UNIVERSIDAD COMPLUTENSE DE MADRID

FACULTAD DE CIENCIAS FÍSICAS

DEPARTAMENTO DE FÍSICA ATÓMICA, MOLECULAR Y NUCLEAR

TESIS DOCTORAL

Measurement of the ^{243}Am capture cross section at the n_TOF facility

Medida de la sección eficaz de captura del ^{243}Am en la instalación n_TOF

MEMORIA PARA OPTAR AL GRADO DE DOCTOR

PRESENTADA POR

Emilio Mendoza Cembranos

Director

Daniel Cano Ott

Madrid, 2014

Universidad Complutense de Madrid

Departamento de Física Atómica, Molecular y Nuclear

DOCTORAL THESIS

Measurement of the ^{243}Am capture cross section at the n_TOF facility

Medida de la sección eficaz de captura del ^{243}Am en la instalación n_TOF

Emilio Mendoza Cembranos

Directed by Daniel Cano Ott

Madrid 2014

Acknowledgements

This work has been supported by ENRESA under the CIEMAT-ENRESA agreement on "Transmutation of high level radioactive waste", by the Spanish Plan on Nuclear and Particle Physics of the Spanish Ministry of Science and Innovation (project FPA2005-06918-C03-01), the European Commission 6th Framework Programme project IP-EUROTRANS (F16W-CT-2004-516520) and the CONSOLIDER-INGENIO project CSD-2007-00042.

I would like to express my gratitude to all those who gave me the possibility to complete this thesis. Foremost, I would like to thank the CIEMAT (which have belonged to three different Spanish ministries along this period: the present Ministerio de Economía y Competitividad, previously the Ministerio de Ciencia e Innovación, and previously the Ministerio de Educación y Ciencia) for my financial support during all these years.

I also would like to thank all my colleagues at CIEMAT, for their valuable help during this time: Aczel, Carlos Sanfrutos, Cayetano, Daniel López, David, Enrique, Eva, Gabriel, Iván, Javi, José Luis, Juan Blázquez, Manolo, Manuel, Mari Carmen Ovejero, Mari Carmen Vicente, Marina, Merche, Miriam, Paco Álvarez, Paco Martín-Fuertes, Raquel, Sara, Trino and Vicente.

My acknowledgement also to all the members of the n_TOF Collaboration, who helped me a lot during all this period: Andrea, Carlos Carrapiço, Carlos Paradela, César Domingo, Cristian Massimi, Cristina, Enrico, Eric, Federica, Frank, Franz, Ingnacio Durán, José Luis Taín, José Manuel Quesada, Jozef Andrzejewski, Marta Sabate, Nicola, Peter Schillebeeckx, Rosa Vlastou, Vasilis, and many others.

Finally, my special thanks to Carlos Guerrero, who helped me a lot, specially in the beginning; and to my supervisor, Daniel Cano, for his enthusiasm, expertise, encouragement and advice.

Contents

Chapter 1

Introduction

This work presents the analysis of the measurement of the neutron capture cross section in the 0.7 eV - 2.5 keV energy range of the ^{243}Am nucleus performed at the n_TOF facility at CERN. At present, there is not any published capture measurement results below 250 eV, excluding thermal measurements, and the present evaluated capture cross sections have been obtained from transmission measurements.

This chapter presents the motivation of this measurement, in Section 1.1, and some theoretical basis, in Section 1.2.

Chapter 2 is dedicated to describe the experimental facility (Section 2.1); the detectors used (Section 2.2); the sample measured (Section 2.3); the experimental set-up (Section 2.4); and the analysis procedures which have been developed and applied (Section 2.5), which goes from the analysis of the signals registered by the detectors up to the procurement of the measured cross section.

In the description of the analysis procedure it is shown that the analysis can be divided in two different parts: the data reduction and the analysis of these data. In the data reduction process all the signals recorded by the different detectors are analyzed and put together in order to create a "reaction yield", which is a data set suitable to deduce the cross section from it. The description of this data reduction process is presented in Chapter 3, whereas Chapter 4 is dedicated to the analysis of the reaction yield.

Finally, a summary and the main conclusions of this work are presented in Chapter 5.

1.1 Motivation

The aim of this measurement is strongly related with the management of the nuclear waste resulting from the operation of nuclear power plants. For this reason, a brief introduction about the nuclear energy production in the world is given in Section 1.1.1, and an introduction concerning the nuclear waste management strategies in Section 1.1.2.

1.1.1 Nuclear energy overview

The first commercial nuclear power plants were built at the end of the 1950 decade. However, the nuclear energy started to be a relevant energy source since the 1970 decade, as it can be observed in Figures 1.1 and 1.2, which show

the contribution of the different sources to the total primary energy (Figure 1.1) and to the electricity generation (Figure 1.2) in the world in the last 40 years (notice that 1 Mtoe=11.63 TWh). As it can be observed, in this period the total primary energy supply has been increased by more than a factor of two, and the electricity generation by a factor of four. The nuclear energy generation has had an strongly increase from 1970 to 1990 (see Figure 1.3), being more than one third of the total electricity generation increase in that period, and a more moderated increase from 1990 up to 2006, where the major increase has been due to carbon and gas power plants. Since 2006, the nuclear energy production has decreased slightly.

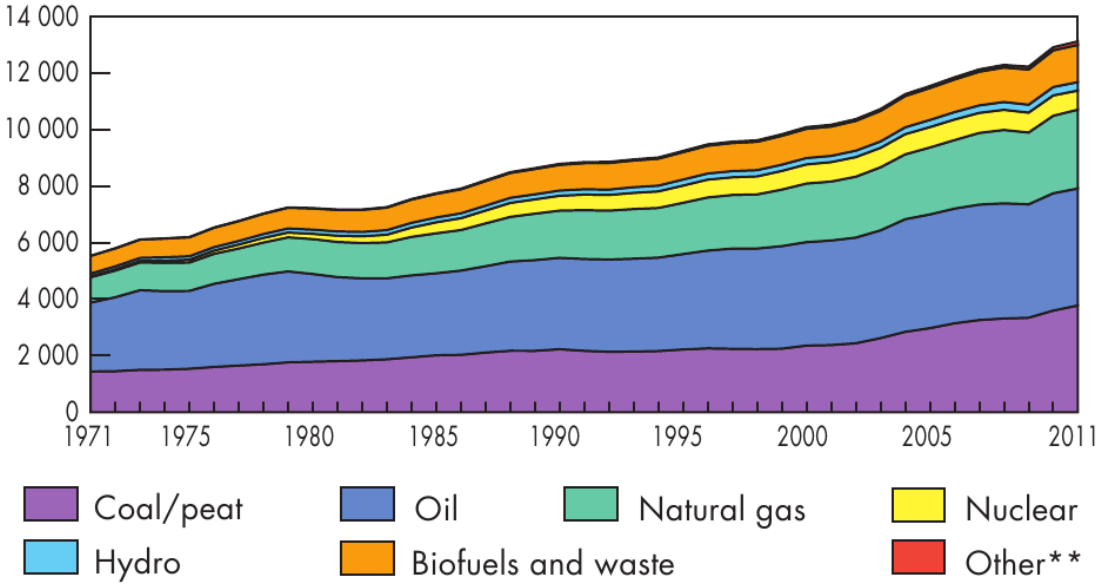

Figure 1.1: World total primary energy supply from 1971 to 2011 by fuel [KWE13]. The Y axis is in million tonnes of oil equivalent (Mtoe). (**) Other includes geothermal, solar, wind, heat, etc.

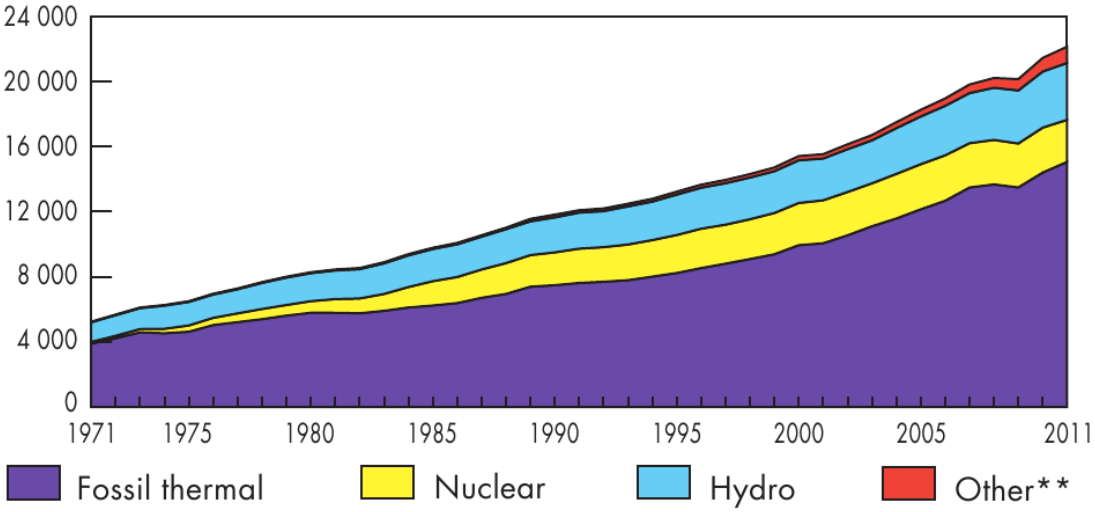

Figure 1.2: World electricity generation from 1971 to 2011 by fuel (TWh) [KWE13]. (**) Other includes geothermal, solar, wind, biofuels and waste, and heat.

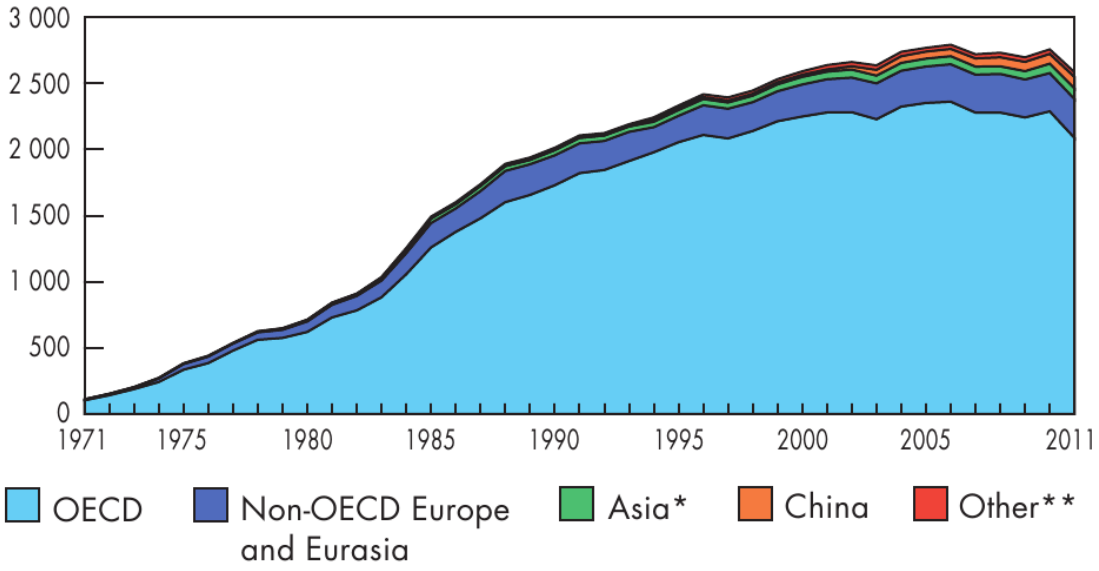

Figure 1.3: Nuclear production from 1971 to 2011 by region (TWh) [KWE13]. (*) Asia excludes China. (**) Other includes Africa, Non-OECD Americas and the Middle East.

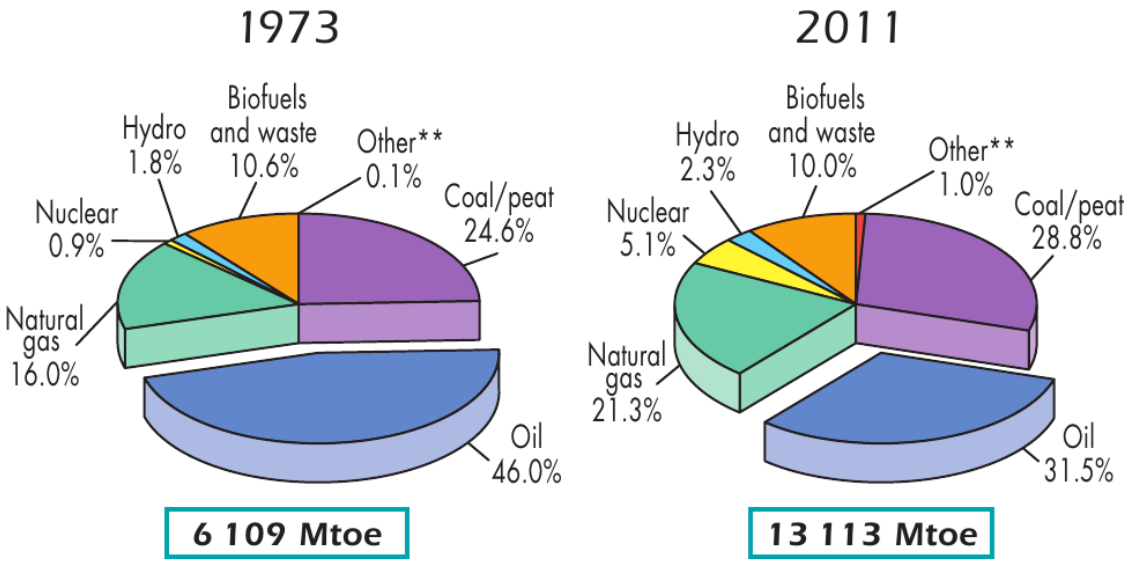

Figure 1.4: 1973 and 2011 world fuel shares of total primary energy supply [KWE13]. (**) Other includes geothermal, solar, wind, heat, etc.

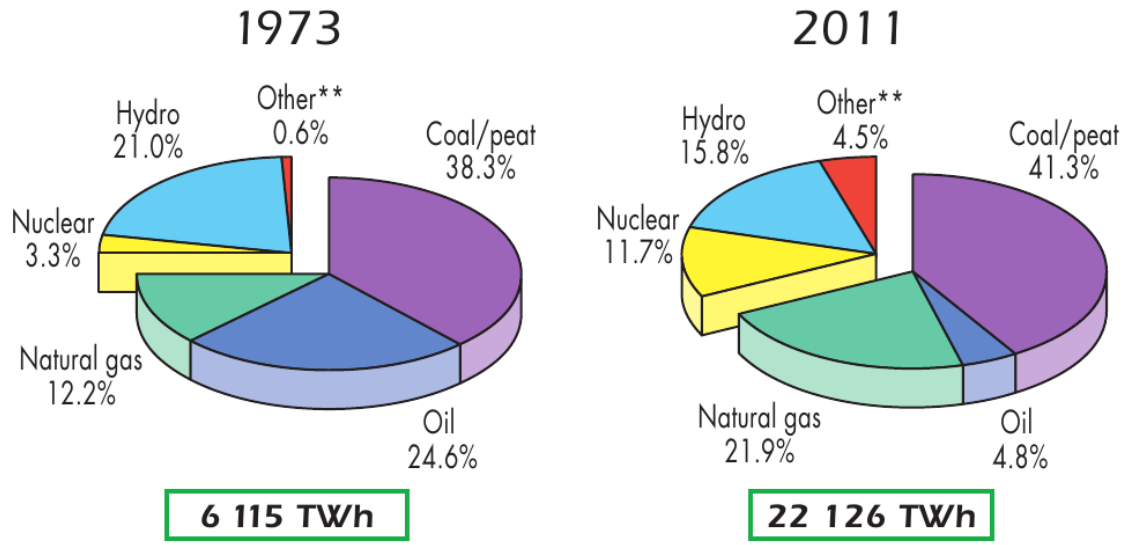

Figure 1.5: 1973 and 2011 world fuel shares of electricity generation [KWE13]. (**) Other includes geothermal, solar, wind, biofuels and waste, and heat.

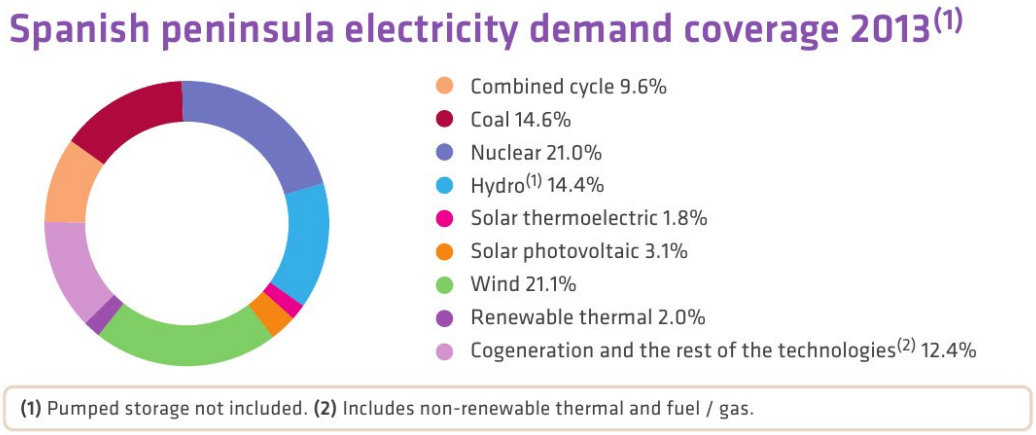

Figure 1.6: Fuel shares of electricity demand in the Spanish peninsula in 2013 [SES13].

In 2011, the nuclear electricity production represented the 5.1% of the total primary energy supply in the world, and a 11.7% of the total electricity production, as it is shown in Figures 1.4 and 1.5. In the Spanish peninsula, the nuclear energy covered 21.0% of the electricity demand in 2013, according to a preliminary report performed by *Red Eléctrica Española* [SES13] as it is shown in Figure 1.6. It was the second source of electricity production, before wind (21.1%).

Concerning the future electricity generation projections, the International Energy Agency (IEA) considered in the *World Energy Outlook 2012* [WEO12] four different future scenarios, based on different assumptions concerning the reduction of CO_2 emissions, to make the future predictions up to 2035:

1. Current Policies Scenario: A scenario that assumes no changes in policies from the mid-point of the year of publication (2012).
2. 450 Scenario: A scenario which sets out an energy pathway consistent with the goal of limiting the global increase in temperature to 2°C by limiting concentration of greenhouse gases in the atmosphere to around 450 parts per million of CO_2.
3. New Policies Scenario: A scenario which takes account of broad policy commitments and plans that have been announced by countries, including national pledges to reduce greenhouse-gas emissions and plans to phase out fossil-energy subsidies, even if the measures to implement these commitments have yet to be identified or announced.
4. Efficient World Scenario: A scenario that presents the potential energy savings if countries adopt current and proven technologies to improve energy efficiency.

These four projections are presented in Figure 1.7, where it is possible to appreciate that in the New Policies Scenario and in the 450 Scenario the CO_2 emissions are reduced with respect to the Current Policies Scenario by reducing the total amount of electricity produced and by reducing the share of fossil fuels electricity production,

thus increasing the share of nuclear and renewable sources. In the four projections, the nuclear electricity generation increases.

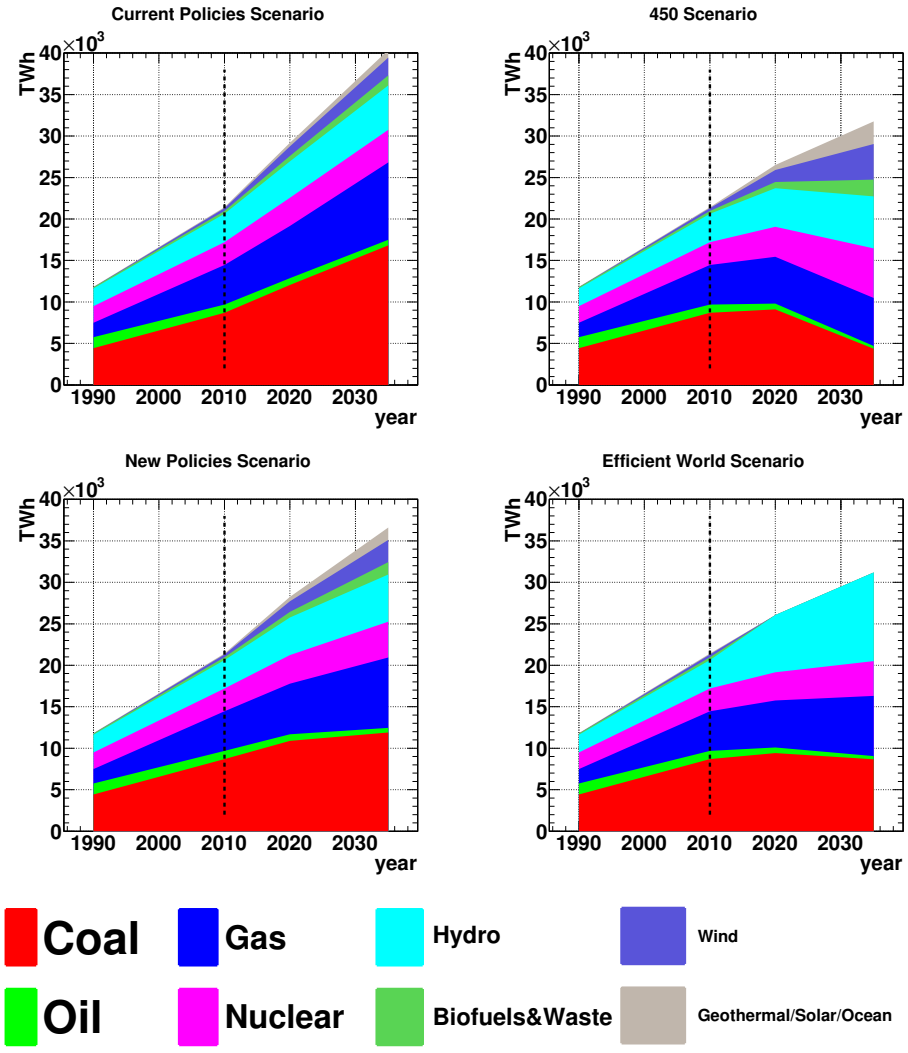

Figure 1.7: Projections of the electricity generation in the world up to 2035 provided by the IEA [WEO12] according to three different scenarios. The vertical dashed line separates historical data (up to 2010) and projections. In the case of the Efficient Word Scenario, all the renewable sources were included in the same light blue color (Hydro).

The Fukushima nuclear accident occurred in Japan in March 2011 produced some uncertainty in the nuclear policy landscape. However, this uncertainty is starting to dissipate, according to the IEA [TCE13]. Most of the countries

have announced that they would not change nuclear deployment targets after the Fukushima accident, a few countries have decided to phase-out nuclear power by closing down or not extending the lifetime of existing plants (Germany, Belgium and Switzerland), and some others are still debating the role of nuclear power in their national energy mix (see the top panel of Figure 1.8). Apparently, the level of public support for nuclear energy has increased since the height of the Fukushima accident in most countries, as it is shown in the bottom panel of Figure 1.8.

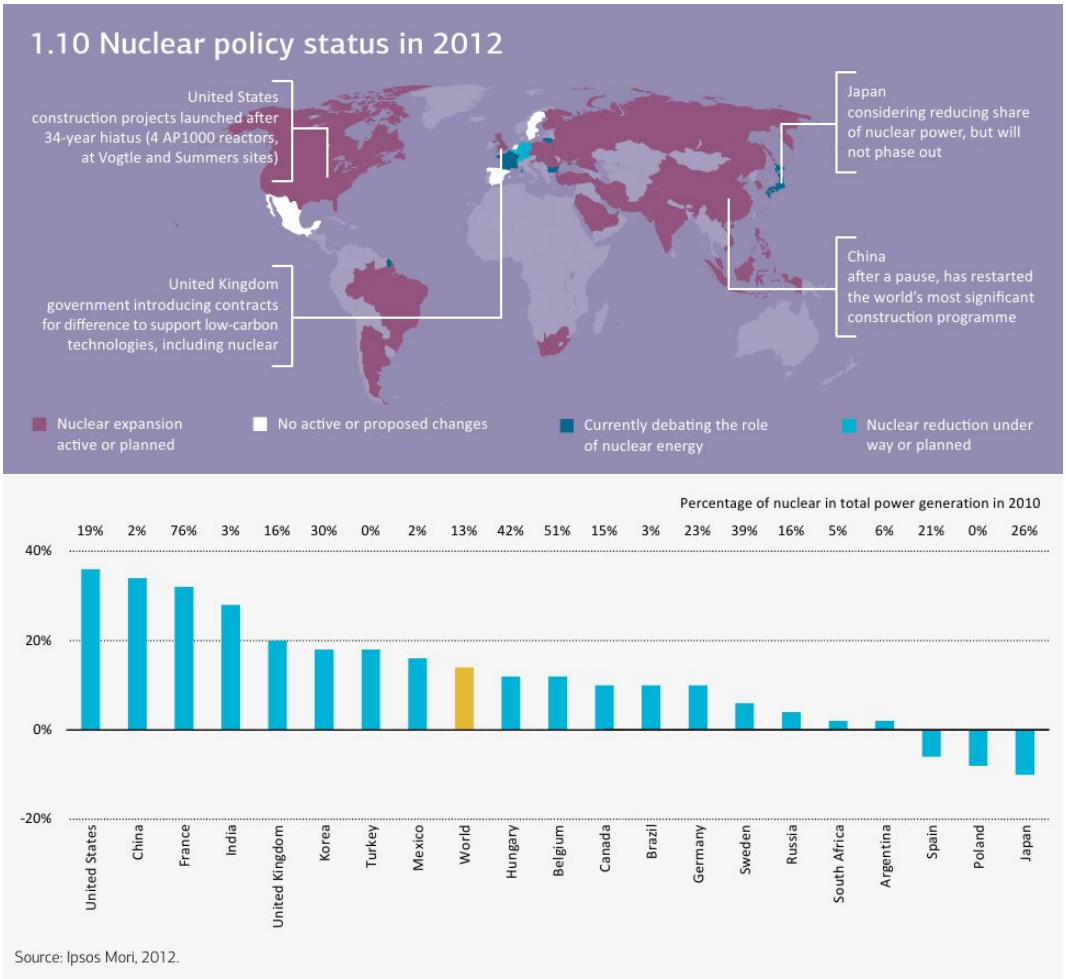

Figure 1.8: Nuclear policy status in 2012 (top); and change in net public support for nuclear power since Fukushima, obtained by comparing attitudes to nuclear energy in April 2011 and September 2012 [TCE13].

Finally, an overview of all the nuclear reactors in the world, for the different countries, is presented in Table 1.1. It can be observed that there are (at 4 March 2014) 435 reactors in operation, 151 in shutdown (149 permanently shutdown and 2 in long term shutdown), 72 under construction and 166 planned for construction.

	shutdown reactors		in operation		under construction		planned construction		nuclear electricity supplied in 2012	
Country	No. reac.	MW(e)	No. reac.	MW(e)	No. reac.	MW(e)	No. reac.	MW(e)	TW(e)·h	% of total
Argentina			2	935	2	717			5.9	4.7
Armenia	1	376	1	375			1	1060	2.1	26.6
Bangladesh							2	2000		
Belarus					1	1109	1	1200		
Belgium	1	10	7	5927					38.5	51.0
Brazil			2	1884	1	1245			15.2	3.1
Bulgaria	4	1632	2	1906			1	950	14.9	31.6
Canada	6	2143	19	13500			2	1500	89.1	15.3
China			21	16890	28	27756	58	62635	92.7	2.0
Czech Rep.			6	3804			2	2400	28.6	35.3
Egypt							1	1000		
Finland			4	2752	1	1600			22.1	32.6
France	12	3789	58	63130	1	1600	1	1720	407.4	74.8
Germany	27	14301	9	12068					94.1	16.1
Hungary			4	1889			2	2400	14.8	45.9
India			21	5308	6	3907	18	15100	29.7	3.6
Indonesia							1	30		
Iran, Isl. Rep			1	915			1	1000	1.3	0.6
Italy	4	1423								
Japan	12	6410	48	42388	2	1325	9	12947	17.2	2.1
Jordan							1	1000		
Kazakhstan	1	52					2	600		
Korea, Rep. of			23	20681	5	6370	6	8730	143.5	30.4
Lithuania	2	2370					1	1350		
Mexico			2	1300					8.4	4.7
Netherlands	1	55	1	482					3.7	4.4
Pakistan			3	690	2	630			5.3	5.3
Poland							6	6000		
Romania			2	1300			2	1310	10.6	19.4
Russia	5	786	33	23643	10	8382	31	32780	166.3	17.8
Slovakia	3	909	4	1815	2	880			14.4	53.8
Slovenia			1	688					5.2	36.0
South Africa			2	1860					12.4	5.1
Spain	3	1067	7	7121					58.7	20.5
Sweden	3	1210	10	9474					61.5	38.1
Switzerland	1	6	5	3308					24.4	35.9
Turkey							4	4800		
UK	29	4225	16	9231			4	6680	64.0	18.1
Ukraine	4	3515	15	13107	2	1900			84.9	46.2
U. Arab Emirates					2	2690	2	2800		
USA	32	13340	100	98560	5	5633	7	8463	770.1	19.0
Vietnam							4	4000		
Total	151	57619	435	371993	72	68344	171	180855	2346.2	

Table 1.1: Overview of all the nuclear reactors in the world for the different countries (at 4 March 2014), including those which have been shut down, in operation, being constructed and planned for construction, together with the nuclear electricity supplied by the reactors in operation in 2012. Together with the number of reactors, the total net electrical capacity is given, in MW(e). The data has been taken from the IAEA [NPR12], except the number of reactions planned for construction, which has been taken from the World Nuclear Association [WNAxx] (data updated on 1 Feb. 2014).

1.1.2 Nuclear waste

In all of the nuclear reactors (constructed or on design) most of the energy is obtained by inducing neutron fission reactions in fissile nuclei (mainly ^{235}U in the nowadays existing reactors). As a consequence of having neutron nuclear reactions inside the reactor, new isotopes are created during the reactor operation, most of them radioactive. These new (they are not present at the beginning of the operation) isotopes are produced by: (1) the fission reactions, which directly produce fission products; (2) other neutron reactions on uranium or higher atomic mass isotopes, especially neutron capture; (3) neutron activation of the water or other structural materials; and (4) the decay of all the radioactive isotopes produced by the previous three mentioned procedures. A schematic view of the creation procedure of transuranic isotopes inside a reactor, which is based essentially in neutron capture reactions and radioactive decays, is presented in Figure 1.9.

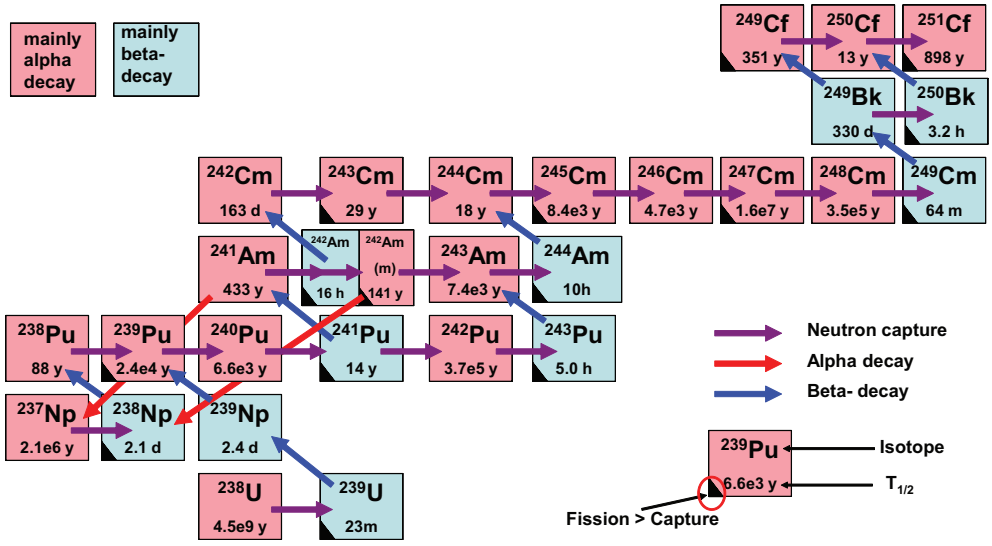

Figure 1.9: Schematic view of the creation of transuranic isotopes in a nuclear reactor from successive neutron capture and decay processes. Only some of the alpha decays have been drawn explicitly. Isotopes in the same row have the same number of protons. Isotopes in the same column have the same number of neutrons.

At the end of its operation, a commercial nuclear reactor will produce a certain amount of radioactive isotopes which constitute radioactive nuclear waste. The management of this nuclear waste depends a lot on its classification. The IAEA classify them in six different classes [CRW09]: exempt waste (EW), very short lived waste (VSLW), very low level waste (VLLW), low level waste (LLW), intermediate level waste (ILW) and high level waste (HLW). The EW do not require any special treatment from the radiological point of view. The VSLW, VLLW and LLW need to be stored until its activity has fallen beneath a certain level, with more or less shielding conditions, but it is always suitable for near surface disposal. ILW need a greater degree of containment and isolation from the biosphere than the one provided by near surface disposal, so a facility between tens and hundreds of meters depth is suitable for them. Finally, the HLW need a greater degree of containment and isolation from the accessible environment than in the ILW.

The HLW arises from the irradiated fuel. It contains the fission products and transuranic elements generated in the reactor core, and there are two distinct kinds: (1) the spent fuel itself, if it is not reprocessed[1]; and (2) separated waste from reprocessing the used fuel. A magnitude used to measure the hazard of these materials is the radiotoxicity. This quantity is proportional to the dose which would be received by that material, and for each radio-nuclei it is defined by multiplying its activity (in Bq) by its dose factor (in Sv/Bq). In Figure 1.10 the contribution of the different materials and isotopes to the total radiotoxicity of a typical spent fuel is presented. In the panel on the left it is possible to observe that the fission fragments are the main contribution to the total radiotoxicity in the first 20 - 30 years. However, after around 500 years its radiotoxicity falls down the levels of the recovered uranium, which has lower radiotoxicity values than the natural uranium used to fabricate the fuel (horizontal line flagged as ^{nat}U in the right panel). On the other hand, the transuranic actinides are the main contribution to the total radiotoxicity after the first 20 - 30 years, becoming almost the total contribution after a few hundreds of years. As it can be seen in the right panel, in the presented case the transuranic actinides do not reach the level of natural uranium in a million of years.

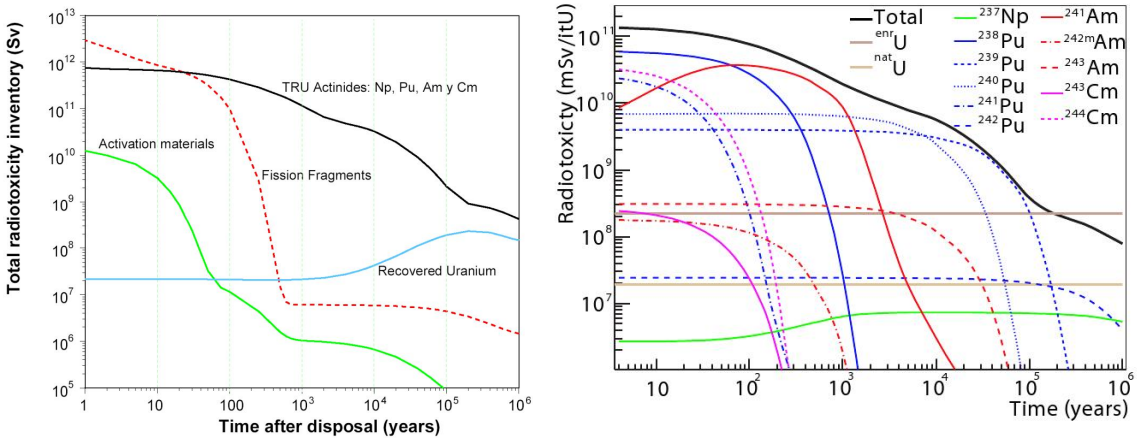

Figure 1.10: Radiotoxicity of different materials of the nuclear waste as a function of time.

Whatever the future of nuclear power, it is universally recognized that safe and acceptable end points must be pursuing for existing and projected inventories of HLW [MFG09]. There is a strong international consensus that the final solution for the disposal of HLW consists in a disposal in stable deep geological repositories [GDR12], where the HLW is isolated from the biosphere for at least hundreds of thousands of years.

A typical 1 GW$_e$ nuclear power plant produces around 27 tonnes of spent fuel per year, and around 10.000 tonnes of spent fuel are produced worldwide per year [Gon00]. If this fuel is not reprocessed it must be considered as HLW. Although there is not any known way to totally destroy these HLW, so in any case the final solution for the disposal of HLW seems to be the deep geological repositories, some procedures to reduce the radiotoxicity and volume of

[1] Reprocessing is to extract, usually by chemically procedures, fissile materials from the spent fuel for recycling and to reduce the volume of high-level wastes. Several European countries, Russia and Japan have had a policy to reprocess used nuclear fuel, although government policies in many other countries have not yet addressed the various aspects of reprocessing.

HLW are being investigated. These procedures are based in the partitioning and transmutation technologies, which are described below.

Partitioning and transmutation [PST06] consists in chemically process the HLW, separating the long-term radiotoxic isotopes (partitioning) and "burning" some of these isotopes (transmutation). "Burning" here means to transform one isotope into another by nuclear reactions. The total radiotoxicity of the HLW is reduced by transforming the isotopes which more contributes to the total radiotoxicity of the spent fuel in others with less or none radiotoxicity. The combination of the partitioning and transmutation processes allows the reduction of the radionuclide masses to be stored, their associated residual heat, and, as a consequence, the volume and the cost of the repositories.

The main procedure to obtain the transmutation of actinides is the nuclear fission, where an actinide is transformed in two fission products. Sometimes the actinide is fissioned directly and sometimes a neutron capture reaction is produced before the fission process. Two examples of these transmutation reactions are given below:

Example 1:

$$n + {}^{239}\text{Pu (24000 years)} \xrightarrow{fission} {}^{134}\text{Cs (2 years)} + {}^{104}\text{Ru(stable)} + 2n + 200\ \text{MeV}$$

$${}^{134}\text{Cs (2 years)} \xrightarrow{\beta^-} {}^{134}\text{Ba (stable)} + \beta^- + \bar{\nu}$$

Example 2:

$$n + {}^{240}\text{Pu (66000 years)} \xrightarrow{capture} {}^{241}\text{Pu (14 years)}$$

$$n + {}^{241}\text{Pu (14 years)} \xrightarrow{fission} {}^{134}\text{Xe (stable)} + {}^{105}\text{Rh(35h)} + 3n + 200\ \text{MeV}$$

$${}^{105}\text{Rh(35h)} \xrightarrow{\beta^-} {}^{105}\text{Pd (stable)} + \beta^- + \bar{\nu}$$

It is clear from the right panel of Figure 1.10 that the main contribution to the radiotoxicity of the actinides of the spent fuel are the Pu isotopes, followed by the Am isotopes. According to [PST06], the long term radiotoxicity inventory can be reduced up to a factor of 10 if all the Pu is recycled and fissioned; and reduction factors higher than 100 can be obtained if, in addition, the minor actinides[2] are also burned.

Many of the isotopes presented in Figure 1.9 have a black triangle in the bottom-left corner of their frame. These are the isotopes where the fission reaction is more probable than the neutron capture in a thermal reactor, which are the isotopes which have an odd number of neutrons. The capture is more probable than the fission reaction in the rest of the isotopes, the ones with an even number of neutrons. This is a consequence of the thermal cross section[3] values (at $\sim$0.025 eV) of the different isotopes. However, the fission cross section of those isotopes with low thermal fission cross section experiments a rapid increase at higher neutron energies (usually close but below 1 MeV), exceeding by far the capture cross section, which, on the other hand, decreases when the neutron energy increases. This behavior can be observed in Figure 1.11, where the capture and fission cross sections of ^{239}Pu, ^{241,243}Am and ^{244}Cm are presented. The ^{239}Pu is an example of an isotope with more fissions than capture reactions at low neutron energies, whereas the ^{241,243}Am and ^{244}Cm isotopes are examples of isotopes with more captures than fission reactions at low neutron energies. The rest of the isotopes presented in Figure 1.9 have capture and fission cross sections which follow the same behavior as the ^{239}Pu or the ^{241,243}Am and ^{244}Cm, depending on their number of neutrons.

[2] The isotopes of Np, Am, Cu and, sometimes, Bq are called minor actinides, whereas isotopes of U and Pu are called major actinides. This is because the spent fuel of a commercial reactor has typical values of a 96% mass of Uranium isotopes, 4% of fission products, 1% of Pu isotopes and much less amount, around a 0.1%, of minor actinides.

[3] The cross section is a measure of the interaction probability and it is defined in the next section.

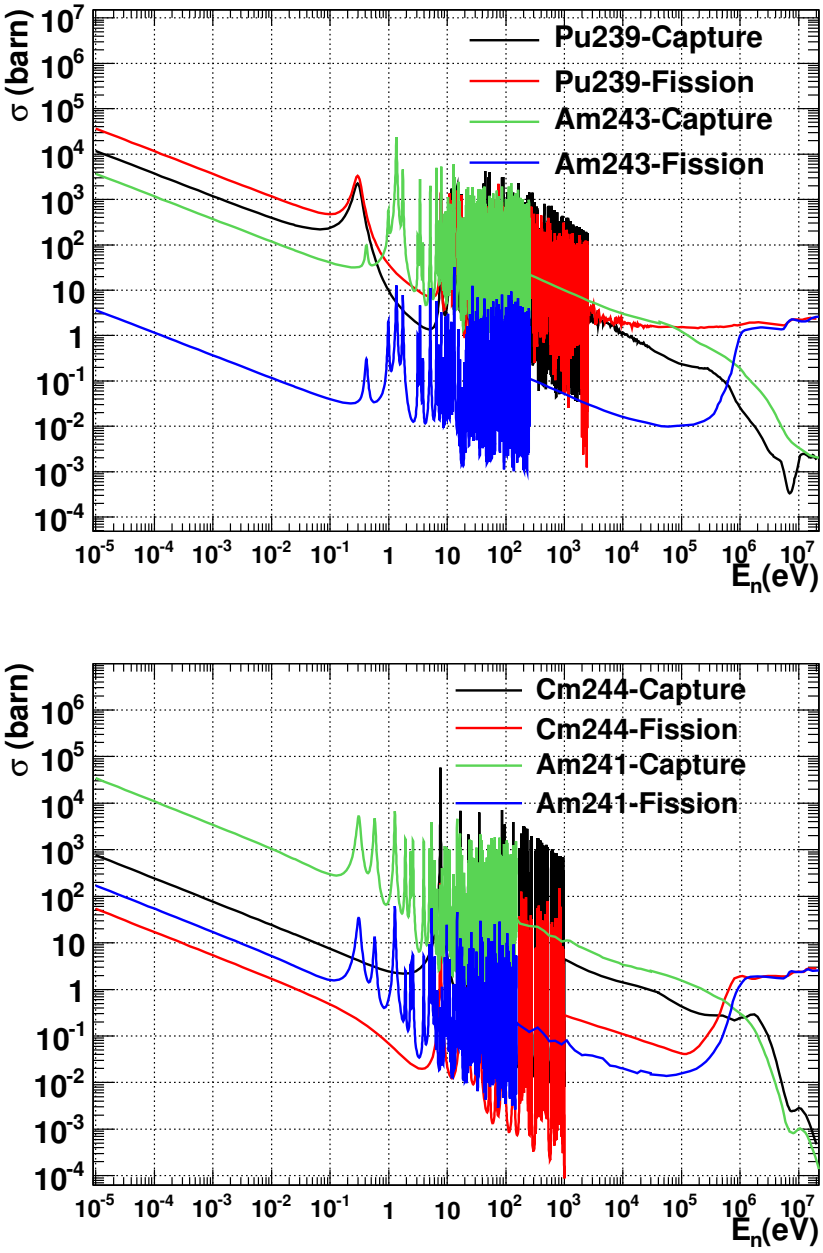

Figure 1.11: Capture and fission cross sections of ^{239}Pu, ^{241,243}Am and ^{244}Cm.

From the explanation given above, it follows that one possibility for the transmutation of actinides is to burn them in fast reactors, which are devices with high energy neutron fluxes (hundreds of eV up to tens of MeV). In principle,

thermal reactors could also be considered for transmutation purposes, since non-fissile nuclei can be transformed in fissile nuclei by neutron capture reactions. However, the large amount of Cm isotopes which would be created by successive neutron captures and decays do not compensate the use of thermal reactors for transmutation. There are two kind of fast reactors which are being considered for the transmutation: critical fast reactors, in particular Generation IV fast reactors, and subcritical fast systems, in particular Accelerator Driven Systems (ADS's) [ADS02].

An ADS is a subcritical system[4] whose neutron source is a proton accelerator coupled to an spallation target. This reactor produces, in general, less electricity than conventional critical reactors but it allows to load fuels with higher concentration of minor actinides, so its utility is focused on transmutation purposes. At this moment it is in the design phase, as well as the Generation IV fast reactors.

Calculations for the design of these new nuclear systems have created the need of improving the neutron cross section knowledge of nuclei or reactions at energies not thoroughly studied so far, because its knowledge is not so relevant for the electricity production in light water nuclear reactors. These are mainly reactions in minor and major actinides, and also in some structural materials, such as Pb, Bi, Ni or Fe. The energy of the neutrons in these systems is larger than in the thermal water reactors, making more important to know with more accuracy than in the past the cross sections at these new energy ranges. There are sensitivity analysis that have been made (and are still being made) to estimate how the present cross section uncertainties affect the accuracy of the calculation of macroscopic parameters of the different nuclear systems (see references [Sal08, Gon09, Ali04, Ali06]), in order to calculate which and how much should the present cross section uncertainties be reduced to reach the required accuracy values for the macroscopic parameters.

One of the first European projects dedicated to produce high precision cross section data of isotopes relevant to the transmutation of nuclear waste and ADS design was the n_TOF-ND-ADS project [Men07] (1998-2002), which was part of the 5^{th} EURATOM framework programme (FP5). This project was followed by the FP6 project EUROTRANS [EUR05, EURxx]: the EUROpean Research Programme for the TRANSmutation of High Level Nuclear waste in Accelerator Driven Systems. EUROTRANS was divided in five domains: (1) DESIGN, related with the development of a reference design of the ADS; (2) ECATS, related with experimental activities on the coupling of the accelerator, the spallation target and the sub-critical blanket; (3) AFTRA, related with the design, development and qualification the reactor fuels; (4) DEMETRA, related with the heavy liquid metal technologies[5] and thermal-hydraulics calculations; and (5) NUDATRA, related with the nuclear data needed for the design. The ^{243}Am neutron capture was one of the measurements decided by the NUDATRA domain[6], together with fission on ^{244}Cm and inelastic reactions on Pb and Bi. These projects have been followed by the FP7 ANDES (2010-2013) and the CHANDA projects (2014-2018).

The decision of measuring the ^{243}Am capture cross section was taken because at that moment there were not any capture measurement of ^{243}Am below 250 eV, excluding the thermal point. Indeed, there were only two measurements performed between 250 eV and 5 keV, and they were not compatible below 2 keV. A third measurement was available, above 5 keV, and it was also not compatible with the mentioned measurements. As it was shown in the right panel of Figure 1.10, the ^{243}Am is the minor actinide which more contributes to the total radiotoxicity of the spent fuel at times after disposal close to 10.000 years. In addition, the capture reaction on ^{243}Am is the main gate to create ^{244}Cm and heavier isotopes. As it can be observed in Figure 1.9, the path to create all the isotopes heavier than ^{244}Cm go through ^{244}Cm; and ^{244}Cm can be created by two different paths: capture on ^{243}Am or

[4] In a critical reactor the fission chain-reaction is auto-sustained: the neutrons which induce the fission reactions are neutrons resulting from previous fission reactions in such a way that the neutron flux remains constant in time. A subcritical system is a device where the chain-reaction needs to be sustained by an external neutron source.

[5] In the main designs of ADS's they are cooled by liquid metals, typically Pb or Pb-Bi.

[6] The EUROTRANS project started in 2005, whereas the ^{243}Am cross section was measured in 2004. However, the decision of measuring the ^{243}Am cross section was taken in the design phase of the EUROTRANS project.

capture on ^{241}Am followed by the decay of ^{242}Am plus two successive neutron captures on ^{242}Cm and ^{243}Cm. The first path, capture on ^{243}Am, is by far the main contribution to the creation of ^{244}Cm.

1.2 Neutron cross section theory

This Section is dedicated to present an overview of the theoretical basis relevant for this work. In Sections 1.2.1 to 1.2.4, the neutron cross section concept is introduced, and the formalisms used for its description, the compound nucleus theory and the R-matrix formalism, are presented. In Section 1.2.5 it is described how the information concerning neutron cross sections is stored for its use in different applications. Finally, Section 1.2.6 is dedicated to present the theoretical basis which describe the decay of the nucleus after neutron capture.

1.2.1 Neutron cross section

The microscopic neutron cross section (σ) is a physical magnitude that quantifies the interaction probability of a neutron with a specific nucleus. If we consider a beam of neutrons with intensity I (neutrons/cm^2/s), incident on a very thin plate of a given isotope with area A (cm^2), density of nuclei N (nuclide/cm^3) and thickness Δx (cm), then the reaction rate R (interactions/cm^2/s) must be proportional to the intensity of the neutron beam (I) and the number of target nuclei ($N \cdot \Delta x \cdot A$):

$$R \propto I \cdot N \cdot \Delta x \cdot A \tag{1.1}$$

The constant of proportionality is the neutron cross section, σ, and it has dimensions of area:

$$R = \sigma \cdot I \cdot N \cdot \Delta x \cdot A \tag{1.2}$$

Since usually there are several allowed reactions, such as elastic scattering, capture, fission, ... There is a *total* reaction rate, an *elastic* reaction rate, a *capture* reaction rate, ... and so there is a *total* cross section (σ_{tot}), an *elastic* cross section (σ_{ela}), a *capture* cross section (σ_γ), ... The total cross section is the sum of all partial cross sections:

$$\sigma_{tot} = \sigma_{ela} + \sigma_\gamma + \sigma_{fission} + ... \tag{1.3}$$

An example of a neutron cross section can be found in Figure 1.12. The nuclear cross sections are usually expressed in "barns" (1 barn=10^{-24}cm^2).

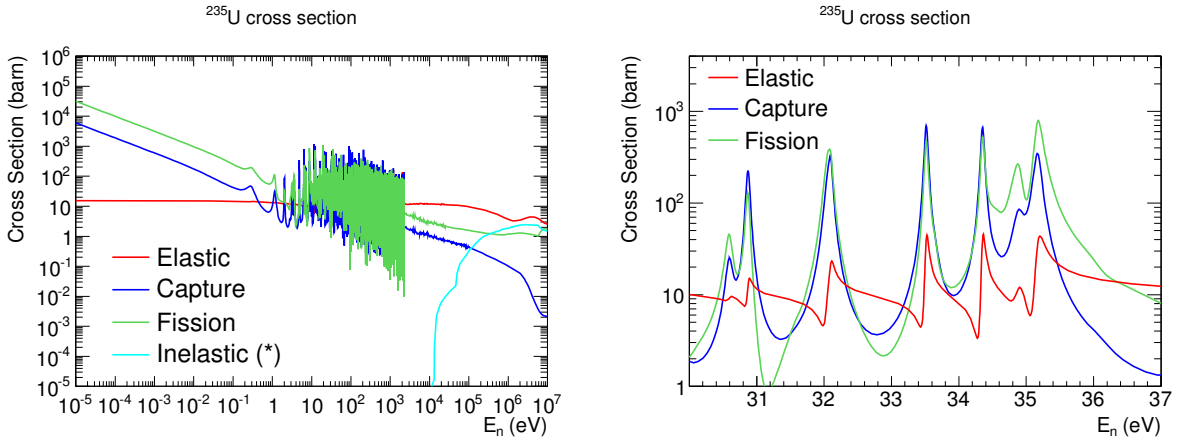

Figure 1.12: ^{235}U partial cross sections, as a function of the neutron energy. The partial cross section called "Inelastic" is a sum over all reactions different from elastic scattering, capture and fission, such as (n,2n), (n,3n), (n,n'), ...

As it can be seen in Figure 1.12, the cross section value is strongly dependent on the incident neutron energy and ranges largely from isotope to isotope. However, some general characteristics can be given for all nuclei:

1. Capture and elastic scattering reactions are always non-threshold reactions, with a very few exceptions concerning the capture (^{3}H, ^{4}He). Fission reactions are non-threshold reactions for heavy nuclei, above Radium. For the rest of the reactions a minimum neutron energy is usually needed, with exceptions such as ^{6}Li(n,t)^{4}He or ^{10}B(n,α)^{7}Li.

2. The structure of the elastic, capture and fission reaction cross sections is always the same, and it can be divided into four regions:

   - Thermal and epithermal region: up to the first resonance, the cross section is found to be smooth and inversely proportional to the square root of the energy ($\sigma \sim 1/\sqrt{E} \sim 1/v$). This is true for all reactions (capture, fission, and also (n,t), (n,α), ...) except for elastic scattering.
   - Resolved Resonance Region (RRR): starting typically in the eV region for heavy nuclei, in the keV region for medium mass nuclei and in the MeV region for light nuclei; a resonant structure appears, with large peak to valley variations. The resonances appear at the same neutron energies in the different reaction channels.
   - Unresolved Resonance Region (URR): above a certain neutron energy value, the resonance widths are comparable to the average resonance spacing. They still do not fully overlap, but the experimental resolution is inadequate to determine the parameters of individual resonances.
   - High energy region: as the neutron energy increases, the distance between resonances is much smaller than their intrinsic widths and resonant structures can not be observed any more. In addition, more and more reaction channels corresponding to threshold reactions open up.

1.2.2 The Compound Nucleus Theory

The resonant structure of neutron cross sections is explained by using the compound nucleus theory, which was initially proposed by Niels Bohr [Boh36, Boh39]. This theory assumes that a compound nuclear system, composed by the neutron and the target nucleus, is formed in the middle of the reaction process, so a reaction $X + a \rightarrow Y + b$ crosses through an intermediate $X + a \rightarrow C^* \rightarrow Y + b$ state, which is the compound nucleus. Thus, the reaction process occurs in two steps: in the first step the compound nucleus is formed and in the second step the compound nucleus decays through the energetically allowed channels. The different decay probabilities are assumed to be independent on the way how the compound nucleus was formed. The origin of the resonances are related with the excitation of nuclear states in the compound nuclear system, at excitation energies above the neutron binding energy. The decay probability of an exit channel "c" is equal to the branching ratio Γ_c/Γ, where Γ_c is the (partial) width related to the decay channel and Γ the total width of the resonance, which is equal to the sum of all partial widths.

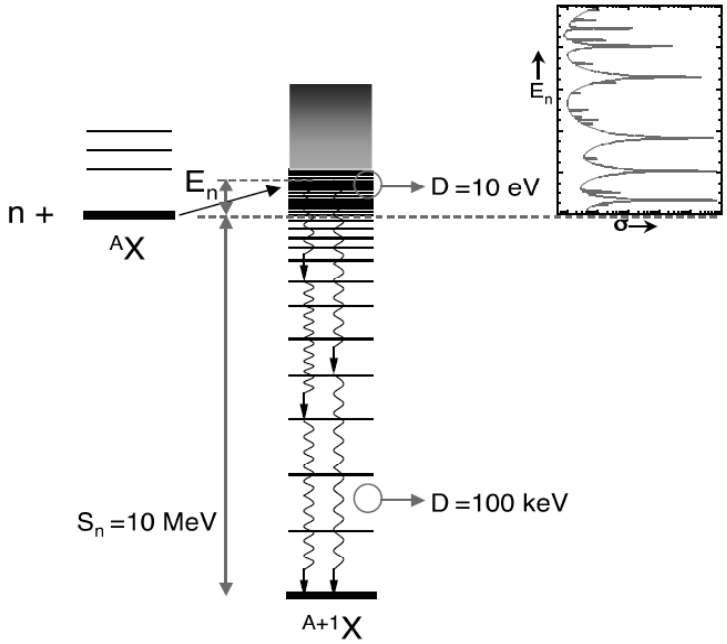

Figure 1.13: Schematic view of the formation of the compound nucleus and its posterior decay via neutron capture. Typical values of the neutron separation energy (S_n) and level spacing (D) are given.

Not all the neutron-nucleus reactions occur by forming a compound nucleus. Direct reactions occur when the incident neutron interact only with one or a few nucleons without forming a compound nucleus. They are important when the De Broglie wavelength of the neutron becomes comparable to the size of nucleons, which is usually at neutron energies higher than about 10 MeV for the heavier nuclei, and lower energies for low mass or closed shell nuclei. The time scale of direct reactions is in the order of $\sim 10^{-22}$s, several orders of magnitude faster than the time scale of compound nucleus reactions, $\sim 10^{-15}$s.

1.2.3 The R-matrix formalism

The R-matrix formalism is the one used to describe more accurately neutron cross sections. This theory was firstly introduced by Wigner and Eisbud [Wig47], and other references of interest are [Lan58, Lyn68, Fro00]. A brief description of the R-matrix theory is given in this Section.

The neutron cross section of a given reaction could be, in principle, calculated if the nuclear wave functions were known. These wave functions could be calculated by solving the Schrödinger equation for the nuclear system, which could be possible if the nuclear potential were known, which is not the case. However, when the incoming and outgoing particles are far away from the nucleus, the interaction between them and the nucleus can be considered absent for neutral particles or the Coulomb interaction for charged particles, and it is possible to calculate the wave functions.

The basic idea of the R-matrix formalism is to divide the geometrical region into two regions for each channel, where a channel is defined with the involved particles with their spins. If the separation between the target nucleus and the ingoing or outgoing particles is smaller than the channel radius, a_c, all nucleons involved in the reaction are close to each other and form a compound nucleus. No interaction (or Coulomb interaction) is assumed if the distance is bigger than the channel radius, and so the Schrödinger equation can be solved. The wave function of the compound nucleus cannot be calculated, but it can be expanded as a linear combination of its eigenstates without solving explicitly the Schrödinger equation of the system. The exact internal value of the internal wave function and its derivatives are only needed to be known at the boundary, to equate them to the external values. The properties of the eigenstates of the compound nucleus are taken together in the R-matrix.

The total wave function in the external region can be calculated and expressed as the superposition of all incoming and outgoing partial waves I_c and O_c with amplitudes y_c and x_c, and summed over all possible channels:

$$\Psi = \sum_c y_c I_c + \sum_{c'} x_{c'} O_{c'} \tag{1.4}$$

The relation between the coefficients of the incoming and outgoing waves is given by the collision matrix, $U_{cc'}$, $x_{c'} \equiv -\sum_c U_{cc'} y_c$.

The cross section is related with the collision matrix with:

$$\sigma_{cc'} = \pi \bar{\lambda}_c^2 \left| \delta_{c'c} - U_{c'c} \right|^2 \tag{1.5}$$

where $\bar{\lambda}_c$is the de Broglie wave length $2\pi\bar{\lambda}_c = \hbar/(\mu_c v_{rel})$, with μ_c the reduced mass and v_{rel} the relative speed between particles. Each channel is defined by the particles involved, α, the total angular momentum, J, the orbital angular momentum, ℓ, and the channel spin, s, which is the sum of the spin of the particle, i, and the spin of the nucleus, I. The $\alpha \to \alpha'$ cross sections are more useful than the channel cross sections, and can be obtained from:

$$\sigma_{\alpha\alpha'}(J) = \pi \bar{\lambda}_\alpha^2 g_J \sum_{l,l',s,s'} \left| \delta_{\ell' s',\ell s} - U_{\ell' s',\ell s} \right|^2 \tag{1.6}$$

$$g_J = \frac{2J+1}{(2i+1)(2I+1)} \tag{1.7}$$

Resonances are introduced by expressing **U** in terms of the channel matrix **R**. After matching boundary conditions (see Lane and Thomas [Lan58]):

$$\begin{aligned} U_{cc'} &= e^{-i(\varphi_c+\varphi_{c'})} P_c^{1/2} \left\{ \left[\mathbf{1} - \mathbf{R}\left(\mathbf{L}-\mathbf{B}\right)\right]^{-1} \left[\mathbf{1} - \mathbf{R}\left(\mathbf{L}^*-\mathbf{B}\right)\right] \right\}_{cc'} P_{c'}^{-1/2} \\ &= e^{-i(\varphi_c+\varphi_{c'})} \left\{ \delta_{cc'} + 2iP_c^{1/2} \left[\left(\mathbf{1} - \mathbf{R}\mathbf{L^0}\right)^{-1} \mathbf{R} \right]_{cc'} P_{c'}^{1/2} \right\}, \end{aligned} \tag{1.8}$$

$$R_{cc'} = \sum_{\lambda} \frac{\gamma_{\lambda c}\gamma_{\lambda c'}}{E_\lambda - E} \tag{1.9}$$

$$L^0_{cc'} \equiv L_{cc'} - B_{cc'} = \left(L_c - B_c\right)\delta_{cc'} \equiv \left(S_c + iP_c - B_c\right)\delta_{cc'} \tag{1.10}$$

where roman subscripts refer to reaction channels and Greek subscripts to compound levels.

Information concerning resonances are present in the R-matrix, with level energies E_λ and probability amplitudes $\gamma_{\lambda c}$ for decay or formation of compound states λ via exit or entrance channels c. φ_c are the hard-sphere phases and L_c their logarithmic derivatives, and they depend only on the (known) ingoing and outgoing radial wave functions I_c and O_c at the channel radius a_c, which defines the boundary between the internal and external region, and it is usually set to $a_c = \left(1.23A^{1/3} + 0.80\right)$fm:

$$\varphi_c \equiv \arg O_c(a_c) = \arctan \frac{Im\, O_c(a_c)}{Re\, O_c(a_c)} \tag{1.11}$$

$$L_c \equiv a_c \frac{O_c'(a_c)}{O_c(a_c)} = \left[r_c \frac{\partial \ln O_c}{\partial r_c} \right]_{r_c = a_c} \tag{1.12}$$

Thus Equation 1.8 defines the collision matrix in terms of the parameters of the R-matrix, E_λ and $\gamma_{\lambda c}$, representing the physical process of the reaction, and the quantities P_c, S_c and ϕ_c, describing the known incoming and outgoing waves, I_c and O_c, outside a sphere with radius a_c. The B_c are logarithmic derivatives of the radial eigenfunctions at the channel radii a_c. They define the eigenvalue problem with eigenvalues E_λ, and their choice is largely a matter of convenience. One of the most used choice is the Wigner-Eisenbud version, with $B_c = -l$.

The collision matrix can alternatively be expressed in terms of the level matrix **A**:

$$U_{cc'} = e^{-i(\varphi_c+\varphi_{c'})} \left(\delta_{cc'} + i \sum_{\lambda,\mu} \Gamma_{\lambda c}^{1/2} A_{\lambda\mu} \Gamma_{\mu c'}^{1/2} \right) \tag{1.13}$$

$$\Gamma_{\lambda c}^{1/2} = \gamma_{\lambda c} \sqrt{2P_c} \tag{1.14}$$

$$\left(\mathbf{A}^{-1}\right)_{\lambda\mu} = \left(E_\lambda - E\right)\delta_{\lambda\mu} - \sum_c \gamma_{\lambda c} L_c^0 \gamma_{\mu c} \tag{1.15}$$

which is related with the R-matrix with:

$$\left(\left[1 - R\left(L - B \right) \right]^{-1} \right)_{cc'} = \delta_{cc'} + \sum_{\lambda\mu} \gamma_{\lambda c} \gamma_{\mu c'} (L_{c'} - B_{c'}) A_{\lambda\mu} \tag{1.16}$$

The resonance parameters E_λ and $\gamma_{\lambda c}$ cannot be theoretically deduced, since they depend on the unknown nuclear interaction, so they are obtained from experimental results.

It is necessary to invert either the **R** channel matrix or the **A** level matrix to calculate the collision matrix, and so the cross section. This is practically impossible in most of the cases, so approximations are commonly used.

Single-level Breit-Wigner approximation (SLBW):

Only one level is considered, so resonances are treated as isolated:

$$\left(\mathbf{A}^{-1} \right)_{\lambda\mu} = \left(\mathbf{A}^{-1} \right) = E_0 - E - \sum_c L_c^0 \gamma_c^2 \equiv E_0 + \Delta - E - i\Gamma/2 \tag{1.17}$$

The resulting cross sections for ℓ=0 (s-waves), and assuming $\kappa a_J \ll 1$ are:

$$Total: \quad \sigma_n^J = 4\pi g_J a_J^2 + 4\pi \bar{\lambda}^2 g_J \left(\frac{\Gamma_n \Gamma}{\Gamma^2 + 4(E_0 - E)^2} + 4k a_J \frac{\Gamma_n (E_0 - E)}{\Gamma^2 + 4(E_0 - E)^2} \right) \tag{1.18}$$

$$Channel: \quad \sigma_{nc}^J = 4\pi \bar{\lambda}^2 g_J \frac{\Gamma_n \Gamma_c}{\Gamma^2 + 4(E_0 - E)^2} \ , c \neq n \tag{1.19}$$

$$Elastic: \quad \sigma_{nn}^J = \sigma_n^J - \sum_{c \neq n} \sigma_{nc} \tag{1.20}$$

where $k = 1/\bar{\lambda}$.

These are the simplest expressions for the cross sections and the following characteristics can be deduced from them:

1. The total neutron cross section expression has three terms: the first one is related with the potential scattering or hard sphere scattering cross section. It is associated with the elastic scattering of the incoming neutron from the potential of the nucleus without forming a compound state, and it is constant at low energies, where the $\kappa a_J \ll 1$ approximation is valid. The second term is associated with the resonant scattering due to the formation of the compound nucleus. The third term is the interference between the potential scattering and the resonant elastic scattering. It is the responsible of the deeps observed in the elastic scattering cross section that can be appreciated in the right panel of Figure 1.12.

2. The cross sections associated with the formation of the compound nucleus (equation 1.19) follow the relation:

$$\sigma_{nc} = \frac{\Gamma_c}{\Gamma} \sigma_n \ , \ \Gamma = \sum_c \Gamma_c \tag{1.21}$$

3. The value of the cross section at the peak of the resonance (of the part associated with the formation of the compound nucleus) is given by setting $E = E_0 \rightarrow \sigma_{n,max} = 4\pi\bar{\lambda}^2 g_J \frac{\Gamma_n}{\Gamma}$, and from equation 1.21:

$$\sigma_{nc,max} = 4\pi\bar{\lambda}^2 g_J \frac{\Gamma_n \Gamma_c}{\Gamma^2} \tag{1.22}$$

4. The area of the resonant part associated with the formation of the compound nucleus can be obtained by integrating the cross section between $E_0 - \Gamma/2$ and $E_0 + \Gamma/2$:

$$Area = 2\pi^2\bar{\lambda}^2 g_J \frac{\Gamma_n \Gamma_c}{\Gamma} \tag{1.23}$$

If the reaction of interest is neutron capture the factor $g_J \frac{\Gamma_n \Gamma_\gamma}{\Gamma}$ is commonly called "radiative kernel". Notice that if $\Gamma_\gamma \gg \Gamma_n, \Gamma_f$, then $\Gamma \simeq \Gamma_\gamma$, and the radiative kernel is proportional to Γ_n. On the contrary, if $\Gamma_n \gg \Gamma_\gamma, \Gamma_f$, then $\Gamma \simeq \Gamma_n$, and the radiative kernel is proportional to Γ_γ. Since the area of a capture resonance is one of the best determined parameters in a capture measurement, then for nuclei with Γ_f small, if a resonance has $\Gamma_\gamma \gg \Gamma_n$, the Γ_n is well determined. For the contrary, if $\Gamma_n \gg \Gamma_\gamma$, the Γ_γ is the well determined parameter. The radiative kernel is very useful to compare the size of the resonances from their parameters, and can be used directly if the resonances have the same energy (values of the same resonance taken from different measurements, for example), or divided by their energy, if the comparison is performed between resonances of different energies, since $\bar{\lambda} \propto 1/\sqrt{E}$.

Multi-level Breit-Wigner approximation (MLBW):

Off-diagonal elements of $\mathbf{A}^{-1}$ are neglected, which means neglecting all interference terms between channels, but not between levels:

$$\left(\mathbf{A}^{-1}\right)_{\lambda\mu} = \left(E_\lambda - E - \sum_c L_c^0 \gamma_{\lambda c}^2\right) \delta_{\lambda\mu} \equiv \left(E_\lambda + \Delta_\lambda - E - i\Gamma_\lambda/2\right) \delta_{\lambda\mu} \tag{1.24}$$

Reich-Moore approximation:

Usually there are many photon channels contributing to the sum $\sum_c \gamma_{\lambda c} L_c^0 \gamma_{\mu c}$ in equation 1.15. While their contributions all add up with the same sign in the diagonal elements, they tend to cancel in the off-diagonal elements because the decay amplitudes have practically random signs but comparable magnitudes. For this reason, the Reich-Moore approximation [Rei58] neglects correlations between photon channels:

$$\left(\mathbf{A}^{-1}\right)_{\lambda\mu} = \left(E_\lambda + \Delta_\lambda - E - i\Gamma_{\lambda\gamma}/2\right) \delta_{\lambda\mu} - \sum_{c \notin \gamma} \gamma_{\lambda c} L_c^0 \gamma_{\mu c} \tag{1.25}$$

This approximation works well for all kind of reactions and nuclei, and it is the recommended approximation to use in cross section data analysis [Lar06].

1.2.4 Statistical properties of the resonances and unresolved resonance region

The R-matrix formalism describes the Resolved Resonance Region (RRR) from a set of parameters: energy, widths and spin from each resonance, plus the channel radius. In the Unresolved Resonance Region (URR) an average

neutron cross section is given. However, the cross section has a (non resolved) resonant structure, which is the opposite than a smooth behavior. For some calculations (shelf shielding) this resonant structure has to be taken into account, and usually a statistical model needs to be applied [MCN08]. All the statistical models need statistical parameters, such as the main level spacing or average widths, in order to model the cross section fluctuations.

The difference of a smooth and a resonant cross section with the same mean value can be easily understood with the following example: the calculation of the amount of neutrons crossing a wall. It can be thick enough that if a smooth average cross section is used in the calculation, then almost every neutron is stopped by the wall. However, if a resonant cross section is used, a certain amount of neutrons with energies in the valleys of the resonances will cross the wall.

According to the theory, the resonance parameters must follow certain statistical rules, which depend on statistical parameters such as the average level spacing or the neutron strength functions. The procedure followed in an analysis usually consists in obtaining the statistical parameters from the RRR and fit some of them in order to reproduce the URR. The procurement of these parameters in the RRR is also used to verify the consistence of the analysis in the RRR. The key publications concerning the study of the statistical model of nuclear resonances can be found in [Por65], and useful information also in [Fro00] and [Lar06]. Some summarized information, however, is presented here.

Average resonance spacing and probability distribution

Each neutron resonance corresponds to an excitation level of the compound nucleus. In the case of heavy nuclei, the amount of levels at the neutron separation energy, S_n, is usually big enough to show the characteristic features of the statistical model.

The average level spacing, $D_{l,,J}$ is one of the statistical parameters used to describe the URR. It is spin dependent, and it is related with the level density as: $\rho_{l,J} = \frac{1}{D_{l,,J}}$. The total amount of resonances with a given spin number is usually assumed to be proportional to the statistical factor, g_J (see Equation 1.7), so $D_{l,,J}$=D_J, and D_l=$\sum_J D_{l,,J}$.

The level density, ρ_l, depends on the excitation energy of the compound nucleus, so D_l=$D_l(E_n)$. However, it can be considered constant in the RRR, since the energy range covered (eV region) is very low compared with the neutron separation energy (several MeV). For this reason, D_l is usually calculated in the RRR, and it can be obtained by dividing the energy interval between two resonances (ΔE) by the number of resonances observed in the energy interval minus one (N-1) [Cap09], as it is presented in Equation 1.26. Then, level density theoretical formulas, such as the Gilbert-Cameron composite formula [Lar06], can be used to calculate D_l at higher neutron energies.

$$D_l = \frac{\Delta E}{N-1} \quad , \quad \frac{\Delta D_l}{D_l} = \frac{0.45\sqrt{\ln N + 2.18}}{N} \approx \frac{1}{N} \tag{1.26}$$

The distribution of level spacings is usually assumed to follow the Wigner's law. If D_k is the level spacing between two resonances of the same JΠ level sequence:

$$p(x)dx = \frac{\pi x}{2} exp\left(-\frac{\pi x^2}{4}\right) dx\,,\ with\ x = \frac{D_k}{D} \tag{1.27}$$

The average value of the distribution is $\langle x \rangle = 1$, and its variance $\sigma^2 = (4/\pi - 1)$, so the relative uncertainty of the average level spacing, calculated from the previous expression and when N resonances are observed is:

$$\frac{\Delta \langle D \rangle}{\langle D \rangle} = \sqrt{\frac{1}{N}\left(\frac{4}{\pi} - 1\right)} \tag{1.28}$$

There is an additional difficulty in the calculation of the level spacing, which is that there are usually a certain amount of resonances which have not been detected, so the calculated level spacing with Equation 1.26 is overestimated. There are several techniques to take this effect into account, and one of them is presented in Section 4.3.6.

Resonance widths distribution

The statistical behavior followed by the resonance widths are usually described by the Porter-Thomas distribution [Por65], which assumes that the distribution of the widths $\Gamma_{\lambda c}$ is given by a χ^2 distribution with ν degrees of freedom:

$$p(x,\nu)dx = \frac{\nu}{2\Gamma\left(\frac{\nu}{2}\right)}\left(\frac{\nu x}{2}\right)^{\frac{\nu}{2}-1} e^{-\frac{\nu x}{2}} dx \quad with \quad x = \frac{\Gamma_{\lambda c}}{\langle \Gamma_{\lambda c} \rangle} \tag{1.29}$$

where ν is the number of possible de-excitations modes of the channel c.

Equation 1.29 can be used for fission and gamma widths. In the capture case ν is usually a huge number, because there are usually a large amount of allowed radiative transitions to lower-lying compound states, so the distribution becomes a delta-like function, and so the radiative width, Γ_γ, is assumed to have nearly the same value for all the resonances. For the fission reaction it has been observed that ν has usually a small value, $\sim 2-3$, not necessarily an integer. This is quite surprising, due to the fact that there are hundreds of possible pairs of fission fragments, each with many possible excited states. This fact is explained by considering that there are a few intermediate states of the compound nucleus before the fission occurs. For the neutron widths, Equation 1.29 can not be used, since they are energy dependent. However, the so called reduced neutron width, defined as:

$$\Gamma^l_{\lambda n} = ka\sqrt{\frac{1}{E_\lambda}}\frac{\Gamma_{\lambda n}}{P^l_n} \tag{1.30}$$

follows the Porter-Thomas distribution. In this case, the number of degrees of freedom are 1 or 2, depending on the multiplicity of J.

Strength function

The average level spacing and the radiative and fission averaged widths are usually calculated in the RRR, and fitted again in the URR. However, instead of the averaged neutron reduced widths, what it is usually calculated is the neutron strength function, S_l, which can be calculated according to:

$$S_l = \frac{\langle g\Gamma^l_n \rangle}{(2l+1)D_l} = \frac{1}{(2l+1)\Delta E}\sum_r g_r \Gamma^l_{nr} \quad , \quad \frac{\Delta S_l}{S_l} = \sqrt{\frac{2}{N}} \tag{1.31}$$

More information concerning all these statistical parameters can be found in Section 4.3.6.

1.2.5 The ENDF-6 format

The cross sections resulting from the R-matrix formalism depends on a large amount of parameters that can not be predicted by the theory with the required accuracy for many applications, and need to be measured experimentally. In order to allow the proper use of the results of these measurements in the different nuclear applications, all the available measurements of a certain material[7] are analyzed together, performing critical comparisons between the different data sets, re-normalizing some results to others, ...; in order to obtain the best possible cross section with the information available. These results are combined with the prediction of nuclear model calculations if the experimental data is missing in a certain energy range of a certain reaction. This process is called an evaluation, and the result is a coherent description of the cross section of the evaluated material, with all the partial cross sections defined in a pre-defined energy range. The evaluation of a certain amount of materials constitute an evaluated library. These libraries are written in computer readable data files, with the purpose of being used by a large variety of computer codes in many different nuclear applications.

The most commonly used evaluated libraries are written in the so called ENDF-6 format [Her09], and several evaluations are distributed by different nuclear energy agencies in this format. The most common evaluated libraries are JEFF (European Union), ENDF/B (USA), JENDL (Japan), BROND and ROSFOND (Russia), and CENDL (China). New experiments are performed constantly, so each evaluated library is updated after a certain period of time. There are several versions of each evaluated library. As an example, the newest ENDF/B evaluations are ENDF/B-VI.8, ENDF/B-VII.0 and ENDF/B-VII.1. This ENDF-6 formatted libraries can be downloaded from the Nuclear Energy Agency [NEDxx], the International Atomic Energy Agency [IADxx] or the Brookhaven National Laboratory Nuclear Data Center [NNDxx] websites, among others.

The information available in the ENDF-6 format evaluated libraries are essentially nuclear reaction cross sections together with the yields and distributions in energies and angles of the secondary reaction products. Covariance matrices which describe the uncertainties and correlations between the different data provided may also be included. Cross sections are described in the ENDF-6 evaluated data format essentially by terms of the parameters described in the previous sections. Therefore, the whole neutron energy range, which is typically between 10^{-5} eV and 20 MeV, is usually divided into three regions:

1. RRR, where the cross section is defined by the channel radius and the resonance parameters. For each resonance it is provided: the orbital angular momentum, l, the total angular momentum, J, the energy of the resonance, E_0, and the partial widths, Γ_c. The representation used for the R-matrix (SLBW, MLBW, Reich-Moore, ...) is explicitly given.

2. URR, where the cross section is defined by the scattering radius, AP, the channel radius, a, and the so called unresolved parameters, which are the mean level spacing, $D_{lJ}(E_n)$, the average reduced neutron widths $\left\langle \Gamma_n^0 \right\rangle_{lJ}(E_n)$, and the average gamma and fission widths, $\langle \Gamma_\gamma \rangle_{lJ}(E_n)$ and $\langle \Gamma_f \rangle_{lJ}(E_n)$, all of them depending on the orbital and total angular momenta and on the neutron energy.

3. High energy region, where the cross section is defined pointwise.

The energy range of this measurement, 0.7 eV - 2.5 keV, covers a part of the RRR and a part of the URR. The analysis described in this manuscript consists in a first part, which is the data reduction, and a second part, which is the cross section analysis. This second part, which is described in Chapter 4, consists in obtaining the previously described resolved and unresolved parameters, together with their uncertainties and the correlations between them.

[7] usually an isotope, but sometimes a mixture of them, typically an element with its natural isotopic composition.

1.2.6 De-excitation electromagnetic cascades after neutron capture

According with the compound nucleus theory, a capture reaction is produced when the compound nucleus decays to the ground state or a metastable level. As a result of this decay, an electromagnetic cascade is emitted. Neutron capture cross sections at n_TOF are measured by the detection of this electromagnetic cascade, and it is necessary to calculate the detection efficiency to infer the amount of capture reactions produced from the amount of capture reactions detected. This efficiency is calculated from simulations, where the starting point is the electromagnetic cascade, so a procedure to generate reliable cascades after neutron capture is needed. These cascades could be reproduced perfectly if the complete level scheme with all the branching ratios between levels of the compound nucleus were known, together with the information concerning the electron conversion. However, the number of levels for heavy nucleus is huge, and only some of them, at low excitation energies, are known. For this reason, a statistical model is normally used to generate the electromagnetic cascades. Some theoretical basis used to the generation of this cascades is presented in this section. More information can be found in references [Kop90], [Wan03] and [HCN06].

In the model most used for the generation of electromagnetic cascades a partial radiation width, $\Gamma_{a\gamma b}$, is defined to calculate the probability of a γ-ray decay from a level with energy E_a to another with energy E_b. The expectation value of this partial radiation width for a given radiation type X (electric or magnetic) and a multipolarity L is assumed to be:

$$\bar{\Gamma}^{(XL)}_{a\gamma b} = f^{(XL)}(E_\gamma) E_\gamma^{2L+1} / \rho(E_a, J_a, \pi_a) \tag{1.32}$$

where $\rho(E, J, \pi)$ is is the nuclear level density, with spin J and parity π, and $f^{(XL)}(E_\gamma)$ is the Photon Strength Function (PSF), which is assumed to depend only in the γ-ray energy and not in the initial and final levels (Brink hypothesis).

There are different models for the nuclear level densities, such as the constant temperature, the Gilbert-Cameron or the Back Shifted Fermi Gas formulas. The later one, in the Digl version, takes the expression:

$$\rho(E, J) = \frac{1}{24\sqrt{2}} \frac{2J+1}{\sigma^3 a^{1/4}} \frac{exp\left[2(a(E-\Delta))^{1/2} - J(J+1)/2\sigma^2\right]}{(E-\Delta+t)^{5/4}} \tag{1.33}$$

where t is the thermodynamic temperature, defined by $E - \Delta = at^2 - t$, σ the spin cut-off parameter, derived theoretically, and a and Δ the parameters of the model, which can be taken from [RP2xx, Dig73].

For the PSF, different Lorentzian-like shapes are usually taken (or sums of them), such as the Standard Lorentzian (SLO), the Enhanced Generalized Lorentzian (EGLO) or the Modified Lorentzian (MLO), which represent different resonant shapes. Each of these Lorentzian-like functions depend on three parameters: E_r,Γ_r and σ_r. As an example, the SLO for the E1 transition, is:

$$f_{E1}(E_\gamma) = 8.674 \cdot 10^{-8} \sigma_r \Gamma_r \frac{E_\gamma \Gamma_r}{\left(E_\gamma^2 - E_r^2\right)^2 + \left(E_\gamma \Gamma_r\right)^2} (MeV^{-3}) \tag{1.34}$$

For some nuclei, there are experimental parameters of these Lorentzian-like resonances. For others, theoretical models can be used to have a first estimation of them. Recommended values taken from [HCN06] and [Kop90] are:

E1 transitions:

Spherical nuclei:

$$\begin{aligned} E_r &\equiv E_0 = 31.2A^{-1/3} + 20.6A^{-1/6}\ MeV \\ \Gamma_r &= 0.026E_r^{1.91}\ MeV \\ \sigma_r &\equiv \sigma_0 = 1.2 \cdot 120NZ/(A\pi\Gamma_r)\ mb \end{aligned} \tag{1.35}$$

Deformed nuclei (two resonances):

$$\begin{aligned} E_{r,1} &= E_{r,2}/\left[0.911\frac{a_0}{b_0} + 0.089\right] \\ \Gamma_{r,1} &= 0.026E_{r,1}^{1.91} \\ \sigma_{r,1} &= \sigma_0/3 \end{aligned} \tag{1.36}$$

$$\begin{aligned} E_{r,2} &= E_0\frac{1}{b_0}\left[1 - 1.51 \cdot 10^{-2} \cdot (a_0^2 - b_0^2)\right] \\ \Gamma_{r,2} &= 0.026E_{r,2}^{1.91} \\ \sigma_{r,2} &= 2\sigma_0/3 \end{aligned} \tag{1.37}$$

where $a_0 = (1 + \alpha_2)/\lambda$ and $b_0 = (1 - 0.5\alpha_2)/\lambda$. α_2 is obtained from the ground state deformation parameters $\alpha_n \equiv \beta_n/\sqrt{(2n+1)/4\pi}$, where β_n can be obtained from [Mol95]. λ can be obtained from the expression: $\lambda^3 = 1 + \frac{3}{5}\alpha_2^2 + \frac{2}{35}\alpha_2^3$.

M1 transitions:

$$\begin{aligned} E_r &= 41 \cdot A^{-1/3}\ MeV \\ \Gamma_r &= 4\ MeV \\ \sigma_r &= adjusted\,to: \\ &\quad 1 - experimental\ f(M1)\ value \\ &\quad 2 - f(M1) = 1.58 \cdot A^{0.47}\ at\ \pm 7MeV \\ &\quad 3 - f(E1)/f(M1) = 0.0588 \cdot A^{0.878}\ at\ \pm 7MeV \end{aligned} \tag{1.38}$$

E2 transitions:

$$\begin{aligned} E_r &= 63 \cdot A^{-1/3}\ MeV \\ \Gamma_r &= 6.11 - 0.021 \cdot A\ MeV \\ \sigma_r &= 0.00014 \cdot Z^2E_r/\left(A^{1/3}\Gamma_r\right)\ mb \end{aligned} \tag{1.39}$$

All this information, together with the experimentally known low-energy levels of the compound nucleus and the electron conversion process, can be used as a starting point for the generation of neutron capture cascades. However, the cascades generated using these recommended theoretical values typically do not reproduce the experimental results, so they need to be varied until the experimental results are reproduced. The information concerning the PSF parameters is valuable itself, since capture measurements are one of the few experiments where PSF are studied below the neutron separation energy.

Chapter 2

The ^{243}Am(n,γ) cross section measurement

This Chapter is dedicated to describe general aspects of the measurement. There are three elements which are necessary to perform a cross section measurement: (1) a sample with the isotope wanted to measure; (2) a neutron source, used to bombard the sample; and (3) a detection system used to "count" the amount of neutron reactions induced in the sample. The first three sections are dedicated to describe the three mentioned elements: in Section 2.1, the n_TOF experimental facility, which is the neutron source; in Section 2.2, the detectors which have been used in the measurement; and in Section 2.3, the ^{243}Am sample. Section 2.4 is dedicated to describe the whole experimental set-up, together with all the characterization and dedicated background measurements performed together with the ^{243}Am capture measurement. Finally, Section 2.5 is dedicated to describe the analysis procedure.

2.1 The n_TOF facility at CERN

The ^{243}Am capture cross section was measured at the n_TOF facility at CERN. Extended information concerning this facility can be found in [NTOxx] and [NTC03], but a brief description is presented here.

The construction of the n_TOF facility was proposed by Rubbia et al. [Rub98] in 1998 and built at CERN in 2000-2001 for performing cross section measurements of isotopes relevant to nuclear astrophysics and the transmutation of nuclear waste. n_TOF has been designed especially to measure low mass and/or radioactive samples, due to its high instantaneous neutron fluence, which minimizes the background to signal ratio.

The neutrons are produced by spallation reactions. Pulses of typically $7 \cdot 10^{12}$ or $4 \cdot 10^{12}$ average number of protons of 16 ns FWHM time width and 20 GeV energy are delivered by the PS accelerator at CERN, and impinge on a lead block of 80x80x60 cm, producing several particles. The neutrons and other accompanying particles travel along a beam line in vacuum of about 185 m until reaching the experimental area. Along the beam line a magnet and two collimators reduce the amount of charged particles which reach the experimental area and give the appropriate shape to the neutron beam. A schematic view of the facility can be seen in Figure 2.1. The beam line ends in a beam dump which consists in a polyethylene block situated after the experimental area. The lead target is surrounded by water, which acts as a coolant and also as a neutron moderator, transforming the initial fast neutron spectrum in the one presented in Figure 2.2.

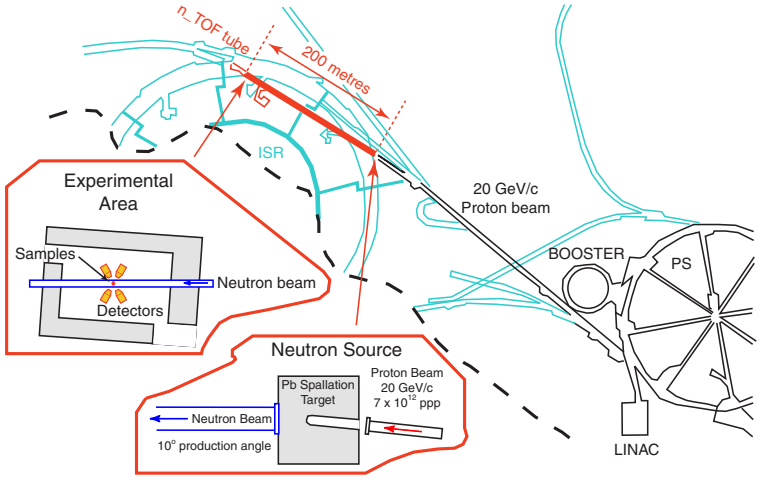

Figure 2.1: Schematic view of the n_TOF facility.

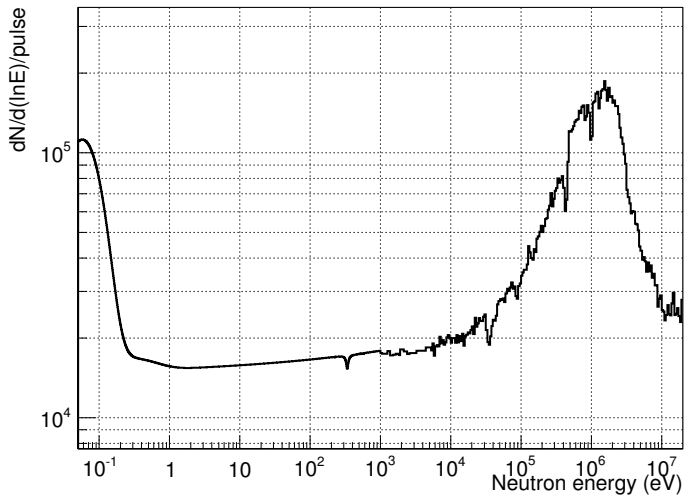

Figure 2.2: Neutron fluence in the experimental area.

The n_TOF neutron source is pulsed. This allows the calculation of the neutron energy by the time of flight method: with the knowledge of the distance between the lead target and the sample L and the time the neutron needs to travel this distance t, its energy can be obtained. In particular, the kinetic energy of a neutron with speed $v = L/t$ can be expressed as:

$$E_n = E - m_n c^2 = \sqrt{c^2 p^2 + m_n^2 c^4} - m_n c^2 = m_n c^2 \left(\frac{1}{\sqrt{1 - \frac{v^2}{c^2}}} - 1 \right) \tag{2.1}$$

and if the kinetic energy of the neutron is low enough:

$$E_n = \frac{1}{2} m_n v^2 = \alpha^2 \frac{L^2}{t^2}, \qquad \alpha = 72.29 \frac{\sqrt{eV}\mu s}{m_n} \tag{2.2}$$

A precise characterization of the neutron beam is necessary to perform the cross section analyses. This characterization consists in the determination of the neutron fluence, the beam profile and the *resolution function*, all three as a function of the neutron energy.

The energy shape of the neutron fluence at the measuring station was determined mainly using two fission chambers absolutely calibrated at PTB (Physikalisch-Technische Bundesanstalt) [PTBxx] and other auxiliary detection systems such as a silicon detector viewing a ^{6}Li foil, C_6D_6 γ-ray detectors and Parallel Plate Avalanche Counters (PPAC). This shape is presented in Figure 2.2, and the total amount of neutrons in different energy ranges in Table 2.1. Two different kind of proton pulses were used in the n_ TOF facility: the TOF, called also dedicated, pulses ($\sim 7 \cdot 10^{12}$ protons) and the EASTC, called also parasitic, pulses ($\sim 4 \cdot 10^{12}$ protons). Values presented in Table 2.1 are for TOF pulses, but it can be easily scaled to other pulse intensities.

Neutron energy	Neutrons/pulse
$<$ 1 eV	3.1×10^5
1 - 10 eV	4.5×10^4
10 - 100 eV	4.7×10^4
100 - 1000 eV	5.1×10^4
1eV - 1keV	1.4×10^5
1 - 10 keV	5.4×10^4
10 - 100 keV	7.1×10^4
100 - 1000 keV	2.3×10^5
1keV - 1 MeV	3.5×10^5
1 - 10 MeV	2.4×10^5
10 - 100 MeV	7.2×10^4
1 - 100 MeV	3.1×10^5
Total (1 - 10^8 eV)	8.0×10^5

Table 2.1: Number of neutrons per pulse for different energy ranges (capture measurements).

The n_ TOF facility is used to measure capture and fission cross sections. The radius of the last neutron collimator is changed from capture to fission measurements, in order to obtain a wider neutron beam in the fission measurements, since fission samples have usually larger diameters than capture samples. For the capture measurements the neutron beam has 2 cm diameter with a quasi-Gaussian spatial profile of $\sigma \sim 0.77$ cm, in the energy range of interest for this work. The beam profile depends on the neutron energy, and it has been measured carefully and compared with the

results of Monte Carlo simulations [Pan04]. However, in the energy range relevant for this work the beam profile remains more or less constant. It is presented in Figure 2.3.

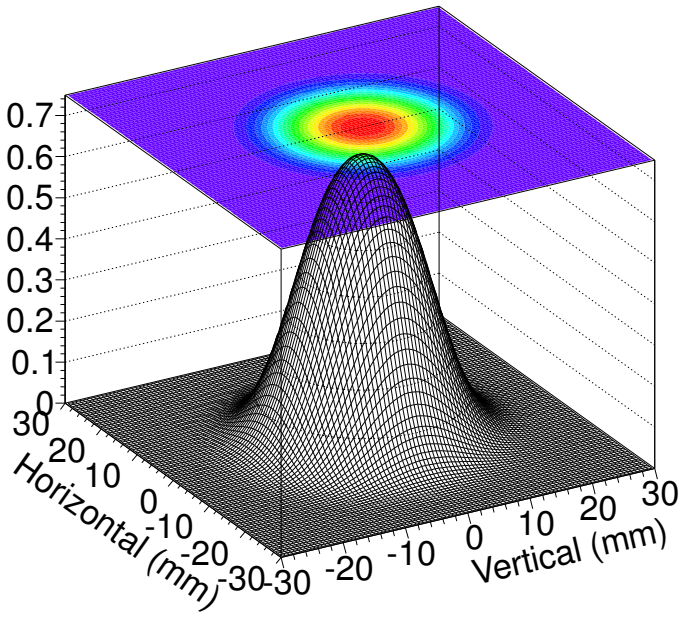

Figure 2.3: Spatial profile of the neutron beam in the experimental area for neutrons between 10 and 100eV.

At a given time, not all the neutrons reaching the sample have exactly the same energy. The neutrons can be produced in different places and times in the spallation lead target and, above all, the moderation time of the neutrons is not always the same. This effect has been characterized and taken into account in the analysis. It is described by the Resolution Function, which has been plotted in Figure 2.4.

Another important characteristic of the n_TOF facility is the so called gamma-flash. At times corresponding more or less to the arrival of the γ-rays produced in the spallation process to the experimental area, the capture detectors get saturated remaining "blind" during a certain period of time. Fission detectors are less sensitive to this effect but a strong signal is also always observed. Its origin is still not clear at present and it is still under study. This effect is usually used to establish a time origin of the detectors, but due to the fact that the capture detectors remain "blind" a certain period of time, it is impossible to measure capture reactions above a certain energy. This energy limit depends on the detector.

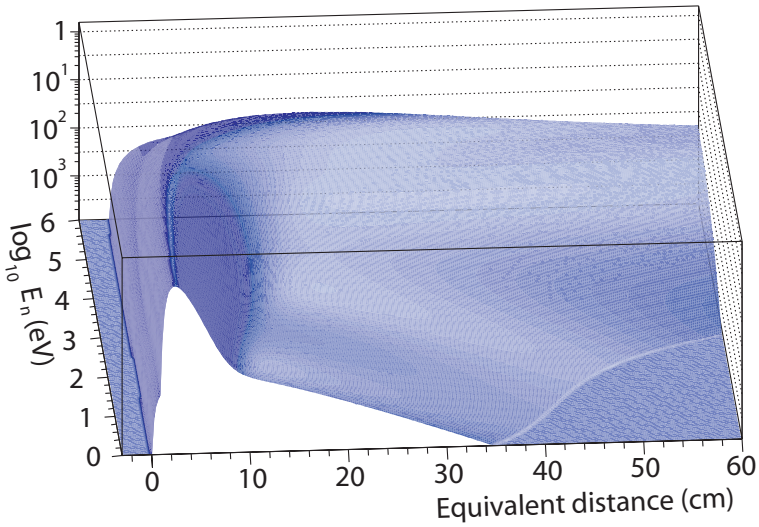

Figure 2.4: Resolution function of the n_TOF facility, expressed as the distribution of the equivalent distance traveled by each neutron as a function of its energy.

2.2 The experimental setup

Four different detectors were used during the ^{243}Am capture measurements: (1) the n_TOF Total Absorption Calorimeter (TAC) [Gue09], used to detect the capture reactions induced in the ^{243}Am sample; (2) the Silicon Flux Monitor (SiMon) [Mar04], used to monitor the intensity of the neutron beam; (3) the Wall Current Monitor (WCM) [NTC03], used to monitor the intensity of the proton beam; and (4) the Beam Current Transformers (BCT) [NTC03], used with the same purpose than the WCM. The signals of the first three mentioned detectors are recorded by a digital Data Acquisition System (DAQ) [Abb05] which registers continuously a certain time window after each proton pulse, typically from 8 to 96 ms. In the case of the BCT, the intensity value of each proton pulse is registered in the DAQ. The detected signals are analyzed offline by dedicated pulse shape analysis routines.

2.2.1 The Total Absorption Calorimeter

The capture reactions in the sample are registered by detecting the γ-ray cascade which follows the neutron capture. This cascade results from the de-excitation of the compound nucleus, at an excitation energy $E_\gamma \cong A/(A+1)\cdot E_n+S_n$, where E_n is the neutron energy and S_n the neutron separation energy, the last one with typical values of 5 - 10 MeV. This de-excitation proceeds in several different paths, determined by all the nuclear levels below the nuclear separation energy and their associated branching ratios. In general, the cascade detection efficiency depends on the decay scheme (levels and branching ratios), which is usually only known at low excitation energies, with the exception of some light nuclei with low level densities. Therefore, it is very difficult to calculate with a reasonable accuracy the detector efficiency for a general case. In order to solve this problem, three different techniques are commonly used in (n,γ) experiments:

- The Moxon-Rae technique [Mox63], which uses a converter to produce secondary electrons that are then detected by a thin plastic scintillator. The detection efficiency is low and nearly proportional to the energy of

the incident γ-ray energy, which makes that the detection probability of a capture event becomes independent of the specific de-excitation cascade, depending only on the total energy of the cascade.

- The Pulse Height Weighting Technique (PHWT), described in detail in [Abb04], which is similar to the previous one, but the γ-rays are not converted into electrons. In the PHWT the detection efficiency is not exactly proportional to the energy of the detected γ-ray, so corrections are needed (*weighting functions*).

- The total absorption technique, which consists in detecting the whole γ-ray cascade. Ideally, the detection efficiency is a 100%, so it do not depend on the specific decay path. In practice, the efficiency detection is very high, 50 - 80%, and the uncertainty in its calculation can be reduced below 3% (see Section 3.5.6). This is the technique used in this work.

The TAC is a 4π segmented array which is made with 40 BaF_2 crystals [Gue09]. Each crystal has been constructed by cutting a BaF_2 cylinder of 14 cm diameter and 15 cm length. There are 12 crystals which have a pentagonal shape and 28 crystals with an hexagonal shape. Both types of shapes are shown in Figure 2.5. Each crystal is covered with two layers of 0.1 mm thick Teflon foil and a 0.1 mm thick polished aluminum sheet on the outside for optimizing the light collection. In order to minimize the amount of background neutrons entering in the crystals, they are put into 1 mm thick ^{10}B loaded carbon fiber capsules. These capsules are coupled to an aluminum cylinder that serves as a housing of the 5" Photonis XP4508B photomultiplier. The whole module is attached to an aluminum honey comb structure, which holds the complete assembly. The whole TAC is divided in two hemispheres that can be opened and closed, as it is shown in Figure 2.6. It forms an spherical shell of 10 cm inner radius and 25 cm outer radius, approximately, covering $\sim$95% of the total solid angle.

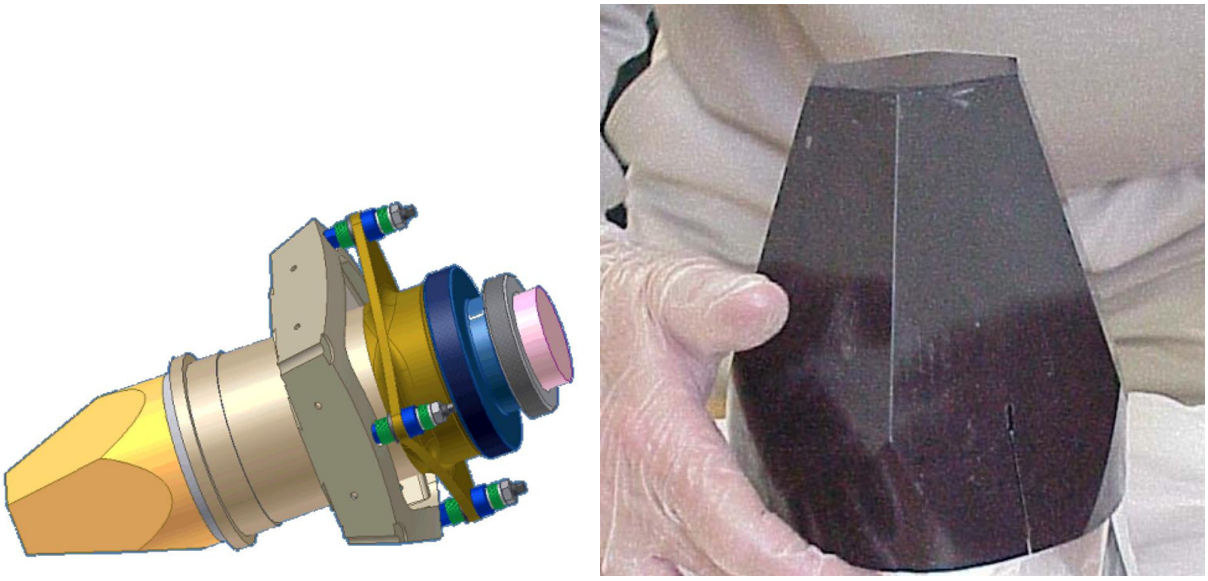

Figure 2.5: Sketch of a pentagonal BaF_2 detector module (left) and picture of an hexagonal BaF_2 detector (right).

The samples are placed in the center of the TAC. A neutron absorber is placed surrounding the sample to reduce the amount of neutrons scattered in the center of the TAC which hit the BaF_2 detectors. Figure 2.6 shows two photographs of the TAC setup. On the left panel, it is possible to see one of the hemispheres. The spherical shell in black corresponds to the neutron absorber and also visible in dark color are the boron loaded carbon fiber capsules. On the right panel, the complete TAC structure and its position inside the n_TOF experimental area is shown.

The neutron absorber is made with a salt with ^{6}Li content, $C_{12}H_{20}O_4{}^6Li_2$, filling a 0.5 mm thick aluminum container. It has an spherical shape with a 5 cm inner radius and 10 cm outer radius, with a cylindrical hole of 2.8 cm radius in the beam line direction. It is made up of two hemispheres surrounding the sample and the beam pipe to allow its placement inside the TAC. The nominal density of the ^{6}Li salt was 1.1 g/cm^3. However, after comparing detailed Monte Carlo simulations with the experimental results, is was found that the ^{6}Li salt should have a density of 0.77 g/cm^3 (see Section 3.5.4), which can be explained by bubbles formed during the manufacture process.

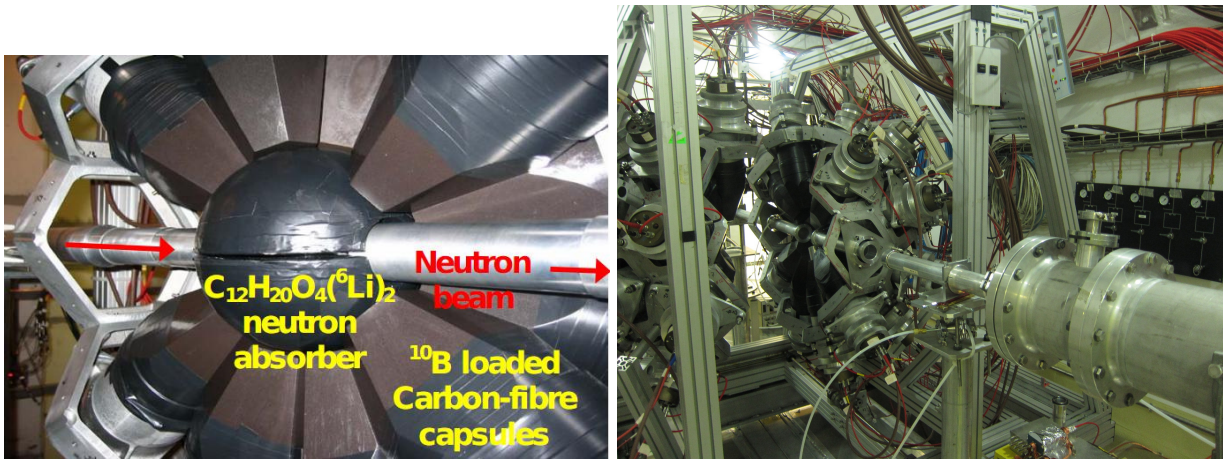

Figure 2.6: Picture of half of the TAC, with the neutron absorber and part of the beam line (left) and the whole TAC setup at the experimental area (right).

The TAC has been constructed to detect in coincidence the γ-rays in the cascade originated after the neutron capture process. This γ-cascade has a total energy which is approximately the neutron separation energy (typically between 5 and 10 MeV) plus the neutron kinetic energy ($E_\gamma \cong A/(A+1) \cdot E_n + S_n$). The whole cascade is emitted usually in a few ps, and the number of emitted γ-rays (multiplicity of the cascade) is usually below 10, with typical values ranging from 2 to 6.

The TAC has a very large detection efficiency. The probability of detecting one single γ-ray is between 80% and 90%, for γ-rays with more than 0.5 MeV, as it is presented in Figure 2.7. For this reason, the TAC efficiency to detect capture cascades is close to 100%. However, conditions on the total deposited energy and in the detected multiplicity are usually applied to the detected events in order to reduce the signal to background ratio (see Section 2.5), so finally the efficiency of the TAC is typically reduced up to values of 50% - 70%.

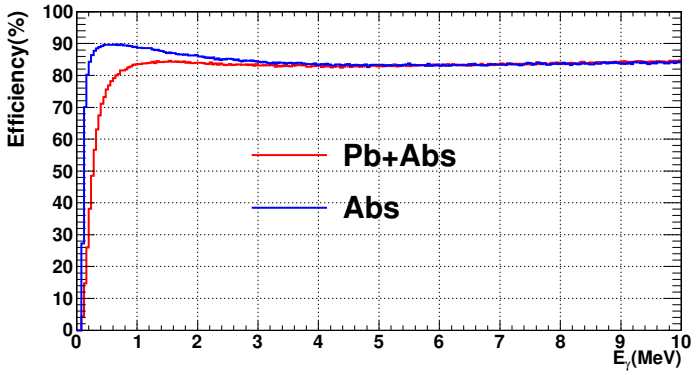

Figure 2.7: Probability of detecting a γ-ray originated isotropically in the center of the TAC as a function of its energy for two different configurations: one with the neutron absorber described in the text (Abs) and the other with the neutron absorber plus a lead cylinder of 1 mm thick placed surrounding the sample and parallel to the beam direction (Pb+Abs). The results have been obtained by Monte Carlo simulations and an energy threshold of 100 keV has been considered in each crystal.

The signals of the BaF_2 detectors are described in Section 3.1, where it is shown that the signals have a fast component of $\sim$0.6 ns. For this reason, time resolutions better than 1 ns can be achieved for each individual module. However, a time coincidence window $\leq$ 20 ns is usually defined to detect the whole capture cascade, as it is described in Section 3.4. Nevertheless, the length of the time window does not affect the time of flight resolution, which is at the end dominated by the resolution function and the Doppler broadening effects (see Section 2.5.2). The energy resolution of the crystals have typical values of 15-18% at 662 keV and 9-11% at 1836 keV, depending on the BaF_2 module. A detailed description is given in Section 3.3.3.

2.2.2 The monitor detectors

The intensity of the neutron beam has been monitored in the ^{243}Am measurement with three different detectors:

- The Silicon Flux Monitor (SiMon), used to monitor the intensity of the neutron beam.
- The Wall Current Monitor (WCM), used to monitor the intensity of the proton beam, which is proportional to the intensity of the neutron beam.
- The Beam Current Transformers (BCT), also used to monitor the intensity of the proton beam. The WCM and BCT detectors are completely independent and use different techniques to determine the proton beam intensity.

The SiMon consists in a very thin ^{6}LiF foil, which intercepts the neutron beam but with a negligible interaction, surrounded by four Silicon detectors, which detect the resulting alpha and tritium products of the ^{6}Li(n,t)^{4}He reaction. A schematic view of the detector can be seen on the left panel of Figure 2.8. The deposited energy spectra of the detected particles in the four Silicon monitors during the ^{243}Am measurements are visible in the right panel. The peak observed at high energies is due to the tritium detection and the part of the spectra at lower energies correspond to alpha detection. More information concerning the SiMon can be found in [Mar04].

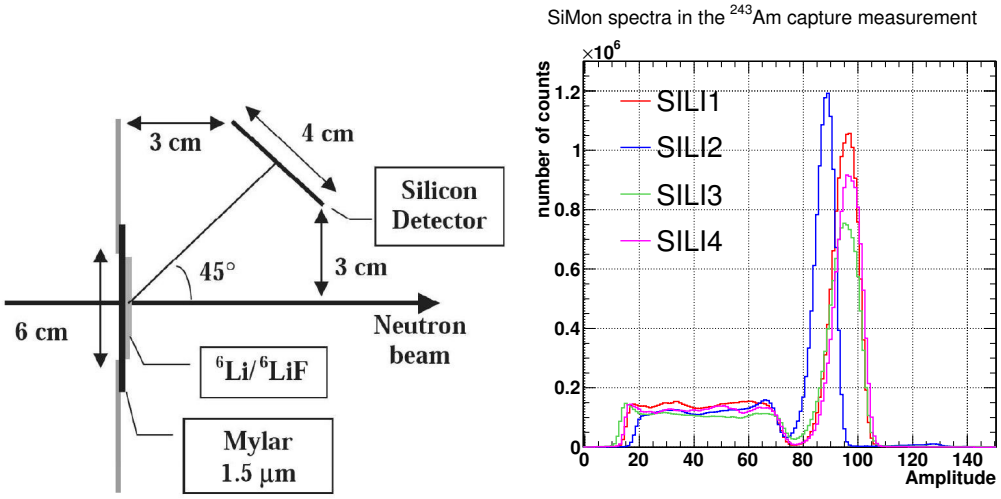

Figure 2.8: Schematic view of the SiMon (left) and deposited energy spectra in the Silicon monitors (right).

The WCM [NTC03] provides a signal proportional to the proton beam intensity. This signal is used to monitor the proton beam intensity and also to establish the time origin of each neutron pulse, which can also be obtained from the gamma-flash. The comparison between the time origin calculated with the WCM and the gamma-flash is provided in Section 3.4.

Finally, the number of protons measured with the BCT, for each proton pulse, is saved in the DAQ files. The comparison between the intensity obtained with these three detectors is provided in Section 3.7.

2.2.3 The Data Acquisition System

The n_TOF experimental set-up uses a fully digital Data Acquisition System (DAQ). The signals produced in the detectors are digitized with Acqiris-DC270 8 bits resolution ADC's, 1 GS/s of maximum sampling rate and 8 MB memory. The sampling rate is adapted to the time characteristic of the detector signals and the time of flight window required (i.e. neutron energies), being typical values 100, 250 and 500 MS/s. Each DAQ channel records continuously after each proton pulse an amount of time given by the ratio between its memory and the selected sampling rate. If all the 8 MB memory is used, this means that it records time of flights of 16, 32 or 80 ms depending if the sampling rate is 500, 250 or 100 MHz, respectively. These values corresponds to record for neutron energies between 0.70, 0.17 or 0.028 eV up to 20 GeV. The PS accelerator provides a signal to the DAQ just before the proton pulse reaches the lead target. This signal is used as a trigger and starts the recording of all the signals detected after the pulse.

After recording the data, a zero suppression algorithm selects the pieces of data containing true detector signals, in order to avoid the storage of large amounts of data without any practical information. These zero suppressed data (the so called raw data) is stored in files together with global information such as the temperature, the date and time of the pulse, the pulse type (dedicated or parasitic) .... Finally, the raw data files are sent to the CERN's

massive CASTOR storage facility [CASxx] for its posterior analysis. These files are organized in "runs", where each run has a specific number and corresponds to the data measured between a start and a stop of the DAQ. The global information concerning each run is accessible from the n_TOF web page [NTOxx], and it includes information such as the type of measurement, the configuration of the detectors or the number of pulses and protons dedicated to the run. The n_TOF DAQ is presented in detail in [Abb05].

In the case of the ^{243}Am capture cross section measurement the DAQ was recording signals of the 40 BaF_2 TAC detectors, operating at 250 MS/s; the 4 silicon detectors of the SiMon, operating at 100 MS/s; and the signal provided by the PS accelerator, with information concerning the WCM, operating at 250 MS/s. The length of the data buffers were limited to 4 MB, instead of 8 MB, due to transfer problems of raw data to the CASTOR storage facility: the high activity of the ^{243}Am sample made the zero suppression completely ineffective. The low energy limit of the measurement was set to 0.70 eV, which corresponds to a time of flight of 16 ms (4 MB recorded at 250 MS/s).

One of the advantages of the digital acquisition systems is that the raw data can be analyzed and manipulated offline. Indeed, this measurement could not have been performed without a fully digital DAQ. Apart from allowing the implementation of different analysis routines to analyze the same data set, this has also allowed to implement additional pileup reconstruction and dead time analysis techniques that would not be possible if an analog acquisition system would be used. These techniques are described in Section 3.2.

2.3 The ^{243}Am sample

The analysis of the ^{243}Am(n,γ) measurement has presented additional difficulties due to the high sample activity with respect to the previous capture measurements performed with the TAC (^{237}Np and ^{240}Pu). The ^{243}Am is a radioactive isotope with a half life of $T_{1/2}$=7370 years, much larger than other Am isotopes but lower than ^{237}Np and ^{240}Pu (see Figure 1.9). The average energy of the γ-rays emitted after the radioactive decay is, however, larger than the ones resulting from the decay of these other isotopes, as it is presented in Figure 2.9. As a consequence, the measured counting rates were considerably larger than in the previous measurements (see beginning of Chapter 3).

The decay chain of the ^{243}Am is the following:

$$^{243}Am \xrightarrow[\alpha]{7370\,y} {}^{239}Np \xrightarrow[\beta^-]{2.35\,d} {}^{239}Pu \xrightarrow[\alpha]{24110\,y} {}^{235}U(T_{1/2} = 7 \cdot 10^8 y)$$

Since $T_{1/2}(^{243}Am) \gg T_{1/2}(^{239}Np)$ and $T_{1/2}(^{239}Pu) \gg T_{1/2}(^{239}Np)$, the activity of ^{239}Np is practically the same as the activity of ^{243}Am, and both of them much higher than the activity of ^{239}Pu (more than 3 orders of magnitude). The activity of each isotope, together with the evolution of the isotopic composition of the sample due to the radioactive decay is presented in Figure 2.10.

The sample was manufactured at IPPE Obninsk. The Am was in the form of oxide powder (AmO_2) deposited on an aluminum backing of 10 mm diameter. The sample with the backing was placed inside a titanium capsule of 15 mm diameter. The full characterization of the sample provided by the manufacturers are given in Table 2.2, and a picture and drawings of the canning in Figure 2.11.

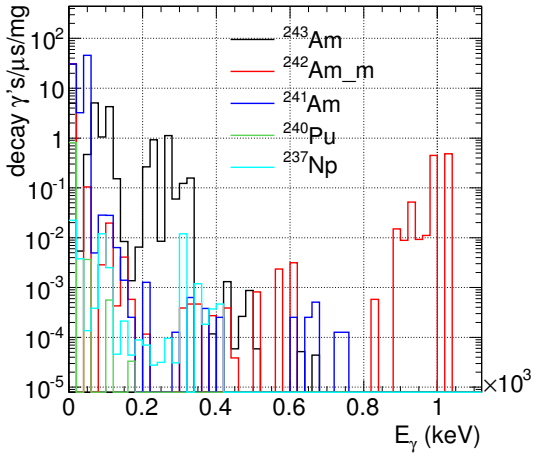

Figure 2.9: γ-ray spectra emitted by one mg of different actinides. All the γ-rays emitted along the entire decay of the isotope have been considered.

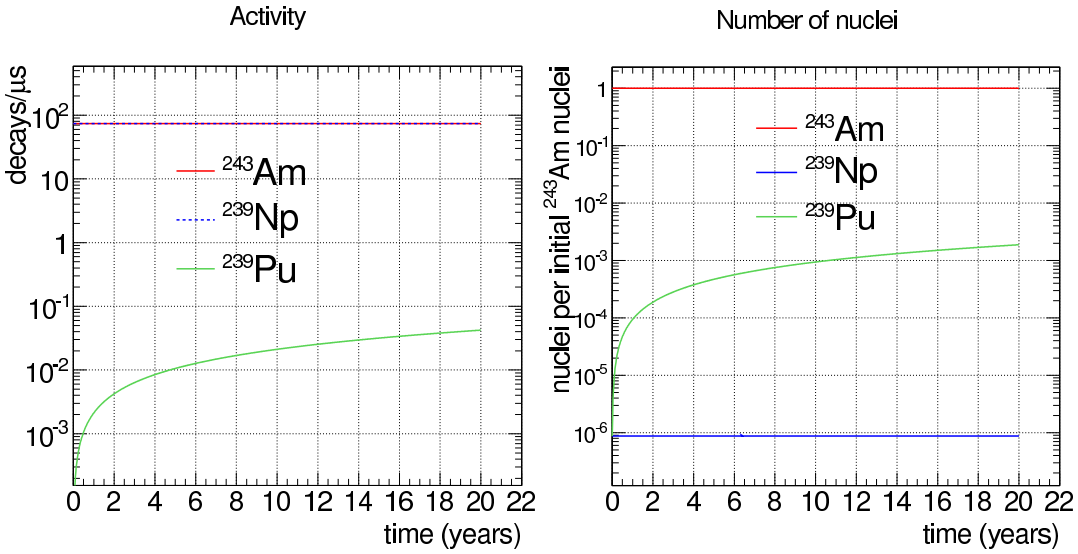

Figure 2.10: On the left panel, the activity of 10 mg of ^{243}Am their decay products, as a function of time. On the right panel, the number of atoms of ^{239}Np and ^{239}Pu created from the decay of ^{243}Am.

A specific and independent sample characterization was performed on arrival at CERN:

- A γ-ray spectrometry measurement, with high resolution Ge detectors, was performed by the radioprotection

Parameter	Data
Total mass (AmO_2)	0.0113 g
Isotopic mass (^{243}Am)	0.0100 g
Isotopic purity	97% mass
α activity	75.11 MBq
Activity	7.36 MBq/mg
Mass of the Al layer	$\lesssim$0.07 g
Capsule material	Titanium GOST 19807
Capsule diameter	15 mm
Capsule thickness above/below sample	0.17/0.18 mm
Date of manufacturing	February 06, 2004

Table 2.2: Parameters of the sample provided by the manufacturer.

service at CERN. Due to the extremely high activity of the sample, the measurement was not carried out under the best conditions, leading to high uncertainties. The results of the activity measured were 54.2($\pm$15.5%)MBq for the ^{243}Am and $\sim$51MBq of ^{239}Np (in equilibrium with the ^{243}Am) and $\sim$6.9MBq of ^{241}Am.

- The total sample (titanium container, actinide deposit and aluminum) was weighted at CERN, obtaining a total value of 0.4209g.

From this results, it is clear that the amount of ^{243}Am measured at CERN differ significantly from the quantity provided by the manufacturer. The mass of a radioactive isotope is related with its activity, A, by the expression given in Equation 2.3, where λ is its decay constant, N the number of atoms, $T_{1/2}$ its half life, N_A the Avogadro constant, m the mass of the sample and m_{iso} its relative atomic mass. According to that expression the ^{243}Am activity is related with the mass by A=7384(MBq/g)·m, since $T_{1/2}(^{243}Am)$=7370 years and $m_{iso}(^{243}Am)$=243.061 u. Thus, the mass of ^{243}Am measured at CERN is 7.34($\pm$15.5%) mg, which is not compatible with the value of 10 mg provided by the manufacturer.

$$A = \lambda N = \frac{ln(2)}{T_{1/2}} \frac{N_A \cdot m}{m_{iso}} \tag{2.3}$$

A third measurement of the sample activity was made with the TAC, which is an excellent rate-meter due to its large intrinsic efficiency. The measurement was limited in resolution with respect to the one performed with Ge detectors due to the much worse intrinsic resolution of BaF_2 crystals. In order to determine the sample activity in the most accurate way, the TAC data were compared with highly detailed Monte Carlo simulations. The event generator was constructed with the most detailed information available in ENSDF [ENSxx] on the ^{243}Am decay, including all the information concerning the different levels and branching ratios of the ^{243}Am and ^{239}Np nuclei, the half life of the levels which can affect the coincidence analysis of the decay cascades, and the electron conversion process. All the γ-rays were generated in a correlated way. The description of the simulation process is given in Appendix B.

The final result for the sample activity was 50 MBq, with a 15% uncertainty, which corresponds to a mass of 6.77($\pm$15%) mg. This value is compatible with the mentioned spectroscopic measurement performed at CERN, 7.34($\pm$15.5%) mg, and not with the 10 mg value provided by the manufacturer. From both activity measurements it can be concluded that the mass value provided by the manufacturer can not be used in the cross section analysis.

Unfortunately, the uncertainty of both activity measurements is too large to determine the mass of the sample as required in a high precision measurement, i.e., $\sigma_{mass} \leq 1\%$. If an average value is performed, a mass of 7.05($\pm$11%) mg is obtained. Therefore a normalization of the measured cross section to previous transmission measurements, leading to a sample mass of 6.23($\pm$4%) mg. This procedure is described in Section 4.2.3.

Concerning the sample impurities, this analysis found that the sample had a high purity content, with only $\sim$0.048 mg of ^{241}Am and $\sim$0.0025 mg of ^{240}Pu (see Section 4.2.4). This amount of ^{241}Am is compatible with what was measured in the mentioned spectroscopic measurement: $\sim$6.9 MBq, which corresponds to $\sim$0.054 mg.

Finally, the sample temperature was assumed to be 293$\pm$4 K, which is the temperature of the n_TOF experimental area. It was verified that the temperature of the sample is not higher than the temperature of the experimental area, due to its interaction with the neutron beam and the activity of the sample. The activity of the sample is much higher than the amount of reactions induced by the neutron beam, and it is around 100 MBq, half of it due to the decay of the ^{243}Am (Q=5.4 MeV) and half of it due to the decay of the ^{239}Np (Q=0.7 MeV). This means a power of $3{\cdot}10^{8}$MeV/s $\simeq 5{\cdot}10^{-5}$W. Making a rough calculation, the heat induced by the sample activity can be assumed to be dissipated by the air, with typical values of 5 W/m^2/K. In equilibrium, all the power is dissipated so P = 5 W/m^2/K$\cdot\Delta$T$\cdot$S, where P = $5{\cdot}10^{-5}$W, being ΔT the temperature difference between the sample and the experimental area and S the surface of the sample which is around $1.6{\cdot}10^{-4}$m^2. With all these values ΔT=0.06 K, which indicates that the sample was at room temperature.

2.4 Configuration of the ^{243}Am capture measurement

The sample was placed in air at the center of the TAC, held between two kapton foils of 25 μm thickness (see Figure 2.11), and surrounded by the neutron absorber. Due to the extremely high counting rate registered by the TAC, a Pb cylinder of 11.5 cm length and 1 mm thickness was placed around the sample. In this way, the amount of high energy γ-rays (200-300 keV) from the ^{243}Am decay reaching the TAC was strongly reduced. However, even with this lead shielding, the counting rate of this measurement was much higher than other previous measurements performed with the TAC.

The experimental configuration of the ^{243}Am capture measurement is schematically described in Figure 2.4. The TAC has been represented in green and the neutron absorber in blue. A vacuum pipe goes from the SiMon to the center of the TAC, and another one from the center of the TAC to the next beam pipe, which goes directly to the beam dump. Apart from the two kapton foils used to hold the sample, there were two additional 50 μm thick kapton vacuum windows inside the TAC attached to to the vacuum pipes and separated by 14 mm. The gap was in air.

Besides the ^{243}Am measurement, a series of characterization and dedicated background measurements were performed with the same configuration. These measurements were:

1. Calibration measurements: used to make the energy calibration of the BaF_2 detectors. The used calibration sources were ^{137}Cs (E_γ=661.7 keV), ^{88}Y (E_γ=898.0 and 1836 keV) and Pu/C (E_γ=6131 keV), which emit

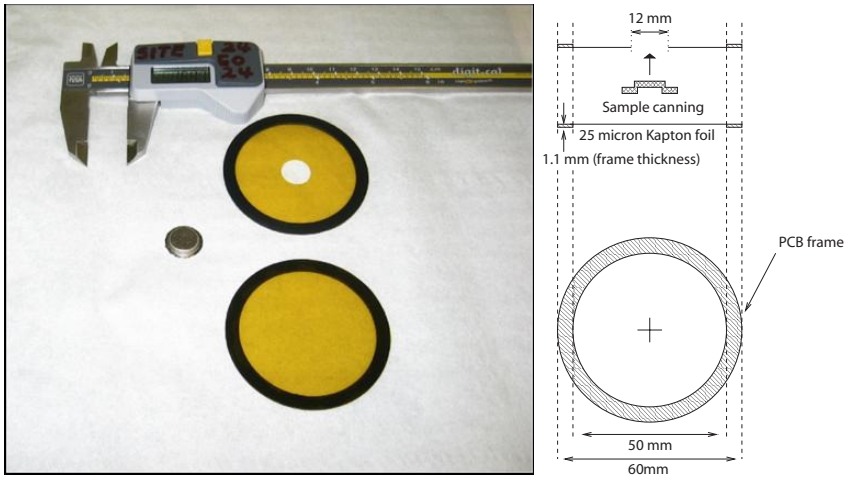

Figure 2.11: Titanium canning with the kapton foils used to place it in the beam line, in the center of the TAC.

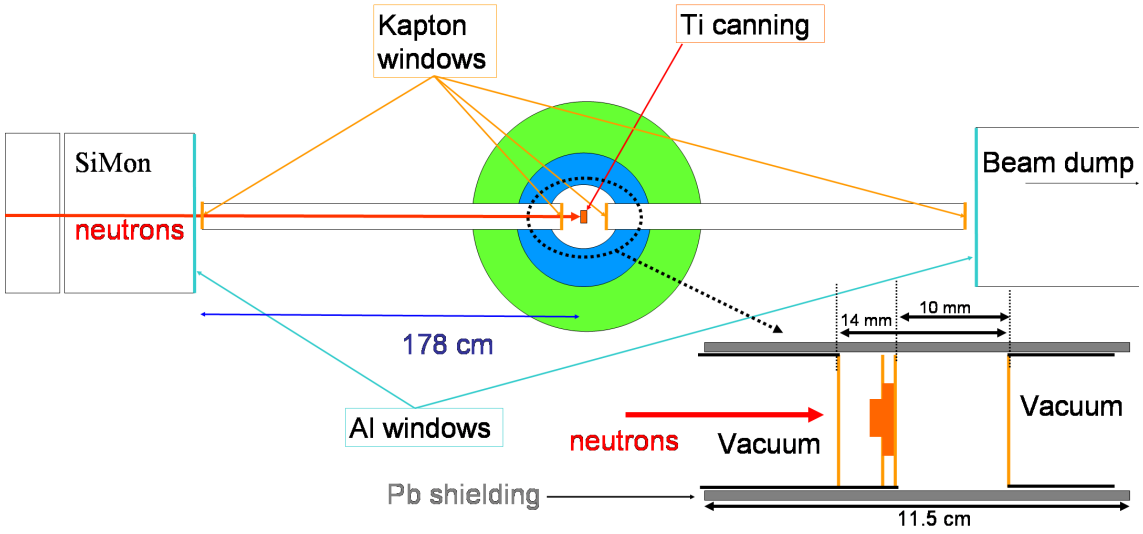

Figure 2.12: Schematic view of the ^{243}Am measurement configuration.

γ-rays with well known energies and are used to perform detector energy calibrations. These measurements were also used to characterize the energy resolution of each BaF_2 detector as a function of the detected γ-ray energy, together with a measurement performed with a ^{24}Na (1369 and 2754 keV) source. These procedures are described with detail in Section 3.3.

2. Background dedicated measurements: used to characterize the background in the ^{243}Am measurement. The results of these measurements are discussed in Section 3.6. Five different types of background were measured

separately:

(a) An environmental background measurement, performed without sample and without beam. This measurement was used to characterize the room background and the intrinsic activity of the BaF_2 crystals.

(b) An ^{243}Am activity measurement, performed with the sample in place, without beam. This measurement was used to characterize the background produced by the activity of the sample.

(c) A measurement performed in the same configuration as the ^{243}Am measurement but without the sample (empty frame). This measurement was used to characterize the background induced by the neutron beam, excluding its interaction with the sample. This background comes from the interaction of the neutrons in the different materials which are intercepting the beam (see Figure 2.4): the vacuum kapton windows of the beam pipes, the kapton foils used to hold the sample, the aluminum windows of the SiMon and the latter vacuum pipe ... When the neutrons interact with these elements, they can be captured, leading to a γ-ray background, or scattered, leading to a background from neutron captures in the TAC or the surrounding materials.

(d) A Ti canning measurement, performed in the same configuration as the ^{243}Am measurement but with an empty titanium canning instead of the sample. This empty titanium canning is similar to the one used with the sample and it is placed in the same position. It was weighted at CERN, and a value of 0.4554 g was obtained, larger than the 0.4209 g of the sample, which also includes the AmO_2 deposited in the aluminum layer. The purpose of this measurement was to characterize the background induced by the titanium canning. Although the mass was greater than expected, the results could be scaled down properly.

(e) A Carbon neutron scatterer measurement, performed with a ^{nat}C sample (graphite) in the same position as the ^{243}Am sample. The purpose of this measurement is to characterize the response of the TAC to scattered neutrons at the same position as the sample. This characterization is used to take into account the contribution to the background of the neutrons scattered in the measured isotope, which can be sizeable at the resonances energies. The carbon material is chosen because its capture cross section is more than four orders of magnitude lower than its elastic cross section in the energy range of interest, so it can neglected.

3. A Reference ^{197}Au measurement, performed with a ^{197}Au sample with the same diameter and in the same position as the ^{243}Am sample. This measurement is used for normalization purposes, to determine accurately the fraction of the neutron beam which is intercepted by the ^{243}Am sample. The results of this measurement are discussed in Section 3.7.

The whole ^{243}Am measurement, including background and other dedicated measurements, was performed in two different periods: between 26-8-2004 and 30-8-2004 and between 23-9-2004 and 7-10-2004. The sequence of these measurements is summarized in Tables 2.3 and 2.4, including the run numbers corresponding to each measurement, the duration of each set of runs, and the number of both TOF ($\sim 7{\cdot}10^{12}$ protons/pulse) and EASTC ($\sim 4{\cdot}10^{12}$ protons/pulse) pulses and dedicated protons. The total number of pulses and protons for each specific measurement is presented in Table 2.5.

Run type	Run number	Time	Pulses-TOF	Protons-TOF	Pulses-EASTC	Protons-EASTC
^{88}Y	7490	30 m	432	-	-	-
^{137}Cs	7491	30 m	261	-	-	-
^{243}Am	7492-7529	3.7 d	35296	$2.21{\cdot}10^{17}$	20742	$6.93{\cdot}10^{16}$
^{88}Y+^{137}Cs	7530	20 m	337	-	-	-

Table 2.3: Description of the runs of the first period.

Run type	Run number	Time	Puls.-TOF	Prot.-TOF	Puls.-EASTC	Prot.-EASTC
Calibration 1 ([3])	7755-7757	2.6 h	4031	-	-	-
^{243}Am ([1])	7758-7815	5.7 d	98949	$6.89{\cdot}10^{17}$	24487	$7.88{\cdot}10^{16}$
Calibration 2 ([3])	7824-7829	8 h	10733	-	-	-
^{197}Au ([2])	7830-7842	1.7 d	19995	$1.40{\cdot}10^{17}$	11744	$3.91{\cdot}10^{16}$
^{243}Am ([1])	7843-7891	4.2 d	51727	$3.57{\cdot}10^{17}$	29579	$9.21{\cdot}10^{16}$
Activity	7892-7893	4 h	5933	-	-	-
Environmental background	7894	9 h	13720	-	-	-
^{197}Au	7895-7896	4.3 h	1875	$1.30{\cdot}10^{16}$	977	$2.66{\cdot}10^{15}$
Calibration 3 ([3])	7897-7901	10 h	13660	-	-	-
Carbon	7903	6.5 h	3756	$2.67{\cdot}10^{16}$	3419	$1.04{\cdot}10^{16}$
Empty frame	7904-7905	7.5 h	1486	$1.04{\cdot}10^{16}$	2258	$6.62{\cdot}10^{15}$
Ti canning	7906-7907	5 h	4157	$2.94{\cdot}10^{16}$	4024	$1.21{\cdot}10^{16}$

Table 2.4: Description of the runs of the second period.

Measurement	Time dedicated	Pulses-TOF	Protons-TOF	Pulses-EASTC	Protons-EASTC
^{243}Am	13.6 d	185972	$1.27{\times}10^{18}$	74808	$2.40{\times}10^{17}$
Activity	10.3 h	15333	-	-	-
Env. background	9 h	13720	-	-	-
^{197}Au	1.9 d	21870	$1.53{\times}10^{17}$	12721	$4.18{\times}10^{16}$
Carbon	6.5 h	3756	$2.67{\times}10^{16}$	3419	$1.04{\times}10^{16}$
Empty frame	7.5 h	1486	$1.04{\times}10^{16}$	2258	$6.62{\times}10^{15}$
Ti canning	5 h	4157	$2.94{\times}10^{16}$	4024	$1.21{\times}10^{16}$
Total	**16.9 d**	**244419**	$\mathbf{1.48{\times}10^{18}}$	**97230**	$\mathbf{3.08{\times}10^{17}}$

Table 2.5: Global time statistics on the pulses and protons dedicated to each specific measurement.

[1] Run numbers 7797, 7815, 7845, 7847 and 7888 were activity measurements, with a total duration of 6.3h, and 9400 pulses.

[2] This measurement was performed with a thicker Au sample than the usually used for normalization purposes.

[3] All the calibration periods include runs with a source of Pu/C and runs with both ^{88}Y and ^{137}Cs calibration sources inside the TAC. In Calibration 1 and 3 the ^{88}Y and ^{137}Cs sources were measured together, whereas in Calibration 2 they were measured separately. Calibration 3 period include also a calibration run with ^{60}Co.

2.5 The analysis procedure

The observable quantity in a capture cross section measurement is the reaction yield, which is the probability of a neutron undergoing a capture reaction after hitting the sample. For this reason, the analysis of the cross section measurement can be divided into two parts.

- First, the procurement of the experimental reaction yield, which is the reduction of the detected data. This process starts with the analysis of the signals of the different detectors and ends with the procurement of the experimental reaction yield, together with all its statistical and systematic uncertainties.
- Second, once the experimental reaction yield is obtained, it is the task of the physicist, and later on of the evaluators, to obtain the neutron capture cross section from the neutron capture yields, typically with standard resonance analysis parameter codes like SAMMY [Lar06] or REFIT [Mox91].

Chapter 3 is dedicated to the description of the data reduction of the ^{243}Am capture measurement and Chapter 4 is dedicated to the analysis of the obtained capture yield. In the following sections we provide a brief description of both parts of the analysis.

2.5.1 The experimental capture yield

The neutron capture yield $Y_\gamma(E_n)$ is defined as the fraction of neutrons which hit the sample with energy E_n that undergo a neutron capture reaction:

$$Y_\gamma(E_n) = \frac{number\,of\,neutrons\,of\,energy\,E_n\,captured\,in\,the\,sample}{number\,of\,neutrons\,of\,energy\,E_n\,hitting\,the\,sample} = \frac{N_\gamma(E_n)}{N_T(E_n)} \tag{2.4}$$

The number of neutrons captured in the sample is calculated by counting the number of reactions and dividing this value by the efficiency of the counting process:

$$N_\gamma(E_n) = \frac{ND(E_n) - BK(E_n)}{\varepsilon} \tag{2.5}$$

where $ND(E_n)$ is the number of detected events, $BK(E_n)$ is the number of detected events which are not coming from neutron capture in the sample (background) and ε is the detection efficiency, i.e. the probability of a neutron capture in the sample of being detected.

The total neutron fluence and its energy dependence have been measured accurately with standard reactions (section 2.1). However, the radius of the sample is lower than the neutron beam radius (0.5 cm and 2 cm, respectively), so only a fraction of the incoming neutrons are hitting the sample. This fraction can be, in principle, obtained from the description of the beam profile presented in 2.1. However, it is calculated with more accuracy by measuring a reference sample with the same radius. The sample used for this purpose was made of ^{197}Au, which has a very strong resonance at 4.9 eV. This resonance is not a standard but is well known. The advantage of using a strong resonance (i.e., saturated) is that almost all the neutrons with energies at the resonance energy get captured in the sample, so the effect of the uncertainty of the evaluated cross section is very low in the determination of the calculation of the number of neutrons which have been captured. The n_TOF fluence is then re-normalized to the value obtained from the ^{197}Au measurement, and the total amount of neutrons in the actinide measurement related

to the ^{197}Au measurement is calculated from the results obtained by the Silicon Flux Monitor (SiMon) (section 2.2), so:

$$N_T(E_n) = N_{T,Au}(E_n) R_{SiMon} \tag{2.6}$$

where $N_{T,Au}$ is the number of neutrons hitting the ^{197}Au sample and $R_{SiMon}$the ratio between the detected ^{6}Li(n,α)^{3}He reactions in both measurements.

Dividing ND(E_n), BK(E_n) and $N_{T,Au}(E_n)$ by time units, number of pulses or number of protons, the total $C(E_n)$ and background $B(E_n)$ counting rates and the incident neutron fluence $\phi(E_n)$ are obtained.

$$\phi(E_n) = \phi_{Au}(E_n) R_{SiMon} \tag{2.7}$$

The experimental capture yield can be finally calculated as:

$$Y_{\gamma,exp}(E_n) = \frac{N_\gamma(E_n)}{N_T(E_n)} = \frac{C(E_n) - B(E_n)}{\varepsilon \phi_{Au}(E_n) R_{SiMon}} \tag{2.8}$$

so all the quantities appearing in the right part of Equation 2.8 should be obtained.

The counting rates are calculated in the following way. First, the individual signals of the BaF_2 detectors are analyzed, identifying the γ-ray signals and discriminating them from signals due to the alpha activity of the crystals[1]. The time of flight and energy of each signal is calculated. In a second step, a coincidence analysis is made: every time the TAC detects a γ-ray, a coincidence window of 20 ns is open, and all the deposited energy in the detector during that period (E_{Sum}) is calculated, together with the number of BaF_2 crystals which have contributed to the detected cascade, called detector multiplicity (m_{cr}). This leads to a collection of "events", each of them characterized by its E_{Sum}, its m_{cr}, and its time of flight (the neutron energy).

As an example, an E_{Sum} distribution is presented in Figure 2.13, for the events which have time of flights corresponding to neutron energies between 1 and 10 eV. The solid red curve corresponds to all the events of the ^{243}Am measurement; and the dashed red curve, the background deduced from the dedicated background measurements described in Section 2.4. The solid and dashed blue curves correspond to the same measurement, but for events with multiplicity greater than 2, $m_{cr}>2$.

If no conditions are applied to the detected events (right panel of Figure 2.13), only a small fraction corresponds to capture reactions in ^{243}Am ($\sim$0.2% of the total detected events, in this case). In order to improve the signal to background ratio, two conditions are applied to the detected events:

1. Conditions on the total deposited energy. The total energy of the capture cascade is, in good approximation, the neutron separation energy of the compound nucleus ($S_n(^{244}Am)$=5363.7 keV) plus the kinetic energy of the incident neutron. For this reason, all the detected events with E_{Sum} greater than 5.5 - 6 MeV (the energy resolution of the crystals must be taken into account) do not correspond to capture reactions in ^{243}Am. These counts can be observed in Figure 2.13, and correspond to the interaction of the neutron beam with different materials along the beam line, such as the kapton windows inside the TAC and the titanium capsule ($S_n(^{49}Ti)$=8142.39 keV). On the other hand, the detected events with E_{Sum} lower than 2 -

[1] The BaF_2 crystals have an intrinsic alpha activity coming from the decay chains of ^{226}Ra and ^{228}Ra impurities. For details, see Section 3.1.

3 MeV are dominated by the background due to the activity of the crystals, the activity of the sample and the environmental background. Thus, if they are not considered, the capture to background ratio improves significantly. As an example, considering only the events with E_{Sum} between 2.5 and 6 MeV, the amount of counts due to neutron capture on ^{243}Am represents ∼70% of the total detected events, instead of the ∼0.2% obtained if no conditions are applied.

2. Conditions on the detected multiplicity. If additional conditions are applied to the detected multiplicity, the capture to background ratio improves. If, in the example presented in Figure 2.13, only events with detected multiplicity greater than 2 are considered (also with E_{Sum} between 2.5 and 6 MeV) then the amount of counts due to neutron capture on ^{243}Am represents ∼84% of the total detected events. This is because there are sources of background which have, on average, lower multiplicities than the capture events:

   (a) all the γ-rays hitting the TAC are absorbed mainly by one or two crystals.

   (b) the intrinsic activity of the crystals, which emit γ-rays with low multiplicity and are absorbed likely in the corresponding crystal.

   (c) neutrons captured by the BaF_2 crystals, where the fact that the capture reaction is produced inside a crystal makes the average detected multiplicity lower than if the capture cascade were originated in the center of the TAC.

   (d) γ-rays emitted due to the sample activity, which is always a low multiplicity background.

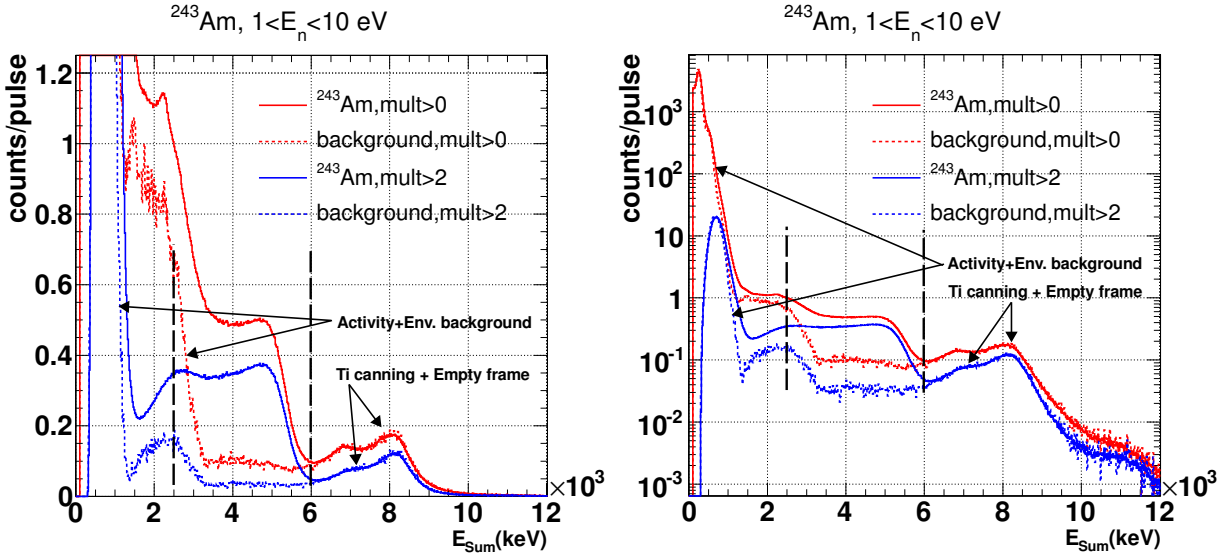

Figure 2.13: Deposited energy spectra in the TAC in a ^{243}Am measurement, for different multiplicities. The right panel is the same as the left panel, but with the Y axis in logarithmic scale.

On the other hand, the more restrictive are the conditions applied to the detected events, the lower is the detection efficiency of the TAC, and thus the statistical uncertainties and the systematic uncertainty on the detection efficiency increase. An optimum compromise between the capture to background ratio improvement and the reduction of the detection efficiency has to be reached. The fact that the uncertainty on the detection efficiency increases as the efficiency decreases is described with detail in Section 3.5. It is because the Monte Carlo simulation of the efficiency is more dependent with the model used to generate the capture γ-ray cascade as the efficiency decreases.

Taking into account the conditions mentioned above, Equation 2.8 can be written as:

$$Y_{\gamma,exp}(E_n) = \frac{N_\gamma(E_n)}{N_T(E_n)} = \frac{C(E_n,\{E_{cuts},m_{CR,cuts}\}) - B(E_n,\{E_{cuts},m_{CR,cuts}\})}{\varepsilon(E_{cuts},m_{CR,cuts},CR)\phi_{Au}(E_n)R_{SiMon}} \tag{2.9}$$

where now the counting rate, the background and the detection efficiency depend on the imposed conditions in the detected events: in the total deposited energy detected (E_{cuts}) and in the detected multiplicity ($m_{\gamma,cuts}$). The detection efficiency also depends on the counting rate (CR), due to pile up effects which lead to an effective dead time. However, it has been assumed that ε does not depend on E_n in the energy range of interest. This is because the total energy of the cascades is always essentially the same and the huge amount of possible decay paths makes indistinguishable for the TAC a capture reaction produced in one resonance or another, as it has been verified[2].

The resulting counting rates of the ^{243}Am measurement (blue), under the conditions defined by $2.5 < E_{Sum} < 6$ MeV and $m_{cr} > 2$, and an estimated background (black), are shown in the left panel of Figure 2.14. It can be appreciated that the background clearly dominates above 2 - 3 keV, due to the huge titanium resonances at those energies, making impossible to analyze the capture data beyond. On the right panel, the capture yield is presented.

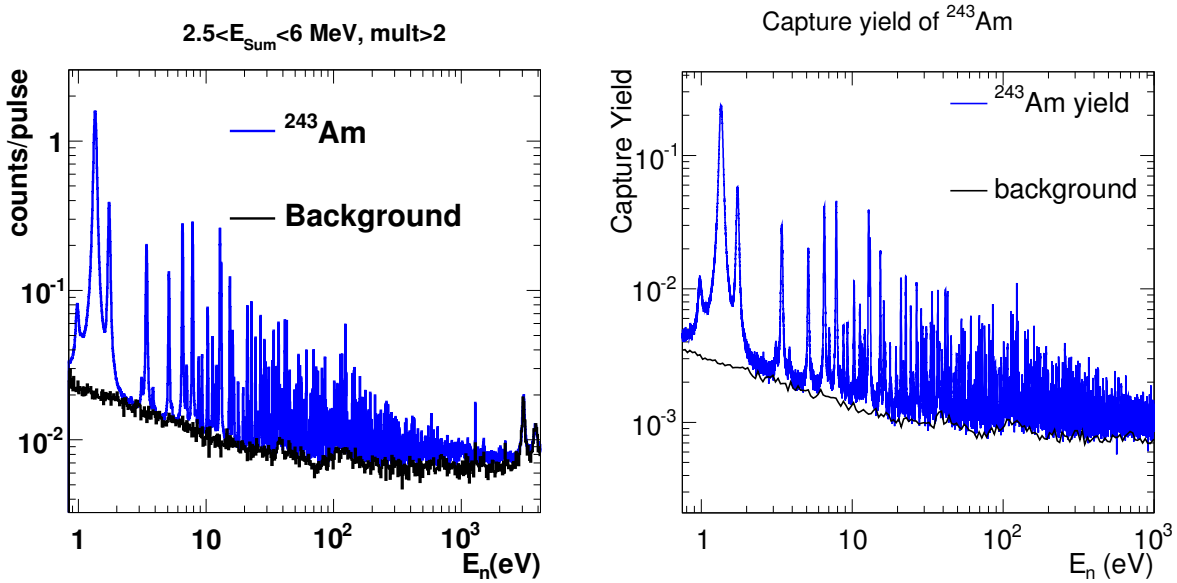

Figure 2.14: Counting rate of the ^{243}Am measurement and the estimated background (left), and the resulting capture yield with the estimated background (right).

[2]Some recent works try to use differences in the deposited energy spectra of different resonances to assign spin values. If these differences exist in the ^{243}Am measurement, they are very small, and can be neglected for the determination of the detection efficiency.

2.5.2 The procurement of the cross section from the experimental capture yield

The capture cross section is obtained by fitting the "theoretical" capture yield calculated from it to the obtained experimental one.

In the resolved resonance region (RRR) the cross section is described in the ENDF-6 format by the scattering radius a and a set of resonance parameters, which are the energy of each resonance E_{0i}, its reaction widths Γ_{xi} and spin S_i:

$$\sigma_x(E) = \sigma_x(E, \{a; E_{01}, \Gamma_{n1}, \Gamma_{\gamma 1}, \Gamma_{f1}, S_1; E_{02}, \Gamma_{n2}, \Gamma_{\gamma 2}, \Gamma_{f2}, S_2; ...\}) \tag{2.10}$$

In the unresolved resonance region (URR), the cross section is described by the scattering radius, the level spacings $\mathrm{D}_{lJ}(\mathrm{E}_n)$ and the average channel widths $\langle \Gamma_n^0 \rangle_{lJ}(E_n)$, $\langle \Gamma_\gamma \rangle_{lJ}(E_n)$, $\langle \Gamma_f \rangle_{lJ}(E_n)$ and $\langle \Gamma_x \rangle_{lJ}(E_n)$, corresponding to the elastic, capture, fission and inelastic widths. All these quantities, except the scattering radius, are provided for each l and J channel quantum numbers and are reported as a function of the neutron energy.

Finally, the high energy region of the cross section is described as energy-cross section pairs. The ^{243}Am measurement covers only parts of the RRR and URR.

Thus, there is a set of parameters which defines the different reaction cross sections of a given nucleus. However, what is directly measured in an experiment is the reaction yield, not the cross section itself. In the case of a transmission measurement, what it is measured is $T = e^{-n\sigma}$, where n is the thickness of the sample (nuclei/barn), while in the case of a reaction channel, if the sample is "thin", $Y_x = (1-T)\frac{\sigma_x}{\sigma}$. However, there are three "broadening" effects that complicate the relation between the cross section and the observables further: the Doppler broadening, the multiple scattering and the resolution function of the facility.

The Doppler broadening

Cross sections are strongly dependent on the neutron energy. Since the measured sample is always at a certain temperature, the thermal motion of the target nucleus makes that, depending on the velocity of the target nucleus when the reaction occurs, the energy value of the incident neutron in the center of mass system actually have different values, for the same laboratory incident neutron energy. This results into a broadening effect of the cross section, which depends on the temperature. The ENDF-6 format files provides the unbroadened cross section values (at 0K temperature), and then the files can be processed in order to broaden the cross section at the temperature needed for an specific application.

In order to calculate the Doppler-broadened cross section from the unbroadened one, it is necessary to know the distribution probability of the velocity of the target nucleus, $\mathrm{p}(\vec{u})\mathrm{d}^3\mathrm{u}$. If ρ_1 and ρ_2 are the densities of beam and target particles, the number of reactions per unit time and unit volume is:

$$\rho_1\rho_2 \int d^3u p(\vec{u}) \left|\vec{v} - \vec{u}\right| \sigma(|\vec{v} - \vec{u}|) \equiv \rho_1\rho_2 v\bar{\sigma}(v) \tag{2.11}$$

where $\bar{\sigma}(v)$ is the Doppler-broadened cross section.

There are different approximations to describe p($\vec{u}$). The most commonly used is the free gas approximation, which uses a Maxwell-Boltzmann distribution. There are also other formulations to take into account the structure of the sample material, which also affects the probability distribution.

In addition, there is also another important effect at low neutron energies: in the elastic scattering reaction, a certain amount of the neutron momentum is transferred to the target nucleus. This quantity depends on the motion of the target nucleus, and also in how the nucleus is bound to the material it belongs, since part of the transferred momentum can be absorbed by the whole material, and not only the target nucleus. This effect is relevant only at low neutron energies, below ~5 eV.

The multiple scattering

If the measured sample is not "thin", a fraction of the neutron beam will induce an (n,x) reaction after 1,2, ... scattering collisions. Thus, the $Y_x = (1-T)\frac{\sigma_x}{\sigma}$ reaction yield has to be corrected by adding the neutron reactions occurring after a certain number of scattering collisions:

$$Y_x = Y_{x0} + Y_{x1} + Y_{x2} + ... \tag{2.12}$$

with:

$$\begin{aligned} Y_{x0} &= (1-T)\frac{\sigma_x}{\sigma} \\ Y_{x1} &= (1-T)\frac{\sigma_n}{\sigma}\left\langle (1-T_1)\frac{\sigma_{x1}}{\sigma_1}\right\rangle_1 \\ Y_{x2} &= = (1-T)\frac{\sigma_n}{\sigma}\left\langle (1-T_1)\frac{\sigma_{n1}}{\sigma_1}\left\langle (1-T_2)\frac{\sigma_{x2}}{\sigma_2}\right\rangle_2\right\rangle_1 \\ &... \end{aligned} \tag{2.13}$$

where $(1-T_i)$ is the probability that after the i collision the neutron interacts somewhere in the sample and $\langle\rangle_i$ denote spatial and angular averages over all possible i^{th} collisions.

The resolution function

The incident neutron energy at the n_TOF facility is obtained by the time of flight method. However, it has to be taken into account that at a certain time the neutrons do not have exactly the same energy. Or, alternatively, not all the neutrons of a certain energy reach the sample at the same time. This occurs mainly because not all the neutrons are created at the same time and in the same position, and because the moderation process in the water surrounding the spallation target is different for each neutron. This effect is modeled as a resolution function (see Figure 2.4), which has been obtained from Monte Carlo simulations and experimentally from the high energy ^{56}Fe resonances.

By taking into account this three effects, it is possible to obtain the capture yield from the parameters which describe the cross section. The theoretical yield is then fitted to the obtained experimental capture yield, by varying the

resonance parameters. The most extended codes for performing the resonance analysis are SAMMY [Lar06] (the one used in this analysis) and REFIT [Mox91]. They take into account all the experimental effects described in this section, and perform a fit of the resonance parameters, calculating also the corresponding uncertainties and covariances.

Chapter 3

The Procurement of the experimental yield

This chapter is dedicated to describe the procedure followed to obtain the experimental capture yield of the ^{243}Am measurement. This procedure has been described briefly in Section 2.5.1, where it is shown that the experimental yield is obtained from the expression:

$$Y_{\gamma,exp}(E_n) = \frac{N_\gamma(E_n)}{N_T(E_n)} = \frac{C(E_n, \{E_{cuts}, m_{CR,cuts}\}) - B(E_n, \{E_{cuts}, m_{CR,cuts}\})}{\varepsilon(E_{cuts}, m_{CR,cuts}, CR)\phi_{Au}(E_n)R_{SiMon}} \tag{3.1}$$

where C is the counting rate of the ^{243}Am measurement, B its associated background, ε the detection efficiency and $\phi(E_n) = \phi_{Au}(E_n)R_{SiMon}$ the neutron fluence, normalized to the ^{197}Au capture measurement.

Many of the tools and procedures needed to obtain the experimental capture yield from the TAC were developed in the past, since other TAC measurements have been analyzed before the one presented in this work [Gue12.2, Gue08]. However, this measurement has presented additional difficulties which have required the improvement or the development of new analysis techniques. These difficulties have been:

1. The high activity of the ^{243}Am sample. As it is discussed in Section 2.3, the γ-ray radiation emitted by the decay of ^{243}Am is much higher, in intensity and also in energy, than the radiation emitted by other actinides measured by the TAC (^{237}Np, ^{240}Pu). The low energy part of the deposited energy spectra (up to $\backsim$1MeV) presented in the left panel of Figure 3.1 correspond mainly to the sample activity detected by the TAC in a ^{237}Np, ^{240}Pu and ^{243}Am measurements. As it can be observed, the ^{243}Am spectrum is around one order of magnitude larger than the ^{237}Np spectrum, and more than two than the ^{240}Pu spectrum. There is a difference of about four orders of magnitude between the counting rate in the 2 - 6 MeV part of the spectrum, which corresponds mainly to ^{243}Am capture events detected by the TAC, and the low energy part, corresponding mainly to the ^{243}Am activity. On the right panel, two digitized data buffers are presented, both corresponding with the signals recorded in one complete pulse (16 ms), in a single BaF_2 detector. The upper buffer corresponds to a ^{197}Au measurement and the lower buffer to an ^{243}Am measurement. As it can be observed, the ^{243}Am buffer is completely filled with signals, whereas in the ^{197}Au buffer, the signals appear reasonably separated in time, with large time periods in between where no signals have been detected. Such a high counting rate causes that:

(a) The pulse shape analysis routine which analyzes the TAC digitized data introduces a sizeable dead time due to the pile up of the detected signals.

(b) There is a non negligible amount of capture events that are detected in random coincidence with activity signals (random "summing").

(c) The detection of the background events during the ^{243}Am sample measurement is distorted by the ^{243}Am sample activity. However, the background measurements (in absence of the sample) are not distorted. As a consequence, the background from the dedicated measurements can not be subtracted directly from the capture data and corrections are needed.

(d) It has been observed that the gain of the BaF_2 detectors vary with the time when a measurement is performed under high counting rate conditions, making the energy calibration of the detectors unstable, i.e., with sizeable variations in time.

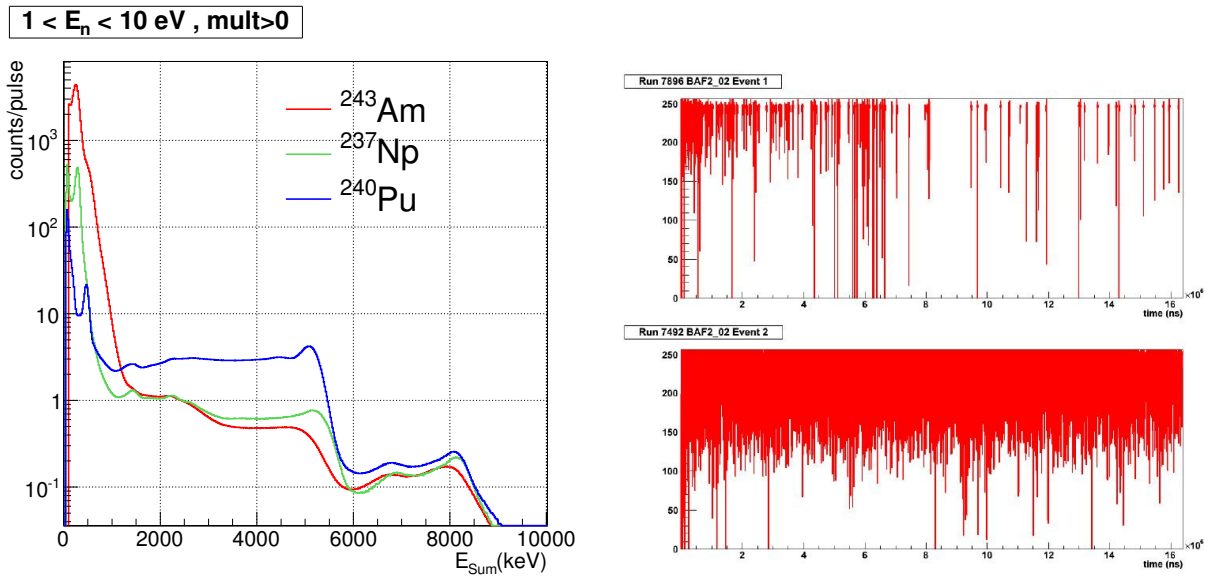

Figure 3.1: Deposited energy spectra for different measurements (left) and data buffer examples (right), for a ^{197}Au measurement (up) and a ^{243}Am measurement (down).

2. The large uncertainty in the sample mass (15%). As it is discussed in Section 2.3, the sample value provided by the manufacturer is not correct. Before starting this analysis there was a spectroscopic measurement performed at CERN which was not compatible with the mass value provided. However, since the spectroscopic measurement could be, in principle, also wrong, a great effort has been dedicated to demonstrate that the sample mass was really not the same as the value provided by the manufacturer. Unfortunately, it has been not possible to obtain the sample mass with good accuracy, and the measurement was finally normalized to previous existing transmission measurements.

In this chapter we describe the data reduction procedures and the corrections related with the mentioned high counting rate. In particular:

1. Section 3.1 is dedicated to describe the performance of the pulse shape analysis routine. This routine analyzes the digitized BaF_2 signals, fitting them to a reference shape which depends on parameters, which are used to deduce the time and energy of the signals, together with the discrimination between alpha and γ-ray particles. The performance of the analysis routine was characterized under high counting rates and under lower sampling rates (250 MS/s instead of 500 MS/s).

2. A detailed characterization of the dead time , which is described in Section 3.2, and was used:

   (a) for the reconstruction of the simulation results performed to calculate the TAC detection efficiency and the sample activity, the latter measured by the TAC and directly related with the sample mass.

   (b) to transform the dedicated background measurements into background data that would have been obtained if they were performed under the same high counting rate conditions than in the ^{243}Am capture measurement.

3. The energy calibration process is described in Section 3.3. It includes a static energy calibration, performed by analyzing the measurements with standard calibration sources; and a dynamic energy calibration, motivated for the change of the gain of the detectors run by run. This dynamic calibration has been performed by analyzing the changes with the time of the intrinsic activity alpha spectrum of each BaF_2 detector.

4. The time calibration is described in Section 3.4. This procedure consists in the synchronization of the different flash ADC-modules, which has to be performed with the best possible precision, since the capture events are detected in coincidence; and the calculation of the time origin, necessary to obtain the time of flight used to calculate the neutron energies.

5. Section 3.5 is dedicated to present the calculation of the detection efficiency, which has been performed by Monte Carlo simulation. The simulation code includes a realistic event generator which reproduces the γ-ray cascades emitted after a neutron capture; a detailed geometry of the TAC; and a reconstruction process that performs the coincidence analysis in the same way as it is done for the experimental results, including the experimental conditions such as the energy resolution of the detectors and the dead time/pile up effects.

6. The calculation of the background is presented in Section 3.6. A part of the background has been calculated with the transformed dedicated background measurements. There is also other part related with the interaction of neutrons in the ^{243}Am sample, which has a resonant structure and includes the interaction with the impurities present in the sample and the fission and elastic reactions that are detected with the TAC as if they were capture reactions.

7. The normalization process is described in Section 3.7, where the fraction of the beam intercepted by the ^{243}Am sample and the way to normalize one measurement to another are calculated.

8. Finally, all the information described in the previous sections is combined to obtain the capture yield, identifying all the statistical and systematic uncertainties. This process is described in Section 3.8.

3.1 The reconstruction of the digital data

The BaF_2 crystals have two scintillation decay modes:

1. A fast component of ∼0.7 ns which is used for the determination of the signal time.
2. A slow component of ∼620 ns which is used to calculate the energy of the signal.

The pulse shape analysis routine developed for the TAC performs least squares fits of the following shape to the digitized data:

$$s(t) = \begin{cases} b(t) & for\ t < t_0 \\ b(t) - A_{fast} \cdot e \cdot \frac{t-t_0}{\tau} \cdot \exp\left(-\frac{t-t_0}{\tau}\right) + A_{slow}\left[\exp\left(-\frac{t-t_0}{\tau}\right) - \exp\left(-\frac{t-t_0}{620ns}\right)\right] & for\ t \geq t_0 \end{cases} \quad (3.2)$$

where s(t) is the signal, b(t) the baseline, A_{fast} and A_{slow} are the fast and slow component maximum amplitude respectively, t_0 the starting time of the signal and τ the fast decay constant (∼0.7 ns). An example of the fits to the digital signals is shown in Figure 3.2 and more information concerning the pulse shape analysis routine can be found in [Mar06.1].

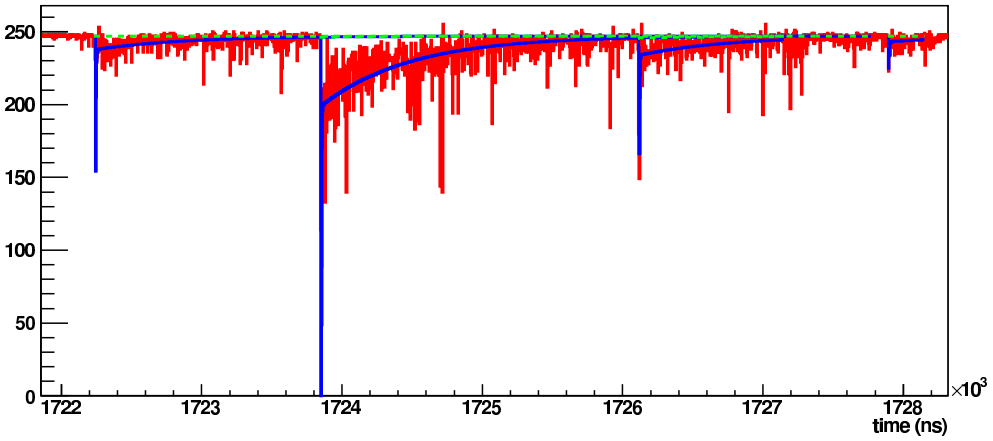

Figure 3.2: Example of the fit of some BaF_2 signals.

The pulse shape analysis leads to parameters such as the fast and slow amplitudes and the time of the signal, which are used during the analysis for obtaining the time and energy of the signal, as well as for separating γ-rays from alpha particles produced by the intrinsic activity of the BaF_2 crystals. The performance of the pulse shape analysis routine was thoroughly tested for digital signals sampled with a 500 MS/s and for less radioactive nuclei. As it

is said in Section 2.2.3, the sampling rate had to be reduced to 250 MS/s in this measurement, due to the large amount of data recorded by the TAC. For this reason, the performance of the pulse shape analysis routine had to be re-investigated for the lower sampling rate of 250 Ms/s and the real conditions of the experiment.

It is well known that BaF_2 crystals have an intrinsic alpha activity from the decay chains of ^{226}Ra and ^{228}Ra, impurities which are present in the crystals due to similar chemical properties of Ba and Ra. However, it is possible to distinguish alpha particles from γ-rays by pulse shape discrimination, thus reducing the intrinsic background produced inside the crystals. Furthermore, the alpha decay lines provide an excellent internal energy calibration which has been used to correct the gain shifts of the individual crystals. In Figure 3.3 a gamma and an alpha signals are shown. The signal on the left has a strong fast component and corresponds to a gamma particle. The signal on the right lacks the fast component and corresponds to an alpha particle.

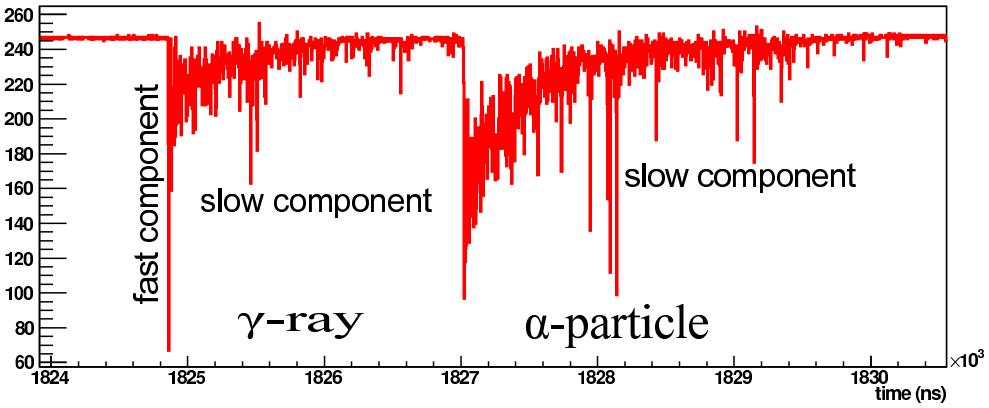

Figure 3.3: Example of the difference between a gamma (left) and an alpha (right) signal. The fast component of the signal is not observed for alpha particles.

The left panel of Figure 3.4 shows the two dimensional histogram used to separate the alphas and γ-rays in a ^{88}Y + ^{137}Cs calibration measurement, sampled at 250 MS/s. The horizontal axis represents ratio between fast amplitude to the fitted signal integral. For alpha particles, the fast component is strongly suppressed, thus showing a distribution at values below 2. On the contrary, the gamma rays show A_{fast}/Area ratios above 2, thus allowing an excellent separation. The vertical axis represents the ratio between the real signal width and the expected one taking into account the 620 ns decay mode. For real signals, the value should be close to unity, as it is the case for the alpha and γ-ray lobes. In this way, signals showing a ratio below 0.4 are labeled as noise, and can be suppressed efficiently. As it can be observed, the degree of mixing between the different lobes is negligible, thus proving that the 250 MS/s sampling rate is still acceptable for an efficient particle discrimination and noise suppression. The right panel of Figure 3.4 shows the energy deposition spectra for γ-rays (in red) and alpha particles (in blue).

As a final check, the data from an ^{88}Y + ^{137}Cs calibration measurement in both sampling rate conditions, 250 MS/s and 500 MS/s, were compared. The results are presented in Figure 3.5, where an example of the deposited

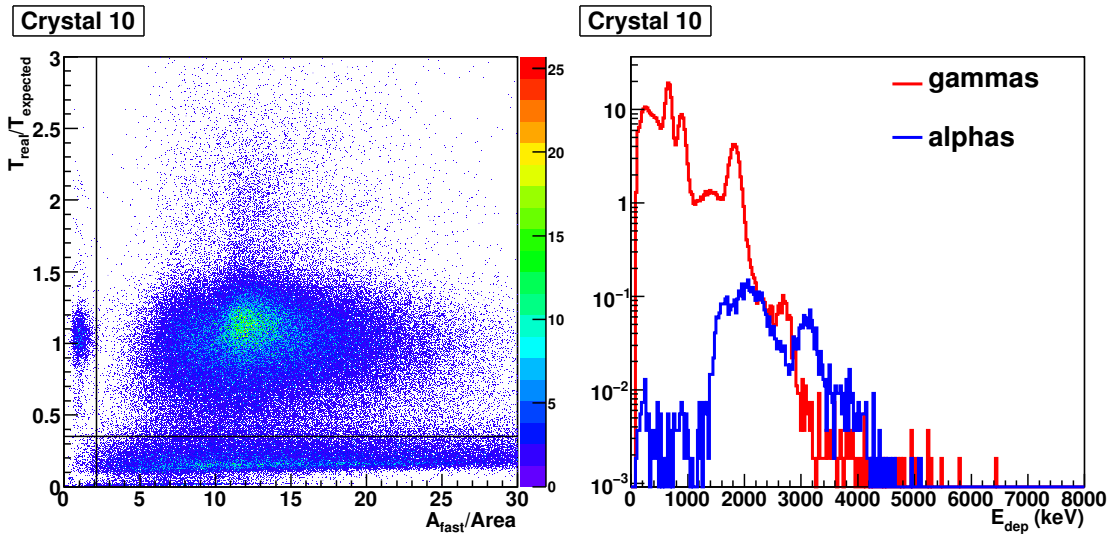

Figure 3.4: Pulse shape discrimination, for signals detected in crystal 10 in a ^{88}Y+^{137}Cs calibration measurement, sampled with 250 MS/s. See the text for more details.

energy spectra is presented in the left panel and shows that the same result is obtained for both configurations for one crystal. In the panel on the right, the integrals of the deposited energy spectra of all the BaF_2 crystals are presented, showing similar results for both configurations.

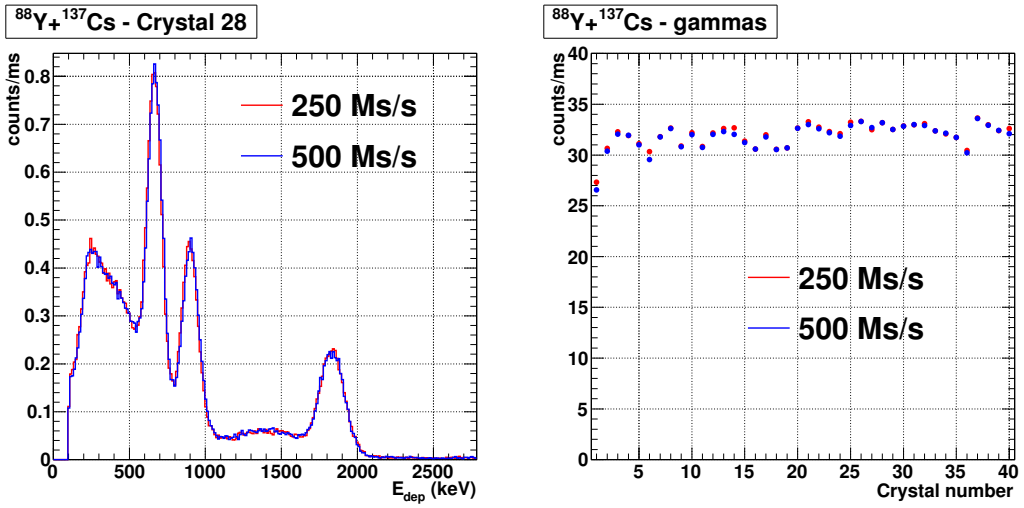

Figure 3.5: Comparison between the results obtained from the same ^{88}Y + ^{137}Cs calibration measurement, performed at both 250 MS/s and 500 MS/s. In the left panel, the deposited energy spectra in a single crystal. In the right panel, the integrals of the deposited energy spectra of each crystal.

The next step is to study the performance of the analysis routine at the very high counting rates in the ^{243}Am measurement. Figure 3.6 shows the same type of distributions than the ones presented in Figure 3.4, but for an ^{243}Am measurement. It can be observed in the right panel that despite the larger ^{243}Am counting rate, the pulse shape discrimination works well, since the alpha spectrum is similar to the one in Figure 3.4. There is a small fraction of low energy γ-ray particles that are detected as alpha particles. However, they are a negligible fraction of the total amount of γ-rays, about $\sim$0.1%, a similar quantity than the one observed in the calibration measurement (Figure 3.4).

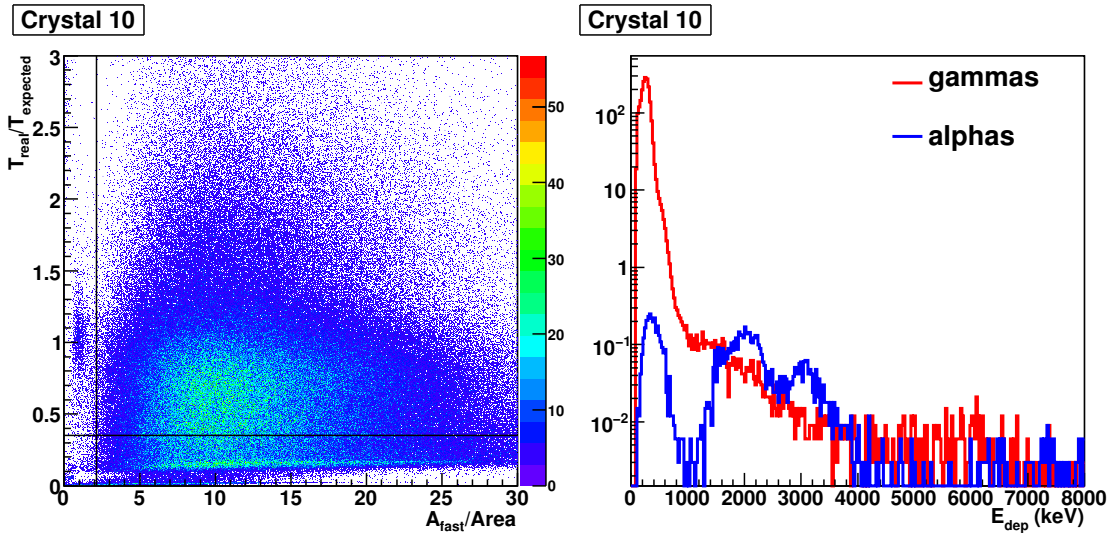

Figure 3.6: Pulse shape discrimination, for signals detected in crystal 10 in a ^{243}Am measurement, sampled with 250MS/s.

Another test was also performed by comparing the alpha spectra between two measurements with high and low counting rates. This comparison has been performed between an ^{243}Am measurement and an environmental background measurement (no beam and no sample), which is the one with the lowest counting rate. In Figure 3.7 the alpha counting rate of both measurements and for each BaF_2 crystal is compared. The lower part of the alpha spectra (see right panel of Figure 3.6) have not been taken into account to compute the counting rates, since they do not correspond to alpha particles. As it can be observed, both results are similar, indicating that the analysis routine is working properly also for high counting rates. Nevertheless, a detailed characterization of the behavior of the analysis routine at very high counting rate conditions is studied with more detail in Section 3.2.

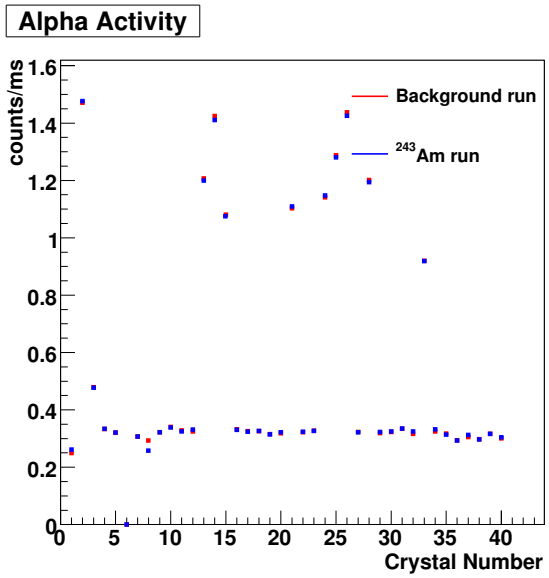

Figure 3.7: Alpha activity in each crystal, taken from an ^{243}Am run and an environmental background run.

3.2 Characterization of the dead time due to pulse pileup

One of the corrections which have to be applied to the measured data in the procurement of the experimental capture yield is related to the dead time in the detection system, which starts to be non-negligible for counting rates higher than a few hundreds of events per ms. Notice that the entire response of each BaF_2 module is digitized every 2 or 4 ns, and thus the detection system does not have a dead time as it is usually defined. However, if two signals are close enough, then the pulse shape analysis routine can have difficulties in resolving the pulse pile-up: either in identifying the two signals or in reconstructing correctly their areas (i.e. energy). In this manuscript the dead time is defined as the (variable) time during which two pile-upped signals are not reconstructed properly by the pulse shape analysis routine.

In previous n_TOF TAC analysis the characterization of the dead time was performed by assuming that, for each signal with energy E_1 followed by another signal with energy E_2, there was a specific time value $DT(E_1, E_2)$ so that if the two signals were separated less than $DT(E_1, E_2)$, then the second signal was not detected. Otherwise, both signals were detected. In both cases, no distortion of the energy values E_1 or E_2 were considered. This $DT(E_1, E_2)$ function was called dead time function, and it was assumed to be the same for all the BaF_2 detectors. It was used in the reconstruction process of the results obtained with the Monte Carlo simulations.

The mentioned dead time function, $DT(E_1, E_2)$, was obtained by analyzing the time distances between consecutive signals. In the saturated resonance at 4.9 eV of the ^{197}Au measurement, the counting rate is constant and high enough so that dead time effects are not negligible. If the time distance between signals histogrammed, as it is shown in Figure 3.8, it can be appreciated that below a given time distance, which was assumed to correspond to the dead time, the second signal is not detected. These dead time values were then calculated as a function of the energies of the first and the second signals. The resulting values are presented in the left panel of Figure 3.9, where it can be appreciated that, as expected, as higher is the energy of the first signal and lower the energy of the second

signal, higher is the dead time, since it is more difficult to detect a small signal after a big one than the opposite.

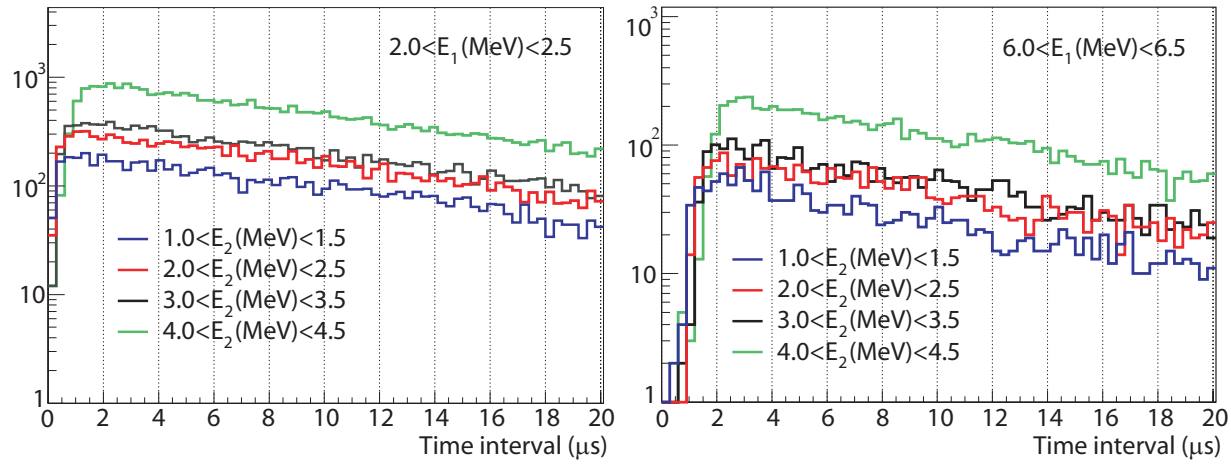

Figure 3.8: Time distance distribution for several E_2 ranges for E_1 between 2 and 2.5MeV and for E_1 between 6 and 6.5 MeV.

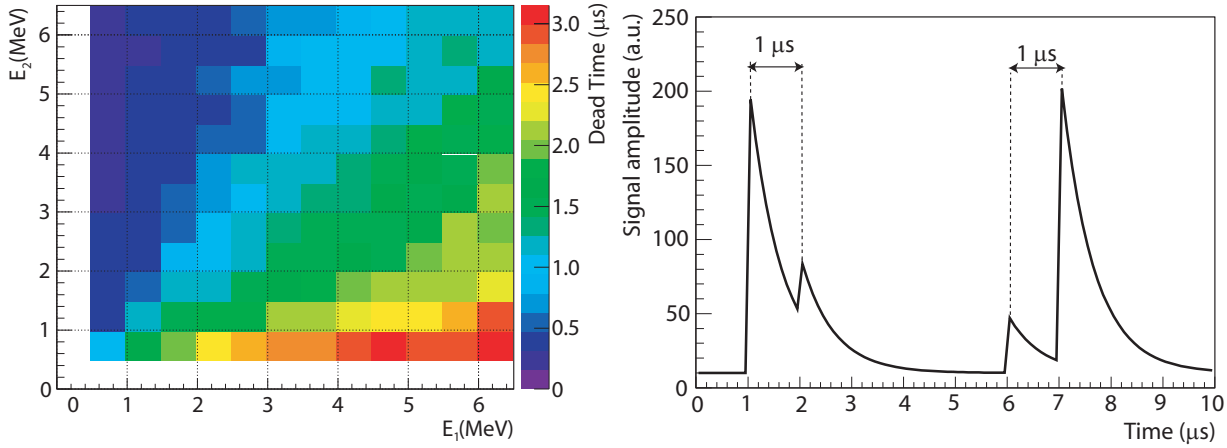

Figure 3.9: Dead time as a function of the energy of the first (E_1) and second (E_2) signals.

This dead time treatment was good enough for the previous n_TOF TAC measurement analysis, but the present measurement has a quite higher counting rate. In particular, the high ^{243}Am sample activity during the capture cross section measurement induced a background of 5.4 events/μs in the TAC. Thus, the average time distance

between two consecutive pulses is comparable to the 620 ns slow scintillation component of the BaF_2 signals. New techniques have been developed to characterize and correct for the pulse pileup and associated dead time effects.

In particular, three harmful situations which distort the data have been identified and treated:

1. The effect of the sample activity background on other measured backgrounds. The background in the TAC measurements, $C_{bkg}(E_n)$, is obtained from dedicated measurements. However, during the ^{243}Am sample measurement the detection of the background events is distorted by the dead time induced by ^{243}Am sample activity, whereas in the background measurement (in absence of the sample) they are not. This causes that the background from the dedicated measurements can not be subtracted directly from the capture data and corrections are needed. In other words, if the different sources of background are measured separately ($C_{bkg,1}(E_n)$, $C_{bkg,2}(E_n)$, ...) and the counting rates are low, then the total background (all the sources measured together) can be calculated as $C_{bkg}(E_n)$=$C_{bkg,1}(E_n)$+$C_{bkg,2}(E_n)$+... . If the counting rates of any of the background sources is high, as it is the case for a highly radioactive sample, then it will affect the detection of the other background sources, and so $C_{bkg}(E_n) \neq C_{bkg,1}(E_n)$+$C_{bkg,2}(E_n)$+...

2. The effect of the sample activity background on the detection of capture cascades. The detection efficiency of the TAC is obtained from Monte Carlo simulations. These Monte Carlo simulations include the generation of the capture cascades, the transportation of the γ-rays in the TAC geometry, and the reconstruction of the detected events. The high background counting rates affect the detection of the capture events in the real experiment, since the probabilities of random summing or pulse pile-up are sizable and it is necessary to include them in the simulation procedure.

3. The effect of capture cascades on subsequent capture cascades. The dead time which appears when the capture counting rates are high enough, usually at time-of-flights corresponding to neutron energies of the strongest resonances, must be corrected for the calculation of the capture yield.

Three different techniques have been developed for the treatment of theses three cases. All of them rely on the offline manipulation of the digitised signals.

3.2.1 Effect of the sample activity background on other measured backgrounds

The ^{243}Am decay γ-rays pile-up with background signals, thus distorting the energy distribution and the number of detected background counts during the capture measurement. However, the dedicated background measurements without ^{243}Am are not distorted by the sample activity. Thus, a method has been developed to distort artificially the data from the dedicated background measurements without ^{243}Am sample. Artificial raw data buffers were created by mixing the digitized signals from the background measurements with signals from an ^{243}Am activity measurement (^{243}Am sample in place, but without neutron beam). The resulting data buffers were analyzed afterwards with the pulse shape analysis routine, in the same way as for the real measured data buffers, so that the measured background signals were analyzed under the effect of the high sample activity.

The addition of the two type of digital data buffers was performed as follows. First, the constant baseline values b_1 and b_2 were calculated for each buffer. Then, the amplitude of the signal of the new created data buffer, $a_{Sum,i}$ (which goes from 0 to 255), at each data point position, i, was calculated according to $a_{Sum,i} = a_{1,i}+a_{2,i}-(b_1+b_2)/2$, where $a_{1,i}$ and $a_{2,i}$ are the amplitudes of the signals of the first and second data buffers, respectively, at the same position. If the resulting value was negative or greater than 255 it was set to 0 or 255, respectively.

The artificial data buffers created with this procedure correspond to a background measurement performed together with the detection of the sample activity, with the exception that the environmental background (measurement without sample and without neutron beam) has been included twice. They will be quoted in this manuscript as "Rad-measurements", to distinguish them from the "real" measurements. Thus, the Ti canning measurement distorted artificially by the sample activity will be called "Rad-Ti canning" measurement, the Empty measurement "Rad-Empty",...

The procedure has been validated by comparing the resulting deposited energy spectra in the TAC (E_{Sum}). In Figure 3.10 three different deposited energy spectra are presented: one corresponding to an ^{243}Am measurement (red), other corresponding to a Ti canning background measurement (green) and the latter to a Ti canning background measurement distorted artificially by the sample activity (blue). In the three cases the contribution of the events coming from the interaction of neutrons in the elements different than the sample or the Ti canning have been subtracted. It should be noticed that all the counts above E_{Sum}=6 MeV correspond to the interaction (elastic scattering or capture) of neutrons in the Ti canning. The total energy of the electromagnetic cascade which follows the ^{243}Am(n,γ) reactions can not exceed the neutron separation energy in the ^{244}Am nucleus, S_n=5.36 MeV, and the no-beam background events have even lower energies.

As it can be observed, there is a sizeable difference between the deposited energy spectrum corresponding to the Ti canning in the ^{243}Am measurement (red) with the one obtained in the background measurement (green). When the corrections described in this section are applied (blue), the difference disappears.

The same procedure was also used as well to characterize the effect of the ^{243}Am activity in the detection of the alpha activity spectra of the crystals, which are used to recalibrate the energy of the detectors run by run. As it is explained with detail in Section 3.3.2, the high counting rate due to the ^{243}Am activity induces a continuous change in the energy calibration of the detectors. This change was corrected by comparing the displacement of the alpha activity spectrum of each crystal between the different runs. For this reason, it is important to characterize the changes in the alpha spectra due to the ^{243}Am activity.

It was shown in Figure 3.7 that the dead time induced in the detection of the alpha particles is very small in terms of total counting rate, i.e., in the integral of the alpha spectra. However, some change in the detected energy (or A_{Slow} parameter) is expected. This change has been characterized by comparing the alpha spectra of a real measurement and the alpha spectra of the same measurement with the corrections described in this section (the real measurement versus the "Rad-measurement")[1].

The characterization were performed by calculating a "multiplication factor" for each crystal, which is defined as the average increase of the detected alpha energy due to the ^{243}Am activity signals. As an example, the left panel of Figure 3.11 presents three different alpha spectra: one obtained from the normal measurement (solid red); one obtained from the corresponding Rad-measurement (solid blue), which is similar to the first one, but with a little displacement to higher energies; and the latter spectra multiplied by a factor in such a way that it matches the first alpha spectrum (dotted blue). This factor is, in this case, the inverse of the "multiplication factor". In the right panel of the Figure, the multiplication factors due to the ^{243}Am activity of all the detectors are presented.

[1] Notice that the Rad-measurements are obtained by mixing two different measurements, so two different alpha spectra are present in each BaF_2 crystal: one for each measurements involved (^{243}Am activity and the other). However, both alpha spectra can be separated by looking at the detection time of each alpha particle.

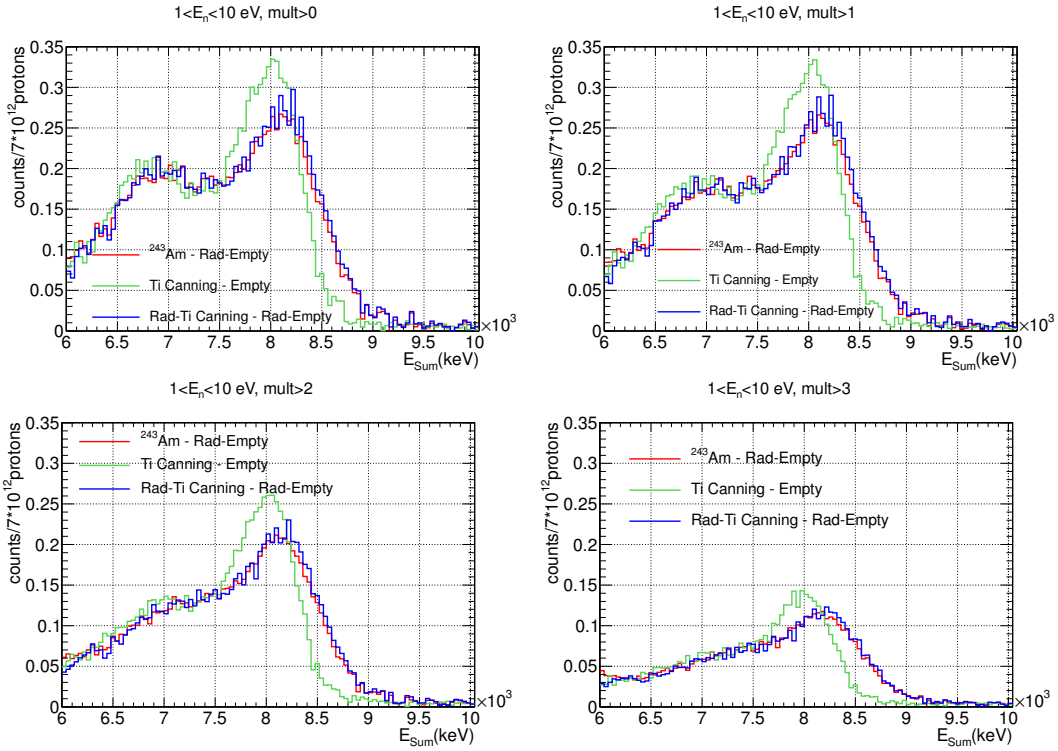

Figure 3.10: Comparison between the deposited energy spectra for the ^{243}Am, the Ti Canning and the Rad-Ti Canning measurements in the high deposited energy region. The Rad-Empty measurement has been subtracted from the ^{243}Am and the Rad-Ti Canning measurements, and the Empty measurement to the Ti Canning measurement, leaving in all the cases only the part of the spectra corresponding to neutron interaction with the Ti capsule.

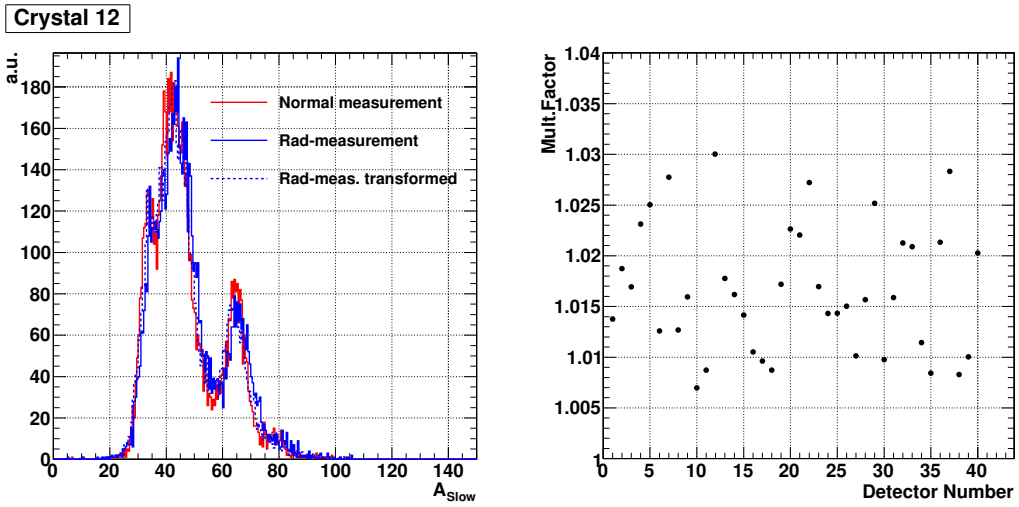

Figure 3.11: Example of an alpha spectrum displaced by the effect of the ^{243}Am activity (left) and average detected alpha energy displacement ("multiplication factor") for each crystal (right).

3.2.2 Effect of the sample activity background on the detection of capture cascades

The detection efficiency of the n_TOF TAC is calculated from Monte Carlo simulations. In the entire simulation process, which is described in detail in Section 3.5, it is necessary to include some experimental effects, such as the energy resolution of the detectors and the pulse pileup. The characterization of the latter is described in this section and in the next one.

The detection of a capture event can be affected by another event if both of them are close in time. This second event can be (i) another capture event or (ii) a background event. The first case might be important in the vicinity of strong resonances, where the counting rate can increase significantly, and it will be treated in the next section. The second case is usually negligible, but in this measurement the sample activity was high enough to affect the detection of the capture cascades. The dead time associated to other sources of background with lower counting rates was neglected.

The effects of the high sample activity in the detection of capture events can be divided in:

1. A background event detected by a certain number of BaF_2 crystals (one or more) can be in coincidence with a capture event detected by other crystals. In this case, the total energy of the capture event and its multiplicity will be increased, but the detection of the individual capture signals would not be affected.

2. The detection of an individual capture γ-ray signal can be affected by a background signal, if both γ-rays hit the same BaF_2 close in time. In this case, it is possible to miss or detect a capture signal with the wrong energy.

The first effect has been taken into account in the reconstruction of the Monte Carlo as follows. Experimental data (energies and multiplicities) from the ^{243}Am activity measurement were added to the Monte Carlo simulated capture

events. The addition of these experimental data was performed randomly, taking into account the experimental counting rate (∼5.4 counts/μs) and the total energy and multiplicity distribution probabilities.

The second effect was taken into account by the following method. Since the activity background is constant in time, the limitations of the pulse shape analysis routine can be characterized as a global effect of the activity signals in the capture signals, and will depend only on the BaF_2 crystal and on the deposited energy by the capture γ-ray. What has been done is to take a ^{197}Au measurement and an ^{243}Am activity measurement. The raw data buffers of both measurements were mixed in the same way as it is described in the previous section. Then, the resulting artificial data buffers were analyzed with the pulse shape analysis routine, and compared with the analysis of the real ^{197}Au measurement. This procedure allows to study the differences between detecting signals with and without the effect of the sample activity, in the entire γ-ray energy range of interest and for all the BaF_2 detectors.

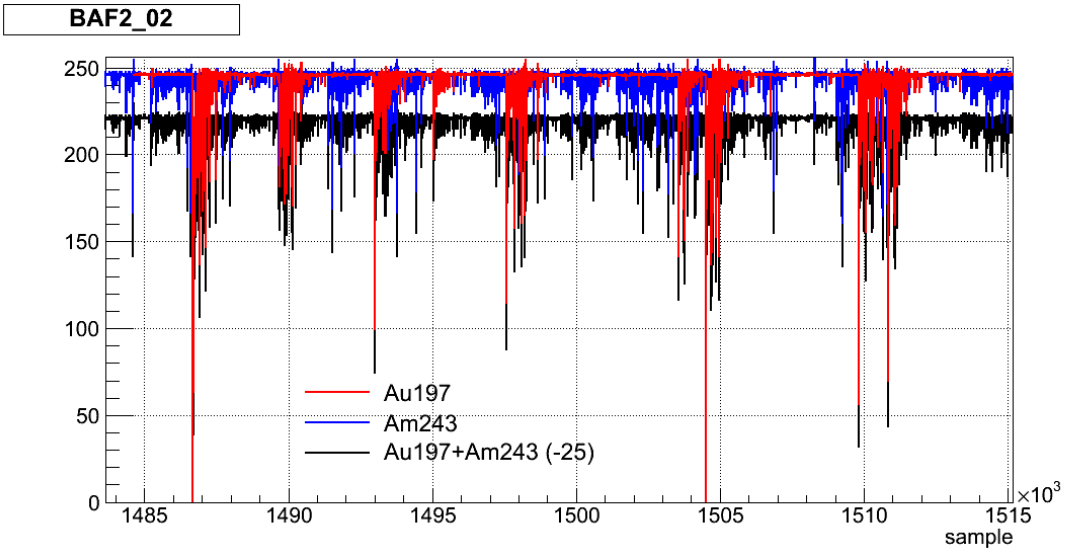

Figure 3.12: Example of a ^{197}Au (red) and an ^{243}Am (blue) buffers, together with the sum of both of them (black), displaced 25 channels down.

The comparison was performed signal by signal: for each signal detected by the analysis routine in the ^{197}Au buffer, it was verified if it was also detected in the new buffer at the same time or if it was masked by a radioactivity background signal. If detected, the difference between the reconstructed energies of the original and the distorted signals was computed. In this way it was possible to characterize the effect of the sample activity background in the rest of the detected signals in terms of:

1. A function for each BaF_2 crystal, $P_{CR}(E_\gamma)$, which provides the probability that the analysis routine does not detect a γ-ray signal in the BaF_2 crystal CR due to the background induced by the ^{243}Am activity, as a function of the detected energy of the signal, E_γ. This function, averaged over all the BaF_2 crystals, is presented in the left panel of Figure 3.13.

2. One probability distribution, $P_{E_\gamma}(\Delta E_\gamma)$, which provides the probability distribution of $\Delta E_\gamma = E_{\gamma,rad} - E_\gamma$, where E_γ is the detected energy of the signal without ^{243}Am activity and $E_{\gamma,rad}$ the detected energy of the signal when it is distorted by the ^{243}Am activity signals, as a function of E_γ. In this case, the result has been averaged over all the crystals. The parametrization of the distribution in terms of E_γ was performed by dividing the energy range of interest in 27 energy intervals[2] and calculating a $P_{E_\gamma}(\Delta E_\gamma)$ distribution for each of these intervals. A few examples of these distribution functions can be found in the right panel of Figure 3.13.

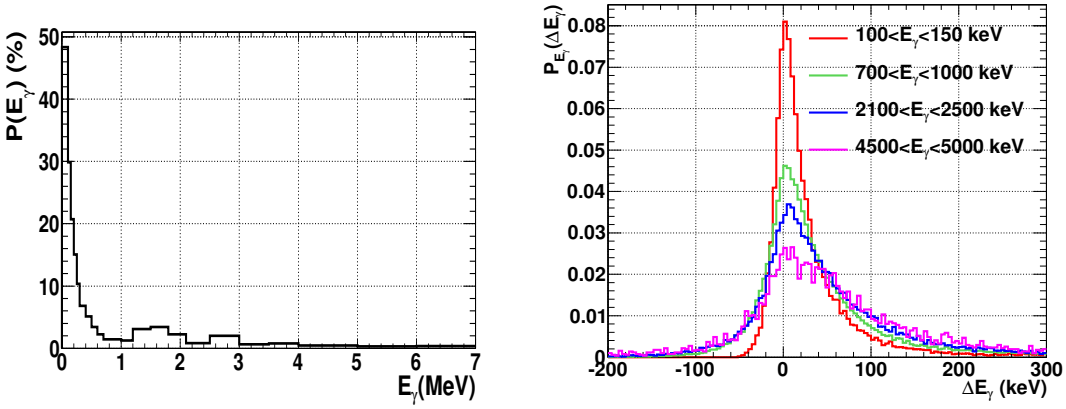

Figure 3.13: Examples of the characterization of the global effect of the ^{243}Am activity in the detection of γ-ray particles. In the left panel, the probability of not detect a γ-ray particle, as a function of its detected energy, averaged over all the BaF_2 detectors. On the right panel, examples of the characterization of the change in the detected energy of an individual γ-ray signal due to the sample activity.

These functions, $P_{CR}(E_\gamma)$ and $P_{E_\gamma}(\Delta E_\gamma)$, are used in the reconstruction of the Monte Carlo data: the $P_{CR}(E_\gamma)$ is used to determine, for every signal, if the simulated signal is detected or not; and the $P_{E_\gamma}(\Delta E_\gamma)$ is applied to each detected signal, to randomize the detected energy. This procedure has been also validated with the Rad-Ti canning and Rad-Au measurements, as it is shown at the end of Section 3.5.4.

3.2.3 Effect of capture cascades on subsequent capture cascades

The purpose of this method is to characterize the dead time induced by capture signals in other capture signals. This effect is important when the capture counting rates are high, usually close to the resonance energies.

The method can be described as follows. First, a certain number of γ-ray signals are selected from the recorded data buffers and stored in a separated file. Only isolated signals are considered, without any observed pile-up with other γ-ray or alpha signals. The buffers have been taken from a low counting rate measurement and for all the

[2]The energy boundaries of these intervals, in units of keV, were: 50, 100, 200, 300, 400, 500, 600, 700, 800, 900, 1000, 1200, 1400, 1600, 1800, 2000, 2300, 2600, 3000, 3400, 3800, 4200, 4600, 5000, 5500, 6000, 6500, 7000.

different BaF_2 detectors, covering the entire energy range of interest (100 keV to 10 MeV). In a second stage, pairs of these signals are stored in artificial data buffers, separated by different time distances. Then, the comparison of the analysis of these artificial data buffers with the analysis of the isolated signals allows to characterize the dead time.

As an example, two signals separated by different time distances and analyzed by the pulse shape analysis routine are presented in Figure 3.14. In the top-left panel, the separation between them is high enough so they are considered as isolated signals. In the top-right panel, the signal on the left modifies the shape of the signal on the right in such a way that the pulse shape analysis routine is not capable of detecting it as a γ-ray signal (in dotted lines, signals which are not considered as γ-rays by the pulse shape analysis routine). In the bottom-left panel, both signals are detected, but their energies have been changed significantly. Finally, in the bottom-right panel, the signal on the right is not detected and the energy value of the left signal provided by the pulse shape analysis routine is close to the sum of the energies of both signals when they are isolated.

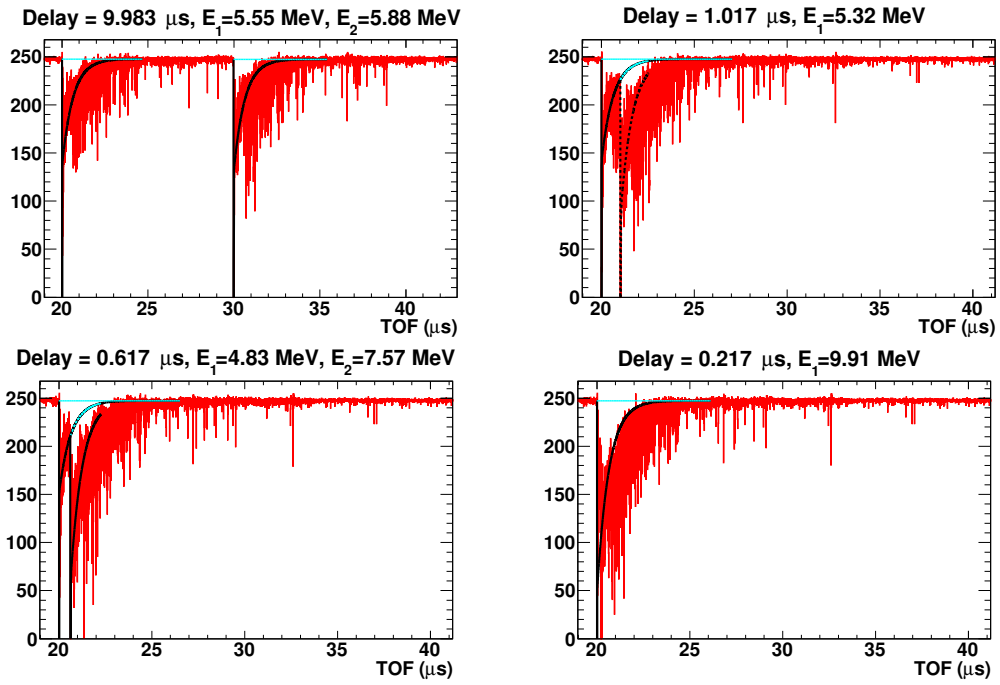

Figure 3.14: Detection of the same two signals separated different time distances. Only the signals presented in solid lines are identified as γ-ray particles by the pulse shape analysis routine. In the top of each panel, the time separation between them (Delay), the energy of the signal on the left (E_1), and the energy of the signal on the right (E_2).

These examples show how the digitized signals can be manipulated in order to characterize the dead and energy distortions induced by the pulse pileup. In the case of the analysis of the $^{243}Am(n,\gamma)$ measurement, 50 isolated signals for each one of the 40 BaF_2 detectors and for 27 different energy intervals were stored. Then, 5000 pairs of

signals were generated for each detector and analyzed. Each pair of signals was analyzed with 300 different time separations uniformly distributed between 0 and 10 μs. The dead time was characterized from the results of all these analyses with:

1. A function, $P(E_1, E_2, \Delta t)$, which provides the probability that the pulse shape analysis routine does not detect a signal with energy E_2 which follows a signal with energy E_1, both of them separated by a time distance Δt.
2. Probability distributions, $P_{\{E_1,E_2,\Delta t\}}(\xi)$, where ξ defines the change in the detected energy of the first signal, E_1, when the second signal, separated by a time Δt and with energy E_2, is not detected. The change was parametrized as $E_1' = E_1 + \xi E_1$, where E_1 is the detected energy of the signal when it is isolated and E_1' when it is followed by the (non-detected) second signal.

In both cases the results were averaged over the 40 BaF_2 crystals. For the $P(E_1, E_2, \Delta t)$ function, the energy values, E_1 and E_2, were discretized in the 27×27 energy interval pairs, and the Δt values in the 300 time separations. For each energy interval pair, ten different $P_{\{E_1,E_2,\Delta t\}}(\xi)$ distributions were obtained, one for each Δt interval uniformly distributed between 0 and 2 μs. Examples of the $P(E_1, E_2, \Delta t)$ projections are presented in Figures 3.15 and 3.16, and examples of $P_{\{E_1,E_2,\Delta t\}}(\xi)$ distributions are given in Figure 3.17.

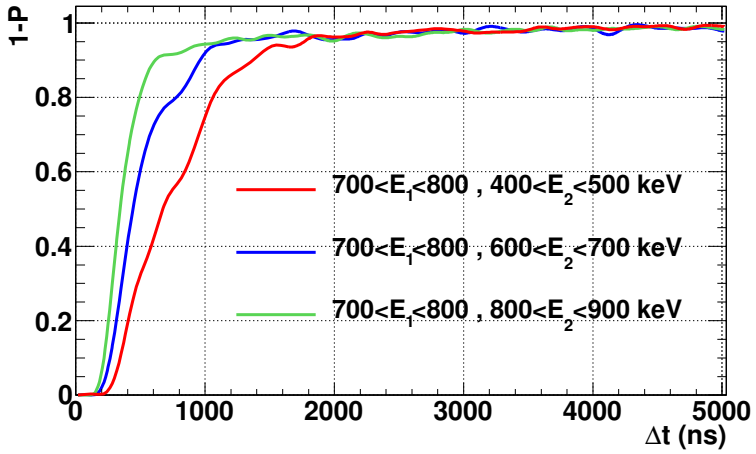

Figure 3.15: Projections of the $P(E_1, E_2, \Delta t)$ function, for different energy interval pairs.

This method has been validated using the saturated resonance at 4.9 eV of the ^{197}Au measurement. First, the deposited energy spectra obtained in the tail of the resonance were reproduced with Monte Carlo simulations, where the dead time effects are negligible. Then, the same capture cascades were simulated to reproduce the deposited energy spectra in the saturated part of the resonance, where the dead time effects are important. The results of these simulations are presented in Section 3.5.4.

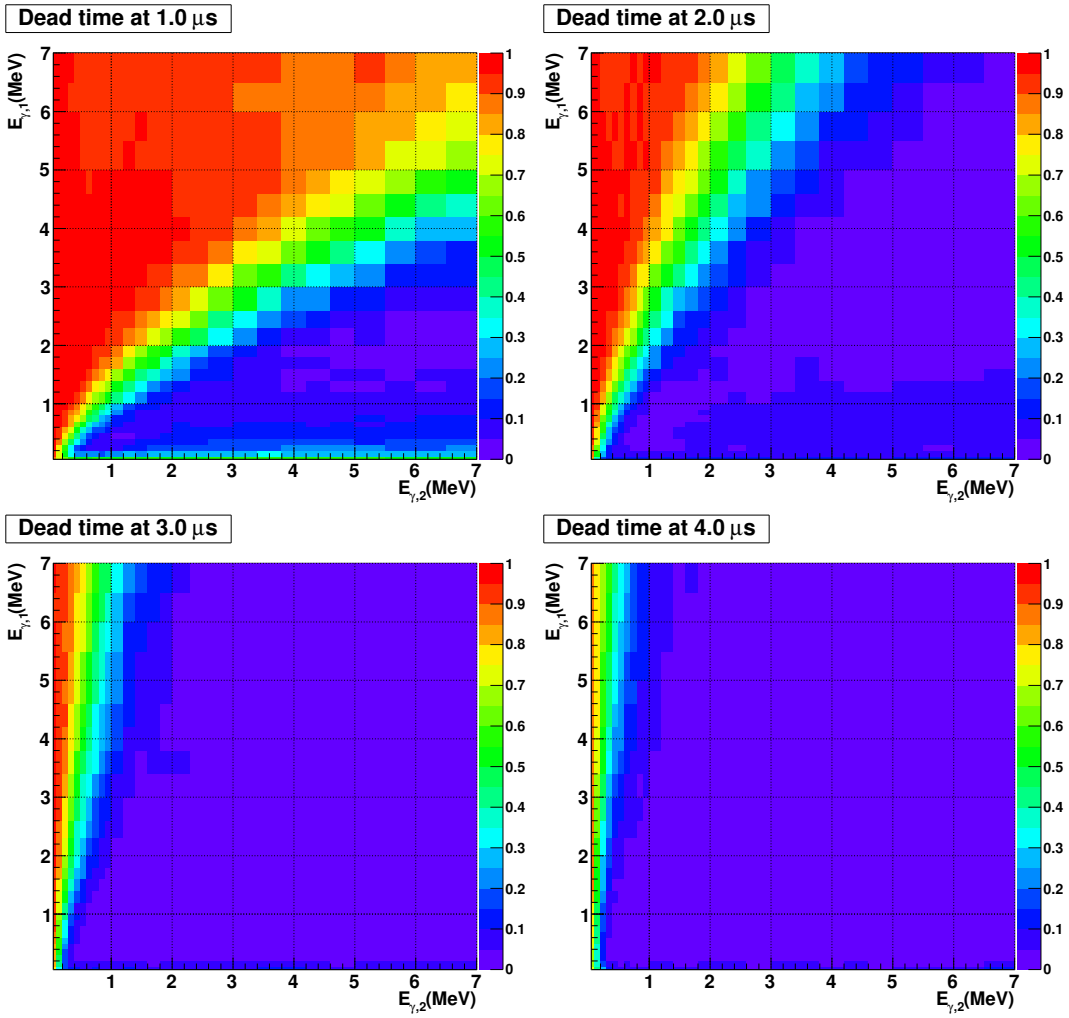

Figure 3.16: Probabilities of not detecting a signal with energy E_2, given by the horizontal axis, which follows a signal with energy E_1, given in the vertical axis, both of them separated by different time distances; i.e., projections of $P(E_1, E_2, \Delta t)$ for different Δt values.

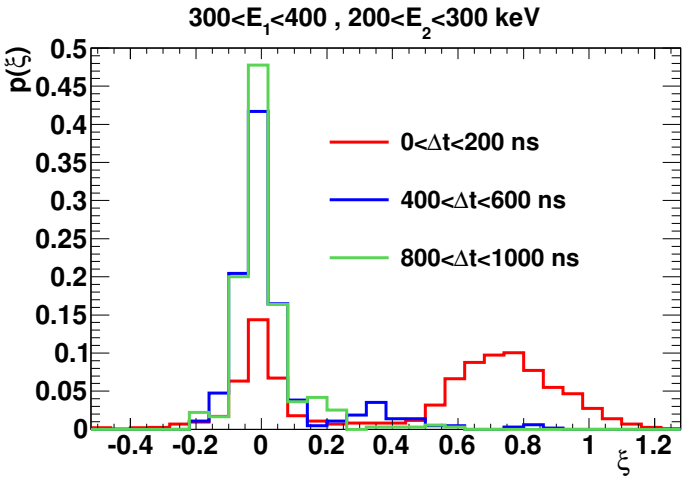

Figure 3.17: Examples of $P_{\{E_1,E_2,\Delta t\}}(\xi)$ distributions, for a fixed energy interval pair and different Δt intervals.

3.3 Energy calibration

In this section we describe the energy calibration performed to the BaF_2 modules. This energy calibration must be done before making the coincidences in the TAC. It is important for the background subtraction, due to the conditions in E_{Sum} applied to the detected events, and for the accurate determination of the detection efficiency.

The energy calibration was performed with three standard calibration sources: ^{137}Cs (E_γ=661.7 keV), ^{88}Y (E_γ=898.0 and 1836 keV) and Pu/C (E_γ=6131 keV). The calibration measurements were made at the beginning at at the end of the two ^{243}Am(n,γ) measurement periods (Section 2.4), and also in the middle of the second period. A schematic view is presented in Figure 3.18, were the calibrations are presented in red and the rest of the measurements in blue, and more detailed information can be found in Tables 2.3 and 2.4. The calibration performed to the three standard calibration sources is presented in Section 3.3.1.

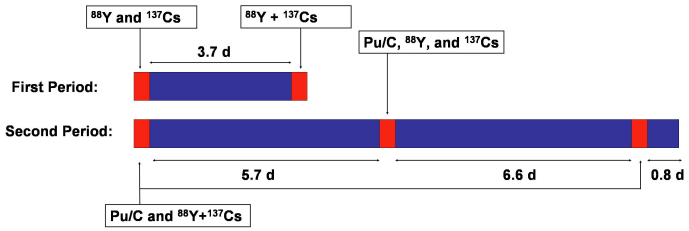

Figure 3.18: Schematic view of the calibrations performed during the ^{243}Am measurement. "^{88}Y+^{137}Cs" means that these two calibration sources were measured together, at the same time.

It was observed that the high ^{243}Am activity counting rate induced appreciable changes in the gains of the BaF_2 detectors. Thus, it was not possible to use directly the energy calibration resulting from the calibration runs along the rest of the measurement. In order to solve this problem, the changes in the alpha energy spectra were used to monitor and correct the changes in the gains of the BaF_2 detectors along the time. A set of "multiplication factors" was obtained, each of them relating the gain of a detector in a certain run with the gain of the detector in a reference run. With this information, the results obtained in the calibration runs were propagated to the rest of the runs, thus performing a different energy calibration for each run. This procedure is described in Section 3.3.2.

Finally, the energy resolutions of the crystals were obtained with the same tool used to perform the energy calibrations, and it is presented in Section 3.3.3.

3.3.1 Calibration performed with the γ-ray sources

There area of the fitted signal (see Equation 3.2) is $A = \int_{-\infty}^{\infty} b(t) - s(t)\,dt = e \cdot A_{fast} \cdot \tau + A_{slow}(620ns - \tau)$, which is in good approximation proportional to A_{slow}, since $\tau \ll 620\,ns$. For this reason, linearity between the A_{slow} parameter and the deposited energy in the detectors is expected, and this is the parameter which were used to obtain the energies of the detected signals.

The correspondence between the A_{slow} parameter and the deposited energy in the detectors was obtained by calculating the position of the different peaks observed in the calibration measurements. In the case of the ^{137}Cs, ^{88}Y and ^{137}Cs+^{88}Y measurements the peaks observed in the A_{slow} distribution spectra were fitted to a Gaussian shape and a linear background, as it is shown in Figure 3.19. In the case of the Pu/C spectra the peak at 6131 keV and the escape peak with an energy of 6131-511 keV were fitted to a straight line, representing the background, and two Gaussians for the peaks. The sigmas of the Gaussians were fixed to the same value (the energy resolution should be approximately the same) and the separation between them was fixed to a factor of (6131-511)/6131, because one of the peaks is an escape peak. Two examples Pu/C calibrations are presented in Figure 3.20, where it can be observed that in the right panel the two peaks are resolved, what is not the case of the left panel, due to a worse energy resolution.

The values obtained with these calibration measurements were then propagated to each run with the mentioned multiplication factors, according to the following expression:

$$A_{slow}^{cr,run2}(E_\gamma) = MF_{cr,run1,run2} A_{slow}^{cr,run1}(E_\gamma)$$

where $A_{slow}^{cr,run1}(E_\gamma)$ is the A_{slow} parameter of the BaF_2 detector cr corresponding to a γ-ray energy E_γ , which has been obtained from the calibration run "run1"; $A_{slow}^{cr,run2}(E_\gamma)$ is the equivalent position of the $A_{slow}^{cr,run1}(E_\gamma)$ value in the run "run2", after multiplying by $MF_{cr,run1,run2}$.

Once the calibration points were appropriately propagated to each run, a parabolic energy calibration of the type $E_\gamma(A_{slow})=A_{slow}(a_1+a_2A_{slow})$ was applied to each crystal, also run by run. The need of a parabola instead of a linear fit can be understood from Figure 3.21. A linear calibration performed with the three lower energy data points (red) does not fit the higher energy point. On the other hand, a linear fit performed with the four data

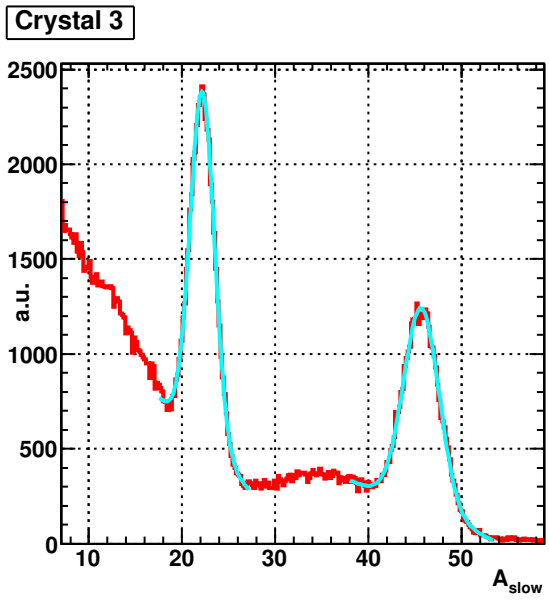

Figure 3.19: Energy calibration performed from a ^{88}Y measurement.

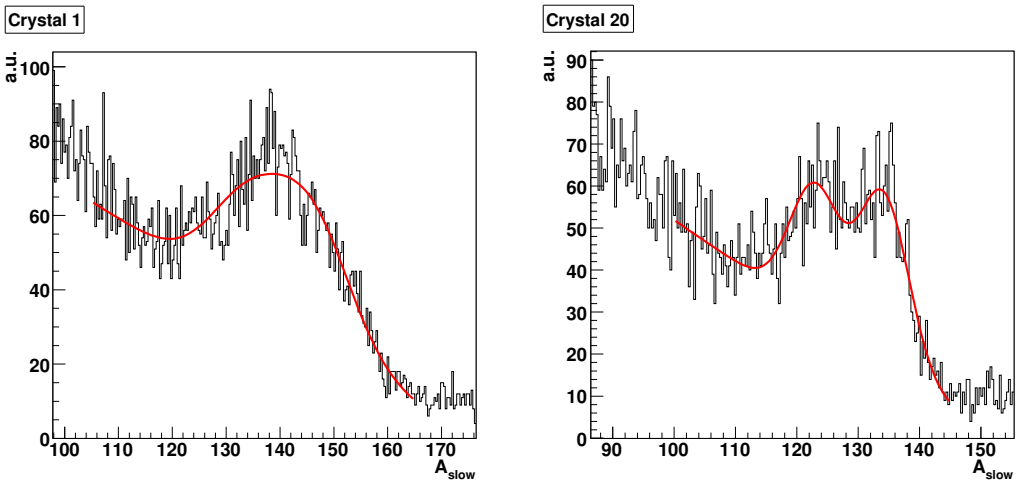

Figure 3.20: Energy calibration performed from a Pu/C measurement.

points (green) deviates significantly from the previous mentioned fit at low energies, which goes close to (0,0), as it is expected. This suggests that the relation between A_{slow} and E_γ is not exactly linear and a parabolic fit (blue) was finally taken, since it fits all the data points and goes through (0,0).

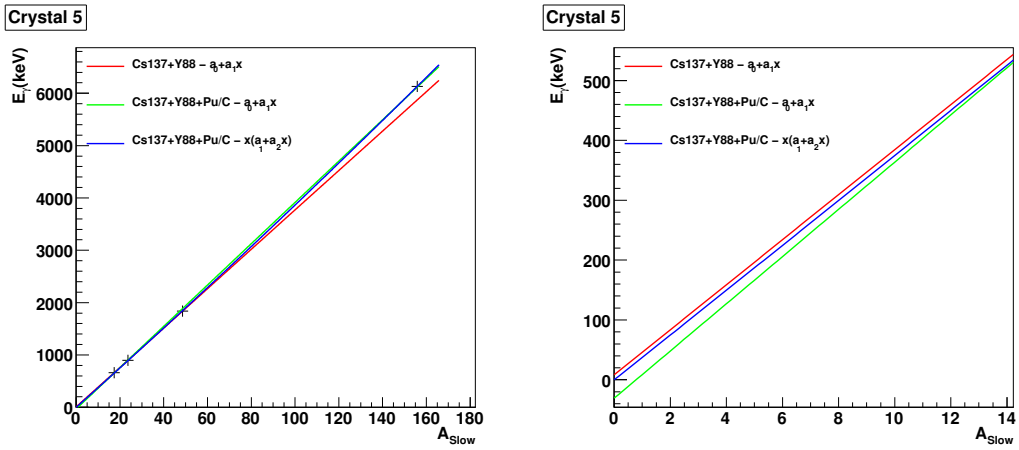

Figure 3.21: Different energy calibrations. The panel on the right is a zoom of the panel on the left. The red line is the result of a linear calibration with the three lower energy points, excluding the Pu/C value; the green line is the result of a linear calibration with all the data points; and the blue line is the result of a parabolic calibration, f(x)=x(a_1+a_2x), with all the data points.

3.3.2 Calibration run by run

All the BaF_2 detectors with the exception one have an intrinsic activity coming from the decay chain of ^{226}Ra impurities. The decay chain of ^{226}Ra is the following:

$$^{226}Ra(1600y) \xrightarrow[4.8\,MeV]{\alpha} {}^{222}Rn(3.8d) \xrightarrow[5.5\,MeV]{\alpha} {}^{218}Po(3.1m) \xrightarrow[6.0\,MeV]{\alpha} {}^{214}Pb(27m) \xrightarrow{\beta^-}$$
$$^{214}Bi(20m) \xrightarrow{\beta^-} {}^{214}Po(164\mu s) \xrightarrow[7.7\,MeV]{\alpha} {}^{210}Pb(22y) \xrightarrow{\beta^-} {}^{210}Bi(5d) \xrightarrow{\beta^-}$$
$$^{210}Po(138d) \xrightarrow[5.3\,MeV]{\alpha} {}^{206}Pb(stable)$$

$$^{228}Ra(5.8y) \xrightarrow{\beta^-} {}^{228}Ac(6.1h) \xrightarrow{\beta^-} {}^{228}Th(1.9y) \xrightarrow[5.4\,MeV]{\alpha} {}^{224}Ra(3.7d) \xrightarrow[5.7\,MeV]{\alpha}$$
$$^{220}Rn(56s) \xrightarrow[6.3\,MeV]{\alpha} {}^{216}Po(0.15s) \xrightarrow[6.8\,MeV]{\alpha} {}^{212}Pb(11h) \xrightarrow{\beta^-} {}^{212}Bi(61m) \longrightarrow$$
$$\longrightarrow \begin{cases} \xrightarrow{\beta^-} {}^{212}Po(310ns) \xrightarrow[8.8\,MeV]{\alpha} {}^{208}Pb(stable) \\ \xrightarrow[6.1\,MeV]{\alpha} {}^{208}Tl(3.1m) \xrightarrow{\beta^-} {}^{208}Pb(stable) \end{cases}$$

where the energies listed correspond to the energy of the alphas emitted in the decays. Some of these decays emit as well a significant amount of γ-rays, which are part of the intrinsic background observed in the crystals. The intensity of the alpha spectra due to the ^{226}Ra decay chain is much higher than the intensity due to the ^{228}Ra decay chain, with alpha energies of E_α=4.8, 5.3, 5.5, 6.0 and 7.7 MeV. An example of alpha spectra, in terms of the A_{slow} parameter, is presented in Figure 3.22, where the highest energy peak corresponds to the alpha emitted by the ^{214}Po, of 7.7 MeV, the lowest energy peak to the alpha emitted by the ^{226}Ra, of 4.8 MeV, and the part in

the middle corresponds mainly to the decays of ^{210}Po, ^{222}Rn and ^{218}Po, with energies E$_\alpha$=5.3, 5.5 and 6.0 MeV, respectively. These lower energy part, with A$_{slow}$<20, corresponds to γ-rays that have not been well discriminated. The amount of γ-rays is negligible compared with the total amount of γ-rays detected at those energies (see 3.1).

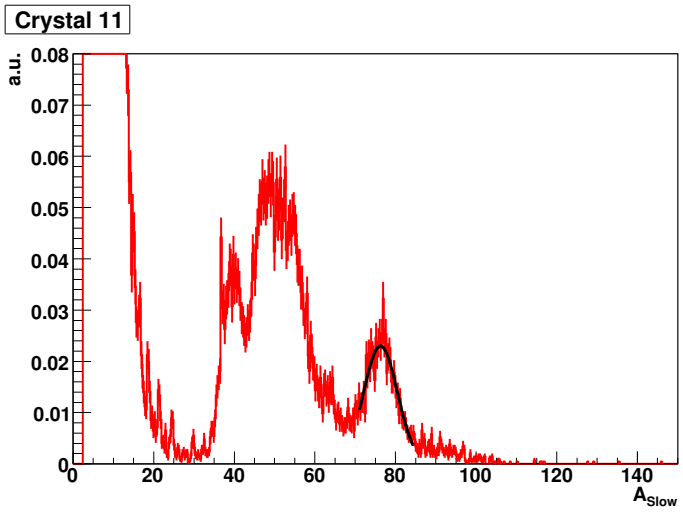

Figure 3.22: Alpha A$_{slow}$ spectrum with a Gaussian fit in the higher energy peak.

The evolution of the centroid of the high energy alpha peak in Figure 3.22 was used to monitor the change in the energy calibration over the time. This was done run by run, by fitting a Gaussian to it. An example of the evolution of this peak is presented in Figure 3.23, where the run numbers covered corresponds with the second period of the ^{243}Am measurement (see Figure 3.18 and/or Table 2.4). This period starts with calibration runs, followed by a ^{243}Am capture measurement (5.7 days). After them, a few calibration runs, followed by a ^{197}Au measurement (1.7 days) and another ^{243}Am capture measurement (4.2 days). At the end, calibration runs and background dedicated measurements were performed.

It can be observed in Figure 3.23 that during the ^{243}Am measurement, with a huge counting rate, the gain of the detectors was decreasing over the time, whereas during the ^{197}Au measurement the gain tended to recover to the original value. The gain varied continuously, and it did not stabilize even after a few days of measurement. In addition, sudden drops in the gain were observed during measurements without beam. Notice that part of this effect is related with the fact that when the ^{243}Am activity is present, the alpha particles are detected with higher energy, ~1-3% according to Figure 3.11.

The changes between the alpha spectra of two different runs allow to calculate the change in the calibration between those runs. However, instead of using the mentioned high energy alpha-peak, the multiplication factor was obtained by transforming linearly one spectrum to match the other; i.e., the A$_{slow}$values of one of the spectra are multiplied by a value in order to match the other spectrum, as it is presented in Figure 3.24.

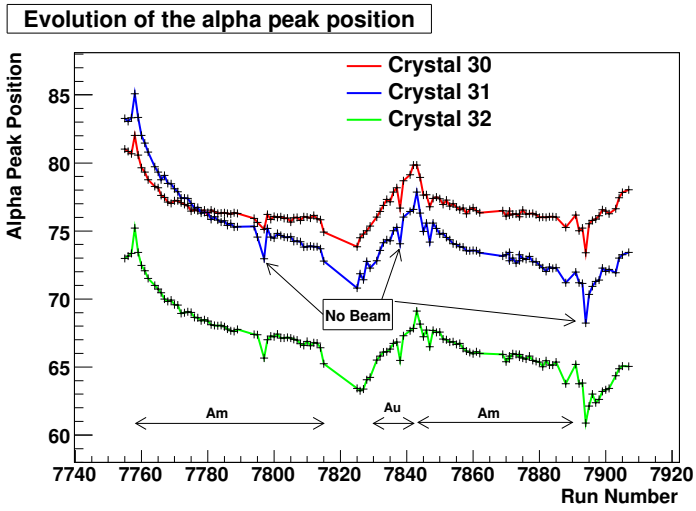

Figure 3.23: Evolution of the alpha peak position for three different crystals. The observed behavior is similar in the rest of the BaF_2 crystals.

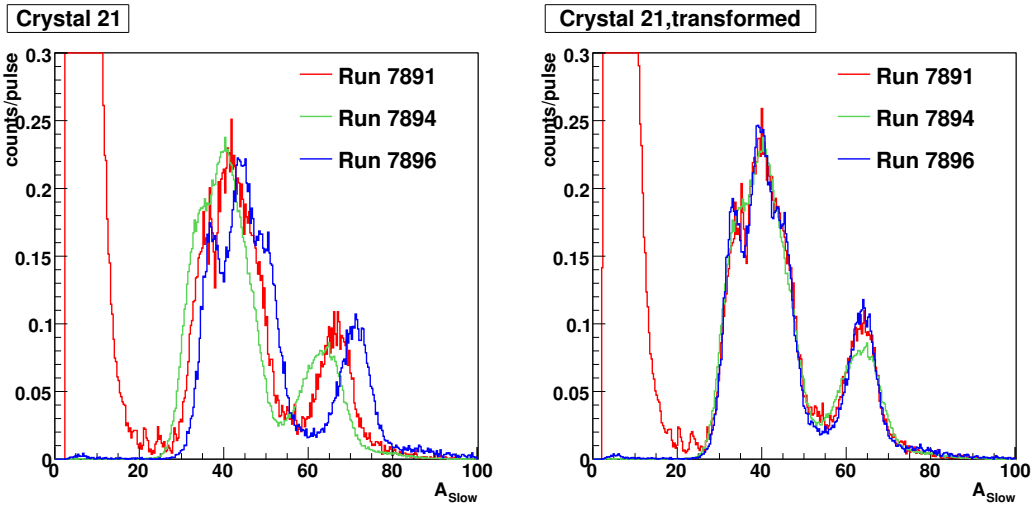

Figure 3.24: Example of the alpha spectra of three different runs (left), and the transformation of them to fit a reference alpha run (right), which is run 7894 (no beam, no source), by multiplying them by the calculated multiplication factor.

Two additional methods were used to check this procedure. The first one was to obtain the multiplication factors with the γ-ray spectra, instead of the alpha spectra, following the same method. The disadvantage of using γ-ray spectra is that the the comparison can be performed only between runs of the same measurement (for example,

it can not be used to compare a run corresponding to a ^{243}Am(n,γ) measurement with a background run). An example of the comparison between both multiplication factors is presented in Figure 3.25. It can be observed that in the left panel the obtained values are practically the same, whereas in the right panel the multiplication factors obtained with the alpha spectra are around 1% higher than the ones obtained with the γ-ray spectra. The differences in the rest of the BaF_2 crystals are in most of the cases negligible, as the ones observed in the left panel, and in some of them similar to the ones on the right panel. Thus, it can be concluded that, on average, the differences between the results obtained with the two methods are lower than 1%.

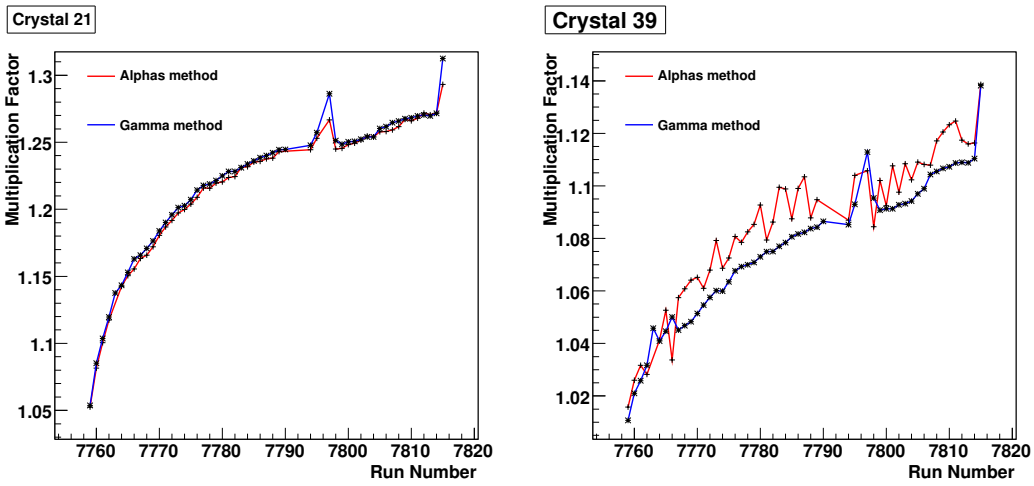

Figure 3.25: Comparison between the multiplication factors obtained using the alpha and γ-ray spectra for two crystals.

The second check was to compare the A_{slow} values corresponding to the same calibration energy , but obtained in different calibration runs (obtained from different ^{137}Cs measurements, for example), after propagating them to the same run, with the calculated multiplication factors. This was done with the four calibration energy points used in the the second period (see Figure 3.18) of the ^{243}Am measurement, where the calibration was performed three times: at the beginning, in the middle and at the end of the measurement. Results are presented in Figures 3.26 and 3.27, showing that most of the obtained differences are below 1%.

The multiplication factors were calculated for every crystal and every run, taking as a reference run an environmental background run (no beam, no sample). With this information, the results of the calibration measurements were propagated to the rest of the runs, thus obtaining an energy calibration for each run and each crystal. In the case of the runs with the ^{243}Am sample in place, it was taken into account that the alpha spectra are distorted due to the ^{243}Am decay γ-rays. The multiplication factors had to be corrected with the values presented in Table 3.11.

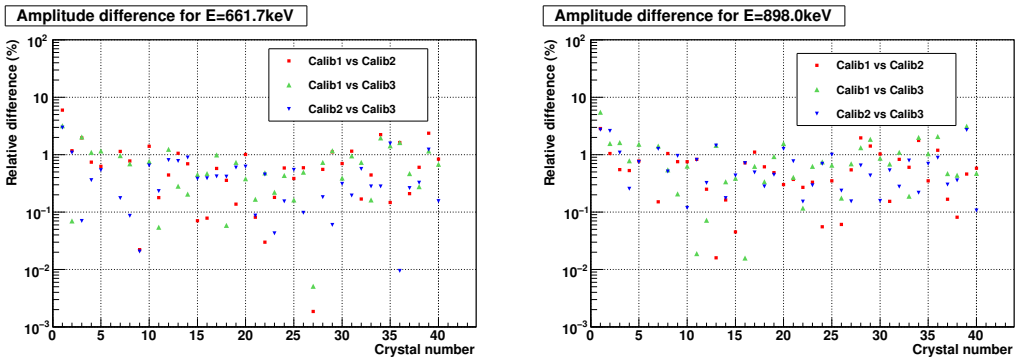

Figure 3.26: Comparison between the calibration A_{slow} values obtained in three different ^{137}Cs measurements (left) and three different ^{88}Y measurements (right). The A_{slow} values have been transported to the same run with the multiplication factors before calculating their difference.

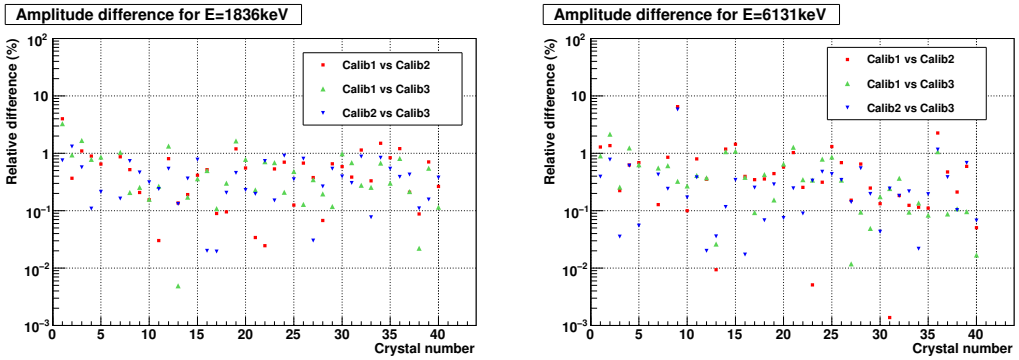

Figure 3.27: Comparison between the calibration A_{slow} values obtained in three different ^{88}Y measurements (left) and three different Pu/C measurements (right). The A_{slow} values have been transported to the same run with the multiplication factors before calculating their difference.

Finally, Figure 3.28 shows the deposited energy spectra of the reconstructed events for different measurements. In the left panel, the same deposited energy spectra were obtained from different run ranges (given in the corresponding legend). All the spectra are matched perfectly. In the right panel, the deposited energy spectra of different background dedicated measurements are presented together with the ^{243}Am capture measurement. Notice that the peak at ∼1.3 MeV are at the same position for the different measurements.

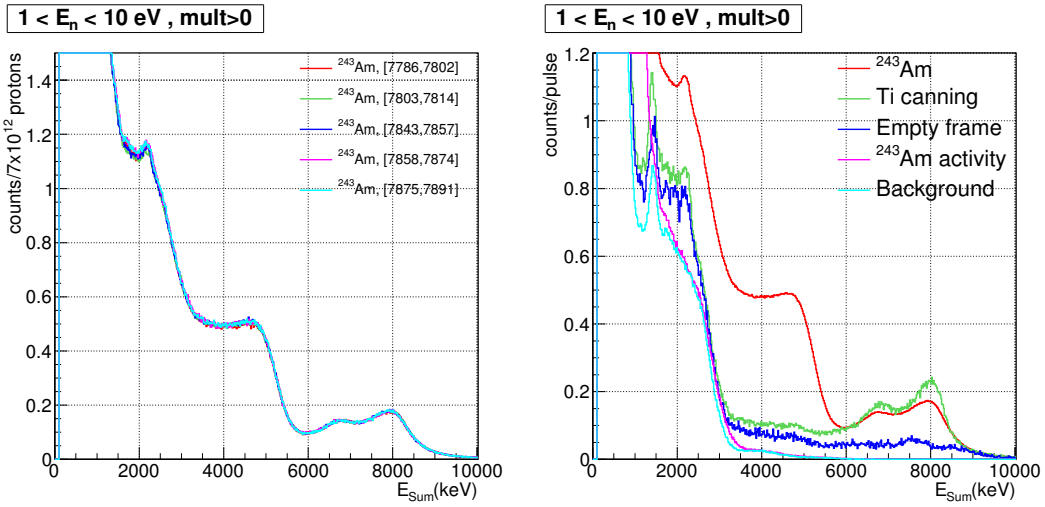

Figure 3.28: Deposited energy spectra obtained from different ^{243}Am run ranges (left) and for different measurements (right).

3.3.3 Energy resolution of the crystals

The characterization of the energy resolution of the crystals is needed for the calculation of the response of the TAC by Monte Carlo simulations.

The energy resolution was determined for each crystal from the detector response to single γ-rays in the ^{137}Cs (662 keV), ^{88}Y (898 and 1836 keV) and ^{24}Na (1369 and 2754 keV) decays. The ^{60}Co (1173 and 1332 keV) data were not used because those two γ-rays are too close in energy and the Pu/C source data because the widths of the Gaussians calculated in the fits were not accurate enough. The same fits used for the energy calibration (Figure 3.19) were used for obtaining the detector resolutions at the energy points mentioned. An expression of the type 3.3:

$$\frac{\Delta E}{E} = \frac{FWHM}{E} = \frac{\sqrt{\alpha + \beta/E}}{E} \tag{3.3}$$

was used for parameterizing the energy resolution of each detector. Figure 3.29 shows the average energy resolution of the detectors, obtained by fitting the average of the experimental points, and one individual crystal. In Table 3.1 the energy resolutions of the ^{137}Cs and the ^{88}Y high energy peaks are presented, for each detector.

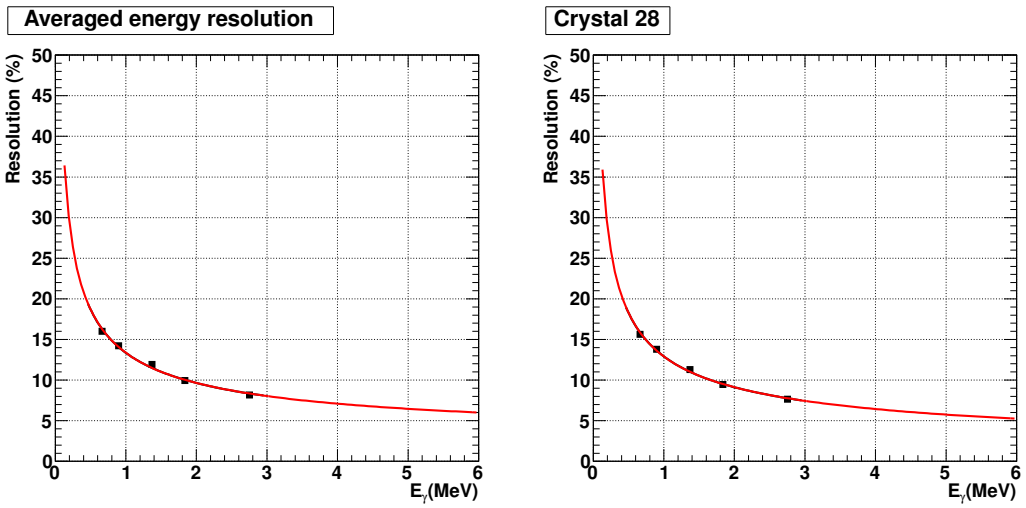

Figure 3.29: Averaged energy resolution of the detectors (left) , and energy resolution of one TAC crystal.

Det	Res1	Res2	Det	Res1	Res2	Det	Res1	Res2	Det	Res1	Res2
1	18.5	14.6	11	15.1	9.2	21	15.5	9.5	31	15.1	9.0
2	19.4	12.4	12	17.0	10.7	22	15.6	9.3	32	15.8	9.5
3	16.1	9.9	13	17.6	10.5	23	15.0	9.1	33	14.8	8.8
4	15.4	9.4	14	15.3	9.2	24	16.5	10.2	34	15.3	9.4
5	17.4	10.9	15	16.3	10.0	25	17.4	11.0	35	15.9	9.9
6	18.4	11.6	16	15.3	9.6	26	15.2	9.0	36	18.9	11.6
7	16.7	9.7	17	16.0	9.6	27	15.2	9.2	37	15.9	9.5
8	16.4	9.7	18	15.2	9.2	28	15.9	9.5	38	16.3	9.7
9	15.6	9.8	19	15.7	9.5	29	15.0	9.0	39	19.6	12.7
10	17.3	10.5	20	16.2	10.0	30	15.2	9.0	40	16.6	10.2

Table 3.1: Energy resolution (%) of the TAC detectors at 662keV (Res1) and 1836keV (Res2).

3.4 Time calibration

3.4.1 Synchronization of the flash-ADC modules

The reconstruction of the total energy deposited in the TAC requires a coincidence over all $BaF2_2$ detectors every time a signal is detected. A time window of 20 ns was adopted. It was necessary to synchronize all the flash-ADC modules, since their internal clocks have an accuracy of only 2ppm, which results in time deviations between detectors of the order of a few tens of ns in the TOF window of 16 ms.

The synchronization of all the BaF_2 detectors are performed in the following way. One of them is taken as a reference, and the rest of them are synchronized to it. The synchronization between two detectors is performed by measuring a radioactive sample which emits two γ-rays in coincidence (^{60}Co or ^{88}Y) and by storing the time

differences between the detected γ-rays (in coincidence), as a function of the time-of-flight. In a second step, the time differences are fitted to a linear function (offset of the start of the different clocks and differences in the clock frequencies). An example is provided in Figure 3.30, where the time differences between the γ-rays detected in an ^{88}Y measurement are presented as a function of the time-of-flight. Only gammas with energy values close to the ones of the ^{88}Y decay have been considered, to avoid spurious coincidences.

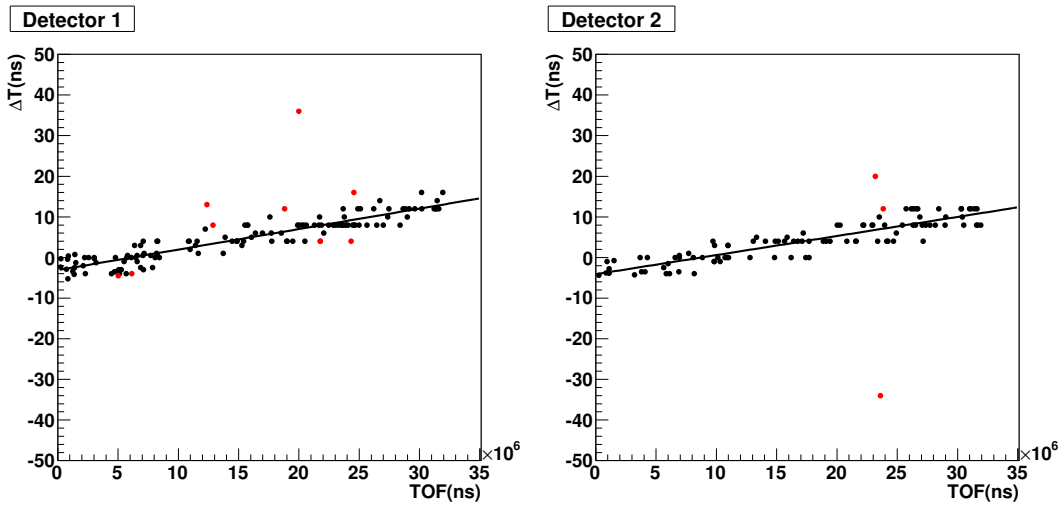

Figure 3.30: Time synchronization of two BaF_2 modules.

After the time synchronization, a check has been done by comparing the deposited energy spectra in the TAC of an ^{88}Y+^{137}Cs calibration measurement in different time-of-flight intervals. If the TAC detectors are not well synchronized, differences in the spectra must be observed. The total length of the recorded buffers is 16 ms. The spectra taken during the entire time interval have been compared to the spectra corresponding to the the first and the last ms. The results are presented in Figures 3.31 and 3.32, for different multiplicity cuts. As it can be observed, all the spectra are in perfect agreement.

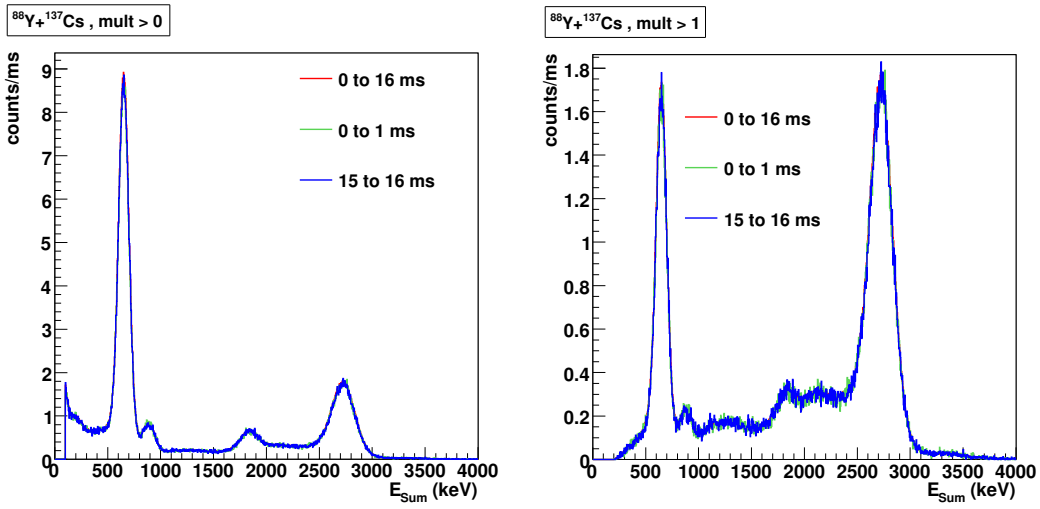

Figure 3.31: Deposited energy spectra in the TAC for an ^{88}Y+^{137}Cs measurement in different time intervals.

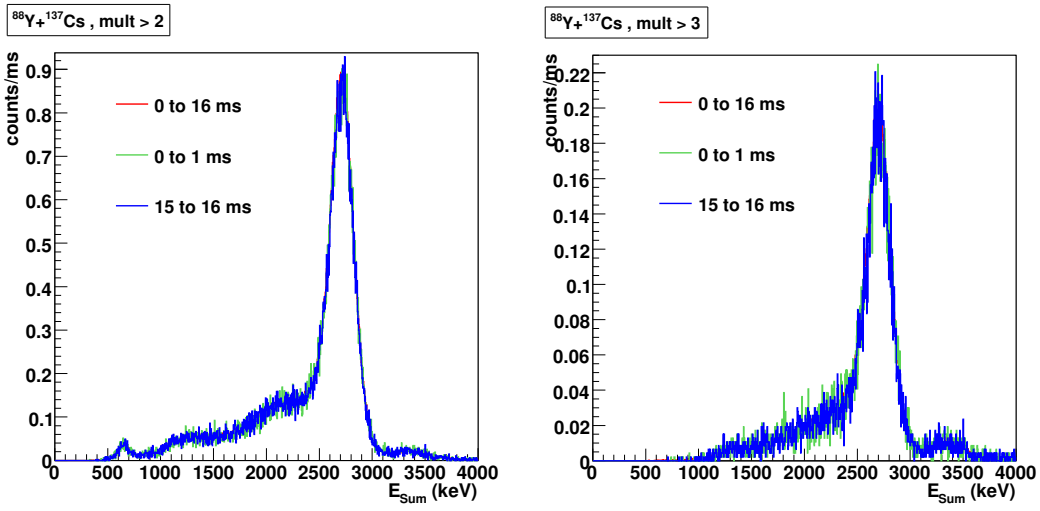

Figure 3.32: Deposited energy spectra in the TAC for an ^{88}Y+^{137}Cs measurement in different time intervals.

The time window value of 20 ns was deduced by making coincidences with a ^{60}Co source with different time window values. It was found that for time window values lower than 11 ns, some γ-rays were missed in the coincidence process. A 20 ns time window was adopted as a safe value.

3.4.2 Time origin

The pulse shape analysis routine calculates the time of each signal, with respect to the beginning of the digital buffer. However, in order to calculate the time of flight of the captured neutrons it is necessary to relate the beginning of the buffer to the time when neutrons are created. This is done with the first particles arriving from the target, the first γ-rays, which saturate the data buffers ("gamma flash"). With this information, it is possible to deduce the time at which these gammas where generated in the spallation target, which is the time when the fastest neutrons were created.

Alternatively, the time of the signal provided by the WCM (usually called PKUP), which provides information concerning the proton intensity (see Section 2.2.2), was used to determine the time origin of each pulse. The reason was that this time value is much easier to obtain. The distance from the PKUP time to the saturation position has been calculated for a certain amount of pulses and the resulting values have been set into a histogram in Figure 3.33. It can be observed that the time difference is always the same, with an spread of $\backsim$20 ns, which has a negligible effect in the energy range of interest.

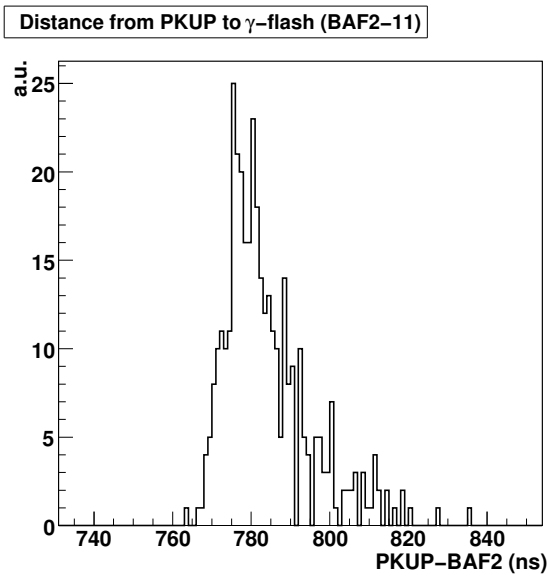

Figure 3.33: Time distance between the PKUP signal and the first saturated channel of the crystal 11 buffer.

3.5 Efficiency calculation

The detection efficiency is the quantity which allows to obtain the reaction rate from the counting rate. It stands for the probability of a capture reaction to be detected, and it depends on the crystal threshold, on the conditions in the total deposited energy and multiplicity (E_{Sum} and m_{cr}), on the nucleus which captures the neutron (the

electromagnetic cascades are different for each isotope), and on the counting rate of the detector (due to pileup and summing effects). Its dependence on the neutron energy is, very often, negligible. This occurs when:

1. The energies of the incident neutrons are much smaller than the neutron separation energy (S_n), so the total energy of the cascade is always the same ($E_{Tot} \cong S_n + E_n$).
2. The level density is large below S_n, i.e. the possible decay paths of the compound nucleus, is large enough, and the "shape" of the cascades are independent from the resonance (level of the compound nucleus) where the capture occurs.

If both conditions are fulfilled, then the shape of the deposited energy spectra by capture cascades in the TAC will be almost identical independently on the neutron energy (notice that the TAC is not very sensitive to the shape of the cascades). This is the case of the ^{243}Am(n,γ) measurement, since it goes only up to 2.5 keV, $S_n(^{244}\text{Am})$=5.4 MeV, and the ^{244}Am nucleus has a very large level density below S_n (there is more than one resonance per eV around S_n).

An accurate calculation of the detection efficiency needs to take into account all the mentioned dependencies can be achieved by means of Monte Carlo simulations. With a simulation code capable of reproducing the measured distributions for all combinations of deposited energy and crystal multiplicity, the simulated detection efficiency is a very accurate estimate of the true value. Such a simulation code needs to include:

1. A realistic event generator of the electromagnetic cascades in the (n,γ) reaction.
2. A reliable Monte Carlo simulation of the cascades, with a detailed description of the TAC geometry and including all the relevant physical processes.
3. An event reconstruction software which makes the coincidence analysis, taking into account the energy resolution of the detector and the dead time and summing effects, in the same way as it happens to the experimental data.

3.5.1 The event generator

The generation of totally realistic capture cascades following the neutron capture reactions requires the knowledge of the complete nuclear level scheme below the neutron separation energy: energies, spins and parities of all the levels together with the corresponding branching ratios. Such information is completely known only for a reduced number of isotopes, usually for the lighter nuclei. The general case is that the level scheme is known only up to a certain excitation energy and the experimental information is scarce above. Hence, the generation of capture cascades has to be based on a model that combines the experimental information at low excitation energies, with theory based assumptions and statistical models at high excitation energies.

The code DecayGen [Tai07, Tai02] has been used for the generation of the capture cascades. It has been applied specifically to the n_TOF TAC measurements in [Gue12.1]. The model implemented in the code considers two different excitation energy ranges:

1. The lower energy range ($E < E_{cut}$) corresponds to the region of known levels (energy, spin and parity), with known transition probabilities. This information is retrieved from the Evaluated Nuclear Structure Data Files (ENSDF) [ENSxx] and allows the exact calculation of the low energy part of the branching ratio matrix. The electron conversion process is modeled for the K, L and M shells from the tabulated values of fluorescence yields and internal conversion coefficients available in the literature [ECWxx].

2. At higher energies ($E > E_{cut}$) the levels and transition probabilities between them are calculated by means of a statistical model. The individual levels are created by sampling the level density distribution given by a model, such as the Back Shifted Fermi Gas (BSFG) or the Gilbert-Cameron models, and the transition probabilities between levels are calculated only for E1, M1 and E2 transitions from the associated Photon Strength Functions (PSF), as it is described in section 1.2.6.

The program starts by reading all the information needed for the simulation of the cascades: the known energy levels and branching ratios from ENSDF, associating an E_{cut} value above the highest known energy level, information concerning the electron conversion process, neutron separation energy of the compound nucleus, A and Z values of the nucleus and parameters for the nuclear level density and PSF models.

Starting from the capture level, the algorithm for generating a cascade is:

1. The branching ratio matrix for E1, M1 and E2 transitions is calculated from the known capture level to all the levels below using the parametrized PSF and the BSFG level density.
2. The transition to a new level is sampled randomly according to the branching ratio matrix.
3. If the new level is in the statistical energy range, a new branching ratio matrix is computed. Otherwise the experimental branching ratio matrix is used.
4. The loop returns to step 2 until the ground or a metastable state is reached. Notice that a level with $T_{1/2}$ greater than the 20 ns time window, such as the first level state of ^{244}Am, with $T_{1/2}$=21 m, is considered metastable.

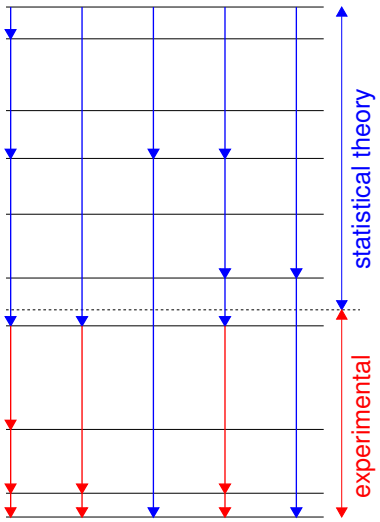

Figure 3.34: Nuclear level scheme used in the cascade generator model. The low energy range is known experimentally, while the upper energy range is described from nuclear level density statistical models and parametrized EM transition probabilities.

3.5.2 The Monte Carlo code

A simulated code based on the GEANT4 [GEAxx] simulation toolkit has been developed. The highly detailed geometry of the experimental setup shown in Figure 3.35 was modeled. This geometry includes the BaF_2 crystals with their capsules, the photomultipliers, the beam pipe, the structure which is holding the crystals and the neutron absorber.

The Monte Carlo code simulates the transport of all particles through the detector until they are completely absorbed or transported outside the TAC. When an interaction takes place in the BaF_2 crystals, the deposited energy, time of flight, event number and crystal identification number of the interaction are recorded for the subsequent event reconstruction.

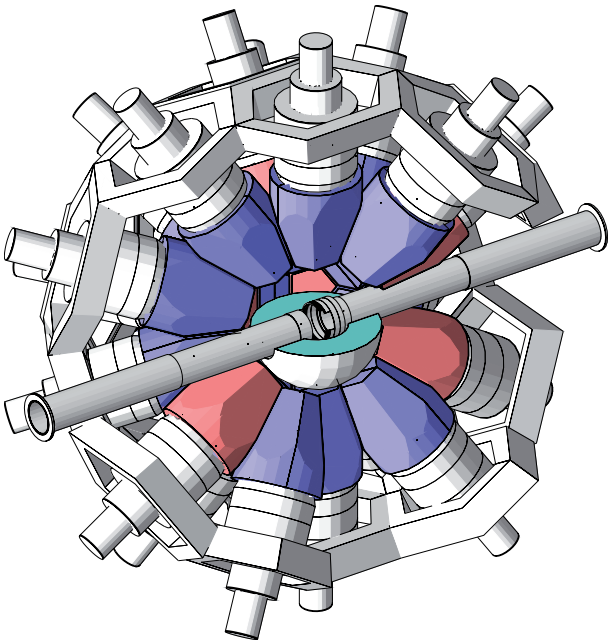

Figure 3.35: TAC geometry (half of it) implemented in GEANT4.

3.5.3 The event reconstruction software

The results obtained from the Monte Carlo code are processed by the event reconstruction software, which is analogous to the reconstruction process of the experimental data:

1. All the "signals" (hits) coming from the Monte Carlo code are read. The deposited energy in each crystal is sampled from the MC value according to the energy resolution of the detector (Section 3.3.3). The uncertainty in the experimental energy calibration produces a broadening in the total energy spectra. In order to take this effect into account, an artificial error in the MC energy calibration is simulated by sampling at the beginning of the simulation a "calibration error factor" for each crystal. This factor is usually sampled according to a Gaussian distribution with $\langle x \rangle$=1 and σ=0.03, which has been obtained by comparison to the experimental results. All the MC energies are then multiplied by its corresponding factor, thus simulating the error committed in the experimental energy calibration process. The starting time of each simulated cascade is sampled according to a certain pre-defined (reaction) rate, and the time between the origin of the cascade and the detection of the γ-rays is given by the Monte Carlo simulation.

2. All signals are ordered in time and two different dead time corrections are applied:

   (a) As it is discussed in Section 3.2.3, the pileup of two signals close in time have been characterized according to a dead time probability function, $P(E_1,E_2,\Delta t)$, which models when a signal is not detected; and a a probability distribution, $P_{\{(E_1,E_2,\Delta t)\}}(\xi)$, which describes the change in the detected energy of a signal if the next signal has not been detected. Hence, $P(E_1,E_2,\Delta t)$ is used to sample for every signal if it is not detected due to the proximity of the previous ones. Then, if it is the case, the energy of the previous signal is modified according to $P_{\{(E_1,E_2,\Delta t)\}}(\xi)$. This correction is done to each individual crystal.

(b) When simulating capture cascades of ^{243}Am, dead time effects resulting from the high sample activity are also taken into account. As it is presented in Section 3.2.2, this effect is characterized by a probability function, $P_{CR}(E_\gamma)$, which characterizes when a signal is not detected due to the ^{243}Am activity; and a probability distribution function, $P_{E_\gamma}(\Delta E_\gamma)$, describing the change in the detected signal energy due to the sample activity. Hence, $P_{CR}(E_\gamma)$ is used to sample, for every signal which has not been "killed" by the previous method, if it is killed or not. Then, if it has been detected, $P_{E_\gamma}(\Delta E_\gamma)$ is used to sample the change in the detected energy.

3. The coincidences are made, in the same way as it is done with the experimental data. With all the signals ordered in time, a coincidence of 20 ns is made. The result is a list of events with a total deposited energy, a detected multiplicity and a time. These events are similar to the experimental ones and are histogrammed in the same way. For the ^{243}Am measurement, the effect of random coincidences must be also included (section 3.2.2): there is a non-negligible probability for a sample activity signal to be in coincidence with the capture signals, changing the total energy and multiplicity of the detected event. In order to take this effect into account, experimental data (energies and multiplicities) from the ^{243}Am activity measurement were added to the Monte Carlo simulated capture events. The addition of these experimental data was performed randomly, taking into account the experimental counting rate ($\sim$5.4 events/μs) and the total energy and multiplicity distribution probabilities.

3.5.4 Validation of the simulation process

The complete simulation code has been validated by comparing different simulated deposited energy spectra with the experimental results. In particular, the following measurements were reproduced:

1. Calibration sources, in different geometrical configurations.
2. ^{nat}Ti(n,γ) cascades.
3. ^{197}Au(n,γ) cascades, with low and high counting rates.
4. Rad-TiCan and Rad-Au (n,γ) cascades.

The complexity of the simulation increases in the order provided. The first simulations, the calibration sources and the ^{nat}Ti(n,γ), do not include any free parameter in the generation of the electromagnetic cascades, so they were used to test the geometry implemented in GEANT4 as well as the general performance of the simulation process. In the simulation of the ^{197}Au(n,γ) cascades it is necessary to modify the PSF parameters until the experimental results are reproduced. It is also possible to check part of the dead time correction model, since the same capture cascades are detected at low and high counting rates. Finally, the Rad-TiCan and Rad-Au (n,γ) cascades include dead time effects associated with the high ^{243}Am activity.

3.5.4.1 Calibration sources

The simplest measurements to compare are the ones performed with the calibration sources, where the generation of the γ-ray cascades follows a simple and well known scheme and the dead time effects are negligible. The comparisons have been performed with ^{137}Cs, ^{88}Y and ^{60}Co calibration sources, with different geometry configurations: with and without neutron absorber and with and without the Pb shielding used in the ^{243}Am measurement. The results are

presented in Figures 3.36 to 3.40. In all these figures, the energy of the experimental spectra has been multiplied by a factor of 1.015 in the case of the ^{137}Cs measurements and by 1.010 in the case of the ^{88}Y and ^{60}Co measurements, which stand for the small errors in the energy calibration procedure (∼1%).

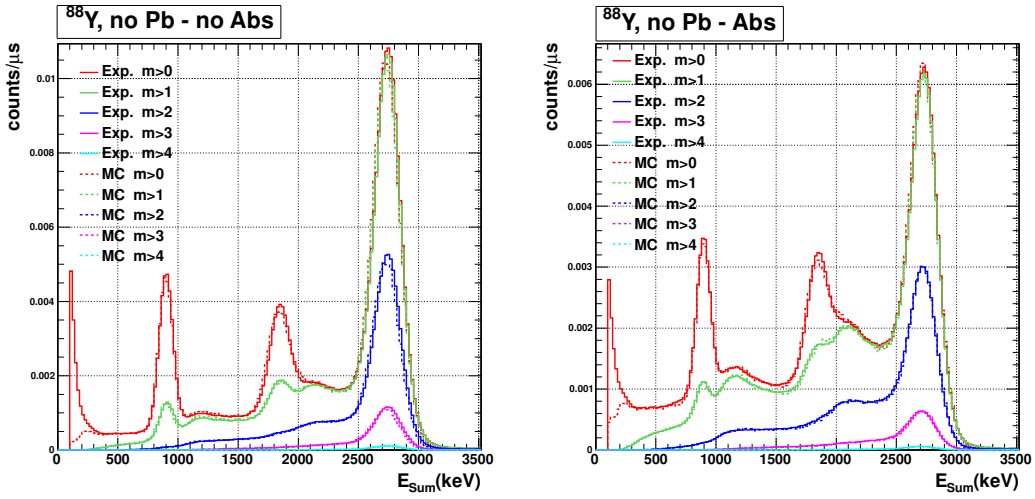

Figure 3.36: Comparison between simulated and experimental results for two different ^{88}Y calibration measurements, both without lead shielding, without absorber (left) and with absorber (right).

The good reproduction of the experimental results indicate that the TAC geometry has been correctly implemented in the MC code, as well as the energy resolution of the detectors in the reconstruction process. It has to be said that in order to reproduce these experimental results, the density of the neutron absorber, which in principle should be 1.1 g/cm^3, has been multiplied by 0.7, due to the wrong specifications available of the neutron absorber. This modification is used for all the rest of the simulations and it is reasonable because: (1) the deposited energy spectra is well reproduced in the same simulations but without neutron absorber (see Figures 3.36 to 3.39); (2) the GEANT4 simulation code is extensively used to simulate detector responses to γ-rays, so the implementation of the corresponding electromagnetic processes have been widely validated; and (3) the neutron absorber was constructed by filling two hemispheric aluminum containers with the ^{6}Li enriched salt in liquid state, so it is perfectly possible the appearance of bubbles in the solidification process, giving a final effective density of 0.77 g/cm^3.

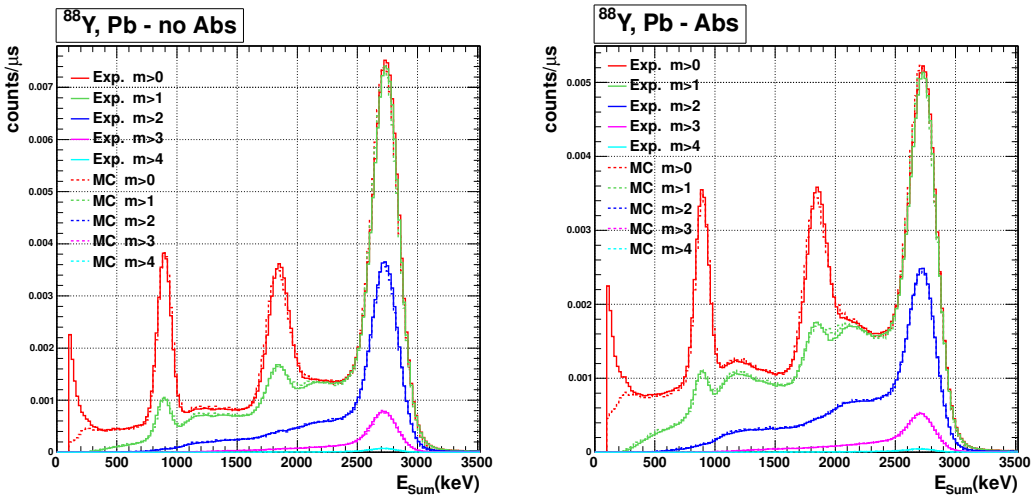

Figure 3.37: Comparison between simulated and experimental results for two different ^{88}Y calibration measurements, both with lead shielding, without absorber (left) and with absorber (right).

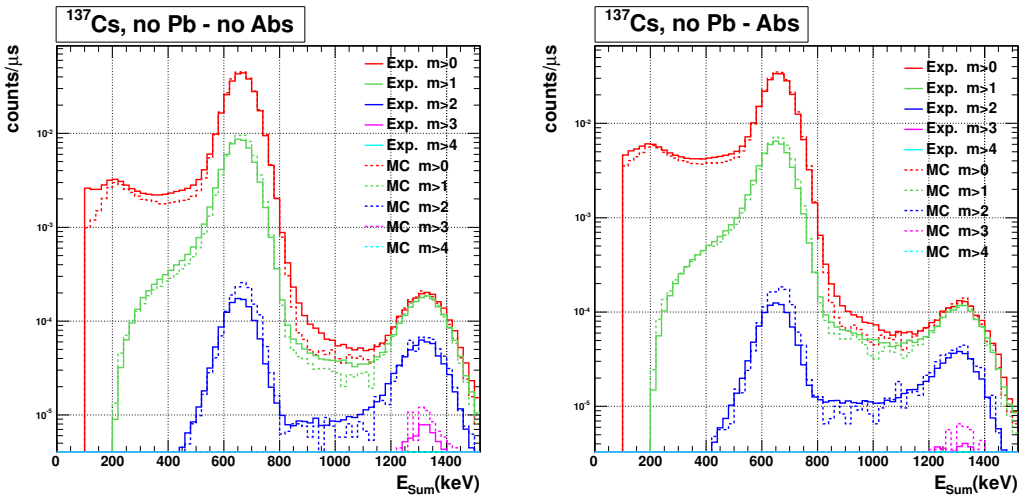

Figure 3.38: Comparison between simulated and experimental results for two different ^{137}Cs calibration measurements, both without lead shielding, without absorber (left) and with absorber (right).

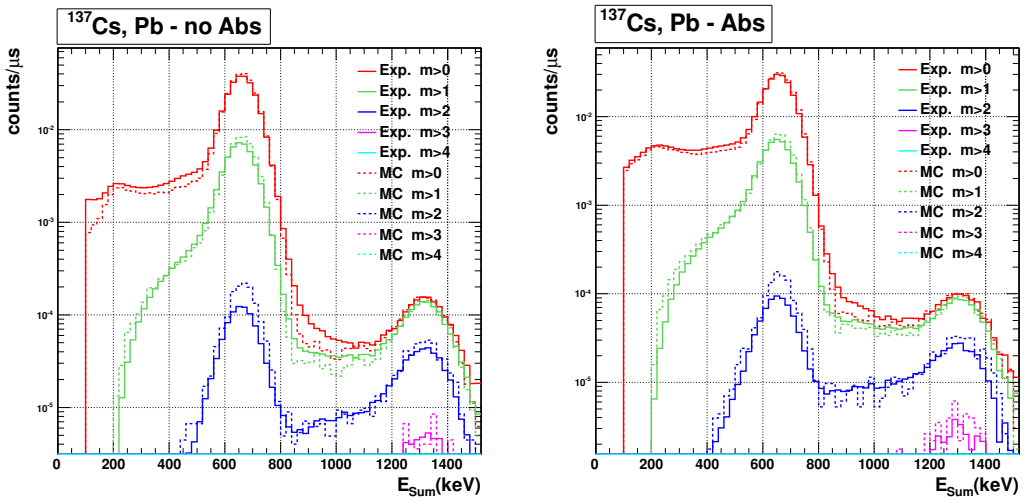

Figure 3.39: Comparison between simulated and experimental results for two different ^{137}Cs calibration measurements, both with lead shielding, without absorber (left) and with absorber (right).

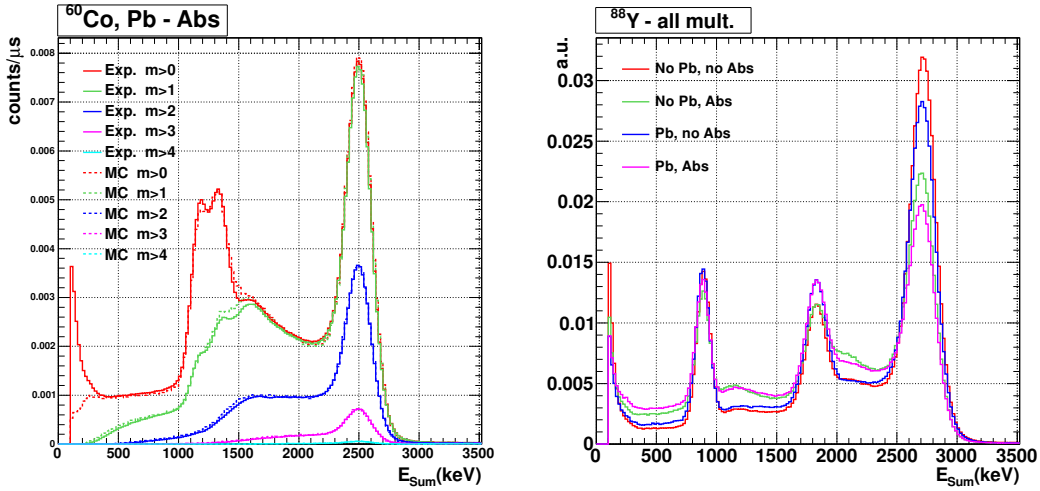

Figure 3.40: Comparison between simulated and experimental results for a ^{60}Co measurement, with lead shielding and absorber (left) and comparison between the experimental ^{88}Y results with the different configurations (right).

3.5.4.2 ^{nat}Ti(n,γ) cascades

A next step in the validation is the simulation of the Ti capture cascades. The Ti contribution to the deposited energy spectrum is obtained by subtracting the empty frame measurement to the Ti canning measurement, after subtracting from both the environmental background measurement. At low energies (few eV) the main contribution to the deposited energy spectra comes from neutron capture in the ^{48}Ti isotope, which represents the 73.45% of the isotopic composition of the natural titanium and also have a higher capture cross section than the rest of the Ti isotopes. This makes that the 95% of the capture reactions occurred in the Titanium capsule between 1 and 10 eV are produced in ^{48}Ti. In this isotope the levels and branching ratios of the corresponding compound nucleus (^{49}Ti) below the neutron separation energy are well known. For this reason, no statistical model is needed in the corresponding cascade event generator. The rest of the isotopes were also included in the simulations, using the mentioned statistical model with the recommended parameters for the Photon Strength Functions[RP2xx]. The contribution of each isotope to the deposited energy spectra was taken accordingly to the fraction of neutron capture reactions in it. Notice that the statistical model is used in only 5% of the generated cascades, so the influence of the statistical model is very small in these simulations.

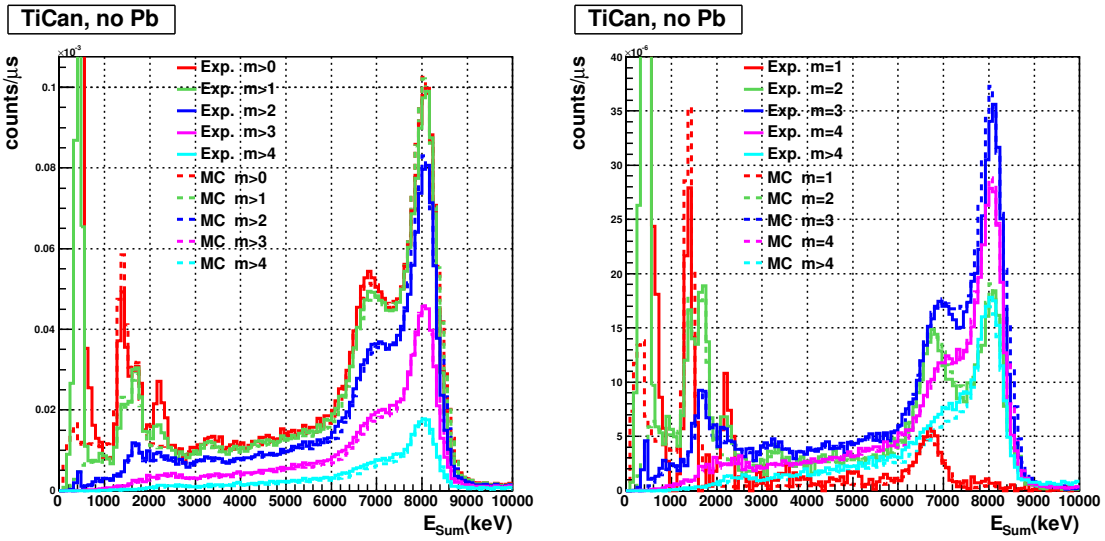

Figure 3.41: Comparison between experimental (Exp.) and simulated (MC) deposited energy spectra of neutron capture cascades in Ti in the 1-10 eV neutron energy range. The geometry does not contain the Pb shielding. The conditions in multiplicities have been selected as greater than some values (left) or equal to some values (right).

The results obtained are compared with the experimental data in Figure 3.41 (without Pb shielding) and in Figure 3.42 (with Pb shielding). It can be appreciated that the experimental results are well reproduced in both cases. The simulation without Pb shielding was normalized to the experimental data, since the exact Ti mass is not

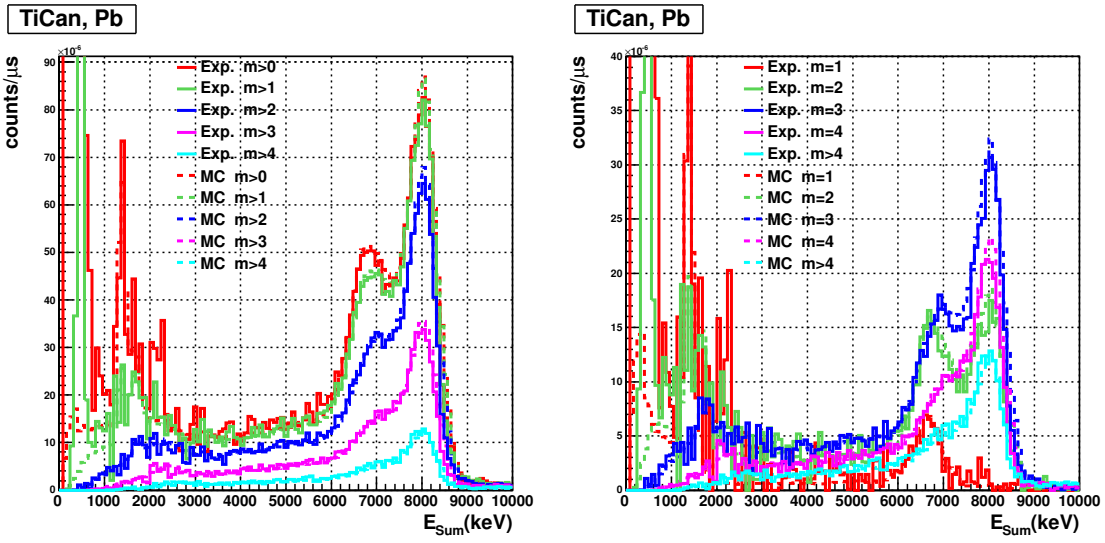

Figure 3.42: Comparison between experimental (Exp.) and simulated (MC) deposited energy spectra of neutron capture cascades in Ti in the 1-10 eV neutron energy range. The geometry contains the Pb shielding. The conditions in multiplicities have been selected as greater than some values (left) or equal to some values (right).

accurately known (see Section 3.6), but the same normalization were also used for the simulation with Pb shielding. These results validate the simulation code for more complex situations. Unlike in the case of the calibration sources described above, the energies of the experimental spectra were not multiplied for any factor. The peak at 2.2 MeV can not be reproduced by the MC simulations because it comes from neutron capture in the absorber, a process which was not included in the simulations.

3.5.4.3 ^{197}Au(n,γ) cascades

A more complex situation are the capture cascades in the ^{197}Au sample. This case is important not only for validation reasons, but also for normalization purposes. The level scheme and branching ratios of the compound nucleus (^{198}Au) are only known up to 1-1.5 MeV, whereas the neutron separation energy is 6.51 MeV. Thus, the unknown part of the level scheme has been described with the statistical model described in Section 3.5.1.

The recommended theoretical values for the PSF [RP2xx] and the level density parameters (see Section 1.2.6) do not reproduce the experimental results, so they have been varied until finding a reasonable agreement between them and the simulated results. The set of parameters (PSF's and level density) which reproduce the experimental results is not unique, but it is reasonable to accept that if a variety of deposited energy spectra, with different multiplicity cuts, are well reproduced, then the generated cascades are close to the real ones and thus the calculated detection efficiency is correct. The parameters used to reproduce the decay of the ^{198}Au nucleus are presented in Table 3.2, where the PSF of the E1 transition has been described with a Enhanced Generalized Lorentzian (EGLO) plus a Standard Lorentzian (SLO), the M1 transition with two SLO, the E2 transition with a SLO, and the level densities with the Back Shifted Fermi Gas formula.

Transition	E_r(MeV)	Γ_r(MeV)	σ_r(mb)
E1,1 (EGLO)	13.72	4.61	541
E1,2 (SLO)	6.7	0.5	230
M1,1 (SLO)	7.05	4.0	4.12
M1,2 (SLO)	5.2	0.3	30
E2 (SLO)	10.8	3.73	5.03

a (1/MeV)	Δ(MeV)
16.09	-1.0

Table 3.2: Parameters used for the Photon Strength Functions of E1, M1 and E2 transitions (up) and for the level density (bottom) used in the generation of ^{197}Au capture cascades.

The resulting ^{197}Au cascades have been compared with the experimental results firstly in the tail of the resonance at 4.9 eV, in the 3.5-4.2 eV neutron energy range (see Figure 3.65). There the statistics achieved in the measurements is enough to perform the comparison with the MC results and the reaction rate ($\sim$0.1 reactions/μs) is low and the dead time effects negligible. The results are presented in Figures 3.43 (without lead shielding) and 3.44 (with lead shielding). In both cases the normalization is the same. In the non-Pb shielding configuration the experimental deposited energy spectra have been multiplied by a factor of 1.01.

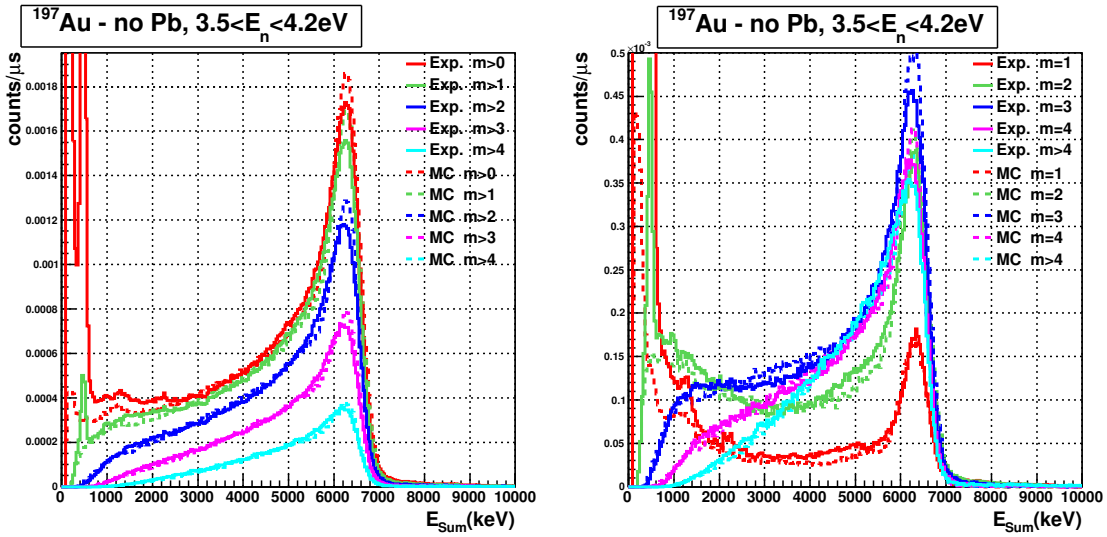

Figure 3.43: Comparison between experimental and simulated deposited energy spectra, for different multiplicities, of neutron capture cascades in ^{197}Au, without Pb shielding.

The PSF and level density parameters were modified not only to reproduce the deposited energy spectra presented in Figures 3.43 and 3.44 but also the experimental results presented in Figure 3.45. In that Figure, the detected

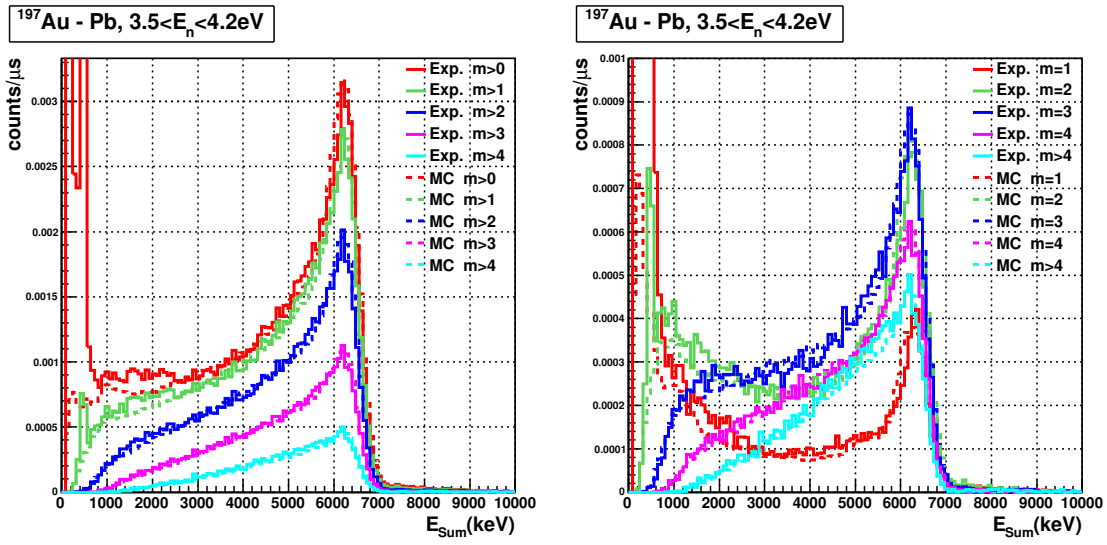

Figure 3.44: Comparison between experimental and simulated deposited energy spectra, for different multiplicities, of neutron capture cascades in ^{197}Au, with Pb shielding.

γ-ray energies contributing to the vicinity of the total absorption peak (5<E_{Sum}<7 MeV) have been histogrammed. Since almost all the cascade has been detected, the detected multiplicity has to be close to the real multiplicity of the cascade. These histograms, one of them for each detected multiplicity, provide valuable information concerning the "shape" of the cascades for each selected multiplicity.

The same simulated ^{197}Au capture cascades have been used to reproduce the 4.8-5 eV neutron energy region, which corresponds to the saturated part of the strongest ^{197}Au resonance (see Figure 3.65). The reaction rate in this region is $\sim$1 captures/μs, so the dead time effects are relevant, thus providing an excellent opportunity to test the dead time correction methods presented in Section 3.2.3 (effect of capture cascades on subsequent capture cascades). The obtained results are presented in Figures 3.46 (without lead shielding) and 3.47 (with lead shielding). In order to show the effects of the dead time, the same experimental spectra presented in Figure 3.46 has been also plotted in Figure 3.48 together with the simulated results obtained when no dead time corrections are applied (i.e., similar to those presented in Figure 3.43). As in the case of the 3.5-4.2 eV neutron energy interval, in the non-Pb shielding configuration the experimental deposited energy spectra have been multiplied by a factor of 1.01.

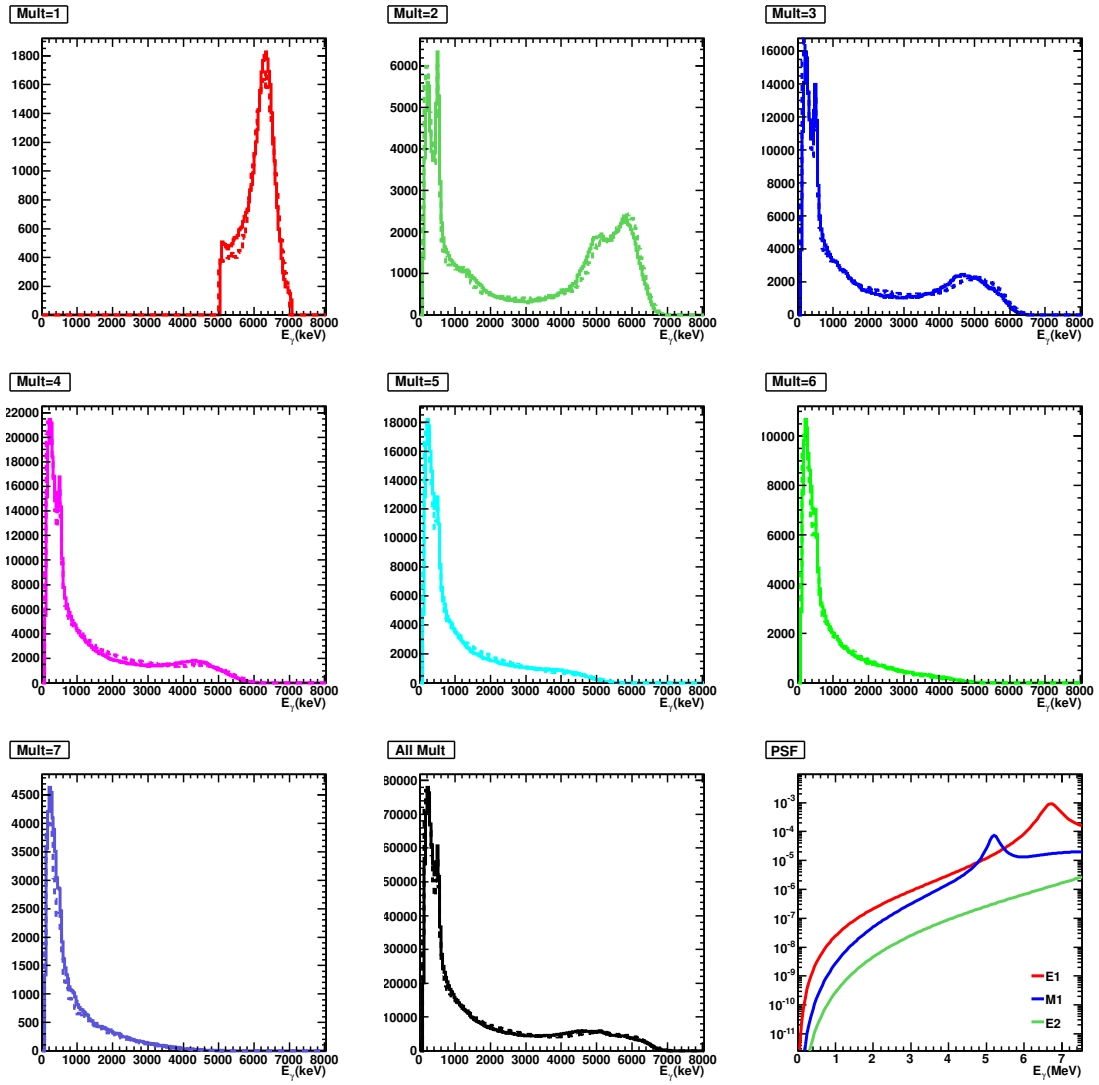

Figure 3.45: Individual γ-ray energy spectra detected by the TAC in the ^{197}Au measurement (without Pb shielding), in the 3.5-4.2 eV neutron energy range. The different spectra have been constructed only with the detected γ-rays contributing to the $5<E_{Sum}<7$ MeV interval, for different multiplicities. The solid lines correspond to the experimental results whereas the dotted lines to the simulation results. The right bottom figure corresponds to the used PSF's, where the Y axis is $f_{XL}(E_\gamma)\cdot E_\gamma{}^{2L+1}$(dimensionless), as it appears in Equation 1.32.

All the presented results concerning the ^{197}Au measurement validate, up to a certain point, the statistical model implemented to generate the electromagnetic cascades produced after neutron capture, since many different total deposited energy spectra and individual γ-ray spectra have been reproduced. The dead time correction model developed to simulate the pileup effect of capture cascades on subsequent capture cascades, has also been validated,

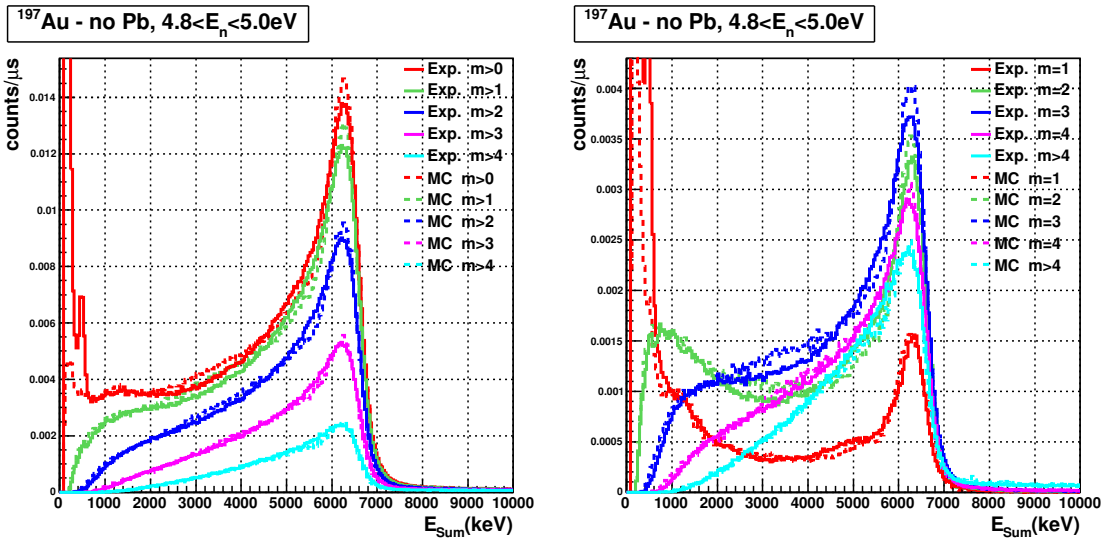

Figure 3.46: Comparison between experimental and simulated deposited energy spectra, for different multiplicities, of neutron capture cascades in the saturated part of the strongest ^{197}Au resonance, without Pb shielding. The dead time effects are relevant in this energy region.

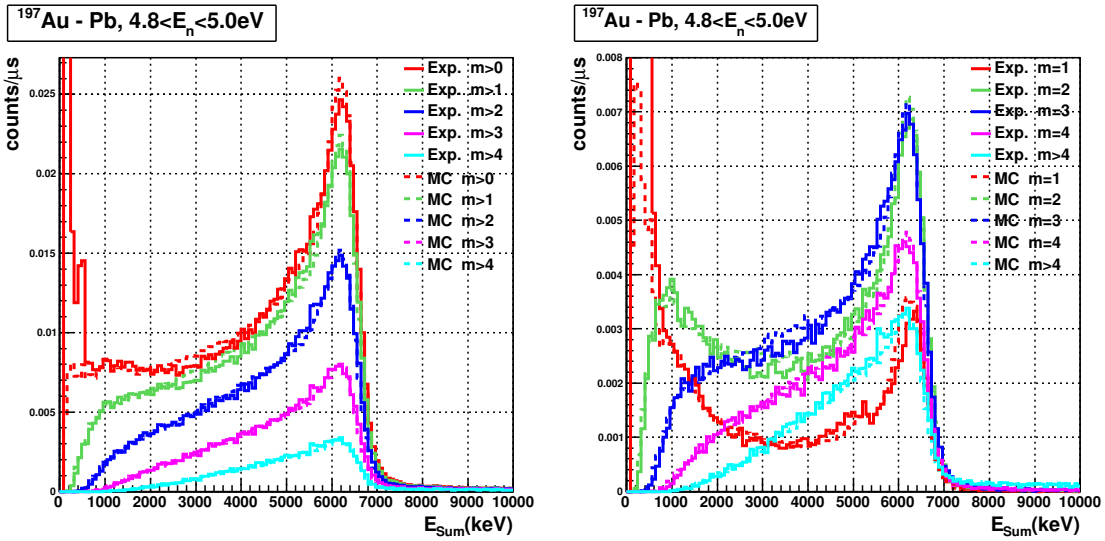

Figure 3.47: Comparison between experimental and simulated deposited energy spectra, for different multiplicities, of neutron capture cascades in the saturated part of the strongest ^{197}Au resonance, with Pb shielding. The dead time effects are relevant in this energy region.

since the deposited energy spectra of the ^{197}Au capture cascades have been reproduced also for high counting rates.

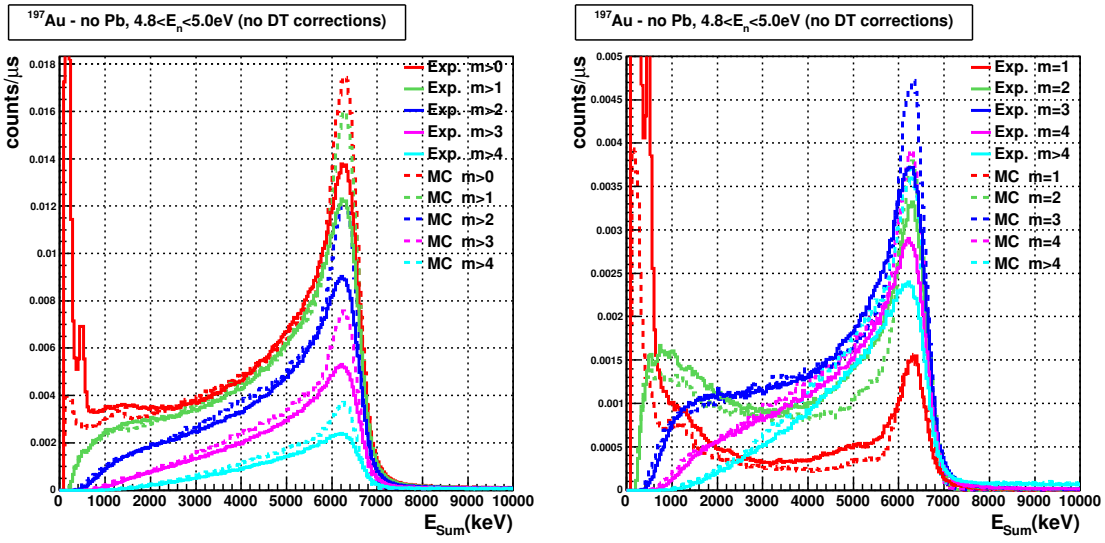

Figure 3.48: Comparison between experimental and simulated deposited energy spectra, for different multiplicities, of neutron capture cascades in the saturated part of the strongest ^{197}Au resonance, without Pb shielding. No dead time corrections have been used in the simulation process. The normalization is the same than the one in Figure 3.46.

Note that the simulated ^{197}Au capture cascades were the same as the ones used in the low counting rate simulations. The only difference was the time distance between them.

3.5.4.4 Rad-TiCan and Rad-Au (n,γ) cascades.

Finally, the Rad-TiCan and Rad-Au measurements, i.e. the ^{nat}Ti(n,γ) and ^{197}Au(n,γ) measurements combined with the ^{243}Am activity measurement, were used to validate the dead time correction method presented in Section 3.2.2 (effect of the sample activity background on the detection of capture cascades).

The same cascades generated in the simulations of the ^{nat}Ti(n,γ) and ^{197}Au(n,γ) measurements were used to reproduce the Rad-TiCan and Rad-Au measurements. In this case, the dead time correction method which models the effect of the ^{243}Am activity in the detection of capture cascades was used during the event reconstruction process. The results for the Rad-TiCan measurement are presented in Figure 3.49, where the experimental deposited energy spectra have been obtained by subtracting the Rad-Empty measurement to the Rad-Ti Canning measurement, in order to obtain just the contribution of the Ti canning. As it can be observed, the simulation reproduces the experimental results, thus validating the mentioned dead time model.

Finally, the Rad-Au measurement has been used to test the situation of having both dead time models at the same time: high capture rate and high ^{243}Am activity background. The comparison of the Rad-Au spectra in the 4.8-5.0 eV energy region ($\sim$1 capture/μs) with the simulation results are presented in Figure 3.50. The same normalization than for the previous ^{197}Au cases has been used. Again, the simulation reproduces the experimental results, validating the performance of both dead time models used at the same time.

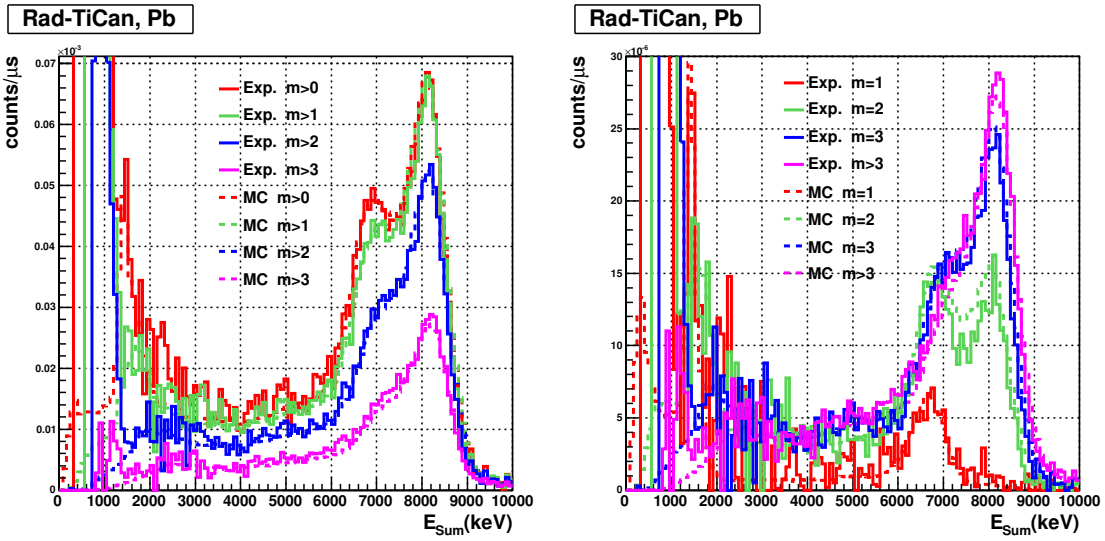

Figure 3.49: Comparison between the experimental deposited energy spectra of the Rad-TiCan measurement and the simulated ones, with Pb shielding and in the 1-10 eV neutron energy range.

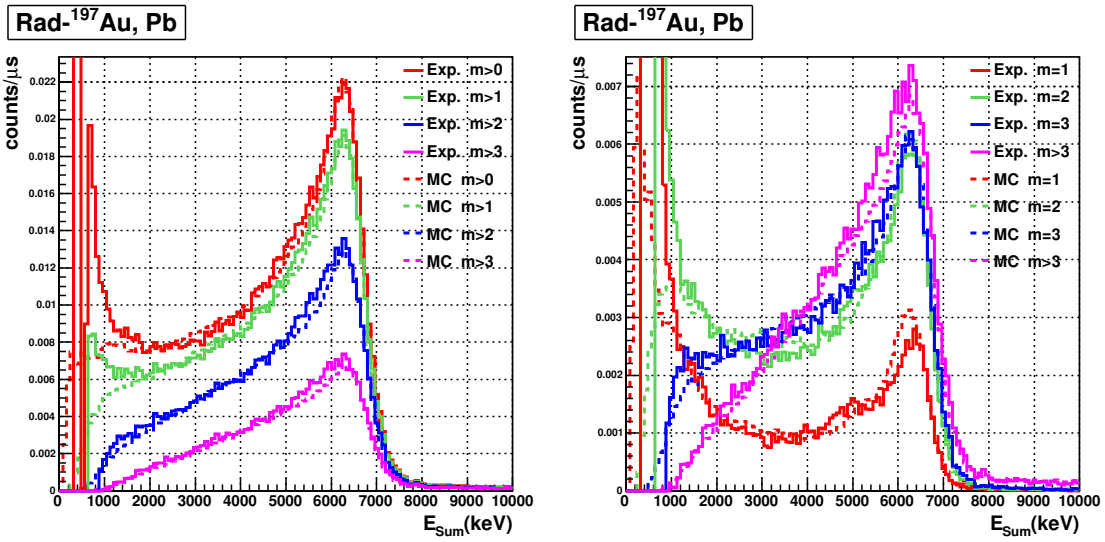

Figure 3.50: Comparison between the deposited energy spectra of the Rad-Au measurement and the simulated ones, with Pb shielding and in the 4.8-5 eV neutron energy range.

3.5.5 ^{243}Am and ^{197}Au capture cascades efficiency detection

Theoretical values of the ^{244}Am PSF parameters were obtained from the formulas presented in Section 1.2.6, since there is not any experimental information available. There are two different expressions for the E1 transitions: one for spherical nuclei (Equation 1.35) and another for deformed nuclei (Equations 1.36 and 1.37). The ^{244}Am nucleus is, in principle, a deformed nucleus. However, the results obtained using the PSF parameters resulting from the spherical nuclei equations are much closer to the experimental results than the ones resulting from the deformed nuclei equations. For this reason, the spherical nuclei parameters were used as a starting point, and they were modified until the experimental results were reproduced. The Gilbert-Cameron model was used to describe the level density, with the parameters proposed in [RP3xx]. The final values are presented in Table 3.3.

Transition	E_r(MeV)	Γ_r(MeV)	σ_r(mb)
E1,1 (EGLO)	13.25	3.6	733
E1,2 (SLO)	4.4	0.7	50
E1,3 (SLO)	0.1	0.6	0.4
M1,1 (SLO)	6.58	4.0	17.5
M1,2 (SLO)	2.3	0.7	2.0
E2 (SLO)	10.1	1.0	2.0

Utop (MeV)	E_0(MeV)	E_{match}(MeV)	a_∞(MeV^{-1})	Δ(MeV)	dW (MeV)	γ (MeV)
0.342	-0.733	2.28	26.34	0	1.98	0.069

Table 3.3: PSF parameters used for the description of the decay of the ^{244}Am nucleus (top). In the E1 transition, below 0.55 MeV, a constant value of $8{\cdot}10^{-9}$ has been assumed for $f^{E1}(E_\gamma){\cdot}E_\gamma^3$. On the bottom, the parameters used for the Gilbert-Cameron level density formula (same as the ones recommended in [RP3xx]).

The simulated and the experimental results were compared for the strongest ^{243}Am resonance, at 1.35 eV. The comparison of the deposited energy spectra are presented in Figure 3.51, with the initial theoretical values ("nominal values"), and in Figure 3.52, with the calculated values. As in some of the previous cases, the energies of the experimental spectra were multiplied by 1.01. The detected γ-rays contributing to the vicinity of the total absorption peak ($4<E_{Sum}<6$ MeV) have been set into histograms in Figure 3.53, like in the case of the ^{197}Au nucleus.

Notice that all these calculations are made to obtain the detection efficiency of the TAC to capture cascades in ^{197}Au and ^{243}Am. However, valuable information concerning the PSF's of both nuclei have been obtained during this process. Indeed, a future systematic work about PSF's in actinides measured at n_TOF will be performed.

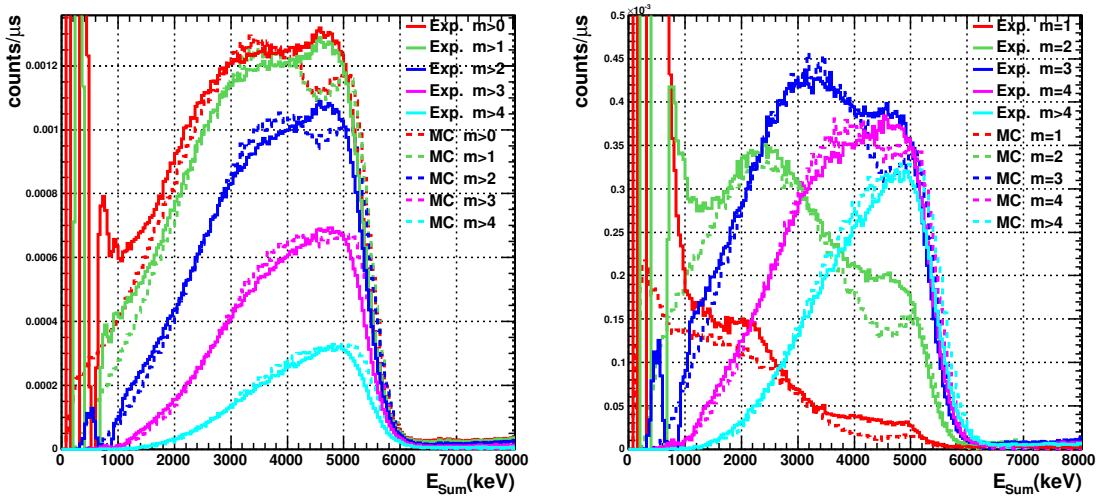

Figure 3.51: Comparison between experimental and simulated deposited energy spectra, for different multiplicities, of neutron capture cascades in ^{243}Am, in the 1.34 - 1.36 eV neutron energy range. Theoretical values for the PSF have been taken.

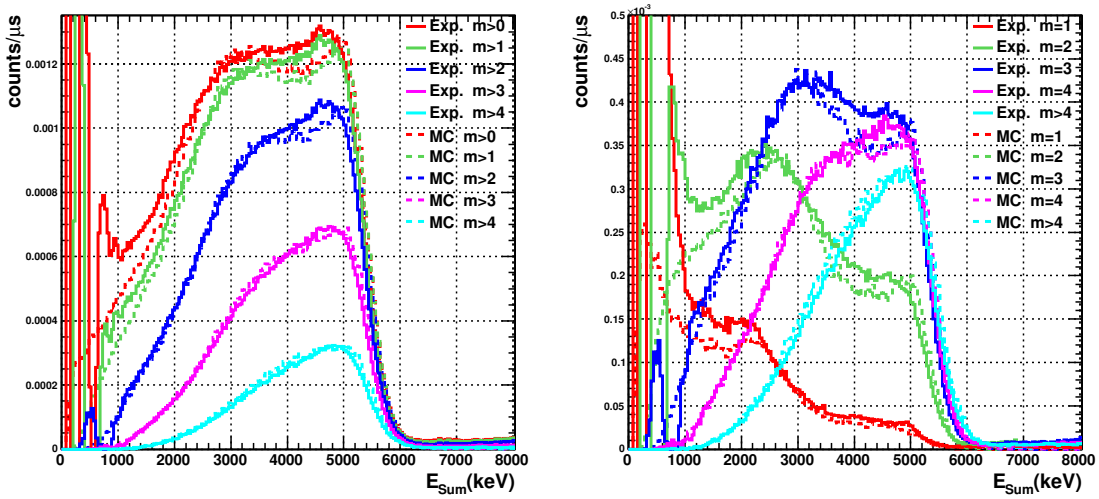

Figure 3.52: Comparison between experimental and simulated deposited energy spectra, for different multiplicities, of neutron capture cascades in ^{243}Am, in the 1.34 - 1.36 eV neutron energy range. Calculated values for the PSF have been taken.

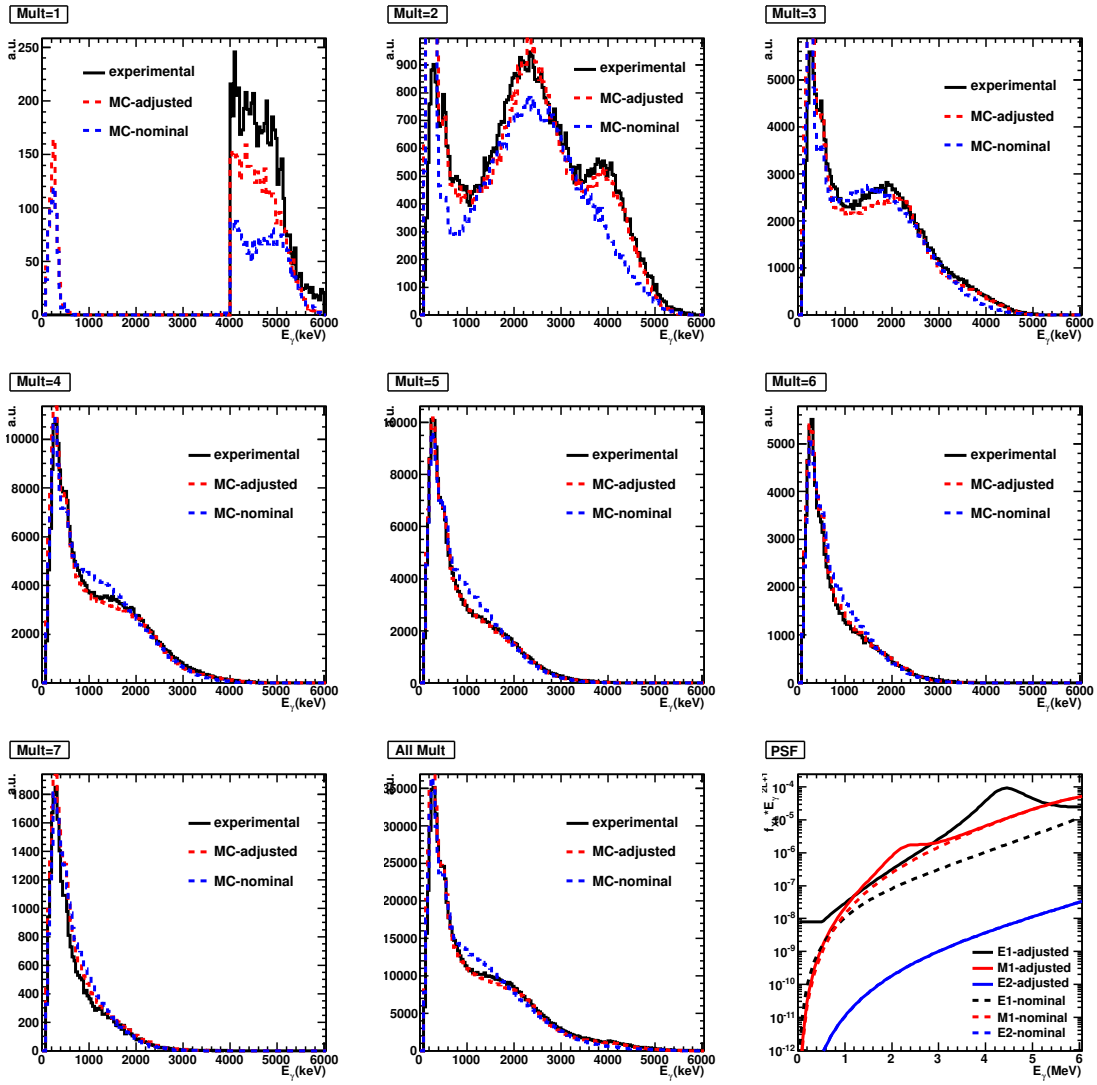

Figure 3.53: Individual γ-ray energy spectra detected by the TAC in the ^{243}Am measurement , in the 1.34-1.36 eV neutron energy range. The different spectra have been constructed only with the detected γ-rays contributing to the $4<E_{Sum}<6$ MeV interval, for different multiplicities. The right bottom figure corresponds to the used PSF's, where the Y axis is $f_{XL}(E_\gamma)\cdot E_\gamma{}^{2L+1}$(dimensionless), as appears in Equation 1.32.

Since several deposited energy spectra are well reproduced for the ^{197}Au and the ^{243}Am, the simulation code can be used to calculate the detection efficiency of neutron capture in both nuclei. This efficiency depends on: (1) the nucleus which captures the neutron; (2) the selected conditions in deposited energy and multiplicity of the detected events; and (3) in the counting rate. In addition, if the changes in the counting rate are fast enough, extra corrections would be needed: the efficiency at a given neutron energy could depend not only on the counting

rate at the corresponding time of flight, but also in the counting rate at lower time of flight values (higher neutron energies).

Once the PSF's have been modified to reproduce the experimental results the detection efficiency can be calculated with the simulation code, as a function of the counting rate. Some examples are provided in Figures 3.54 (^{243}Am), 3.55 (^{197}Au, without lead shielding) and 3.56 (^{197}Au, with lead shielding). In all the three cases the detection efficiency in the left panel is plotted as a function of the reaction rate, for different E_{Sum} and m_{cr} conditions. The lower energy limit (2.5 MeV) has been chosen to avoid the 2.2 MeV neutron capture γ-rays in the ^{1}H of the neutron absorber and the higher energy limits (6 MeV for the ^{243}Am and 7 MeV for the ^{197}Au) from the neutron separation energies ($S_n(^{244}Am)$=5.4 MeV, $S_n(^{198}Au)$=6.5 MeV). The experimental counting rates are plotted in the right panels. The horizontal dotted lines represent the counting rate values in which the efficiencies vary more than 1% due to the dead time effects.

As it can be observed, the detection efficiency for the presented conditions in deposited energy and multiplicity of the detected events is essentially constant in the energy range of interest for the case of the ^{243}Am measurement, i.e., has a very low dependency on the counting rate. This is an important conclusion because it implies that no corrections due to fast changes in the counting rate are needed. On the other hand, the ^{197}Au measurement has a much higher counting rate, so the dead time corrections are important. At high neutron energies (E_n~keV) the rapid variations of the counting rate has to be taken into account in the dead time correction model. However, in this work, only the saturated resonance at 4.9 eV is used, where the variations of the counting rate are slow, and no dead time effects related to variable counting rates need to be considered.

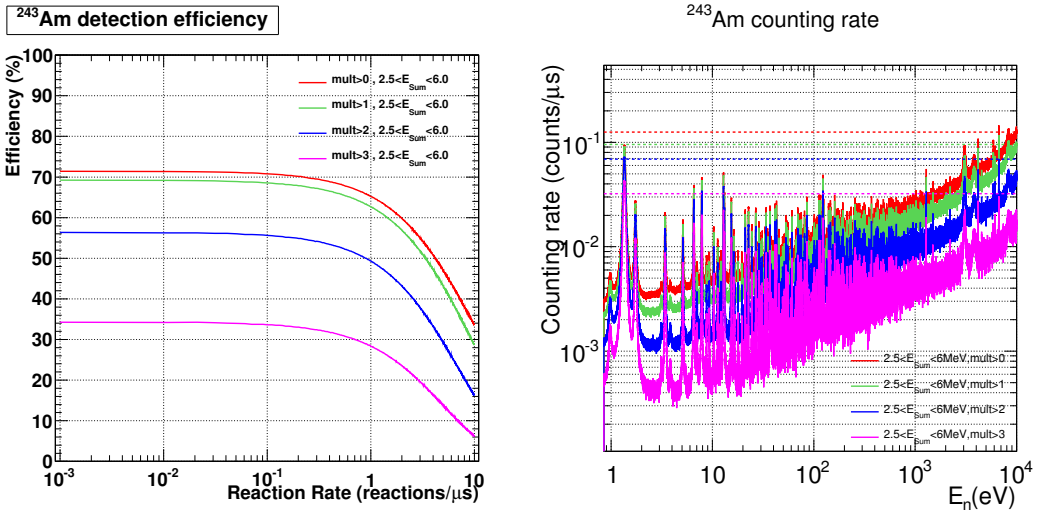

Figure 3.54: Calculated detection efficiency for the ^{243}Am capture cascades, as a function of the reaction rate (left). Counting rate of the ^{243}Am measurement (right). The dotted horizontal lines indicate the counting rate values when the efficiency changes more than 1% from the low counting rate efficiency value.

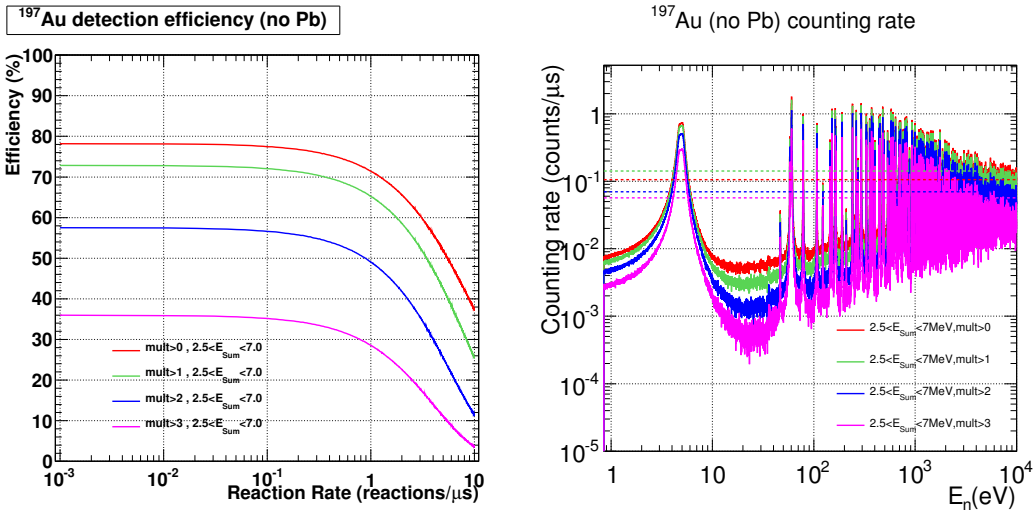

Figure 3.55: Calculated detection efficiency for the ^{197}Au (without lead shielding) capture cascades, as a function of the reaction rate (left). Counting rate of the ^{197}Au measurement, without lead shielding (right). The dotted horizontal lines indicate the counting rate values when the efficiency changes more than 1% from the low counting rate efficiency value.

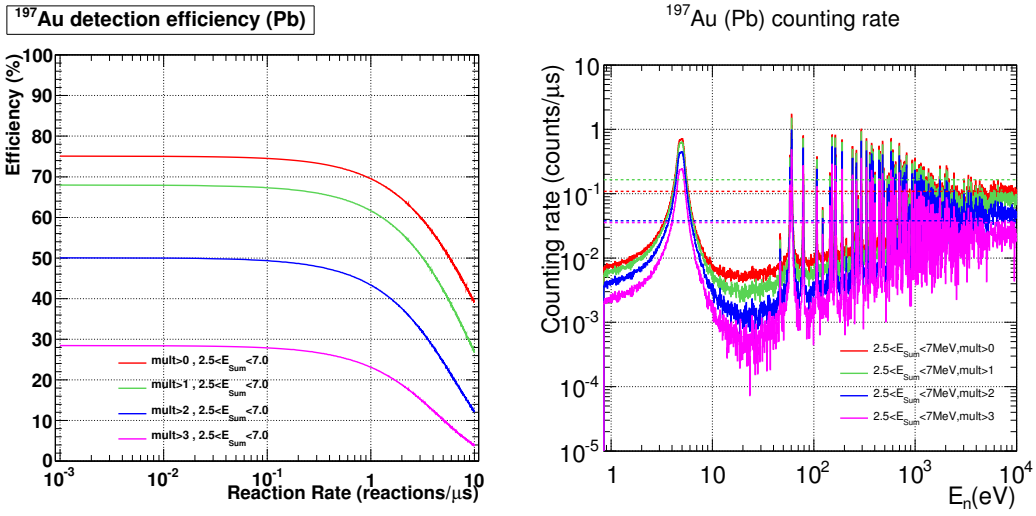

Figure 3.56: Calculated detection efficiency for the ^{197}Au (with lead shielding) capture cascades, as a function of the reaction rate (left). Counting rate of the ^{197}Au measurement, with lead shielding (right). The dotted horizontal lines indicate the counting rate values when the efficiency changes more than 1% from the low counting rate efficiency value.

3.5.6 Uncertainties in the efficiency calculation.

It is not straightforward how to assign a systematic uncertainty to the calculated efficiency. Its estimation has been performed separately for each of the three parts of the simulation process (event generator, GEANT4 transportation and event reconstruction).

Uncertainty related with the event generator

A large number of calculations was made in order to see how the values of the calculated PSF parameters affect the detection efficiency values. The PSF parameter values were varied in a reasonable range, in order to see the change in the calculated efficiency. The procedure was the following:

1. The following PSF parameters were varied uniformly for the ^{243}Am (see Table 3.3):
   - $\Gamma_r(E1,2)$ in the [0.5,0.9] MeV range.
   - $\sigma_r(E1,2)$ in the [25,75] mb range.
   - $\Gamma_r(M1,2)$ in the [0.5,0.9] MeV range.
   - $\sigma_r(M1,2)$ in the [1,3] mb range.
   - $f^{E1}(E_\gamma)\cdot E_\gamma^3$ has been assumed to be constant below a certain value. This value has been varied between 0.30 and 0.70 MeV, and the constant value between $0.5\cdot10^{-8}$ and $1.1\cdot10^{-8}$.
2. A certain number of cascades were generated for each set of varied parameters.
3. The generated cascades were transported with the GEANT4 code, and the results were reconstructed in the same way as it has been presented in the previous sections. For each set of varied parameters, a set of simulated deposited energy histograms were obtained, one for each m_{cr}.
4. The simulated spectra were compared with the experimental ones. For this purpose, a "distance" between them were defined as:
$$D = \frac{1}{N_2}\sum_{mult}\frac{1}{N_1}\sum_{i}\left(y_i^{exp} - y_i^{MC}\right)^2 \tag{3.4}$$
which is a least squares difference: y_i^{exp} and y_i^{MC} are the bin contents of the experimental and simulated histograms, respectively, with multiplicities m_{cr}=1,...,4 and m_{cr}>4 between the energy cut values (2.5<E_{Sum}<6MeV for the ^{243}Am and 2.5<E_{Sum}<7MeV for the ^{197}Au), N_1 is the number of bins in this energy range and N_2=5, the number of histograms with different multiplicities. This "distance" can be used to determine if the experimental results are reproduced or not with a certain set of PSF parameters.

A total number of 5000 sets of parameters were produced. The computational time to perform that amount of simulations is huge, and therefore a new method for the generator of the response function was developed:

- Individual γ-rays were simulated in the energy range of interest: from 10 keV up to 10 MeV, every 10 keV. 10000 events were generated for each energy.
- The results were stored in a list mode file, containing the deposited energy in each crystal for each event.

- These results were used instead of the complete simulation process. For each γ-ray of each simulated capture cascade, a random result from that file were taken (one of the 10000 results of the closest energy value), instead of performing the true Monte Carlo simulation.
- In addition, in order to make the calculations even faster, each initial cascade were "transported" 15 times. Thus, instead of producing 450000 different cascades, which is a relatively slow process, only 30000 cascades were produced for each set of PSF parameters, and these cascades were simulated 15 times.

This method was used to calculate the *distance* between the deposited energy spectra corresponding to the 5000 different sets of PSF parameters and the experimental ones. The results for the ^{243}Am are presented in Figure 3.57. In the left panel, the 5000 points have been plotted. The X axis corresponds to the efficiency obtained for the conditions {2.5<E_{Sum}<6 MeV; m_{cr}>1}, and the Y axis to the mentioned distance. In the right panel, the efficiency values have been histogrammed, showing a distribution whose shape is close to a Gaussian. The uncertainty in the calculation of the efficiency due to the statistical model used to generate the capture cascades were estimated with the standard deviation of this distribution (or a similar one, if other conditions to the detected events were considered). In this case, only those efficiencies corresponding to points with distances lower than twice the minimum obtained distance where histogrammed, assuming that the rest of the points correspond to PSF values which do not reproduce the experimental results. An example of a simulated deposited energy spectra with distance to the experimental results twice the minimum distance found is presented in Figure 3.58.

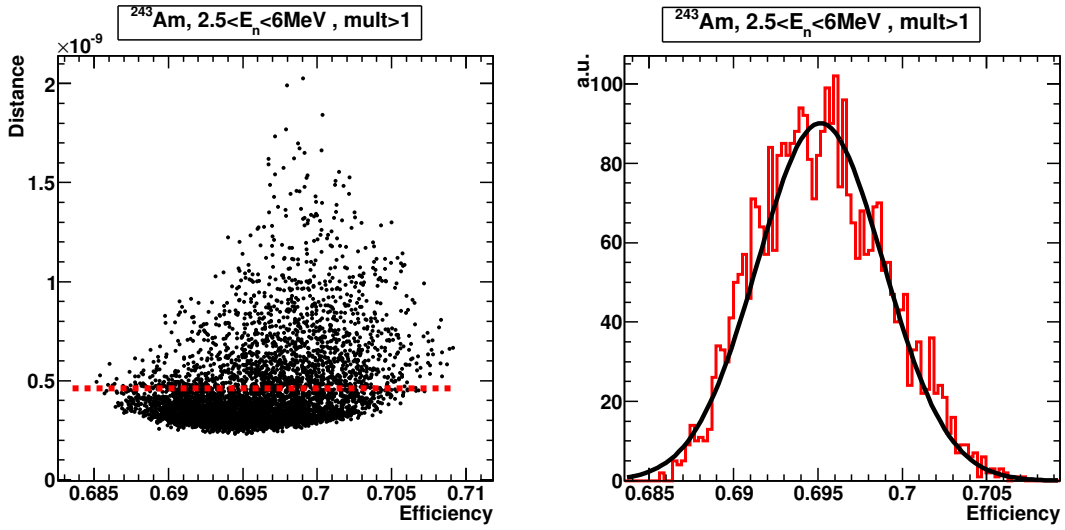

Figure 3.57: In the left panel, the (efficiency,distance) pairs for 5000 different simulations have been plotted. The efficiency values with distances below two times the minimum distance (horizontal red line) have been set into a histogram in the right panel, and fitted to a Gaussian.

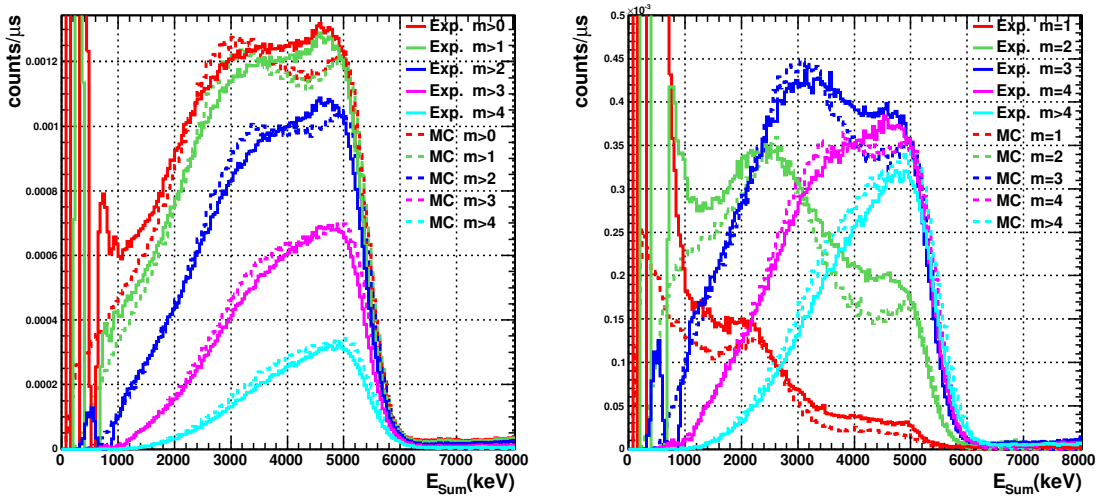

Figure 3.58: Comparison between experimental and simulated deposited energy spectra, for different multiplicities, of neutron capture cascades in ^{243}Am, in the 1.34 - 1.36 eV neutron energy range. With these PSF parameters, the distance of the MC results to the experimental results is twice the minimum distance found.

This procedure has been applied to both ^{197}Au and ^{243}Am measurements, considering conditions in the total deposited energy of 2.5<E_{Sum}<6 MeV (^{243}Am) and 2.5<E_{Sum}<7 MeV (^{197}Au), and different m_{cr}. In the case of the ^{197}Au measurement, two different counting rates were considered, by taking the deposited energy histograms of the two previous mentioned neutron energy ranges (see Section 3.5.4, Figures 3.43 and 3.46): 4.8-5.0 eV, with a reaction rate of ∼1.0 captures/μs; and 3.5-4.2 eV, with a reaction rate of ∼0.1 captures/μs. Two different conditions have been applied to the points included in the histogram previously mentioned: distances lower than twice the minimum distance and no conditions at all. The results are presented in Table 3.4.

^{243}Am	mult>0	mult>1	mult>2	mult>3
no conditions	0.4%	0.6%	1.7%	3%
dist<2·min_dist	0.4%	0.5%	1.2%	2.3%
^{197}Au (∼0.1capture/μs)	mult>0	mult>1	mult>2	mult>3
no conditions	0.6%	1.3%	3%	5%
dist<2·min_dist	0.6%	1.4%	3%	4%
^{197}Au (∼1capture/μs)	mult>0	mult>1	mult>2	mult>3
no conditions	0.6%	1.4%	3%	5%
dist<2·min_dist	0.4%	1.0%	2%	3%

Table 3.4: Estimated uncertainties for the detection efficiencies, associated with the statistical model used to generate the capture cascades, under different conditions.

Thus, what it is presented in Table 3.4 is an estimation of the detection efficiency uncertainty related to the cascade generation model. It can be appreciated that the uncertainty increases when the conditions in m_{cr} are more restrictive. That is reasonable, since the TAC efficiency, without any condition in the detected events is nearly 100%, with a very low dependence in the shape of the electromagnetic cascade produced after the neutron capture. The more restrictive the conditions applied to the detected events are, the larger become the efficiency differences between different cascade shapes. In other words, more restrictive the conditions in the detected events introduce a larger dependence of the efficiency on the shape of the cascade.

Uncertainty related to the TAC geometry

In order to estimate the uncertainty due to the GEANT4 Monte Carlo simulation, the most relevant geometrical parameter has been varied, which is the inner radius of the TAC. After performing simulations with the inner TAC radius changed in ±1 mm (value assumed for the uncertainty in the radius), the difference between the different efficiency values were computed. The uncertainties in the calculated efficiencies due to the geometry implemented in the MC simulations have been assumed to be half of this difference. The obtained results are provided in Table 3.5.

	mult>0	mult>1	mult>2	mult>3
^{243}Am - 2.5<E_{Sum}<6 MeV	1.4%	1.5%	1.9%	2.6%
^{197}Au (∼0.1capture/μs) - 2.5<E_{Sum}<7 MeV	1.0%	1.2%	1.2%	2.1%
^{197}Au (∼1capture/μs) - 2.5<E_{Sum}<7 MeV	1.0%	1.1%	1.5%	1.9%

Table 3.5: Estimated uncertainties of different detection efficiencies, due to the geometry implemented in the MC simulations.

Uncertainty related to the reconstruction process

Finally, the uncertainties related to the reconstruction process have been considered negligible compared with the other sources of uncertainty. In principle, it seems reasonable to think that the dead time correction model could introduce a sizeable uncertainty to the detection efficiency. Figure 3.59 shows the differences in the deposited energy spectra with and without dead time corrections. The differences in the efficiency values can be appreciated by performing the ratio of the integrals between between both simulations. The results corresponding to 2.5<E_{Sum}<6 MeV and m_{cr}>0, ..., m_{cr}>4 are 0.990, 0.984, 0.957, 0.912 and 0.855, respectively. Again, the difference in the efficiency values increases as more restrictive are the conditions. These differences are twice 0.5%, 0.8%, 2.1%, 4.4% and 7.2% (the uncertainties are being estimated as half of these differences), for m_{cr}>0, ..., m_{cr}>4. However, the obtained results when no dead time corrections are applied do not reproduce the experimental results. As a consequence, the values of the uncertainty in the efficiency associated to the dead time model should be considerably lower. Thus, if the conditions applied to the detected events are not very restrictive, this source of uncertainty can be considered quite lower compared to the other sources of uncertainty presented in this Section.

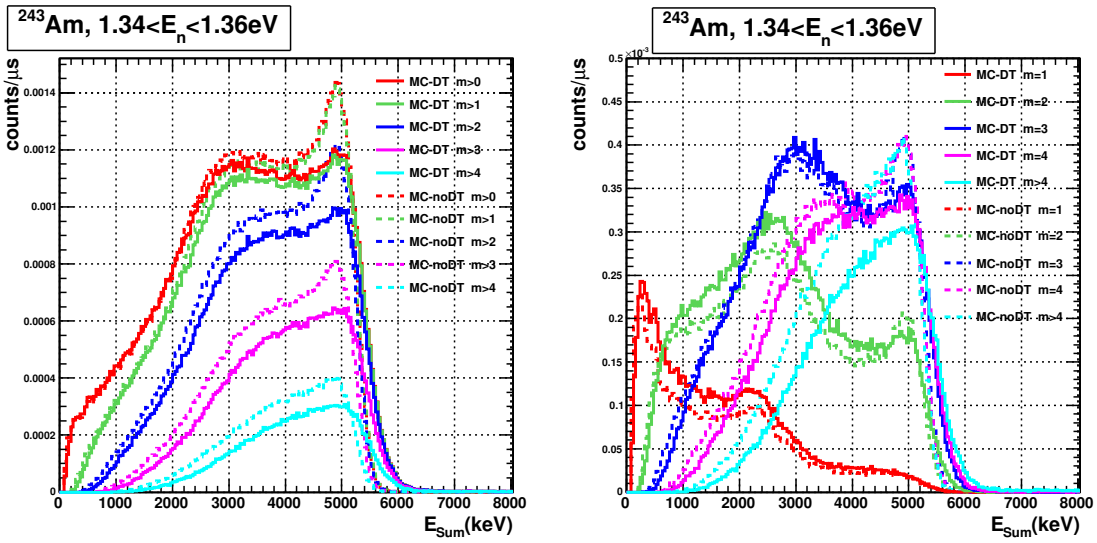

Figure 3.59: Comparison of the Monte Carlo results of the ^{243}Am capture cascades in the normal case (MC-DT) and in the case where no dead time corrections are applied (MC-noDT).

Total uncertainties in the detection efficiencies

In order to provide a final value for the uncertainties in the detection efficiencies, the values obtained in Tables 3.4 (dist<2·min_dist) and 3.5, which correspond to the estimated uncertainties related with the generation of the capture cascades and with the geometry implemented in the MC simulations, have been added quadratically ($\sigma^2_{tot} = \sigma^2_{cascades} + \sigma^2_{geometry}$). The results are provided in Table 3.6.

	mult>0	mult>1	mult>2	mult>3
^{243}Am - 2.5<E$_{Sum}$<6 MeV	1.5%	1.6%	2.2%	3.5%
^{197}Au (∼0.1capture/μs) - 2.5<E$_{Sum}$<7 MeV	1.2%	1.8%	3.2%	4.5%
^{197}Au (∼1capture/μs) - 2.5<E$_{Sum}$<7 MeV	1.1%	1.5%	2.5%	3.6%

Table 3.6: Estimated uncertainties for different efficiency values.

3.6 Background

The sources of background in the ^{243}Am(n,γ) measurement can be classified as follows:

1. ^{243}Am activity.
2. Intrinsic activity of the BaF_2 crystals and environmental background.

3. Interaction of the neutron beam with other materials different than the Ti capsule and the sample.
4. Interaction of the neutron beam with the Ti capsule.
5. Interaction of the neutron beam with the ^{243}Am sample: fission and elastic scattering.

For the ideal case with no pile-up or random coincidences between the different sources, i.e., if the counting rates are small, the first four sources of background can be obtained from the dedicated background measurements described in Section 2.4:

1. ^{243}Am activity: ^{243}Am Activity measurement - Environmental background measurement.
2. Activity of the BaF_2 crystals and environmental background: Environmental background measurement.
3. Interaction of the neutron beam with the Ti capsule: (Ti canning measurement - Environmental background measurement) - (Empty frame measurement - Environmental background measurement). Notice that it is necessary to subtract the environmental background measurement because the ratios between the number of protons and the number of pulses dedicated to each measurement can be different.
4. Interaction of the neutron beam with other materials: Empty frame measurement - Environmental background measurement.

However, all these types of background were measured without the presence of the ^{243}Am activity, which is by far the main contribution to the total counting rate in the ^{243}Am capture measurement. The effect of the ^{243}Am activity signals in the rest of the detected events has been described in Section 3.2.2 (see Figure 3.10), where there are presented the so called "Rad-measurements", constructed by artificially adding the data buffers of an ^{243}Am activity measurement to the different dedicated background measurements. This "Rad-measurements" have been used instead of the real ones to construct the different background contributions in the ^{243}Am capture measurement, so the effect of the ^{243}Am activity is taken into account.

An example of the different contributions to the total background is presented in Figure 3.60. There are presented the deposited energy spectra corresponding to the interaction of the neutron beam with the Ti canning (Ti canning contribution), the rest of the materials intercepting the beam (Empty contribution), and the contribution of the ^{243}Am activity, the environmental background and the activity of the BaF_2 crystals (No beam contribution). On the left panel, the different contributions have been calculated from the dedicated background measurements. As it can be observed, the calculated total background is not correct, since it does not match the shape of the ^{243}Am capture measurements at total deposited energies greater than 6 MeV, where no capture events are expected. On the contrary, when the mentioned Rad-measurements are used (right panel), the total background fits the ^{243}Am measurements at high total deposited energies, as expected. The full characterization of the background over the entire neutron energy range is detailed in Appendix A.

The corresponding time of flight spectra are given in Figure 3.61. The "TiCan" contribution (red) corresponds to the Ti canning contribution to the total background; the "Empty" contribution (green) to the rest of the beam interaction contributions, except with the ^{243}Am sample; and the "Activity" contribution to the activity of the ^{243}Am sample plus the activity of the BaF_2 crystals and the environmental background. When the three contributions are added (magenta) the total background is obtained, with the exception of the contribution due to the interaction

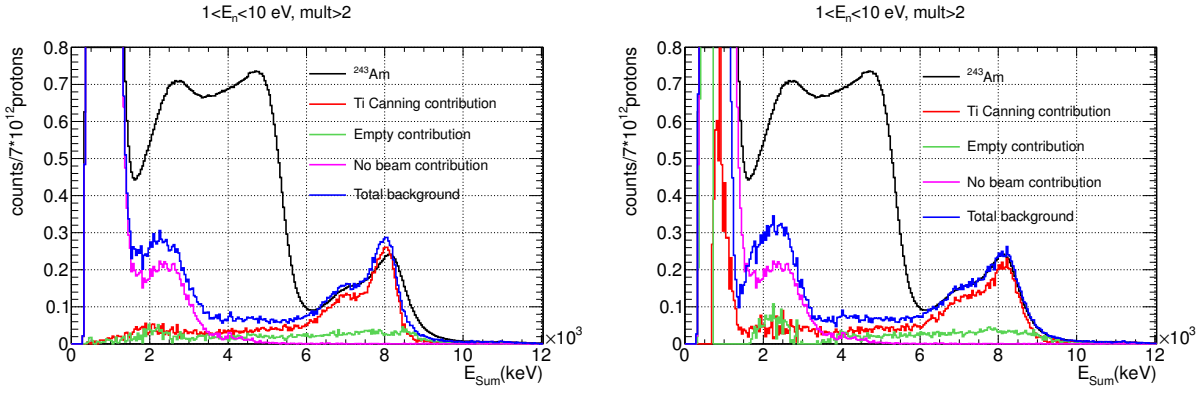

Figure 3.60: Deposited energy spectra of the different contributions to the background, calculated with the dedicated measurements (left) and with the "Rad-measurements" (right). The Ti canning contribution has been multiplied by 0.883 in both cases (see the text below).

of neutrons in the ^{243}Am sample (see the beginning of this Section). This total background has large statistical fluctuations, as it can be observed, and this is because the first two contributions have large statistical uncertainties. The contribution related to the backgrounds which are time independent have negligible statistical uncertainties. For this reason, a smoothing algorithm was applied to the total background (black dotted line), under the assumption that change of the background has to be smooth.

This is reasonable because the background comes from the interaction of the neutron beam with the different elements present in the beam line: Ti, Al, kapton (H, C, N, O), and all these elements are made by isotopes which do not have resonances in the energy range of interest. There is an exception, which are the Ba isotopes of the TAC: neutrons scattered anywhere can be captured in the BaF_2 crystals, producing a capture cascade which can be detected, being part of the background. The different isotopes of natural Barium have resonances in the energy range of interest, suggesting that there can be any non-smooth behavior. However, it has been determined experimentally in other measurements with the TAC that, although the general structure of the Ba resonances can be observed, the background remains relatively smooth [Gue08].

The algorithm used for smoothing the background is described in [Bur83]. It was adopted among other smoothing algorithms such as the moving average or the Savitzky-Golay algorithms [Sav64] because better results were achieved, in the sense that a smaller χ^2 between the fitted and the experimental yield data points was obtained. In addition, the data were also analyzed without performing any smoothing of the background, and the obtained differences were used to estimate the systematic uncertainties due to the uncertainties in the background. This procedure is described in detail in Section 4.3.2.

In the subtraction procedure, it was observed that little changes in the energy calibration of different measurements lead to sizeable differences in the final obtained background. These differences are due to the fact that, in the total deposited energy spectra, the contribution of the activity of the BaF_2 crystals has a high slope in the range $2<E_{Sum}<4$ MeV, so little changes in the energy calibration lead to sizeable differences in the integrated spectra. However, this effect introduces an error in the background calculation which is not time dependent, so a correction

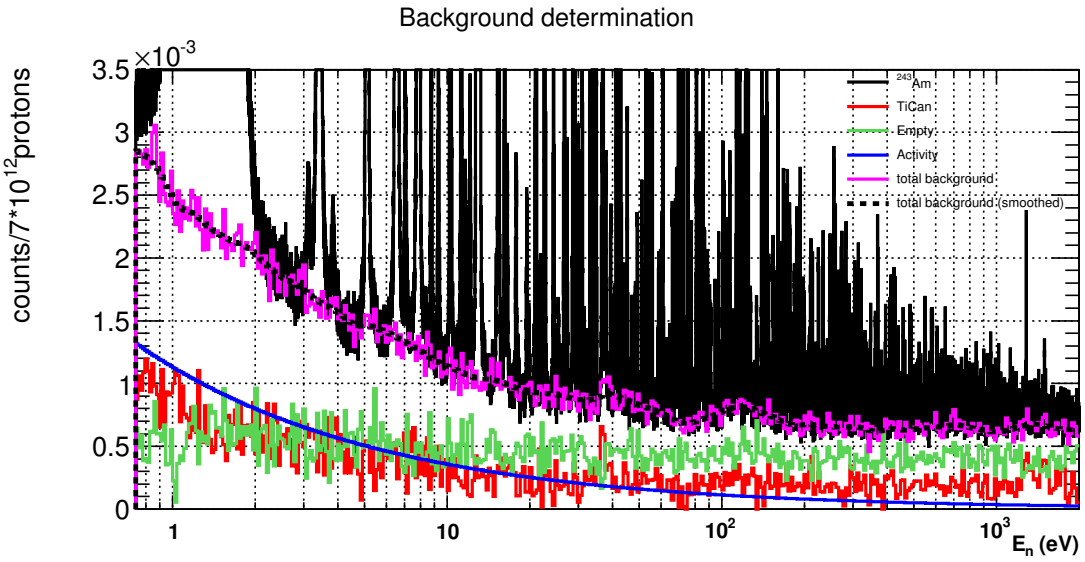

Figure 3.61: Estimated background for the ^{243}Am measurement, for 2.5<E$_{Sum}$<6 MeV, mult.>2.

to the obtained background can be easily performed in the fitting procedure, by adding a term constant in time to the calculated background, i.e., proportional to $1/\sqrt{E_n}$ (i.e. 1/V, being V the neutron velocity).

In addition, the Ti capsule used for the dedicated background measurements is slightly different that the one which contains the ^{243}Am sample. According to the measured masses of both Ti capsules and taking into account the ^{243}Am mass, the ratio between the masses of both capsules should be 0.8994 (^{243}Am/Ti). However, the ^{243}Am sample has been deposited in an Al layer of around 0.07g mass (see Section 2.3), so the normalization factor which has to be used with the dedicated Ti canning measurement is not 0.8994. This normalization factor has been obtained from the ratio of the integral of the deposited energy spectra above E$_{Sum}$=6.5 MeV (no ^{243}Am capture contribution) of the ^{243}Am and Rad-Ti canning measurements. The Rad-Empty contribution has been subtracted from both spectra before calculating the ratio. The results are presented in Figure 3.62, where a normalization factor of 0.883 was used. The total deposited energy spectra of the different measurements are shown in different neutron energy ranges: between 1 and 10 eV (top-right), 10 and 100 eV (bottom-left), and 100 and 1000 eV (bottom-right). The ratio between the integrals of the ^{243}Am and the Ti canning measurements (top-left) is also presented as a function of the neutron energy. This comparison was used to obtain the final normalization factor of 0.883.

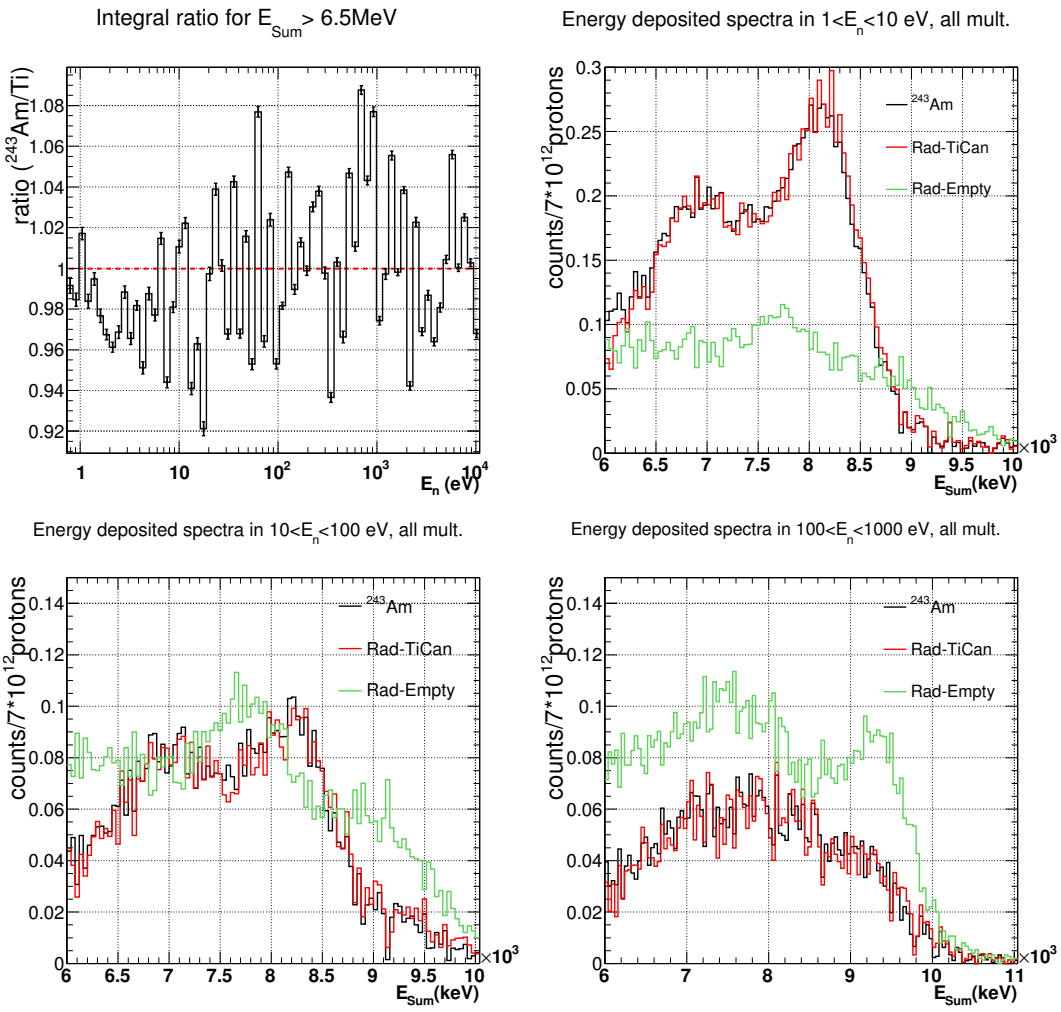

Figure 3.62: Deposited energy spectra for different measurements. The Rad-Empty contribution has been subtracted to the ^{243}Am and the Rad-Ti measurements (up-right and bottom). Ratio between the integrated deposited energy spectra above 6.5MeV between the ^{243}Am measurement and the Rad-Ti measurement, once the Rad-Empty contribution has been subtracted (up-left).

Interaction of neutrons with the sample

The background due to fission and elastic scattered neutrons in the ^{243}Am sample has the same structure as the ^{243}Am cross section: it is a resonant background, and cannot be derived directly from another measurements, since it depends on the ^{243}Am partial cross sections. Fortunately, this background contribution is negligible in this measurement.

The SAMMY code can be used to calculate the theoretical reaction yields, i.e., the yields derived from an existing

evaluated cross section. The fission yield can be calculated directly with the code, and the number of scattered neutrons who exit the sample (Y_n) can be obtained from the transmission and the capture (Y_γ) and fission (Y_f) yields as: Y_n=(1-Transmission)-Y_γ-Y_f. This latest expression is valid if only elastic, capture and fission channels are open. Once these yields are obtained, they need to be multiplied by the detection efficiency, in order to obtain the background contribution.

The efficiency of detecting a scattered neutron (here called neutron sensitivity[3]) can be obtained from the carbon sample measurement (see Section 2.4). The differences with the empty frame measurement are related with the detection of scattered neutrons, since neutron capture in Carbon is negligible. The elastic cross section of Carbon is well known, as well as the neutron flux in the experimental area. This allows to calculate the number of scattered neutrons, at each incident neutron energy. By comparing this quantity with the results of the carbon sample measurement, it is possible to obtain the neutron sensitivity, as a function of the neutron energy and the different conditions in multiplicity and total deposited energy applied to the detected events. The calculated neutron sensitivity is presented in Figure 3.63.

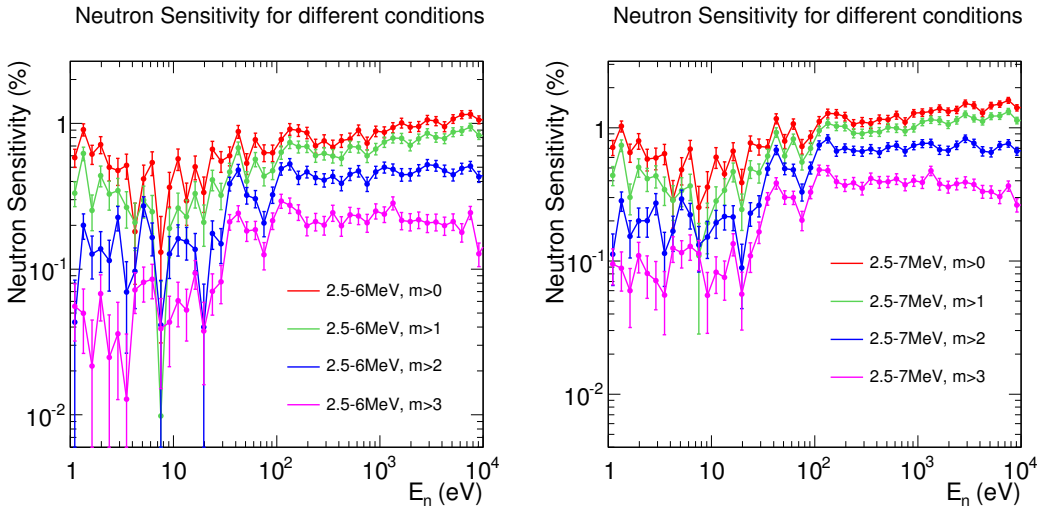

Figure 3.63: Measured neutron sensitivity, for different conditions on E_{Sum} and m_{cr}.

The yields mentioned above have been calculated and multiplied by its detection efficiency, and the obtained results are presented in Figure 3.64, where the ENDF/B-VII.0 cross sections have been used. The detection efficiency for the elastic scattered neutrons is the neutron sensitivity, and the capture and fission efficiencies have been approximated to 50%. On the left panel these quantities are presented in the resolved resonance region of the ^{243}Am nucleus. As it can be appreciated, the backgrounds due to elastic scattering and fission reactions are completely negligible. On the right panel, it is presented the neutron energy region corresponding to the ^{197}Au resonance at 4.9 eV, used for normalization purposes. Again, the background due to scattered neutrons in the sample is negligible.

[3]Sometimes the neutron sensitivity is defined as the ratio between detected an scattered neutron divided by the capture detection efficiency.

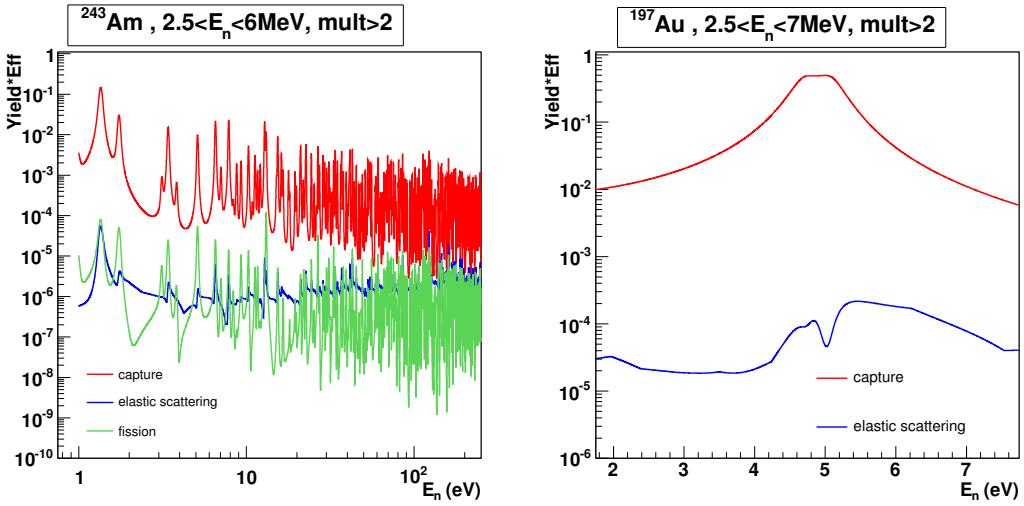

Figure 3.64: Different yields calculated with SAMMY from the ENDF/B-VII.0 evaluation, multiplied by the detection efficiency of each reaction.

Finally, the unresolved resonance region of the ^{243}Am should be also investigated, from 250 up to 2500 eV, the upper energy limit of this measurement. According to the ENDF/B-VII.0 evaluation, the fission channel is more than two orders of magnitude lower than the capture in the whole energy range, so its contribution to the background must be less than a 1%. The elastic reaction, however, remains more or less constant, whereas the capture reaction decreases with the neutron energy. This makes that the elastic reaction is up to 2.3 times greater than the capture reaction, in the mentioned energy range. However, for the same conditions presented in Figure 3.64, 2.5<E_{Sum}<6 MeV and m_{cr}>2, the neutron sensitivity is around 0.5% (Figure 3.63). Since, under the mentioned conditions, the capture efficiency is around 55%, it can be obtained that the background due to elastic scattered neutrons in the ^{243}Am sample can represent up to a 2.3×0.5/55=2% of the measured events.

As a summary, it can be concluded that, for the conditions used in the analysis (2.5<E_{Sum}<6 MeV and m_{cr}>2):

1. The background due to scattered neutrons in the sample is negligible in the ^{197}Au measurement, in the vicinity of the resonance at 4.9 eV.

2. The background due to fission and elastic scattered neutrons in the sample is negligible in the ^{243}Am measurement in the resolved resonance region.

3. The background due to fission and elastic scattered neutrons in the sample is below 1% and 2%, respectively, in the ^{243}Am measurement between 250 and 2500 eV.

3.7 Normalization of the neutron capture yield

Fraction of neutrons intercepted by the sample

The neutron fluence at the n_TOF experimental area was obtained from measurements performed with different detectors, as it is described in Section 2.1. However, the measured sample has 0.5 cm radius, so only intercepts a fraction of the neutron beam, which has 2 cm radius. For this reason, what it is well known is the shape of the neutron fluence, but not its absolute value. The calculation of the fraction of neutrons which are intercepted by the sample has been performed by means of the saturated resonance method [Mac79]. In this way, the uncertainty in the normalization due to the uncertainty in the evaluated cross section is minimized. A ^{197}Au(n,γ) measurement was performed for this purpose, with a sample of the same radius as the ^{243}Am sample. The saturated resonance at 4.9 eV is not a standard, but is enough known. The yield is saturated in the vicinity of the resonance energy, making the uncertainty in the calculated normalization associated to the uncertainty of the evaluated cross section very low, since (almost) all the neutrons intercepted by the ^{197}Au sample are captured in it.

The measured neutron capture yield of the ^{197}Au sample has been compared with the capture yield resulting from the ENDF/B-VII.0 evaluation. In the procurement of the experimental yield, the background was obtained from the dedicated background measurements (see Section 2.4), and the detection efficiency from the simulations presented in Section 3.5. The background due to scattered neutrons is negligible, as it is demonstrated in Section 3.6. The shape of the neutron fluence is also known, so the only quantity needed to obtain the capture yield is the fraction of neutrons which are intercepted by the sample (here called beam factor). This beam factor is then obtained by fitting the experimental yield to the theoretical one, as it is presented in Figure 3.65.

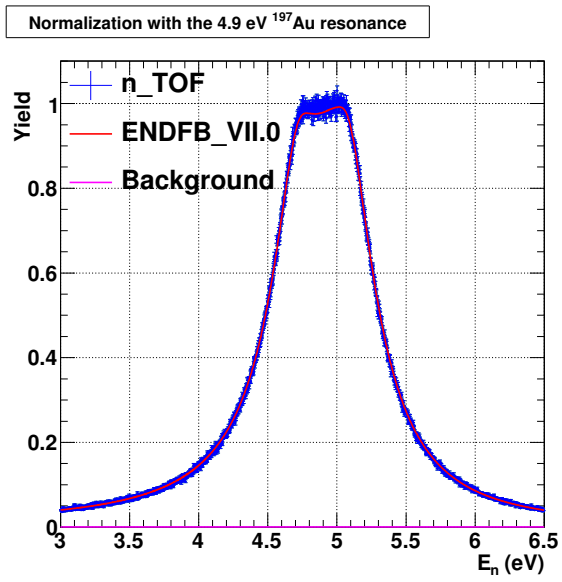

Figure 3.65: Calculation of the fraction of the neutron beam intercepted by the sample, by using the 4.9 eV ^{197}Au saturated resonance.

The beam factor has been calculated from different ^{197}Au measurements (with and without lead shielding), and using different multiplicity conditions. The results are presented in Table 3.7, where the provided uncertainties were calculated by adding quadratically the estimated efficiency uncertainties presented in Section 3.5.6 (Table 3.6) to an estimated uncertainty of 1% associated to the uncertainty in the evaluated cross section. These two uncertainties dominates over the rest of uncertainty sources.

	mult>0	mult>1	mult>2	mult>3
Without Pb shielding	0.198(3)	0.196(4)	0.196(5)	0.200(7)
With Pb shielding	0.194(3)	0.194(4)	0.196(5)	0.199(7)

Table 3.7: Beam factors obtained using different measurements and different conditions in the detected events.

As it can be appreciated, the spread in the values presented in Table 3.7 is compatible with the individual uncertainties, as it is expected. The final beam factor for the ^{197}Au measurement used in this work was 0.196(3), which is a reasonable value if the individual uncertainties and the dispersion of the different values are taken into account.

The beam factor obtained from the parametrization provided in [Pan04] is 0.190, a 3% lower than the one calculated here. However, the beam factor determined experimentally of this work is more accurate than the one deduced from [Pan04]. There can also be a certain misalignment between the ^{197}Au and the ^{243}Am samples. In order to take this effect into account, the beam factor was calculated for different sample positions, with the theoretical parametrization. It was assumed that the misalignment is less than 1 mm, so the beam factor was calculated with the sample centered in the (0,0), (0,1), (1,0) and (1,1) positions (in mm) of the plane perpendicular to the neutron beam. The standard deviation of the obtained beam factors was then calculated, obtaining a σ=0.27%, which is negligible compared with the ^{197}Au beam factor uncertainty (1.5%).

Finally, the mentioned parametrization was also used to obtain the dependence of the beam factor with the neutron energy, finding that there are not significant changes in the beam shape in the energy range of interest (0.7 eV - 2.5 keV). Thus, the calculated beam factor can be considered constant with the neutron energy in this work. If higher energies were reached, an energy dependent beam factor should be used.

Normalization between the different measurements

In order to compare one measurement to another, it is necessary to know the number of neutrons and the number of pulses used in each measurement. The number of pulses is perfectly registered in each measurement, and does not present any problem. The number of neutrons, however, must be calculated. It can be obtained from each of the three monitor detectors, described in Section 2.2.2: the Silicon Flux Monitor (SiMon), which measures the number of neutrons; or the Wall Current Monitor (WCM) or the Beam Current Transformers (BCT), which measure the number of protons, which is proportional to the number of neutrons.

Here it is shown that the values obtained from the SiMon are in perfect agreement with the values provided by the BCT, being both detectors are completely independent. In order to perform this comparison, the tritium peak of the amplitude spectra obtained from each of the four silicon detectors have been integrated (see Figure 2.8), for each individual measurement (see Section 2.4). The obtained values have been divided by the proton intensities given by the BCT, and compared to each other. The results are presented in Table 3.8, where the uncertainties given

in parentheses are only related to the statistical uncertainties of the mentioned SiMon integrals. The uncertainties due to the BTC and systematic uncertainties in the calculation of the mentioned integrals have not been taken into account. Each column corresponds to the ratio of each silicon detector, except the column on the right, where the ratio has been calculated from the sum of the four integrated values. As it can be appreciated, all the results are in good agreement, with the exception of the values obtained from the Empty frame measurement, where it has been verified that the SiMon was not working properly. The results obtained from the rest of the measurements are totally compatible, as it can be appreciated from the standard deviations presented in the bottom line.

In this work the values provided by the BCT have been used to normalize each measurement to the corresponding number of protons. The uncertainty in this normalization has been considered very small compared with other sources of uncertainty, due to the perfect agreement between the silicon detectors and the BCT, and has been neglected.

Measurement	SILI1/p	SILI2/p	SILI3/p	SILI4/p	SILI_tot/p
^{243}Am	$9.868(3)\cdot10^{12}$	$8.672(3)\cdot10^{12}$	$8.307(3)\cdot10^{12}$	$8.914(3)\cdot10^{12}$	$3.5761(5)\cdot10^{11}$
^{197}Au (with Pb shielding)	$9.86(3)\cdot10^{12}$	$8.68(3)\cdot10^{12}$	$8.28(3)\cdot10^{12}$	$8.90(3)\cdot10^{12}$	$3.571(6)\cdot10^{11}$
^{197}Au (without Pb shielding)	$9.88(1)\cdot10^{12}$	$8.68(1)\cdot10^{12}$	$8.39(1)\cdot10^{12}$	$8.94(1)\cdot10^{12}$	$3.590(2)\cdot10^{11}$
Ti Canning	$9.90(2)\cdot10^{12}$	$8.68(2)\cdot10^{12}$	$8.37(2)\cdot10^{12}$	$8.92(2)\cdot10^{12}$	$3.587(3)\cdot10^{11}$
Empty frame	$8.12(3)\cdot10^{12}$	$9.66(3)\cdot10^{12}$	$8.70(3)\cdot10^{12}$	$7.32(3)\cdot10^{12}$	$3.380(6)\cdot10^{11}$
Carbon	$9.92(2)\cdot10^{12}$	$8.67(2)\cdot10^{12}$	$8.43(2)\cdot10^{12}$	$8.91(2)\cdot10^{12}$	$3.593(4)\cdot10^{11}$
Standard deviation (σ)	0.23%	0.05%	0.66%	0.15%	0.8%

Table 3.8: Ratios between the 4 silicon detector results and the number of protons given by the BTC, for different measurements (dedicated pulses). The uncertainties given in parentheses have been calculated taking into account only the statistical uncertainties of the SiMon spectra. In the bottom line, the standard deviation of the values of each column are presented, excluding the values of the Empty frame measurement for the calculation.

3.8 The experimental capture yield

With all the information presented in this chapter the experimental ^{243}Am capture yield was calculated according to Equation 2.9:

$$Y_{\gamma,exp}(E_n) = \frac{N_\gamma(E_n)}{N_T(E_n)} = \frac{C(E_n,\{E_{cuts},m_{\gamma,cuts}\}) - B(E_n,\{E_{cuts},m_{\gamma,cuts}\})}{\varepsilon(E_{cuts},m_{\gamma,cuts},CR)\phi_{Au}(E_n)R_{SiMon}}$$

Different conditions in the detected events can be chosen to obtain the capture yield. As more restrictive are these conditions, the better is the signal to background ratio, but lower is the detection efficiency, so a compromise between these two quantities must be reached. Notice that a lower detection efficiency means larger the statistical uncertainties and a larger uncertainty in the calculated efficiency.

Two different conditions to the detected events have been defined: conditions in the total deposited energy and conditions in the detected multiplicity. Concerning the energy cuts, it is clear from all the deposited energy spectra presented in this work (see Appendix A, for example) that almost all the events with total deposited energy greater

than 6 MeV do not correspond to neutron capture reactions in ^{243}Am, since $S_n(^{244}Am)$=5.4 MeV. For this reason, it seems reasonable to take 6 MeV as the high energy limit for the detected events.

The detected efficiency and the signal to background ratio are presented in Figure 3.66 as a function of the low energy cut and the detected multiplicity. The detection efficiencies were obtained from the Monte Carlo simulations presented in Section 3.5, and the signal to background ratios by dividing the integral of the ^{243}Am capture yield by the corresponding calculated background in the 50-400 eV neutron energy range. As it can be appreciated, the best signal to background ratios are achieved for E_{min} values between 2 and 4.5 MeV, and the detection efficiency decreases with E_{min}, being the slopes considerably higher above E_{min}= 2 MeV. In order to avoid the detection of the 2.2 MeV gammas resulting from the neutron capture in the ^{1}H present in the neutron absorber, which increases significantly the neutron sensitivity, the low energy cut was set to 2.5 MeV, since with higher values the efficiency decreases significantly and the improvement in the signal to background ratio is not too much. Finally, the multiplicity cut was set to $m_{cr}>2$, since the signal to background ratio is improved significantly with respect to $m_{cr}>0$ and $m_{cr}>1$, without reducing so much the detection efficiency. More restrictive conditions in the detected multiplicity leads to unacceptably low detection efficiencies.

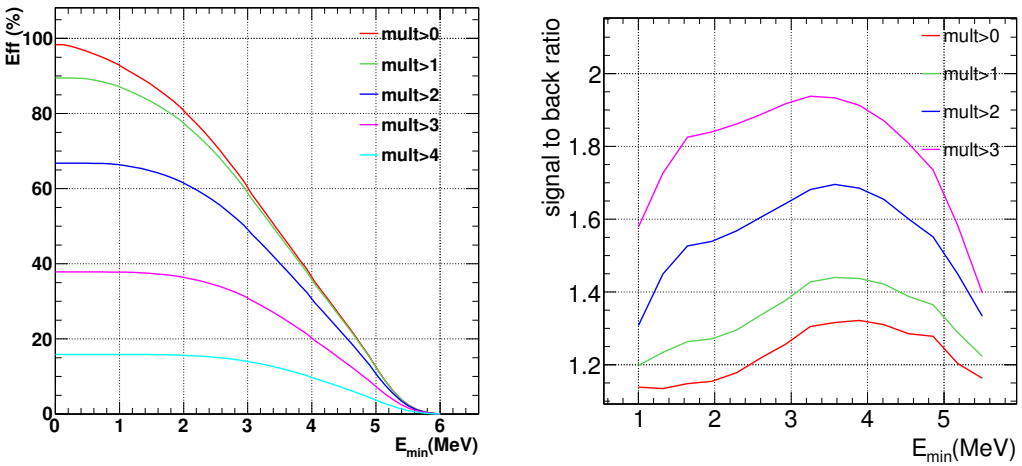

Figure 3.66: On the left panel, the detection efficiency of the TAC as a function of the low energy cut, assuming a high energy cut of 6 MeV, for different multiplicities. On the right panel, the measured signal to background ratio in the 50-400 eV neutron energy range, as a function of the low energy cut and for different multiplicities.

It has been verified that the capture yields constructed from different conditions in the detected events are equivalent, as it is presented in Figure 3.67. The experimental ^{243}Am capture yield obtained from the selected conditions in the detected events is presented in Figure 3.68.

The correlation between the different yield data points is negligible, except from the correlation induced by the normalization uncertainty and the background. A typical source of correlation between the data points are the dead time corrections. However, since these corrections are very low (always below 1%, as it is presented in Section 3.5.5), the introduced correlation can be considered negligible.

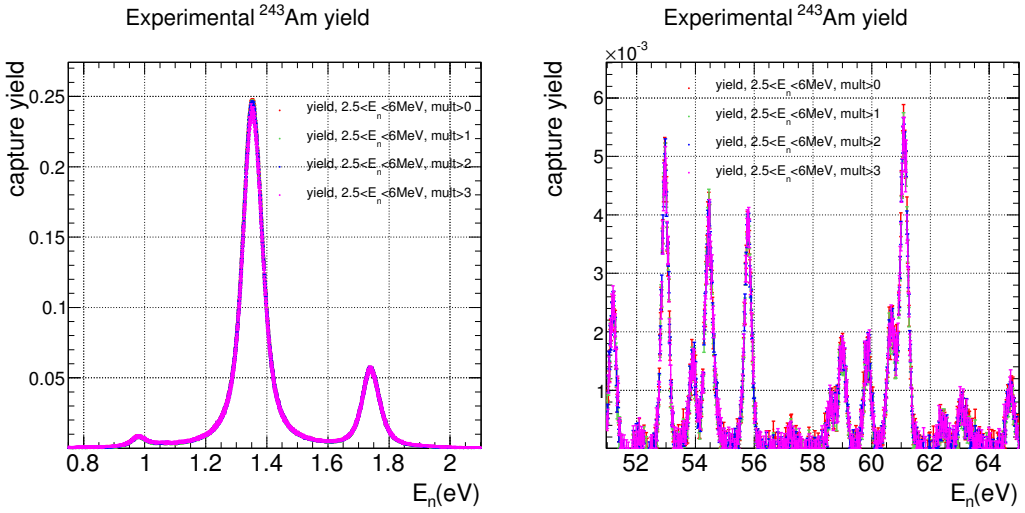

Figure 3.67: Experimental ^{243}Am capture yield obtained from different event cuts. The corresponding backgrounds have been subtracted.

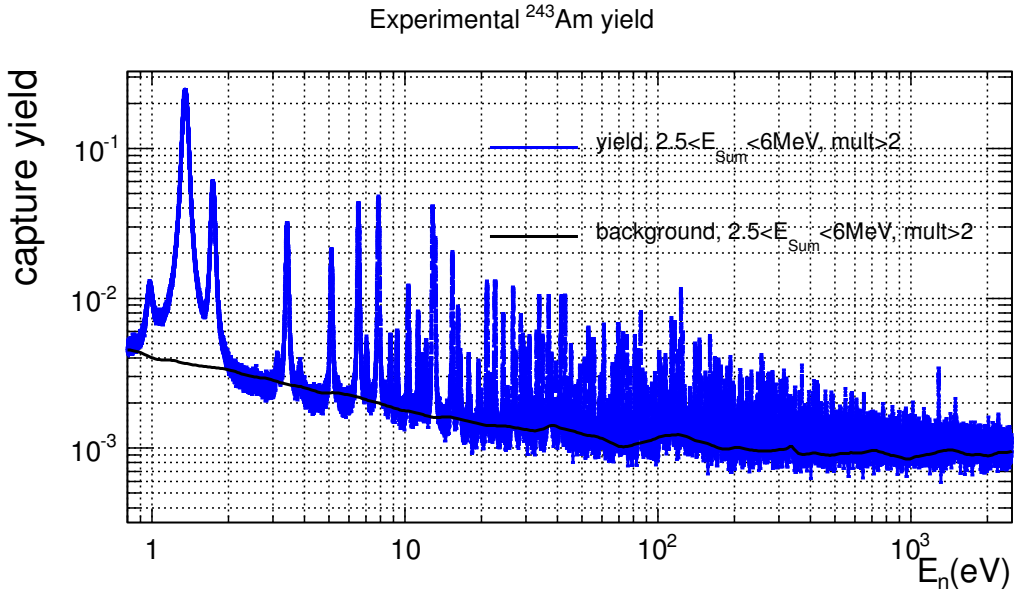

Figure 3.68: Experimental ^{243}Am capture yield obtained with the selected cuts of {2.5<E$_{Sum}$<6 MeV; mult>2}, with his associated background. There is a component proportional to $1/\sqrt{E_n}$ that has to be still fitted in the background.

The capture yield, including the statistical uncertainties of each data point, and together with the calculated backgrounds (smoothed and non-smoothed) will be included in the EXFOR database, in order to make them available to the nuclear physics community. The rest of the information needed to perform a resonance analysis of the n_TOF capture measurement, which should be also included in EXFOR is:

1. Both calculated backgrounds have a component proportional to $1/\sqrt{E_n}$, or 1/V, that must be fitted.
2. The normalization uncertainty, which is obtained from the detection efficiency and the beam factor uncertainties, which are 2.2% and 1.5%, respectively. If these two quantities are quadratically added, a total normalization uncertainty of 2.7% is obtained. If they are linearly added, the resulting normalization uncertainty is 3.7%. However, this uncertainty is negligible compared to the uncertainty in the sample mass (11%).
3. The information concerning the measured sample (dimensions, temperature, ...), available in Section 2.3.
4. The n_TOF resolution function.

Chapter 4

Resonance analysis of the capture yield

This Chapter is dedicated to the procurement of the ^{243}Am cross section from the analysis of the experimental capture yield. The SAMMY code [Lar06], which is widely used by the nuclear data community, has been used to perform this analysis. SAMMY allows to fit the resonance parameters which describe the neutron cross sections in the resolved and unresolved resonance regions (RRR and URR) to one or several experimental transmission and/or yield data sets. In both RRR and URR, a Bayesian analysis is performed by the code to obtain the cross section parameters, together with their uncertainties and correlations.

In the RRR, several approximations to the R-matrix formalisms can be used to obtain the cross section from the resonance parameters. In this analysis, the Reich-Moore approximation was selected. SAMMY uses the theoretical cross section to obtain the corresponding transmission or reaction yield, which is then compared to the experimental data. In this process, the experimental effects such as the Doppler broadening, the multiple scattering and the resolution broadening are taken into account.

For the analysis of the URR, a version of the FITACS code [Fro89] is implemented in SAMMY, which uses Hauser-Feshbach theory with width fluctuations. In this case, the unresolved resonance parameters allow to construct the theoretical cross section, which is then compared to the experimental value and not to the transmission or the reaction yields.

In this Chapter the comparison of the fitted and experimental capture and transmission yields is given in a large number of figures, all with the same structure; the upper part showing the overlap of the theoretical and experimental curves, and the lower part showing the residuals. The residuals are the distances of the experimental data points to the theoretical fitted yield, divided by the statistical uncertainties of the data points. They represent the distance, in units of σ, from the experimental points to the fitted values, and in all the cases the the Y axis range from -5σ up to +5σ.

In Section 4.1, a summary of all the relevant ^{243}Am measurements performed up to now is presented.

Section 4.2 is dedicated to the procurement of the experimental capture yield:

1. The time of flight distance is used to calculate the energies of the captured neutrons. It has been calibrated by fitting the measured ^{197}Au resonance energies to the values present in the ENDF/B-VII.0 evaluated library.
2. The background of the n_TOF capture yield was obtained from dedicated measurements. However, a component proportional to $(E_n)^{-1/2}$ (or 1/V) had to be included.

3. The uncertainty of the n_TOF capture yield due to the normalization (efficiency and beam interception factor) is 2.7%, as it is said in Section 3.8. However, the sample mass has an estimated uncertainty of 11%, due to its wrong characterization. For this reason, the n_TOF capture measurement has been normalized to the existing transmission measurements.

4. It was found that the sample contains impurities. Its amount was determined from the measured capture yield, since their strongest resonances are visible in it. The impurities have been taken into account in the cross section analysis, as a component of the background. Although this procedure is described in Section 4.2.4, its contribution was included in the total background in the calculations of the normalization and the $(E_n)^{-1/2}$ background component.

Section 4.3 is dedicated to describe the analysis performed in the RRR. The analysis includes the procurement of the resonance parameters, E_0, $g\Gamma_n$ and Γ_γ of each resonance, since the data is not sensitive neither to the fission widths nor to the spins of the resonances and the channel radius. It also includes the calculation of the different uncertainties. The statistical uncertainties have been obtained with the SAMMY code. The systematic uncertainties, however, have been calculated with other methods, since it was found that the results obtained by SAMMY seem to be underestimated. Finally, a statistical analysis of the obtained resonance parameters is presented at the end of the Section. The result of this latter analysis is a set of average resonance parameters that are usually used to predict cross sections at higher energies, if no experimental data is available.

The analysis of the URR is presented in Section 4.4, where the n_TOF data is analyzed up to 2.5 keV. In addition, other differential and integral data have been used to fit the capture cross section up to higher energies.

4.1 Previous measurements and evaluations

All the differential capture and transmission measurements performed up to now are presented in Figure 4.1 and listed in Table 4.1. There are also other fission, inelastic and (n,2n) differential cross section measurements available in the EXFOR [Sch08] database. In addition, there are also thermal and integral measurements, some of them presented in Sections 4.3.5 and 4.4.4. A brief summary can also be found in [Har14].

As it can be observed, there is not any published result of a differential capture measurement below 250 eV, and the capture cross section of all the present evaluations for the resolved resonance region have been obtained from the transmission measurements. However, there are three capture measurements which cover the resolved resonance region which have been performed recently, apart from the one presented in this work. The first two measurements (M. Jandel et al. [Jan09]) were performed at Los Alamos National Laboratory (LANL), in the years 2005 and 2007, with two different samples. In [Jan09], only a brief description of the experiment is presented. The third one (J. Hori et al. [Hor09]) was performed at the Research Reactor Institute of the Kyoto University, in the energy range from 0.01 to 400 eV. The only publication available ([Hor09]) only describes the experiment and provides the capture resonance integral. The resonance parameters provided by Kimura et al. have been obtained from a capture measurement where the ^{243}Am was an impurity, and thus the values provided are probably not very accurate. Indeed, the amount of ^{243}Am in the sample was estimated from the measured yield.

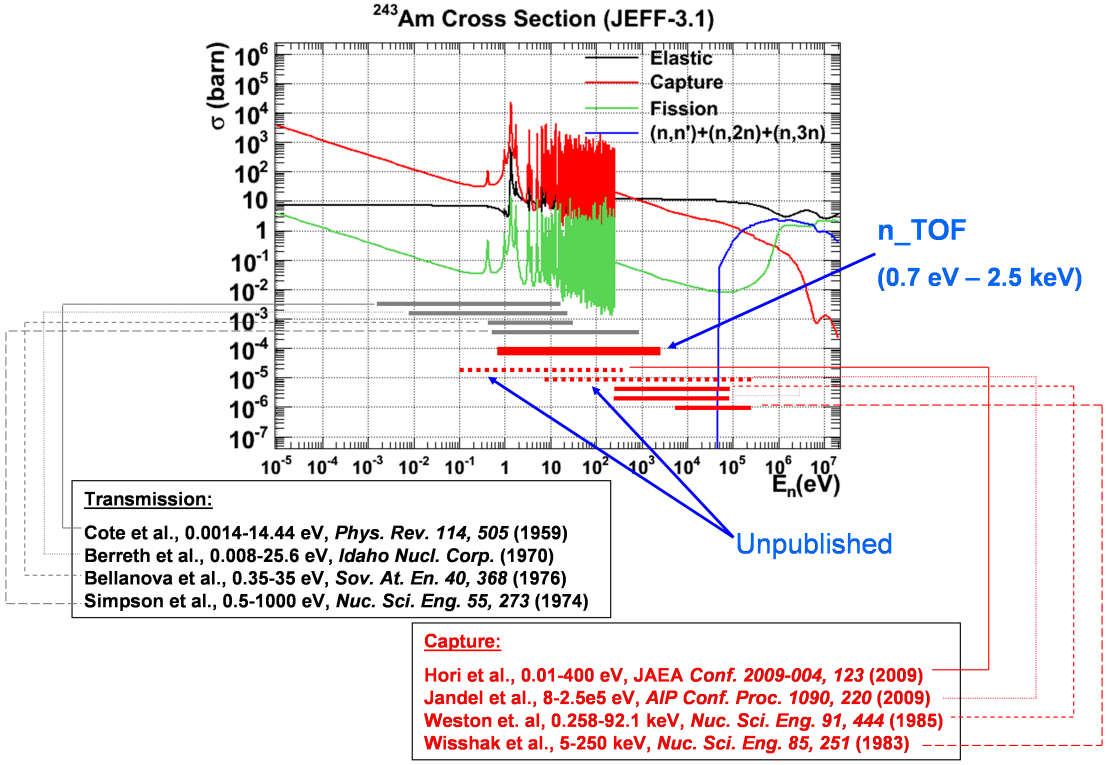

Figure 4.1: Differential transmission and capture measurements of ^{243}Am performed up to now.

A comparison between the four capture cross sections calculated from the transmission data is presented in Figure 4.2. The cross sections have been constructed from the resonance parameters provided in the publications. As it can be appreciated, there are sizeable differences between them. The same occurs with the capture measurements at higher energies. In this case, there are two different data sets available in EXFOR for each measurement, corresponding to different experimental configurations. As it can be appreciated in Figure 4.3, the two data sets provided by Weston et al. are not compatible below 2 keV. In addition, the data provided by Wisshak et al. is between 10% and 15% lower than the Weston et al. results.

The cross sections available in the standard ENDF format libraries are based in evaluations performed with the experimental data described above. In all of them the resolved resonance region (RRR) goes up to 250 eV, and the unresolved resonance region (URR) up to 40-42 keV[1], depending on the evaluated library. Taking into account only

[1]Excluding the Russian libraries, BROND-2.2 and ROSFOND-2010, where the URR goes up to 30 and 20 keV, respectively.

Reference	Type of measurement	Energy range
T.S.Bellanova et al. (1976) [Bel76]	Transmission	0.35 eV - 35 eV
O.D.Simpson et al. (1974) [Sim74]	Transmission	0.5 eV - 1 keV
J.R.Berreth et al. (1970) [Ber70]	Transmission	0.008 eV - 25.6 eV
R.E.Cote et al. (1959) [Cot59]	Transmission	0.0014 eV - 15.44 eV
L.W.Weston et al. (1985) [Wes85]	Capture	258 eV - 92.1 keV
K. Wisshak et al. (1983) [Wis83]	Capture	5 - 250 keV
Kobayashi et al. (1999) [Kob99]	Fission	0.056 eV - 7.94 keV
H-H. Knitter et al (1988) [Kni88]	Fission	1 eV - 10 MeV
P.A.Seeger et al. (1970) [See70]	Fission	0.489 eV - 2.97 MeV
M. Jandel et al. (2009) [Jan09]	*Capture*	*8 eV - 250 keV*
J. Hori et al. (2009) [Hor09]	*Capture*	*0.01 - 400 eV*
This work	Capture	0.7 - 2500 eV
Kimura et al. , 2012 [Kim12]	*Capture*	-
Alekseev et al. , 2011 [Ale12]	*Fission*	-

Table 4.1: Differential transmission, capture and fission ^{243}Am measurements performed up to now. In the case of the fission measurements, only those performed in the energy range of this work have been considered. The results of the M. Jandel et al. and J. Hori et al. measurements have not been published yet (neither the yield nor the resulting cross sections). Kimura et al. only provide the resonance parameters of the resonance at 1.35 eV , and Alekseev et al. the resonance parameters below 17 eV.

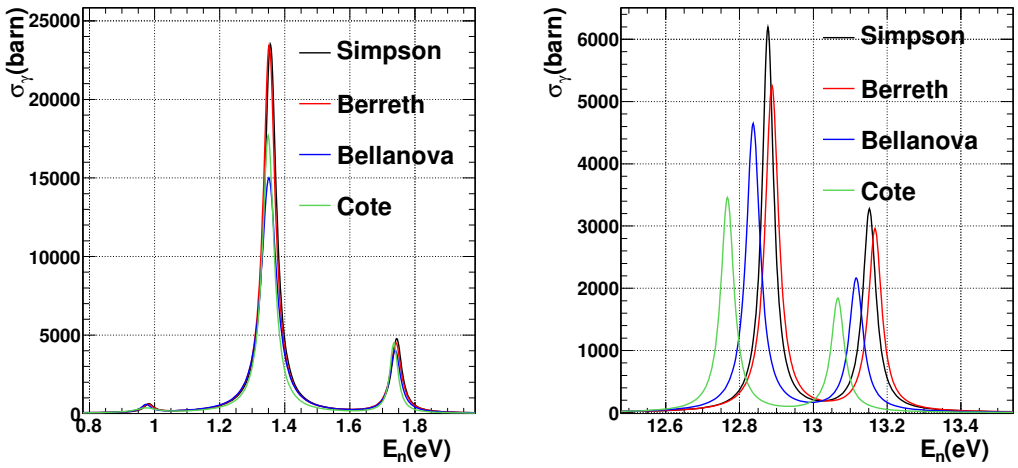

Figure 4.2: Comparison between the ^{243}Am capture cross sections obtained from the resonance parameters available in the different transmission measurement publications [Bel76, Ber70, Sim74, Cot59].

the elastic and capture cross sections in the resolved and unresolved resonance regions the most recent libraries rely on the following evaluations:

1. The evaluation adopted by the ENDF-B/VI library, which has been also maintained for the ENDF/B-VII.0

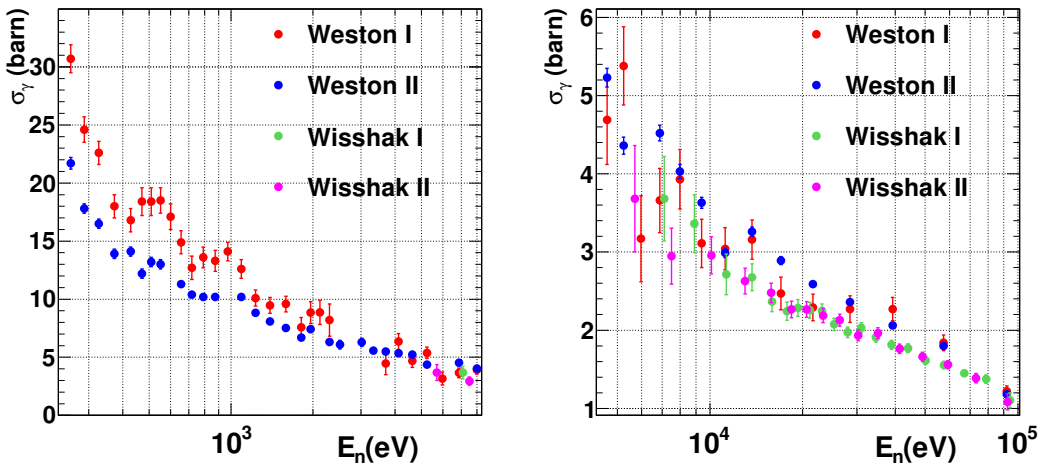

Figure 4.3: Comparison between the ^{243}Am capture cross sections provided by Weston et al. [Wes85] and Wisshak et al. [Wis83].

library. It is based in the Simpson et al., the Weston et al. and the Wisshak et al. measurements.

2. The evaluation adopted by the ENDF/B-VII.1 library, which is similar but not the same as the one adopted by the previous ENDF/B versions in the RRR. The main change was performed in the biggest resonance at 1.35 eV, in order to reproduce the integral measurement performed by Ohta et al. [Oht06]. A different evaluation of the URR was also carried out.

3. The evaluation adopted by the JEFF-3.1, JENDL-3.3 and CENDL-3.1 libraries, which are mainly based in an evaluation performed by Maslov et al. [Mas96], which uses the same experimental data as the ENDF-B/VI and ENDF/B-VII.0 libraries.

4. The evaluation adopted by the JENDL-4.0 library, which is based in JENDL-3.3, with modifications in the lower energy resonances to reproduce the integral measurement performed by Ohta et al. [Oht06]; and also with modifications in the URR.

5. The evaluation adopted by the ROSFOND-2010 and BROND-2.2 libraries, where the RRR of the Maslov evaluation is adopted, but with changes in the URR. Both ROSFOND-2010 and BROND-2.2 URR are slightly different. In particular, the URR of the BROND-2.2 evaluation goes up to 30 keV, whereas the ROSFOND-2010 evaluation goes up to 20 keV.

Thus, in all the cases the Simpson et al. data were used to obtain the resonance parameters in the RRR. This is because they have more quality than the Bellanova et al. and the Cote et al. measurements, and are quite compatible with the Berreth et al. measurement. An additional reason is that it is the only dataset above 35 eV. One should notice that the same experimental data have lead to different evaluated cross sections.

In Figures 4.4 and 4.5 part of the transmission measurement performed by Simpson et al. is presented together with the transmission yields obtained from the evaluations. In the left panel of Figure 4.4 it can be appreciated that the JENDL-4.0 library does not reproduce the experimental results, whereas the ENDF/B-VII.1 library has

increased the size of the resonance at 1.35 eV (see left panel of Figure 4.6) in such a way that it still reproduces quite well the Simpson et al. data. Above 1.8 eV the JENDL-4.0 library has the same resonance parameters as the rest of the non-ENDF/B libraries, and they do not to reproduce the experimental data in the right panel of Figure 4.4. In the left panel of Figure 4.5 all the evaluations present more or less the same result, with the exception of the ENDF/B-VII.1 library, probably due to a mistake. In the right panel of Figure 4.5 two different results can be observed. The one which reach lower values corresponds to the ENDF/B libraries and the other to the rest of the libraries. In this case it is less clear which result is in better agreement with the experimental results.

At higher energies, above 40 - 42 keV, almost all the evaluations differ from the others. In all the cases the capture cross section was obtained from the available experimental results and with optical model calculations. More comparisons between the experimental data and the evaluated libraries are presented in Sections 4.4.3, 4.4.4 and 5.2.

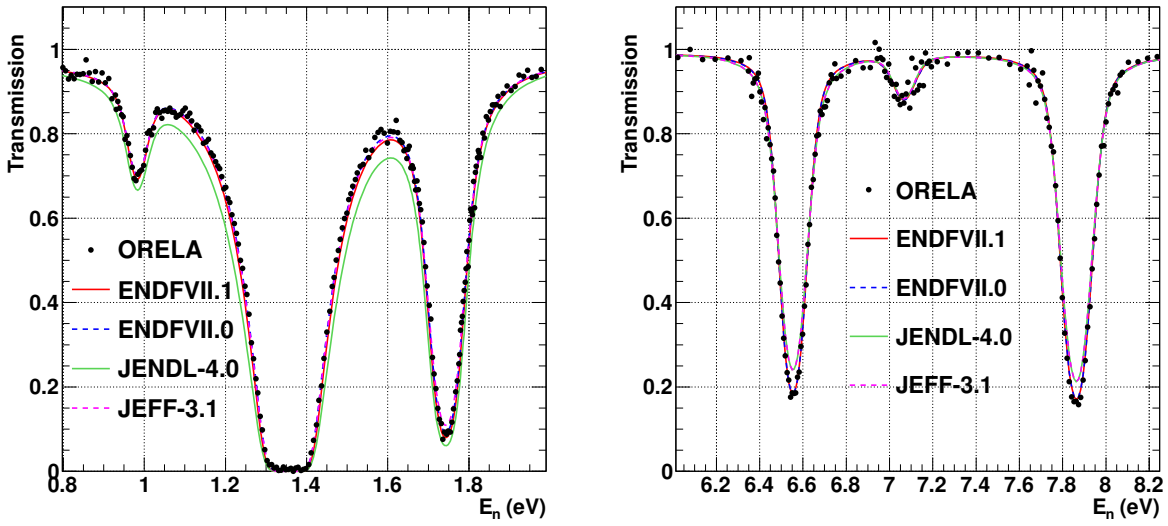

Figure 4.4: Transmission yield obtained by Simpson et al. at the ORELA facility together with the theoretical yields obtained from different libraries and the ORELA experimental conditions.

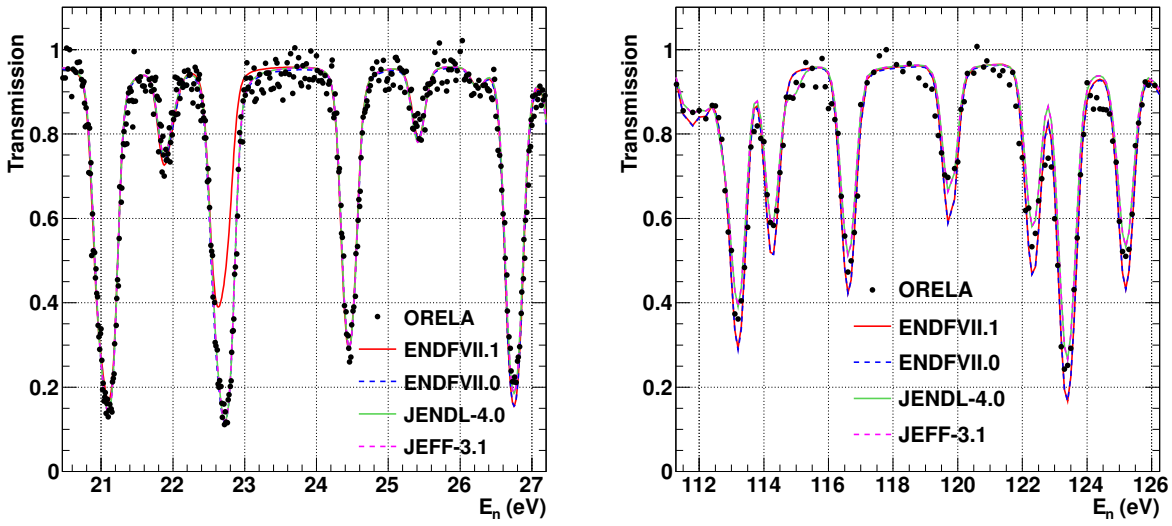

Figure 4.5: Transmission yield obtained by Simpson et al. at the ORELA facility together with the theoretical yields obtained from different libraries and the ORELA experimental conditions.

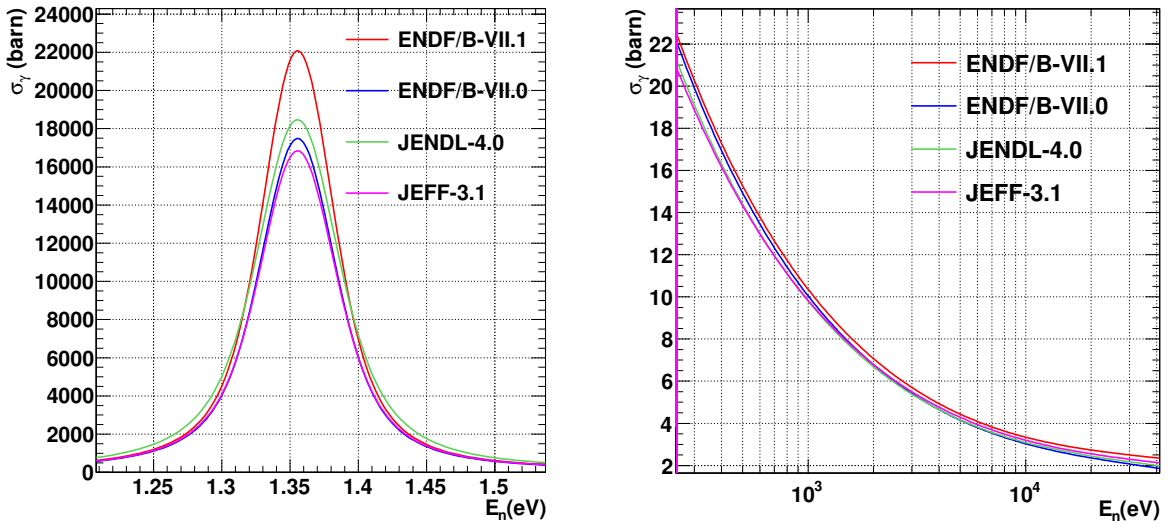

Figure 4.6: Different evaluations of the ^{243}Am capture cross section, in the strongest resonance at 1.35 eV (left) and in the unresolved resonance region (right).

4.2 Procurement of the experimental capture yield

This Section is dedicated to describe some final modifications performed to the obtained capture yield: the calibration of the time of flight distance, the determination of the background component constant in time, the normalization to the existing transmission measurements and the determination of the sample impurities.

4.2.1 Time of flight distance calibration of the measurement

The time of flight distance of the n_TOF data has been calibrated to the ^{197}Au resonance energies present in the ENDF/B-VII.0 library. This has been done by first fitting the ^{197}Au resonance parameters to the n_TOF data, assuming a time of flight distance of 185.005 m, which is one of the values used in previous experiments, and then by comparing them with the evaluated ones in the 1 eV - 1 keV energy range. The calibration has been performed by minimizing the following quantity:

$$D = \sum_i \left[\left(E_i^{ENDF} - E_i^{Adj} \right) \cdot RK_i^{ENDF} \right] \tag{4.1}$$

where E_i^{ENDF} and E_i^{Adj} are the E_0 (resonance energy) parameter of the i^{th} resonance in the ENDF/B-VII.0 evaluation and in the n_TOF fit, respectively, and RK_i is the radiative kernel (see equation 1.23) of the resonance, which is introduced to weight the resonances proportionally to their size. Then, the n_TOF distance has been varied in order to make D=0. The result is a time of flight distance of 184.878 m.

Alternative definitions of D, such as the quadratic difference between the resonance energies, or omitting the RK weight, lead to very close results (differences smaller than 0.003%).

Thus, the energy values of this ^{243}Am resonance analysis have been referenced to the ^{197}Au evaluation present in the ENDF/B-VII.0 library.

4.2.2 Determination of the background constant

As it was presented in Section 3.6, the background of the n_TOF capture measurement has been determined from dedicated background measurements. However, as a consequence of the uncertainties in the energy calibration of the different measurements, a background component constant in time had to be added. When the capture yield is expressed as a function of the neutron energy, a background component which is constant in time has an energy dependency proportional to $1/\sqrt{E_n}$. Thus, the determination of this component consists in fitting a single parameter "a", where B(E)=B_p(E)+a/$\sqrt{E_n}$, being B(E) the fitted background and B_p(E) the background calculated from the dedicated measurements.

The procurement of the background constant "a" was performed by making several fits of the ^{243}Am resonance parameters together with the background constant to the n_TOF capture data in different energy ranges. The fits were carried out with the SAMMY code, and the results are summarized in the left panel of Figure 4.7. Each fit was performed in the energy range which goes from {1,1.5,2,2.5,...,10} eV (value of the X axis) up to 50 eV (red line) , 75 eV (blue line) or 100 eV (green line), thus covering a large amount of energy intervals. The final background constant value was set to -7.7·$10^{-4}\sqrt{eV}$, and it is represented by an horizontal continuous black line. Its associated uncertainty was set to 4%, as represented by the dashed black lines. The value and its uncertainty is compatible with all the fits within one σ.

The normalization (i. e. the sample mass or the sample thickness) has to be determined together with the background constant. In principle, it is not evident if both parameters are correlated in the fit. In order to answer this question, the background constant was obtained for different thickness values. In the right panel of Figure 4.7 the background constant has been fitted, together with the resonance parameters, for three different thicknesses, in the energy ranges between the value given by the X axis and 50 eV. The three thickness values used were $2{\cdot}10^{-5}$ atoms/barn, which is the value used in the left panel, and $2{\cdot}10^{-5}{\pm}15\%$ atoms/barn. These values correspond, approximately, to the mean value of the sample mass calculated in Appendix B and a variation of ±15%, which is an overestimation of the uncertainty in the sample mass. This Figure shows that the dependence of the fitted value of the background constant with the sample thickness is very low. Thus, the correlation has been neglected and both parameters have been determined separately.

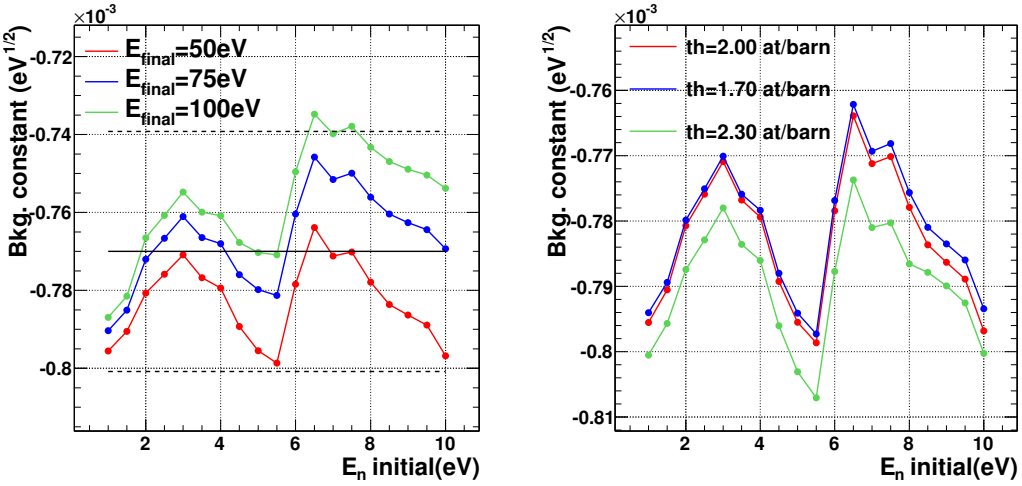

Figure 4.7: On the left panel, the fitted values of the background constant are represented. The thickness of the sample has been set to $2{\cdot}10^{-5}$atoms/barn and the fits have been performed between an initial energy given by the X axis and a final energy which is 50 eV (red line), 75 eV (blue line) or 100 eV (green line). The final value for the background constant and errors are represented with the black lines. On the right panel, three different thicknesses have been used for the fits, all of them between an initial energy given by the X axis and 50 eV.

Finally, in order to show the size of the effect of the 4% uncertainty in the background constant, the relative difference in the total background between using a background constant of $-8.00{\cdot}10^{-4}\sqrt{eV}$ (mean value plus 4%) and a background constant of $-7.40{\cdot}10^{-4}\sqrt{eV}$ (mean value minus 4%) has been calculated. The results are presented in Figure 4.8, where it is shown that this relative difference is around 2% for 1 eV, 1.25% for 10 eV, 0.5% for 100 eV and 0.25% for 1 keV. Notice that the uncertainty in the final background associated with the uncertainty in the background constant is half of these values, so 1%, 0.6%, 0.25% and 0.13% for 1 eV, 10 eV, 100 eV and 1 keV, respectively. A detailed study of the effect of this uncertainty in the uncertainty of the calculated resonance parameters can be found in Sections 4.3.2 and 4.3.4.

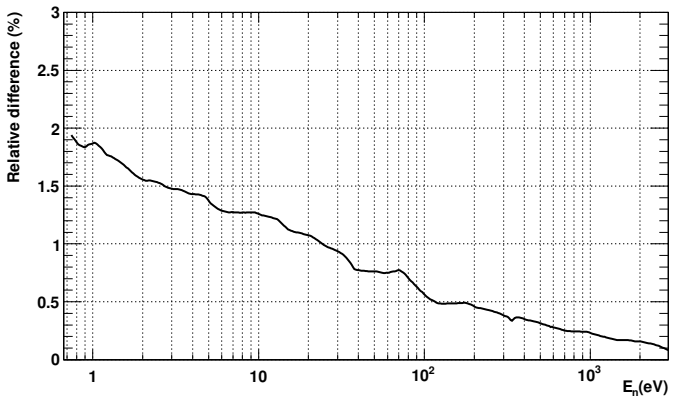

Figure 4.8: Relative difference in the final total background B(E)=B$_p$(E)+a/$\sqrt{E_n}$ between using a background constant of a= -8.00·10$^{-4}\sqrt{eV}$ (mean value plus 4%) and a background constant of a= -7.40·10$^{-4}\sqrt{eV}$ (mean value minus 4%).

4.2.3 Normalization

The capture cross section is obtained by comparing the theoretical capture yield, calculated from the capture cross section and the thickness of the sample and taking into account the broadening effects (Doppler, multiple scattering and resolution broadening), with the experimental capture yield. As it was presented in Section 3.8, the uncertainty in the normalization of the experimental capture yield, without taking into account the uncertainty in the sample mass, is 2.7%. However, the 11% uncertainty associated to the sample mass (i.e., to the sample thickness and thus to the theoretical capture yield) gives a total uncertainty in the normalization of the capture cross section of σ=$\sqrt{0.027^2+0.11^2}\backsimeq$11%. In order to reduce it, the n_TOF capture measurement was normalized to other existing ^{243}Am cross section measurements.

The only experimental data available to normalize the n_TOF capture yield are the four transmission measurements presented in Table 4.1 and the Weston et al. capture data above 250 eV. Integral measurements (see Table 4.7) cannot be used because the discrepancies and uncertainties are too high, among other reasons that will be discussed later. On the other hand the Weston et al. data provide two different measurements of the same ^{243}Am sample, which are incompatible below 2 keV. For this reason, it was decided to normalize the n_TOF measurement to the transmission measurements. As a result, the normalized n_TOF data are compatible with one of the mentioned Weston et al. data sets.

The normalization procedure was performed with two different methods, that lead to compatible results:

1. The Simpson et al. data have more quality than the rest of the data sets, and the experimental information needed to perform the analysis of the data is more complete. For this reason, they have been used to normalize the n_TOF capture data by performing a sequential SAMMY fit of both data sets. The preparation of the transmission data, needed for the analysis, is presented in Section 4.2.3.1, and the determination of the n_TOF sample mass with these data in Section 4.2.3.2.

2. The information available concerning the experimental conditions of the rest of the transmission measurements is too poor to perform a resonance analysis. However, the results of the analysis performed with these data

are available in [Bel76, Ber70, Cot59], as a set of fitted resonance parameters. These parameters, together with the ones provided by the evaluations relying on the Simpson et al. data, have been used to normalize the n_TOF capture measurement. This second procedure performed to normalize the n_TOF data is presented in Section 4.2.3.3.

All the normalization values obtained from the different methods are discussed together in Section 4.2.3.4.

4.2.3.1 Preparation of the transmission data

The best way to perform a resonance analysis is by fitting all the available data sets simultaneously, in order to reduce the correlations between resonance parameters, which can become large when only one data set is analyzed. The Simpson et al. experimental data are available in the EXFOR database [EX1xx, EX2xx]. The information concerning the experimental conditions needed for the analysis, such as the temperature of the sample or some parameters used to construct the resolution function, was obtained from [Sim74]. Unfortunately, the EXFOR database does not contain the experimental uncertainties of the Simpson et al. transmission data, as well as other parameters needed to implement the resolution function. For this reason, it has been impossible to perform a rigorous resonance analysis with both data sets at the same time. However, the information available was good enough to perform a reasonable normalization of the n_TOF capture yield at low energies (E_n<50 eV).

The ORELA experimental conditions, together with some assumptions concerning the uncertainty of the data and the time of flight distance adjustment to the n_TOF capture data are described below.

Samples

Two different samples were measured by Simpson et al., with inverse thicknesses of 279.3 barn/atom, with data available in the 0.5-1000 eV energy range [exf02] and 1288.2 barn/atom, with data available in the 0.5-76 eV energy range [exf01].

Doppler broadening and resolution function

As it is found in [Sim74], the temperature of the sample was assumed to be 320K. Concerning the resolution function, it is said in [Sim74] that a Gaussian resolution function was used, but they no information on its width and energy dependency was provided. The specific implementation of the ORELA [ORExx] resolution function in the SAMMY code was used. This resolution function has four components: the electron burst, the ORELA moderator, the neutron detector and the time of flight channel width. All of those four components depend on parameters, which have been taken from the paper [Sim74]. In some cases this information was not available and the parameters were taken from examples related to the ORELA facility distributed together with SAMMY.

Two additional problems with the transmission data have been found. First, the Simpson et al. resonance parameters seems to be not the best ones to fit the data of some resonances (see right panel of Figure 4.9), and this only happens at energies where the resolution function is relevant. Second, the n_TOF capture data and the Simpson et al. transmission data seems to be compatible at low energies, but not totally compatible at higher energies (above 50-100 eV).

Figure 4.9 shows the transmission yield obtained with and without resolution functions, with the resonance parameters provided by Simpson et al., in two different energy ranges. As it can be observed, at low energies (left panel) the effect of the resolution broadening is negligible, whereas at higher energies (right panel) it has an important

effect. The effect of the resolution function starts to be relevant at around 25 eV. For this reason, the normalization of the n_TOF capture measurement to the transmission data was performed mainly below 25 eV, as it is discussed in Section 4.2.3.2.

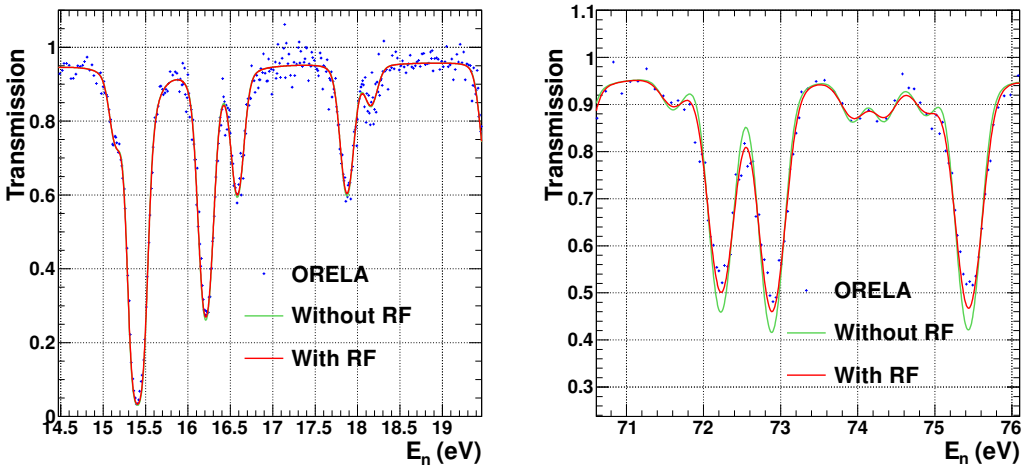

Figure 4.9: Transmission yield obtained with the Simpson et al. resonance parameters, for the thick sample. One yield has been obtained using the resolution function which is used in this work (red) and the other without using any resolution function (green).

Data uncertainty

As it was mentioned above, neither the EXFOR database nor the Simpson et al. paper [Sim74] provide the uncertainties in the data or the information necessary for their calculation/estimation. Thus, the following assumptions have been adopted in order to make the fit with SAMMY:

1. The uncertainties in the data points are constant (in certain energy ranges) and uncorrelated.
2. The distribution of the distances from the data points to the theoretical transmission constructed from the resonance parameters follows a normal distribution with a mean equal to zero and an standard deviation equal to the uncertainty of the data points; i.e., the distribution of the distances of the data points to the fit, divided by their uncertainties, has an standard deviation equal to 1.

The first condition is arbitrary, and has been established because it is not possible to deduce which data points have a larger or lower uncertainty, since this depends on the statistics, the background subtraction and the technique. The second condition, however, is fulfilled for any good fit, if only statistical uncertainties are present.

Since the transmission yields constructed from the resonance parameters provided by Simpson et al. should be a reasonable fit of the data, both of them (for the thick and the thin samples) have been calculated and compared

to the data. Then, constant uncertainties have been established in different energy ranges following the previous assumptions. The energy ranges have been chosen in such a way that the uncertainties do not vary too much between consecutive regions, and the limits were always placed between resonances. The results are provided in Table 4.2.

Sample	Energy range (eV)	uncertainty	Sample	Energy range (eV)	uncertainty
Thick	0.5-3	0.011	Thick	50-100	0.024
Thick	3-8.5	0.015	Thick	100-150	0.034
Thick	8.5-14.5	0.021	Thick	150-200	0.026
Thick	14.5-20.5	0.026	Thick	200-250	0.024
Thick	20.5-30.5	0.034	Thin	0.5-2.5	0.013
Thick	30.5-40	0.030	Thin	2.5-8.5	0.014
Thick	40-50	0.028	Thin	8.5-75	0.023

Table 4.2: Uncertainties assigned to the Simpson et. al transmission data.

The final distributions of the distances in the entire energy ranges considered are presented in Figure 4.10. It is necessary to insist that with the method adopted the uncertainties of the transmission data are not calculated but estimated from educated guesses.

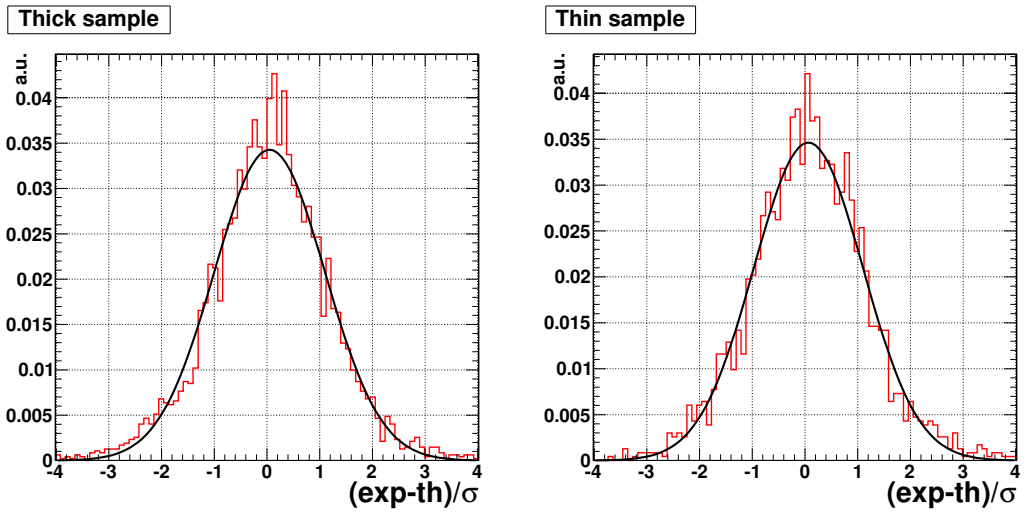

Figure 4.10: Distribution of the distances of the experimental data points to the calculated yield, divided by their uncertainties, for the thick sample data between 0.5 and 250 eV (left) and for the thin sample between 0.5 and 75 eV (right). The adopted uncertainties in the transmission data have been used. The parameters of the Gaussians are: main_{thick}=0.050, σ_{thick}=1.05, main_{thin}=0.065 and σ_{thin}=1.03.

Calibration of the time of flight

The energy of the transmission data was calibrated to the n_TOF capture measurement. A similar procedure than the one described in Section 4.2.1 has been followed. In this case the t_0 value has been calibrated together with the TOFD, in order to obtain a better compatibility between both data sets. The ^{243}Am ENDF/B-VII.0 evaluation, which matches perfectly the energies of the Simpson et al. transmission data, has been used to compare with the resonance parameters fitted to the n_TOF capture data. The following quantity has been minimized:

$$D = \sum_i \left[\left(E_i^{ENDF} - E_i^{nTOF} \right)^2 \cdot RK_i^{ENDF} \right] \tag{4.2}$$

where E_i^{ENDF} and E_i^{nTOF} are the energies of the resonances in the ENDF/B-VII.0 evaluation and in the fit performed to the n_TOF data, respectively. The comparison has been performed by taking all the resonances in the 3-150 eV energy range. The lower energy limit was chosen because the normalization was performed above 3 eV, avoiding the ^{243}Am strongest resonance at 1.35 eV. The upper energy limit was chosen because the transmission data looses quality as the energy increases, and the compatibility between the n_TOF and the Simpson et al. data sets is lower as the energy increases. Equation 4.2 was used instead of Equation 4.1 because two parameters are being calculated at the same time.

The minimization of D results in a TOFD of 18.5502 m and a t_0 of -38.08 ns for the transmission measurement. The TOFD used by Simpson et al., which is the same as the used in the ^{243}Am ENDF/B-VII.0 evaluation, was 18.576 m. This also means that the resonance energies obtained in this work will be shifted by a factor of approximately (considering $t_0 = 0$) 0.997 from the present evaluated ones.

4.2.3.2 Sequential fit of the transmission and capture data

The n_TOF capture yield has been fitted together with the ORELA Simpson et. al transmission data. The fitting procedure consists in a sequential SAMMY fit. The transmission data has been fitted first, and then the capture data using the obtained covariances as prior uncertainties and correlations. This is a common practice in Bayesian fitting procedures, as it is explained in [Lar06]. The fit has been performed in the 3 - 50 eV energy range, in order to avoid the resonance at 1.35 eV, which presents problems that will be discussed later. The limit of 50 eV has been chosen mainly because it is not clear that the resolution function used in this work for the transmission data is the most appropriate one, as it was explained in Section 4.2.3.1. The resolution function starts to be sizeable at around 25 eV, but up to 50 eV its effect is quite low. A secondary reason is that the uncertainty in both data sets, capture and transmission, worsens as the energy increases.

The fitted parameters were:

1. The energy and the neutron and capture widths of all the resonances in the mentioned energy range.
2. The normalization of the capture yield, which is defined in SAMMY as the "N" parameter in the relation: $Y(E) = N \cdot Y_u(E) + B(E)$, where $Y(E)$ is the theoretical yield, $Y_u(E)$ the uncorrected theoretical yield and $B(E)$ the background.

The fitting procedure has been performed with a sample thickness of 2×10^{-5}atoms/barn[2]. Thus, the calculated thickness of the sample will be the the latter value multiplied by the fitted normalization factor.

[2]The sample mass estimated from the activity measurements is 6.7 mg, with an uncertainty of 11%. This leads to a sample thickness between $1.88 \cdot 10^{-5}$ and $2.34 \cdot 10^{-5}$ atoms/barn (the radius of the sample is 0.5 cm).

The fitted yields are presented in Figures 4.11 (thick sample) and 4.12 (thin sample). In both cases the fits were performed in the 3 - 50 eV energy range. Similar fits were also performed in other energy ranges, and all the results are presented in Table 4.3. The different energy ranges have been chosen in order to take the most appropriate energy intervals for the normalization procedure, which consists in using strong resonances, which are the ones which are best defined, but avoiding the saturated ones. This are the cases of the 3 - 10 eV and 10 - 17 eV energy ranges for the thin sample and the 8.5 - 10.5 eV and 14 - 25 eV energy ranges for the thick sample. In order to show the effect which has the uncertainty in the determination of the background constant (see Section 4.2.2) in the normalization values, all the fits were performed using three different backgrounds: one constructed with the main value of the background constant, $\langle a \rangle$, and the other two with $\langle a \rangle + \sigma$ and $\langle a \rangle - \sigma$, where σ=4% ,the uncertainty of a. The dispersion[3] of each normalization value obtained with these three fits is reflected by the uncertainties provided in Table 4.3, which corresponds to the uncertainties in the normalization values due to the uncertainty in the background constant. The discussion of the obtained results is performed in Section 4.2.3.4.

Sample	Range (eV)	Norm	Sample	Range (eV)	Norm
Thick	3-50	0.983(4)	Thin	3-50	0.9565(18)
Thick	3-25	0.969(5)	Thin	3-25	0.9530(18)
Thick	3-10	0.974(6)	Thin	3-10	0.9490(19)
Thick	8.5-12.5	0.965(4)	Thin	8.5-12.5	0.985(5)
Thick	10-17	0.961(3)	Thin	10-17	0.9628(14)
Thick	14-25	0.963(3)	Thin	14-25	0.9704(24)

Table 4.3: Results of the normalization fitted to the transmission data, for both the thick and thin transmission samples, in different energy ranges. In parentheses, the uncertainties due to the uncertainty of the background constant.

[3] This "dispersion" has been calculated as the highest value minus the lowest value, divided by two.

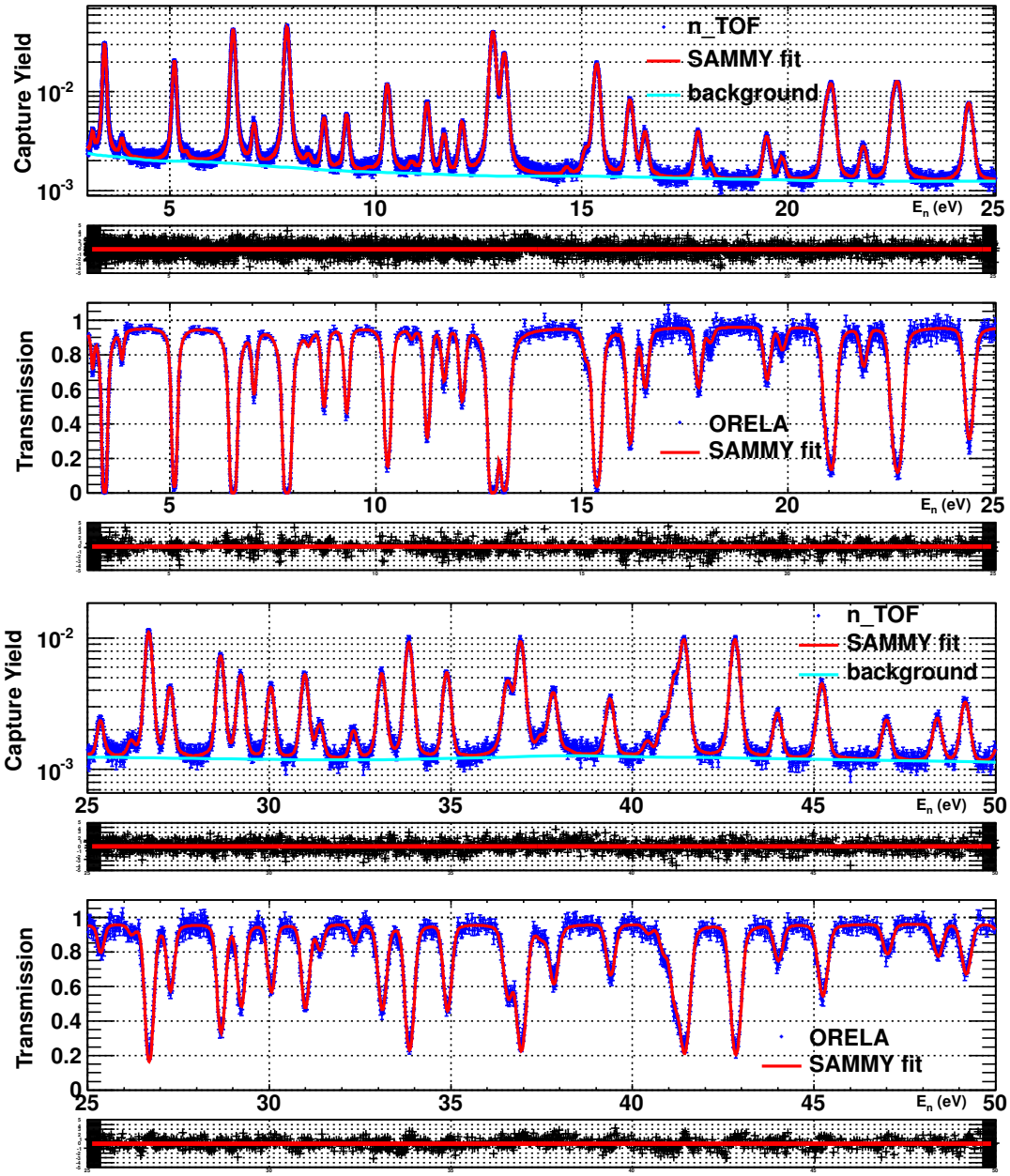

Figure 4.11: Sequential fit of the n_TOF capture data and the ORELA transmission data, for the thick transmission sample data, in the 3 - 25 eV (top) and 25 -50 eV (bottom) energy ranges.

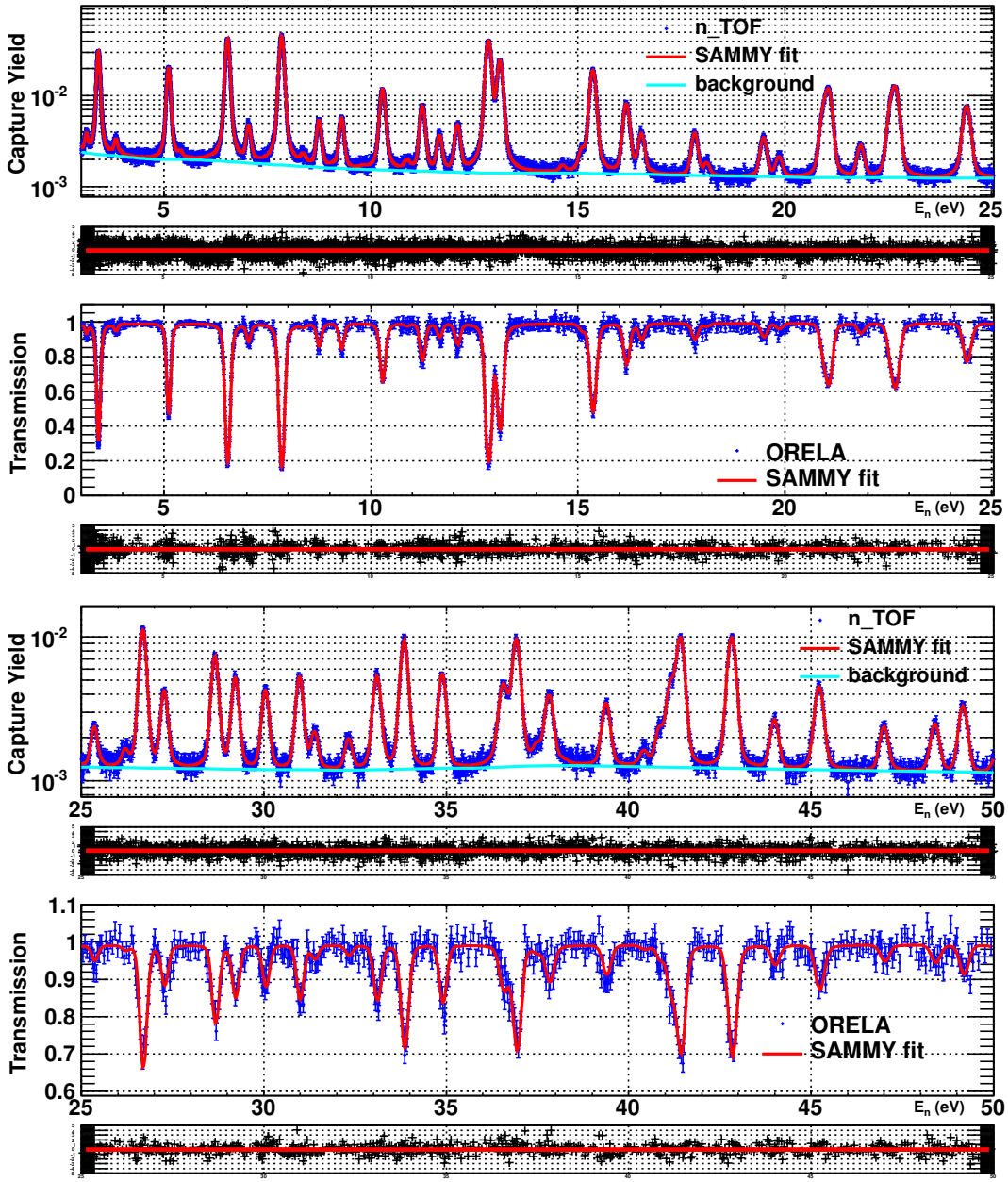

Figure 4.12: Sequential fit of the n_TOF capture data and the ORELA transmission data, for the thin transmission sample data, , in the 3 - 25 eV (top) and 25 -50 eV (bottom) energy ranges.

4.2.3.3 Normalization to evaluated data

An alternative normalization procedure has been followed. The procedure consists in normalizing the n_TOF data to the theoretical capture yield resulting from the different resonance parameters obtained by the experimentalists and the evaluators. The resonance parameters obtained in the four transmission experiments available (see Section 4.1) have been taken from the published papers. Two different evaluations have been also considered: the one of the ENDF/B-VII.0 library, which is very similar to the one available in the ENDF/B-VII.1 evaluation in the RRR, excluding the 1.35 eV strongest resonance; and the Maslov evaluation, used in the rest of the newest evaluated libraries, except for the lower energy resonances in the JENDL-4.0 evaluation (see Section 4.1).

Each set of resonance parameters has been used to perform a SAMMY fit to the n_TOF capture data, where only the normalization and the energies of the resonances have been varied. The energy range used in the fits was 3 - 50 eV, as in the previous normalization procedure. In some cases, the measured energy range does not reach 50 eV and smaller ranges were used. The sample thickness was set to 2×10^{-5}atoms/barn.

The results are summarized in Table 4.4. Together with the normalization values, the Bayesian reduced chi square χ^2/n (see [Lar06]) and the ratio between the areas of the experimental and the normalized theoretical yields are provided. All the fits were performed using three different backgrounds: one constructed with the main value of the background constant, $\langle a\rangle$, and the other two with $\langle a\rangle+\sigma$ and $\langle a\rangle-\sigma$, where σ=4% ,the uncertainty of a. The dispersion[4] of each normalization value obtained with these three fits is reflected by the uncertainties provided in parentheses. Thus, the uncertainties provided are the uncertainties induced in the fitted normalization values due to the uncertainty in the background constant.

The Bayesian χ^2/n allows to know if the different resonance parameters calculated reproduce the n_TOF capture data. From the values available in Table 4.4, it is clear than the Berreth et al., the Simpson et al. and the ENDF/B-VII.0 evaluations, which are pretty close to each other, are in reasonable agreement with the n_TOF capture data, followed by the evaluation performed by Maslov. On the other hand, the parameters provided by Bellanova et al. and Cote et al. do not reproduce the n_TOF capture measurement and were therefore excluded.

Data	Range (eV)	Norm	χ^2/n (Bayes)	$\text{Area}_{th}/\text{Area}_{exp}$
Bellanova et al. [Bel76]	3-34	1.0270(18)	14.2	0.957
Berreth et al. [Ber70]	3-25	0.9939(17)	1.82	0.994
Simpson et al. [Sim74]	3-50	0.9466(15)	1.51	0.983
Simpson et al.	3-25	0.9417(15)	1.46	0.990
Simpson et al.	25-50	0.9913(20)	1.48	0.989
Cote et al. [Cot59]	3-16	1.3416(17)	22.4	0.890
Maslov evaluation (JEFF,JENDL, ...)	3-50	0.9664(16)	3.75	0.988
ENDF/B-VII.0	3-50	0.9849(17)	1.53	0.994

Table 4.4: Normalization values obtained from different transmission measurements and evaluations. Together with the fitted values, the reduced Bayesian chi square obtained in the fits and the ratio between the fitted and the experimental capture yields are provided. The values in parentheses are the uncertainties in the normalization values associated with the uncertainty in the $1/\sqrt{E_n}$ background constant.

[4] This "dispersion" has been calculated as the highest value minus the lowest value, divided by two.

The normalization at higher energies with this procedure is not straightforward. This is because at higher energies the evaluated parameters are less compatible with the n_TOF capture data. The best way to compare the n_TOF capture data with previous evaluations is by comparing the integral of the capture cross section obtained after the n_TOF data resonance analysis with the integrals obtained from the evaluated libraries, in different energy ranges. This comparison is presented in Section 5.2.

4.2.3.4 The normalization adopted for the n_TOF data

All the results obtained in Tables 4.3 and 4.4 have been represented in Figure 4.13, with the exception of the values obtained from the resonance parameters from Cote et al. and Bellanova et al.. The order of the points is the same as they appear in the tables: the first 6 points correspond to the fits to the Simpson et al. thick sample data, the next 6 points to the Simpson et al. thin sample data, and the latter 6 points to the values obtained by fitting to the different resonance parameters, in the order that they appear in Table 4.4.

The mean of all the normalization values is 0.970, and it is represented in the Figure by the horizontal continuous blue line. The standard deviation is 0.0154 (1.6%), and it is represented by the dashed horizontal green lines. Notice that here the standard deviation does not have an straightforward statistical meaning, since most of the data points come from the same data set (the Simpson et. al data). It just gives an estimate of the dispersion of the normalization values.

The mean value of 0.970 has been then adopted for the normalization of the n_TOF capture measurement. Its associated uncertainty has been finally set to 3%, in order to cover all the values presented in Figure 4.13. This 3% uncertainty is graphically represented by the two horizontal dashed blue lines.

The n_TOF capture measurement was then normalized to the transmission data. The 3% uncertainty is associated with the normalization procedure, and it is a conservative value. In order to give an overall normalization uncertainty, the normalization uncertainties of the transmission measurements should also be taken into account, but these values have not been reported by the experimentalists. However, it has to be considered that the Simpson et al. transmission measurements were performed with two samples with different thicknesses, and the Berreth et al. transmission measurement with the same two samples plus a third one [Ber70, exf03]. Transmission measurements usually have low normalization uncertainties, if the sample masses are well known. In this case three different samples have been considered, so it indicates that they have probably low normalization uncertainties.

Before normalizing the n_TOF capture measurement to the existing ^{243}Am cross section data, there were two sources of uncertainty concerning the normalization: the sample mass (11%) and the normalization of the experimental capture yield (2.7%). Both of them give an overall normalization uncertainty in the capture cross section of 14% or 11%, depending if they are added linearly or quadratically, respectively. This normalization uncertainty has been reduced down to a 3%. This is because what has been done in all this procedure is to fit the normalization of the ^{243}Am *capture cross section* to the available transmission data, neither the sample mass nor the experimental capture yield.

The experimental capture yield can be expressed as $Y_{exp}=N_{exp}\cdot Y^{abs}_{exp}$, where Y^{abs}_{exp} is the experimental yield without normalization uncertainty and $N_{exp}=1$, which includes the 2.7% normalization uncertainty. In the thin sample approximation (self shielding and hence multiple scattering corrections are negligible) the theoretical capture yield is proportional to the sample thickness, so it can be also expressed as $Y_{th}=N_{th}\cdot Y^{abs}_{th}$, where $N_{th}=1$ and includes the

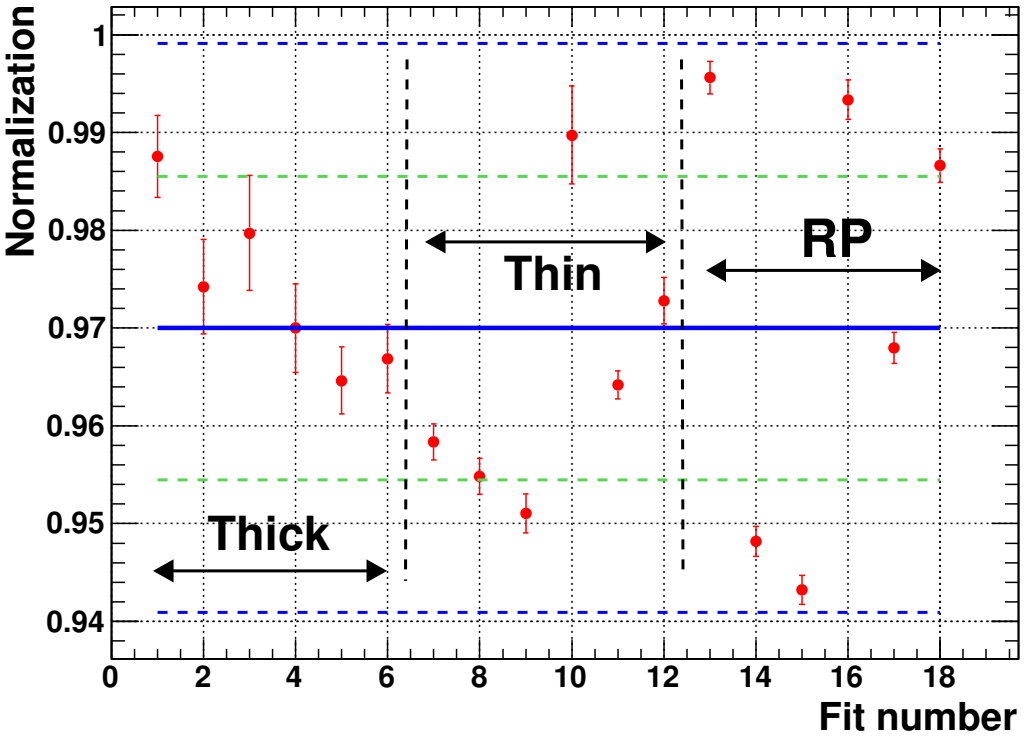

Figure 4.13: Normalization values presented in Tables 4.3 and 4.4. The uncertainty of each normalization point is the uncertainty in the calculated normalization value due to the uncertainty of the background constant. The order of the points is the same as they appear in the Tables, so it is arbitrary.

11% normalization uncertainty due to the sample mass. By fitting the n_TOF capture data to the transmission measurements, what has been calculated is the parameter N=N_{exp}/N_{th}, which has an uncertainty of 3%, the normalization uncertainty of the measured cross section.

The sample thickness used in the normalization fits was $2{\cdot}10^{-5}$ atoms/barn, so the thickness was finally fitted to $1.94{\cdot}10^{-5}$ atoms/barn, with a 3% uncertainty plus a 2.7% uncertainty in the normalization of the experimental capture yield, following the previous reasoning. For this reason, the final uncertainty in the sample thickness (or in the sample mass) is 4%, if both uncertainties are added quadratically. This value corresponds to a mass of 6.23(25) mg, which is totally compatible with the value obtained by simulating the activity of the sample (Appendix B), which was 6.7(1.0) mg and with the value resulting from the γ-ray spectrometry measurement performed at CERN, which was 7.3(1.1) mg.

All the previous reasonings are true if the sample is considered to be homogeneous and with the certified radius of 0.5 cm. It does not need to be considered as a thin sample. If the sample is not homogeneous, the thickness can vary from one spatial point to other. Two different situations have to be taken into account:

1. The thin sample approximation is valid. In this case the shape of the capture yield does not depend on the

thickness (i.e. on the inhomogeneities), and the results of the cross section analysis are totally correct, and they will still have a normalization uncertainty of a 3%. Moreover, if the neutron beam is assumed to be spatially homogeneous, the previous value provided for the sample mass (6.23±0.25 mg) is still correct, since the number of capture reactions will only depend on the sample mass and not in how that mass is spatially distributed. According to the parametrization of the spatial n_TOF beam profile available in [Pan04], the ratio between the amount of neutrons in the center and in the border of the sample is about 0.9, so the central part of n_TOF neutron beam is not far from being homogeneous.

2. The thin sample approximation is not valid. In this case the shelf shielding and multiple scattering corrections are important, so the shape of the capture yield will depend on the thickness and/or in the inhomogeneities. Hence, there will be an additional uncertainty in the analyzed cross section related with these effects.

For this reason, it is important to know if the thin sample approximation is valid or not. Taking into account only shelf shielding effects (no multiple scattering) the reaction yield can be expressed as:

$$Y_x = \left(1 - e^{-n\sigma}\right) \frac{\sigma_x}{\sigma} \overset{thin}{\simeq} n \cdot \sigma_x \tag{4.3}$$

where n is the sample thickness, σ_x the reaction cross section and σ the total cross section. In the right part of Equation 4.3 the thin target approximation has been applied. In order to check if the thin target approximation is valid or not, the ratios between the yields calculated without and with using the thin target approximation have been considered: $\left[1 - exp(-n\sigma)\right]/n\sigma$. The closer to unity is that factor, the better is the thin target approximation. This factor is presented in Figure 4.14, where a sample thickness of $2{\cdot}10^{-5}$atoms/barn has been assumed. The ratio is higher than 0.99 for all the resonances, except the one at 1.35 eV, where the ratio reaches 0.84, and other 7 resonances, where the ratio is between 0.97 and 0.99.

In order to quantify the shelf shielding correction for those 8 resonances, the capture yield has been calculated for two samples, one with $2{\cdot}10^{-5}$ atoms/barn and other with $4{\cdot}10^{-5}$ atoms/barn. If the shelf shielding correction is negligible, the yield obtained with the thicker sample has to be the same as the one obtained with the thinner, multiplied by a factor of 2. The comparison is shown in Figure 4.15, where the four strongest resonances of ^{243}Am are presented. It is possible to appreciate that the correction is strong for the resonance at 1.35 eV, but very small for the rest of the resonances. A more extensive study of this effect can be found in Sections 4.3.2 and 4.3.4.

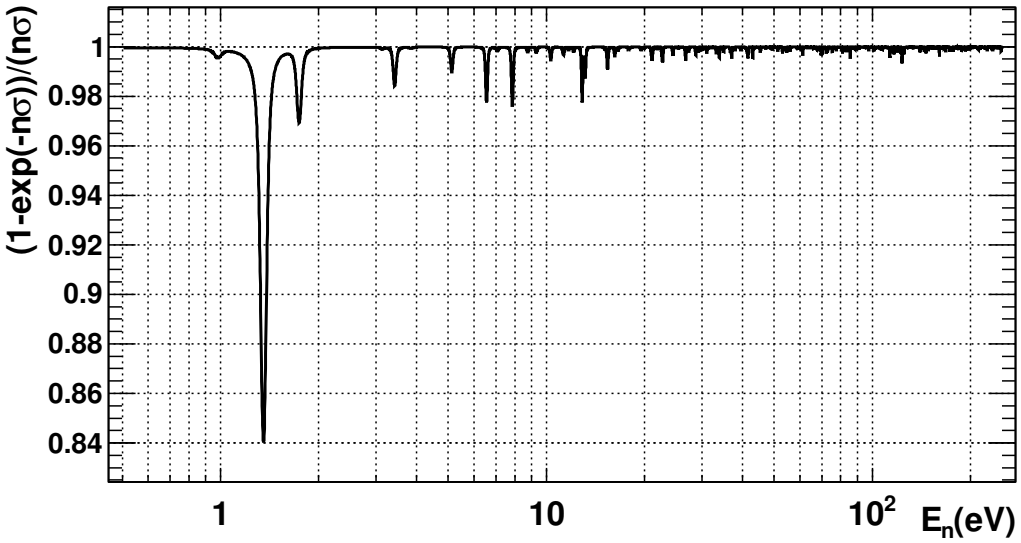

Figure 4.14: Value of the factor $[1 - exp(-n\sigma_{tot})]/n\sigma_{tot}$ for the ^{243}Am total cross section taken from ENDF/B-VII.0, which has been Doppler-broadened using a temperature of 300 K. A thickness of $2{\cdot}10^{-5}$atoms/barn has been considered.

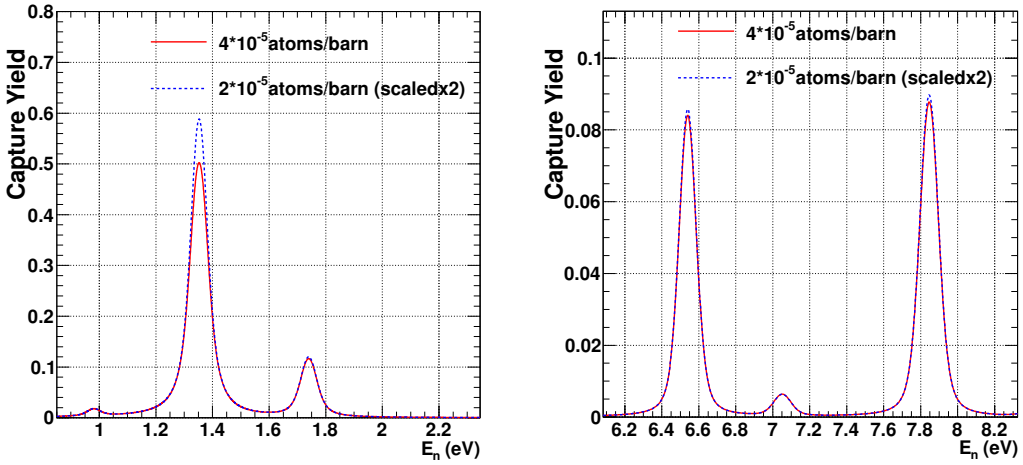

Figure 4.15: ^{243}Am capture yields obtained from the ENDF/B-VII.0 resonance parameters. Two different samples have been considered, one with half of the thickness of the other, but with its corresponding yield scaled by a factor of 2. This plot indicates that for thicknesses lower than $4{\cdot}10^{5}$atoms/barn, the thin target approximation is valid for all the resonances, except for the one at 1.35 eV.

4.2.4 Impurities

Two impurities have been detected in the n_TOF capture data by observing resonances at low energies that do not correspond to the ^{243}Am(n,γ) reaction.

The first of these impurities is ^{241}Am, whose strongest resonances are clearly visible in the n_TOF capture data, as it is shown in Figure 4.16. The ^{241}Am capture yield has been obtained from the ENDF/B-VII.0 library and calibrated in energy according to the n_TOF data. Then, it has been scaled properly and included in the pointwise background, which has been used for the rest of the SAMMY resonance analysis. These calculations suggest that there is around 1.5×10^{-7}atoms/barn of ^{241}Am, which is around 0.77% of the sample mass.

The second of these impurities is ^{240}Pu. Only its strongest resonance at 1.05 eV is visible, and the influence of the rest resonances is negligible. In this case, instead of including the contribution of the impurity in the pointwise background, a new resonance has been added to the ^{243}Am resonance set, and its energy and resonance parameters have been fitted as if it were a real ^{243}Am resonance. This procedure was followed because its size and position is not as clear as in the previous case, as it can be observed in Figure 4.17. The fitted ^{240}Pu resonance has a radiative kernel ($g\frac{\Gamma_\gamma\Gamma_n}{\Gamma_{tot}}$) of 9.62×10^{-4}meV. Since it should be 2.27 meV, according the ENDF/B-VII.0 library, it can be concluded that there are $\sim8.2\times10^{-9}$atoms/barn of ^{240}Pu, which stands for a $\sim$0.04% of the sample mass.

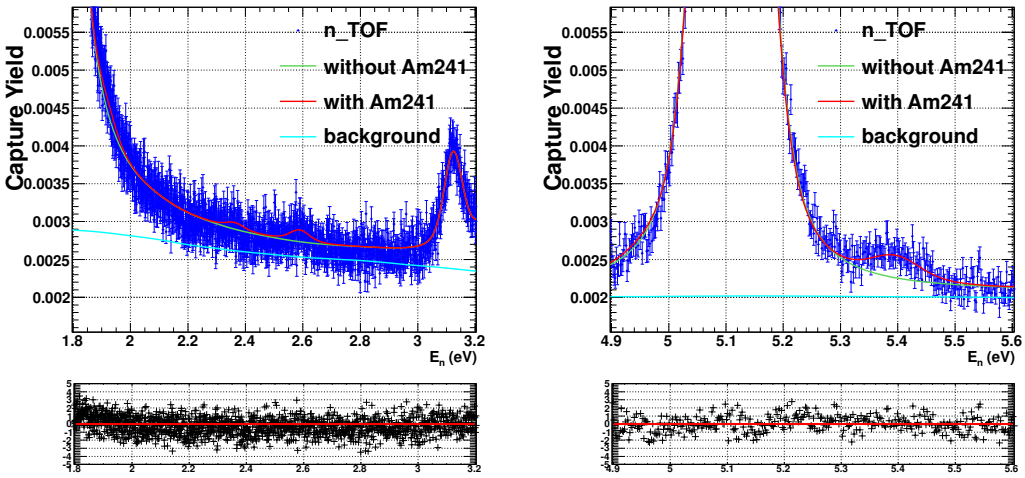

Figure 4.16: Fits performed to the n_TOF capture data with and without including the ^{241}Am impurities in the background. In both panels, the backgrounds do not include the impurities and the residuals correspond to the fits where the impurities were included.

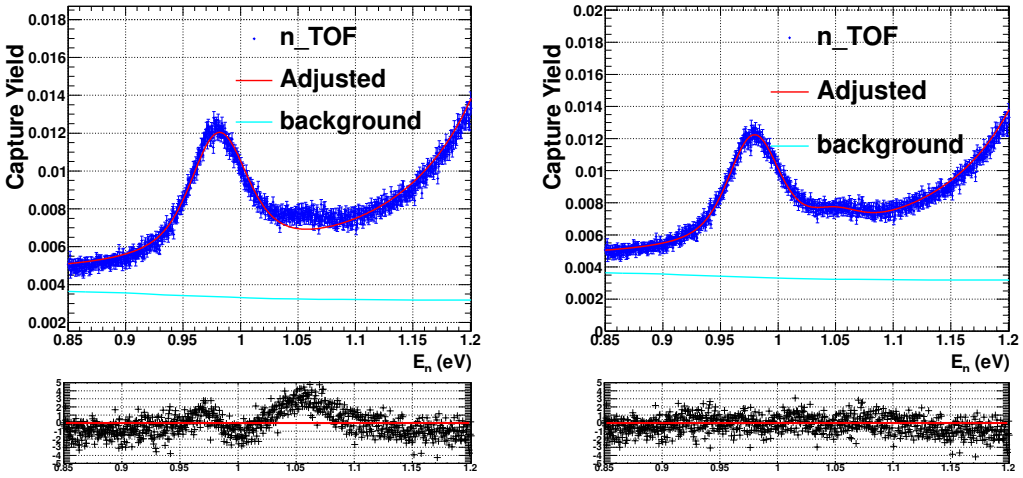

Figure 4.17: Fits performed to the n_TOF capture data performed with (right) and without (left) including a resonance at around 1.05 eV, which is set to take into account the ^{240}Pu impurities.

4.3 Analysis of the Resolved Resonance Region

4.3.1 Fit of the resonance parameters

The Resolved Resonance Region (RRR) has been analyzed with the SAMMY code. In the present evaluations, the RRR extends up to 250 eV. However, the low statistical uncertainties and the good resolving power of the n_TOF capture data has made possible to extend it up to 400 eV. The fitted capture yield, together with the experimental one, are presented in Figures 4.19 to 4.28.

In the analysis process, the energy E_0, gamma width Γ_γ, and neutron width Γ_n, of each resonance have been obtained. For the fission widths, the values present in ENDF/B-VII.0 have been adopted, but their effect in the fitted parameter values is negligible. The channel radius has been also fixed to the value present in the ENDF/B-VII.0 evaluated library (9.7 fm), since the n_TOF capture measurement is not sensitive to it (it is usually obtained from transmission measurements), as it is shown in Sections 4.3.2 and 4.3.4.

Concerning the spin assignment, it has been considered that all resonances have orbital spin l=0, according to the calculations presented in Section 4.3.6.1. The total spin values have been assigned randomly to its two possible values J=2,3 (the spin of the ^{243}Am nucleus in the ground state is 5/2), since there has not been possible to distinguish between them. This is shown in Figure 4.18, where two of the strongest resonances have been fitted with both total spin values.

It is a common practice (when the capture reaction is dominant) to fit the Γ_γ parameters only in the lower energy resonances, which are the strongest ones and thus present the lowest statistical uncertainties. Then, since it is expected that all the Γ_γ parameters have very similar values, an average value is calculated and the Γ_γ parameters

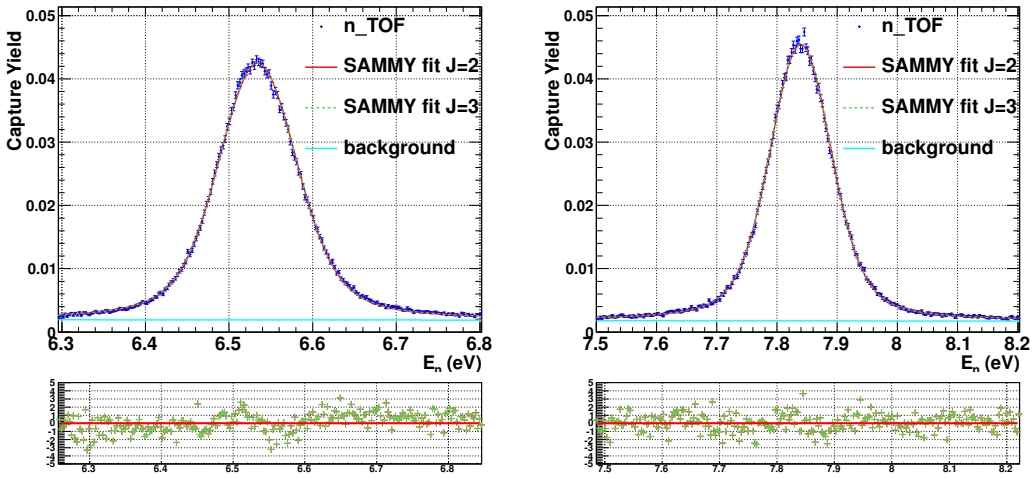

Figure 4.18: n_TOF capture yield fitted with SAMMY, using both spin assignments.

of the rest of the resonances are fixed to it. This is made because, with the exception of these low energy resonances, the capture yield is not sensitive to the Γ_γ parameters, i.e., the uncertainty in the fitted Γ_γ parameters is too large. This is because the Doppler broadening is by far the main contribution to the width of the broadened capture yield (see Figure 4.38 of Section 4.3.2), and therefore the Γ_γ parameters are only well determined in resonances described with a large amount of points, all of them with good enough statistics. Since the radiative kernel is essentially proportional to $g\Gamma_n$ (in nuclei where the capture reaction is dominant, $\Gamma_\gamma \gg \Gamma_n$), $g\Gamma_n$ is well determined for all the resonances.

For this reason, the Γ_γ parameters have been varied only below 50 eV, and only for those resonances with a low statistical uncertainty in the fitted Γ_γ parameter (less than 10%). For the rest of the resonances, the Γ_γ values have been fixed to the mean value, and verified that the values calculated by SAMMY of the Γ_γ parameters were compatible with the mean value, within their uncertainties. Details of the calculation of the mean value can be found in Section 4.3.3.

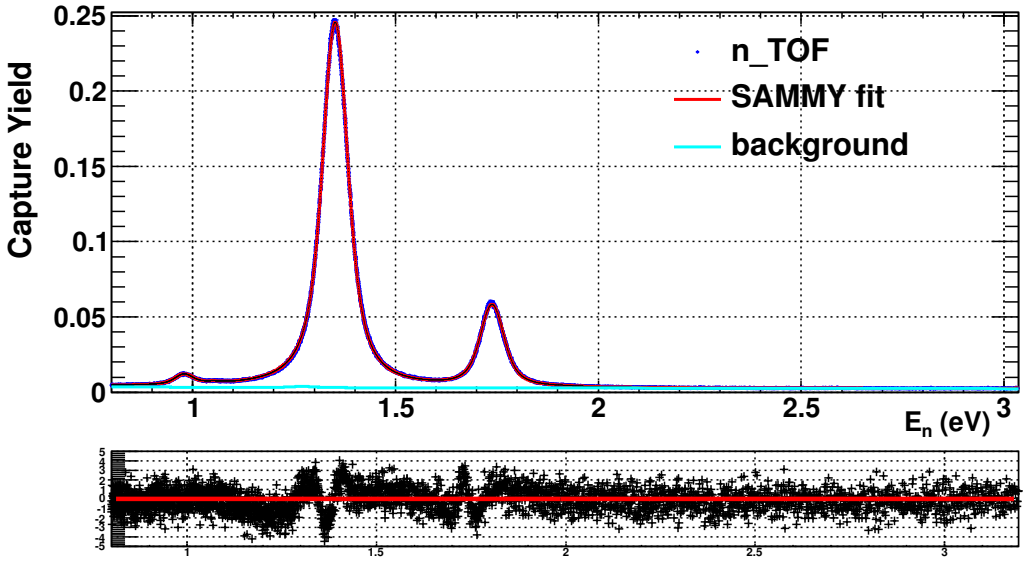

Figure 4.19: n_TOF capture yield fitted with SAMMY.

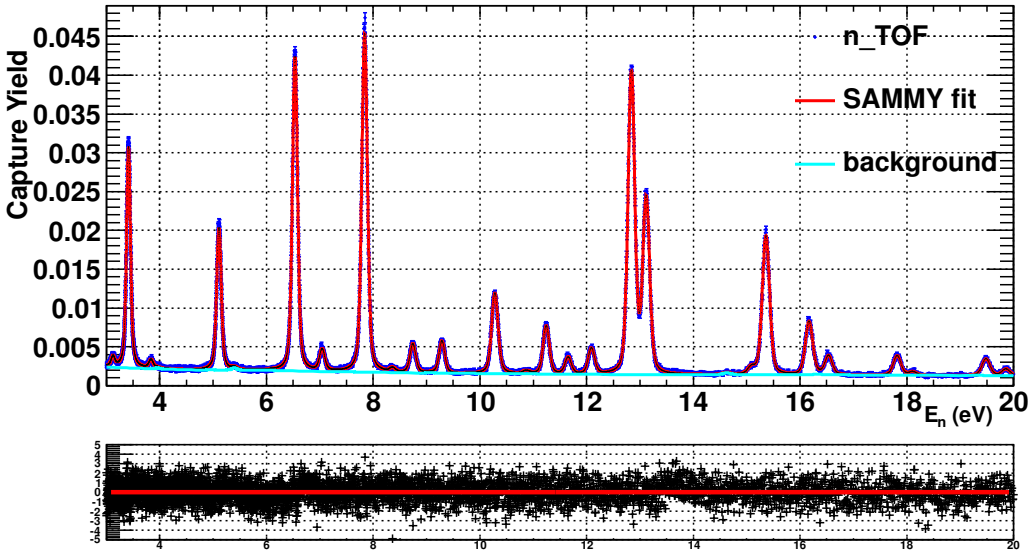

Figure 4.20: n_TOF capture yield fitted with SAMMY.

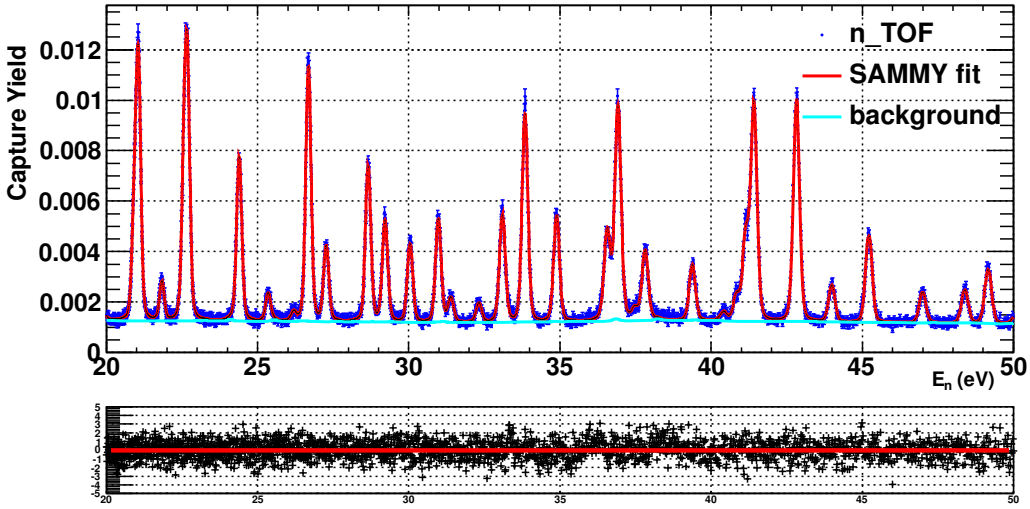

Figure 4.21: n_TOF capture yield fitted with SAMMY.

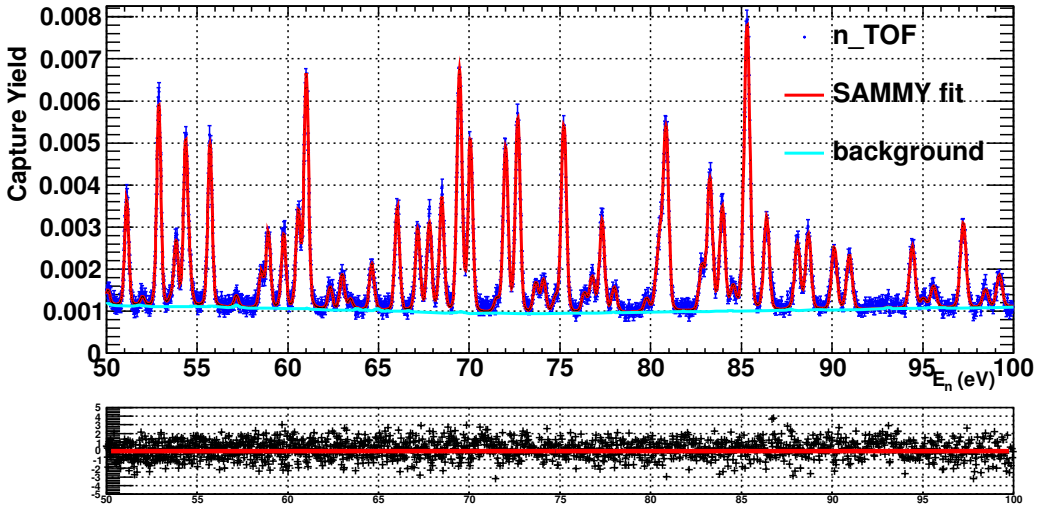

Figure 4.22: n_TOF capture yield fitted with SAMMY.

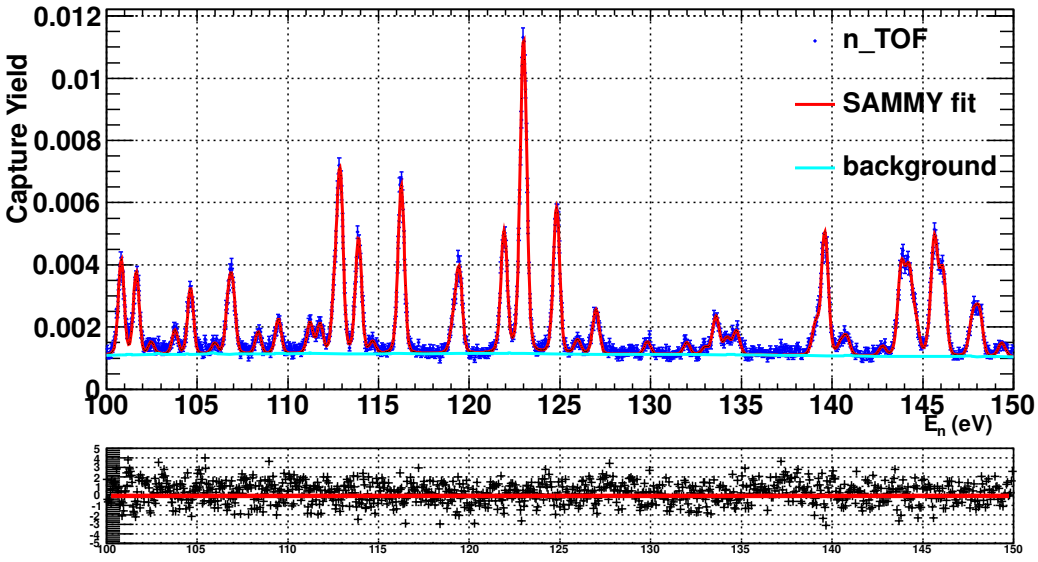

Figure 4.23: n_TOF capture yield fitted with SAMMY.

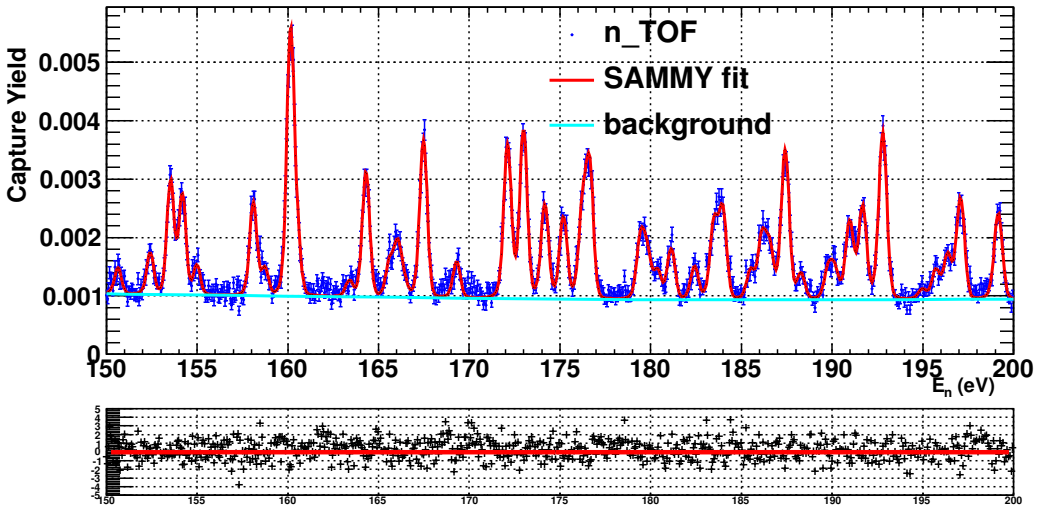

Figure 4.24: n_TOF capture yield fitted with SAMMY.

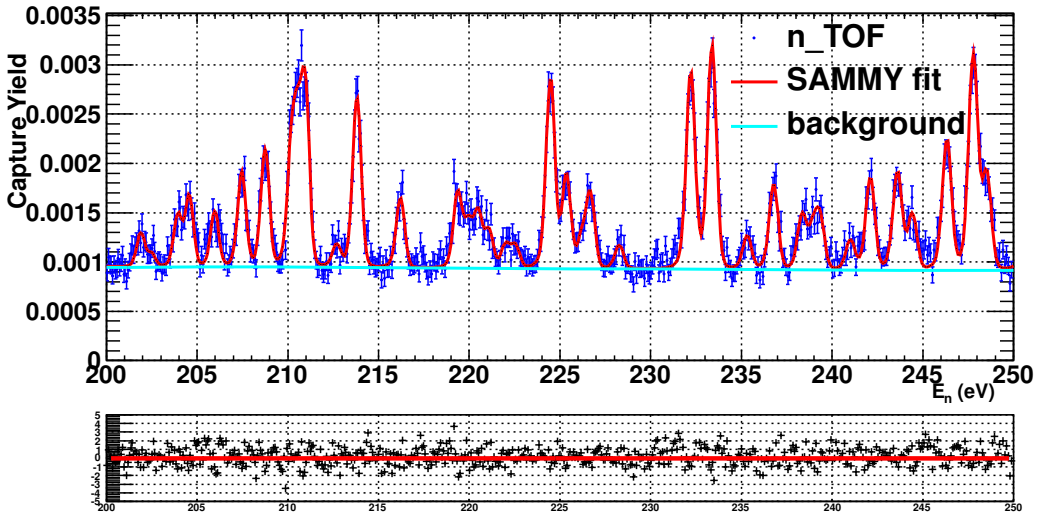

Figure 4.25: n_TOF capture yield fitted with SAMMY.

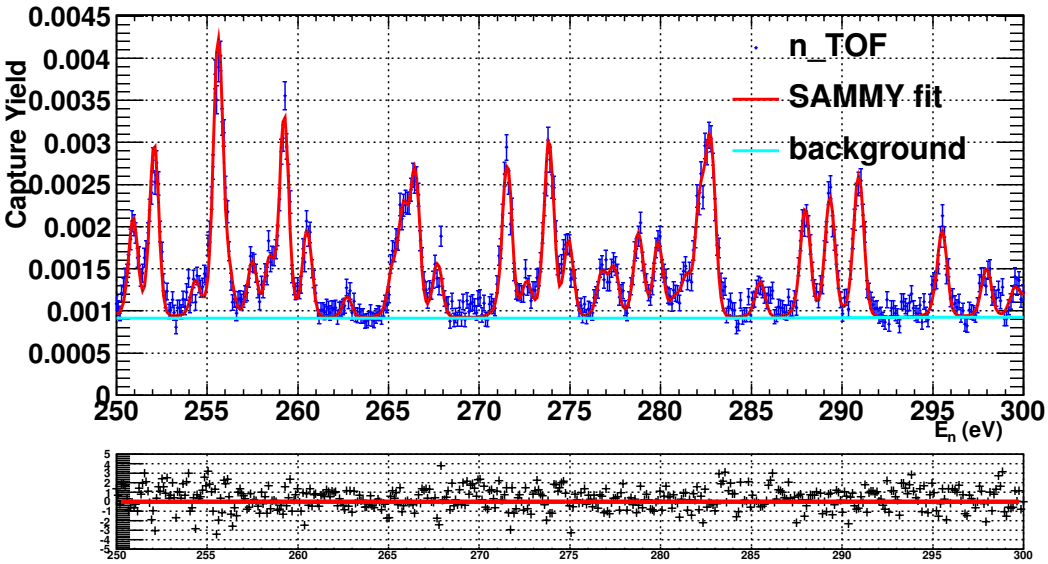

Figure 4.26: n_TOF capture yield fitted with SAMMY.

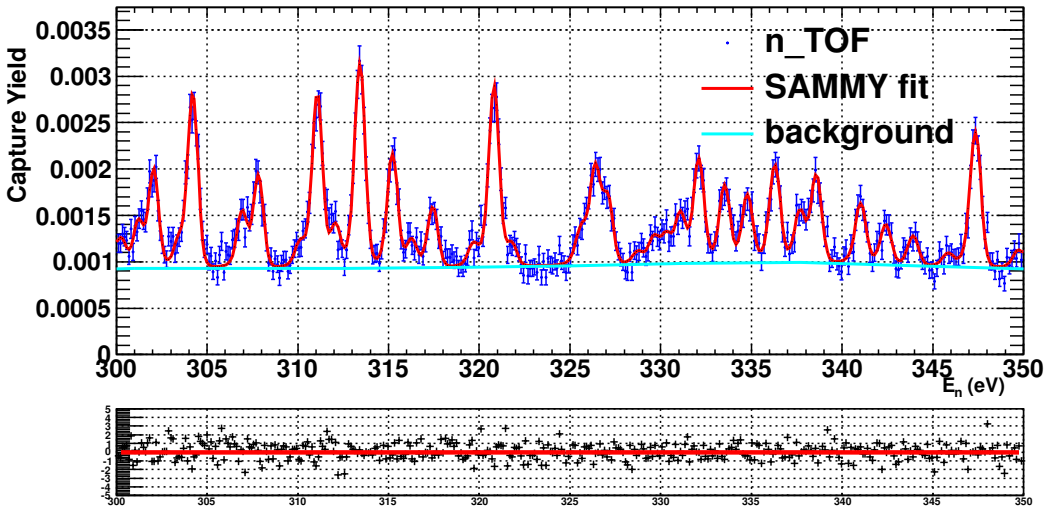

Figure 4.27: n_TOF capture yield fitted with SAMMY.

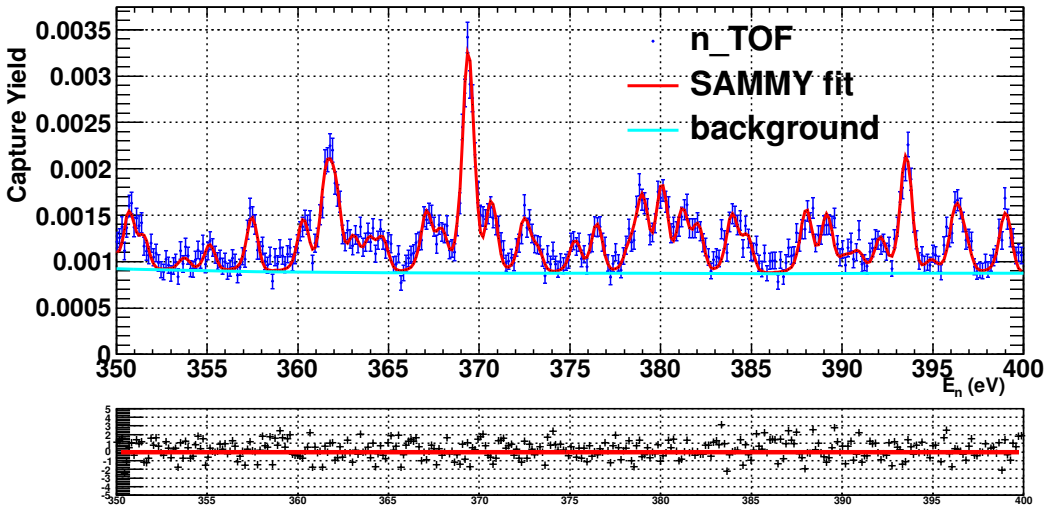

Figure 4.28: n_TOF capture yield fitted with SAMMY.

The distribution of the differences between the experimental and the fitted yield data points, divided by their statistical uncertainties, are given in Figure 4.29, for two different energy ranges. It is possible to appreciate that, in both cases, the standard deviations are close to 1, what is expected if only statistical uncertainties are present. The mean value is expected to be close to 0, as it is in the 0.8 - 50 eV energy range. However, that is not the case for the 50 - 400 eV energy range, where $\bar{x}$=0.23, which means that the experimental yield data points tend to be higher than the fitted ones. This could be due to weak resonances that are not strong enough to be appreciated (the so called "missing resonances"). The number of missing resonances increases with the resonance energy, as it is discussed in Section 4.3.6.2.

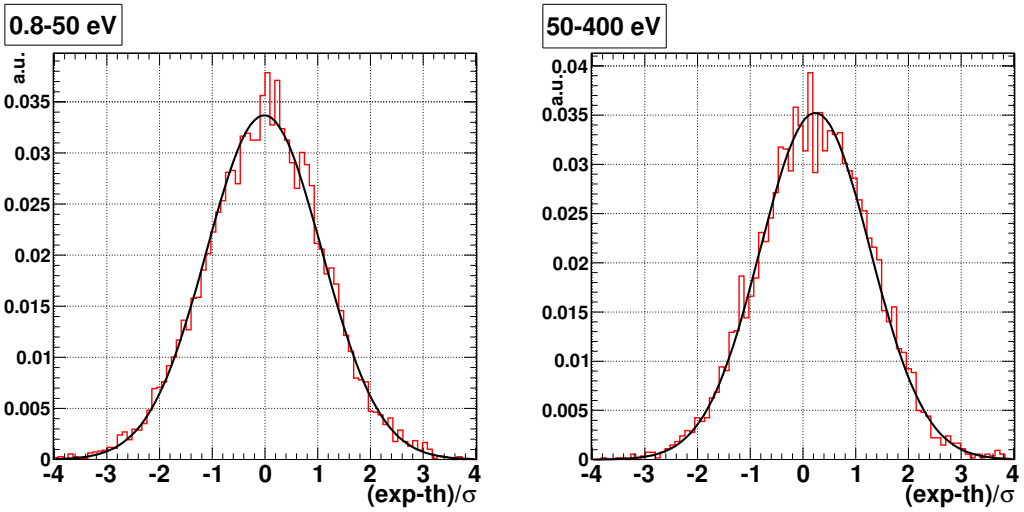

Figure 4.29: Distributions of the differences between the experimental and the fitted yield data points, divided by their statistical uncertainties, in the 0.8-50 eV energy range (left) and in the 50-400 eV energy range (right). The mean and standard deviation of the left figure are $\bar{x}$=-0.013, σ=1.09 , and for the right figure $\bar{x}$=0.23, σ=1.04.

4.3.2 Estimation of the systematic uncertainties of the resonance parameters in the 0.7 - 50 eV energy region

The uncertainties of the resonance parameters depend on:

1. The statistical uncertainties in the experimental capture yield.
2. Systematic uncertainties of the measurement, such as the normalization, temperature, the backgrounds, the resolution function ...
3. Uncertainties associated to the models used to calculate the theoretical capture yield, such as the Doppler broadening model, the multiple scattering, ...

The statistical and part of the systematic uncertainties are, in principle, taken into account in the fits performed with the SAMMY code. The statistical uncertainties are provided to SAMMY together with the experimental capture yield, in the same data file. Correlations between the different data points are also given. Both uncertainties and correlations are present in the Bayesian equations used by SAMMY to perform the Bayesian fit. The systematic uncertainties are treated via de so called PUP parameters (see the SAMMY reference manual [Lar06]), which are parameters that are not fitted by SAMMY, but whose uncertainties are, in principle, propagated properly. Additional sources of uncertainty, such as the ones associated to the models used to calculate the theoretical capture yield can not be easily included in a SAMMY calculation. These uncertainties can be estimated by performing the same fit with different models and see how the calculated parameters vary.

However, it has been found that SAMMY tends to underestimate the uncertainties in the resonance parameters associated to the uncertainties in the PUP parameters, i. e., SAMMY underestimates the systematic uncertainties. This can be seen in the following example. As it is said in Section 1.2.3, if the capture cross section is much larger than the other partial reaction cross sections, as it is for the ^{243}Am nucleus, then the area of a resonance is essentially proportional to $g\Gamma_n$. This means that the uncertainty value of the normalization should induce the same uncertainty in the Γ_n parameters, i. e., if the normalization uncertainty is 3%, then the Γ_n parameters should have, at least, a 3% systematic uncertainty. This behavior was not observed in the calculations performed with SAMMY, as it is presented in Figure 4.30. When a 3% uncertainty was set in the normalization parameter, the strongest resonances, where the statistical uncertainties are very low, have an uncertainty in the Γ_n parameter which is below 3% (around 1.2%).

For this reason, and also because there are sources of uncertainty that can not be handled by SAMMY, a total Monte Carlo method has been applied in order to estimate all the possible systematic uncertainties which affect the resonance parameters. The idea of this method is to calculate the variation of each resonance parameter when one of the external parameters is varied. An external parameter here means all the possible parameters (or theoretical models) which may affect the value of the fitted resonance parameters: the normalization, temperature, background, Doppler model, ... Thus, the method consists in performing a large number of SAMMY fits of the resonance parameters, and for each fit, some external parameters are varied according to their uncertainties. Then, the standard deviation of each resonance parameter is calculated, and such quantity is assumed to be the systematic uncertainty of the resonance parameter induced by the corresponding external parameters.

By using this method, the following systematic uncertainties have been estimated:

1. Uncertainty due to the choice of the initial resonance parameters. For each SAMMY fit it is necessary to provide an initial value of all the resonance parameters. It has been observed that the results of the fitted parameters can (usually for very small resonances) depend on their initial value. In order to take this effect into account, 1000 different fits were performed, each of them with different initial values of the resonance parameters. The variations were performed according to a Gaussian distribution with a 10% standard deviation. For each parameter, the standard deviation of its 1000 values was calculated, and the resulting value was assumed to be its systematic uncertainty due to the choice of its initial parameter.

2. Uncertainty due to the uncertainty in the normalization. It has been calculated in the same way as for the previous case. 1000 different fits were performed, each of them with a different normalization value, varied according to a Gaussian distribution with a mean equal to 1 and a 3% standard deviation, which is the uncertainty associated to the normalization, as it is presented in Section 4.2.3.4.

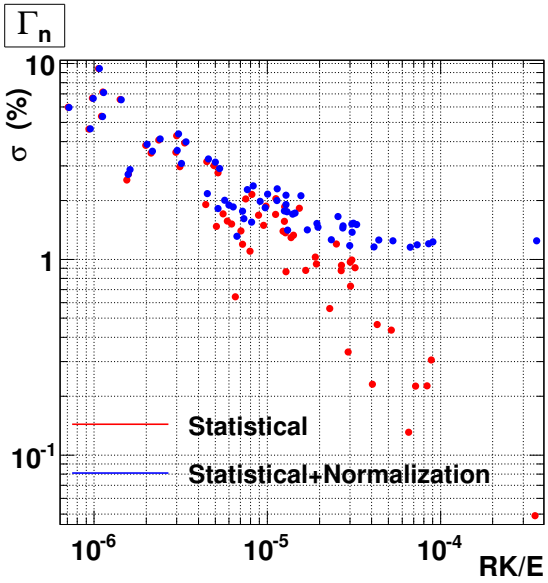

Figure 4.30: Relative uncertainties provided by SAMMY for the Γ_n parameters of the resonances in the 0.7 - 50 eV energy range. In one case (red points), the unique uncertainties provided to make the fit were the statistical uncertainties of the capture yield. The other case (blue points) corresponds to the same calculation but setting also a 3% uncertainty in the normalization. The resonances have been ordered (X axis) by its RK/E value, which means the ratio between the radiative kernel and the energy of the resonance, which is approximately proportional to the resonance capture area.

3. Uncertainty due to the uncertainty in the sample temperature. It has been calculated in the same way as for the previous cases. The temperature of the sample was 293±4 K (see Section 2.3). 1000 fits were then performed with temperatures distributed according to a Gaussian with a mean of 293 K and a standard deviation of 4 K.

4. Uncertainty due to the uncertainty of the 1/V background component. The 1/V background component (background constant in time) was fitted to -7.7·10$^{-4}\sqrt{eV}$±4% (Section 4.2.2). The propagation of this uncertainty to the resonance parameters was performed as in the cases above, with 1000 fits in which this parameter was varied according to a Gaussian with a -7.7·10^{-4} mean and a 4% standard deviation.

5. Uncertainty due to the pointwise background. It was presented in Section 3.6 that the background of the capture measurement was determined from dedicated background measurements, with the exception of the mentioned 1/V background. Due to the large statistical uncertainties of the dedicated background measurements the resulting background was smoothed, under the assumption that it has no resonant behavior. In order to estimate the uncertainty due to this background, two fits were performed: one with the smoothed background and other with the calculated background, without any smoothing. From the results of these fits, the systematic uncertainty of each resonance parameter were obtained as in the previous cases, by calculating the standard deviation of the two resulting values.

6. Uncertainty due to the Doppler broadening model used. In this work the free gas model was used to perform the Doppler broadening of the capture cross section. This model assumes that the nuclei have the same

velocity distribution than an ideal gas, which is only an approximation. Another commonly used Doppler broadening model is the crystal-lattice model, which assumes that the nucleus is part of the atom, which is bound to the rest of the atoms composing the solid. This solid has a phonon spectrum, which is taken into account to simulate the velocity distribution of the nucleus. The model requires a phonon spectrum of the solid, and this spectrum (AmO_2) hasn't been measured. However, what has been assumed is that the phonon spectrum of the AmO_2 should not be so different to the spectrum of the UO_2, which has been measured and is available. Thus, in order to estimate the uncertainty due to the Doppler broadening model used, two different fits were compared: one with the free gas model and other with the crystal-lattice model, using the UO_2 phonon spectrum. The uncertainty was calculated from the standard deviation of the results of both fits.

7. Uncertainty due to the inhomogeneities of the sample. As it is said in Section 4.3.5, there are indications that the sample is not homogeneous. Unfortunately, it has been impossible to calculate the size and spatial distribution of these inhomogeneities. An estimation of this source of uncertainty has been performed by comparing two different fits: one with the nominal thickness of $1.94{\cdot}10^{-5}$ atoms/barn and other with a double thickness. In the second fit the normalization was set to 0.5, so it has been performed with the same sample mass. The differences between the two fits are only due to the shelf shielding and multiple scattering effects. The uncertainty was calculated from the standard deviation of the results of both fits. Notice that this calculation, more than an estimation of the uncertainty, provides information concerning which parameters would be more affected by the presence of inhomogeneities. The absolute value of the obtained uncertainties depends of how large are the mentioned inhomogeneities, which is unknown.

All the computed quantities are presented in Figure 4.31, for the Γ_γ resonance parameters, and in Figure 4.32 for the Γ_n resonance parameters. All those parameters are the resonance parameters of the resonances between 0.7 and 50 eV, with the exception of 27 Γ_γ parameters whose statistical uncertainty exceeds 10% and have been fixed to the $\langle\Gamma_\gamma\rangle$ value. It is possible to appreciate, for example, that the uncertainty of the Γ_n parameters due to the normalization uncertainty is now ~3%, as it is expected. All the parameters have been ordered in increasing resonance capture area, which is in good approximation proportional to the radiative kernel ($g\Gamma_\gamma\Gamma_n/\Gamma$) divided by the resonance energy. This allows to visualize some tendencies with the increase of the resonance area, such as the decrease of the statistical uncertainty, the increase of the uncertainty due to the inhomogeneities, and the constant behavior of the uncertainty due to normalization.

In order to visualize which sources of uncertainty are more relevant for each resonance parameter, the relative contribution of each source of uncertainty has been represented in Figures 4.33 and 4.34. In both cases the resonances have been ordered by increasing RK/E value, for the same reason mentioned above. In Figure 4.33 the quantities $\sigma_i/\sum\sigma_i$ have been represented, which means that the different uncertainties are added linearly, so $\sigma_{tot}=\sum\sigma_i$. In Figure 4.34, the uncertainties are added quadratically, so $\sigma_{tot}^2=\sum\sigma_i^2$, and hence the represented quantities are $\sigma_i^2/\sum\sigma_i^2$. In the second representation, the largest contributions appear larger than in the first representation, and the smallest contributions appear smaller.

By looking at these Figures, the following conclusions can be reached:

Concerning the Γ_γ parameters, it is possible to appreciate that:

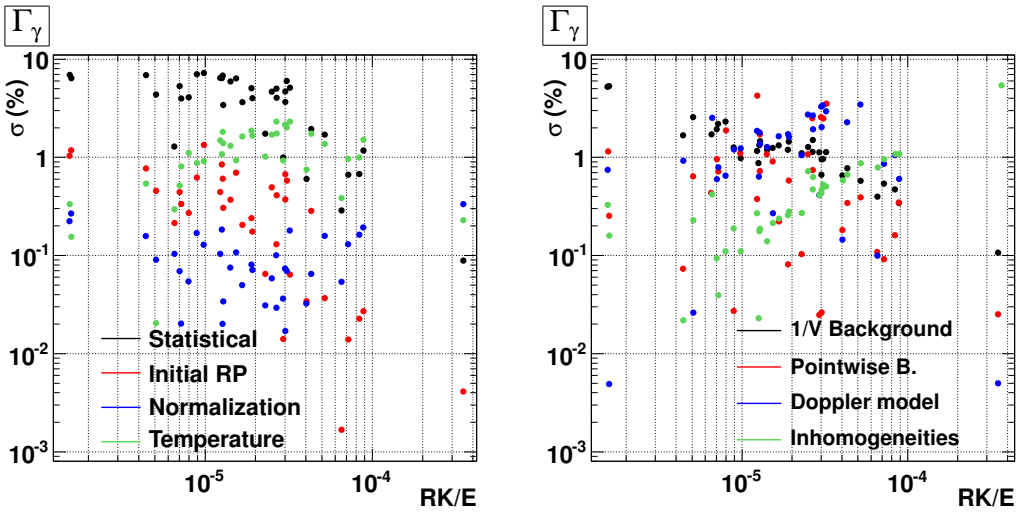

Figure 4.31: Statistical and systematic uncertainties of the Γ_γ parameters of the resonances between 0.7 and 50 eV. The sources of systematic uncertainties are those described in the text: the choice of the initial resonance parameters, the normalization, the temperature, the 1/V background component, the pointwise background, the Doppler broadening model used in the calculation and the inhomogeneities present in the sample. The resonances have been ordered (X axis) by its RK/E value, the ratio between the radiative kernel and the energy of the resonance, which is approximately proportional to the resonance capture area.

- The main source of uncertainty corresponds to the statistical uncertainty, which comes from the statistical uncertainties of the capture yield data points and it is calculated by the SAMMY code, except for the strongest resonances.
- The uncertainties due to the temperature and the Doppler model are of the same size, being the contribution in both cases larger as the resonance area increases, mainly due to the fact that the statistical uncertainty decreases (both sources of uncertainty remains more or less constant, as it can be appreciated in Figure 4.31).
- The uncertainties due to the 1/V background are the systematic uncertainties dominant for the weaker resonances.
- The uncertainties due to the pointwise background are relevant for almost all the resonances, but its relevance is lower.
- The uncertainties due to inhomogeneities in the sample are relevant only for the strongest resonances.
- The uncertainties due to the normalization and the choice of the initial values for the resonance parameters are very small and can be neglected.

Concerning the Γ_n parameters,

- The main source of uncertainty is the normalization, whose absolute value is constant for all the energy range, except for the weakest resonances. Since the rest of the uncertainties (with the exception of the one related to

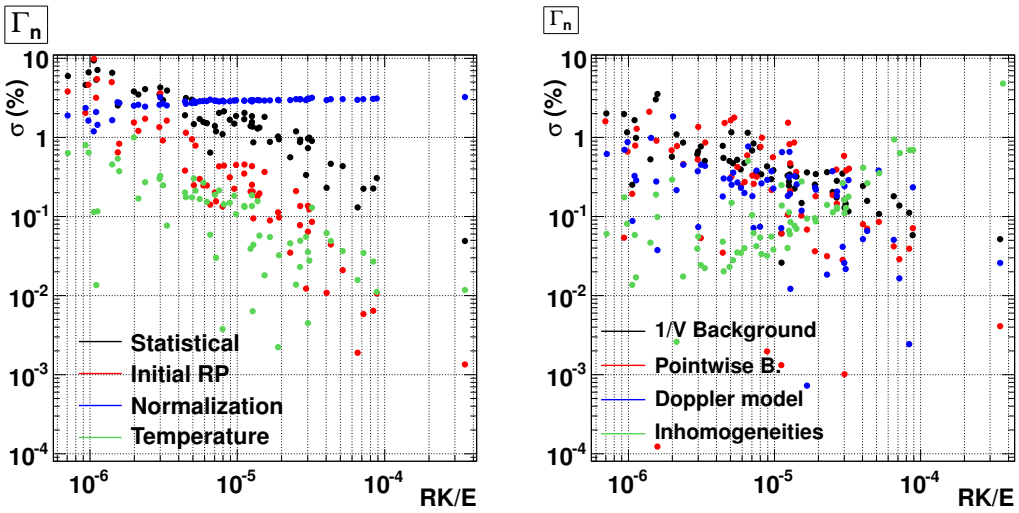

Figure 4.32: Statistical and systematic uncertainties of the Γ_n parameters of the resonances between 0.7 and 50 eV. The sources of systematic uncertainties are those described in the text: the choice of the initial resonance parameters, the normalization, the temperature, the 1/V background component, the pointwise background, the Doppler broadening model used in the calculation and the inhomogeneities present in the sample. The resonances have been ordered (X axis) by its RK/E value, the ratio between the radiative kernel and the energy of the resonance, which is approximately proportional to the resonance capture area.

the sample inhomogeneities) decrease when the radiative kernel increases, the contribution of the uncertainty due to the normalization to the total uncertainty increases as the capture area increases.

- The statistical uncertainties are relevant in the whole capture area range, being more important at lower capture area ranges.
- The uncertainty due to the choice of the initial values for the resonance parameters are the dominant systematic uncertainties for small radiative kernel values. Its contribution to the total uncertainty decreases as the capture area increases, being negligible for high radiative kernel values.
- The uncertainties due to the 1/V background and due to the pointwise background are smaller than the previous contribution, but are still relevant and more or less constant in the whole capture area range.
- Uncertainties due to inhomogeneities in the sample are relevant only for the strongest resonances.
- Uncertainties due to the temperature and the Doppler broadening model can be neglected.

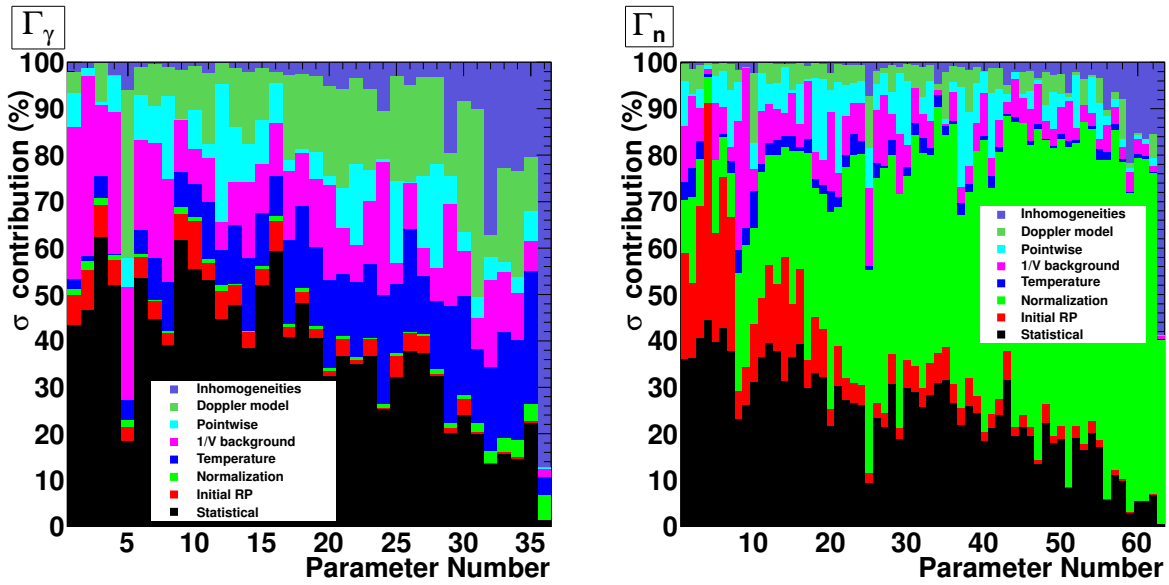

Figure 4.33: Relative contributions to the total uncertainty. The uncertainties have been added linearly, so the computed quantities are $\sigma_i / \sum \sigma_i$. The resonances have been ordered by its RK/E value (RK: radiative kernel, E: resonance energy), in increasing order, so the parameter number 1 corresponds to the resonance with lower RK/E value and the highest parameter number to the resonance with higher RK/E value.

Some of these systematic uncertainties have been compared with the ones calculated by SAMMY. For the calculation of the systematic uncertainties provided by SAMMY, it has been assumed that the relation between the total σ_{TOT}, the statistical σ_{STAT} and the systematic σ_{SYS} uncertainties is given by $\sigma_{TOT} = \sqrt{\sigma_{STAT}^2 + \sigma_{SYS}^2}$, since with SAMMY it is only possible to obtain σ_{TOT} or σ_{STAT}[5]. The ratio between the SAMMY uncertainties and the ones calculated in this work are presented in Figure 4.35: one on the left, the ratio between the systematic uncertainties, and on the right, the ratio between the total uncertainties. Three different uncertainties have been considered: the one related with the normalization in the Γ_n parameters, and the ones related with the temperature and the 1/V background in the Γ_γ resonance parameters. These three uncertainties have been chosen because they are the more relevant systematic uncertainties calculated in this work that can be handled by SAMMY.

It can be observed that the uncertainties associated with the normalization in the Γ_n parameters and with the 1/V background in the Γ_γ parameters are clearly underestimated by SAMMY for all the resonances. Moreover, it can be appreciated that there are only 7 points related to the 1/V background uncertainties in the left panel. For the rest of the resonances, the calculated SAMMY uncertainties were larger when the fit was performed without including the systematic uncertainty in the 1/V background than when it was included, which has no sense. Those 7 points correspond to the Γ_γ resonance parameters of the lower energy resonances, where the 1/V ($1/\sqrt{E_n}$) background component has a larger influence. The systematic uncertainties in the Γ_γ resonance parameters due to the sample temperature calculated with both methods are similar, except for the resonances with larger radiative kernels.

[5] It is only possible to calculate σ_{TOT} , but σ_{STAT} can be obtained from a fit performed without considering systematic uncertainties.

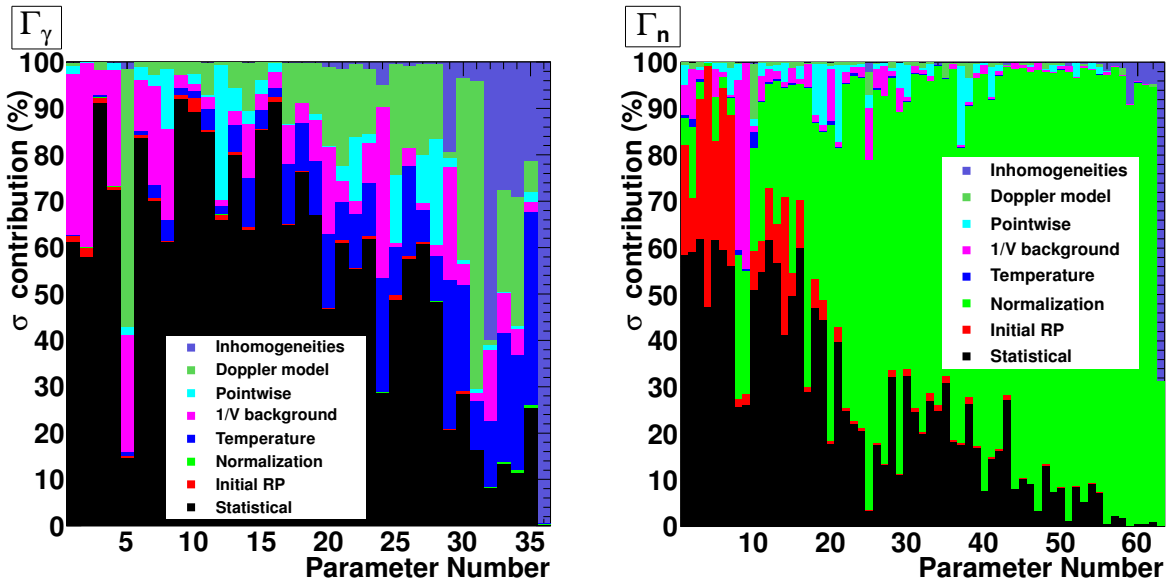

Figure 4.34: Relative contributions to the total uncertainty. The uncertainties have been added quadratically, so the computed quantities are $\sigma_i^2/\sum\sigma_i^2$. The resonances have been ordered by its RK/E value (RK: radiative kernel, E: resonance energy), in increasing order, so the parameter number 1 corresponds to the resonance with lower RK/E value and the highest parameter number to the resonance with higher RK/E value.

The correlations provided by SAMMY between the fitted Γ_γ and Γ_n parameters of the resonances in the 0.7-50 eV energy range are presented in Figure 4.36. The systematic uncertainties mentioned above, such as the normalization, temperature, ... have not been taken into account. It is possible to appreciate that only parameters of the same resonance or of resonances which are close one to the other are correlated, as it is expected.

The correlation of the resonance parameters with the normalization, temperature and 1/V factor have been also estimated with the method mentioned above. From the 1000 different fits performed for each of those three parameters, the correlation coefficients between the resonance parameters and the three mentioned factors have been calculated. With a few exceptions of resonances with very low capture area, the obtained results were:

- Correlations with the normalization: Γ_γ parameters show a correlation of +1 and Γ_n parameters a correlation of -1. This means a linear dependency with a positive (Γ_γ) or negative (Γ_n) slope. In the case of the Γ_n parameters, it is clear that, if the normalization increases, the capture area of the resonances, which are essentially proportional to Γ_n, decreases.

- Correlations with the temperature: Γ_γ parameters show a correlation of -1 and Γ_n parameters a correlation of +1. In the case of the Γ_γ parameters, it is clear that, if the temperature increases, the Doppler broadened resonances will be wider, so the fitted Γ_γ, which gives essentially the width of the resonance, will decrease to fit the experimental results.

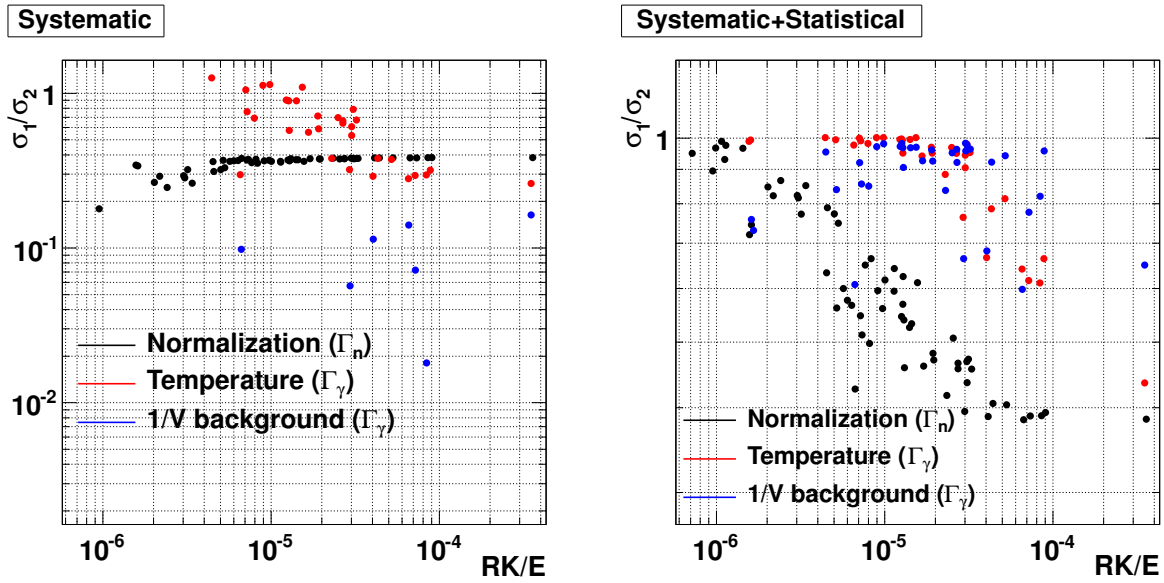

Figure 4.35: Ratio between systematic (left) and total (right) uncertainties computed by the SAMMY code (σ_1) and the ones obtained in this work (σ_2).

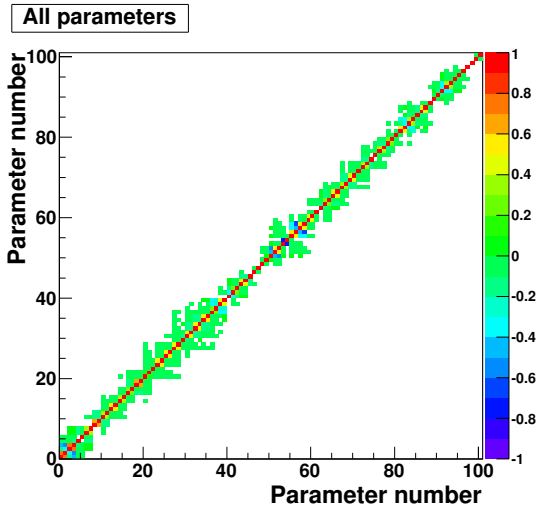

Figure 4.36: Correlation matrix between all the Γ_γ and Γ_n parameters fitted in the 0.7-50 eV energy region. The parameters have been ordered by increasing resonance energy. Correlations between parameters which are exactly 0 (according to the SAMMY calculation) are represented in white color.

- Correlations with the 1/V factor: in this case both Γ_γ and Γ_n show a correlation of -1. This is because when the 1/V parameter increases, then the background increases, so the resonances appear smaller (and thus the

Γ_n will decrease) and broader (and thus Γ_γ parameters will also decrease).

All the resonance parameters calculated in this work, together with their uncertainties, and the more relevant correlation coefficients are listed in Appendix C.

Finally, it has to be said that there are more sources of uncertainty that the ones mentioned above. This sources of uncertainty have been considered negligible, but are described below:

8. Uncertainty due to the dead time model used. As it is presented in Section 3.5.5 (see Figure 3.54), the corrections due to dead time effects are always below 1%.

9. Uncertainty due to the n_TOF resolution function. The description of the n_TOF resolution function has also its uncertainties, that may affect the resonance analysis. However, in the resolved resonance energy range the broadening due to the Doppler effect is much larger than the broadening due to the resolution function. For this reason, the uncertainties due to the resolution function have not been taken into account. A comparison between both broadening effects in the whole energy range can be found in Figure 4.37, and a comparison of both effects at 100 eV and 400 eV in Figure 4.38. In the latter, it is possible to appreciate that the resolution broadening is negligible at 100 eV and much smaller than the Doppler broadening at 400 eV.

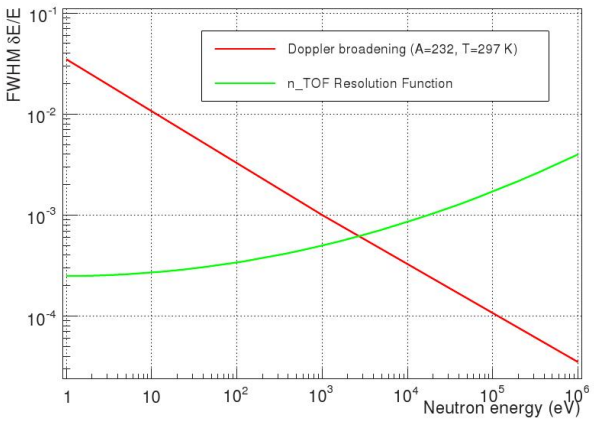

Figure 4.37: Resonance broadening due to the Doppler effect and the resolution function, as a function of the neutron energy. For the Doppler effect the free gas model has been considered, for a nucleus with mass A=252.

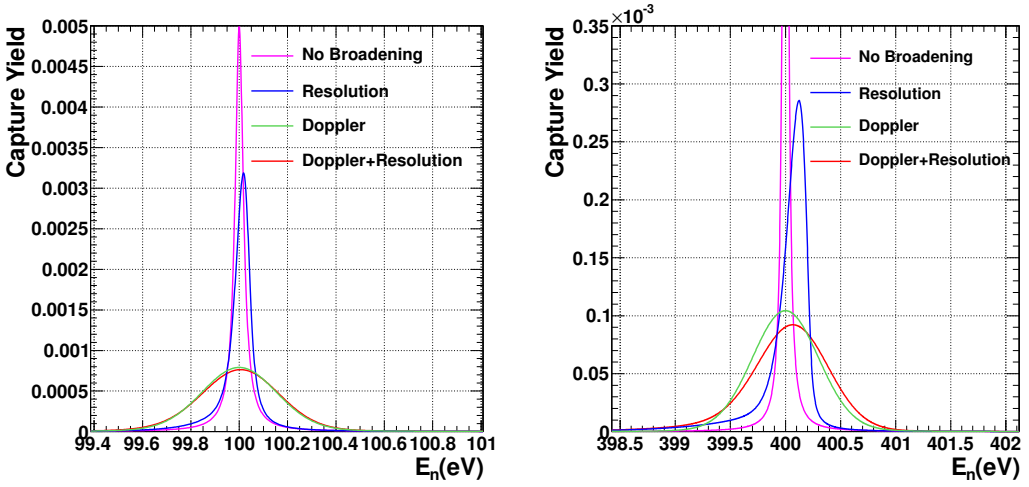

Figure 4.38: Resonance broadening due to the Doppler effect and the resolution function, for a resonance at 100 eV (left) and at 400 eV (right). In both cases, four different broadening treatments have been applied to the resonance: no broadening effects have been applied (magenta), only the broadening due to the resolution function (blue), only Doppler broadening (green) and both of them (red).

4.3.3 Calculation of the radiative width

The mean value of the radiative width has been obtained from the values of the Γ_γ parameters in the 3 - 50 eV energy range. Notice that 63 resonances are found in the 0.7 - 50 eV energy range, but the Γ_γ parameter has been obtained from only 36 of them. For the remaining 27 resonances the uncertainty was too large, so they have been fixed to the calculated mean value. The three resonances between 0.7 and 3 eV have been excluded because the parameters of the strongest resonance at 1.35 eV could not be well determined (this is presented in Section 4.3.5), and the parameters of the resonances at 0.98 and 1.74 eV are correlated with them.

Thus, the $\langle\Gamma_\gamma\rangle$ value has been obtained from the 33 resonance values presented in Figure 4.39. An horizontal blue line has been represented at 42 meV, which is the obtained $\langle\Gamma_\gamma\rangle$ value. Two different techniques have been used in order to compute the $\langle\Gamma_\gamma\rangle$ value from the individual Γ_γ values, their uncertainties and their correlations. The first one is to use the weighted mean, where the correlation between parameters is not taken into account. The second one is to use the generalized weighted mean, which considers the correlations between them. This mean can be defined according to Equation 4.4 [Cox06]:

$$\bar{x} = \sigma^2_{\bar{x}} \left(W^T C^{-1} X\right) \quad \sigma^2_{\bar{x}} = \left(W^T C^{-1} W\right)^{-1} \tag{4.4}$$

where X=$[x_1, ..., x_n]$, C is the covariance matrix and W=$[1, 1, ..., 1]$ is the design matrix. Due to the fact that the correlations between parameters of different resonances are quite low (see Section 4.3.2) the results obtained with both methods are very similar, as it can be observed in Table 4.5.

In the calculation mentioned above, only statistical uncertainties were taken into account. As it was presented in Section 4.3.2, the main sources of systematic uncertainties for the Γ_γ parameters are the temperature, the 1/V

background factor, the Doppler broadening model, and the inhomogeneities. In order to estimate this systematic uncertainties, the $\langle\Gamma_\gamma\rangle$ value was computed from SAMMY fits performed at different temperatures (the nominal temperature $\pm\sigma_{temp}$), with different 1/V factors (the nominal value $\pm\sigma_{1/V}$), using the Doppler lattice crystal model with the phonon structure of the UO_2, and with a double sample thickness, in the same way as it is presented in Section 4.3.2. All the resulting values are presented in Table 4.5, and the deduced uncertainties in Table 4.6.

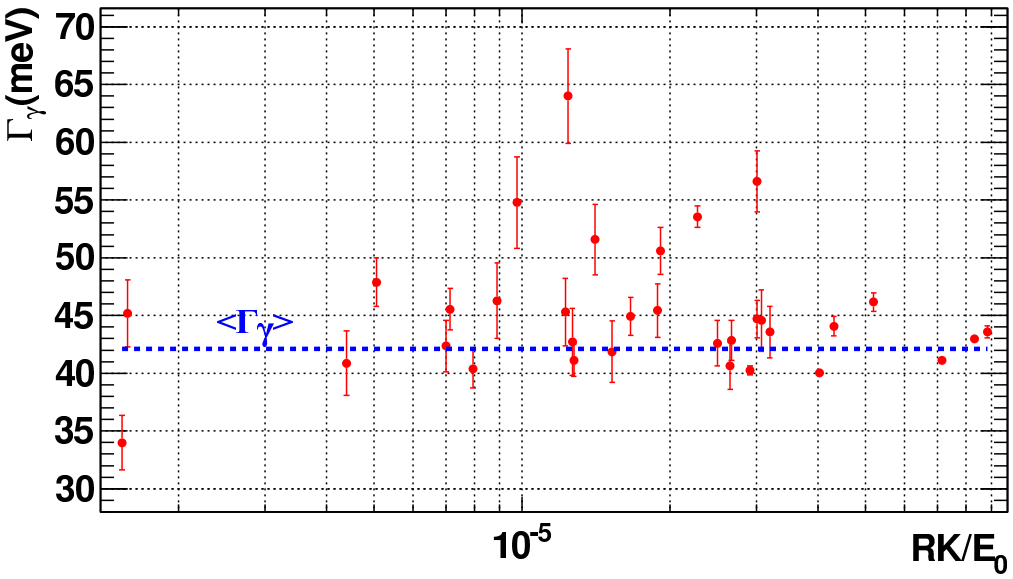

Figure 4.39: Values of the Γ_γ parameters.

Conditions	C-Matrix	Weighted
Nominal values	41.94(12)	41.74(13)
Temp=289K	42.39(12)	42.19(13)
Temp=297K	41.49(12)	41.30(13)
1/V factor = -7.4·$10^{-4}\sqrt{eV}$	41.61(12)	41.45(13)
1/V factor = -8.0·$10^{-4}\sqrt{eV}$	42.26(12)	42.03(13)
Lattice Doppler model	41.20(12)	41.05(13)
Thickness x2	41.31(12)	41.11(13)

Table 4.5: $\langle\Gamma_\gamma\rangle$ values (in meV) calculated with different temperatures, 1/V background constants, Doppler models and thicknesses. For all the cases, the $\langle\Gamma_\gamma\rangle$ value has been obtained by performing a weighted mean of the fitted Γ_γ parameters (Weighted) and by performing a generalized weighted mean (C-Matrix), using the whole covariance matrix.

$\langle\Gamma_\gamma\rangle$	σ_{stat}	σ_{temp}	$\sigma_{1/V}$	$\sigma_{Doppler}$	σ_{Inhom}	σ_{tot}^{lin}	σ_{tot}^{quad}
42.00	0.12	0.5	0.3	0.7	0.6	2.2	1.1

Table 4.6: $\langle\Gamma_\gamma\rangle$ value with its statistical uncertainty (σ_{stat}) and the estimated uncertainties due to the temperature (σ_{temp}), the 1/V factor ($\sigma_{1/V}$), the Doppler model used ($\sigma_{Doppler}$) and the sample inhomogeneities (σ_{Inhom}). All these quantities have been added linearly (σ_{tot}^{lin}) and quadratically (σ_{tot}^{quad}). All the values are expressed in meV.

4.3.4 Estimation of the systematic uncertainties of the resonance parameters in the 50 - 400 eV energy region

The estimation of the systematic uncertainties in the 50 - 400 eV energy region has been performed in the same way as for the 0.7 - 50 eV energy region (Section 4.3.2). The only difference is that above 50 eV all the Γ_γ parameters have been fixed to the average value (Section 4.3.3), so only the Γ_n parameters have been calculated.

The relative contribution of the different sources of uncertainty to the total uncertainty is shown in Figures 4.40 and 4.41 , in the same way as it was performed in Section 4.3.2. It is possible to appreciate that now the dominant source of uncertainty is the statistical uncertainty, followed by the systematic uncertainties related with the choice of the initial parameter values and the normalization. All these values are presented in Figure 4.42. The rest of systematic uncertainties are quite lower than these and can be neglected. There is an exception, which is the uncertainty due to the pointwise background in the 325 - 350 eV energy region, which can be appreciated in the left panel of Figure 4.40 (region close to the parameter number 250). This uncertainty was obtained by comparing the fitted results obtained when using the smoothed background and when using the pointwise without smoothing. The χ^2/n of both fits were computed in the mentioned energy range, finding values of 0.74 and 0.85 for the smoothed background and for the non-smoothed background cases, respectively. This indicates that the fit is significantly better when the smoothed background is used. For this reason, it has been assumed that, in this case, the pointwise uncertainty has been overestimated and thus, it has been neglected for the Γ_n parameters of the resonances in the whole 50 - 400 eV energy range.

Concerning the three relevant uncertainties, it is possible to appreciate that the statistical uncertainties are larger than in the 0.7 - 50 eV energy range case, and that they decrease as the resonance capture area increases (see right panel of Figure 4.42). The normalization uncertainty is close to 3%, as expected, except for resonances with low capture area, where the uncertainties due to the choice of the initial values are larger. The uncertainties related to the choice of the initial values follow a similar behavior than the statistical ones, and are quite important for weak resonances. However, this source of uncertainty is always smaller than the statistical uncertainty, as it is shown in Figure 4.43.

Notice that this uncertainty related to the choice of the initial parameters has been obtained by sampling each initial parameter according to a Gaussian distribution with a standard deviation of 10%. Thus, it is expected a maximum obtained uncertainty of a 10%, which is the case for the weaker resonances, as it can be appreciated in Figure 4.42. Indeed, it is reasonable to assume that all the uncertainties significantly lower than a 10% have been estimated correctly, whereas those uncertainties with values close to a 10% may be larger. The solution could be to sample the initial parameters using a Gaussian distribution with standard deviation larger than 10%. However, this has been done and it has been observed than with higher initial standard deviations not all the fits converge for all the resonances. For this reason, and since there are only 13 resonances of a total of 291 with relative errors greater than a 9% (38 greater than an 8%), the results with the 10% initial standard deviation have been adopted.

Finally, the correlations between the different Γ_n parameters are presented in Figure 4.44. The systematic uncertainties have not been taken into account. It can bee appreciated that the correlation matrix is quasi-diagonal, which means that only parameters of resonances which are very close one to the other are correlated. The correlation of all the Γ_n parameters with the normalization is -1, as expected. They have been calculated from the 1000 fits performed with different normalization values.

The obtained resonance parameters, together with their uncertainties, and with the correlation between parameters of neighboring resonances are presented in Appendix C.

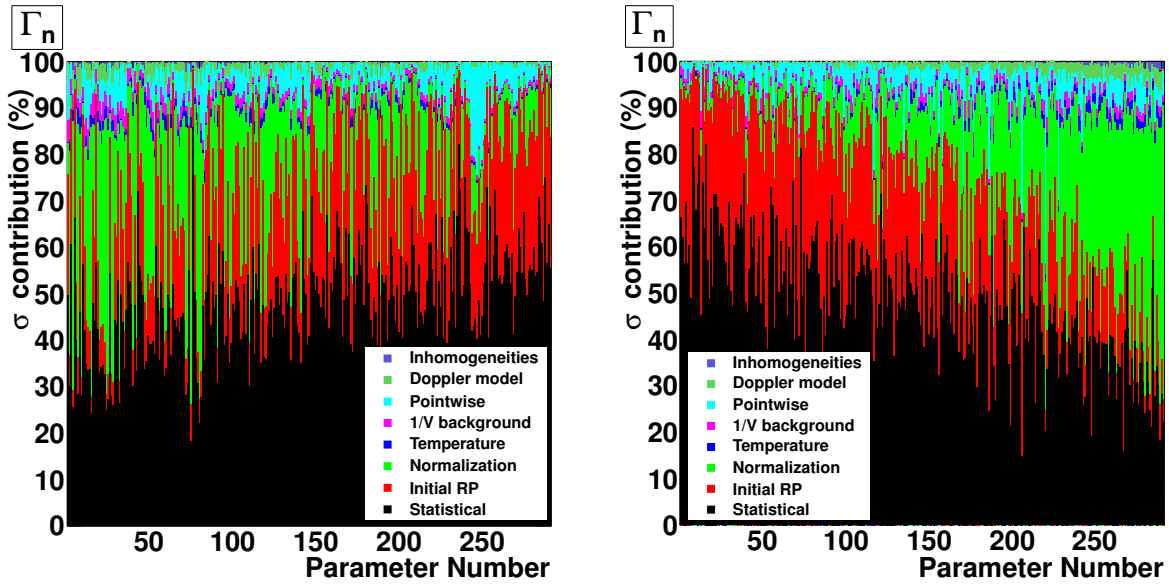

Figure 4.40: Relative contribution to the Γ_n total uncertainties (50 - 400 eV energy range) of the different sources of uncertainties. The uncertainties have been added linearly, so the computed quantities are $\sigma_i / \sum \sigma_i$. The resonances have been ordered by energy (left panel) and by its RK/E value (right panel).

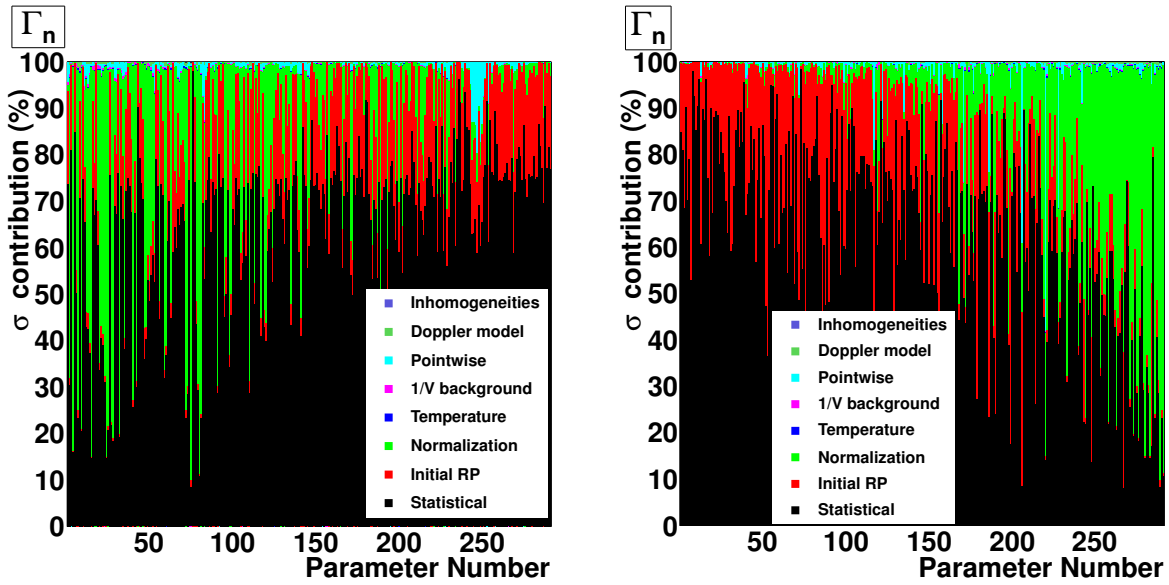

Figure 4.41: Relative contribution to the Γ_n total uncertainties (50 - 400 eV energy range) of the different sources of uncertainties. The uncertainties have been added quadratically, so the computed quantities are $\sigma_i^2/\sum\sigma_i^2$. The resonances have been ordered by energy (left panel) and by its RK/E value (right panel).

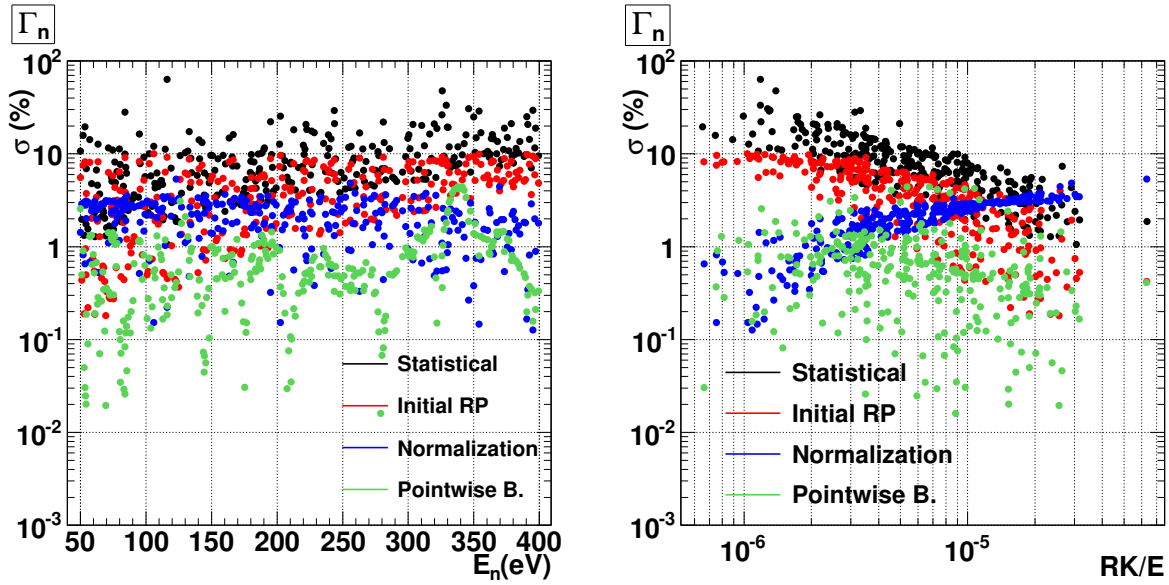

Figure 4.42: Statistical and systematic uncertainties of the Γ_n parameters in the 50 - 400 eV energy range. Only the main sources of systematic uncertainties have been considered: choice of initial resonance parameter values, normalization and pointwise background. The resonances have been ordered by its energy (left) and by its RK/E value (right).

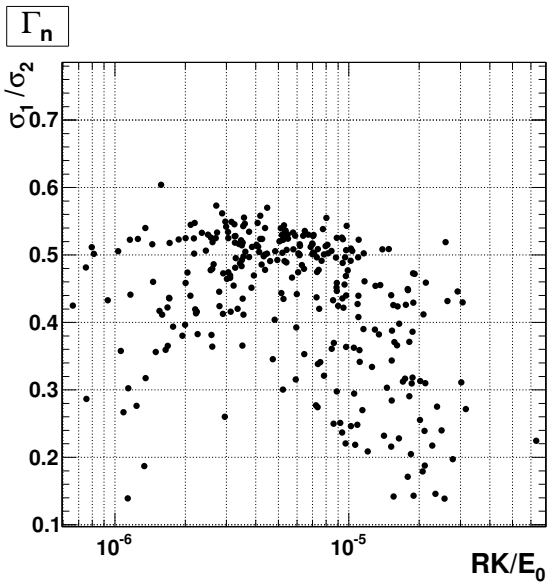

Figure 4.43: Ratio between the uncertainty due to the choice of the initial Γ_n values (σ_1) and the statistical uncertainties (σ_2), for the Γ_n parameters of the resonances in the 50 - 400 eV energy region, ordered by increasing capture area.

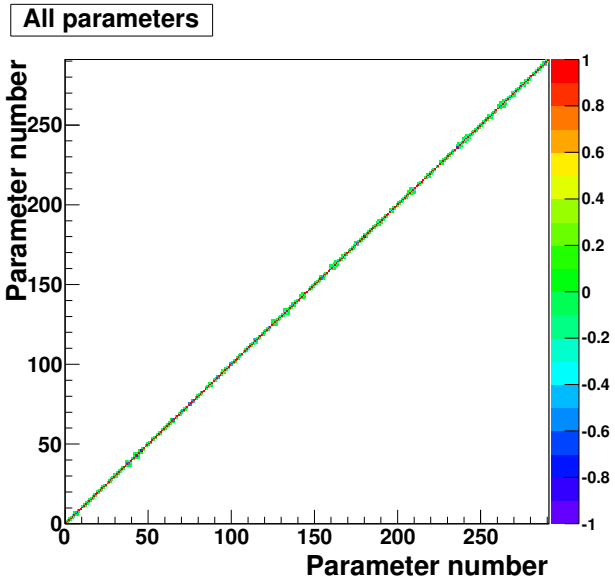

Figure 4.44: Correlation matrix between all the Γ_n parameters fitted in the 50 - 400 eV energy region. The parameters have been ordered by increasing resonance energy. Correlations between parameters which are exactly 0 (according to the SAMMY calculation) are represented in white color.

4.3.5 Negative resonances and the at 1.35 eV resonance

Besides the differential measurements used to normalize the n_TOF capture data, there are integral measurements that can also be compared to the n_TOF capture measurement. These integral measurements are not compatible with the results obtained in this work, which suggests that the parameters calculated in this work for the resonance at 1.35 eV, which is by far the main contribution to these integral measurements, are not correct.

In Table 4.7 there is a list of the available capture resonance integrals, defined as $I_0 = \int_{0.5eV}^{\infty} \frac{\sigma_\gamma(E)}{E} dE$, together with the thermal capture cross sections and the ratio between them. Some of the capture resonance integrals have been obtained from integral measurements, and others have been derived from the resonance parameters. As it can be appreciated, many values are incompatible. The thermal capture cross are scattered mainly between 73 and 85 barn, and the resonance integrals between 1800 and 2300 barn, approximately.

The resonance integrals of the ENDF/B-VII.0 and the JEFF-3.1 (which is the same evaluation as JENDL-3.3) evaluations are around 1800 barn, whereas the ENDF/B-VII.1 and JENDL-4.0, which are the most recently evaluated libraries, have capture resonance integrals close to 2050 barn. This change has been motivated in both cases, according to the documentation provided by the libraries, by the measurement performed by Ohta et al.. This measurement gives a resonance integral of 2250(300) barn, if the thermal cross section value of Marie et al. (81.8 barn) is assumed (for lower assumed thermal cross section values, the resonance integral increases). This value of 2250(300) barn is not compatible with some of the measured values listed in Table 4.7. In both evaluated libraries, the resonance integral has been increased by modifying the resonance at 1.35 eV (see Figure 4.6 of Section 4.1), which is clearly the main contribution to the resonance integral, as can be appreciated from the values presented in Table 4.8.

In Table 4.8 it can also be appreciated that the resonance integral of the n_TOF capture measurement is significantly lower than the rest of evaluated and measured values, and that the discrepancy comes from the integral of the 1.35 eV resonance contribution. It can be observed in Table C.1 (Appendix C) or in Figures 4.33 and 4.34 (Section 4.3.2) that this resonance could be strongly affected by the presence of inhomogeneities, due to shelf shielding and multiple scattering effects (Figure 4.14). As it is discussed, for example, in [Kop07], inhomogeneities can be very strong in thin powder samples, such as the one used in the n_TOF measurement. If the sample is inhomogeneous, then the multiple scattering corrections have not been performed correctly, which causes a wrong determination of the resonance parameters. For the rest of the resonances the uncertainty in the resonance parameters due to sample inhomogeneities is very small or negligible (Section 4.2.3.4).

Reference	σ_0(barn)	I_0(barn)	I_0/σ_0
Hori et al. (2009) [Hor09]	76.6[a]	1970(110)	25.7(15)
Marie et al. (2006) [Mar06.2]	81.8(36)		
Ohta et al. (2006) [Oht06]		2250(300)[b]	28(4)
Y. Hatsukawa et al. (1997) [Hat97]	84.4		
Gavrilov et al. (1977) [Gar76]	83(6)	2200(150)	26.5(26)
Simpson et al. (1974) [Sim74]		1819(80)[c]	
Eberle et al. (1971) [Ebe71]	77(2)	1930(50)[c]	25.1(9)
Berreth et al. (1970) [Sim74]	85(4)	1824(80)[c]	21.5(14)
Folger et al. (1968) [Fol68]	78	2250[d]	29
Bak et al (1967) [Bak67]	73(6)	2300(200)	32(4)
Ice et al. (1966) [Ice66]	$66<\sigma_0<84$		
Butler et al (1957) [But57]	73.6(1.8)	2290(50)	31(1)
Harvey et al (1954) [Har54]	140(50)		
Stevens et al. (1954) [Ste54]	115		
Mughabghab (2006) [Mug84]	75.1(18)	1820(70)	24.2(11)
ENDF/B-VII.1 [Cha11]	80.4	2051	25.5
ENDF/B-VII.0 [Cha06]	75.1	1820	24.2
JENDL-4.0 [Shi11]	79.3	2040	25.7
JEFF-3.1 [JND06]	76.7	1788	23.3

Table 4.7: Thermal capture cross sections, resonance integrals and ratios between them provided by different experiments and evaluations.

[a] Value assumed to normalize, so I_0 is proportional to it.

[b] The thermal value of Marie et al. has been assumed. The Ohta et al. measured value was $\hat{\sigma} = 174.5(5.3)$barn, and α=0.0418(45), where $I_0=\hat{\sigma}/\alpha+(0.45-1/\alpha)\sigma_0$.

[c] Cut-off energy was taken as 0.625 eV

[d] Cut-off energy was taken as 0.83 eV

	0.5 - 1 eV	1 - 2 eV	2 - 50 eV	50 - 250 eV	250 eV - 20 MeV	Total
ENDF/B-VII.1	59.2	1576	320	53.8	42.7	2051
ENDF/B-VII.0	57.6	1338	322	53.6	40.6	1820
n_TOF	58.2	1196	325	58.1	43.8	1681

Table 4.8: Values of the capture resonance integral in different energy ranges, in barn, for the ENDF/B-VII.1 and ENDF/B-VII.0 evaluations and for the result of the n_TOF capture measurement. In the case of the n_TOF capture measurement, the integral between 400 eV and 20 MeV of the ENDF/B-VII.1 evaluation has been adopted, which is 33.4 barn.

The resonance parameters obtained for the 1.35 eV resonance are presented in Table 4.9, together with other measurements and evaluations, and together also with the quantity $g\Gamma_n\Gamma_\gamma/(2g\Gamma_n+\Gamma_\gamma)$, which is approximately

proportional to the resonance capture area (it is the radiative kernel, but with $2g\Gamma_n$ in the denominator, instead of Γ_n, which is an average value of Γ_n between both spin assignments). It can be observed that the resonance capture area obtained in this work is lower than the rest, with the exception of the Cote et al. and the Bellanova et al. measurements, which are not compatible with the n_TOF measurement, as it was discussed in Section 4.2.3.3.

Reference	$2g\Gamma_n$(meV)	Γ_γ(meV)	$g\Gamma_n\Gamma_\gamma/(2g\Gamma_n+\Gamma_\gamma)$ (meV)
n_TOF	0.97(5)	48.6(2.5)	0.481
Cote et al.	0.82(8)	43.0(3.3)	0.402
Berreth et al.	1.106	43	0.539
Bellanova et al.	0.890(7)	56(1)	0.438
Simpson et al.	1.107(47)	43(2)	0.540
ENDF/B-VII.1	1.32	38.6	0.638
ENDF/B-VII.0	1.11	43	0.541
JENDL-4.0	1.28	50	0.624
JEFF-3.1	1.09	45.15	0.532

Table 4.9: Different values of the resonance parameters of the resonance at 1.35 eV. The quantity $g\Gamma_n\Gamma_\gamma/(2g\Gamma_n+\Gamma_\gamma)$ is approximately proportional to the resonance capture area. Uncertainties in the values obtained in the n_TOF measurement are an estimation of the systematic uncertainties due to the presence of sample inhomogeneities.

In order to appreciate how the inhomogeneities affect the parameters of the resonance at 1.35 eV, the same fit has been performed with different sample thicknesses (and by varying the normalization accordingly). The results are presented in Table 4.10, where it is possible to appreciate how the resonance integral increases with the sample thickness. In Figure 4.45, the different yields are presented.

	$2g\Gamma_n$(meV)	Γ_γ(meV)	$g\Gamma_n\Gamma_\gamma/(2g\Gamma_n+\Gamma_\gamma)$ (meV)	I_0(barn)
nominal thickness	0.972	48.6	0.476	1681
nominal thickness x 1.50	1.016	46.2	0.497	1730
nominal thickness x 2.00	1.070	43.6	0.522	1788
nominal thickness x 2.50	1.136	40.7	0.553	1859
nominal thickness x 3.00	1.221	37.5	0.591	1948

Table 4.10: Resonance parameters of the 1.35 eV resonance, together with the radiative kernel (proportional to the resonance capture area) and the resulting resonance capture integral, for different thickness values (nominal thickness is $1.94{\cdot}10^{-5}$ atoms/barn). For the resonance capture integral above 400 eV the value of 33.4 barn from the ENDF/B-VII.1 evaluation has been used.

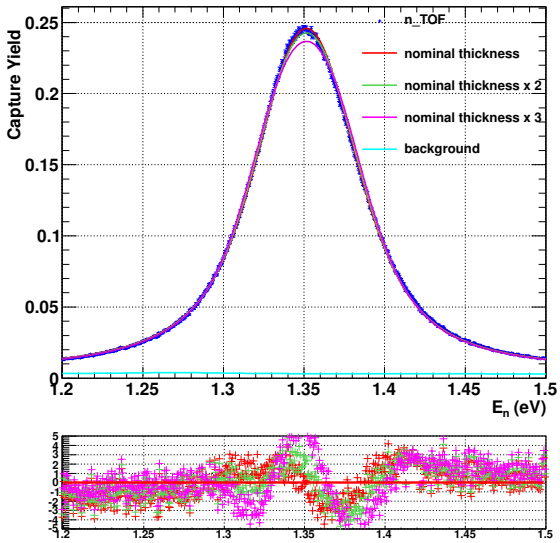

Figure 4.45: Fit performed to the resonance at 1.35 eV assuming different thicknesses.

Thus, it can be concluded that:

1. The inhomogeneities affect severely the values of the resonance parameters at 1.35 eV, and thus, the resonance capture integral.
2. The discrepancies between the n_TOF capture measurement and most of the measurements suggest that the sample is inhomogeneous.
3. Since there is no way to characterize these inhomogeneities, there is no mechanism to obtain reliable values for the 1.35 eV resonance parameters from this sample, and thus, for the resonance capture integral.

However, it was shown in Section 4.2.3.3 that the n_TOF measurement is quite compatible with the Simpson et al. and the Berreth et al. measurements. As an example, the resonance parameters obtained from these three measurements of the four strongest resonances are given in Table 4.11. As it can be observed, the values of the resonances at 1.74, 6.54 and 7.84 eV do not differ so much from one measurement to another. In addition, it has to be said that the Simpson et al. measurement was performed with samples of $3.58{\cdot}10^{-3}$ and $7.76{\cdot}10^{-4}$ atoms/barn, so the resonance at 1.35 eV was saturated; however, the Berreth et al. measurement was performed with those two samples plus a $1.66{\cdot}10^{-4}$ atoms/barn sample, which does not saturate. Indeed, the Simpson et al. evaluation of the resonance at 1.35 eV probably comes from the Berreth et al. resonance parameters. This indicates that the most reliable values could be the ones provided by Berreth et al..

All the newest evaluations, with the exception of the ENDF/B-VII.1 and JENDL-4.0, have resonance integrals close to 1800 barn, similar to the one provided by Berreth et al., whereas the mos recent ones have modified the parameters of the resonance at 1.35 eV in order to be compatible with the Ohta et al. measurement, and have resonance integrals close to 2050 barn. However, these modifications are incompatible with the Berreth et al. measurement. In addition, for resonance integrals larger than 2000 barn, the n_TOF results could only be

understood if the inhomogeneities were huge (Table 4.10). All of this indicates that the mentioned changes in the ENDF/B-VII.1 and JENDL-4.0 libraries are perhaps going in a wrong direction. The publication of the two unpublished measurements mentioned in Section 4.1, [Jan09, Hor09], might solve this problem. Alternatively, a new measurement with a very thin sample should be performed in order to determine with reasonable accuracy the resonance parameters at 1.35 eV.

	This work		Simpson et al.		Berreth et al.	
E_0(eV)	$2g\Gamma_n$(meV)	Γ_γ(meV)	$2g\Gamma_n$(meV)	Γ_γ(meV)	$2g\Gamma_n$(meV)	Γ_γ(meV)
1.35	0.972(48)	48.6(25)	1.107(47)	43(2)	1.106	43
1.74	0.2293(22)	40.1(4)	0.240(11)	38(2)	0.239	40
6.54	0.965(6)	41.0(7)	0.998(38)	37(3)	0.911	42
7.84	1.363(10)	42.9(8)	1.374(56)	39(4)	1.276	42

Table 4.11: Parameters of the four strongest ^{243}Am resonances.

Finally, some considerations concerning the negative resonances will be presented. The negative resonances are usually used to fit the thermal region, and they are supposed to represent an average effect of the levels below the neutron separation energy. In this work, the negative resonance of the ENDF/B-VII.0 has been adopted (there is only one for the ^{243}Am), as well as the value of the resonance at 0.415 eV, which is also out of the n_TOF capture measurement energy range. One doubt that arises up is if this negative resonance affects the ^{243}Am cross section above 0.7 eV, in the energy range of the n_TOF measurement. This question is answered in Figure 4.46, where different ^{243}Am cross sections have been constructed: the n_TOF fitted cross section (black); the same cross section, but without including the negative resonance (blue); the cross section resulting from only the 1.35 eV resonance (green); and the cross section resulting from only the negative resonance (red). It is possible to appreciate that the effect of the negative resonance is negligible in the n_TOF energy range. Moreover, the main contribution to the thermal cross section value comes from the resonance at 1.35 eV, and not from the negative resonance.

The only information that can be obtained concerning the thermal cross section from the n_TOF measurement comes from the fact that this measurement is compatible with the Weston et al. capture measurement (see Section 4.4.3). The integrated cross section in the n_TOF measurement (normalized to the transmission measurements at low energies) between 250 eV and 2.5 keV is 5($\pm$3.8)% lower than the Weston et al. results. The previous uncertainty is only due to statistical uncertainties. According to [Wes85], the Weston et al. measurement was normalized at thermal energies to 74.8 barn, and the systematic uncertainty related with the normalization in the keV region relative to thermal was estimated in 5%. All this information suggests that the thermal cross section could be closer to 75 barn than to 85 barn, but the arguments are too weak to reach a conclusion.

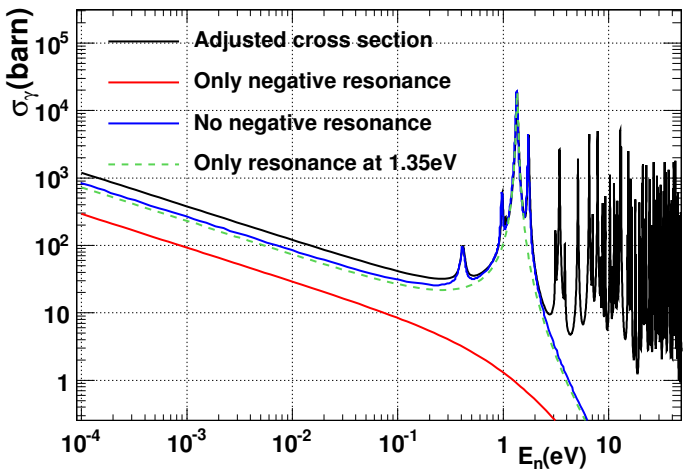

Figure 4.46: Effect of the negative resonance in the ^{243}Am capture cross section.

4.3.6 Statistical properties of the resolved resonance region

The neutron resonance parameters are expected to follow a specific statistical behavior, as it was discussed in Section 1.2.4. A statistical analysis of the resonance parameters in the Resolved Resonance Region (RRR) is usually performed with two purposes. First, to check the consistency of the resonance parameters, and second, to deduce average resonance parameters which are needed for nuclear reaction calculations. In particular, they are the basis for the neutron cross sections calculation above the RRR.

The resonance properties required for the calculation of the elastic and capture cross sections above the RRR are:

1. The average gamma widths, $\langle \Gamma_\gamma^l \rangle$, which, for l=0, was calculated in Section 4.3.3. The distribution of the Γ_γ^l parameters are expected to follow a χ^2 distribution with a large number of degrees of freedom (a delta-like distribution), which leads to assume that all the Γ_γ^l parameters have the same value.

2. The average resonance spacings (or average level spacings), D_l, which are the average distances between two consecutive resonances with the same orbital angular momentum, l. Its value and statistical uncertainty can be calculated, according with [Cap09], with Equation 4.5, where ΔE is the energy interval between two resonances and N is the number of resonances in the interval.

$$D_l = \frac{\Delta E}{N-1} \quad , \quad \frac{\Delta D_l}{D_l} = \frac{0.45\sqrt{\ln N + 2.18}}{N} \approx \frac{1}{N} \tag{4.5}$$

3. The neutron strength functions, S_l, which are defined by the relationship given in Equation 4.6, where Γ_n^l are the reduced neutron widths, defined in Equations 4.7 and 4.8, g is the statistical weight factor, g=$\frac{1}{2}$(2J+1)/(2I+1), V_l are the penetrability factors, k is the neutron wave number, which can be calculated with k=2.19677·10$^{-3}\frac{A}{A+1}\sqrt{E/1eV}$ ·10^{12}cm^{-1}, and R is the scattering radius, R=0.080+0.123A$^{1/3}$·10^{-12}cm.

$$S_l = \frac{\langle g\Gamma_n^l \rangle}{(2l+1)D_l} = \frac{1}{(2l+1)\Delta E}\sum_r g_r \Gamma_{nr}^l \quad , \quad \frac{\Delta S_l}{S_l} = \sqrt{\frac{2}{N}} \tag{4.6}$$

$$\Gamma_n^l = \sqrt{\frac{1eV}{E}}\frac{\Gamma_n}{V_l} \tag{4.7}$$

$$V_0 = 1 \quad , \quad V_1 = \frac{(kR)^2}{1+(kR)^2} \quad , \quad V_2 = \frac{(kR)^4}{9+3\,(kR)^2+(kR)^4} \tag{4.8}$$

All these quantities, $\langle\Gamma_\gamma^l\rangle$, D_l and S_l, depend on the neutron energy. However, in the energy range of the RRR their variation is negligible, and they can be considered as constants. Notice that these parameters provide information concerning the density of resonances in the nucleus and the average values of the different widths. With appropriate models which describe their energy dependence and the shape of the distribution probabilities of the widths and the distance between consecutive levels, average cross sections can be calculated, together with an statistical treatment of their fluctuations due to their resonant behavior.

All these quantities are also defined for each total angular momentum value, J, so $\langle\Gamma_\gamma^{l,J}\rangle$, $D_{l,J}$ and $S_{l,J}$ have the same definitions as above, but taking into account only resonances with the same l and J values. When the J values of the resonances are unknown, and this happens very often, it is recommended to use the so called 2J+1 law of the level density, which means that $1/D_{l,J} \propto (2J+1)$ (see Appendix D of [Her09]).

4.3.6.1 Orbital momentum of the resonances measured in the RRR

In this Section it will be demonstrated that all the ^{243}Am resonances which have been measured in the RRR are s-wave (l=0) resonances.

Each resonance is defined by its energy, its partial widths (Γ_n, Γ_γ, Γ_f) and its angular momentum quantum numbers (orbital l and total J). Sometimes it is possible, with the shape of a resonance, to determine its angular momentum quantum numbers. In this work it was assumed that all resonances have orbital momentum l=0, and it was shown (Section 4.3.1) that it has not found any way to distinguish the total angular momentum of the resonances. For this reason, the parameter which has been determined for each resonance is $g\Gamma_n$, instead of Γ_n.

There is another way to determine (or suggest) the orbital momentum of a resonance, different from the analysis of the shape of the resonance. This method is based in the Porter-Thomas distribution of the neutron widths, which is different for each orbital (and, in principle, total) momentum. Thus, if a resonance has a certain $g\Gamma_n$ value, it is possible to assign a probability for that resonance of being an l=0,1,2,... wave resonance. This can be done if the different $\langle\Gamma_n^l\rangle$ values are known.

The Porter-Thomas distribution is given in Equations 4.9 and 4.10, for two possible degrees of freedom μ=1,2, which is the number of exit channels, equal to the multiplicity of J. The multiplicity of J is the number of possible channel spins for a specific value of J. The channel spin is the vector sum of the target spin and the neutron spin. For example, if the target nucleus has spin I=5/2, then its channel spin can be 2 or 3, and for l=1 there are four possible values of J, which are J=1,2,3,4; two of them with multiplicity equal to 1: J=1,4, and two of them with multiplicity equal to 2: J=2,3.

$$p(x)dx = \frac{1}{\sqrt{2\pi x}}e^{-x/2}dx \ , \ with \ \ x = \Gamma_n^l / \langle\Gamma_n^l\rangle \qquad for \ \ \mu = 1 \tag{4.9}$$

$$p(x)dx = e^{-x}dx \ , \ with \ \ x = \Gamma_n^l / \langle\Gamma_n^l\rangle \qquad for \ \ \mu = 2 \tag{4.10}$$

Using Equations 4.9, 4.10 and 4.6, and assuming the 2J+1 law of the level density, the Equation 4.11 can be obtained. Complete details can be found in [Oh00]. This equation gives the probability of a resonance with a certain $g\Gamma_n$ value of having orbital spin 0, 1 or 2. The Equation contains a coefficient, β_l, which depends of the spin of the target nucleus, I, and their values are given in Table 4.12.

$$P(g\Gamma_n|l=0,1,2) = \left(\frac{\beta_l}{\sqrt{2\pi S_l D_0 \sqrt{E} V_l g\Gamma_n}} + \frac{1-\beta_l}{2S_l D_0 \sqrt{E} V_l} \right) \exp\left(-\frac{g\Gamma_n}{2S_l D_0 \sqrt{E} V_l} \right) \tag{4.11}$$

	l=0	l=1	l=2
I=0	1	1	1
I=1/2	1	2/3	2/3
I=1	1	1/2	1/2
I=3/2	1	1/2	2/5
I≥2	1	1/2	1/3

Table 4.12: β_l statistical factors to be used in Equation 4.11, as a function of the spin of the target nucleus (I).

With Equation 4.11 it is possible to demonstrate that, in the case of the ^{243}Am nucleus, all the detected resonances are s-wave resonances. This has been done by adopting the D_0 and S_l values from the ENDF/B-VII.1 evaluation, which are D_0= 0.66 eV, S_0= $0.98{\cdot}10^{-4}$, S_1= $2.60{\cdot}10^{-4}$ and S_2= $0.98{\cdot}10^{-4}$. With this values the probabilities of s, p and d-waves are presented in Figure 4.47, as a function of $g\Gamma_n$, for two resonance energy values, 1 and 400 eV, which are the energy limits for the RRR considered in this work. The range of $g\Gamma_n$ values obtained in this ^{243}Am analysis has also been included, showing that only s and p waves have to be considered.

Finally, the probability of each detected resonance of being a p-wave resonance has been calculated, finding that in all the cases the probability of being a p or d-wave resonance is less than 10^{-20}. Results are shown in Figure 4.48. Notice that the Y axis is in double logarithmic scale, due the extremely large range of values covered. There are also p and d-wave resonances in the 1 - 400 eV energy range, but they not been detected for being too weak. Its contribution to the cross section increases with the neutron energy, as it is presented in Section 4.4.2.

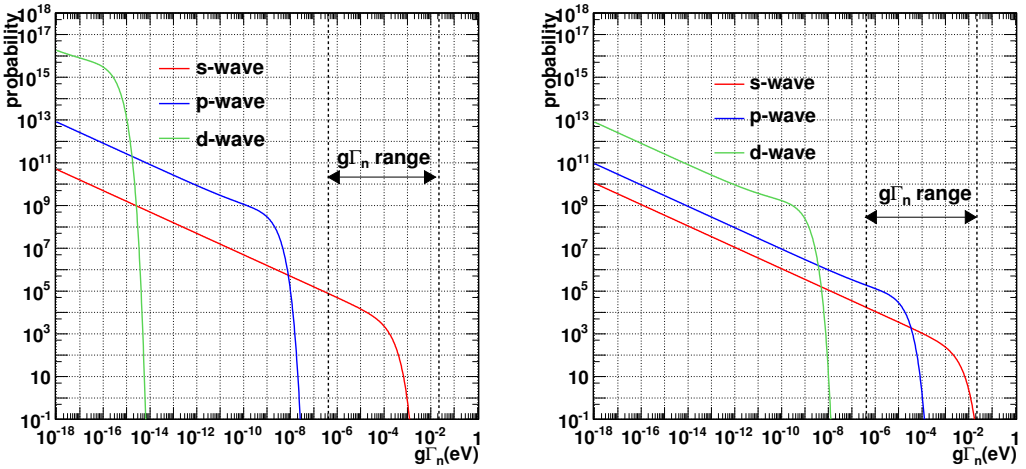

Figure 4.47: s, p and d-wave probabilities for the ^{243}Am nucleus, as a function of gΓ_n, for resonance energies of 1 eV (left) and 400 eV (right). The gΓ_n ranges provided correspond to the range of gΓ_n parameters obtained in this work.

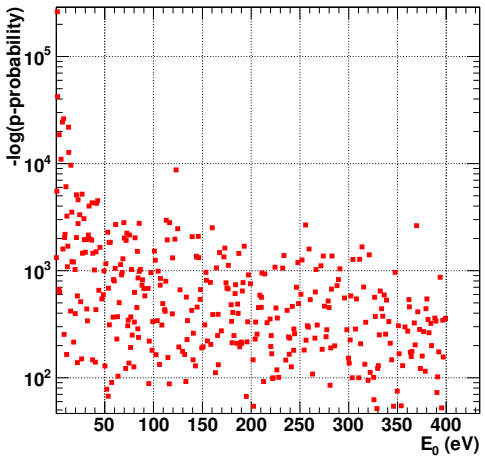

Figure 4.48: Probability of each analyzed resonance, given by its energy E_0, of being a p-wave resonance.

4.3.6.2 Calculation of the average level spacing and the strength function

D_0 can be calculated, in principle, from Equation 4.5. However, as well as the p and d-wave resonances have not been detected in the n_TOF measurement for being too weak, there are also a certain amount of s-wave resonances which are too weak for being detected. These resonances are the so called missing resonances, and there are several methods used to estimate the number of them [Cap09].

One of the most common used methods is based on fitting the reduced neutron width distribution, which is assumed to follow the Porter-Thomas law (Equation 4.9, since μ_l is always 1 for s-wave resonances). One of the problems associated with this method is that in the ^{243}Am nucleus there are , in principle, two Porter-Thomas distributions for the s-wave resonances, one for each possible J=2,3 value. However, together with the (2J+1) law of the level density, which means that $1/\mathrm{D}_{l,J} \propto (2\mathrm{J}+1)$, it is also usually assumed (see Appendix D of [Her09]) that $\mathrm{S}_{l,J} = \mu_{l,J} S_l$. For s-wave resonances $\mu_{0J} = 1$, so $\mathrm{S}_{0J} = S_0$, hence $\left\langle \Gamma^0_{nJ} \right\rangle / D_{0J} = \left\langle \Gamma^0_n \right\rangle / D_0$ and thus $\left\langle (2J_1+1)\Gamma^0_{n,J_1} \right\rangle = \left\langle (2J_2+1)\Gamma^0_{n,J_2} \right\rangle$, so finally $\left\langle g_{J_1}\Gamma^0_{nJ_1} \right\rangle = \left\langle g_{J_2}\Gamma^0_{nJ_2} \right\rangle = \left\langle g\Gamma^0_n \right\rangle$. This means that the value of $\left\langle g_J\Gamma^0_{Jn} \right\rangle$ does not depend on the J value, and thus both Porter-Thomas distributions are the same and all the s-wave resonances can be studied together.

Following this approach, the number of missing resonances can be calculated according to the plots presented in Figure 4.49. The Y axis is the number of resonances with $\left(g\Gamma^0_n\right)^{1/2}$ values greater than the value given by the X axis. The black curve is a fit to the experimental values, taking into account resonances in the 0 - 40 eV energy range. The fitted function is the one given in Equation 4.12, which is deduced directly from the Porter-Thomas distribution, and where the fitted parameters are $\left\langle g\Gamma^0_n \right\rangle$ and N, which is the real number of resonances in the energy interval, including the missing resonances.

$$f(x) = N \frac{2}{\sqrt{\pi}\sqrt{2\left\langle g\Gamma^0_n \right\rangle}} \int_x^\infty e^{-\frac{y^2}{2\left\langle g\Gamma^0_n \right\rangle}} dy \tag{4.12}$$

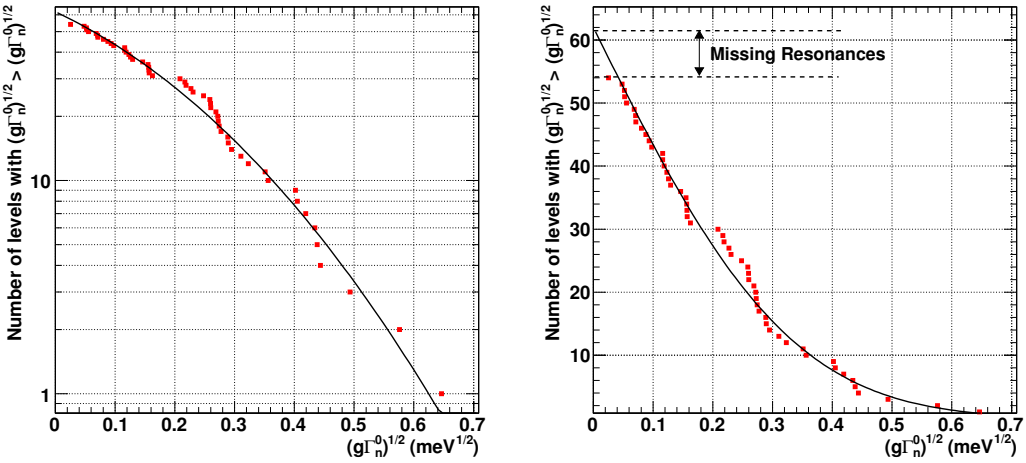

Figure 4.49: Estimation of the number of missing resonances. The Y axis represents the number of levels with $\left(g\Gamma^0_n\right)^{1/2}$ greater than the value given by the X axis, in the 0 - 40 eV energy range. The experimental points have been fitted to the function given in Equation 4.12. Both figures are the same, but with logarithmic Y axis (left) or linear Y axis (right).

Range (eV)	Error applied	Observed	Missing	D_0 - simple (eV)	D_0 - corrected (eV)	$\langle g\Gamma_n^0 \rangle$ (meV)
0 - 30	abs. const.	42	3.4	0.703(19)	0.650(18)	0.0733
0 - 30	rel. const.	42	2.1	0.703(19)	0.669(18)	0.0769
0 - 40	abs. const.	54	6.4	0.736(16)	0.656(14)	0.0742
0 - 40	rel. const.	54	7.6	0.736(16)	0.644(14)	0.0694
0 - 50	abs. const.	64	9.3	0.774(14)	0.675(12)	0.0731
0 - 50	rel. const.	64	12.4	0.774(14)	0.647(12)	0.0649

Table 4.13: D_0 and $\langle g\Gamma_n^0 \rangle$ values obtained by considering different energy ranges and using two different assumptions to perform the fit used to estimate the number of missing resonances: all the points with the same absolute error (abs. cont.) or with the same relative error (rel. const.). The number of observed and missing resonances in the energy ranges and the obtained fitted values of $\langle g\Gamma_n^0 \rangle$ are also presented.

The D_0 values obtained, for different energy ranges, are presented in Table 4.13. The *D_0-simple* values have been obtained only with the observed resonances, whereas the *D_0-corrected* values include the number of missing resonances. In both cases, the uncertainties of the D_0 values represent the statistical uncertainties obtained from Equation 4.5. The mean and standard deviation of the corrected D_0 values presented in the table are 0.657 and 0.011 eV, respectively, and one half of the difference between the highest and the lowest value, 0.016 eV. Taking into account that they are not independent, a final value of D_0= 0.66(3) eV has been adopted. The mean value of the obtained $\langle g\Gamma_n^0 \rangle$ values is 0.0720 meV, and one half of the difference between the highest and the lowest value amounts to 0.0060 meV.

Only energy intervals at low neutron energies have been considered, since the amount of missing resonances increases with the neutron energy. This is because the capture area is, in good approximation if $\Gamma_\gamma \backsimeq \Gamma$, proportional to $\Gamma_n/E = \Gamma_n^0/\sqrt{E}$. Such a behavior is well observed in Figure 4.50, where the cumulative number of levels is represented as a function of the neutron energy. If there were no missing resonances, the measured values should follow the red dashed line.

Finally, the S_0 value can be calculated with Equation 4.6. In this case, the missing resonances do not need to be taken into account, since their contribution to the $\sum g\Gamma_n^0$ is negligible. If the entire energy range is taken, from 0 up to 400 eV, the resulting value is S_0=1.11(8)·10^{-4}. Another possibility is to make a linear fit of $\sum g\Gamma_n^0$ as a function of the neutron energy, as it is presented in the left panel of Figure 4.51. In this case the obtained value is S_0=1.08(8)·10^{-4}, which is compatible with the previous one.

The calculation of S_0 has also been performed in different energy ranges. On the right panel of Figure 4.51, the red curve shows the value of S_0 obtained from applying Equation 4.6 in the energy range between 0 and the value of the X axis. All these obtained values are compatible, within their uncertainties. The value S_0=1.08(8)·10^{-4}, which is the result of the linear fit, has been finally adopted. With this value, $\langle g\Gamma_n^0 \rangle$= D_0×S_0= 0.0713 meV, which is compatible with the values presented in Table 4.13.

Concerning the systematic uncertainties, the main source for the Γ_n values comes from the normalization, which does not affect the calculation of D_0 but propagates in a 3% into the S_0 value.

A comparison between these values and the ones provided by the evaluations and previous measurements are given in Section 5.2.

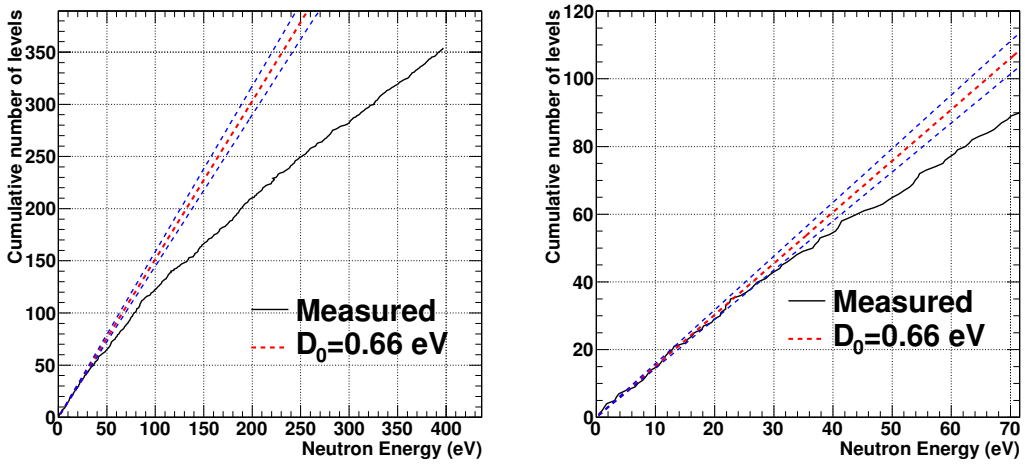

Figure 4.50: Cumulative number of measured resonances (levels) as a function of the resonance energy. The red dashed line represents the real expected value assuming a D_0 value of 0.66 eV. The two blue dashed lines represent the 0.03 eV uncertainty in the D_0 value. The right panel is a zoom to low energies of the left panel.

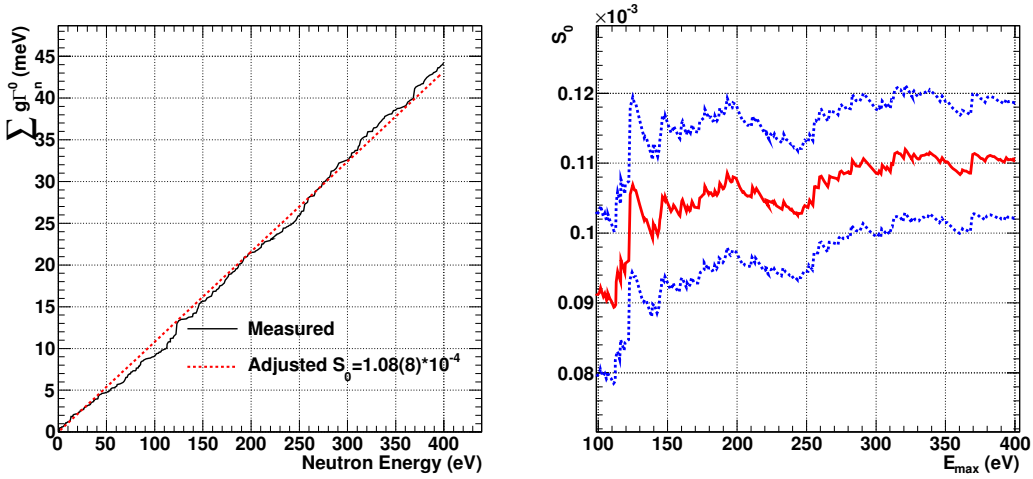

Figure 4.51: On the left panel, a linear fit of $\sum g\Gamma_n^0$ as a function of the neutron energy is presented. S_0 is in this case the slope of the straight line. In the right panel it is represented (red line) the S_0 values obtained from Equation 4.6, if the energy ranges between 0 and the value given by the X axis are considered. The blue dashed lines show the statistical uncertainty of each S_0 value.

4.4 Analysis of the unresolved resonance region

In all the present evaluations, the Resolved Resonance Region (RRR) extends up to 250 eV, and the Unresolved Resonance Region (URR) ranges from 250 eV up to 40 - 42 keV, depending on the evaluation. In this work, the RRR has been extended up to 400 eV. Above this energy, the resonant structure in the n_TOF capture yield is still visible, but the resonances overlap too much to allow a resonant treatment.

4.4.1 Procurement of the URR experimental cross section

The measured capture yield between 250 and 3500 eV is presented in Figure 4.52, together with the obtained backgrounds, smoothed an non-smoothed (see Section 3.6), used in the analysis of the RRR. The resonance observed at around 3100 eV corresponds to the Titanium of the sample capsule. This resonance is followed by strong Ti resonances, which makes impossible the analysis above 2500 eV, which has been set as the high energy limit for the analysis of this measurement. The low energy limit in the analysis of the URR has been chosen to be 250 eV, instead of 400 eV, in order to make a more direct comparison with previous measurements and evaluations. Thus, the energy region between 250 and 400 eV has been analyzed in both the RRR and the URR formalisms.

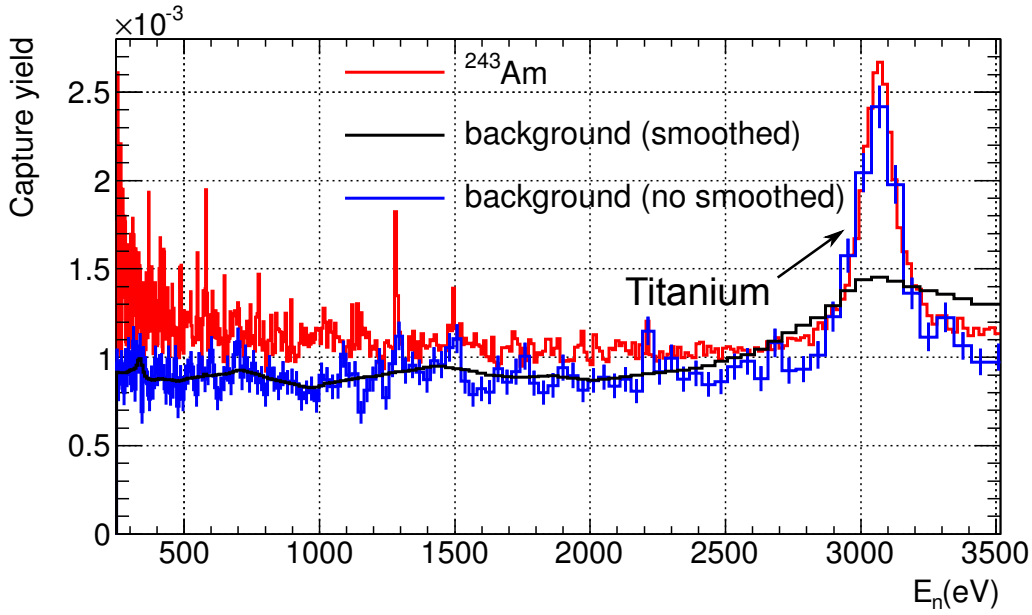

Figure 4.52: Measured ^{243}Am yield between 250 and 3500 eV, together with the measured background and with the smoothed background used in the analysis of the RRR.

Concerning the two presented backgrounds, the smoothed background fits the non-smoothed background up to ~2000 eV, but it is too large above that energy. The reason is that the smoothing of the ^{47}Ti resonance at 3.078

keV distorts artificially the spectrum at lower energies. It is also not straightforward to check, as in the RRR, if the smoothed background fits the measured yield between separated resonances. For these reasons, only the non-smoothed background has been considered in the URR analysis.

The analysis of the URR has been performed with the SAMMY code, which uses as an input the experimental σ_γ, and not the reaction yield, Y_γ. In this energy region the shelf-shielding and multiple scattering effects are negligible (see discussion in Section 4.2.3.4), and thus the two quantities are related by $Y_\gamma(E_n) = n \cdot \sigma_\gamma(E_n)$, where n is the sample thickness. The resulting cross section is presented in Figure 4.53, where the 250 - 2500 eV energy region has been divided in 30 energy intervals, using logarithmic and linear binnings. As it can be observed, the statistical uncertainties are in both cases large. This is a consequence of the large statistical uncertainties of the dedicated background measurements. As it can be seen in the bottom panel of Figure 4.53, the linear case has lower uncertainties than the logarithmic case at lower neutron energies, whereas it has higher uncertainties at higher energies. In order to have lower uncertainty differences between the different experimental points, the logarithmic bins have been adopted for the URR analysis. However, the fits have been performed as well with the linear data set, obtaining compatible results with the logarithmic data set.

Concerning the systematic uncertainties, a 3% normalization uncertainty should be added to the statistical uncertainties presented in Figure 4.53. Other sources of systematic uncertainties have been neglected:

1. Uncertainties in the temperature of the sample, in the Doppler broadening model, or in the description of the resolution functions are not relevant, since the cross section is being integrated in large energy bins.
2. Uncertainties due to the dead time model are not relevant for the same reason as in the RRR: corrections due to the dead time effect are below 1% (see Figure 3.54). Thus, the error committed due to the dead time correction model are negligible.
3. Uncertainties due to the inhomogeneities in the sample do only affect the strongest ^{243}Am resonances, which are located at very low neutron energies.
4. The uncertainty due to the fitted 1/V component is the only one that could be taken into account. It has been verified that the 4% uncertainty in the 1/V factor induces a 0.10% uncertainty in the integral of the measured background between 250 and 2500 eV (the statistical uncertainty is 0.87%), which means a 0.44% uncertainty in the total capture integral (statistical uncertainty of 3.7%). Concerning the unresolved parameters, the statistical uncertainty of the fitted S_0 , which is the most sensible parameter to the n_TOF data (see below), is around 3%, whereas the induced uncertainty of the 1/V background is 0.5%. If both 3% and 0.5% are added quadratically the resulting value is again 3%. For this reason, this source of uncertainty has been neglected.

The background due to fission or elastic scattered neutrons was not taken into account. As it is shown in Section 3.6, both components are below 1% and 2%, respectively, so the size of statistical uncertainties make these background contributions very small.

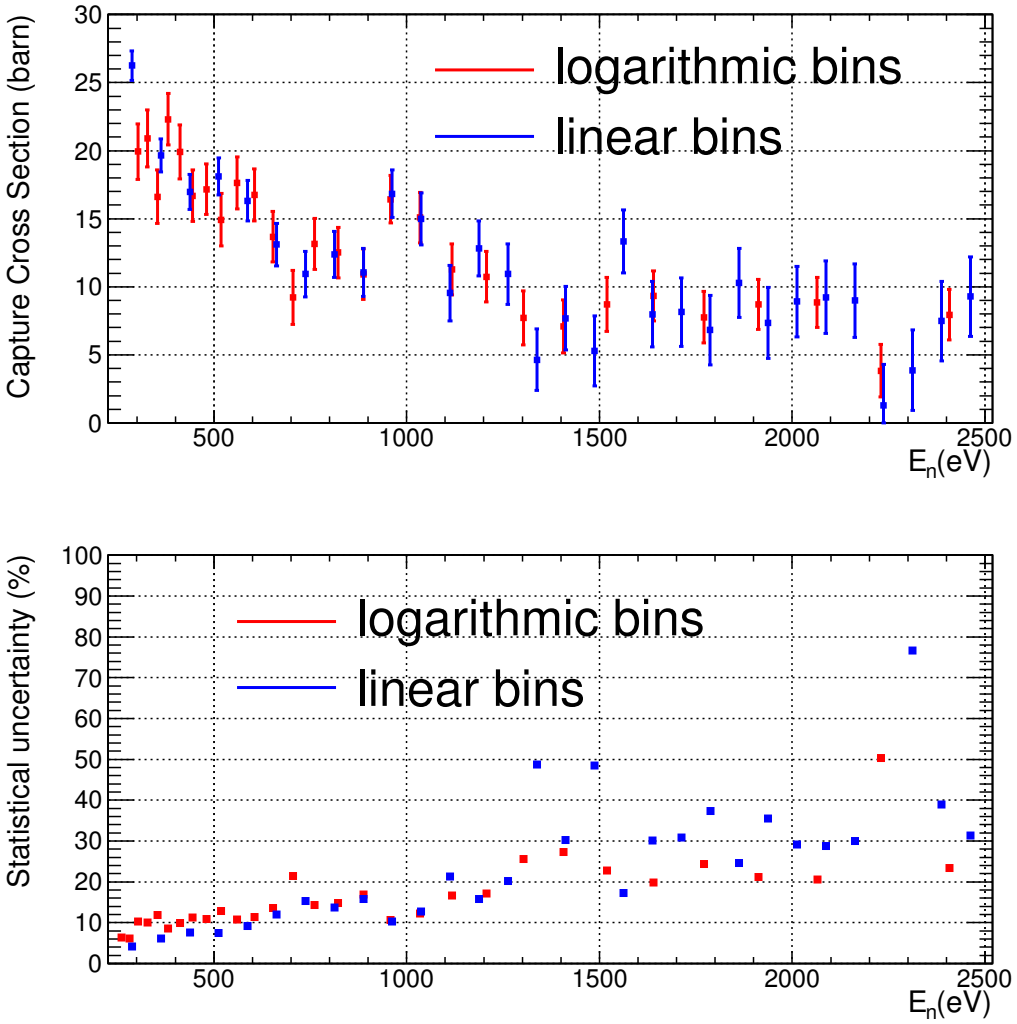

Figure 4.53: ^{243}Am capture cross section between 250 and 2500 eV using 30 bins per decade (top) with their associated relative uncertainties (bottom). All the presented uncertainties are statistical uncertainties. Logarithmic and linear binnings have been considered.

4.4.2 SAMMY analysis of the URR

The SAMMY code contains a modified version of the FITACS code [Lar06, Fro89] for the analysis of the URR. This code uses the Hauser-Feshbach theory [Hau52] with width fluctuations.

In the ENDF-6 format, the URR is described by the scattering radius, AP, the channel radius, a (AP and a are the same for all the channel quantum numbers and constant in energy), the level spacings $D_{lJ}(E_n)$ and the average

channel widths $\langle\Gamma_n^0\rangle_{lJ}(E_n)$, $\langle\Gamma_\gamma\rangle_{lJ}(E_n)$, $\langle\Gamma_f\rangle_{lJ}(E_n)$ and $\langle\Gamma_x\rangle_{lJ}(E_n)$, corresponding to the elastic, capture, fission and inelastic widths. All these quantities but the scattering radius are provided for each l and J channel quantum numbers and are reported as a function of the neutron energy. Each width is distributed according to a chi-squared distribution with a certain number of degrees of freedom, which are provided for each neutron and fission (l,J) channels.

In the SAMMY-FITACS code the URR is described in a slightly different way (see [Lar06]):

- The channel radius, a, and the distant-level parameters R_l^∞, which depend on l and are related with the AP scattering radius via $AP = a(1 - R_l^\infty)$. The difference between the scattering radius and the channel radius, which have the same value in many evaluations, is that the channel radius is defined to be the geometric boundary in the R-matrix formalism, and it is used to compute some quantities such as the penetrabilities, P_l(ka), the shift factors, S_l(ka), or the hard-sphere phase shifts, φ(ka). The scattering radius is introduced in the ENDF-6 format to give more flexibility, and it can be used instead of the channel radius for the calculation of the hard-sphere phase shifts, φ(ka), which define the potential scattering cross section.
- The mean level spacing is only provided for $D_{l=0}(E_n = 0)$. The mean level spacings for l>0, as well as its J dependency, are calculated via the Bethe formula, and their energy dependency via the Gilbert-Cameron composite formula.
- Strength functions S_l are used, instead of average neutron reduced widths. They are supposed to depend only on l, not on J neither on the neutron energy.
- The radiation widths $\langle\Gamma_\gamma\rangle$ are assumed to depend only on the parity and on the energy (so $\langle\Gamma_\gamma\rangle_0 = \langle\Gamma_\gamma\rangle_2$). It is provided for $E_n = 0$ and the energy dependency is calculated with the giant dipole resonance model.
- The fission widths are provided for E_n=0, for each (l,J) values. Its energy dependency is calculated with the Hill-Wheeler fission barrier transmission coefficients (also provided).
- It is recommended to not use the inelastic widths.
- The number of degrees of freedom is provided only for the fission channels, since for the capture channels this number is assumed to be infinite and for the neutron channels it can only be 1 or 2, and it can be calculated from l and J.

From all the mentioned parameters, only a fraction of them can be fitted. These are the neutron strength functions, S_l, the distant level parameters, R_l^∞, and the average radiation and fission widths at E_n=0, $\langle\Gamma_\gamma\rangle_l(E_n = 0)$ and $\langle\Gamma_f\rangle_l(E_n = 0)$.

In this analysis, the following values have been used:

1. It has been verified that the channel radius, a, and the distant level parameters, R_l^∞, have a negligible effect in the calculated capture cross section. For this reason, the channel radius has been fixed to a=9.7 fm, the value used in the RRR, and the distant level parameters to $R_l^\infty = 0$.
2. The fission channels have also a negligible effect in the calculated capture cross section, and thus the values of the ENDF/B-VII.1 evaluated library, $\langle\Gamma_f\rangle_l$=2.25·10^{-4} eV, have been adopted.
3. The $D_{l=0}(E_n = 0)$ value cannot be fitted, and it has been fixed to the value obtained in the statistical analysis of the RRR (Section 4.3.6.2), D_0=0.66 eV.

Following these conditions, only the S_l and $\langle\Gamma_\gamma\rangle_l$ values need to be fitted. According to the ENDF/B-VII.1 evaluation, only the l=0 and l=1 values are relevant in the energy range of interest, as it is shown in Figure 4.54. Indeed, the s-wave dominates in all the energy range of interest, being the p-wave contribution to the total capture cross section of only a 11.1% at 2.5 keV, according to this evaluation.

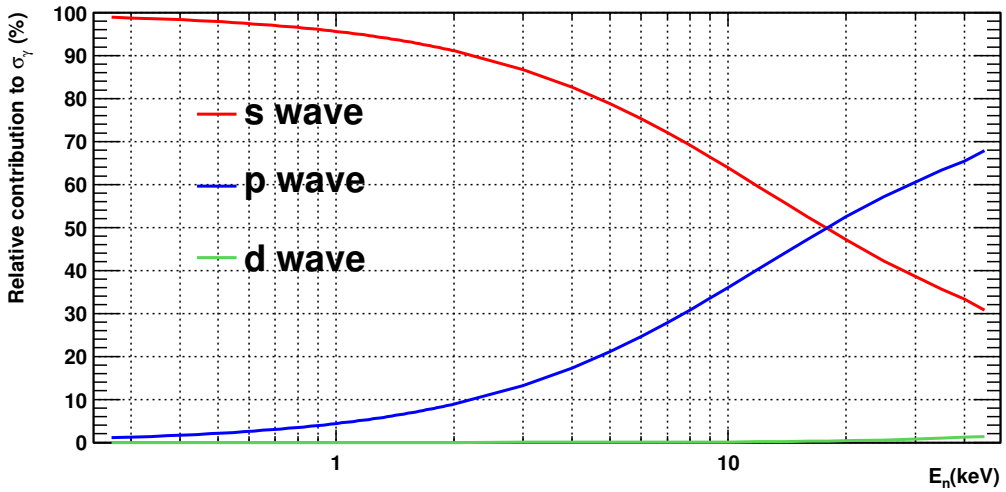

Figure 4.54: Relative contributions of the s, p and d-waves to the capture cross section of the ^{243}Am, according to the ENDF/B-VII.1 evaluation.

There are, in principle, four parameters which can be calculated: S_0, S_1, $\langle\Gamma_\gamma\rangle_0$ and $\langle\Gamma_\gamma\rangle_1$. However, it has been verified that the fit is not sensitive to the $\langle\Gamma_\gamma\rangle_1$ value, and thus it has been fixed to the value obtained for $\langle\Gamma_\gamma\rangle_0$ in the RRR: $\langle\Gamma_\gamma\rangle_1$= 42 meV. The fit is very sensitive to S_0 and less sensitive to S_1 and $\langle\Gamma_\gamma\rangle_0$. On the other hand, the fact that the p-wave contribution is only relevant in the higher energy region (and always below 11%), makes impossible a reliable calculation of S_1 with the n_TOF data. For this reason, the calculation has been performed varying only S_0 and $\langle\Gamma_\gamma\rangle_0$. The S_1 parameter has been fixed to $2.0{\cdot}10^{-4}$, which is an intermediate value of those provided by the most recent evaluations (see Table 5.3). It has been verified that a variation of 25% in the S_1 value induces a variation of around 0.5% in the value of S_0, and a negligible variation in the $\langle\Gamma_\gamma\rangle_0$ parameter.

On the contrary, the results depend largely on the energy range considered in the calculation. Figure 4.55 shows the averaged cross sections when the calculation is performed in the 250 - 2500 eV and 400 - 2500 eV energy ranges. A visible difference can be appreciated between the two results because of the two lower energy points, which have larger values than expected from the rest of the data points. This makes the results to vary significantly when those points are included or not. Notice that this is a strong argument to increase the RRR up to, at least, 300-350 eV. It can also be observed that the URR cross section obtained from the statistical parameters calculated in the RRR reproduces perfectly the measurement, being very close to the calculated values, specially to those obtained from the fit in the 400 - 2500 eV energy range.

Several results are presented in Table 4.14, in order to show their dependence with the energy range considered, varied between 250 and 500 eV. For the initial parameters, the values obtained in the RRR have been used, S_0=1.08(8)·10^{-4} and $\langle\Gamma_\gamma\rangle_0$= 42(2) meV, but three different initial uncertainties have been considered: the uncertainties obtained in the RRR, the same values multiplied by 4, and a 100% large uncertainties. It can be deduced from Table 4.14 that in the three cases the results with low energy limits higher or equal than 300 eV are compatible, and differ from the E_{min}= 250 eV case, where S_0 is larger and $\langle\Gamma_\gamma\rangle_0$ lower than in the rest of the cases. The results can be interpreted as follows:

1. The results obtained in the first case (RRR uncertainties) are the results obtained when it is assumed that the measurement of S_0 and $\langle\Gamma_\gamma\rangle_0$ in the RRR and in the URR are independent. Thus, the results are not the results of the URR fit, but the final result taking into account both measurements.

2. When a 100% initial uncertainties are considered, no prior information of the parameters is assumed. In this case large uncertainties are obtained for both parameters, specially for $\langle\Gamma_\gamma\rangle_0$(∼60-70%). However, they are strongly correlated, and thus when one parameter is fixed, the uncertainty in the other parameter is strongly reduced. In particular, if $\langle\Gamma_\gamma\rangle_0$ is fixed to 42 meV, or any other value, the uncertainties in S_0 decrease to values similar to those obtained in case 1.

3. An intermediate situation is when 4 times the initial uncertainties of case 1 are used. In this case some prior information is assumed, but not all the information obtained in the RRR is taken into account. With these results it is possible to conclude that the results obtained in the URR are totally compatible with those obtained in the RRR (notice that this conclusion can not be reached from the results of the first case).

Notice also that the $\langle\Gamma_\gamma\rangle_0$ parameter is not very sensitive to the n_TOF URR data, since the uncertainties obtained after the fit are more or less the same as the initial uncertainties.

The final result is presented in Table 4.15. It has been obtained from an average of the first case (RRR initial uncertainties), in part because the uncertainty in $\langle\Gamma_\gamma\rangle_0$ could be not much larger than the value obtained in the RRR. The fit with E_{min}= 250 eV has been excluded. Concerning the systematic uncertainties, the 3% normalization uncertainty is the only one which is non-negligible (see Section 4.4.1). It induces a 3% uncertainty in the S_0 parameter, but do not affect $\langle\Gamma_\gamma\rangle_0$. This result has been obtained in the same way as in the RRR, by performing fits with different normalizations.

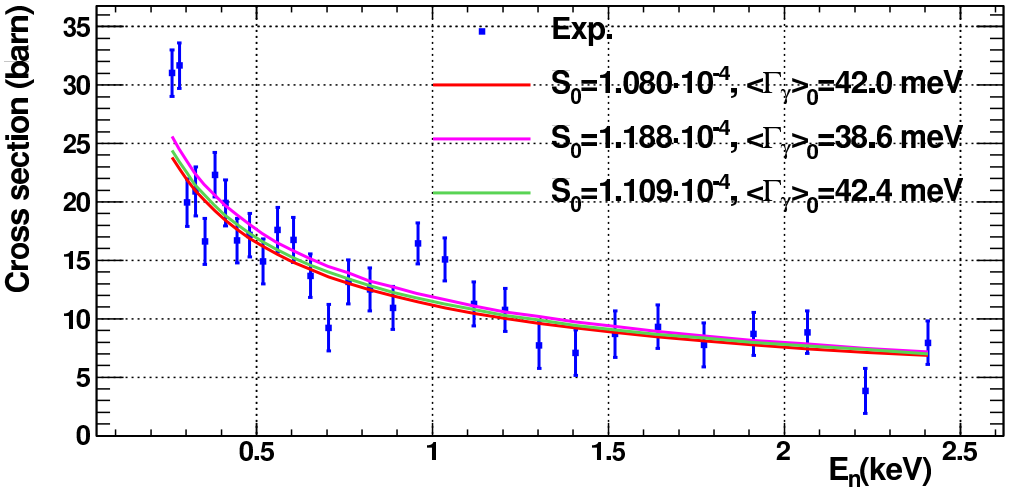

Figure 4.55: Averaged cross sections in the URR for the S_0 and $\langle\Gamma_\gamma\rangle_0$ values obtained in the RRR (red), together with the results of the fit in the 250 - 2500 eV energy region (magenta) and in the 400 - 2500 eV energy region (green).

	RRR initial uncertainties			4 x RRR initial uncertainties			100% initial uncertainties		
E_{min}(eV)	$S_0(10^{-4})$	$\langle\Gamma_\gamma\rangle_0$(meV)	Corr	$S_0(10^{-4})$	$\langle\Gamma_\gamma\rangle_0$(meV)	Corr	$S_0(10^{-4})$	$\langle\Gamma_\gamma\rangle_0$(meV)	Corr
250	1.156(32)	42.0(20)	-0.30	1.188(57)	38.6(69)	-0.81	1.42(22)	22(8)	-0.98
300	1.087(33)	42.1(20)	-0.26	1.082(52)	43.5(80)	-0.74	1.02(10)	62(42)	-0.95
350	1.099(36)	42.1(20)	-0.25	1.099(57)	42.9(79)	-0.74	1.06(13)	53(36)	-0.96
400	1.104(39)	42.1(20)	-0.23	1.109(62)	42.4(78)	-0.72	1.09(16)	46(31)	-0.96
450	1.106(42)	42.1(20)	-0.21	1.113(67)	42.3(78)	-0.70	1.10(18)	45(33)	-0.96
500	1.106(44)	42.1(20)	-0.20	1.114(70)	42.2(78)	-0.69	1.10(19)	45(33)	-0.96

Table 4.14: Values of S_0 and $\langle\Gamma_\gamma\rangle_0$, with their correlations (Corr), obtained from fits performed in energy ranges which go from E_{min} up to 2500 eV. In the columns on the left the initial values for the input parameters were S_0=1.08(8)·10^{-4} and $\langle\Gamma_\gamma\rangle_0$= 42(2) meV, which correspond to the values obtained in the RRR analysis. In the columns on the center, the same values were used, but with the uncertainties multiplied by 4. In the columns on the right, the same values were also used, but with uncertainties of a 100%.

D_0	S_0	$\langle\Gamma_\gamma\rangle_0$	Correlation (S_0,$\langle\Gamma_\gamma\rangle_0$)
0.66(3) eV	1.10(4)·10^{-4}	42.1(20) meV	-0.23

Table 4.15: Final values of D_0, S_0 and $\langle\Gamma_\gamma\rangle_0$, with their statistical uncertainties and the correlation between S_0 and $\langle\Gamma_\gamma\rangle_0$. The S_0 parameter has also a 3% systematic uncertainty due to the normalization uncertainty.

4.4.3 Comparison with previous measurements

There are two previously published capture measurements in the URR: one is the measurement performed by Weston and Todd [Wes85], in the 0.258 - 92 keV energy range, and the other is the measurement performed by Wisshak and Käppeler [Wis83], in the 5 - 250 keV energy range. The n_TOF capture measurement can be compared only with the Weston and Todd measurement.

Weston and Todd provide two different data sets, since the measurement was performed with two different techniques. Both data sets are plotted together with the n_TOF data in Figure 4.56, where the "Weston I" and "Weston II" data sets correspond to the thermal [exf04] and the high-repetition-rate [exf05] data sets, respectively, described in [Wes85]. The data provided by Weston and Todd contain information concerning the center of the bins where the data were integrated, but not on the bin widths. However, if one bin limit is defined, then the rest of the bin limits follow automatically. It has also been assumed that the center between the first two values is a bin limit, and it has been verified that the results do not depend so much on this assumption, if the chosen bin limit is not too close to the center of a bin.

Together with the statistical uncertainties presented in Figure 4.56, there is a 3% normalization uncertainty in the n_TOF data. According to the paper, the Weston and Todd data have a 6% normalization uncertainty, plus an 8% systematic uncertainty in the shape. This uncertainty is estimated to be strongly correlated over factors of two in neutron energy and weakly correlated over the full range of neutron energy[6]. The normalization was performed to the thermal capture cross section at 0.0253 eV of 74.8 b (ENDF/B-V) with the thermal data set, and the high-repetition-rate data set were normalized to the thermal data set in the 4 - 40 eV region. A 5% of the 6% normalization uncertainty comes from the estimated systematic uncertainty in the measurement at keV neutron energies relative to thermal.

Figure 4.56 shows that the two data sets provided by Weston are not compatible below 1 keV. In the paper it is said that the discrepancies were not understood. It is also clear that the n_TOF data is more compatible with the thermal Weston data than with the high-repetition-rate data set.

A statistical comparison between the measurements is provided in Table 4.16, where the highest energy point has been removed, since its uncertainty is very large in the n_TOF data and affects significantly the calculation of the capture area. As it is shown, the normalization is $5(\pm 3.8)\%$ higher in the Weston thermal data set than in n_TOF, and $20(\pm 5)\%$ lower in the high-repetition-rate data set. Taking into account the systematic uncertainties, the normalization of the n_TOF and the Weston thermal data sets are compatible. The χ^2 values between the measurements are also provided, together with the corresponding degrees of freedom of the chi-squared distribution which has to be used to determine the compatibility of the different data[7]. The values of the integrals are the probabilities of obtaining chi-square values greater than the ones which have been obtained, if it is assumed that the compared data sets are compatible. Thus, values close to 0.5 indicate that the data are compatible, values close to 1 indicate that the calculated uncertainties are overestimated, and values close to 0 indicate that the data are not compatible.

[6] This sentence appears literally in the Weston and Todd paper. We understand that there are no correlations between energies which differ more than a factor of two.

[7] When the comparison is made without normalizing the data sets, the number of degrees of freedom is equal to the number of compared data points. When the normalization is performed, the number is reduced in 1. Notice that in the high-repetition-rate data set, some points are missing.

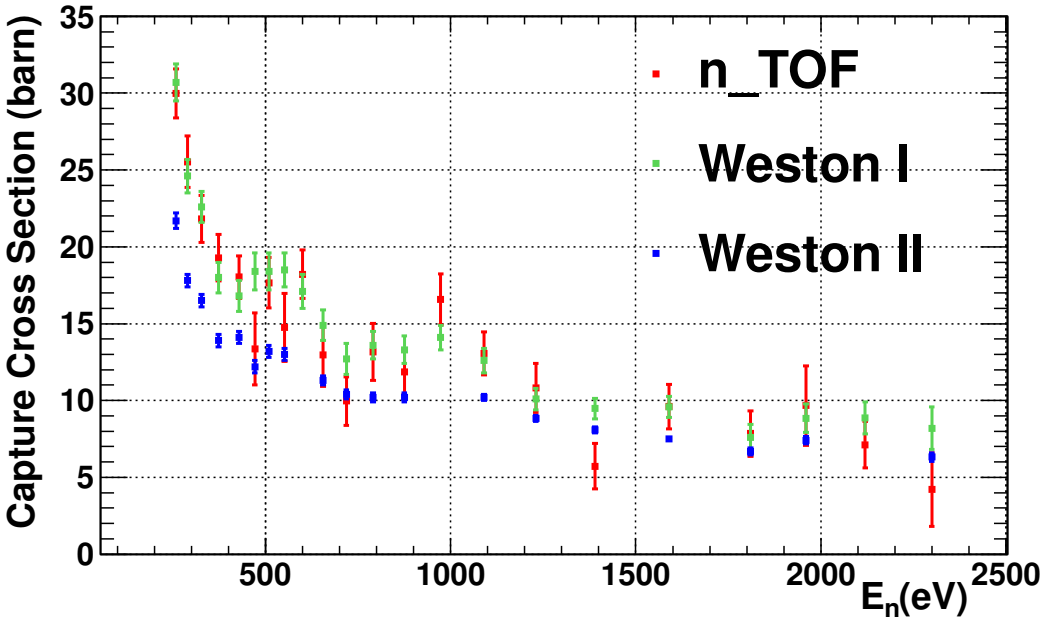

Figure 4.56: Comparison between the n_TOF capture data in the URR and the two different data sets provided by Weston and Todd: Weston I is the thermal data set and Weston II is the high-repetition-rate data set. The error bars represent the statistical uncertainties.

		Non-Normalized			Normalized		
	Area(n_TOF/Weston)	χ^2	d.o.f.	$\int_t^\infty \chi^2(x)dx$	χ^2	d.o.f.	$\int_t^\infty \chi^2(x)dx$
Weston I	0.950(38)	20.01	21	0.52	19.8	20	0.47
Weston II	1.194(46)	98.92	18	$3.49{\cdot}10^{-13}$	29.5	17	0.030

Table 4.16: Statistical comparison between the n_TOF and the Weston data sets. For each data set it is provided: the ratio between the integrated cross section areas with its statistical uncertainties, the chi-squared values with the number of degrees of freedom (d.o.f.) and the integral value of the chi-squared function above the obtained value. The comparison were performed normalizing and non normalizing the Weston data sets to the n_TOF data.

From the values shown in Table 4.16, it is clear than the n_TOF data is compatible with the Weston thermal data, and not with the high-repetition-rate data set. Notice also that the n_TOF capture data were normalized essentially to the transmission data provided by Simpson et al. (see Section 4.2.3), whereas the Weston data were normalized to the thermal cross section of ENDF/B-V of 74.8 b, so both normalizations are independent and compatible. This is an important confirmation of the reliability of the n_TOF capture data normalization.

A last comparison is shown in Figure 4.57, where the distribution of the residuals between the n_TOF and the thermal Weston data are represented. This distribution has the expected shape, thus consolidating the idea that both measurements are compatible.

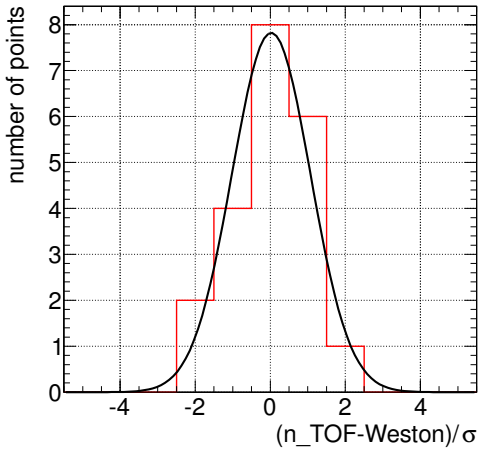

Figure 4.57: Distribution of the residuals (distances in units of σ) between the n_TOF and the Weston thermal data points, which have been normalized to the n_TOF data. The fitted Gaussian has a mean value of μ =0.02±0.27 and a standard deviation of σ =1.04±0.24.

4.4.4 Data analysis above 2.5 keV

The n_TOF data energy ranges up to 2.5 keV. However, the Weston and Wisshak measurements together with integral measurements can be used to analyze the ^{243}Am capture cross section at higher energies. In this section a brief analysis above 2.5 keV is presented.

A capture analysis above 2.5 keV should include the determination of the high energy part of the URR, which means the determination of the S_1 and $\langle\Gamma_\gamma\rangle_1$ parameters, and the determination of the cross section in the high energy range, above the URR. This high energy range cross section is given in the ENDF-6 format evaluations as a pointwise curve obtained from measurements, if they exist, and complemented with nuclear model calculations. In our analysis, the S_1 and $\langle\Gamma_\gamma\rangle_1$ parameters have been fitted to the existing data, but no nuclear calculation has been performed for the high energy region. Alternatively, the existing high energy cross sections of several neutron libraries have been compared with the experimental results.

The Wisshak et al. measurement [Wis83] was performed in eight different runs, each of them with different experimental parameters. Four of those runs the measurement covered the 5 - 90 keV energy region [exf06], other two the 7 - 90 keV energy region [exf07], other one the 30 - 250 keV energy region [exf08], and the latest one the 40 - 250 keV energy region [exf09]. The 7 - 90 keV (Wisshak I) and 5 - 90 keV (Wisshak II) measurements are presented together with the Weston data and the capture cross sections of the ENDF/B-VII.1, ENDF/B-VII.0, JENDL-4.0 and JEFF-3.1 libraries in Figure 4.58. The Wisshak capture cross section was measured relative to the ^{197}Au capture cross section of ENDF/B-V, and in this work it was renormalized to the ^{197}Au capture cross section of ENDF/B-VII.1.

It can be observed that the two Weston data sets differ at low energies, but are compatible above 2 keV. The two Wisshak data sets presented in Figure 4.58 are also compatible, but they are between 10% and 15% (depending on the energy range considered) lower than the Weston data. It is also important to notice that the present evaluations are closer to the Weston II data in the lower energy region of the URR, whereas the n_TOF data is compatible with Weston I and not with Weston II.

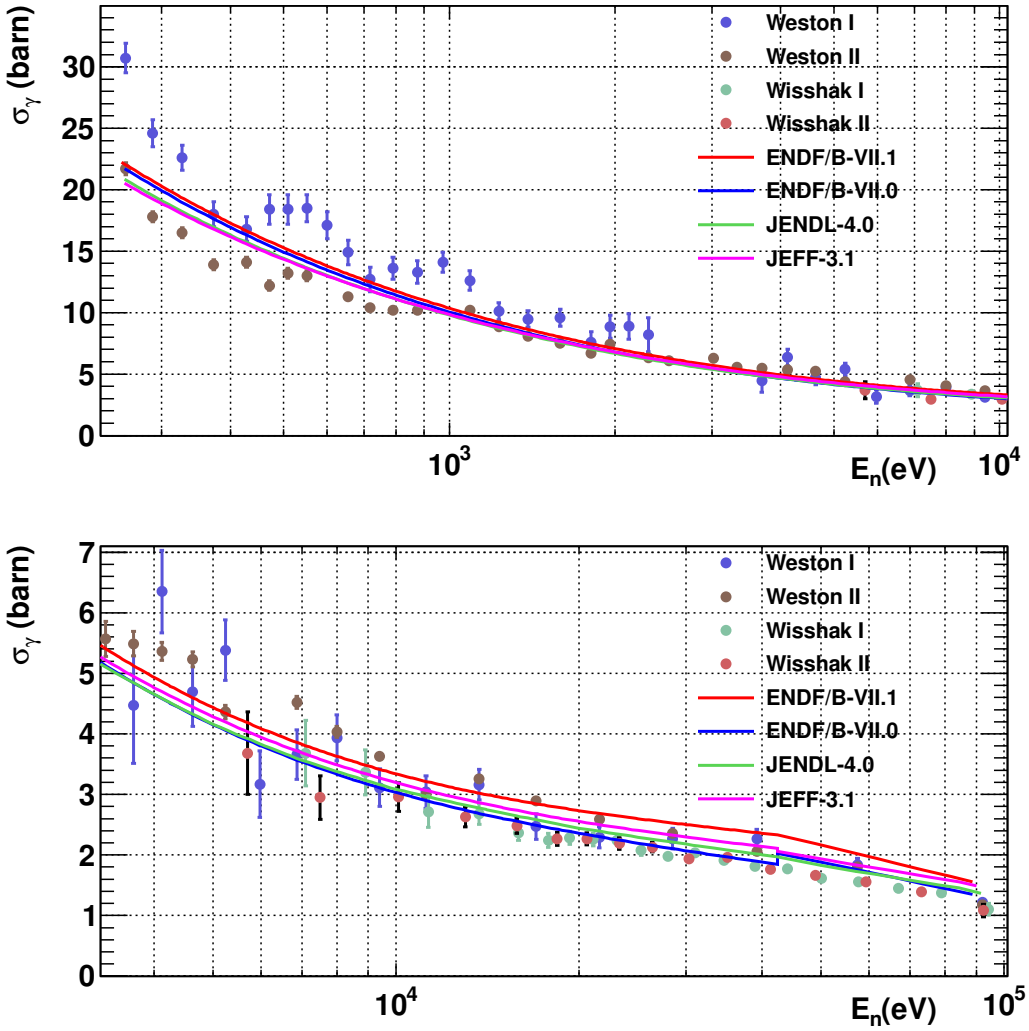

Figure 4.58: Different evaluations plotted together with the capture data available in EXFOR for the URR. Weston I data is compatible with n_TOF data up to 2.5 keV.

These data sets have been used to calculate the S_1 and $\langle\Gamma_\gamma\rangle_1$ parameters. The fits have been performed in the 0.4 - 42 keV energy range for the Weston data and in the 5 - 42 keV or 7 - 42 keV for the Wisshak data. The upper energy limit of 42 keV, which is where the first inelastic channel is open, has been chosen for being the upper energy limit of the URR in most of the evaluations. However, the fit has also been performed up to 92 keV, obtaining compatible values. The results are presented in Table 4.17, where two different calculations are shown. In one of them, the S_1 and $\langle\Gamma_\gamma\rangle_1$ parameters were fitted at the same time, obtaining uncertainties close to 100% in $\langle\Gamma_\gamma\rangle_1$, and a very strong correlation between both parameters. In order to compare more easily the results, another calculation is shown, where $\langle\Gamma_\gamma\rangle_1$ has been fixed to 42 meV. In all the cases the S_0 and $\langle\Gamma_\gamma\rangle_0$ parameters have been fixed to the values obtained in this work and provided in Table 4.15. Since the normalization of the Weston I data is 5% higher than the n_TOF normalization, it has also been fitted renormalized by a factor of 0.95.

The systematic uncertainties have not been calculated in this case, since they are not described in the Weston et al. paper: it is only said that there is a 6% normalization uncertainty and an 8% systematic uncertainty in the shape. The only additional information provided for the second one is a non very precise comment about the correlations (see the beginning of Section 4.4.3).

As expected, the results obtained with Weston I and Weston II data are compatible, and differ from the values obtained with the Wisshak data sets, since the latter are 10% - 15% below. One of the reasons which indicates that the Weston results are better than the Wisshak data is that they are compatible with the values obtained in this work, and other reason is that they are more compatible with the PROFIL-1 integral experiment [Kah11].

	S_1 and $\langle\Gamma_\gamma\rangle_1$ fit			$\langle\Gamma_\gamma\rangle_1$ fixed to 42 meV
Data set	$S_1(\times10^{-4})$	$\langle\Gamma_\gamma\rangle_1$(meV)	Correlation	$S_1(\times10^{-4})$
Weston I (×0.95)	1.29(16)	78(67)	-0.72	1.40(13)
Weston I	1.65(24)	52(34)	-0.82	1.71(14)
Weston II	1.844(76)	40.0(59)	-0.89	1.821(34)
Wisshak I	1.08(11)	67(46)	-0.93	1.169(45)
Wisshak II	1.09(11)	65(43)	-0.91	1.176(51)

Table 4.17: Results of the fits of S_1 and $\langle\Gamma_\gamma\rangle_1$ to the different available data sets in the 0.4 - 42 keV neutron energy range. S_0 and $\langle\Gamma_\gamma\rangle_0$ have been fixed to the values provided in Table 4.15. The statistical uncertainties are given in parentheses.

Integral experiments performed in nuclear reactors are very useful for the validation of neutron cross sections. These measurements are usually performed by irradiating a sample inside a reactor with a well known flux and during a well known period of time, and analyzing afterwards its isotopic composition. With this information it is possible to determine the number of reactions of a certain kind that have occurred, which is given essentially by $\int \phi(E)\sigma_x(E)dE$, where ϕ is the neutron flux and σ_x the reaction cross section. Some of the experimental results provided in Section 4.3.5 come from integral measurements, but in thermal reactors, where little information on keV region can be inferred.

Useful information concerning the capture cross section of ^{243}Am in and above the URR can be obtained from integral experiments performed in fast nuclear reactors, where most of the neutrons have energies from tens of keV up to several MeV. It was not possible to use in this work the data from [Mur96, Tsu03, Ohk05] due to the lack of information on the reactor neutron flux. However, it was possible to obtain the neutron flux used in the

PROFIL-1 irradiation experiment performed at the PHENIX reactor in 1974. Part of the results can be found in [Pal05, Kah11], which provide the calculated to experimental ratio (C/E) of the $\sigma_{cap} = \int \phi(E)\sigma_\gamma(E)dE$ value obtained when using different neutron data libraries. This values are provided in Table 4.18. It has to be said that in [Pal05] the library used is ENDF/B-VI.8 instead of ENDF/B-VII.0, but the capture cross sections of ^{243}Am are exactly the same in both evaluated libraries. The observed differences between the two references for the C/E values obtained for the ENDF/B-VII.0 evaluation are probably due to the different neutron fluxes used to obtain the calculated σ_{cap} values: in [Pal05] the flux was calculated by Monte Carlo simulations, whereas in [Kah11] an experimental flux was used, as it is described in [Pal11]. In the right part of Table 4.18, the ratios of the different C/E values respect to the C/E values of the ENDF/B-VII.0 evaluation are given. This quantities are the same as the σ_{cap} ratios, and they have been compared with the same ratios obtained in this work.

Reference	JEFF-3.0 (1)	ENDF/B-V (2)	ENDF/B-VII.0 (3)	ENDF/B-VII.1 (4)	(1)/(3)	(2)/(3)	(4)/(3)
Kahler [Kah11]			0.834	0.939			1.126
Palmiotti [Pal05]	0.99	0.62	0.85		1.165	0.729	

Table 4.18: C/E values for σ_{cap} for the PROFIL-1 irradiation experiment obtained by using different libraries. The experimental uncertainty provided is 5%. On the right, the ratios between the different C/E values respect to the C/E value of the ENDF/B-VII.0 evaluation (same as ENDF/B-VI.8 for the ^{243}Am capture reaction).

The shape of the neutron flux of the PHENIX reactor was obtained from MCNPX Monte Carlo simulations. The flux used in this work is presented in Figure 4.59, and it corresponds to the flux obtained at the center of the reactor (where the sample was placed) at the beginning of the operation (when the sample was irradiated). Figure 4.59 also presents the flux multiplied by the ^{243}Am(n,γ) cross section of different libraries, showing that almost all the neutron captures are produced between 100 eV and 2 MeV, and that the most important energy region is between 10 and 100 keV. The cumulative integrals of the previous quantities are presented in the bottom, on the left normalized to the total integral ($\int_0^E \phi(E')\sigma(E')dE' / \int_0^\infty \phi(E')\sigma(E')dE'$), and on the right to the total neutron flux ($\int_0^E \phi(E')\sigma(E')dE' / \int_0^\infty \phi(E')dE'$). These last two figures show that 60% of the captures are produced below 42 keV, the upper energy limit of the URR, and the rest of the capture reactions, 40%, above the URR. They also show that 20-25% of the neutron captures are produced below 2.5 keV, which is the limit of the n_TOF measurement.

With this neutron flux it is possible to calculate ratios between different σ_{cap}, each of them obtained from different ^{243}Am capture cross sections. The total values of σ_{cap} can not be calculated, since we do not have the absolute normalization of the neutron flux. These ratios are presented in Table 4.19 (the values which are not in parentheses), where different σ_{cap} have been divided by the σ_{cap} calculated with the cross section of the ENDF/B-VII.0 evaluation:

- The values of the second column ("This work") are the σ_{cap} values obtained from the capture cross sections of the libraries on the first column, divided by the σ_{cap} value obtained from the capture cross section of the ENDF/B-VII.0 evaluation.
- The values of the third column ("References") are the values obtained from [Kah11, Pal05], presented in Table 4.18.

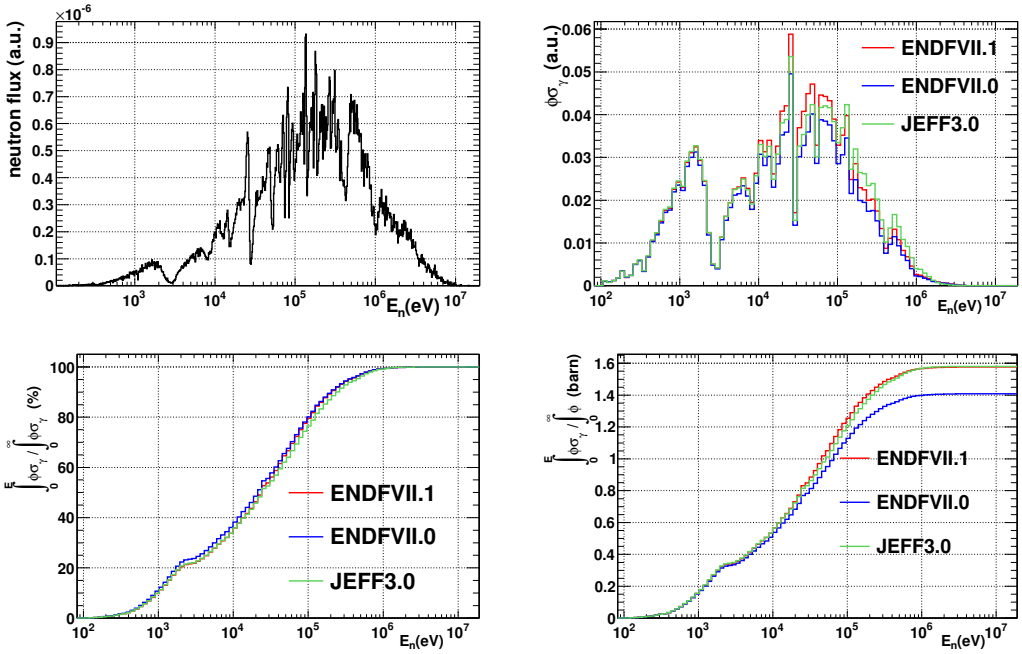

Figure 4.59: Neutron flux in the center of the PHENIX reactor obtained from Monte Carlo simulations (top left), this flux multiplied by different ^{243}Am capture cross sections (top right), cumulative number of captures divided by the total number of captures (bottom left), and cumulative number of captures divided by the total neutron flux (bottom right).

- The fourth, fifth and sixth columns ("n_TOF+Weston+library") are the ratios between the following two σ_{cap} quantities:
  - the σ_{cap} values obtained from the cross sections constructed from:
    - the RRR obtained in this work,
    - the URR constructed with the S_0 and $\langle\Gamma_\gamma\rangle_0$ parameters from this work and the S_1 and $\langle\Gamma_\gamma\rangle_1$ parameters from the fit of the Weston data, provided in Table 4.17,
    - the cross section above the URR taken from the different evaluations, listed in the first column.
  - the σ_{cap} value obtained from the capture cross section of the ENDF/B-VII.0 evaluation (same as the ones used in the second column).

The numbers in parentheses are the values on their left, but multiplied by the C/E value provided by [Kah11] for the ENDF/B-VII.0 evaluation (0.834), which is the C/E value which is obtained if it is assumed that the values of σ_{cap} calculated in [Kah11] and in this work are the same.

It can be observed that the result obtained from the ENDF/B-VII.1 evaluation (second column) is almost the same as the one provided by [Kah11] (third column), with a difference of around 0.5%. In the other two comparable results, the ones from the JEFF-3.0 and the ENDF/B-V.0 evaluations, a difference of 4% is found respect with the

values provided by [Pal05]. Notice that the results provided by both references are not exactly the same: there is a difference of 2% in the C/E value calculated with the ENDF/B-VII.0 library. These results indicate that the PHENIX neutron flux used in this work is compatible with the fluxes used in the references.

	Evaluated library		n_TOF+Weston+library		
library	This work	References [Kah11, Pal05]	Weston I (×0.95)	Weston I	Weston II
ENDF/B-VII.1	1.120 (0.934)	1.126 (0.939)	1.104 (0.810)	1.126 (0.939)	1.135 (0.947)
ENDF/B-VII.0	1.000 (0.834)	(0.834 - 0.85)	1.043 (0.870)	1.066 (0.889)	1.074 (0.896)
JENDL-4.0	1.022 (0.852)		1.061 (0.885)	1.084 (0.904)	1.092 (0.911)
JEFF-3.1	1.069 (0.892)		1.091 (0.910)	1.114 (0.929)	1.122 (0.936)
JEFF-3.0	1.122 (0.936)	1.165 (0.99)	1.127 (0.940)	1.150 (0.959)	1.158 (0.966)
CENDL-3.1	1.092 (0.911)		1.113 (0.928)	1.136 (0.947)	1.144 (0.954)
ROSFOND-2010	0.960 (0.801)		1.007 (0.840)	1.031 (0.860)	1.039 (0.867)
ENDF/B-V.0	0.701 (0.585)	0.729 (0.62)	0.852 (0.711)	0.875 (0.730)	0.883 (0.736)

Table 4.19: Ratios between σ_{cap} obtained from different evaluations and σ_{cap} obtained from the ENDF/B-VII.0 evaluation. On the left ("Evaluated library"), the values calculated from the evaluated cross sections ("This work") are compared by the ones provided by [Kah11, Pal05] ("References"). On the right ("n_TOF+Weston+library"), the values of σ_{cap} were obtained from the cross sections constructed by taking the RRR and the S_0 and $\langle\Gamma_\gamma\rangle_0$ parameters resulting from this work, the S_1 and $\langle\Gamma_\gamma\rangle_1$ from the values provided in Table 4.17, and the cross section above 42 keV from the corresponding evaluated library of the left column. In parentheses, the σ_{cap} ratios have been multiplied by the C/E value provided by [Kah11] (0.834), which is the C/E value if it is assumed that values of $\sigma_{cap}^{ENDF/B-VII.0}$ calculated in [Kah11] and in this work are the same.

All the C/E values (in parentheses) of the fourth, fifth and sixth columns of Table 4.19 are below 1. However, only some of them are compatible with the 5% uncertainty of the experimental value of σ_{cap}. The same calculations were performed also with the S_1 and $\langle\Gamma_\gamma\rangle_1$ parameters obtained from the fit of the Wisshak data, obtaining C/E values which are a 4 - 5% lower than the values presented for the Weston I data. For this reason, they have not been presented here.

Concerning the URR, the Weston I results are around 0.7% lower than the Weston II results, and the renormalization of the Weston data by 0.95 reduce in a 2% the C/E values. For this reason, the values which are in best agreement with the integral experiment are the Weston II results, followed by Weston I and then by Weston I renormalized by 0.95[8]. Above the URR, the high energy cross sections provided by the ENDF/B-VII.0 (same as ENDF/B-VI.8), JENDL-4.0, ROSFOND-2010 and ENDF/B-V.0 evaluations do not agree with the integral experiment, whereas the ENDF/B-VII.1, JEFF-3.1 (same as JENDL-3.3), JEFF-3.0 and CENDL-3.1 do.

All the mentioned cross sections are presented in Figure 4.60. On the top, they appear together with all the Weston and Wisshak data. The Wisshak data has been renormalized by 1.15, which is reasonable since it is 10 - 15% lower than the Weston data. The figure on the middle is a zoom of the figure on the top. In the figure on the bottom,

[8]The renormalization by 0.95 was performed because the n_TOF data normalization is 5% lower than the Weston I data in the overlapping energy region. However, this 5% difference has a statistical uncertainty which makes both data sets compatible even if they are not normalized one to the other. Notice that the Weston I data without renormalization are more compatible with the PROFIL-1 integral measurement.

the evaluated cross sections are presented together with the cross sections obtained from the n_TOF+Weston data (Table 4.17).

It can be appreciated that the ENDF/B-VII.1 library is not compatible with the experimental results below 100 keV, and JEFF-3.0 is not compatible at higher energies, whereas JEFF-3.1 and CENDL-3.1 are compatible with the experimental data. On the other hand, the latter coincide more or less with the non-renormalized Weston cross sections at 42 keV, the border between the URR and the high energy region. This matching is not continuous in the case of the renormalized Weston data.

As a conclusion, it seems that the best choice for the ^{243}Am capture cross section in the URR and high energy region is to adopt the S_0 and $\langle\Gamma_\gamma\rangle_0$ parameters from this work, the S_1 and $\langle\Gamma_\gamma\rangle_1$ parameters from the fit to the Weston data (Table 4.17), without renormalization, and a high energy cross section similar to the ones implemented in the JEFF-3.1 (same as JENDL-3.3) or CENDL-3.1 evaluations. This capture cross section: (1) fits the n_TOF and the Weston I data between 0.25 and 2.5 keV; (2) fits the Weston data between 2.5 and 42 keV; (3) fits the Wisshak data up to 250 keV, if they are normalized to the Weston data; (4) is compatible with the integral experimental results of the PROFIL-1 irradiation experiment; and (5) there is a continuous matching between the URR and the high energy region, at 42 keV.

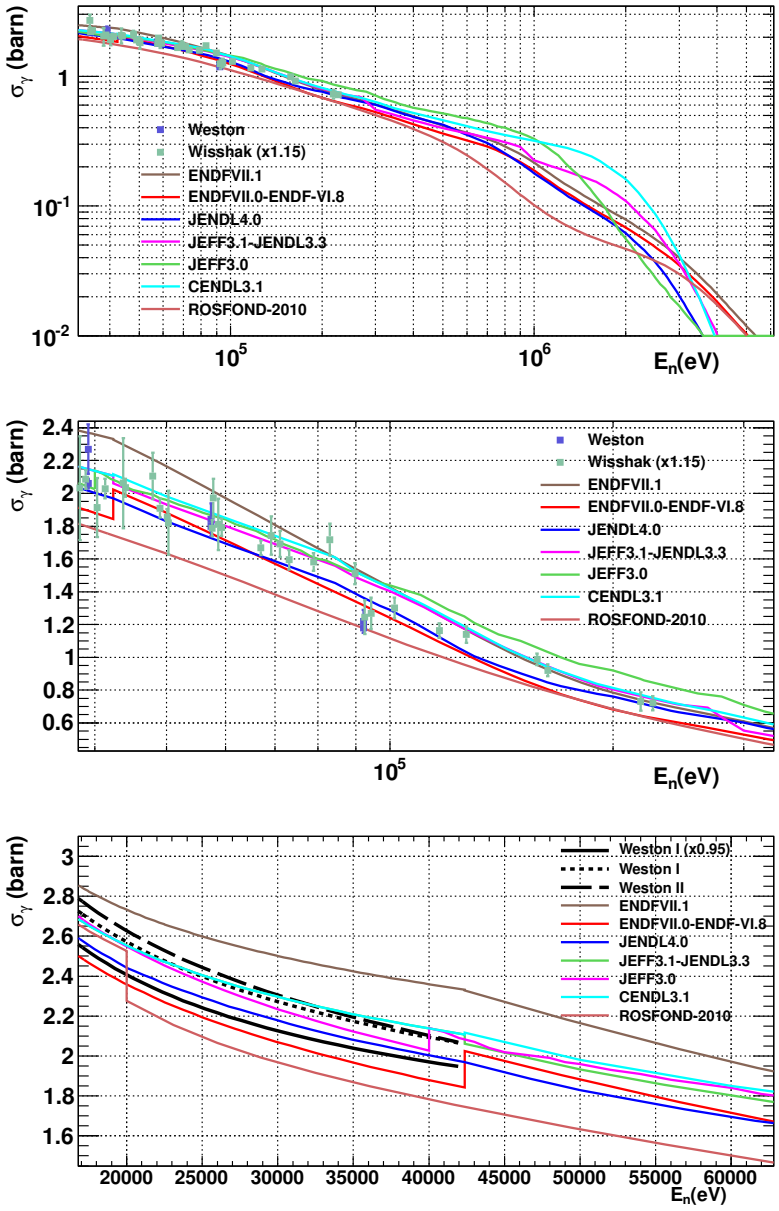

Figure 4.60: Top and center: different evaluated ^{243}Am capture cross sections together with the Weston and Wisshak data, the latest renormalized by 1.15. Bottom: cross sections obtained in this work (Table 4.17), up to 42 keV, together with the evaluated cross sections.

Chapter 5

Summary and conclusions

Nuclear data for minor actinides are necessary for improving the design and performance of advanced reactors and transmutation devices for the incineration of radioactive nuclear waste [Sal08, Gon09, Ali04, Ali06]. In particular, the ^{243}Am isotope is relevant since it is the minor actinide which contributes more to the radiotoxicity of the nuclear waste between $\sim 3 \cdot 10^3$ and $\sim 3 \cdot 10^4$ years. In addition, the neutron capture in ^{243}Am is the main gate to the creation of ^{244}Cm and higher mass isotopes.

The purpose of the this work is to provide experimental data on the ^{243}Am(n,γ) for improving the current evaluations. At present, there is no published neutron capture measurement of ^{243}Am below 250 eV, and all the existing evaluations of the elastic and capture cross sections are based essentially on a single transmission measurement [Sim74]. Above 250 eV there are only a few capture measurements available [Wes85, Wis83], which show discrepancies that make them incompatible. Due to the lack of experimental data on ^{243}Am the standard ENDF-6 format libraries present sizeable differences between each other.

This manuscript describes the analysis of the measurement, including the data reduction and the cross section analysis. The capture yield has been calculated together with all the statistical and systematic uncertainties, and will be included in the EXFOR data base to make it available to the nuclear data community for future evaluations. This yield has been analyzed and compared with previous measurements and evaluations, which have also been used to obtain the cross section which better reproduces all the experimental results performed up to now.

The main result of this work are the capture yield, which will be delivered to EXFOR, and the results of the cross section analysis, which have been compared with other data and evaluations. In addition, valuable information has been obtained concerning the ^{198}Au and ^{244}Am photon strength functions at low energies. Last, but not least, the analysis has required to develop a new set of tools and methodologies which allow to extend the use of the TAC to very high counting rates. All methods have been validated conveniently.

5.1 The procurement of the experimental capture yield

The ^{243}Am neutron capture cross section was measured in the 0.7 eV - 2.5 keV energy range at the n_TOF facility during the 2004 campaign. This measurement was performed with the n_TOF Total Absorption Calorimeter (TAC), which is composed by 40 BaF_2 crystals covering almost the entire solid angle. The high segmentation

of the TAC and its high geometric and intrinsic efficiencies make it an excellent device for measuring low mass and/or radioactive samples. The ^{243}Am sample was placed in the center of the TAC and the capture reactions were measured by detecting in coincidence the electromagnetic cascades following the neutron capture. The detector signals were recorded by a digital data acquisition system operating at 250 MSamples/s and with 8 bits resolution, recording continuously a time of flight of 8 ms for each pulse. The neutron energy was obtained by the time of flight technique. Conditions on the energy and multiplicities of the detected events were applied in order to obtain a good capture signal to background ratio without degrading in excess the detection efficiency. The background was obtained by dedicated measurements. Two additional difficulties were found with respect to previous measurements with the TAC at n_TOF:

1. The very high counting rate detected by the TAC due to the sample activity of 5.4 counts/μs, the largest measured up to now at n_TOF. This high counting rate induced changes in the gain of the BaF_2 detectors and enhances dead time effects in the detected ^{243}Am capture and background events. New methods have been developed to deal with these effects without affecting significantly the final cross section uncertainty.

2. The ^{243}Am sample had a high purity with a small contaminations of about 0.048 mg of ^{241}Am and 0.0025 mg of ^{240}Pu. However, the certified mass of the sample (10 mg) did not agree with a spectroscopic characterization of the sample performed at CERN, which gave a mass of 7.34 ($\pm$15%) mg. For this reason, a detailed Monte Carlo simulation of the sample activity measured with the TAC was performed, giving a mass of 6.77 ($\pm$15%) mg, thus confirming the results of the spectroscopic measurement. The analysis of the time of flight data was finally performed by normalizing the n_TOF measured capture cross section to the transmission data of Simpson et al. [Sim74] at low neutron energies (3 - 50 eV), obtaining a final sample mass of 6.23 ($\pm$4%) mg, in agreement with the spectroscopic measurements. With this normalization, the n_TOF capture data is totally compatible with one of the two published capture data by Weston in the 0.25 - 2.5 keV energy region [Wes85]. It was also found as well that the sample has inhomogeneities. This fact made impossible the analysis of the largest ^{243}Am resonance at 1.35 eV, the only one affected significantly by shelf shielding and multiple scattering.

5.2 Analysis of the capture yield

5.2.1 Resolved Resonance Region

All the detected resonances below 400 eV have been analyzed with the Reich Moore formalism. The resulting energies and reduced neutron and gamma widths of each resonance, together with their statistical and systematic uncertainties and the most relevant correlations between them, are listed in Appendix C. There are two exceptions, which are: (1) the resonance at 0.415 eV, which is below the n_TOF measurement energy range; and (2) the strongest resonance at 1.35 eV, which could not be analyzed due to inhomogeneities in the sample (see Section 4.3.5). The spins of the resonances, the channel radius and the fission widths have not been determined, and the reference values from ENDF/B-VII.0 were adopted. A statistical analysis of the resonances of the RRR have been performed, and the results are summarized in Table 5.1.

	mean value	σ_{stat}	σ_{norm}	σ_{temp}	$\sigma_{1/V}$	$\sigma_{Doppler}$	σ_{Inhom}	σ_{tot}^{lin}	σ_{tot}^{quad}
D_0(eV)	0.66	0.03	-	-	-	-	-	0.03	0.03
$S_0(\times 10^{-4})$	1.08	0.08	0.03 (3%)	-	-	-	-	0.11	0.09
$\langle\Gamma_\gamma\rangle$(meV)	42.00	0.12	-	0.5	0.3	0.7	0.6	2.2	1.1

Table 5.1: Statistical parameters obtained from the analysis of the RRR. The mean values are presented together with the statistical uncertainties (σ_{stat}) and the estimated systematic uncertainties due to the normalization (σ_{norm}), the temperature (σ_{temp}), the 1/V factor ($\sigma_{1/V}$), the Doppler model used ($\sigma_{Doppler}$) and the sample inhomogeneities (σ_{Inhom}). All these quantities have been added linearly (σ_{tot}^{lin}) and quadratically (σ_{tot}^{quad}).

Excluding the the fission widths, which have no visible effect in the calculation of the elastic and capture cross sections, there are essentially three different evaluations of the RRR resonance parameters in the ENDF format distributed neutron data libraries:

1. The evaluation performed by Mughabghab [Mug06], which is adopted by the ENDF/B-VII.1 library.
2. The evaluation performed by Weston [Her09], adopted by the ENDF/B-VII.0 and ENDF/B-VI libraries.
3. The evaluation performed by Maslov [Mas96], which is adopted by the rest of the most recent libraries: JEFF-3.1, JEFF-3.1.1, JEFF-3.1.2, JENDL-3.3, JENDL-4.0, BROND-2.0, ROSFOND-2010 and CENDL-3.1. In the JENDL-4.0 evaluation, the strongest resonance at 1.35 eV and the two neighboring resonances at 0.98 and 1.74 eV, have been modified with respect to the Maslov evaluation.

The evaluations performed by Mughabghab and Weston are very similar, with the exception of the resonance at 1.35 eV, and their resonance parameters are very close to those provided by Simpson et al. [Sim74]. The main difference found between them is in the resonance at 22.74 eV, presented in the left panel of Figure 5.1, where the ENDF/B-VII.1 library seems to have a wrong Γ_n parameter.

A comparison between the yields obtained with the Mughabghab and Maslov resonance parameters and the n_TOF fitted yield is provided in Figures 5.1 - 5.4. The energy scales of the Mughabghab and Maslov evaluations have been fitted to the one used in this work. In addition, the cumulative number of levels and the evolution of $\sum g\Gamma_n^0$ with the neutron energy for the different evaluations are presented in Figure 5.5, in order to make a general comparison between the number and the size of the resonances. Finally, the ratios between the obtained capture and elastic cross sections integrated in wide energy intervals are provided in Figure 5.6, in the 3 - 250 eV energy range.

In the comparison procedure it has observed that:

1. Excluding the negative resonances, the Mughabghab (and Weston) evaluation contain 218 resonances, the Maslov evaluation 238, and the n_TOF evaluation 248 resonances up to 250 eV, and 105 additional resonances between 250 and 400 eV.
2. Up to 70 - 80 eV, the three evaluations are, in general, in good agreement, with the exception of the stronger resonances for the Maslov evaluation (see Figures 5.1 and 5.2): it seems that in the evaluation procedure the shelf shielding or multiple scattering effects in the Simpson et al. transmission data were overestimated.
3. Above 70 - 80 eV, the differences between the three evaluations increase with the neutron energy, as expected since the n_TOF measurement have greater resolving power than the Simpson et al. measurement.

4. Some small resonances have been rejected (see resonance at ∼171 eV in the left panel of Figure 5.4) and some of them have been added (see resonance at ∼180.5 eV in the left panel of Figure 5.4). Most of the resonances proposed by Maslov which are not present in the Mughabghab evaluation have been confirmed.

5. The n_TOF capture cross section is, in general, larger than the other evaluations: on average, 6% higher than the Mughabghab and Weston evaluations and 13% higher than the Maslov evaluation. Notice that the difference with the latest is greater despite it has more resonances than the Mughabghab and Weston evaluations. The greater differences are found in the 100 - 150 eV energy region, where the n_TOF cross section is 26% and 12% higher than the Maslov and Mughabghab-Weston evaluations, respectively.

6. The n_TOF elastic cross section is, on average, 3% lower than the Mughabghab and Weston evaluations and 7% higher than the Maslov evaluation. However, the comparison depends largely on the energy range considered. Again, the largest differences are found in the 100 - 150 eV energy region.

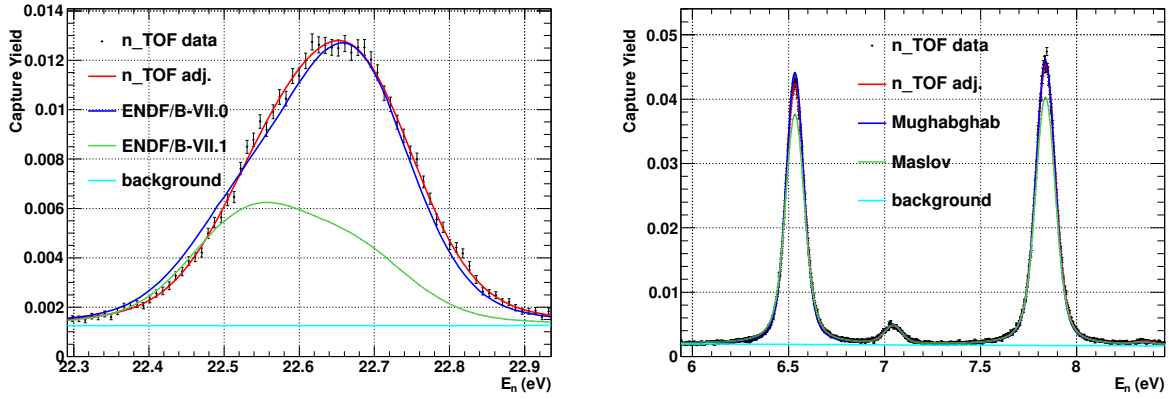

Figure 5.1: Comparison between the n_TOF data, the n_TOF fitted yield and the yields obtained with the resonance parameters from other evaluations.

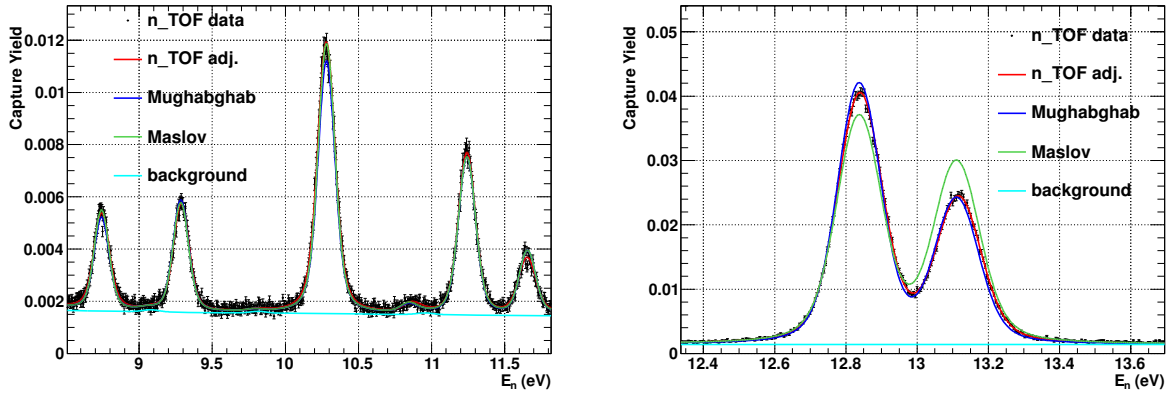

Figure 5.2: Comparison between the n_TOF data, the n_TOF fitted yield, and the yields obtained with the resonance parameters from other evaluations.

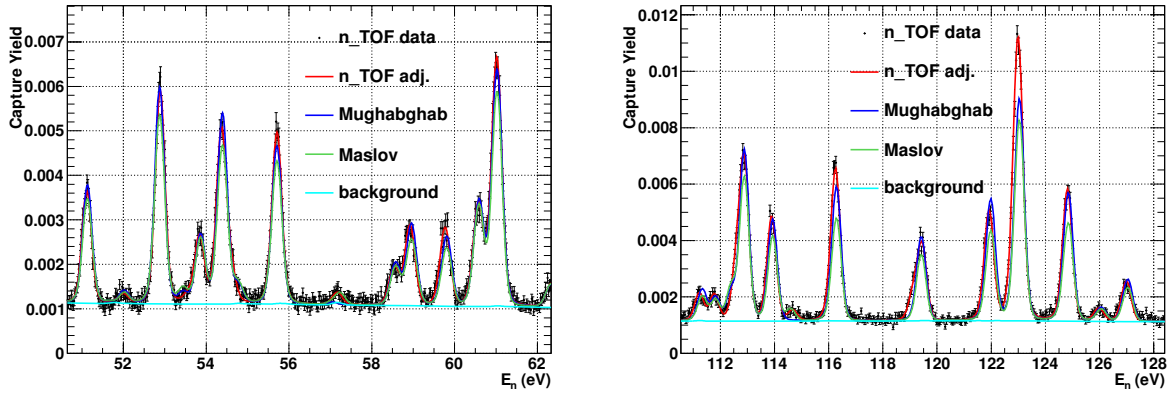

Figure 5.3: Comparison between the n_TOF data, the n_TOF fitted yield and the yields obtained with the resonance parameters from other evaluations.

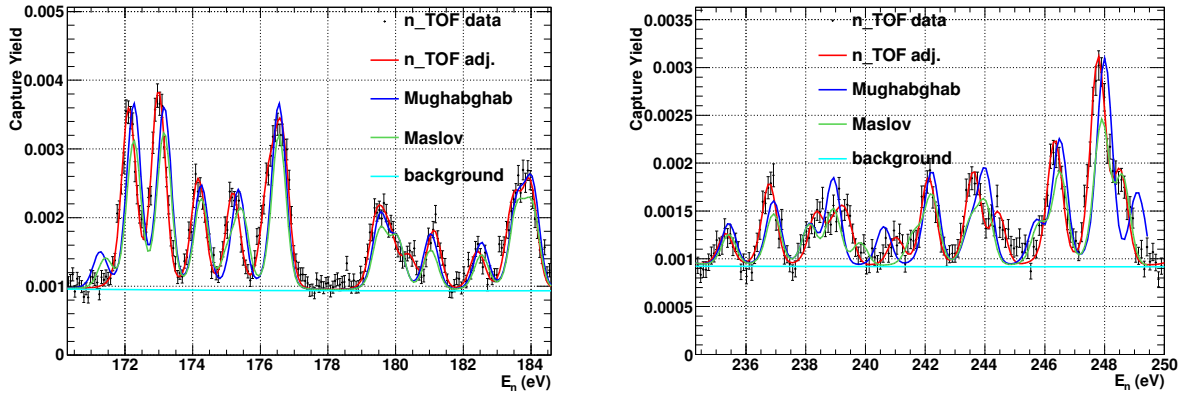

Figure 5.4: Comparison between the n_TOF data, the n_TOF fitted yield, and the yields obtained with the resonance parameters from other evaluations.

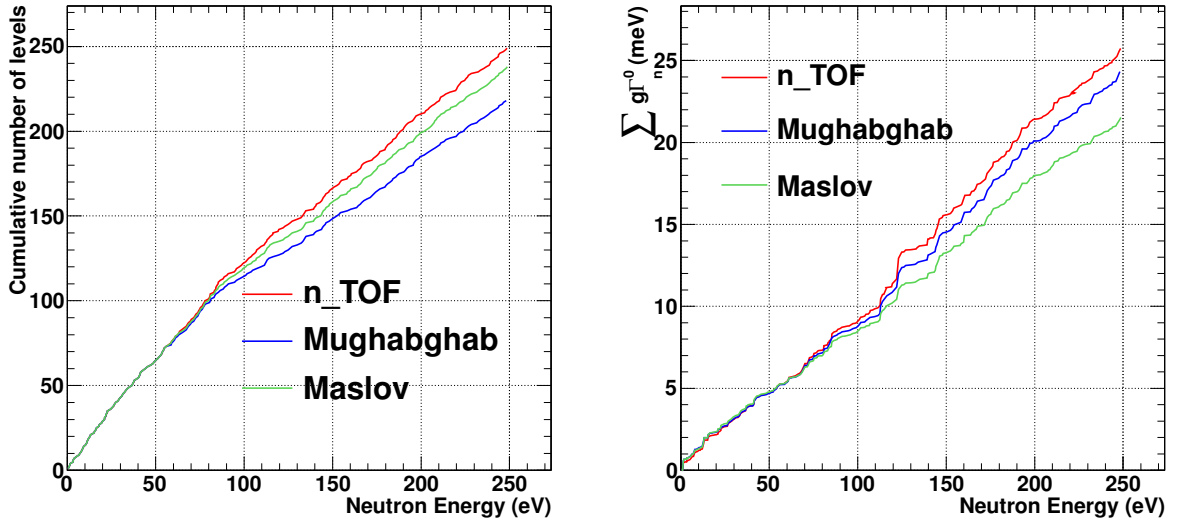

Figure 5.5: Cumulative number of levels (left) and $\sum g\Gamma_n^0$ (right) for the n_TOF resonance parameters compared with the Mughabghab and Maslov evaluations.

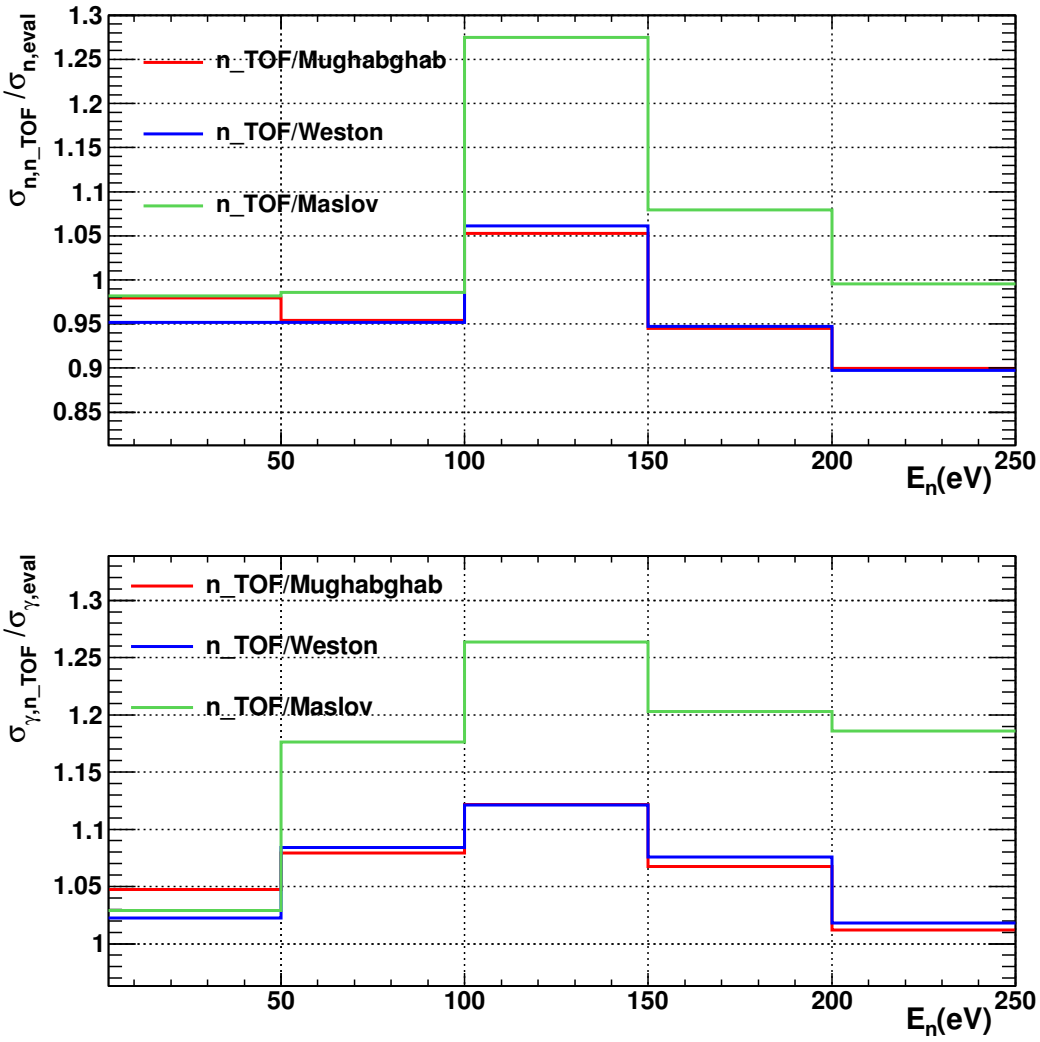

Figure 5.6: Comparison between the n_TOF fitted elastic (top) and capture (bottom) cross section and the Mughabghab (ENDF/B-VII.1), Weston (ENDF/B-VII.0, ENDF/B-VI) and Maslov (latest versions of JEFF, JENDL, BROND and CENDL libraries) evaluations. The lower limit of the first bin is 3 eV.

5.2.2 Unresolved Resonance Region

The URR has been analyzed in the 0.25 - 2.5 keV energy range with the n_TOF data, where only the s-wave (i.e., l=0) contribution is significant. D_0 was fixed to the value obtained in the RRR, and S_0 and $\langle\Gamma_\gamma\rangle_0$ have been fitted to the experimental data taking into account the prior knowledge of the statistical analysis in the RRR. If no prior knowledge of the statistical parameters is assumed, the results are compatible to those obtained in the RRR, but larger uncertainties and correlations are obtained. It was also observed that the cross section between 250 and 350 eV is not well reproduced with the obtained unresolved parameters. For this reason, it is strongly recommended to extend the RRR up to 350 - 400 eV, with the resolved resonance parameters obtained in this work.

The Weston et al. experimental data, which is compatible with the n_TOF results in their common energy range (0.25 - 2.5 keV), has been used to extend the analysis of the URR up to 42 keV. This analysis was performed by fitting S_1 and $\langle\Gamma_\gamma\rangle_1$ to the experimental results, with the s-wave parameters fixed to the values obtained from the n_TOF data. The systematic uncertainties of S_1 and $\langle\Gamma_\gamma\rangle_1$ could not be obtained in this case, due to the lack of information available in the Weston et al. publication. The scattering radius and the fission widths could not be determined from these experimental data sets. They should be obtained from transmission and fission experimental data. The results are provided in Table 5.2.

Finally, the Wisshak et al. experimental data and the results of the PROFIL-1 integral experiment have been used to obtain information about the ^{243}Am(n,γ) cross section above 42 keV. It has been found that the capture cross section constructed with the RRR of this work, the URR with the parameters provided in Table 5.2, and the high energy region (>42 keV) of the JEFF-3.1 (JENDL-3.3) or the CENDL-3.1 evaluations is the one which better reproduces the measurements performed up to now.

	D_0(eV)	$S_0(\times10^{-4})$	$\langle\Gamma_\gamma\rangle_0$(meV)	corr(S_0,$\langle\Gamma_\gamma\rangle_0$)	$S_1(\times10^{-4})$	$\langle\Gamma_\gamma\rangle_1$(meV)	corr(S_1,$\langle\Gamma_\gamma\rangle_1$)
mean value	0.66(3)	1.10(4)	42.1(20)	-0.23	1.65(24)	52(34)	-0.82
σ_{norm}	0	3%	0		-	-	

Table 5.2: URR parameters obtained in this work, with their statistical uncertainties in parentheses. corr(a,b) means the correlation between a and b. The normalization uncertainty (σ_{norm}) has been calculated for the l=0 parameters, and is the only non negligible systematic uncertainty. The l=1 parameters have been obtained from the n_TOF+Weston data fit, and their systematic uncertainties have not been calculated.

The URR parameters obtained in this work are presented together with those obtained in other experiments and evaluations in Table 5.3. Note that in all the cases the parameter values are at E_n=0, and in the case of the n_TOF data the evolution of the URR parameters with the neutron energy is the one described in [Lar06].

The fitted n_TOF capture data is presented in Figure 5.7, together with the only two available capture data sets at present in this energy range, tagged as "Weston I" and "Weston II". Both of them range from 250 eV up to 92 keV, and they differ significantly below 1.5-2 keV. The n_TOF data is compatible, in normalization and shape, with the Weston I data set, whereas it is not with the Weston II data. On the other hand, all the present evaluations are much closer to the Weston II data set, underestimating the ^{243}Am capture cross section in this energy region between 7% and 20%. The ratio between the n_TOF results and the capture cross sections of the different evaluations are presented in Figure 5.8.

	D_0(eV)	$S_0(\times 10^{-4})$	$\langle\Gamma_\gamma\rangle_0$(meV)	$S_1(\times 10^{-4})$	$\langle\Gamma_\gamma\rangle_1$(meV)
This work	0.66(3)	1.10(5)	42.1(20)	1.65(24)$^{(*)}$	52(34)$^{(*)}$
Bellanova [Bel76]	0.62	0.95			
Berreth [Ber70]			42		
Simpson [Sim74]	0.68	0.96(10)	39		
Cote [Cot59]			43(3)		
RIPL-3 [RP3xx]	0.73(6)	0.98(6)	39(3)		
Mughabghab [Mug84]	0.60(6)	0.98(9)	39(1)		
Maslov [Mas96]	0.566(49)	0.873(146)	43	2.176	43
BROND-2.2	0.67	0.93	39	2.44	39
JENDL-4.0	0.44	0.864	39	1.687	39
ENDF/B-VII.0	0.75	0.98	39	2.2	44
ENDF/B-VII.1	0.66	0.98	39.1	2.6	69.8

Table 5.3: URR parameters (at E_n=0) obtained in this work compared with those obtained in other evaluations. In the URR, the capture cross section of the ENDF/B-VI library is the same as ENDF/B-VII.0. The Maslov evaluation has been adopted by JEFF-3.1, JENDL-3.3 and CENDL-3.1, and also by ROSFOND-2010 at low energies, but in the latter case the dependence of the resonance parameters with the neutron energy is different. $^{(*)}$Values obtained from the n_TOF+Weston data fit.

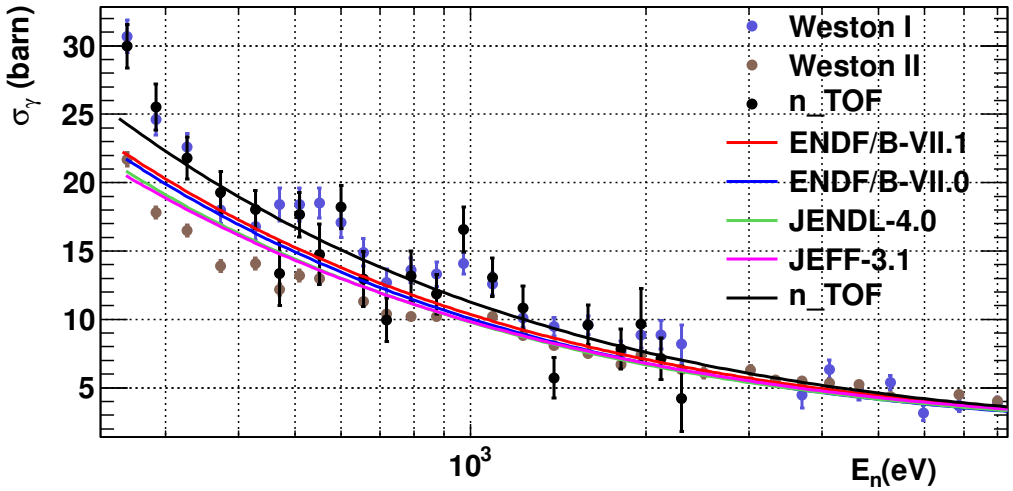

Figure 5.7: n_TOF data in the low energy part of the URR together with the only two published ^{243}Am capture data below 5 keV, "Weston I" and "Weston II". The cross sections available in the ENDF/B-VII.1, ENDF/B-VII.0, JENDL-4.0 and JEFF-3.1 (same as JENDL-3.3 and CENDL-3.1) libraries are also presented, together with the cross section obtained in this work. Notice that all the libraries are close to the Weston II results, whereas the n_TOF data are close to Weston I.

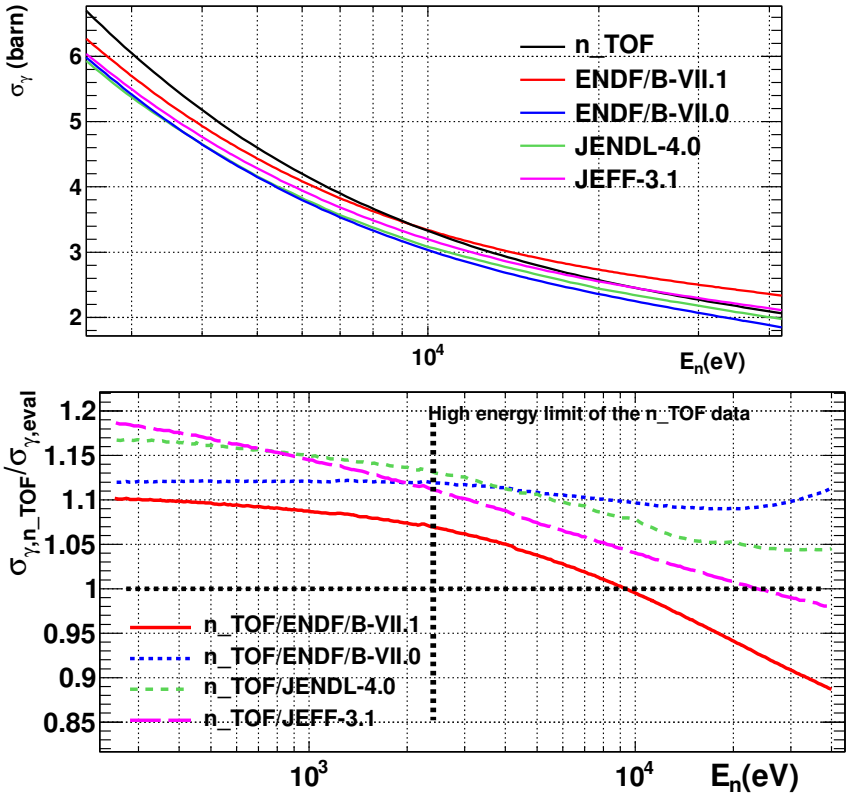

Figure 5.8: n_TOF+Weston ^{243}Am capture cross section in the URR together with some evaluated libraries in the 2.5 - 42 keV energy range (top) and the ratio between them in the entire URR (bottom). Notice that the URR cross section obtained in this work has a shape very similar to the one of the ENDF-B/VII.0 library, but 10-12% larger.

5.2.3 Status of the ^{243}Am capture cross section and future measurements

The result of this analysis suggest changes in the present evaluated libraries in the resolved energy region and in the range between 400 eV and 2.5 keV. With these results included in the evaluated libraries, the ^{243}Am(n,γ) cross section presents its largest uncertainties:

1. At thermal energies, since measured data are scattered mainly between 75 and 85 barn (see Table 4.8).
2. At the strongest resonance energy of 1.35 eV (see Section 4.3.5).
3. In the fast range for reactor applications (see Section 4.4.4).

The experimental results of Jandel et al. and Hori et al. could reduce further some of the mentioned uncertainties. Otherwise, with a low-mass sample (no shelf shielding corrections) it would be very easy to measure the resonance of 1.35 eV at n_TOF with the TAC. The fast range for reaction applications can be also measured at n_TOF, not with the TAC, but with detectors with a faster recovery after the "gamma-flash", and with a sample with a larger mass.

5.3 Additional results

An important effort has been made for the development of methodologies and analysis tools:

1. A new dead time correction model for digital acquisitions systems (DAQ) has been developed and validated. This method is based in the offline manipulation of the digital buffers recorded by the DAQ and can be used to:

   (a) Characterize the effects in the detection of signals of the same detector which are close to each other. This characterization can be used afterwards in the reconstruction process of Monte Carlo simulated results.

   (b) Characterize the effects in the detection of signals detected under a high counting rate constant in time. As in the previous case, this characterization can be included in the reconstruction of simulated data.

   (c) Obtain the contribution of different sources of background of a high counting rate measurement, when they have been measured separately, under non-high counting rate experimental conditions.

2. Valuable information concerning the Photon Strength Functions (PSF) of ^{198}Au and ^{244}Am at low energies has been obtained. In addition, a new method which can be used to perform fast Monte Carlo simulations has been developed. This method is based in performing the transport of particles only once, obtaining the response of the detector to single γ-rays. The simulation results are then used to construct the response of the TAC to whole capture cascades. This allows to perform a large amount of simulations with different parameters of the models used to generate the cascades. In this work, this tool has been useful to fit the PSF parameters to the experimental results, and to estimate the uncertainty in the detection efficiency. However, it can also be used to perform more rigorous studies of the PSF of actinides measured with the TAC. Some work has been done in this direction, by coupling it with a minimization algorithm. It is possible to define a "distance" function between the simulated and the experimental results which depends on the PSF parameters, as it has been done in this work. Then, the problem of finding PSF parameters which reproduces the experimental results has been transformed in a minimization problem, which can be studied with minimization algorithms. At the moment, the code has been coupled with minuit [Jam06], but some problems need to be solved so the complete program is not still finished. This tool will be used in a future to perform a systematic study of PSF of actinides measured with the TAC.

3. It has been demonstrated that the treatment of the systematic uncertainties performed by the SAMMY code, which is widely used by the nuclear data community, is not satisfactory. The systematic uncertainties of the fitted resonance parameters provided by the code are, in general, underestimated. This has been taken into account in the resonance analysis process, and a different method, based in the variation of the experimental parameters according to their systematic uncertainties, has been used to calculate the systematic uncertainties in the resonance parameters.

4. New analysis software has been developed, which has been used in the analysis of more recent measurements performed at n_TOF. In particular:

   (a) A computer program capable to analyze automatically the results of a calibration measurement has been developed. This program calculates the position of the calibration peaks of the 40 BaF_2 detectors, making possible an automatic energy calibration of the TAC.

   (b) A software capable to characterize the changes in the alpha spectrum of each BaF_2 detector has been developed. This program allows to correct the changes in the energy calibration of each BaF_2 detector produced along the time.

   (c) A visualization software which permits to easily see the performance of a developed pulse shape analysis routine has been developed. This software allows to visualize the fit of any analysis routine to the digitized signals, in a user-friendly way. It has been very useful in the development of new pulse shape analysis routines of different detectors used at n_TOF.

5.4 Improvements for future measurements

Three other actinide capture measurements have been performed with the TAC after the ^{243}Am measurement described in this work: ^{241}Am in the 2010 campaign, ^{238}U in the 2011 campaign and ^{235}U in the 2012 campaign. The latter was performed with fission tagging detectors, in order to distinguish between capture and fission events detected by the TAC. Some of the limitations found during the analysis of this measurement have been taken into account for improving the performance of these new measurements. However, some of the limitations remain:

1. During this manuscript it has been shown that many problems arise when the measurements are performed under high counting rate conditions. This was solved in the ^{241}Am measurement by shielding the sample with 2 mm lead, instead of 1 mm. This simple solution, together with the reduction of the high voltage of the detector, was enough to perform the measurement without large variations of the gain of the detectors, observed in the beginning of the measurement, where only 1 mm shielding was used.

2. The amount of neutron beam dedicated to measure the backgrounds in the ^{243}Am measurement was not sufficient to have an accurate description of the background in the entire energy range. It was necessary to smooth it in the RRR, and their large statistical uncertainties have been the highest source of uncertainty in the URR. This has been taken into account in all the measurements described previously, and considerably more beam time was dedicated to the background measurements.

3. A big effort should be performed in the improvement of the quality and the characterization of the measured samples: inhomogeneities do not allow to measure resonances with a non-negligible shelf shielding effect, and a poor sample characterization leads to unacceptable large systematic uncertainties.

4. The ISO2929 Ti container requested by the CERN radioprotection has not allowed to measure above 2.5 keV. This problem has been solved thanks to the design of new containers, and also to the changes performed to the n_TOF experimental area, which fulfills now the "class A" radio protection requirements.

5. If the background allows the measurement at higher energies, another limitation that has not been present in this analysis arises. This limitation is the gamma flash, which "blinds" the capture detectors during a certain period of time, preventing the measurements with the TAC above 10 - 30 keV. It is still not clear which is the origin of this gamma flash, and its identification might permit to find solutions to reduce it.

6. The origin of the background related to the neutron beam that does not correspond to the interaction of neutrons with the sample or the container is still not clear. This source of background has not supposed a big problem in this measurement, but if samples with lower mass and/or capture cross sections want to be measured, this source of background can be one of the highest sources of uncertainty. For this reason, the origin of this background should be investigated in a future, in order to reduce it.

Appendix A

Experimental spectra

A.1 Deposited energy spectra

In Figures A.1-A.3 there are presented the deposited energy spectra of different dedicated background and ^{243}Am capture measurements (see Section 2.4). Each plot corresponds to a certain neutron energy range and to certain conditions applied to the multiplicity of the detected events, given in the upper part of the different panels.

In Figures A.4 and A.5 there are presented the different contributions to the background, calculated as it is explained in Section 3.6, with the "Rad-measurements".

All the histograms presented in this section have 40 keV/bin.

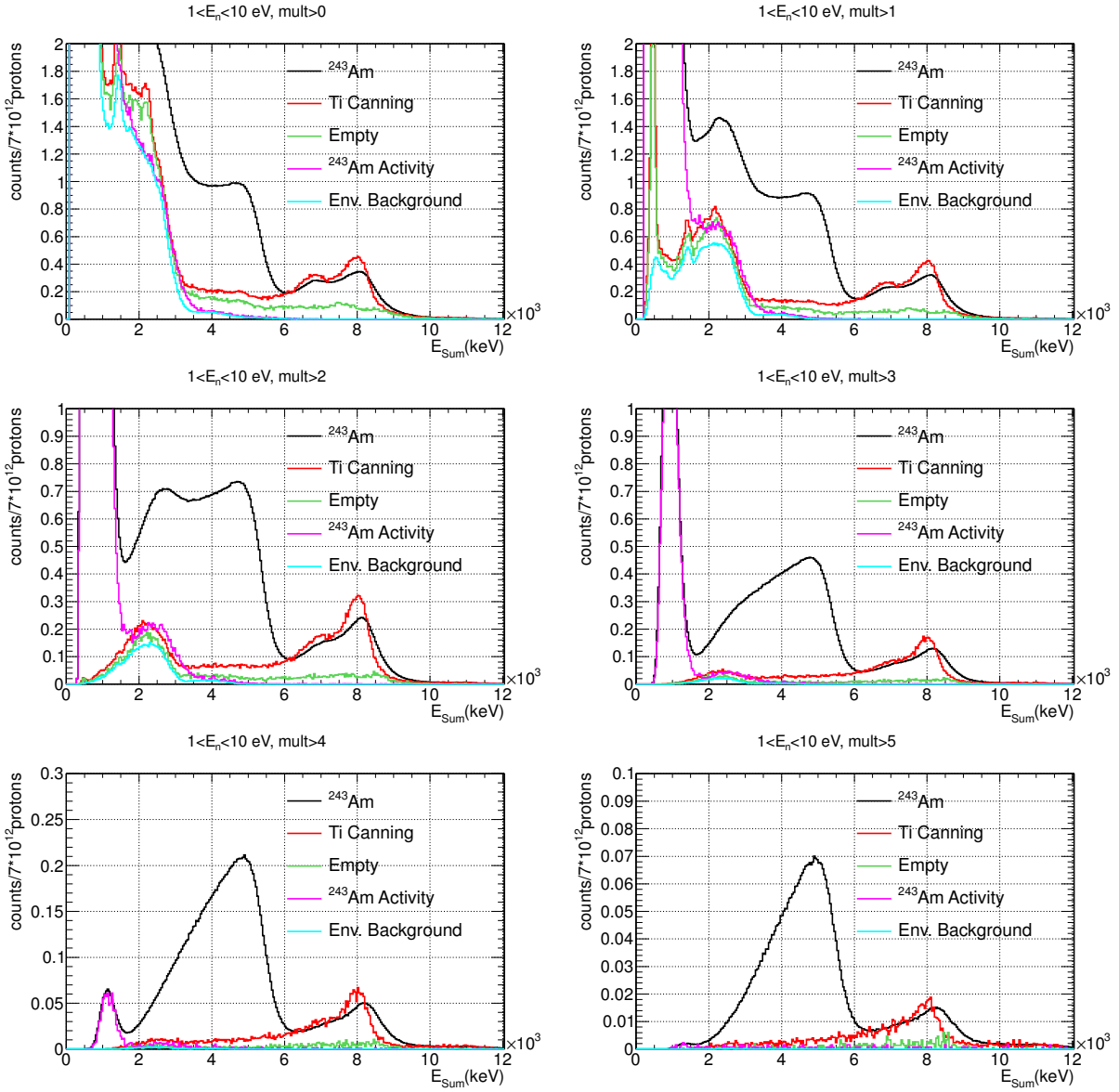

Figure A.1: Deposited energy spectra for the ^{243}Am capture measurement and different background dedicated measurements.

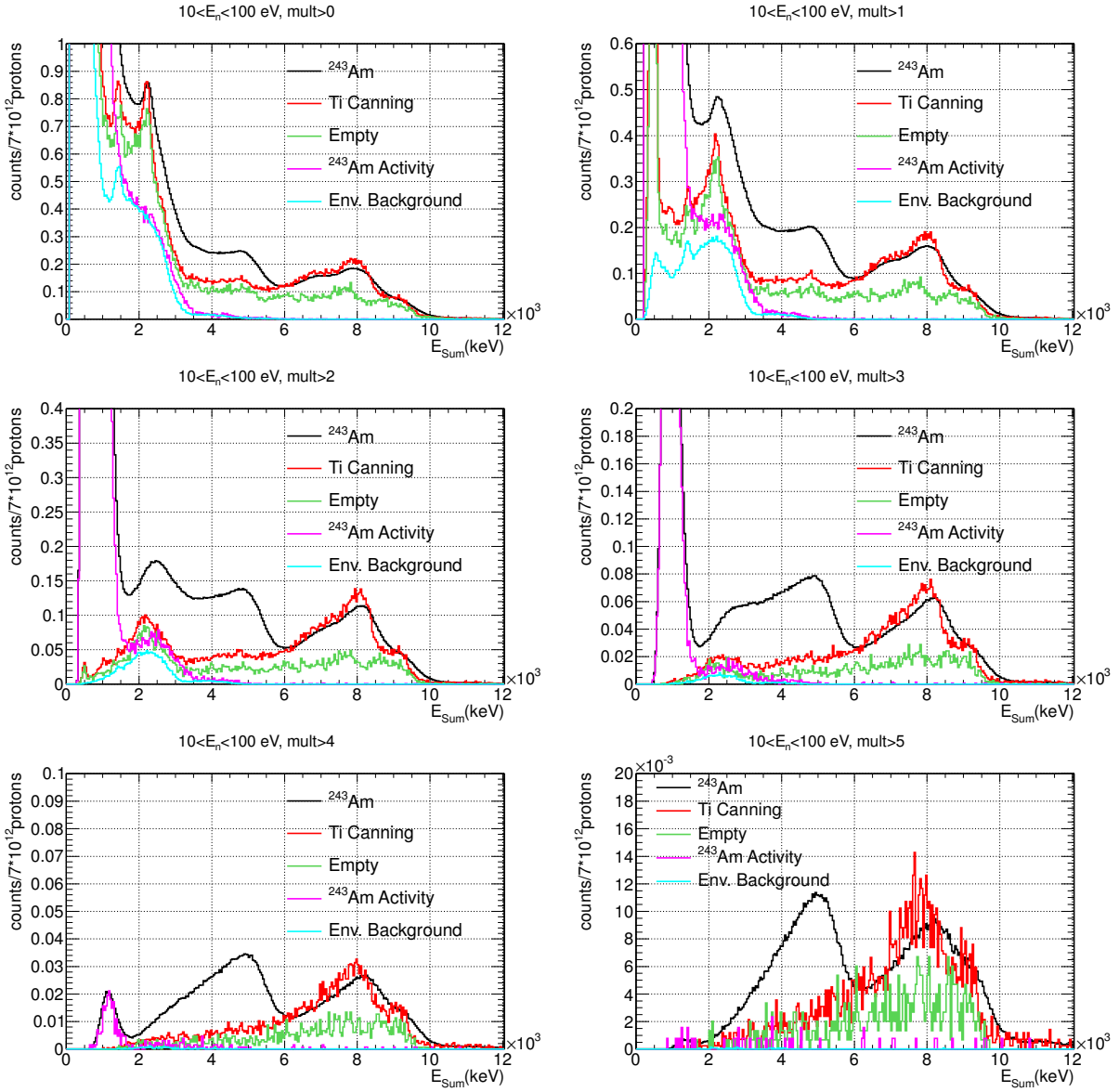

Figure A.2: Deposited energy spectra for the ^{243}Am capture measurement and different background dedicated measurements.

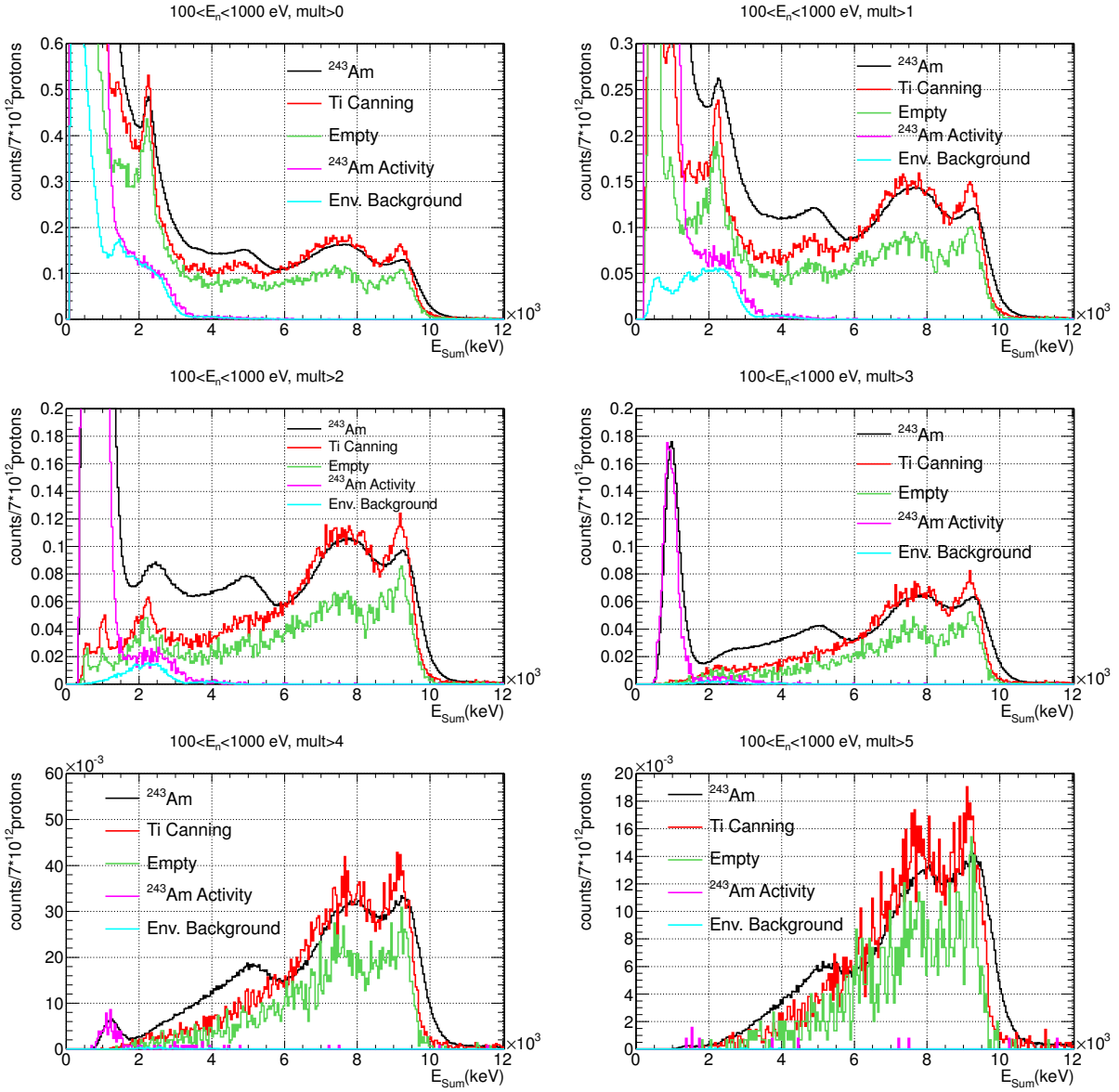

Figure A.3: Deposited energy spectra for the ^{243}Am capture measurement and different background dedicated measurements.

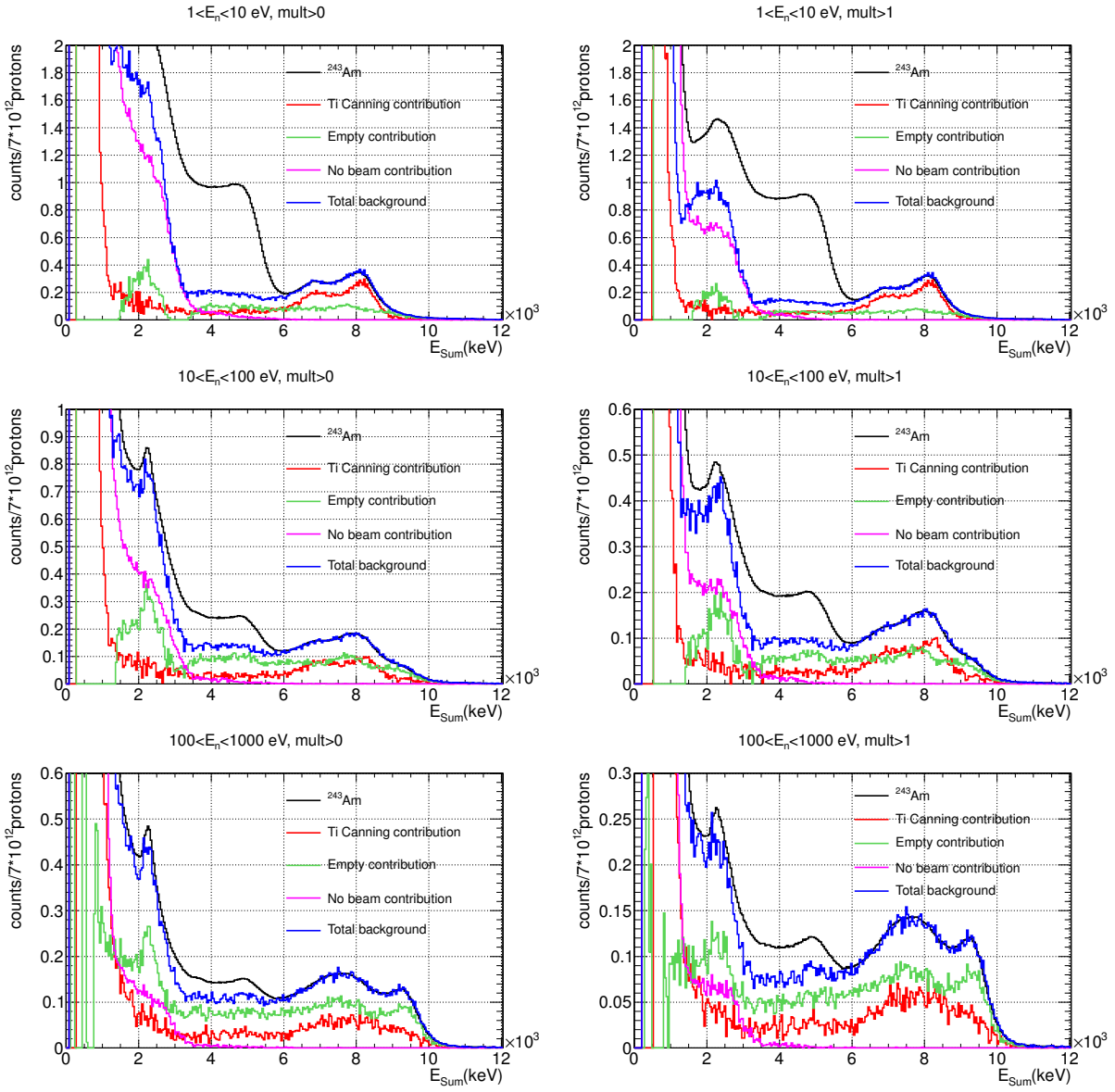

Figure A.4: Deposited energy spectra of the different contributions to the background of the ^{243}Am capture measurement, obtained from the "Rad-measurements" (see Section 3.6).

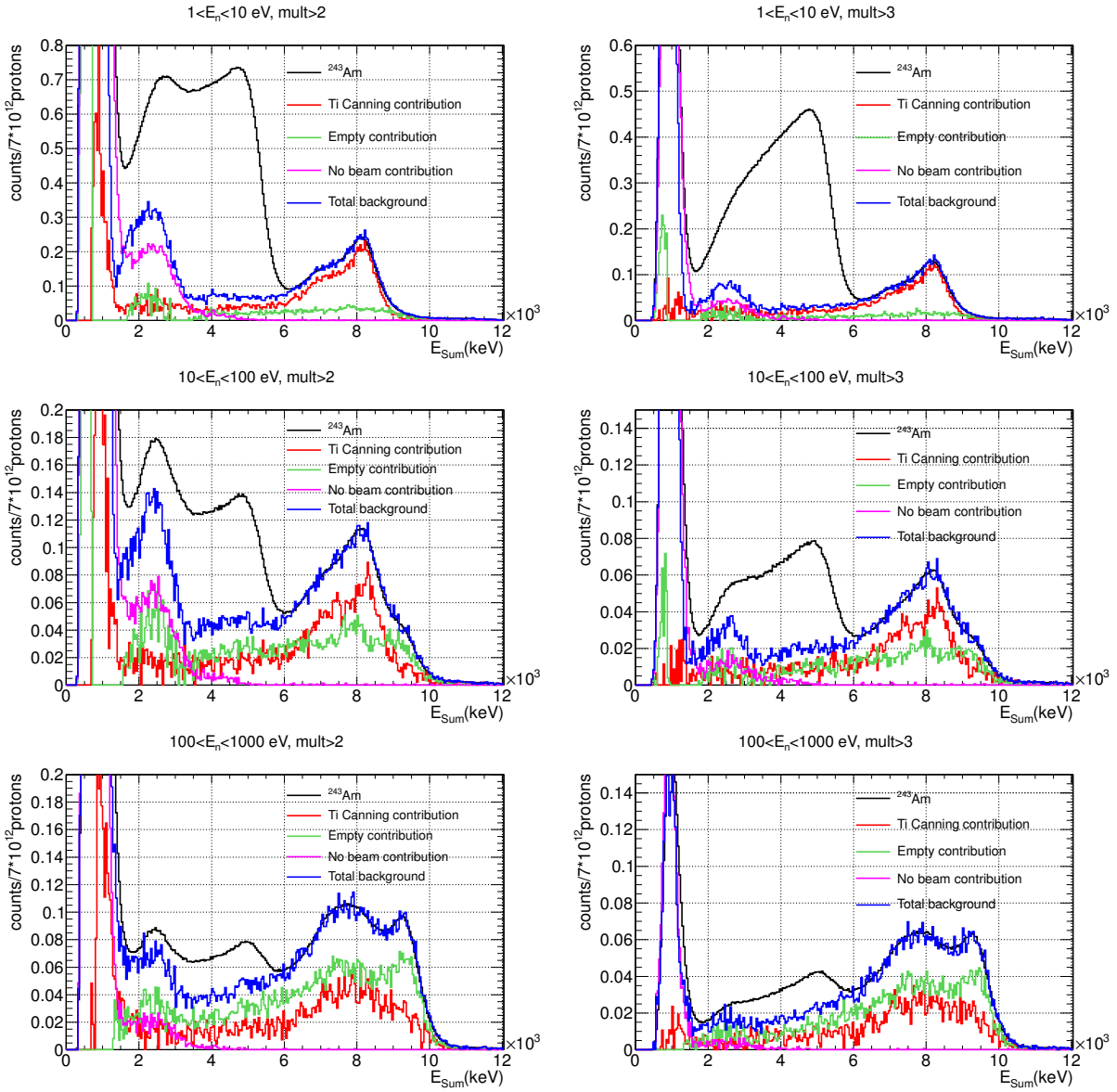

Figure A.5: Deposited energy spectra of the different contributions to the background of the ^{243}Am capture measurement, obtained from the "Rad-measurements" (see Section 3.6).

A.2 Counting rates

In Figures A.6-A.9 there are presented the number of detected events, as a function of the neutron energy, in the dedicated background and ^{243}Am capture measurements (see Section 2.4). Each plot corresponds to different conditions applied to the detected events, given in the upper part of the different panels.

In Figures A.10 and A.11 there are presented the counting rates, as a function of the neutron energy, of the dedicated background and ^{243}Am capture measurements, which are obtained from the histograms of the previous Figures, divided each bin by its corresponding time of flight width.

In Figure A.12 there are presented the different contributions to the background, calculated as it is explained in Section 3.6, with the "Rad-measurements".

All the histograms presented in this section have 200 bins per decade.

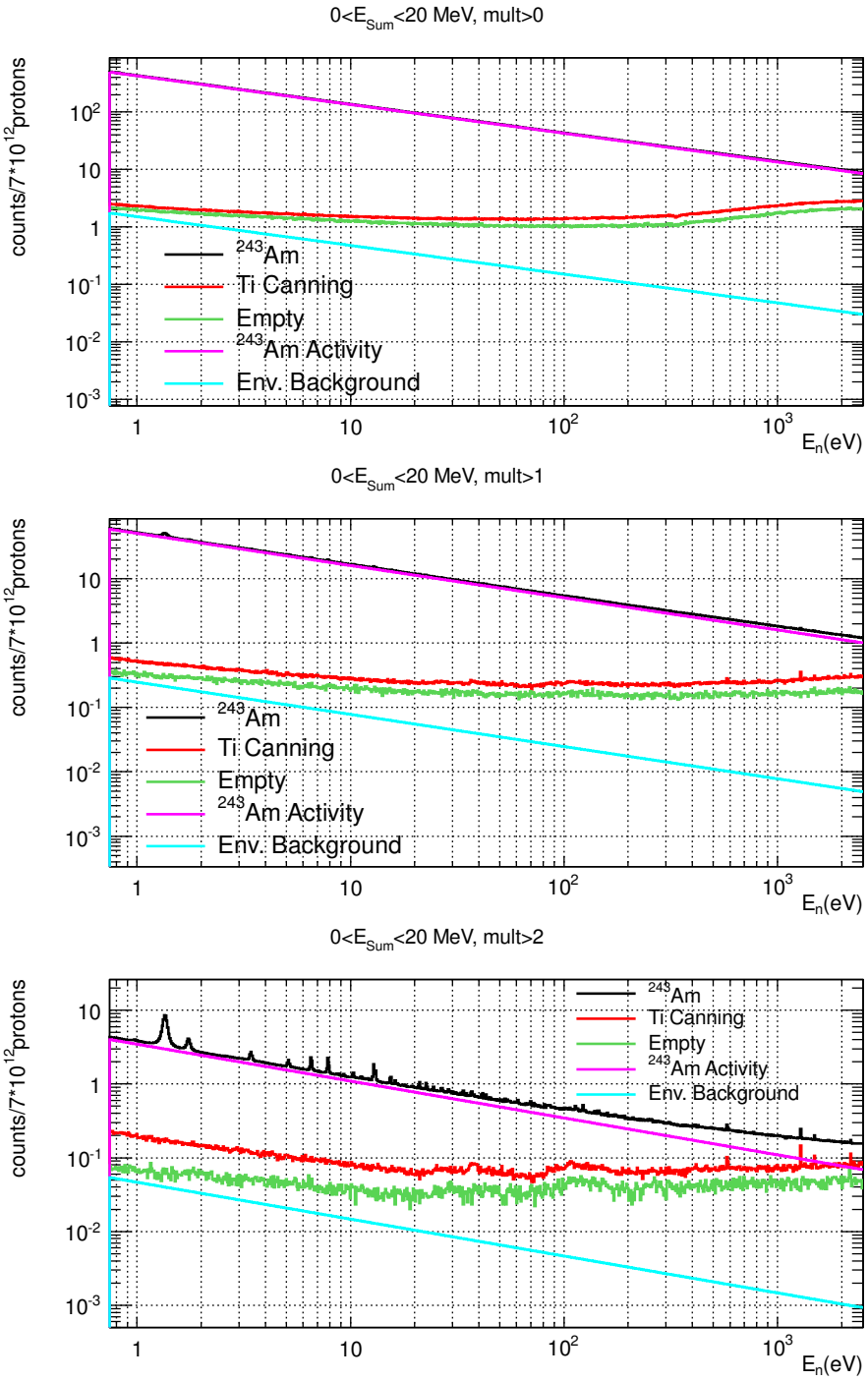

Figure A.6: Number of detected events per proton pulse as a function of the neutron energy for the ^{243}Am capture measurement and for different background dedicated measurements.

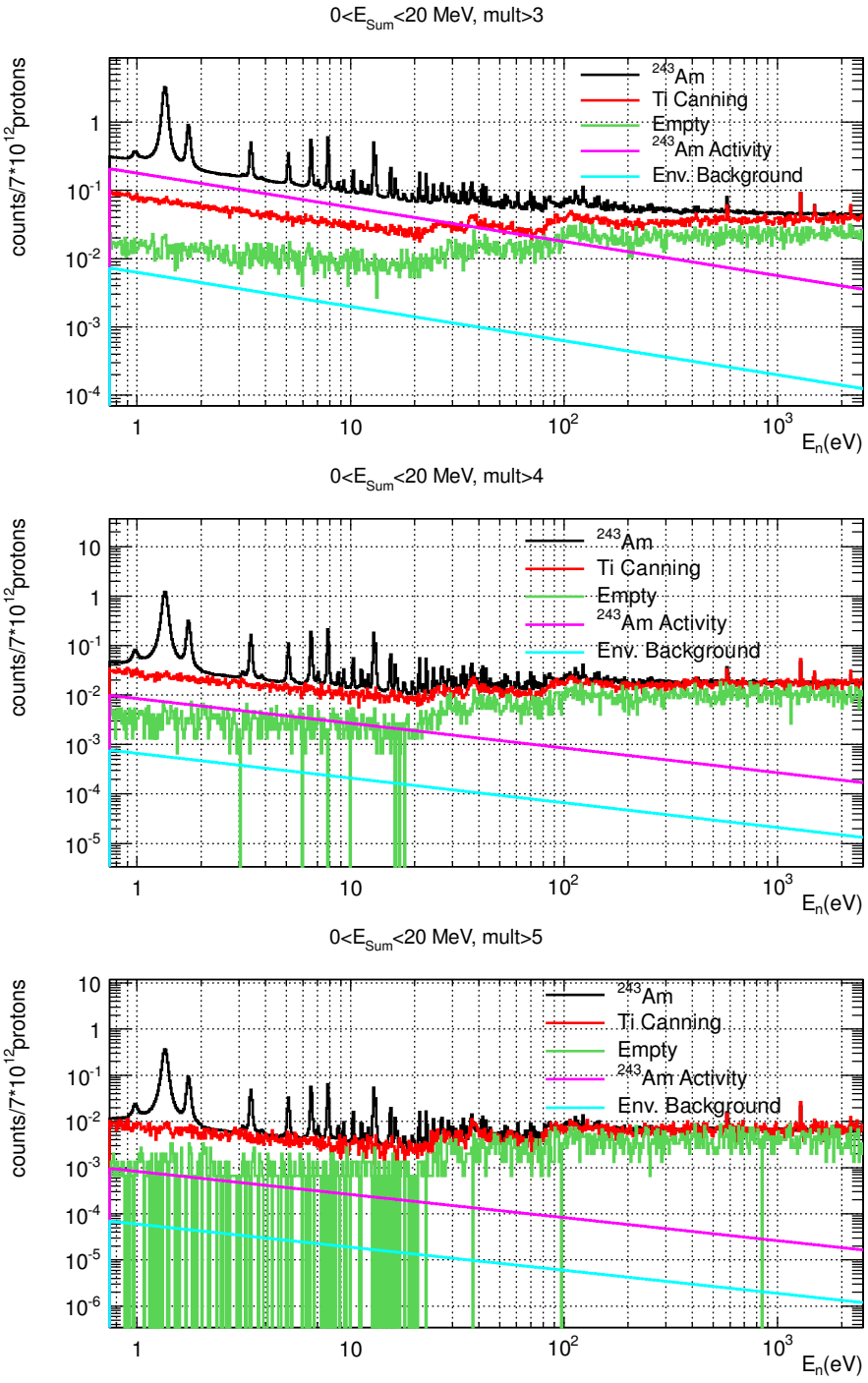

Figure A.7: Number of detected events per proton pulse as a function of the neutron energy for the ^{243}Am capture measurement and for different background dedicated measurements.

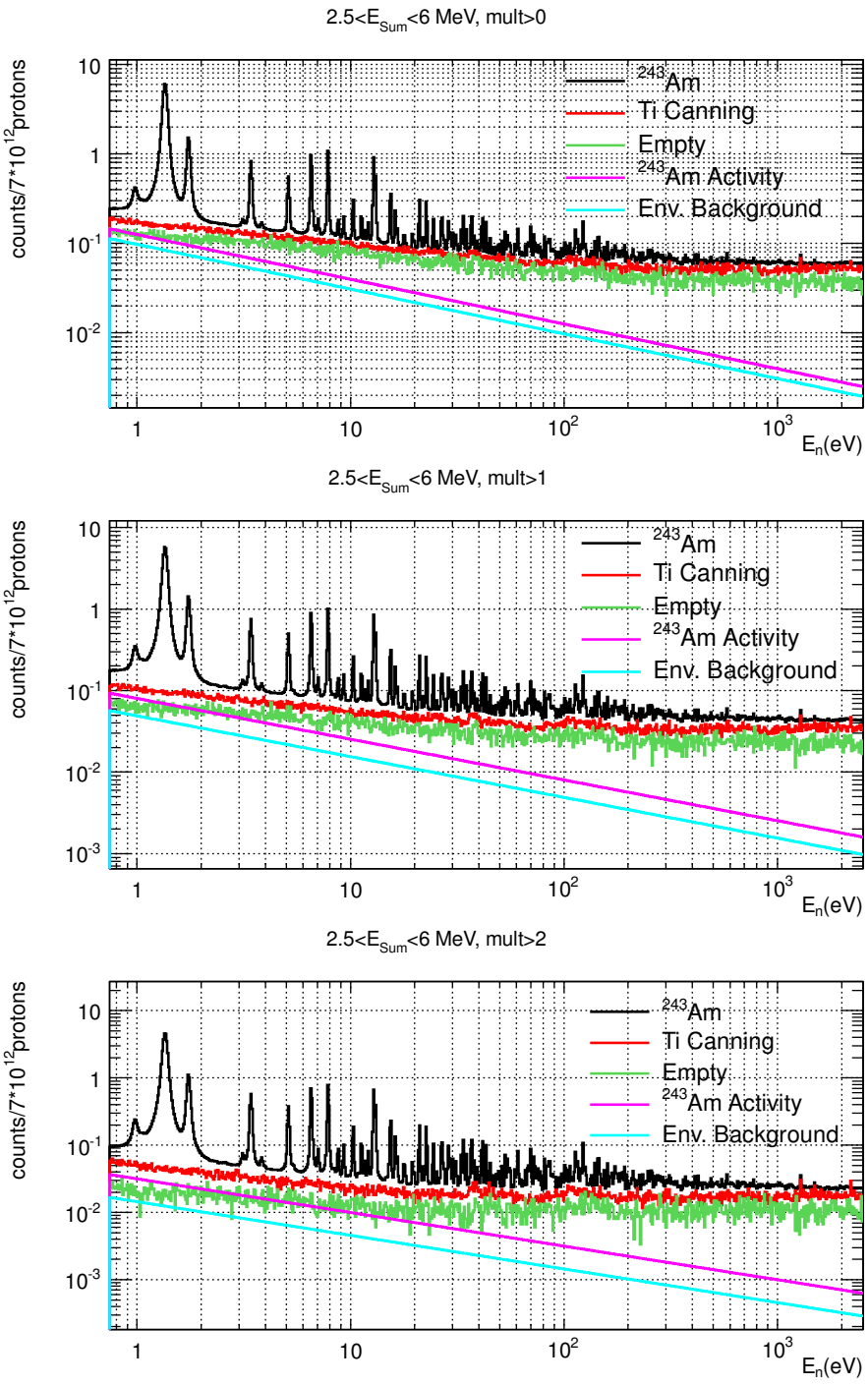

Figure A.8: Number of detected events per proton pulse as a function of the neutron energy for the ^{243}Am capture measurement and for different background dedicated measurements.

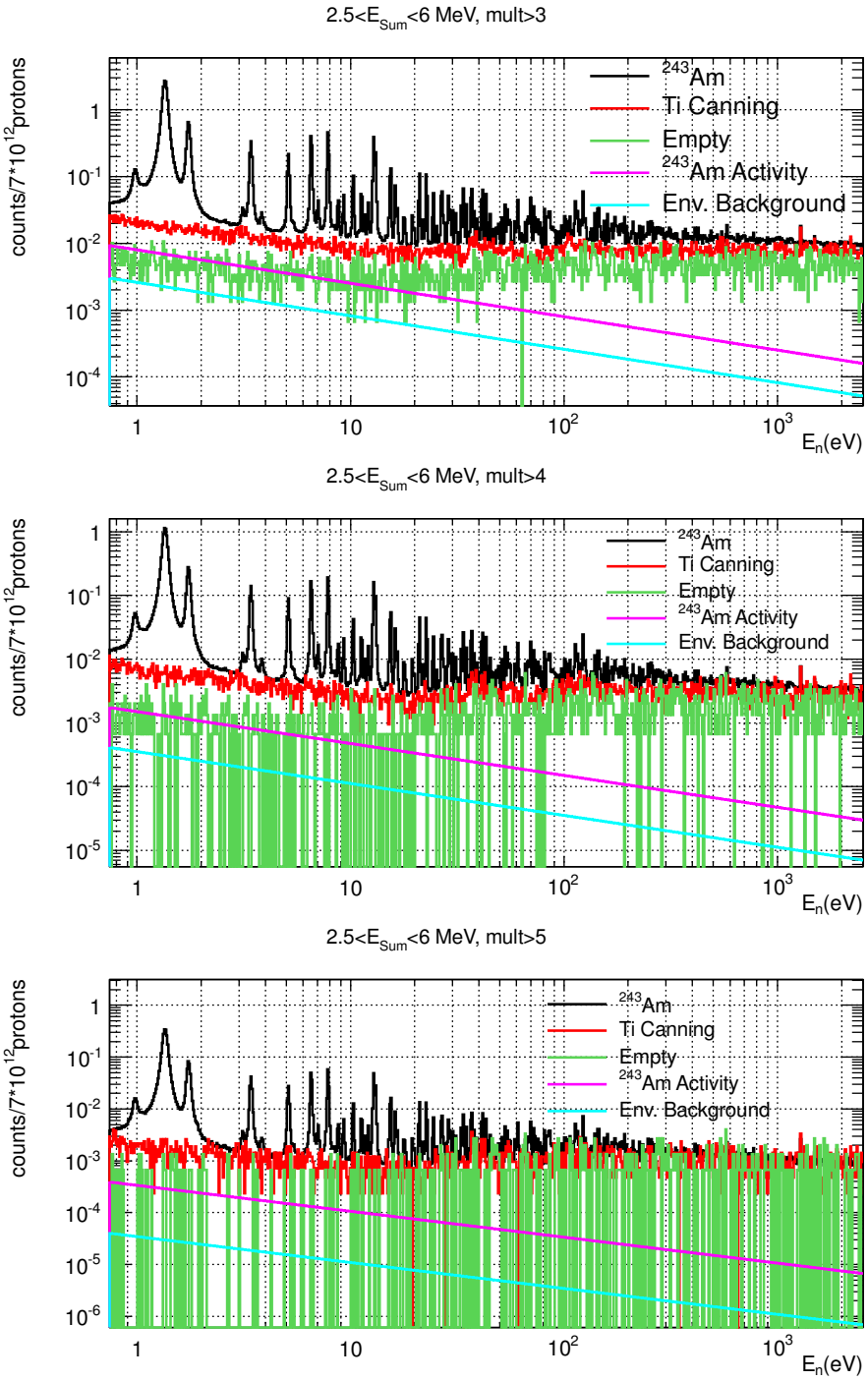

Figure A.9: Number of detected events per proton pulse as a function of the neutron energy for the ^{243}Am capture measurement and for different background dedicated measurements.

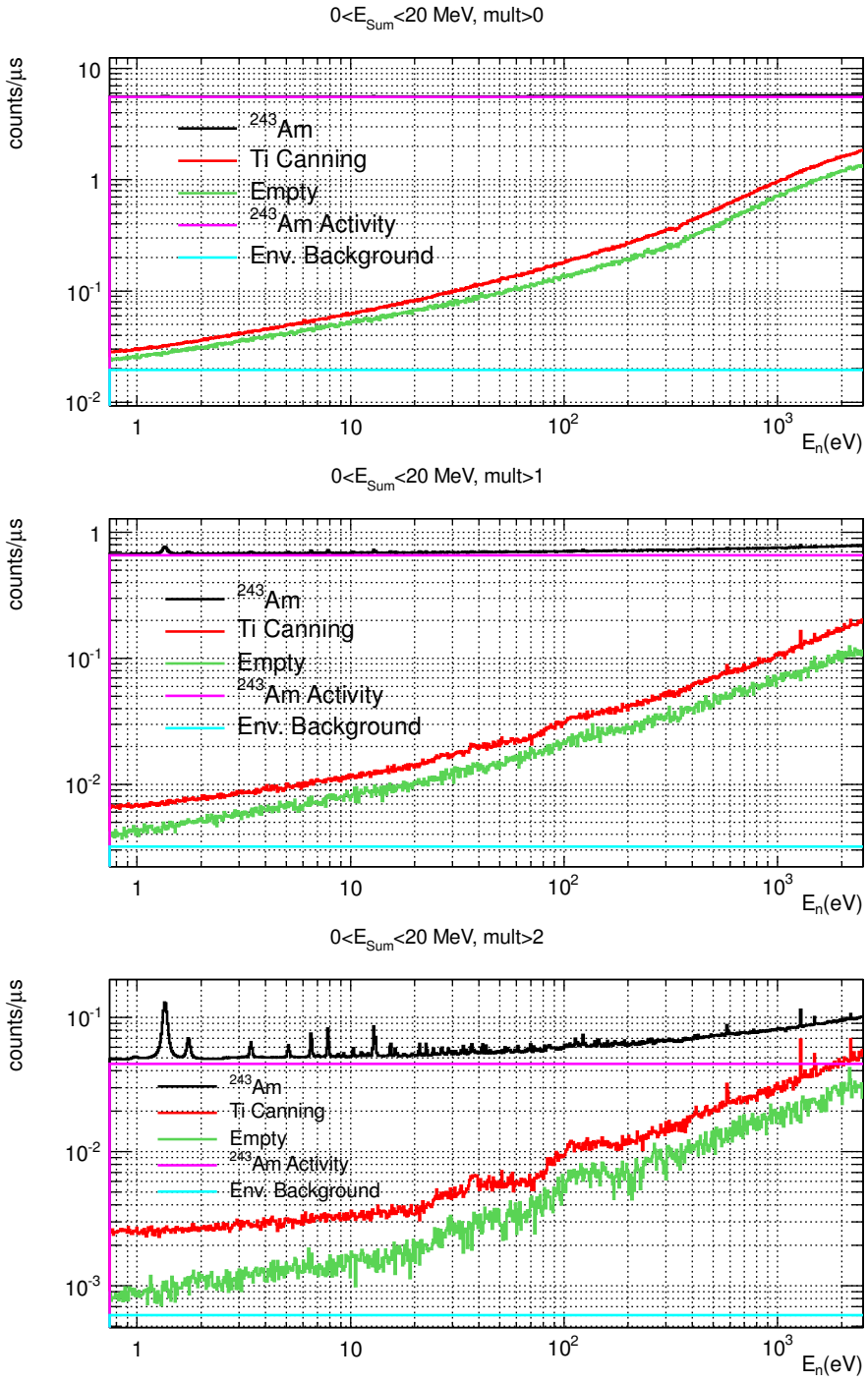

Figure A.10: Detected counting rate as a function of the neutron energy for the ^{243}Am capture measurement and for different background dedicated measurements.

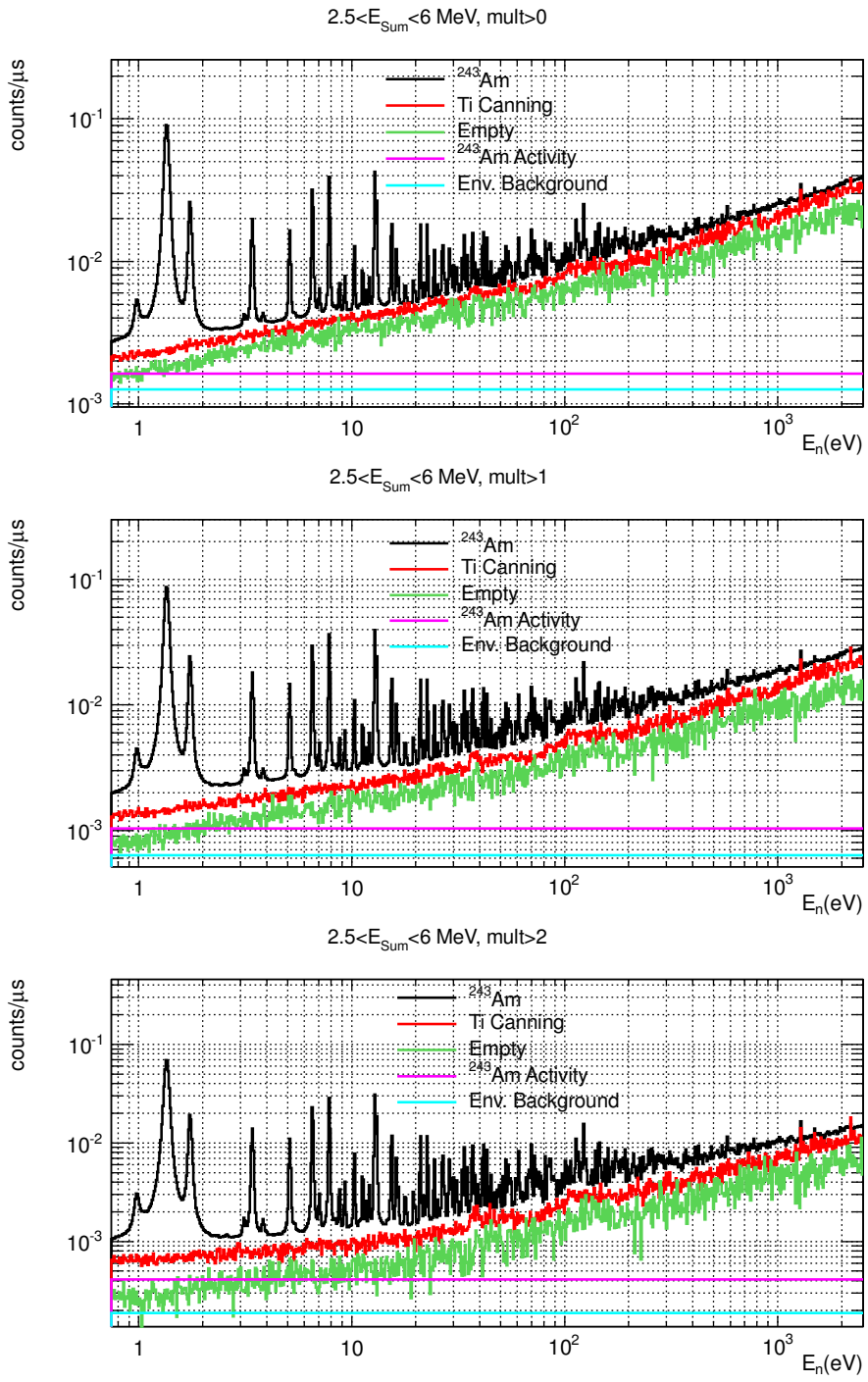

Figure A.11: Detected counting rate as a function of the neutron energy for the ^{243}Am capture measurement and for different background dedicated measurements.

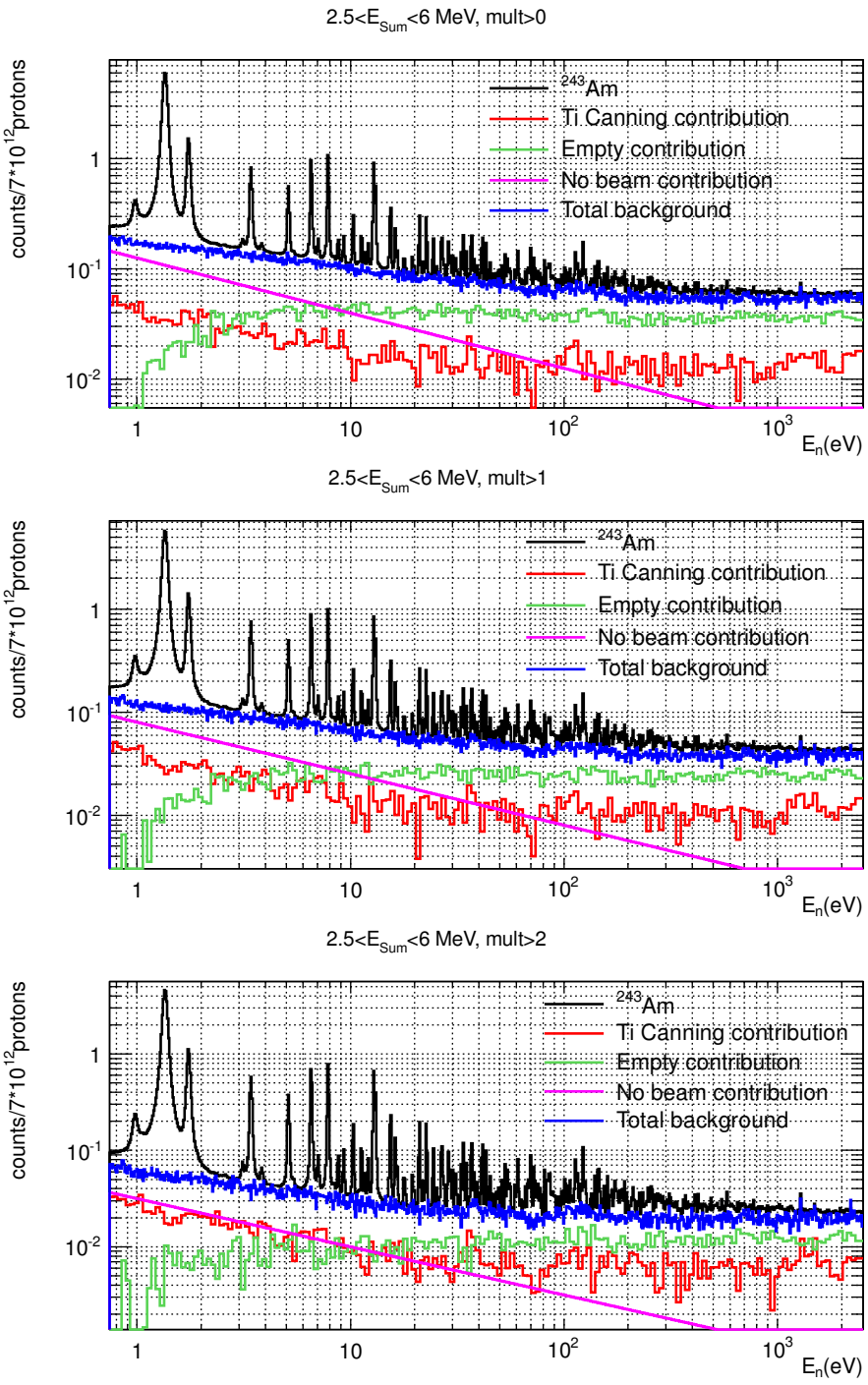

Figure A.12: Number of detected events per proton pulse as a function of the neutron energy for the ^{243}Am capture measurement and for different background dedicated measurements.

Appendix B

Determination of the sample mass with the TAC

The same simulation code used to determine the detection efficiency (Section 3.5) has been used to determine the sample mass by reproducing the ^{243}Am activity measurement:

- The event generator was performed with all the available information taken from ENSDF concerning levels, branching ratios, electron conversion and decay chains (see Section 2.3).
- The Monte Carlo code was the same used for the rest of the simulations.
- In the reconstruction process, the dead tine model used was the one which models the behavior of the analysis routine when there are two signals one close to the other, i.e., the one described in paragraph 2a of Section 3.5.3. The dead time model used under high counting rates constant in time (2b) have not been used in this case, since the ^{243}Am activity is not an external source of signals, but the ones which are being simulated.

Some results are presented in Figures B.1 and B.2, comparing the deposited energy spectra of simulations with 73.6 MBq (nominal mass, 10 mg) and 46.5 MBq (6.3 mg) with the experimental results. As it can be seen, if the nominal mass is assumed, the Monte Carlo results do not reproduce the experimental ones, whereas if a mass around 40% lower is assumed, the experimental results can be acceptably reproduced. In both Figures, an energy threshold of 113 keV has been used in the simulations (100 keV in the reconstruction of the experimental data), and the same energy resolution than for previous simulations. If a higher energy resolution is taken, better results can be achieved.

From these results, it can be concluded that the certified value of the sample mass is not correct, and that its true value should be around 6 mg. However, these Monte Carlo simulations have their limitations, and it has not been possible to obtain an accurate value for the sample mass.

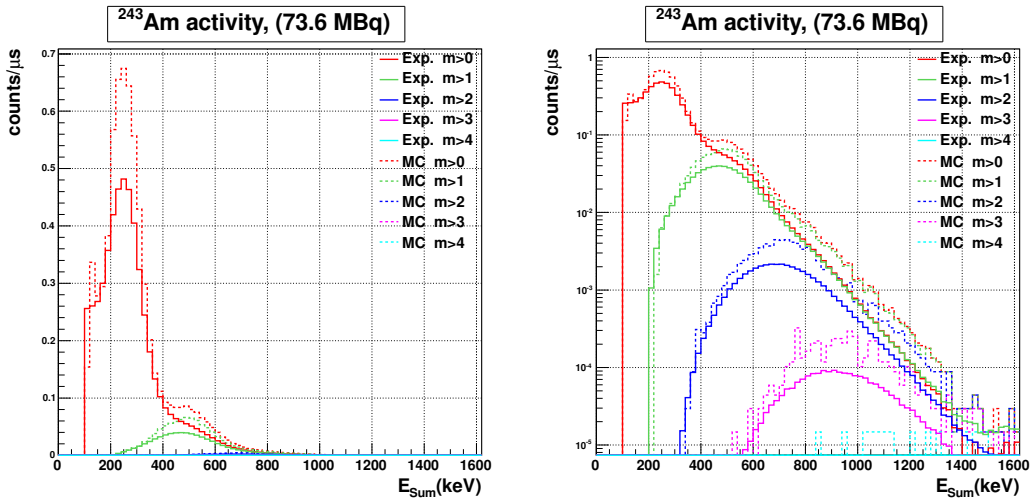

Figure B.1: Comparison between the experimental activity measurement and the simulated results, assuming an activity of 73.6 MBq, which corresponds to a 10mg sample mass. The left panel is in linear scale whereas the right panel is in logarithmic scale.

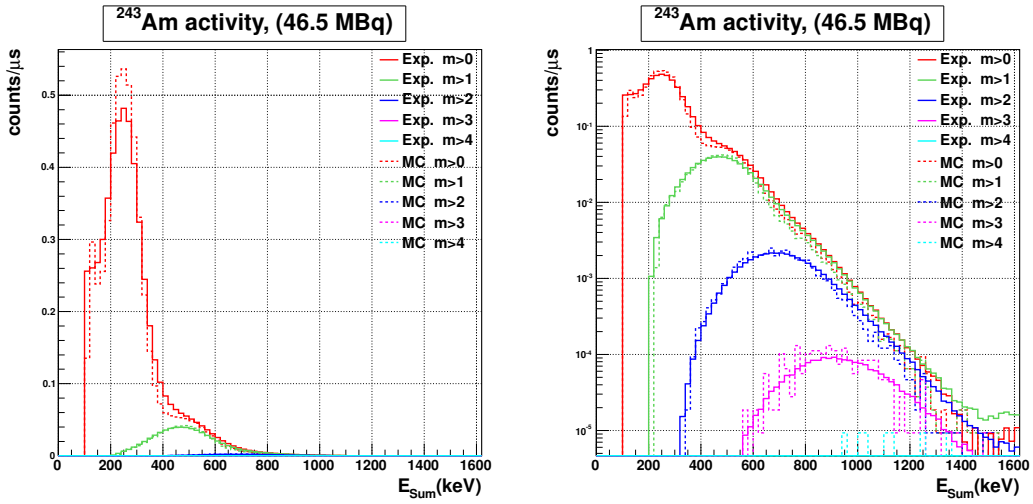

Figure B.2: Comparison between the experimental activity measurement and the simulated results, assuming an activity of 46.5 MBq, which corresponds to a 6.3mg sample mass. The left panel is in linear scale whereas the right panel is in logarithmic scale.

In this case the energy of the simulated γ-rays are lower than in the rest of the cases presented above. It can be seen in Section 2.3 (see Figure 2.9) that the γ-rays emitted in the ^{243}Am decay have, in general, energies lower than 350 keV (only a 5% have greater energies). This fact make that the results of the simulations are especially sensitive to the energy resolution of the crystals and the energy threshold applied in the reconstruction process.

Indeed, after performing several simulations, it was observed that the uncertainty in the sample mass determination was dominated by these two factors. Notice also that the energy calibration and the resolution of the γ-rays below the ^{137}Cs peak (662 keV) were obtained by extrapolating higher energy values (see Sections 3.3.1 and 3.3.3).

In order to assign a central value and an uncertainty to the sample mass calculated from this procedure, several simulations were performed by varying these two parameters in a reasonable range, for different activity values. In particular, the activity was modified between 40 and 60 MBq, the energy threshold between 80 and 130keV and the energy resolution was multiplied by a factor between 0.8 and 1.4. The following quantities were computed, in order to compare with the experimental results:

1. A difference between the experimental and simulated results was defined as:

$$D_{rel} = \sum_m D^m_{rel} \quad ; \quad D^m_{rel} = \frac{1}{N} \sum_{i=i_1}^{i=i_N} \left(\frac{y^{exp}_{m,i} - y^{MC}_{m,i}}{y^{exp}_{m,i}} \right)^2 \tag{B.1}$$

   where $y^{exp}_{m,i}$ and $y^{MC}_{m,i}$ are the i-bin contents of the experimental and simulated deposited energy spectra with multiplicities greater than m. Histograms with multiplicities greater than 0, 1, 2 and 3 have been considered and the operation on the right was performed in different energy ranges, depending of the multiplicity of the histogram: 150-1200 keV for m>0, 250-1200 keV for m>1, 350-1200 keV for m>2, and 600-1200 keV for m>3.

2. A difference between the areas of the experimental and simulated results was defined as:

$$D_{areas} = \sum_m D^m_{areas} \quad ; \quad D^m_{areas} = \left(1 - \frac{Area^m_{MC}}{Area^m_{exp}} \right)^2 \tag{B.2}$$

   where $Area^m_{exp}$ and $Area^m_{MC}$ are the areas of the experimental and simulated deposited energy spectra, with multiplicities greater than m. The areas were computed in the previously mentioned energy ranges.

Both quantities were arbitrarily defined, but they try to express the closeness of the MC results to the experimental ones. As lower are these quantities, better the experimental results are reproduced. Notice that defining a chi-squared function has no sense here, since the statistical uncertainties are negligible in the experimental histograms and can be "infinitely" reduced in the simulated ones.

In Figure B.3 they are presented the results obtained for D_{rel} and D_{areas} for each different threshold and resolution computed values, for a constant activity of 50 MBq. As it can be observed, both D_{rel} and D_{areas} values are much more sensitive to the threshold value than to the resolution of the crystals, but the latter has also some effect.

In order to make an estimation of the uncertainty of the sample mass calculated with this procedure, what has been done is to select, for each simulated activity, the lowest D_{rel} and D_{areas} values. These results are presented in Figure B.4, where it can be seen that both values are too high below 42 MBq and above 57 MBq. These limits have been taken to establish the uncertainty in the sample mass calculation. One of the best results obtained in the simulations is presented in Figure B.5 (49.5 MBq) and the best results obtained from the low and high activity limits in Figures B.6 (56.8 MBq) and B.7 (42.1 MBq).

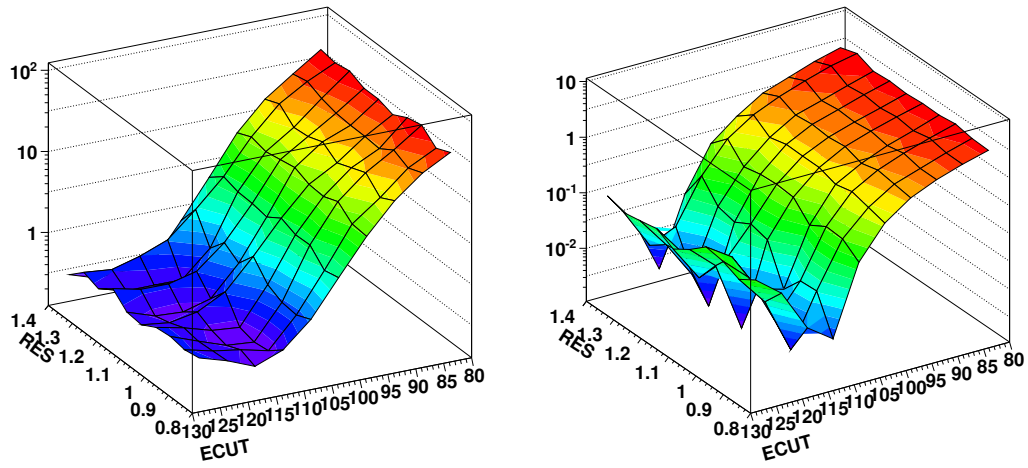

Figure B.3: Results obtained with a simulated activity of 50 MBq for different energy thresholds (ECUT, in keV) and resolution factors (RES). In the left panel, the Z axis corresponds to the D_{rel} defined value, and in the right panel to D_{areas}. It can be seen that the effects of changing the threshold are higher than the effects changing the resolution factor. This behavior is the same for the rest of the computed activity values.

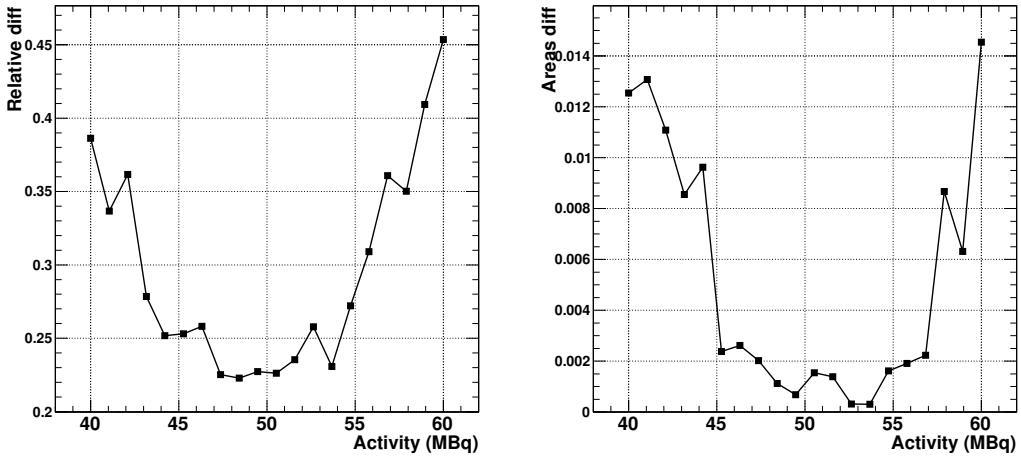

Figure B.4: Minimum D_{rel}(left) and D_{areas}(right) values obtained for all the computed energy thresholds and energy resolution factors for each activity value.

So it can be finally concluded that the sample activity is between 42 MBq and 57 MBq, which corresponds to a mass between 5.7 mg and 7.7 mg. Or, what is the same, an activity of 50 MBq or a mass of 6.7 mg, both with an uncertainty of 15%.

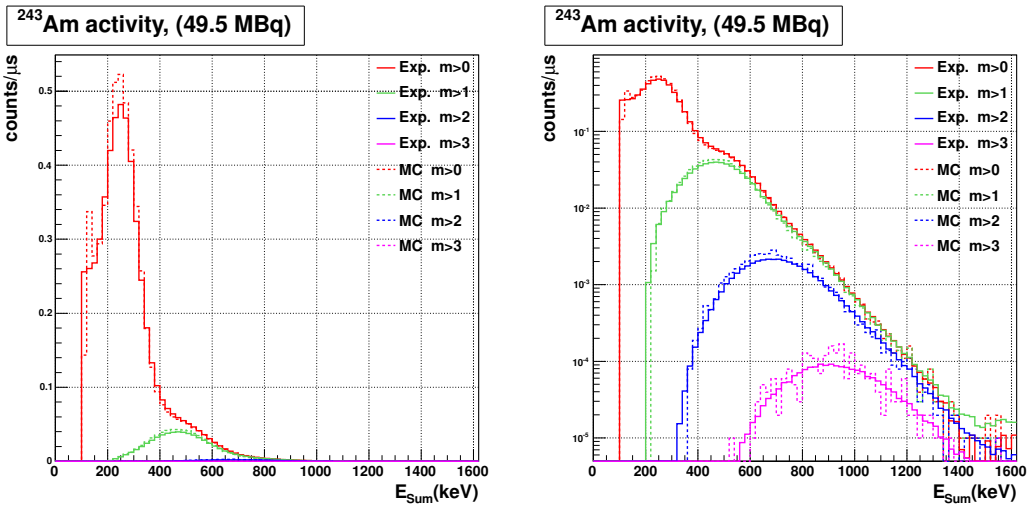

Figure B.5: Comparison between the experimental activity measurement and the simulated result, assuming an activity of 49.5 MBq. The left panel is in linear scale whereas the right panel is in logarithmic scale. The simulated energy threshold is 113 keV and the energy resolution factor 1.4.

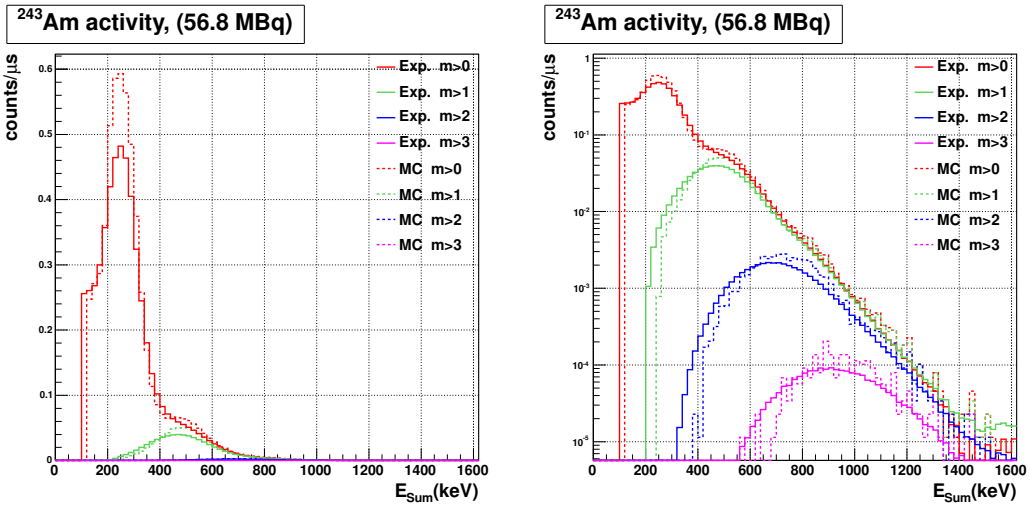

Figure B.6: Comparison between the experimental activity measurement and the simulated result, assuming an activity of 56.8 MBq. The left panel is in linear scale whereas the right panel is in logarithmic scale. The simulated energy threshold is 124 keV and the energy resolution factor 1.07.

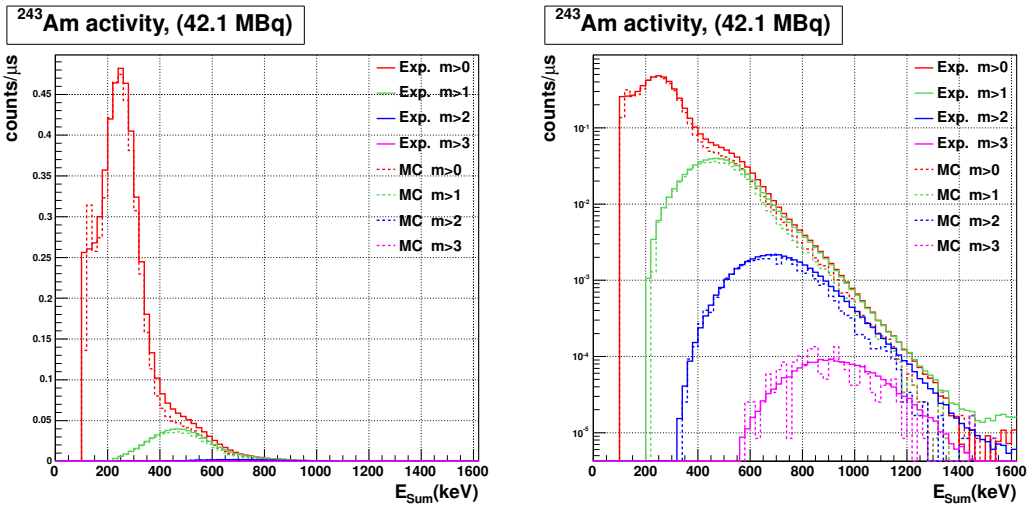

Figure B.7: Comparison between the experimental activity measurement and the simulated result, assuming an activity of 42.1 MBq. The left panel is in linear scale whereas the right panel is in logarithmic scale. The simulated energy threshold is 113 keV and the energy resolution factor 1.4.

Appendix C

Values of the resonance parameters

E_0(eV)	$g\Gamma_n$	$\sigma_{n,s}$	$\sigma_{n,i}$	$\sigma_{n,v}$	$\sigma_{n,h}$	$C_{n,n}$(%)	Γ_γ	$\sigma_{\gamma,s}$	$\sigma_{\gamma,t}$	$\sigma_{\gamma,v}$	$\sigma_{\gamma,p}$	$\sigma_{\gamma,d}$	$\sigma_{\gamma,h}$	$C_{n,\gamma}$(%)
-2.000	0.57350	-	-	-	-	-	39.0	-	-	-	-	-	-	-
0.4151	0.00042	-	-	-	-	-	39.0	-	-	-	-	-	-	-
0.9798	0.006433	0.00004	0.000009	0.00007	0.00003	-4	34.41	0.4	0.10	0.6	0.15	0.9	0.15	71
1.3526	0.48579	0.00024	-	0.0003	0.024	-7	48.5672	0.04	0.11	0.05	0.012	0.0024	2.5	0
1.7395	0.11465	0.00015	-	0.00021	0.0011	0	40.11	0.12	0.15	0.16	0.04	0.04	0.3	33
3.1251	0.004856	0.00012	0.00003	0.00015	0.000009	-14	34.0	2.4	-	1.8	0.4	0.3	-	62
3.4160	0.1389	0.0003	-	0.0003	0.0006	-7	39.93	0.24	0.3	0.3	0.07	0.06	0.23	35
3.8382	0.00608	0.00017	0.00005	0.00022	-	-1	45.2	3	-	2.4	-	-	-	59
5.1122	0.1512	0.0005	-	0.0005	0.0004	-1	40.21	0.4	0.4	0.5	-	0.17	0.17	37
6.5378	0.4824	0.0011	-	0.0007	0.003	-7	41.03	0.3	0.4	0.22	0.04	0.3	0.4	20
7.0467	0.03587	0.0005	0.00009	0.0004	0.00005	-3	47.77	2.1	-	1.2	0.3	-	0.11	60
7.8434	0.6813	0.0015	-	0.0008	0.005	-3	42.91	0.3	0.4	0.20	0.07	0.4	0.5	14
8.3658	0.00788	0.0004	0.00016	0.00016	-	-7	-	-	-	-	-	-	-	-
8.7480	0.06302	0.0008	0.00010	0.0005	0.00004	-8	45.5	1.8	0.4	1.0	0.3	0.4	-	56
9.2931	0.07448	0.0008	0.00010	0.0006	-	-3	40.3	1.6	0.4	0.9	0.8	0.3	-	54
10.286	0.23845	0.0013	0.00008	0.0009	0.0003	-3	53.52	0.9	0.5	0.6	0.06	0.6	0.14	41
10.870	0.00769	0.0005	0.0003	0.00015	-	-8	-	-	-	-	-	-	-	-
11.249	0.14578	0.0013	0.00014	0.0006	0.00012	-13	41.10	1.4	0.6	0.6	0.3	0.6	0.08	50
11.661	0.05176	0.0010	0.00020	0.0004	-	-11	40.81	3	0.22	0.7	-	0.4	-	55
12.098	0.08549	0.0012	0.00017	0.0006	0.00009	-4	42.27	2.2	0.22	0.8	0.4	0.3	-	55
12.846	1.1890	0.004	-	0.0007	0.008	-25	43.48	0.5	0.7	0.15	0.15	0.3	0.5	29
13.124	0.7134	0.003	-	0.0008	0.003	0	46.05	0.8	0.6	0.3	0.18	1.5	0.4	40
15.098	0.03001	0.0011	0.0005	0.00017	0.00009	-20	-	-	-	-	-	-	-	-
15.369	0.6881	0.003	0.0003	0.0011	0.0018	-5	44.05	0.9	0.8	0.3	0.15	1.0	0.3	29
16.178	0.27246	0.0024	0.00024	0.0010	0.0003	-13	44.92	1.6	0.7	0.6	0.10	0.7	0.11	48
16.543	0.09784	0.0015	0.00024	0.0004	-	0	-	-	-	-	-	-	-	-
17.830	0.1115	0.0017	0.0003	0.0005	-	-7	-	-	-	-	-	-	-	-
18.120	0.0200	0.0011	0.0006	0.0003	-	0	-	-	-	-	-	-	-	-
19.496	0.1089	0.0019	0.0003	0.0006	-	-4	-	-	-	-	-	-	-	-
19.869	0.0425	0.0015	0.0005	0.0005	-	1	-	-	-	-	-	-	-	-
20.933	0.2356	0.004	0.0008	-	0.0006	-56	-	-	-	-	-	-	-	-
21.071	0.5822	0.005	0.0008	0.0016	0.0007	-2	42.8	1.7	0.7	0.6	0.3	0.8	0.3	51

Table C.1: Fitted $g\Gamma_n$ and Γ_γ parameters of the ^{243}Am nucleus in the 0 - 21.5 eV energy range, together with their resonance energy (E_0), their statistical uncertainties ($\sigma_{n,s}$, $\sigma_{\gamma,s}$), and their systematic uncertainties due to the choice of the initial values for the fit ($\sigma_{n,ini}$), the 1/V background component ($\sigma_{n,v}$,$\sigma_{\gamma,v}$), the sample inhomogeneities ($\sigma_{n,h}$,$\sigma_{\gamma,h}$), the temperature of the sample ($\sigma_{\gamma,t}$) and the Doppler broadening model ($\sigma_{\gamma,d}$). The correlation of each $g\Gamma_n$ parameter with the $g\Gamma_n$ parameter of the next resonance ($C_{n,n}$) and the Γ_γ parameter of the same resonance ($C_{n,\gamma}$) are also included. All the $g\Gamma_n$ resonance parameters have also a 3% normalization uncertainty. All the values in the table, except E_0, $C_{n,n}$ and $C_{n,\gamma}$ are in meV. Resonances below 0.8 eV are out of the n_TOF capture measurement energy range and the values of the ENDF/B-VII.0 are presented here. Systematic errors below a 5% of the corresponding statistical uncertainty have been omitted. All the omitted Γ_γ values have been fixed to $\langle\Gamma_\gamma\rangle$ = 42 meV.

E_0(eV)	$g\Gamma_n$	$\sigma_{n,s}$	$\sigma_{n,i}$	$\sigma_{n,v}$	$\sigma_{n,h}$	$C_{n,n}$(%)	Γ_γ	$\sigma_{\gamma,s}$	$\sigma_{\gamma,t}$	$\sigma_{\gamma,v}$	$\sigma_{\gamma,p}$	$\sigma_{\gamma,d}$	$\sigma_{\gamma,h}$	$C_{n,\gamma}$(%)
21.840	0.0657	0.003	0.0024	0.0004	-	-71	-	-	-	-	-	-	-	-
21.851	0.0237	0.0022	0.0023	-	-	0	-	-	-	-	-	-	-	-
22.580	0.3509	0.006	0.0013	0.0005	0.0010	-69	41.8	3	0.4	0.5	0.4	-	-	55
22.695	0.5875	0.007	0.0012	0.0012	0.0007	-1	42.5	2.0	0.7	0.5	0.5	1.1	0.3	53
24.404	0.4761	0.005	0.0005	0.0016	0.0004	-2	50.58	2.0	0.8	0.7	0.3	0.8	0.14	40
25.365	0.0797	0.0024	0.0007	0.0006	-	0	-	-	-	-	-	-	-	-
26.208	0.0257	0.0017	0.0012	0.0003	-	-6	-	-	-	-	-	-	-	-
26.695	0.8469	0.006	0.0005	0.0014	0.0014	-8	44.60	1.6	1.0	0.4	-	0.9	0.21	21
27.284	0.2452	0.004	0.0008	0.0011	-	-1	46.2	3	0.4	0.6	-	0.5	-	45
28.673	0.5589	0.006	0.0006	0.0014	0.0005	-11	45.30	2.3	0.8	0.5	-	0.8	0.12	35
29.230	0.3650	0.005	0.0008	0.0012	-	-2	45.29	3	0.7	0.5	0.17	0.8	-	44
30.058	0.2916	0.004	0.0007	0.0009	-	-2	-	-	-	-	-	-	-	-
30.994	0.4023	0.005	0.0008	0.0014	-	-12	42.6	3	0.8	0.6	0.7	0.8	-	39
31.406	0.0937	0.003	0.0013	0.0006	-	0	-	-	-	-	-	-	-	-
32.339	0.0768	0.003	0.0013	0.0007	-	-3	-	-	-	-	-	-	-	-
33.115	0.4816	0.006	0.0009	0.0015	0.0003	-6	51.5	3	0.7	0.6	0.5	0.6	-	37
33.862	0.9399	0.008	0.0007	0.0016	0.0012	-1	40.62	2.0	0.9	0.5	1.0	1.1	0.19	23
34.908	0.4928	0.006	0.0009	0.0011	0.0004	0	-	-	-	-	-	-	-	-
36.583	0.4657	0.009	0.0020	0.0013	0.0005	-32	63.9	4	0.7	0.6	3	0.4	-	51
36.940	1.1680	0.011	0.0016	0.0015	0.0013	-7	56.57	3	1.2	0.4	1.4	1.8	0.24	37
37.498	0.0532	0.003	0.003	0.0003	-	-16	-	-	-	-	-	-	-	-
37.837	0.3786	0.007	0.0017	0.0015	-	-1	54.8	4	0.5	0.5	0.6	0.7	-	40
39.399	0.3007	0.006	0.0013	0.0011	-	0	-	-	-	-	-	-	-	-
40.438	0.0456	0.003	0.0025	0.0005	-	-3	-	-	-	-	-	-	-	-
40.861	0.1369	0.005	0.0022	0.0007	-	-13	-	-	-	-	-	-	-	-
41.165	0.4730	0.010	0.0022	-	0.0007	-32	-	-	-	-	-	-	-	-
41.438	1.3417	0.013	0.0017	0.0020	0.0017	-1	44.51	3	0.9	0.4	1.1	1.5	0.23	32
42.845	1.4935	0.014	0.0013	0.0017	0.003	-1	43.52	2.2	1.0	0.5	1.6	1.2	0.22	-5
44.016	0.2311	0.006	0.0018	0.0011	-	0	-	-	-	-	-	-	-	-
45.242	0.5887	0.009	0.0015	0.0014	-	0	-	-	-	-	-	-	-	-
47.018	0.2125	0.007	0.0024	0.0012	-	0	-	-	-	-	-	-	-	-
48.418	0.2416	0.007	0.0023	0.0012	-	-1	-	-	-	-	-	-	-	-
49.189	0.4093	0.009	0.0018	0.0014	-	-	-	-	-	-	-	-	-	-

Table C.2: Fitted $g\Gamma_n$ and Γ_γ parameters of the ^{243}Am nucleus in the 21.5-50 eV energy range, together with their resonance energy (E_0), their statistical uncertainties ($\sigma_{n,s}$, $\sigma_{\gamma,s}$), and their systematic uncertainties due to the choice of the initial values for the fit ($\sigma_{n,ini}$), the 1/V background component ($\sigma_{n,v}$,$\sigma_{\gamma,v}$), the sample inhomogeneities ($\sigma_{n,h}$,$\sigma_{\gamma,h}$), the temperature of the sample ($\sigma_{\gamma,t}$) and the Doppler broadening model ($\sigma_{\gamma,d}$). The correlation of each $g\Gamma_n$ parameter with the $g\Gamma_n$ parameter of the next resonance ($C_{n,n}$) and the Γ_γ parameter of the same resonance ($C_{n,\gamma}$) are also included. All the $g\Gamma_n$ resonance parameters have also a 3% normalization uncertainty. All the values in the table, except E_0, $C_{n,n}$ and $C_{n,\gamma}$ are in meV. Systematic errors below a 5% of the corresponding statistical uncertainty have been omitted. All the omitted Γ_γ values have been fixed to $\langle\Gamma_\gamma\rangle$=42 meV.

E_0(eV)	$g\Gamma_n$ (meV)	σ_s (meV)	σ_i (meV)	$C_{n,n}$(%)	E_0(eV)	Γ_n (meV)	σ_s (meV)	σ_i (meV)	$C_{n,n}$(%)
50.107	0.058	0.006	0.003	-1	83.309	1.371	0.03	0.006	-15
51.144	0.5068	0.010	0.0022	-1	83.963	0.27	0.07	0.03	-4
52.026	0.039	0.006	0.003	-1	84.011	0.79	0.08	0.03	-95
52.916	1.0431	0.014	0.0020	-2	84.599	0.227	0.016	0.008	-7
53.579	0.035	0.007	0.003	-24	85.267	0.92	0.06	0.03	-4
53.868	0.325	0.010	0.003	-5	85.391	2.59	0.07	0.03	-79
54.393	0.871	0.015	0.004	-41	86.436	0.983	0.024	0.006	-1
54.617	0.153	0.011	0.006	-1	88.133	0.725	0.023	0.007	0
55.737	0.9120	0.014	0.0020	0	88.740	0.819	0.024	0.007	-6
57.194	0.051	0.007	0.004	0	90.165	0.697	0.023	0.008	-1
58.572	0.200	0.010	0.004	-14	91.002	0.607	0.022	0.008	-2
58.953	0.447	0.012	0.003	-1	94.474	0.749	0.03	0.009	0
59.803	0.444	0.012	0.003	-1	95.081	0.105	0.017	0.007	-6
60.605	0.590	0.014	0.003	-10	95.642	0.252	0.020	0.010	-7
61.049	1.527	0.020	0.003	-1	97.283	1.098	0.03	0.009	0
62.370	0.139	0.009	0.005	-2	98.509	0.218	0.020	0.011	-1
63.032	0.226	0.010	0.004	-8	99.280	0.402	0.023	0.011	-2
63.489	0.067	0.009	0.004	-1	100.870	1.833	0.04	0.009	0
64.664	0.314	0.012	0.004	0	101.701	1.531	0.04	0.008	-3
66.067	0.728	0.015	0.003	-1	102.521	0.212	0.021	0.013	-2
67.194	0.602	0.015	0.004	-3	103.830	0.438	0.03	0.013	-1
67.836	0.644	0.015	0.004	-3	104.690	1.264	0.03	0.009	-2
68.524	0.870	0.018	0.004	-1	106.032	0.182	0.022	0.011	-1
69.502	1.928	0.03	0.003	-5	106.793	0.964	0.05	0.020	-3
70.102	1.402	0.023	0.005	0	107.022	1.118	0.05	0.021	-58
71.530	0.094	0.011	0.006	-8	108.425	0.426	0.03	0.014	0
72.035	1.392	0.023	0.004	-4	109.531	0.678	0.03	0.012	-1
72.711	1.647	0.024	0.005	-1	111.280	0.613	0.03	0.014	0
73.713	0.235	0.013	0.006	-14	111.831	0.596	0.03	0.014	-11
74.131	0.266	0.014	0.006	-3	112.651	1.137	0.05	0.023	-3
74.785	0.111	0.012	0.006	-12	112.945	4.196	0.08	0.022	-46
75.253	1.669	0.03	0.005	-1	113.955	2.793	0.06	0.014	-2
76.385	0.158	0.013	0.007	-13	114.731	0.236	0.03	0.014	-4
76.818	0.301	0.015	0.007	-7	116.120	0.139	0.09	0.012	-58
77.362	0.832	0.020	0.005	-3	116.316	4.179	0.04	0.019	0
78.040	0.212	0.014	0.007	0	119.186	0.620	0.04	0.021	0
79.821	0.114	0.013	0.007	-6	119.507	2.044	0.06	0.021	-43
80.396	0.290	0.022	0.012	-59	121.983	3.141	0.06	0.014	0
80.611	0.540	0.03	0.015	-40	123.055	14.08	0.3	0.06	-4
80.899	1.751	0.03	0.008	0	124.880	4.072	0.08	0.015	-1
82.862	0.410	0.018	0.007	-15					

Table C.3: Fitted values of the ^{243}Am $g\Gamma_n$ resonance parameters in the 50 - 125 eV energy range, together with their resonance energy (E_0), their statistical uncertainty (σ_s), their uncertainty due to the choice of the initial values for the fit (σ_i) and the correlation with the Γ_n parameter of the next resonance ($C_{n,n}$). All the $g\Gamma_n$ resonance parameters have also a 3% normalization uncertainty.

E_0(eV)	$g\Gamma_n$ (meV)	σ_s (meV)	σ_i (meV)	$C_{n,n}$(%)	E_0(eV)	Γ_n (meV)	σ_s (meV)	σ_i (meV)	$C_{n,n}$(%)
126.037	0.338	0.03	0.017	-2	166.120	1.01	0.07	0.03	-36
127.053	1.134	0.04	0.015	0	166.469	0.353	0.06	0.025	-48
129.891	0.321	0.03	0.018	0	167.567	3.80	0.11	0.03	-2
132.060	0.310	0.03	0.017	-1	169.394	0.73	0.05	0.03	-1
133.064	0.180	0.03	0.014	-10	172.200	3.60	0.10	0.03	0
133.669	1.049	0.05	0.019	-11	173.081	4.40	0.13	0.04	-6
134.271	0.432	0.04	0.021	-17	174.257	2.12	0.08	0.03	-2
134.795	0.647	0.04	0.020	0	175.280	1.91	0.08	0.03	-3
139.162	0.841	0.05	0.023	-20	176.326	1.89	0.10	0.05	-3
139.682	4.075	0.09	0.021	-4	176.727	3.13	0.11	0.04	-41
140.529	0.303	0.04	0.020	-43	179.537	1.39	0.09	0.05	0
140.871	0.53	0.05	0.03	0	179.911	0.98	0.08	0.04	-47
142.862	0.275	0.04	0.019	-2	180.470	0.63	0.06	0.03	-23
143.893	2.80	0.08	0.03	-33	181.226	1.19	0.07	0.03	-9
144.317	2.75	0.10	0.04	-39	182.516	0.75	0.06	0.03	-1
144.701	0.95	0.06	0.03	-3	183.579	1.82	0.09	0.04	-3
145.705	4.35	0.11	0.03	-25	184.070	2.21	0.09	0.04	-29
146.182	2.78	0.08	0.03	0	185.608	0.65	0.06	0.03	-1
147.839	1.16	0.07	0.03	-44	186.227	1.49	0.09	0.04	-19
148.190	1.44	0.07	0.03	-1	186.654	1.22	0.08	0.04	-39
149.436	0.427	0.04	0.022	-1	187.517	4.42	0.14	0.04	-7
150.717	0.443	0.04	0.024	0	188.382	0.62	0.06	0.03	-6
152.491	0.712	0.05	0.024	-2	189.884	0.69	0.08	0.04	-1
153.616	2.19	0.08	0.03	-12	190.250	0.67	0.08	0.04	-49
154.267	1.860	0.07	0.023	-5	191.064	2.04	0.10	0.04	-8
155.065	0.52	0.05	0.03	0	191.783	2.45	0.10	0.04	-12
158.180	1.85	0.07	0.03	-12	192.902	5.38	0.17	0.05	-3
158.815	0.50	0.05	0.03	-1	195.077	0.235	0.05	0.019	0
160.229	6.05	0.15	0.05	-39	195.821	0.72	0.07	0.04	-9
160.612	0.96	0.07	0.04	0	196.473	1.11	0.08	0.04	-16
163.471	0.293	0.04	0.020	-4	197.187	3.01	0.12	0.05	-13
164.396	2.664	0.08	0.025	-1	199.272	2.53	0.11	0.04	0
165.683	0.64	0.06	0.03	-36					

Table C.4: Fitted values of the ^{243}Am $g\Gamma_n$ resonance parameters in the 125 - 200 eV energy range, together with their resonance energy (E_0), their statistical uncertainty (σ_s), their uncertainty due to the choice of the initial values for the fit (σ_i) and the correlation with the Γ_n parameter of the next resonance ($C_{n,n}$). All the $g\Gamma_n$ resonance parameters have also a 3% normalization uncertainty.

E_0(eV)	$g\Gamma_n$ (meV)	σ_s (meV)	σ_i (meV)	$C_{n,n}$(%)	E_0(eV)	Γ_n (meV)	σ_s (meV)	σ_i (meV)	$C_{n,n}$(%)
201.999	0.52	0.07	0.04	-18	246.467	3.24	0.16	0.07	-1
202.586	0.204	0.05	0.015	-1	247.913	5.54	0.21	0.08	-2
204.043	0.82	0.08	0.04	-19	248.655	2.32	0.15	0.08	-16
204.673	1.17	0.08	0.04	-1	251.053	2.88	0.16	0.07	0
206.078	0.92	0.08	0.04	-1	252.214	6.00	0.3	0.11	-5
207.572	1.63	0.09	0.04	-2	254.482	0.90	0.11	0.06	-1
208.859	2.14	0.11	0.05	-1	255.742	12.9	0.6	0.3	-5
210.283	1.67	0.13	0.07	-57	256.329	1.12	0.13	0.07	-30
210.640	2.05	0.17	0.09	-46	257.622	1.53	0.13	0.07	-2
211.071	3.47	0.17	0.08	-1	258.561	1.49	0.13	0.07	-8
212.793	0.36	0.07	0.03	-3	259.384	7.91	0.3	0.14	-16
213.932	3.47	0.14	0.05	0	260.652	2.70	0.16	0.07	-4
216.325	1.25	0.09	0.04	0	262.868	0.58	0.10	0.04	0
219.483	1.39	0.10	0.05	-26	265.358	1.23	0.14	0.07	0
220.063	0.78	0.10	0.05	-31	265.951	3.28	0.22	0.11	-31
220.603	0.99	0.10	0.05	-24	266.598	5.32	0.3	0.12	-27
221.197	0.68	0.08	0.04	-1	267.837	1.64	0.14	0.07	-4
222.118	0.41	0.08	0.03	-6	271.683	5.93	0.3	0.12	0
222.656	0.42	0.08	0.03	-27	272.757	1.02	0.12	0.06	-6
224.599	4.32	0.17	0.07	-9	273.987	7.42	0.3	0.14	-5
225.471	1.82	0.11	0.05	-8	275.076	2.55	0.17	0.09	-6
226.315	0.50	0.09	0.04	-36	276.909	1.35	0.14	0.08	-1
226.798	1.49	0.11	0.06	-1	277.563	1.57	0.15	0.08	-26
228.388	0.44	0.07	0.03	0	278.924	2.91	0.19	0.09	-3
232.332	4.45	0.17	0.06	-4	280.013	2.55	0.18	0.09	-6
233.502	5.88	0.23	0.09	-1	280.910	0.51	0.11	0.04	-9
235.447	0.65	0.09	0.04	-1	281.542	1.10	0.15	0.07	-26
236.908	1.87	0.12	0.06	-1	282.317	3.81	0.3	0.14	-20
238.468	1.08	0.10	0.05	-27	282.897	7.77	0.4	0.19	-36
239.061	0.75	0.12	0.05	-50	285.633	1.18	0.13	0.07	0
239.468	1.06	0.12	0.06	-1	288.117	4.23	0.24	0.11	0
241.136	0.59	0.09	0.04	-4	289.485	4.86	0.3	0.12	-4
242.239	2.10	0.13	0.06	-1	291.076	6.17	0.3	0.13	-2
243.670	0.84	0.25	0.06	-90	295.672	3.39	0.22	0.11	0
243.781	1.31	0.3	0.08	-14	298.124	1.76	0.16	0.09	0
244.558	1.20	0.11	0.06	-1	299.693	0.97	0.14	0.07	-2

Table C.5: Fitted values of the ^{243}Am $g\Gamma_n$ resonance parameters in the 200 - 300 eV energy range, together with their resonance energy (E_0), their statistical uncertainty (σ_s), their uncertainty due to the choice of the initial values for the fit (σ_i) and the correlation with the Γ_n parameter of the next resonance ($C_{n,n}$). All the $g\Gamma_n$ resonance parameters have also a 3% normalization uncertainty.

E_0(eV)	$g\Gamma_n$ (meV)	σ_s (meV)	σ_i (meV)	$C_{n,n}$(%)	E_0(eV)	Γ_n (meV)	σ_s (meV)	σ_i (meV)	$C_{n,n}$(%)
300.418	0.88	0.14	0.07	-10	350.889	2.43	0.3	0.13	-10
301.363	1.43	0.16	0.09	-15	351.673	1.35	0.20	0.10	-21
302.211	3.65	0.24	0.11	-3	353.935	0.47	0.14	0.04	-1
303.571	0.66	0.14	0.06	-20	355.336	1.08	0.18	0.08	-3
304.369	8.06	0.4	0.19	0	357.665	2.44	0.24	0.13	-1
307.084	1.86	0.18	0.10	-13	360.478	2.26	0.24	0.13	0
307.989	3.52	0.24	0.12	0	361.742	4.42	0.4	0.21	-7
310.268	0.69	0.14	0.06	-13	362.279	3.81	0.4	0.19	-46
311.234	8.34	0.4	0.20	-10	363.254	1.47	0.21	0.10	-14
312.223	1.40	0.17	0.09	-6	364.130	1.35	0.22	0.10	-17
313.586	11.0	0.6	0.3	-2	364.859	1.50	0.22	0.11	-27
315.387	4.71	0.3	0.15	-8	367.281	2.76	0.3	0.15	-1
316.432	0.93	0.15	0.07	-6	368.092	1.74	0.24	0.12	-22
317.607	2.25	0.20	0.10	-1	369.593	22.2	1.6	0.9	-8
319.832	0.68	0.14	0.06	-8	370.875	3.56	0.3	0.17	-10
320.986	9.6	0.5	0.3	-11	372.679	2.46	0.3	0.14	-2
321.949	0.81	0.15	0.06	0	373.365	1.09	0.21	0.08	-29
325.890	0.47	0.22	0.04	-67	375.489	1.42	0.21	0.11	-1
325.731	0.74	0.20	0.07	-18	376.691	2.39	0.3	0.13	-8
326.558	3.98	0.3	0.16	-28	378.523	1.05	0.22	0.09	-2
327.256	2.66	0.3	0.13	-1	379.189	3.92	0.4	0.18	-35
328.915	0.40	0.13	0.05	-13	380.270	4.85	0.4	0.21	-12
329.789	0.90	0.18	0.07	-25	381.400	3.15	0.3	0.16	-10
330.480	0.96	0.19	0.08	-21	382.246	2.39	0.3	0.15	-21
331.261	1.84	0.22	0.11	-11	384.143	2.92	0.3	0.15	-2
332.280	4.68	0.3	0.17	-4	384.967	1.84	0.25	0.12	-22
333.703	3.23	0.3	0.15	-5	388.234	3.33	0.3	0.17	0
334.963	2.78	0.3	0.13	-3	389.368	3.14	0.3	0.16	-10
336.479	4.38	0.3	0.16	-4	390.358	0.71	0.18	0.05	-11
337.849	1.92	0.23	0.12	-15	391.073	0.98	0.20	0.08	-24
338.761	3.97	0.3	0.16	-1	392.314	1.66	0.24	0.12	-6
341.211	2.55	0.25	0.13	-4	393.751	8.1	0.6	0.3	-6
342.592	1.62	0.21	0.10	-3	395.109	0.53	0.16	0.04	-5
344.105	1.16	0.19	0.09	-1	396.471	3.29	0.4	0.20	-5
346.021	0.45	0.14	0.04	-3	396.987	1.52	0.3	0.12	-49
347.545	7.48	0.5	0.24	-1	399.229	3.45	0.3	0.17	-1
349.886	0.62	0.16	0.06	-10					

Table C.6: Fitted values of the ^{243}Am $g\Gamma_n$ resonance parameters in the 300 - 400 eV energy range, together with their resonance energy (E_0), their statistical uncertainty (σ_s), their uncertainty due to the choice of the initial values for the fit (σ_i) and the correlation with the Γ_n parameter of the next resonance ($C_{n,n}$). All the $g\Gamma_n$ resonance parameters have also a 3% normalization uncertainty.

Appendix D

Resumen en español (Summary in Spanish)

Este trabajo presenta el análisis de la medida de captura neutrónica del ^{243}Am realizada en la instalación n_TOF del CERN, en el rango de enrgías de 0.7 eV hasta 2.5 keV. La importancia de esta medida está relacionada con el diseño de nuevos reactores nucleares, especialmente en lo relacionado con la transmutación de residuos radioactivos. En este momento no existe ninguna publicación con resultados finales de ninguna medida de captura del ^{243}Am por debajo de 250 eV, excluyendo el punto térmico. Sí se han realizado algunas medidas de captura, pero sus resultados no están publicados aún. Las secciones eficaces de captura del ^{243}Am que se encuentran en las evaluaciones actuales se basan fundamentalmente en medidas de transmisión.

D.1 Introducción

En estos últimos años los datos nucleares de actínidos minoritarios (normalmente se llama así a los isótopos de Np, Am y Cm) han ganado importancia debido a que son necesarios para el diseño y mejora de reactores nucleares avanzados y dispositivos para la transmutación de residuos nucleares [Sal08, Ali04, Ali06]. En concreto, el ^{243}Am es el actínido minoritario que más contribuye a la radiotoxicidad del combustible gastado en tiempos próximos a su vida media (7370 años). Además, la mayor parte del ^{244}Cm que se produce en reactores nucleares lo hace a través de la reacción ^{243}Am(n,γ). Éste último isótopo, ^{244}Cm, es importante porque es un potente emisor de neutrones y porque es la puerta para crear cualquier isótopo más pesado.

En la Tabla D.1 se muestran todos los datos diferenciales (en función de la energía) disponibles en este momento que son útiles para la evaluación de la sección eficaz de la reacción ^{243}Am(n,γ) . Como puede verse, en este momento sólo hay dos medidas de captura por debajo de 250 eV, excluyendo ésta, y sus resultados finales no han sido publicados ni tampoco están disponibles en EXFOR. La sección eficaz de captura del ^{243}Am por debajo de 250 eV en las librerías de datos nucleares actuales (en este momento las últimas versiones son JEFF-3.1.2, ENDF/B-VII.1, JENDL-4.0, ROSFOND-2010 y CENDL-3.1) se basa principalmente en la medida de transmisión de Simpson et al., que es la única que se extiende por encima de 35 eV. Los resultados diferenciales se complementan con los datos integrales de la Tabla D.2, entre los que se pueden apreciar diferencias significativas.

Referencia	Tipo de medida	Rango de energías
T.S.Bellanova et al. (1976) [Bel76]	Transmisión	0.35 eV - 35 eV
O.D.Simpson et al. (1974) [Sim74]	Transmisión	0.5 eV - 1 keV
J.R.Berreth et al. (1970) [Ber70]	Transmisión	0.008 eV - 25.6 eV
R.E.Cote et al. (1959) [Cot59]	Transmisión	0.0014 eV - 15.44 eV
L.W.Weston et al. (1985) [Wes85]	Captura	258 eV - 92.1 keV
K. Wisshak et al. (1983) [Wis83]	Captura	5 - 250 keV
Kobayashi et al. (1999) [Kob99]	Fisión	0.056 eV - 7.94 keV
H-H. Knitter et al (1988) [Kni88]	Fisión	1 eV - 10 MeV
P.A.Seeger et al. (1970) [See70]	Fisión	0.489 eV - 2.97 MeV
M. Jandel et al. (2009) [Jan09]	*Captura*	*8 eV - 250 keV*
J. Hori et al. (2009) [Hor09]	*Captura*	*0.01 - 400 eV*
Este trabajo	Captura	0.7 - 2500 eV
Kimura et al. , 2012 [Kim12]	*Captura*	-
Alekseev et al. , 2011 [Ale12]	*Fisión*	-

Table D.1: Medidas diferenciales del ^{243}Am realizadas hasta ahora. En el caso de las medidas de fisión, sólo aparecen aquellas cuyo rangeo de energías solapa con el de este trabajo. Los resultados de M. Jandel et al. y J. Hori et al. no se han publicado aún (ni la tasa de reación ni la sección eficaz). Kimura et al. sólo dan los parámetros de la resonancia a 1.35 eV , y Alekseev et al. los parámetros de las resonancias que están por debajo de 17 eV.

Referencia	σ_0(barn)	I_0(barn)	I_0/σ_0
Hori et al. (2009) [Hor09]	76.6[a]	1970(110)	25.7(15)
Marie et al. (2006) [Mar06.2]	81.8(36)		
Ohta et al. (2006) [Oht06]		2250(300)[b]	28(4)
Y. Hatsukawa et al. (1997) [Hat97]	84.4		
Gavrilov et al. (1977) [Gar76]	83(6)	2200(150)	26.5(26)
Simpson et al. (1974) [Sim74]		1819(80)[c]	
Eberle et al. (1971) [Ebe71]	77(2)	1930(50)[c]	25.1(9)
Berreth et al. (1970) [Sim74]	85(4)	1824(80)[c]	21.5(14)
Folger et al. (1968) [Fol68]	78	2250[d]	29
Bak et al (1967) [Bak67]	73(6)	2300(200)	32(4)
Ice et al. (1966) [Ice66]	$66<\sigma_0<84$		
Butler et al (1957) [But57]	73.6(1.8)	2290(50)	31(1)
Harvey et al (1954) [Har54]	140(50)		
Stevens et al. (1954) [Ste54]	115		
Mughabghab (2006) [Mug84]	75.1(18)	1820(70)	24.2(11)
ENDF/B-VII.1 [Cha11]	80.4	2051	25.5
ENDF/B-VII.0 [Cha06]	75.1	1820	24.2
JENDL-4.0 [Shi11]	79.3	2040	25.7
JEFF-3.1 [JND06]	76.7	1788	23.3

Table D.2: Secciones eficaces térmicas de captura σ_0, valores de $I_0=\int_{0.5eV}^{\infty}\sigma_\gamma(E)/EdE$ y cocientes entre ambos resultantes de varios experimentos y evaluaciones.

[a] Valor utilizado para normalizar, por lo que I_0 es proporcional a él.

[b] Se ha adoptado el valor térmico de Marie et al.. El valor medido de Ohta et al. fue $\hat{\sigma}$ = 174.5(5.3)barn, y α=0.0418(45), siendo $I_0=\hat{\sigma}/\alpha+(0.45\text{-}1/\alpha)\sigma_0$.

[c] La energía inferior de la integral es 0.625 eV en lugar de 0.5 eV.

[d] La energía inferior de la integral es 0.83 eV en lugar de 0.5 eV.

Por encima de 250 eV existen dos medidas, una entre 250 eV y 5 keV, Weston et al., que consta de dos conjuntos de datos que difieren por debajo de 2 keV, y otra entre 5 y 250 keV, Wisshak et al., cuyos resultados son un 10-15% menores que los obtenidos por Weston et al.. Además de estas medidas diferenciales, existen medidas integrales realizadas en reactores rápidos que dan información sobre la sección eficaz de captura del ^{243}Am en la parte rápida (por encima de las decenas de keV, principalmente). Las mayor parte de las evaluaciones no están de acuerdo con algunos de estos experimentos integrales [Pal05, Kah11], lo que ha motivado cambios como los introducidos en ENDF/B-VII.1 [Cha11].

La ausencia de datos, las inconsistencias que se acaban de presentar, y el reciente interés en el diseño de nuevos reactores nucleares, han motivado nuevas medidas de captura neutrónica en ^{243}Am, como la que se presenta en este trabajo o las de Jandel et al. y Hori et al..

D.2 Configuración experimental

D.2.1 La instalación n_TOF del CERN

La instalación n_TOF del CERN (fase 1[1]) [NTC03] consta de una fuente pulsada de neutrones acoplada a una línea de haz en vacío de casi 200 m de longitud que termina en un área experimental. Está diseñada para estudiar reacciones neutrónicas en núcleos atómicos para energías del neutrón que van desde unos pocos meV hasta varios GeV. Los neutrones se producen en reacciones de espalación inducidas por un haz de protones de 20 GeV/c, 16 ns de anchura temporal (*FWHM*) y con una tasa de repetición típica de 0.4 Hz. La fuente de espalación es un bloque de 80x80x60 cm^3 de plomo rodeado por 5.8 cm de agua, que sirve como refigerante y al mismo tiempo como moderador del inicialmente rápido espectro de neutrones. Los neutrones viajan por la línea de vacío, orientada unos 10º respecto del haz de protones, hasta alcanzar el área experimental. Durante este trayecto, dos colimadores dan forma al haz y un imán deflecta las partículas cargadas. La instalación n_TOF se ha usado principalmente para medir reacciones de fisión y de captura relevantes para la astrofísica nuclear y para la tecnología nuclear.

D.2.2 El sistema de detección

Hay tres detectores distintos que monitorizaron el haz de neutrones durante la medida: un *wall current monitor* [NTC03] y un *wall current transformer* [NTC03], que se usaron para monitorizar la corriente del haz de protones, y un *silicon flux monitor* [Mar04], que se utilizó para monitorizar la intensidad del haz de neutrones directamente. Éste último se situó unos dos metros antes de la muestra irradiada.

Las reacciones de captura en ^{243}Am se midieron con el Calorímetro de Absorción Total (TAC) [Gue09], mediante la detección en coincidencia de los gammas emitidos tras la reacción ^{243}Am(n,γ). El TAC, que se muestra en la Figura D.1, es un detector segmentado de tipo 4π compuesto por 40 cristales de BaF_2. Cada cristal se ha construido cortando cilindros de BaF_2 de 14 cm de diámetro y 15 cm de largo. Para minimizar la detección de neutrones dispersados en el centro del calorímetro los detectores están metidos en unas cápsulas de fibra de carbono con un alto contenido en ^{10}B. El TAC está dividido en dos semiesferas, que se pueden abrir y cerrar, formando una esfera de unos 10 cm de radio interno y 15 cm de espesor, cubriendo aproximadamente el 95% del ángulo sólido. Para minimizar aún más la detección de neutrones dispersados, se situó un absorbente neutrónico de unos 5 cm de espesor hecho de $Li_2C_{12}H_{20}O_4$ entre la muestra y el TAC.

[1] n_TOF se cerró en 2004, abriéndose de nuevo en 2009 (fase 2) con un blanco de espalación diferente.

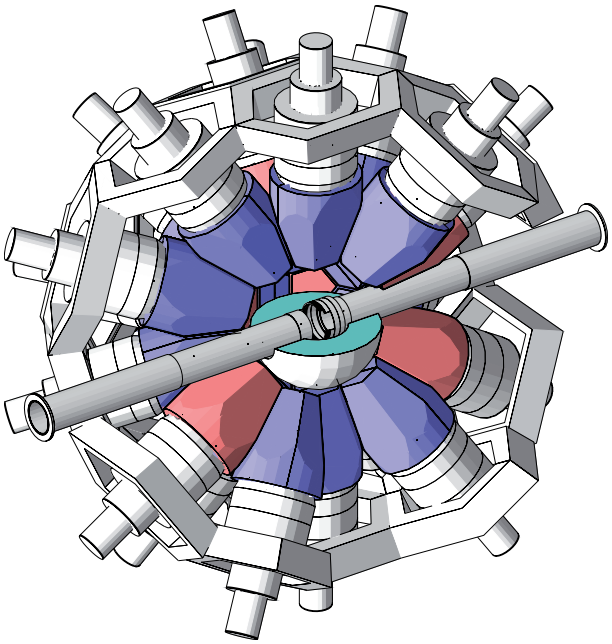

Figure D.1: Geometría del TAC implementada en el código de simulación Monte Carlo GEANT4 [GEAxx].

Las señales del detector se grabaron con un sistema de adquisición digital [Abb05], basado en digitalizadores Acqiris-DC270 de 8 bits de resolución, operando a 250 MHz y grabando de manera continua 16 ms de tiempo de vuelo por cada pulso, lo que se corresponde con grabar todas las señales registradas correspondientes a neutrones incidentes con energías superiores a 0.7 eV. Los datos registrados se analizaron posteriormente con una rutina de reconstrucción de pulsos diseñada especialmete para el TAC. Esta rutina viene descrita en [Ber04], y una referencia más accesible de una rutina parecida es [Mar06.1]. Para cada señal la rutina devuelve el tiempo de vuelo, el área, y otros parámetros necesarios para diferenciar la partícula detectada: γ o α, viniendo la última de la desintegración de impurezas de Ra presente en los cristales. Cada detector se calibró en energías con medidas realizadas con fuentes de calibración estándar (^{137}Cs, ^{60}Co, ^{88}Y, ^{24}Na y Pu/C), y las variaciones en la ganancia de los detectores a lo largo del tiempo fue corregida a partir de los cambios observados en los espectros α de energía depositada en cada cristal. Una vez que los detectores fueron calibrados en energías y en tiempos, se realizó un análisis de coincidencias, siendo agrupadas las señales de cada detector en *eventos*, estando cada uno de éstos caracterizado por su tiempo de vuelo, su energía depositada total (suma de cada una de las señales en coincidencia) E_{Sum} y por su multiplicidad de detección (número de detectores en coincidencia) m_{cr}. Para realizar este análisis de coincidencias se utilizó una ventana temporal de 20 ns. Los valores de E_{Sum} y m_{cr} se utilizaron para imponer condiciones en los eventos detectados, y de esta manera mejorar la relación señal-ruido.

D.2.3 Muestras y medidas

La muestra de ^{243}Am se fabricó en el IPPE, situado en Obsnik (Rusia) en Febrero de 2004. El Am estaba en forma de óxido (AmO_2), formando un polvo que estaba depositado en una lámina de Al de 10 mm de diámetro y menos de 70 mg, de acuerdo con los fabricantes. Todo ello estaba dentro de una cápsula de titanio de 15 mm de diámetro y 0.17 y 0.18 mm de grosor por delante y por detrás de la muestra. Toda ella fue pesada en el CERN, obteniendo como resultado 420.9(1) mg. De acuerdo con los fabricantes, la masa del depósito de AmO_2 tenía que ser de 11.3 mg, y la masa de ^{243}Am, 10 mg. Sin embargo, este valor de la masa no concuerda con lo obtenido de una medida de la actividad de la muestra hecha con detectores de Ge en el CERN (7.34±15% mg) ni con los resultados obtenidos de medir la actividad con el TAC (6.77±15% mg). Por este motivo, la medida ha sido normalizada a medidas de transmisión disponibles en EXFOR, en concreto a las realizadas por Simpson et al. [Sim74], consiguiéndose una incertidumbre en la normalización de un 3%, y una masa de la muestra de 6.23±4% mg, que está de acuerdo con las dos medidas de la actividad antes mencionadas. Las impurezas en la muestra se determinaron durante el análisis de las resonancias, encontrándose unos 0.048 mg de ^{241}Am y 0.0025 mg de ^{240}Pu. La temperatura de la muestra durante la medida fue de 293±4 K, que es la temperatura del área experimental.

La muestra se situó en el centro del TAC durante la medida, sostenida por dos láminas de kapton de 25 μm de espesor y rodeada por el absorbente neutrónico. Dada la alta tasa de contaje, se rodeó también de un cilindro de plomo de 1 mm de espesor y 11.5 cm de largo, rodeando el tubo del haz de 5.2 cm de diámetro, impidiendo la detección de la mayoría de los rayos γ de baja energía (200-300 keV) producidos en la desintegración de la muestra. Aún así, la detección de estas desintegraciones han hecho que la tasa de contaje registrada por el TAC haya sido la mayor de todas las medidas hechas con el TAC hasta la fecha.

Otras tres muestras se midieron también, con las mismas condiciones experimentales: (i) una cápsula de titanio vacía, similar a la utilizada en la medida de ^{243}Am pero con una masa ligeramente diferente; (ii) una muestra de grafito de 10 mm de diámetro y 70.0(1) mg, que sirve para determinar la respuesta del TAC a neutrones dispersados; y (iii) una muestra de ^{197}Au de 10 mm de diámetro y 185.4(1) mg, que vale para determinar la fracción del haz interceptada por la muestra y para validar las técnicas de análisis.

Además de éstas, se hicieron otras medidas para caracterizar el fondo: una medida sin haz y sin muestra, otra sin haz y con muestra, y otra con haz pero sin ninguna muestra. Todas ellas se detallan en la Tabla D.3

Medida	#pulsos	#protones
^{243}Am	$1.86{\cdot}10^{5}$	$1.27{\cdot}10^{18}$
Fondo ambiental	$1.37{\cdot}10^{4}$	–
Actividad	$1.53{\cdot}10^{4}$	–
^{197}Au	$2.19{\cdot}10^{4}$	$1.53{\cdot}10^{17}$
Grafito	$3.76{\cdot}10^{3}$	$2.67{\cdot}10^{16}$
Cápsula de Ti	$1.49{\cdot}10^{3}$	$1.04{\cdot}10^{16}$
Haz sin muestra	$4.16{\cdot}10^{3}$	$2.94{\cdot}10^{16}$

Table D.3: Número de pulsos y protones dedicados a cada medida.

D.3 Reducción de datos

En esta Sección describiremos el proceso de análisis que lleva a la obtención de la tasa de captura experimental, que puede calcularse a partir de:

$$Y_{n,\gamma}(E_n) = \frac{C_{tot}(E_n) - C_{bkg}(E_n)}{\varepsilon \cdot F_{BIF} \cdot \phi(E_n)} \tag{D.1}$$

donde $C_{tot}(E_n)$ y $C_{bkg}(E_n)$ son el número de cuentas de la medida y del fondo registradas por el TAC, respectivamente, bajo ciertas condiciones en E_{Sum} y m_{cr}; ε es la eficiencia de detección bajo esas condiciones; $\phi(E_n)$ es la fluencia total de neutrones y F_{BIF} la fracción de neutrones del haz interceptados por la muestra.

Todo el proceso de reducción de datos es similar al descrito en [Gue12.2], con la excepción de algunas técnicas que se han desarrollado en este trabajo para tener en cuenta los efectos derivados de tener una tasa de contaje mucho más alta que las tenidas hasta este momento (5.4 eventos/μs), y que se deben a la detección de la actividad de la muestra.

D.3.1 Caracterización del fondo

El fondo en la medida puede dividirse en dos contribuciones: (i) eventos que vienen de neutrones dispersados o fisionados en los núcleos de ^{243}Am; y (ii) el resto del fondo, que es la suma del fondo ambiental, la actividad intrínseca de los cristales de BaF_2, el debido a la actividad de la muestra y el debido al haz de neutrones salvo su interacción con los núcleos de ^{243}Am.

Esta segunda contribución podría obtenerse directamente, en principio, a partir de las distintas medidas de fondo presentadas en la Tabla D.3, tras normalizar, sumar y restar apropiadamente las distintas contribuciones. Sin embargo, durante la medida del ^{243}Am la detección de los eventos de fondo está distorsionada por los efectos de apilamiento de pulsos (*pulse pile-up* en inglés) y tiempo muerto inducidos por la actividad de la muestra, mientras que en las medidas de fondo no lo están. Esto hace que el fondo no pueda obtenerse directamente de las medidas de fondo, habiendo sido necesario hacer algunas correcciones. Estas correcciones se describen en detalle en [Men14], y se basan en la manipulación de las señales digitalizadas almacenadas en memoria.

En la Figura D.2 se presenta el espectro de energía depositada en el TAC obtenido durante la medida de ^{243}Am(n,γ), para neutrones de entre 1 y 10 eV, junto con varias contribuciones al fondo: el fondo total (*dummy sample*), todas las contribuciones menos la que viene de la interacción de los neutrones del haz con la cápsula de titanio (*sample out*), y la contribución no relacionada con el haz de neutrones (*No beam*). La parte de los espectros que está por debajo de $\sim$2 MeV se corresponde principalmente con eventos relacionados con la actividad de la muestra, mientras que por encima de 6 MeV los eventos registrados se deben a fondo relacionado con el haz de neutrones, ya que la energía total de la cascada emitida tras la captura en ^{243}Am no puede exceder la energía de separación neutrónica del núcleo compuesto $S_n(^{244}\text{Am})$=5.36 MeV, y los eventos de fondo no debidos al haz tienen energías menores. Por este motivo, por encima de E_{Sum}=6 MeV el espectro de fondo total debería coincidir con el de la medida de ^{243}Am(n,γ). Como puede verse, ésto sólo ocurre si las correcciones de apilamiento de pulsos se tienen en cuenta (panel de la derecha).

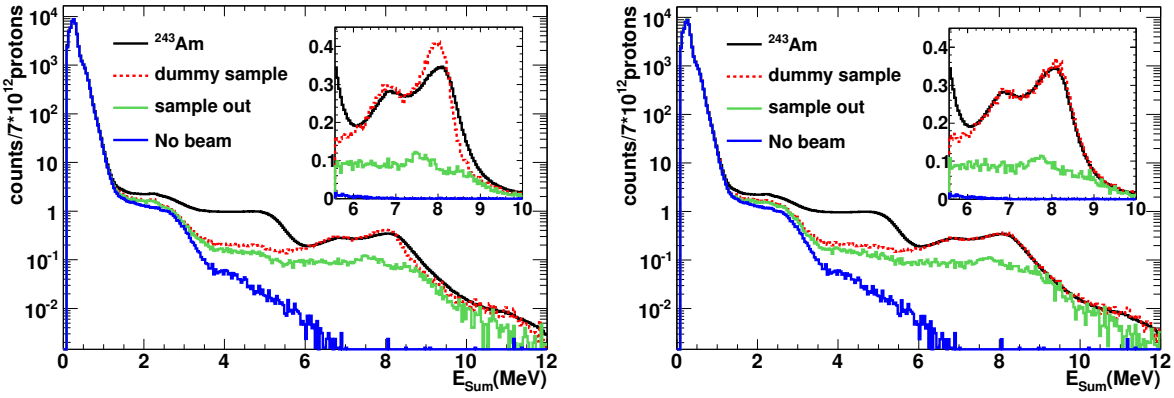

Figure D.2: Espectros de energía depositada en el TAC en la medida de ^{243}Am junto con varias contribuciones al fondo, sin aplicar (izquierda) y aplicando (derecha) las correcciones de apilamiento de pulsos en la obtención de los fondos. En la parte superior izquierda de cada gráfico, se presenta un zum de la parte de altas energías. Los histogramas presentados se corresponden con energías del neutrón de entre 1 y 10 eV.

Puede también observarse en la Figura D.2 que la relación señal-ruído mejora sustancialmente si no se tienen en cuenta los eventos que están por debajo de E_{Sum}=2 MeV ni los que están por encima de E_{Sum}=6 MeV. Ocurre lo mismo si además se ponen condiciones en la multiplicidad de detección (m_{cr}), ya que los eventos de captura tienen, en promedio, mayor multiplicidad que los debidos al fondo. Por otra parte, hay que tener en cuenta que cuanto más restrictivas son las condiciones en E_{Sum} y m_{cr}, menor es la eficiencia de detección. Tras un análisis detallado, se ha llegado a la conclusión que las condiciones óptimas en E_{Sum} y m_{cr} vienen dadas por 2.5<E_{Sum}<6 MeV y m_{cr}>2, y son las que se han utilizado en el análisis. El número de eventos detectados por pulso bajo esas condiciones se presenta en la Figura D.3, en función de la energía del neutrón. Puede verse que el fondo es relativamente suave hasta E_n=2-3 keV, donde comienzan a ser relevantes las resonancias del ^{nat}Ti. Estas resonancias no han permitido medir por encima de 2.5 keV, el límite superior en energías de esta medida. El límite inferior de 0.7 eV viene dado por los 16 ms de tiempo de vuelo grabados.

Como consecuencia de pequeñas diferencias en la calibración en energías debidos al método de corrección del apilamiento de pulsos [Men14], no ha sido posible determinar experimentalmente una componente del fondo constante en el tiempo. Esta componente se ha obtenido tras hacer un ajuste del fondo de la tasa de reacción obtenida. Su incertidumbre puede expresarse como a=0$\pm 3\cdot 10^{-5}\sqrt{eV}$, siendo el fondo total B(E_n)+a/$\sqrt{E_n}$. La incertidumbre relativa del fondo debido a esta componente es 1%, 0.6%, 0.3% y 0.13% a 1, 10, 100 y 1000 eV, respectivamente.

La componente del fondo relacionada con la interacción de los neutrones del haz con los núcleos de ^{243}Am sigue una estructura resonante similar a la de la sección eficaz de la reacción ^{243}Am(n,γ). Es posible hacer una estimación de estas contribuciones a partir de las secciones eficaces evaluadas si se conocen las probabildades de detectar una fisión o un neutrón dispersado en ^{243}Am. La última se ha obtenido a partir de la medida de la muestra de grafito, si se asume que los ángulos y energías de los neutrones dispersados en grafito y en ^{243}Am son parecidos. Esta probabilidad depende de las condiciones en E_{Sum} y m_{cr}, que se han sido seleccionadas para hacer pequeña dicha

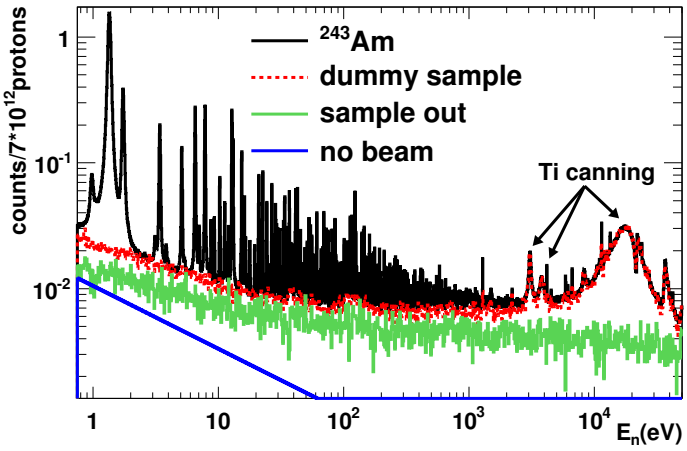

Figure D.3: Número de eventos detectados por pulso en la medida de ^{243}Am(n,γ) en función de la energía del neutrón, junto con distintas contribuciones al fondo y bajo las condiciones de 2.5<E_{Sum}<6 MeV y m_{cr}>2.

probabilidad. Tomando ésta junto con las secciones eficaces que aparecen en ENDF/B-VII.0 se obtiene que la contribución al fondo debida a los neutrones dispersados es menor del 0.5% en todo el rango de energías, incluso en el centro de las resonancias. El mismo cálculo se ha realizado con los eventos de fisión, en este caso asumiendo una eficiencia de detección sobreestimada del 100%, encontrando que la contribución de la fisión al total de eventos registrados es menor del 1% en todo el rango de energías. Por este motivo, ambas contribuciones se han considerado despreciables y no se han tenido en cuenta en el análisis.

D.3.2 Eficiencia de detección y determinación de la actividad de la muestra

La eficiencia de detección se ha obtenido a partir de simulaciones Monte Carlo. Las simulaciones constan de tres partes: (i) la generación de las cascadas de captura, que ha sido realizada con el código DECAYGEN [Tai07, Tai02]; (ii) el transporte de dichas cascadas con el código GEANT4 en la geometría del TAC; y (iii) la reconstrucción de los eventos detectados, que se hace de la misma manera que en un experimento real, teniendo en cuenta efectos instrumentales como la resolución en energías de los detectores y los efectos de apilamiento de pulsos. La generación de las cascadas de captura incluye modelos estadísticos que dependen de unos parámetros. Estos parámetros se ajustan hasta que se reproducen los resultados experimentales. Una descripción de este proceso puede encontrarse en [Gue12.1], y el método ha sido utilizado también en [Gue12.2]. La principal diferencia introducida en este análisis ha sido la relacionada con las correcciones de tiempo muerto [Men14].

Los parámetros de los modelos estadísticos antes mencionados se han ajustado manualmente hasta reproducir los espectros de energía depositada presentados en la Figura D.4. No se han encontrado diferencias en la forma de los espectros de energía depositado de una resonancia a otra, por lo que se ha asumido que la eficiencia de detección es constante para unas condiciones en E_{Sum} y m_{cr} dadas, salvo por efectos de apilamiento de pulsos, que dependen de la tasa de contaje CR. Así, $\varepsilon = \varepsilon(E_{Sum}, m_{cr}, CR)$, y las variaciones en la eficiencia en función de la energía del neutrón se deben exclusivamente a las variaciones en la tasa de contaje. Las simulaciones Monte Carlo permiten calcular la eficiencia para cualesquera condiciones en E_{Sum} y m_{cr} , y para cualquier tasa de contaje. En el caso

concreto de las condiciones en E_{Sum} y m_{cr} adoptadas en este análisis, la eficiencia de detección es de 56.3(12)% para bajas tasas de contaje, variando siempre menos de un 1% en todo el rango de energías considerado. La estimación de las incertidumbres se ha obtenido teniendo en cuenta las incertidumbres en la generación de las cascadas y en la geometría del TAC.

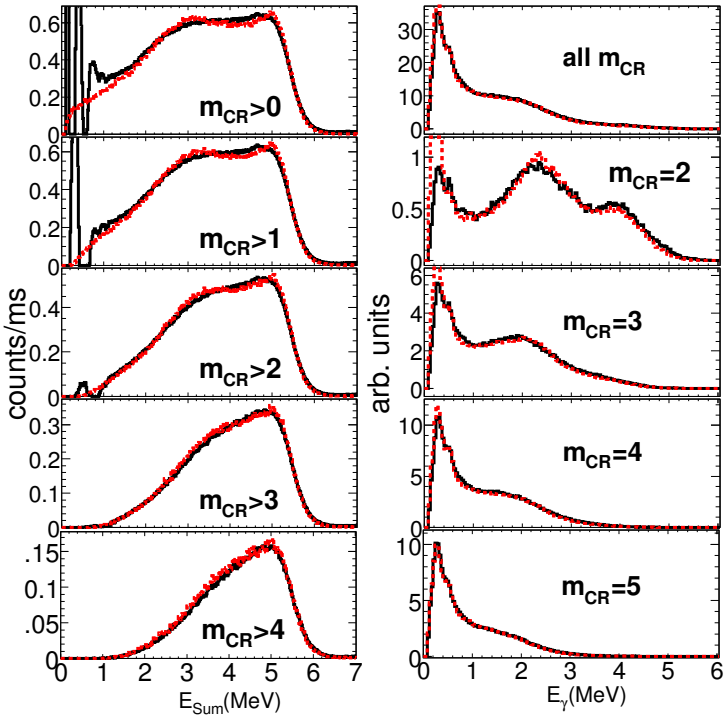

Figure D.4: Espectros de energía depositados en el TAC experimentales (líneas contínuas) y simulados (líneas de puntos) debido a cascadas de capura en ^{243}Am, bajo distintas condiciones en m_{cr}. A la izquierda, la energía total (E_{Sum}) depositada. A la derecha, los espectros de energía depositada por rayos-γ individuales. En este último caso, sólo se han tenido en cuenta los que contribuyen a eventos con $4<E_{Sum}<6$ MeV, en los que la mayoría de la cascada ha sido detectada. Los resultados se han obtenido de los rayos-γ de captura en la resonancia mayor del ^{243}Am, a 1.35 eV.

El mismo código Monte Carlo y las mismas técnicas se han utilizado para obtener la respuesta del TAC a la actividad de la muestra. En este caso las cascadas emitidas tras las desintegraciones se han tomado de ENSDF, sin ajustar ningún parámetro. A partir de este estudio, se ha determinado la masa de la muestra, resultando 6.77±15% mg de ^{243}Am, que es consistente con la otra medida de la actividad realizada en el CERN con detectores de Ge, que dio como resultado 7.34±15% mg, y no con los 10 mg que indican los fabricantes. La comparación entre los resultados obtenidos de las simulaciones y los obtenidos experimentalmente se muestra en la Figura D.5. La incertidumbre relativa es mucho mayor que la de la eficiencia de detección debido a la menor energía de los rayos-γ involucrados, en este caso próximos al umbral de los cristales de BaF_2.

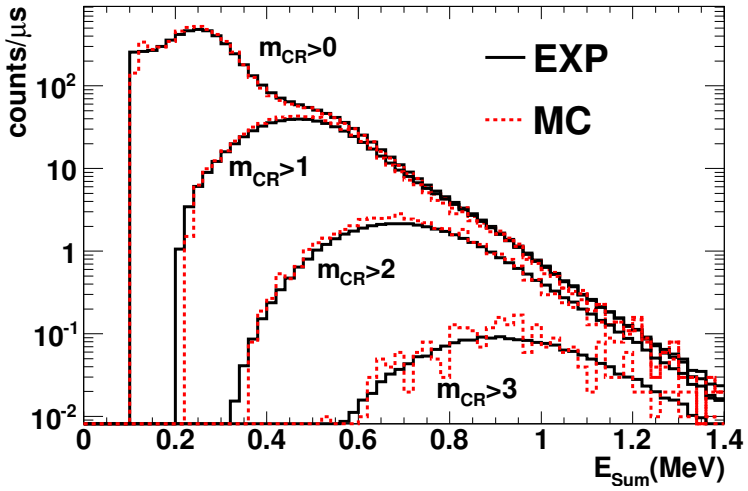

Figure D.5: Espectros de energía depositada en el TAC debido a la actividad de la muestra de ^{243}Am. En línea contínua, los espectros experimentales, mientras que en línea punteada, los resultados de las simulaciones, para las que se ha asumido una masa de ^{243}Am de 6.77 mg.

D.3.3 Normalización

La medida se ha normalizado por el método de la resoanancia saturada [Mac79], utilizando la resonancia a 4.9 eV del ^{197}Au. Con ésto básicamente lo que se calcula es la fracción de neutrones que son interceptados por la muestra, aunque en el cálculo queda incluída también la normalización al número de neutrones utilizados en la medida. La incertidumbre en la normalización de la tasa de reacción viene dada por la incertidumbre obtenida en la normalización a la resonancia del ^{197}Au (un 1.5%) y por la incertidumbre en la eficiencia de detección (2.2%). La suma de ambas cantidades da un 3.7% o un 2.7%, según sean sumadas de manera lineal o cuadrática, respectivamente. Sin embargo, a la hora de calcular la incertidumbre en la normalización de la sección eficaz hay que añadir también la incertidumbre en la masa de la muestra, que en este caso es mucho mayor (11%). Como ésto daría lugar a una incertidumbre en la normalización inaceptable, lo que se ha hecho es normalizar a las medidas de transmisión existentes (ver Tabla D.1). Esta normalización se ha llevado a cabo con el código SAMMY [Lar06], ajustando la tasa de captura obtenida en n_TOF con los datos existentes. Ésto se ha realizado de dos maneras:

1. Ajustando simultáneamente la tasa de captura con los datos de transmisión, donde en el ajuste se dejaron libres la normalización de los datos de captura y los parámetros de las resonancias. Ésto se hizo sólo con los datos de Simpson et al., ya que la información experimental existente para los demás datos de transmisión resultó insuficiente.

2. Ajustando la tasa de captura obtenida en n_TOF con las tasas de captura construídas a partir de los parámetros de las resonancias obtenidos por las personas que analizaron las medidas de transmisión, y que están disponibles en [Cot59, Ber70, Sim74, Bel76]. En este caso, el único parámetro a ajustar fue la normalización de la tasa de captura obtenida en n_TOF.

Los datos de transmisión de Simpson et al. se obtuvieron a partir de dos muestras diferentes, una [exf01] más gruesa que la otra [exf02]. La normalización se hizo a ambos conjuntos de datos, en seis rangos distintos de energía. Estos datos de transmisión se utilizaron sólo para normalizar y no para hacer el análisis de los parámetros de las resonancias por dos razones. Primero, proque los datos disponibles en EXFOR vienen dados sin incertidumbres (son necesarias para el ajuste, por lo que se asignaron siguiendo ciertas hipótesis); y segundo, porque la función de resolución del haz de neutrones del experimento de transmisión (la que da la información relativa a la relación energía-tiempo de los neutrones) no pudo obtenerse con suficiente precisión. Esta falta de información en los datos de transmisión no impidió que se utilizaran para normalizar la medida de n_TOF, pero hacen que no puedan usarse para un análisis de resonancias.

Del segundo método mencionado, se vio que los datos de n_TOF son incompatibles con los resultados proporcionados por Cote et al. y Bellanova et al., mientras que parecen ser razonablemente compatibles con los de Simpson et al. y los de Berreth et al., además de con las evaluaciones hechas por Mughabghab [Mug06] y Maslov [Mas96].

Los resultados obtenidos se muestran en la Figura D.6. Los primeros 6 puntos se corresponden con normalizaciones hechas a los datos de transmisión de Simpson et al. obtenidos con la muestra más gruesa, los 6 siguientes a los obtenidos con la muestra menos gruesa, y los 6 últimos a los ajustes realizados con las tasas de captura obtenidas a partir de parámetros de las resonancias. En todos los casos los ajustes se hicieron por encima de 3 eV, para evitar así efectos de auto absorción debidos a la resonancia más grande a 1.35 eV. Las incertidumbres que se muestran son las debidas a la incertidumbre en la constante de fondo constante en el tiempo, ya que se trata de la contribución dominante.

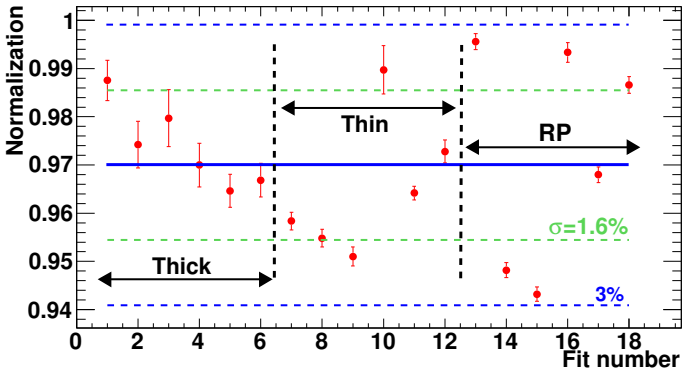

Figure D.6: Resultados de 18 normalizaciones distintas de los datos obtenidos en n_TOF. En todos los casos el espesor inicial de la muestra de ^{243}Am considerado fue de $2{\cdot}10^5$ átomos/barn, lo que se corresponde con una masa de 6.34 mg.

La media de todos los valores de normalización que hay en la Figura D.6 es 0.970, que se corresponde con un espesor de la muestra de $1.94{\cdot}10^5$ átomos/barn, o a una masa de 6.23 mg de ^{243}Am. La desviación estándar de estos valores es del 1.6%, pero, debido a que éstos no son independientes, se ha tomado finalmente una incertidumbre en la normalización de un 3%. Para el cálculo de la incertidumbre en la masa hay que añadir el 2.7% de incertidumbre debido a la normalización de la tasa de captura obtenida experimentalmente, con lo que se obtiene una incertidumbre final en la masa de ^{243}Am de un 4%, si ambas cantidades se suman cuadráticamente.

D.4 Obtención de la sección eficaz

D.4.1 Análisis de la zona de resonancias resueltas

La zona de resonancias resueltas se ha analizado con SAMMY (versión 7.0.0), extendiendo dicha zona de los 250 eV presente en las evaluaciones actuales hasta los 400 eV. Se han ajustado los valores de la energía E_0, la anchura neutrónica Γ_n y la anchura radiativa Γ_γ de cada resonancia del rango de energías de entre 0.7 y 400 eV, utilizando la aproximación de Reich-Moore. Los parámetros de las resonancias negativas y los de la primera resonancia a 0.415 eV, todas las anchuras de fisión Γ_f y el radio de dispersión (*scattering radius*, en inglés) se han tomado de ENDF-B/VII.0, tras verificar que fuertes variaciones de dichos parámetros no afectan significativamente a la tasa de captura resultante. Se ha comprobado que las resonancias observadas son todas de onda s, tras aplicar las técnicas descritas en [Oh00]. No ha sido posible distinguir entre los dos posibles espines totales J=2,3, por lo que únicamente quedan determinados los valores de $g\Gamma_n$. La relación energía-tiempo se obtuvo ajustando la distancia de tiempo de vuelo para reproducir las energías de las resonancias del ^{197}Au de ENDF/B-VII.0, obteniendo 184.878 m. La tasa de captura experimental se presenta junto con los resultados de los ajustes en la Figura D.7, para varios rangos de energía.

Se han tomado las incertidumbres estadísticas en los parámetros ajustados proporcionados por SAMMY, junto con las correspondientes correlaciones. En lo que se refiere a las incertidumbres sistemáticas, se han considerado las siguientes contribuciones:

1. Incertidumbres debidas a la normalización. Se han estimado haciendo varios (1000) ajustes, cada uno de ellos con una normalización diferente que varía aleatoriamente de acuerdo a una distribución gaussiana con desviación estándar igual la incertidumbre en la normalización (3%). Las incertidumbres sistemáticas de cada parámetro debidas a la normalización se estimaron entonces como la desviación estándar de los valores obtenidos.

2. Incertidumbres debidas a la temperatura de la muestra. Se obtuvieron igual que en el caso anterior, variando la temperatura de la muestra de acuerdo con 293±4 K.

3. Incertidumbres debidas a la componente del fondo constante en el tiempo. Se obtuvieron igual que en los casos anteriores, a partir de $a = 0 \pm 3 \cdot 10^{-5}\sqrt{eV}$.

4. Incertidumbre debida a la forma del fondo. Debido al escaso tiempo de haz dedicado a las medidas del fondo (Tabla D.3), fue necesario integrar el fondo en intervalos de energía del neutron relativamente grandes para reducir las fluctuaciones estadísticas. Sin embargo, dado que la forma del fondo es suave (Figura D.3) se utilizó un fondo suavizado para el análisis de resonancias. Para estimar las incertidumbres en los parámetros de las resonancias debidos al proceso de suavizado, lo que se ha hecho es comparar los resultados de un ajuste realizado con el fondo suavizado y otro realizado con el fondo sin suavizar. Las incertidumbres se estimaron como las desviaciones estándar de los resultados obtenidos.

5. Incertidumbre debida al modelo de ensanchamiento Doppler. Al igual que en los casos anteriores, esta incertidumbre se estimó realizando un ajuste usando el modelo de gas libre y otro usando el modelo de red cristalina [Lar06]. En este último caso usando el espectro de fonones del UO_2, ya que el del AmO_2 no se ha medido. Las incertidumbres se estimaron como las desviaciones estándar de los resultados obtenidos.

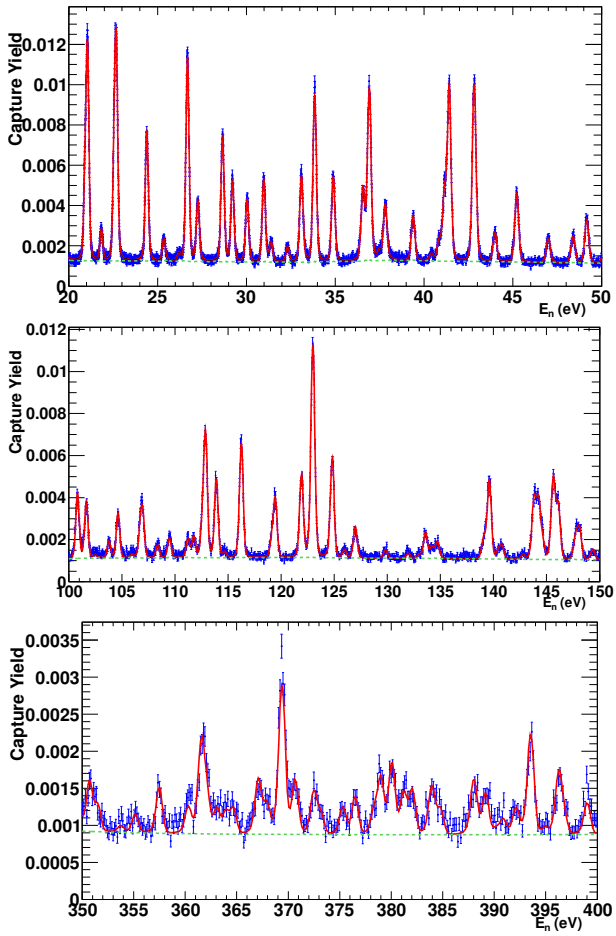

Figure D.7: Ejemplos de la tasa de captura obtenida en n_TOF, en varios rangos de energía.

6. Incertidumbre debida a inhomogeneidades en la muestra. Se ha visto que el valor de $I_0 = \int_{0.5eV}^{\infty} \sigma_\gamma(E)/EdE$ obtenido en n_TOF I_0=1681 barn, es significativamente menor que los obtenidos en otras medidas (Tabla D.2). Esta discrepancia puede explicarse con la existencia de inhomogeneidades en la muestra, ya que afectan a las correcciones de auto absorción y de dispersión múltiple. La resonancia más grande a 1.35 eV es la única donde estas correcciones son importantes (∼15%), y ésta contribuye alrededor de un 70-80% al valor de I_0. Para el resto de resonancias la corrección es mucho menor (8 resonancias con correcciones entre el 3% y el 1% y el resto con correcciones por debajo del 1%). De todas formas, para hacer una estimación de la incertidumbre en los parámetros debida a estas inhomogeneidades se ha hecho un ajuste con el espesor nominal de la muestra y otro con el doble de espesor. De nuevo, las incertidumbres se estimaron como las desviaciones estándar de los resultados obtenidos. En este caso, la imprecisión en el cálculo de estas incertidumbres es grande, ya que lo de considerar el doble de espesor es arbitrario. No obstante, sirve para saber qué parametros están afectados por posibles inhomogeneidades y cuáles no lo están.

El resto de contribuciones, como las relacionados con las correcciones por apilamiento de pulsos o las debidas a la fución de resolución del haz de neutrones, se han considerado despreciables y no se han tenido en cuenta. Los valores de los parámetros de las resonancias junto con cada una de sus incertidumbres, estadísticas y sistemáticas, se encuentran en el Apéndice C.

El cociente entre la sección eficaz de captura obtenida en este análisis y las evaluaciones más recientes se muestra en la Figura D.8. El cociente se hecho con tres evaluaciones distintas: la de Mughabghab, que es la que adopta la librería ENDF/B-VII.1; la de Weston, que es la que adoptaron versiones anteriores de ENDF/B; y la de Maslov, que es la que utilizan el resto de evaluaciones en este rango de energías. En el intervalo que va de 3 a 250 eV la sección eficaz obtenida en n_TOF es, en promedio, un 6% mayor que la de Mughabghab y la de Weston, y un 13% mayor que la de Maslov, llegando en este último caso a ser más de un 25% mayor en promedio entre 100 y 150 eV. Hay que decir también que se han encontrado nuevas resonancias en este rango de energías, además de las 105 nuevas resonancias entre 250 y 400 eV. En concreto, las evaluaciones de Mughabghab y Weston tienen 218 resonancias, la de Maslov 238, y la de n_TOF 248, por debajo de 250 eV.

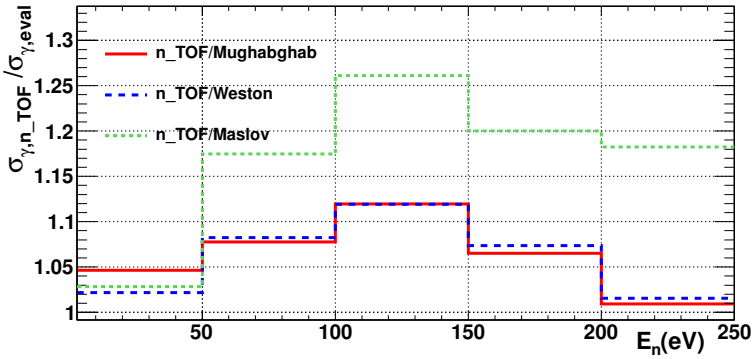

Figure D.8: Cociente entre la sección eficaz de captura obtenida en n_TOF y las que hay en las differentes librerías ($\int_{E_1}^{E_2} \sigma_{\gamma,n\_TOF}(E)dE / \int_{E_1}^{E_2} \sigma_{\gamma,eval}(E)dE$), integradas en varios rangos de energía. El límite inferior del primer intervalo es 3 eV, para evitar el efecto de la resonancia a 1.35 eV.

D.4.2 Análisis estadístico de los parámetros de las resonancias

La anchura radiativa promedio, $\langle\Gamma_\gamma\rangle$, se ha determinado a partir de los valores obtenidos de las anchuras Γ_γ de cada resonancia, teniendo en cuenta sólo aquellas cuyos errores estadísticos eran menores del 10%. Se ha utilizado una media ponderada generalizada [Cox06], que tiene en cuenta las incertidumbres estadísticas y las correlaciones entre los parámetros. Para estimar las incertidumbres sistemáticas, lo que se ha hecho es calcular $\langle\Gamma_\gamma\rangle$ a partir de parámetros obtenidos con distintas temperaturas, normalizaciones, modelos doppler, ..., y calculando las desviaciones estándar de los resultados obtenidos. Es decir, se han obtenido de la misma manera de la que se obtuvo para cada uno de los parámetros de las resonancias. El resultado del análisis ha sido $\langle\Gamma_\gamma\rangle = 42.00 \pm 0.12 \pm 0.5 \pm 0.3 \pm 0.7 \pm 0.6$ meV, donde las incertidumbres son, respectivamente: estadística, debido a la temperatura, debido a la componente de fondo constante en el tiempo, debido al modelo utilizado de ensanchamiento Doppler, y

debido a las inhomogeneidades de la muestra. La incertidumbre sistemática total es 2.1 o 1.1 meV, según se sumen las cantidades de forma lineal o de forma cuadrática.

En principio, se puede obtener una estimación de la distancia promedio entre niveles de onda s D_0 a partir de $D_0 = \Delta E/(N-1)$, con $\Delta D_0/D_0 \approx 1/N$ [Cap09], donde N es el número de resonancias observadas entre E_1 y E_2, y $\Delta E = E_2 - E_1$. Sin embargo, normalmente existe un cierto número de resonancias de tamaño pequeño que no han llegado a observarse, siendo necesario estimar su número. Existen varios métodos para hacer esto. Uno de los más comunes se basa en asumir que los valores de $\Gamma_n^0 = \Gamma_n(E_0/1eV)^{-1/2}$ se distribuyen, para cada valor del espín total J, de acuerdo con una distribución de Porter-Thomas de un grado de libertad $p(x)dx = e^{-x/2}/\sqrt{2\pi x}dx$, donde $x = \Gamma_{n,J}^0/\langle\Gamma_{n,J}^0\rangle$. Dado que no se han determinado los espines de las resonancias, es necesario asumir que $1/D_{0,J} \propto (2J+1)$ y que $S_{0,J} = S_0$ (ambas vienen justificadas en el Apéndice D de [Her09]), donde $S_0 = \langle g\Gamma_n^0\rangle/D_0$. De lo anterior se sigue que $\langle g_J\Gamma_{n,J}^0\rangle = \langle g\Gamma_n^0\rangle$, es decir, que el valor de $\langle g\Gamma_n^0\rangle$ es el mismo para los dos espines, y por lo tanto puede considerarse una única distribución de Porter-Thomas para los dos, tras hacer el cambio de variable de $x = \Gamma_n^0/\langle\Gamma_n^0\rangle$ a $y = g\Gamma_n^0/\langle g\Gamma_n^0\rangle$. Con esto, y tras manipular un poco la distribución de Porter-Thomas, es posible llegar a que el número de resonancias con $\sqrt{g\Gamma_n^0}$ mayores que una cierta cantidad x viene dada por:

$$f(x) = N\frac{2}{\sqrt{\pi}\sqrt{2\langle g\Gamma_n^0\rangle}}\int_x^\infty \exp\left(-\frac{y^2}{2\langle g\Gamma_n^0\rangle}\right)dy \tag{D.2}$$

donde N es el número de resonancias en el intervalo de energías considerado. Se ha utilizado esta fórmula para obtener el número de resonancias no detectado, ajustando los valores de N y de $\langle g\Gamma_n^0\rangle$ tal y como se muestra en el panel izquierdo de la Figura D.9. El resultado obtenido finalmente fue D_0=0.66(3) eV, donde la incertidumbre se estimó a partir de la incertidumbre estadística debida al número de resonancias considerado y de calcular D_0 en distintos rangos de energía.

El valor de S_0 puede obtenerse a partir de $S_0 = \sum_\lambda g\Gamma_{n,\lambda}^0/\Delta E$ y $\Delta S_0/S_0 = \sqrt{2/N}$ [Cap09], y se calculó a partir de la pendiente de la suma cumulativa, tal y como se muestra en el panel derecho de la Figura D.9. El resultado fue $S_0 = 1.08(8)\cdot 10^{-4}$, con una incertidumbre adicional del 3% debida a la normalización.

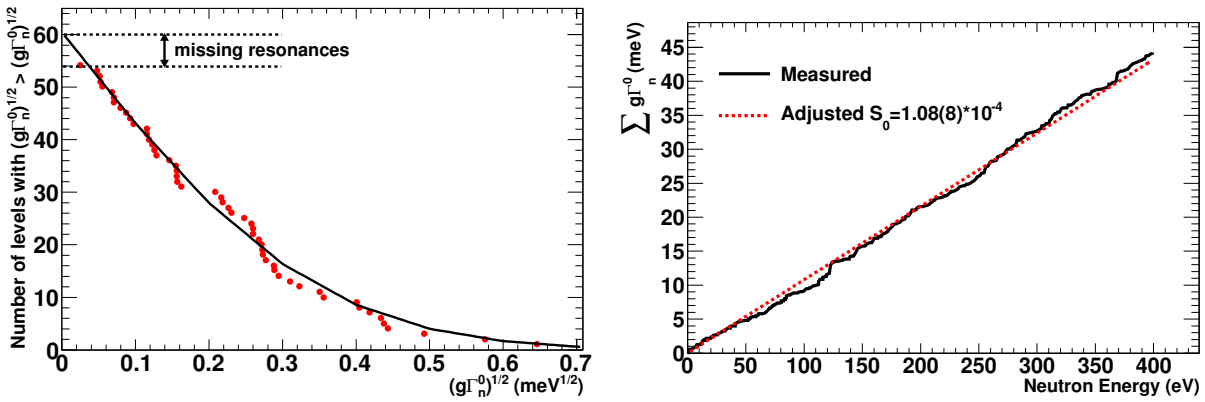

Figure D.9: A la izquierda, estimación del número de resonancias en onda s no observadas en el intervalo de energías de entre 0 y 40 eV. Los puntos experimentales se han ajustado a la ecuación D.2. A la derecha, ajuste lineal de $\sum_\lambda g\Gamma_{n,\lambda}^0$ en función de la energía del neutrón.

D.4.3 Análisis de la zona de resonancias no resueltas

Se ha analizado la región de entre 250 eV y 2500 eV como zona de resonancias no resueltas, con lo que la región que va de 250 a 400 eV se ha analizado de las dos maneras. Ésto se ha hecho por comparación con las librerías existentes, que fijan 250 eV como el límite entre ambas regiones. Para el análisis se ha utilizado el código SAMMY, que contiene una versión modificada del código FITTACS [Lar06, Fro89].

Los ajustes en SAMMY se hacen directamente a la sección eficaz experimental, en lugar de a la tasa de reacción. Ésta se ha obtenido directamente de dividir la tasa de captura por el espesor de la muestra, $\langle\sigma_\gamma(E_n)\rangle = \langle Y_\gamma(E_n)\rangle/n$, ya que en este rango de energías los efectos de auto apantallamiento y de colisiones múltiples son despreciables. El fondo se ha restado sin hacer ningún tipo de suavizado, ya que no esposible comprobar si el suavizado se hace de manera correcta mirando si éste se encuentra a la altura de la tasa de captura entre resonancias distantes, tal y como puede hacerse en la zona de resonancias resueltas. En lo que se refiere a las incertidumbres, todas las incertidumbres sistemáticas mencionadas en la Sección D.4.1 son despreciables en este rango de energías, con excepción de la incertidumbre debido a la normalización. La mayor contribución a las incertidumbres estadísticas viene de la substracción del fondo.

Los únicos parámetros que se han ajustado con los datos de n_TOF son S_0 y $\langle\Gamma_\gamma\rangle_0$, ya que el resto de parámetros no son sensibles a esta medida: o lo son a transmisión, o a rangos de energía más elevados. En concreto, la contribución en onda p, de acuerdo con ENDF/B-VII.1, es de un 11% a 2.5 keV, y una variación de un 25% del valor de S_1 induce un cambio en el valor ajustado de S_0de tan sólo un 0.5%.

Los valores e incertidumbres obtenidos en la zona de resonancias resueltas de S_0 y $\langle\Gamma_\gamma\rangle_0$ se han utilizado como incertidumbres *a priori* para el ajuste, y la distancia promedo entre niveles se fijó al valor obtenido de $D_0 = 0.66$ eV. Los resultados del ajuste fueron $S_0 = 1.10(4)\cdot 10^{-4}$ y $\langle\Gamma_\gamma\rangle_0 = 42.1(20)$ meV, con una correlación entre ambos de -0.23. A esas incertidumbres y correlaciones, que son estadísticas, hay que añadirle un 3% de incertidumbre al valor de S_0 debido a la normalización.

El ajuste de los datos de n_TOF se presenta en la Figura D.10, junto con los dos únicos conjuntos de datos de captura disponibles en este momento en este rango de energías, ambos de Weston et al.. Éstos últimos aparecen etiquetados en la figura como "Weston I" [exf04] y "Weston II" [exf05], y no son compatibles por debajo de ∼1.5-2 keV. Los datos de n_TOF son compatibles en normalización y forma con los de Weston I, y no lo son con los de Weston II. Nótese que la normalización de los datos de n_TOF se ha realizado a bajas energías. Por otra parte, todas las evaluaciones que existen actualmente se encuentran mucho más cercanas a Weston II que a Weston I, infraestimando la sección eficaz de captura en este rango de energías entre un 7% y un 20%.

El análisis se ha extendido hasta 42 keV (límite de la zona de resonancias no resueltas en la mayoría de las evaluaciones) con ayuda de los datos de Weston et al., ya que son compatibles con los de n_TOF en su rango común de energías. El otro conjunto de datos disponibles, el de Wisshak et al. (Tabla D.1), tiene una sección eficaz de captura un 10%-15% menor. Lo que se ha hecho es hacer un ajuste de S_1 y $\langle\Gamma_\gamma\rangle_1$ a los datos de Weston et al. entre 2.5 y 42 keV (los dos conjuntos de datos son compatibles en este rango de energías), con los valores de S_0 y $\langle\Gamma_\gamma\rangle_0$ fijados a los obtenidos en el análisis de los datos de n_TOF. Los resultados obtenidos fueron $S_1 = 1.65(24)\cdot 10^{-4}$ y $\langle\Gamma_\gamma\rangle_1 = 52(34)$ meV, con una correlación entre ellos de -0.82. Las incertidumbres sistemáticas de estos valores no se pudieron calcular, debido a la falta de información suministrada por Weston et al..

Los valores de los parámetros de la zona de resonancias no resueltas obtenidos en este trabajo se muestran junto con los obtenidos en otros experimentos y otras evaluaciones en la Tabla D.4. El cociente entre la sección eficaz

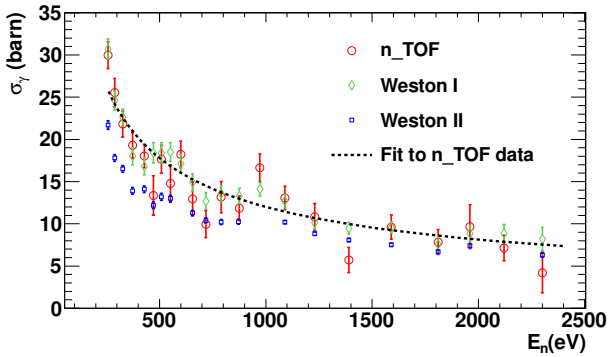

Figure D.10: Sección eficaz de captura obtenida experimentalmente en n_TOF, junto con su ajuste a la sección eficaz promedio y junto con los datos reportados por Weston et al., entre 250 y 2500 keV.

obtenida en este análisis y las de las distintas evaluaciones se muestra en la Figura D.11. A bajas energías, la secciones eficaces evaluadas son un 7%-20% menores que la obtenida en este trabajo, debido a que las evaluaciones se acercan más a *Weston II* que a *Weston I*, siendo esta última la que es compatible con los datos de n_TOF.

	D_0(eV)	$S_0(\times 10^{-4})$	$\langle\Gamma_\gamma\rangle_0$(meV)	$S_1(\times 10^{-4})$	$\langle\Gamma_\gamma\rangle_1$(meV)
n_TOF+Weston	0.66(3)	1.10(5)	42.1(20)	1.65(24)$^{(*)}$	52(34)$^{(*)}$
Bellanova [Bel76]	0.62	0.95			
Berreth [Ber70]			42		
Simpson [Sim74]	0.68	0.96(10)	39		
Cote [Cot59]			43(3)		
RIPL-3 [RP3xx]	0.73(6)	0.98(6)	39(3)		
Mughabghab [Mug84]	0.60(6)	0.98(9)	39(1)		
Maslov [Mas96]	0.566(49)	0.873(146)	43	2.176	43
BROND-2.2	0.67	0.93	39	2.44	39
JENDL-4.0	0.44	0.864	39	1.687	39
ENDF/B-VII.0	0.75	0.98	39	2.2	44
ENDF/B-VII.1	0.66	0.98	39.1	2.6	69.8

Table D.4: Parámetros de la zona de resonancias no resueltas (a E_n=0) obtenidos en este análisis comparados con otros obtenidos en otras evaluaciones. En la zona de resonancias no resueltas la sección eficaz de captura de ENDF/B-VI es igual a la de ENDF/B-VII.0. La de Maslov es la que hay en JEFF-3.1, JENDL-3.3 y CENDL-3.1, y en ROSFOND-2010 a bajas energías, aunque en este último caso la evolución de los parámetros con la energía del neutrón es distinta.

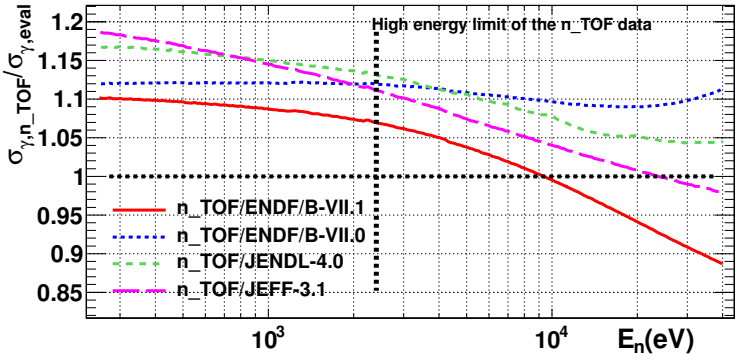

Figure D.11: Cociente entre la sección eficaz de captura obtenida en este trabajo y las de distintas evaluaciones. La sección eficaz de JEFF-3.1 es igual que las de JEFF-3.1.2, JENDL-3.3 y CENDL-3.1, en este rango de energías.

D.4.4 Región de altas energías

Además de los distintos datos experimentales diferenciales (en función de la energía del neutrón) existen medidas integrales hechas en reactores rápidos que son útiles para determinar la sección eficaz de captura. Una de estas medidas es la del experimento PROFIL-1, donde se irradió una pastilla de ^{243}Am en el reactor rápido PHENIX, en 1974 [Pal05, Kah11]. De hecho, ha habido cambios en ENDF/B-VII.1 respecto de ENDF/B-VII.0 motivados por estos resultados [Cha11]. La información que puede obtenerse de PROFIL-1 es la sección eficaz convolucionada con el flujo $\sigma_{cap} = \int \phi(E)\sigma_\gamma(E)dE$. Dado que fue posible acceder a la forma de dicho flujo, se utilizaron los resultados de PROFIL-1 que se proporcionan en [Pal05, Kah11] para sacar conclusiones acerca de la sección eficaz de captura del ^{243}Am por encima de 42 keV. Lo que se hizo fue obtener distintos valores de σ_{cap} a partir de secciones eficaces construídas hasta 42 keV con la obtenida en este análisis y por encima de 42 keV con las que hay en distintas evaluaciones. Dichos valores sec compararon con los resultados experimntales. En concreto, se tomaron las secciones eficaces por encima de 42 keV de las librerías: ENDF/B-VII.1, ENDF/B-VII.0, JENDL-4.0, JEFF-3.1 (misma que JENDL-3..), JEFF-3.0, CENDL-3.1, ROSFOND-2010 y ENDF/B-V.0. La conclusión final del estudio fue que, de éstas, la sección eficaz que mejor reproduce los resultados experimentales que existen en este momento es la que se construye con los resultados obtenidos en este trabajo por debajo de 42 keV y con la sección eficaz de captura de las librerías JEFF-3.1 o CENDL-3.1 por encima de 42 keV. Esta sección eficaz: (i) reproduce los resultados de n_TOF entre 0.7 y 2.5 keV; (ii) reproduce los resultados de "Weston I" entre 0.25 y 2.5 keV; (iii) reproduce los datos de Weston et al. entre 2.5 y 42 keV; (iv) reproduce los datos de Wisshak et al. hasta 250 keV, si se normalizan éstos a los de Weston et al. (que son compatibles con n_TOF); (v) reproducen los resultados del experimento integral PROFIL-1; y (vi) existe continuidad entre la zona de resonancias no resueltas y la zona de altas energías, a 42 keV.

D.5 Conclusiones

La sección eficaz de captura del ^{243}Am se ha medido en la instalación n_TOF usando el calorímetro de absorción total de BaF_2, entre 0.7 eV y 2.5 keV. Hasta ahora no se ha publicado ningún análisis de captura de ^{243}Am por debajo de 250 eV, salvo de la sección eficaz térmica.

La masa de ^{243}Am que certificaron los fabricantes ha resultado no ser correcta, por lo que la medida ha sido normalizada a las medidas existentes de transmisión a bajas energías, por debajo de 50 eV. Con esta normalización

los datos de n_TOF son consistentes con una de las dos únicas medidas de captura publicadas entre 0.25 y 2.5 keV. Además, la masa de la muestra resultante es compatible con los resultados de la actividad medidos tanto con detectores de germanio en el CERN como con el calorímetro de BaF_2.

Debido a la gran distancia de tiempo vuelo de n_TOF (185 m) y a la estadística alcanzada, los resultados obtenidos mejoran el conocimiento existente de la zona de resonancias resueltas, extendiendo ésta de 250 eV hasta 400 eV. En la zona de resonancias no resueltas, los resultados obtenidos indican que las evaluaciones actuales infraestiman la sección eficaz de captura entre un 7% y un 20% por debajo de 2.5 keV. Finalmente, se ha completado el análisis por encima de 2.5 keV con los datos de captura disponibles, encontrando la sección eficaz que mejor reproduce los resultados experimentales que existen en este momento.

Por último, decir que con esta medida la sección eficaz de captura del ^{243}Am presenta sus mayores incertidumbres en el térmico, en la resonancia más grande a 1.35 eV, y por encima de las decenas de keV. Los resultados aún no publicados de Jandel et al. [Jan09] o de Hori et al. [Hor09] podrían reducir algunas de estas incertidumbres.

Appendix E

Summary in English

Background: The design of new nuclear reactors and transmutation devices requires to reduce the present neutron cross section uncertainties of minor actinides.

Purpose: Reduce the ^{243}Am(n,γ) cross section uncertainty.

Method: The ^{243}Am(n,γ) cross section has been measured at the n_TOF facility at CERN with a BaF_2 Total Absorption Calorimeter, in the energy range between 0.7 eV and 2.5 keV.

Results: The ^{243}Am(n,γ) cross section has been successfully measured in the mentioned energy range. The resolved resonance region has been extended from 250 eV up to 400 eV. In the unresolved resonance region our results are compatible with one of the two incompatible capture data sets available below 2.5 keV.

Conclusions: These are the first published analysis results of a differential ^{243}Am(n,γ) measurement below 250 eV. The results of this measurement contribute to reduce the ^{243}Am(n,γ) cross section uncertainty and suggest that this cross section is underestimated up to 25% in the neutron energy range between 50 eV and a few keV in the present evaluated data libraries.

I. INTRODUCTION

Nuclear data for minor actinides have gained importance in the last years because they are necessary for improving the design and performance of advanced nuclear reactors and transmutation devices for the incineration of radioactive nuclear waste [1–3]. In particular, the ^{243}Am is the minor actinide which more contributes to the total radiotoxicity of the spent fuel at times after disposal close to its half life (7370 years). In addition, in a nuclear reactor most of the production of ^{244}Cm, which is a strong neutron emitter and which is in the path of the creation of any heavier isotope, is originated as the result of the ^{243}Am(n,γ) reaction.

The differential data available for the evaluation of the ^{243}Am capture cross section are presented in Table I. As it can be observed, there are only two differential capture measurements covering the energy region below 250 eV, apart from the one presented here. Both of them are recent and their results have not been published yet. In this energy range, only the information provided by the transmission measurements have been used to determine the ^{243}Am capture cross section in the present evaluated data libraries (the last releases at this moment are ENDF/B-VII.1, JENDL-4.0, JEFF-3.1.2 [14], ROSFOND-2010 [15] and CENDL-3.1 [16]). In particular, the present evaluations are based essentially in the Simpson *et al.* results, which are the only ones which extend above 35 eV. This information has been completed with the integral measurements presented in Table II, which provide the thermal capture cross section and resonance integral measurements performed up to now. As it can be observed, there are sizeable differences between the different results.

TABLE I. Differential measurements performed up to now relevant for the evaluation of the ^{243}Am capture cross section.

Reference	Type	Range (eV)
Bellanova *et al.* (1976) [4]	Transmission	0.35 – 35
Simpson *et al.* (1974) [5]	Transmission	0.5 – $1{\cdot}10^3$
Berreth *et al.* (1970) [6]	Transmission	0.008 – 25.6
Cote *et al.* (1959) [7]	Transmission	0.0014 – 15.44
Weston *et al.* (1985) [8]	Capture	258 – $9.2{\cdot}10^4$
Wisshak *et al.* (1983) [9]	Capture	5 – $2.5{\cdot}10^5$
Jandel *et al.* (2009) [10] [a]	Capture	8 – $2.5{\cdot}10^5$
Hori *et al.* (2009) [11] [a]	Capture	0.01 – 400
This work	Capture	0.7 – $2.5{\cdot}10^3$
Kimura *et al.* (2012) [12] [b]	Capture	–
Alekseev *et al.* (2011) [13] [b]	Fission	–

[a] Neither the yield nor the resulting cross sections have been published yet.

[b] Only the resonance parameters of the resonance at 1.35 eV (Kimura *et al.*) or below 17 eV (Alekseev *et al.*) are provided.

TABLE II. Thermal capture cross sections (σ_0), resonance integrals ($I_0 = \int_{0.5eV}^{\infty} \sigma_\gamma(E)/EdE$) and ratios between them provided by different experiments and evaluations.

Reference	σ_0(barn)	I_0 (barn)	I_0/σ_0
Hori *et al.* (2009) [11]	76.6[a]	1970(110)	25.7(15)
Marie *et al.* (2006) [17]	81.8(36)		
Ohta *et al.* (2006) [18]		2250(300)[b]	
Hatsukawa *et al.* (1997) [19]	84.4		
Gavrilov *et al.* (1977) [20]	83(6)	2200(150)	26.5(26)
Simpson *et al.* (1974) [5]		1819(80)[c]	
Eberle *et al.* (1971) [21]	77(2)	1930(50)[c]	25.1(9)
Berreth *et al.* (1970) [6]	85(4)	1824(80)[c]	21.5(14)
Folger *et al.* (1968) [22]	78	2250[d]	29
Bak *et al.* (1967) [23]	73(6)	2300(200)	32(4)
Ice (1966) [24]	66-84		
Butler *et al.* (1957) [25]	73.6(1.8)	2290(50)	31(1)
Harvey *et al.* (1954) [26]	140(50)		
Stevens *et al.* (1954) [27]	115		
Mughabghab (2006) [28]	75.1(18)	1820(70)	24.2(11)
ENDF/B-VII.1 [29]	80.4	2051	25.5
ENDF/B-VII.0 [30]	75.1	1820	24.2
JENDL-4.0 [31]	79.3	2040	25.7
JEFF-3.1 [32]	76.7	1788	23.3

[a] Value assumed for normalization. I_0 is proportional to it.

[b] The thermal value of Marie *et al.* was assumed. The Ohta *et al.* measured value was $\hat{\sigma}$ =174.5(5.3) barn and α=0.0418(45), where $I_0 = \hat{\sigma}/\alpha + (0.45 - 1/\alpha)\sigma_0$.

[c] Cut-off energy was taken as 0.625 instead of 0.5 eV.

[d] Cut-off energy was taken as 0.83 instead of 0.5 eV.

At higher neutron energies there are only two data sets between 250 eV and 5 keV, both of them carried out by Weston *et al.*, which differ significantly below 2

keV. In addition, the results of Wisshak *et al.* are 10-15% lower than the Weston *et al.* data in the energy range of overlap. Together with these differential measurements, there are also integral measurements carried out in fast nuclear reactors, which provide information of the ^{243}Am capture cross section in the fast energy range. The results of the calculations performed with the evaluated libraries do not reproduce necessarily these experimental results [33, 34]. These inconsistencies have motivated, for example, changes in the evaluated ^{243}Am capture cross section in the ENDF/B-VII.1 release with respect to ENDF/B-VII.0 [29].

The lack of data, the inconsistencies presented above, and the recent interest in the design of new nuclear devices, specially those related with the transmutation of the spent fuel, have motivated new ^{243}Am capture cross section measurements, such as the one presented in this work or the ones of Jandel *et al.* and Hori *et al.*.

In Section II we describe the experimental setup of the ^{243}Am(n,γ) measurement carried out at the n_TOF facility at CERN. The reduction of the data which leads to the capture yield, which will be available in the EXFOR database [35], is presented in Section III; and the cross section analysis performed with the resulting yield, in Section IV. Finally, the conclusions of this work are presented in Section V.

II. THE EXPERIMENTAL SETUP

A. The n_TOF facility at CERN

The n_TOF (Phase-1[36]) facility at CERN [37] is a pulsed neutron source coupled to a 200 m flight path designed to study neutron-nucleus interactions for neutron kinetic energies ranging from a few meV to several GeV. The neutrons are produced in spallation reactions induced by a 20 GeV/c proton beam with 16 ns FWHM time resolution and a repetition rate of $\sim$0.4 Hz. The spallation source is a 80x80x60 cm^3 lead block surrounded by 5.8 cm of water, serving as a coolant and as a moderator for the initially fast neutron spectrum. The neutrons travel along a beam line in vacuum orientated at 10° with respect to the proton beam until reaching the experimental area. Along the beam line a magnet avoid the charged particles reaching the experimental area and two collimators give the appropriate shape to the neutron beam. This facility is used mainly to measure fission and capture cross sections relevant for nuclear astrophysics and nuclear technologies.

There are around $1.54{\cdot}10^5$ neutrons per nominal pulse of $7{\cdot}10^7$ protons between 1 eV and 10 keV reaching the irradiation position, placed at 185 m from the spallation source, with a nearly isolethargic energy distribution. Only proton pulses with intensities close to the mentioned nominal intensity have been considered in this analysis. At the irradiation position the neutron beam has a spatial distribution which does not vary significantly in the energy range of this measurement and that resembles a 2D-Gaussian with σ_x=σ_y=0.54 cm [38]. The description of the resolution function can be found in [39].

B. The detection system

Three different detectors were used to monitor the neutron beam during the ^{243}Am(n,γ) measurement: a wall current monitor [37] and wall current transformers [37], used to monitor the intensity of the proton beam; and a silicon flux monitor [40] used to monitor the intensity of the neutron beam. The latter is a ^{6}Li-based silicon monitor placed around 2 m before the irradiated sample.

The ^{243}Am(n,γ) reactions were measured with the n_TOF Total Absorption Calorimeter (TAC) [41], by measuring in coincidence the γ-cascades which follows the neutron capture reactions. The TAC, which is shown in Figure 1, is a 4π segmented array made of 40 BaF_2 crystals with pentagonal and hexagonal shapes. Each crystal has been constructed by cutting a BaF_2 cylinder of 14 cm diameter and 15 cm length. For optimal light collection each crystal is covered with two layers of 0.1 mm thick Teflon foil and a 0.1 mm thick polished aluminum sheet on the outside. In order to minimize the detection of scattered neutrons, the crystals are encapsulated inside a 1 mm thick ^{10}B loaded carbon fiber capsules. Each capsule is coupled to an aluminum cylinder that houses also a 12.7 cm photonis XP4508B photomultiplier and a special voltage divider made at the Instituto Tecnológico e Nuclear in Lisbon that favors its fast recovery. The whole modules are attached to an aluminum honey comb structure, which holds the complete assembly. The TAC is divided in two hemispheres that can be opened and closed, and form a spherical shell of 10 cm inner radius and 25 cm outer radius, approximately, covering around 95% of the entire solid angle. A neutron absorber which consists on a 5 cm thick spherical shell made of $Li_2C_{12}H_{20}O_4$ was placed in the inner hole of the TAC, in order to reduce, together with the ^{10}B loaded carbon fiber capsules, the detection of scattered neutrons in the center of the TAC, where the ^{243}Am sample was placed.

The detector signals were recorded by a digital data acquisition system [42] which used Acqiris-DC270 digitizers with 8 bits resolution operating at 250 MHz and recording continuously a time of flight of 16 ms for each pulse, thus containing the digitized electronic response of each detector for neutron energies above 0.7 eV. The data buffers were then analyzed offline, with dedicated pulse shape reconstruction algorithms. The algorithm used to analyze the BaF_2 signals is described in [43], and a more accessible reference of a similar routine is [44]. It returns for each signal the time-of-flight, the area, and other parameters used to distinguish the detected particle type: γ or α (the latter is produced by the decay of Ra impurities in the crystals). Each detector was calibrated in energies from measurements performed with standard

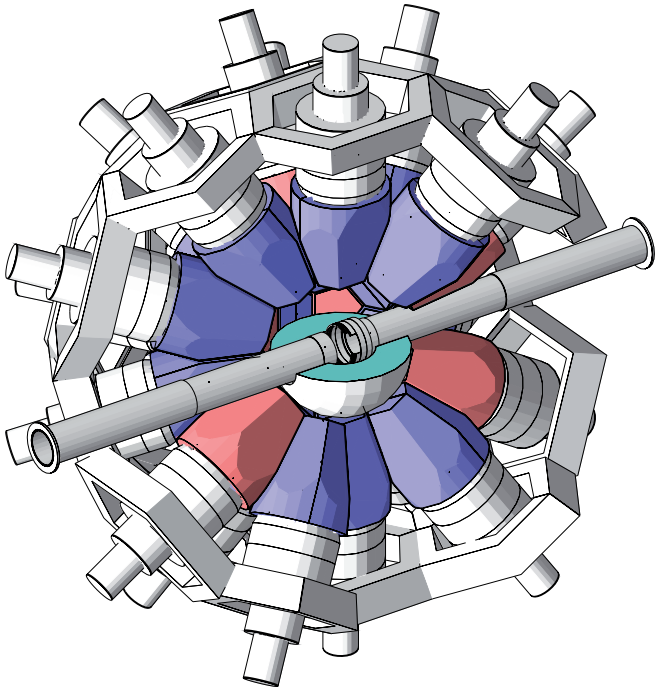

FIG. 1. Schematic view of the n_TOF Total Absorption Calorimeter.

calibration sources (^{137}Cs, ^{60}Co, ^{88}Y, ^{24}Na, and Pu/C), and the gain drifts occurred along the entire measurement were monitored with the changes observed in the α deposited energy spectra in each BaF_2 detector. The individual detector signals are grouped into TAC events, using a coincidence window of 20 ns. Each TAC event is characterized by their time-of-flight, the total energy deposited (E_{Sum}) and the crystal multiplicity (m_{cr}), which is the number of detectors contributing to the event. The E_{Sum} and m_{cr} values are used to apply conditions to the detected events in order to improve the capture over background ratio. In this paper, the word *event* always refers to these TAC events.

C. The ^{243}Am and auxiliary samples and measurements

The ^{243}Am sample was manufactured at IPPE Obninsk (Russia) in February 2004. It was in form of oxide power (AmO_2) deposited on an Al backing of 10 mm diameter and less than 70 mg, according to the specifications provided by the manufacturers. The sample was encapsulated inside a Ti canning of 15 mm diameter and 0.17 and 0.18 mm thickness above and below the sample. The whole sample (AmO_2, Al backing and Ti canning) was weighted at CERN, obtaining a value of 420.9(1) mg. According to the specifications provided by the manufacturers, the total mass of the AmO_2 deposit was 11.3 mg, and the isotopic mass of ^{243}Am, 10.0 mg. However, this value does not agree with a spectroscopic characterization of the sample performed at CERN, which resulted into an ^{243}Am mass of 7.34±15% mg. An additional sample activity measurement performed with the TAC resulted into a mass of 6.77±15% mg. The data were finally normalized to the transmission measurements available in EXFOR (see Section III C), specially to the one performed by Simpson *et al.* [5] , obtaining a normalization uncertainty of 3%, and an associated sample mass of 6.23 (±4%) mg, which is in agreement with the spectroscopic measurements. The impurities were determined during the resonance analysis process, finding around 0.048 mg of ^{241}Am and 0.0025 mg of ^{240}Pu. The temperature of the sample was assumed to be 293±4 K, which is the average temperature of the n_TOF experimental area.

TABLE III. Number of pulses and protons dedicated to each measurement.

Measurement	#pulses	#protons
^{243}Am	$1.86{\cdot}10^5$	$1.27{\cdot}10^{18}$
Env. background	$1.37{\cdot}10^4$	–
Activity	$1.53{\cdot}10^4$	–
^{197}Au	$2.19{\cdot}10^4$	$1.53{\cdot}10^{17}$
Graphite	$3.76{\cdot}10^3$	$2.67{\cdot}10^{16}$
Ti canning	$1.49{\cdot}10^3$	$1.04{\cdot}10^{16}$
Empty frame	$4.16{\cdot}10^3$	$2.94{\cdot}10^{16}$

The sample was placed in the center of the TAC, held by two kapton foils of 25 μm thickness and surrounded by the neutron absorber. Due to the high sample activity, a Pb cylinder of 11.5 cm length and 1 mm thickness was placed around the sample, surrounding the 5.2 cm diameter vacuum tube. In this way, the amount of high energy gamma rays (200-300 keV) originated in the sample decay and reaching the TAC were strongly reduced. However, even with this lead shielding, the counting rate of this measurement was much higher than other previous measurements performed with the TAC.

Three other samples were also measured for the determination of the ^{243}Am(n,γ) cross section, with the same experimental conditions: (i) an empty Ti-Al canning similar to the one encapsulating the sample, with the same diameter but with a slightly different mass, 455.4(1) mg, used for background determination purposes; (ii) a graphite sample of 10 mm diameter and 70.0(1) mg mass used to determine the TAC response to scattered neutrons; and (iii) a ^{197}Au sample of 10 mm diameter and 185.4(1) mg mass used to determine the fraction of the beam intercepted by the ^{243}Am sample, and also used for validation of the analysis tools.

Other measurements were also performed to determine the different background components: a measurement without beam and without sample in place (Env. Background), a measurement without beam and with the sample in place (Activity) and a measurement with neutron beam but without any sample (Empty frame). All of them are presented in Table III.

III. DATA REDUCTION

In this Section we describe the analysis process which leads to the experimental capture yield, which can be calculated from:

$$Y_{n,\gamma}(E_n) = \frac{C_{tot}(E_n) - C_{bkg}(E_n)}{\varepsilon \cdot F_{BIF} \cdot \phi(E_n)} \quad (1)$$

where $C_{tot}(E_n)$ and $C_{bkg}(E_n)$ are the number of measured and background counts registered by the TAC, respectively, under certain E_{Sum} and m_{cr} conditions; ε is the detection efficiency under the same conditions; $\phi(E_n)$ is the total neutron fluence; and F_{BIF} is the *Beam Interception Factor*, i.e., the fraction the neutron beam intercepted by the measured sample.

The data reduction process is quite similar to the one described in [45], with some additional features specially developed to deal with the much higher counting rates (5.4 events/μs) observed in the ^{243}Am(n,γ) measurement due to the sample activity.

A. Background and selection of the analysis conditions

The background events in the ^{243}Am(n,γ) measurement can be divided in two contributions: (i) events coming from fission reactions and scattered neutrons in the ^{243}Am nuclei; and (ii) the rest of the background, which results from the environmental background, the activity of the BaF_2 crystals, the sample activity and the interaction of the neutron beam with all the materials except with the ^{243}Am nuclei.

The second contribution can be obtained directly, in principle, from the different background measurements presented in Table III, by subtracting and adding properly the different contributions. However, during the ^{243}Am sample measurement the detection of the background events was distorted by the pile-up and dead time induced by the high ^{243}Am sample activity, whereas in the background measurements it was not. This causes that the background can not be calculated directly from the dedicated background measurements and some corrections are needed. The procedure followed to take this effect into account is described in detail in [46], and it is based in the offline manipulation of the digitized detector signals and the parametrization of the response of the pulse shape analysis routine.

The deposited energy spectrum obtained from the ^{243}Am(n,γ) measurement in the 1-10 eV neutron energy range is presented in Fig. 2, together with different background contributions: the total contribution (dummy sample), the total contribution except the one related with the interaction of the neutron beam with the Ti capsule (sample out), and the contribution not related with the neutron beam (No beam). The part of the spectra below ~2 MeV corresponds mostly to sample activity

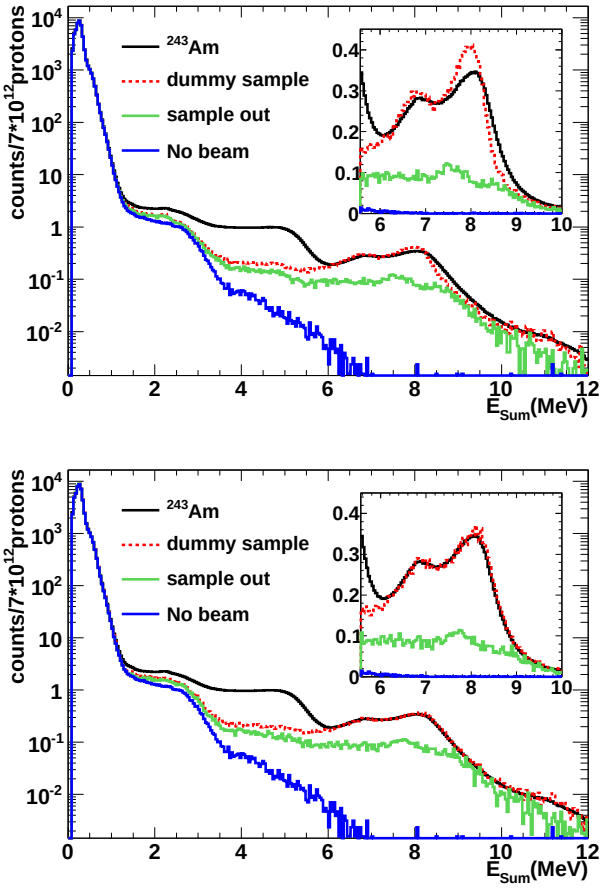

FIG. 2. Deposited energy spectrum of the ^{243}Am(n,γ) measurement together with different background contributions, without (top) and with (bottom) applying pile-up corrections in the calculation of the backgrounds. A zoom of the high energy part is presented in the top-right corner of each panel. The data corresponds to neutron energies between 1 and 10 eV.

events, whereas above 6 MeV the events are due to background events related with the neutron beam, since the total energy of the γ-cascade emitted after a capture reaction in ^{243}Am can not exceed the neutron separation energy of the compound nucleus, $S_n(^{244}\text{Am})$=5.36 MeV. For this reason, above E_{Sum}=6 MeV the dummy sample spectrum should match the results of the ^{243}Am(n,γ) measurement. As it can be observed, this only happens if the mentioned pile-up corrections are applied (bottom panel).

It can also be observed that the capture to background ratio is highly improved if the low (E_{Sum} <2 MeV) and high (E_{Sum} >6 MeV) energy events are not considered. The same occurs if some conditions are applied on the m_{cr}, since the capture events have, in general, higher multiplicity than the background ones. On the other hand, the detection efficiency becomes lower as the conditions in E_{Sum} and m_{cr} are more restrictive. A detailed

analysis has lead to the optimum conditions, adopted in the analysis, of m_{cr} >2 and 2.5<E_{Sum} <6 MeV. The number of events detected per proton pulse under these conditions is presented in Fig. 3, as a function of the neutron energy. It can be appreciated that the background is smooth until E_n=2-3 keV, where the resonances of the Ti capsule start. These Ti resonances have not allowed to measure above 2.5 keV, which is the high energy limit of this measurement. The low energy limit of 0.7 eV is given by the 16 ms recording time.

Due to small differences in the energy calibration caused by the dead time correction method [47], there was a background component constant in time that could not be determined from the measurements and had to be fitted. The uncertainty due to this fit can be expressed by considering the background as $B(E_n)+a/\sqrt{E_n}$, where $a = 0 \pm 3 \cdot 10^{-5}\sqrt{eV}$. The relative uncertainty of the background due to this component is 1%, 0.6%, 0.3% and 0.13% at 1, 10, 100 and 1000 eV, respectively.

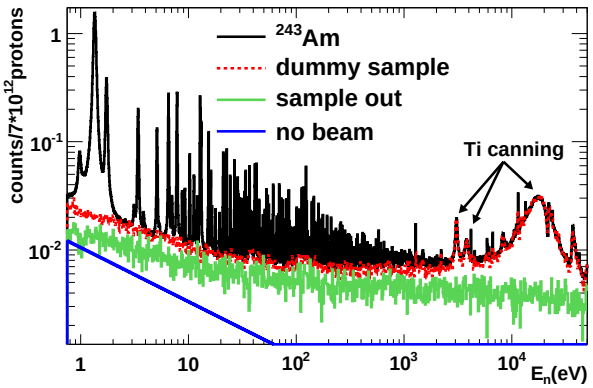

FIG. 3. Number of events detected in the ^{243}Am(n,γ) measurement as a function of the neutron energy, together with different background contributions and under the conditions of m_{cr} >2 and 2.5<E_{Sum} <6 MeV.

The background contribution related with the interaction of neutrons in the ^{243}Am nuclei follows a similar resonant behavior than the ^{243}Am(n,γ) cross section. An estimation of this contribution can be performed with the evaluated cross sections if the probability of detecting a scattered neutron (neutron sensitivity, in this paper) and a fission reaction are known. The neutron sensitivity has been obtained from the measurement performed with the graphite sample (Table III), by assuming that the neutrons scattered in Carbon have similar energies and angles than the neutrons scattered in ^{243}Am. The neutron sensitivity depends on the neutron energy and also in the E_{Sum} and m_{cr} conditions considered. With the conditions used in this analysis, the 2.2 MeV gammas resulting from neutron capture in the H of the neutron absorber are avoided, thus reducing the neutron sensitivity significantly. This calculated neutron sensitivity was used, together with the ^{243}Am evaluated cross section present in the ENDF/B-VII.0 library, to estimate the background induced by the neutrons scattered in the AmO_2 sample, finding that its contribution to the total background is below 0.5% in the entire energy range of the measurement, even in the center of the resonances. For the fission events, if a detection efficiency of 100% is assumed then its contribution to the total background is higher than the previous one in the center of certain ^{243}Am resonances. However, this contribution is always below 1% the capture yield. As a consequence, both contributions, elastic scattering and fission in the sample, have been neglected in the analysis.

B. Detection efficiency and determination of the sample activity

The detection efficiency has been calculated from Monte Carlo simulations. The entire process starts with the generation of the electromagnetic cascades which follows the neutron capture, which has been performed with the DECAYGEN code [48]. The resulting cascades are then transported with a code based in the GEANT4 package [49]. In the last step the Monte Carlo results are reconstructed in the same way as it is done in a real experiment, including all the experimental effects such as the energy resolution of the crystals or the dead time effects. The generation of the capture cascades includes statistical models for the description of the level densities and photon strength functions. These models depend on parameters, which are adjusted until the experimental results are reproduced. A detailed description of the entire process is given in [50], and this method has been also used in [45]. The main difference introduced in this analysis is that a new dead time correction method was developed, specially due to the strong effect of the high sample activity [46].

The mentioned statistical parameters have been tuned to reproduce: (i) the deposited energy (E_{Sum}) distributions for different detection multiplicities (m_{cr}); and (ii) the individual γ-ray energy spectra contributing to events with 4<E_{Sum} <6 MeV, where most of the capture cascade has been detected. The experimental spectra have been obtained for the strongest ^{243}Am resonance at 1.35 eV, where the capture to background ratio is maximum. An example of how the experimental results are well reproduced is shown in Fig. 4.

We have not found any significant difference in the shape of the deposited energy distributions between several resonances, and thus it was assumed that the detection efficiency depends only on the analysis conditions in E_{Sum} and m_{cr} and in the detected counting rate, CR, due to the associated pile up and dead time effects. Thus, $\varepsilon = \varepsilon(E_{Sum}, m_{cr}, CR)$, and the variations in the detection efficiency with the neutron energy are only due to changes in the detected counting rate. The Monte Carlo simulations allow to determine the detection efficiency for any E_{Sum} and m_{cr} conditions, and for any detected

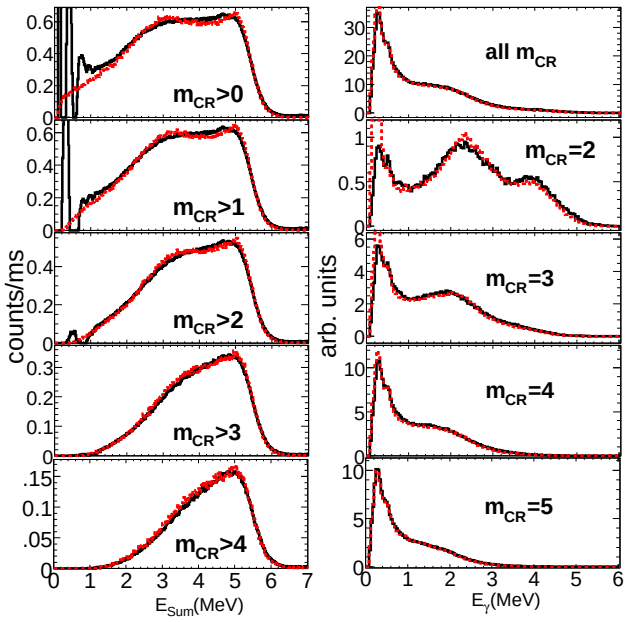

FIG. 4. Experimental (solid lines) and simulated (dotted lines) deposited energy spectra from ^{243}Am capture cascades, under different conditions in multiplicity. On the left, the total γ-ray energy deposited in the TAC (E_{Sum}). On the right, the individual γ-ray energy spectra obtained by gating on the total γ-ray energy in the 4<E_{Sum} <6 MeV region. The results have been obtained from the strongest ^{243}Am resonance at 1.35 eV.

counting rate. For the conditions used in this analysis, 2.5<E_{Sum} <6 MeV and m_{cr} >2, the calculated detection efficiency for low counting rates is 56.3(12)%, and it vary less than 1% in the entire neutron energy range of the analysis. The estimation of the uncertainty in the efficiency was performed taking into account uncertainties in the generation of the cascades and uncertainties in the simulated TAC geometry. More details can be found in [51, 52].

The same tools used to calculate the detection efficiency were used to reproduce the energy response of the TAC to the sample activity. In this way, the value of the sample mass could be deduced by comparing the Monte Carlo simulations with the data. We obtained a sample mass of 6.77±15% mg, which is consistent with the results of the spectroscopic characterization of the sample performed at CERN (7.34±15% mg) and not with the value provided by the manufacturers (10 mg). An example of the comparison between the experimental and the simulated results is given in Fig. 5. The estimated uncertainty is much larger than the one of the detection efficiency due to the lower energies of the γ-rays involved in the simulation, which in this case are close to the threshold of the BaF_2 crystals.

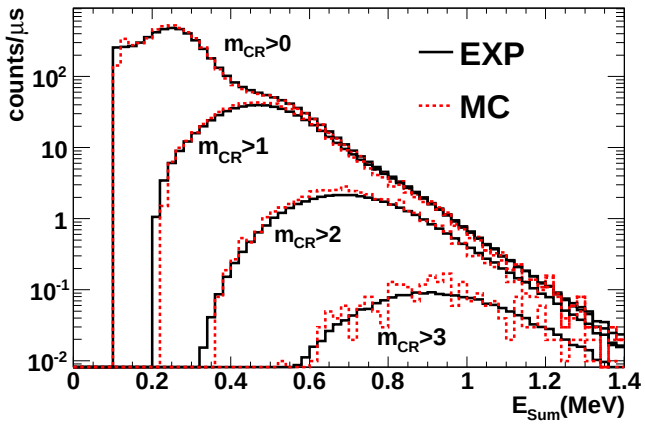

FIG. 5. Experimental (solid lines) and simulated (dotted lines) deposited energy spectra due to the detection of the sample activity. A sample mass of 6.77 mg of ^{243}Am has been used.

C. Normalization

The Beam Interception Factor, F_{BIF}, is the fraction of the neutron beam intercepted by the measured sample. It has been calculated by measuring a thick ^{197}Au sample of the same diameter as the ^{243}Am one (Section II C), placed at the same position. The strongest ^{197}Au resonance at 4.9 eV has been used to measure the F_{BIF} by means of the saturated resonance method [53] obtaining a value of 19.6(3)%, which is consistent with other measured values [38, 45] for the same sample diameter.

The uncertainty in the normalization of the experimental capture yield is dominated by the uncertainties in the detection efficiency (2.2%) and the F_{BIF} (1.5%), which added linearly or quadratically give total uncertainties of 3.7% or 2.7%, respectively. However, the uncertainty in the sample mass is much larger (11%), so the n_TOF capture measurement was finally normalized to the previous existing transmission measurements (Table I). The normalization procedure was performed with the SAMMY code [39], by fitting the obtained capture yield to the existing transmission data. Two different methods were used:

1. A simultaneous fit of the n_TOF capture yield and the transmission measurements, where the resonance parameters and the normalization of the n_TOF capture yield were varied. Only the Simpson *et al.* data sets were used for these analyses, due to the lack of experimental information available for the rest of the transmission measurements, necessary to perform the fits.

2. A normalization of the n_TOF data to the resonance parameters provided by the experimentalists of the transmission measurements [4–7], or the evaluators [28, 54].

The Simpson *et al.* transmission measurement was performed with two ^{243}Am samples, one thicker [55] than the other [56]. The normalization of the n_TOF capture data was performed to both data sets in six different energy ranges [57]. These transmission data were only used to normalize the capture data, and not to perform the resonance analysis, for two reasons. First, the uncertainties in the transmission data available in EXFOR are not given and thus realistic assumptions are necessary to perform the resonance analysis. It was estimated that reasonable assumptions can be made to perform a normalization, but are not sufficient to perform a resonance analysis. Second, the resolution function of the measurement was not reported and thus it had to be taken from a different reference. This is why the normalization was performed only at low neutron energies, below 50 eV, were the effect of the resolution function is very low.

In the second method we fitted the n_TOF capture yield to the theoretical capture yield resulting from the different resonance parameters obtained by experimentalists and evaluators. We found that our data are incompatible with the values provided by Cote *et al.* and Bellanova *et al.* (see Table I), but are in a reasonable agreement with the resonance parameters provided by Simpson *et al.*, Berreth *et al.*, and some evaluations such as the ones performed by Mughabghab [28] or Maslov [54].

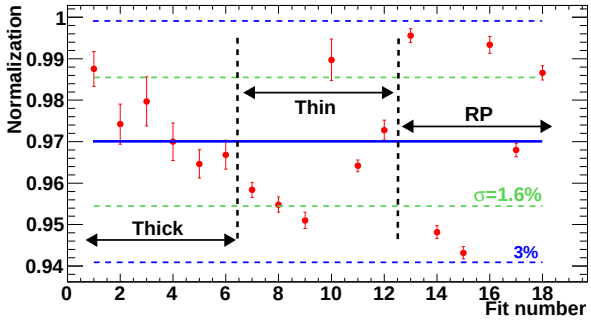

FIG. 6. Results of 18 different normalization fits performed with SAMMY. In all the cases, the initial thickness of the ^{243}Am sample considered was $2{\cdot}10^5$ atoms/barn, which corresponds to a mass of 6.34 mg.

The results of all these normalization values are presented in Fig. 6. The first 6 points correspond to the fits performed to the Simpson *et al.* thick transmission sample, the fits 7 to 12 to the Simpson *et al.* thin transmission sample, and the latter 6 points to the fits performed to the different resonance parameters. In all the cases the fits were performed above 3 eV, to avoid the strongest ^{243}Am resonance at 1.35 eV. The uncertainties in the normalization data points are due to the uncertainty in the background component constant in time presented in Section III A, which is the dominant contribution. More information concerning the normalization procedure can be found in [52].

The mean value of all the normalization values presented in Fig. 6 is 0.970, which corresponds to a sample thickness of $1.94{\cdot}10^5$ atoms/barn, or a mass of 6.23 mg of ^{243}Am. The standard deviation is 1.6%, but the different values are not independent and thus a 3% uncertainty in the normalization was adopted, which is more conservative. Note that this 3% uncertainty is the uncertainty in the normalization of the capture cross section. In the calculation of the uncertainty of the sample mass, the 2.7% uncertainty in the normalization of the experimental capture yield (due to the detection efficiency and the F_{BIF}, without taking into account the normalization to transmission) has to be added. Thus, the fitted sample mass (or thickness) has an uncertainty of 4%, if both quantities are added quadratically.

IV. CROSS SECTION ANALYSIS

A. Analysis of the Resolved Resonance Region

The Resolved Resonance Region (RRR) has been analyzed with the SAMMY code (version 7.0.0) up to 400 eV (250 eV is the high energy limit of the RRR in the present evaluations). We have fitted the energy E_0, the neutron width Γ_n, and the radiative capture width Γ_γ of each resonance in the measured energy range, using the Reich-Moore approximation. The resonance parameters of the negative and the first resonance at 0.415 eV, and all the fission widths and the scattering radius were fixed to the values present in the ENDF/B-VII.0 evaluation, after verifying that strong variations of these parameters do not affect significantly the resulting capture yield. All the observed resonances are s-wave resonances (orbital spin $l = 0$), as it can be confirmed, after performing the fit, by applying the techniques described in [58]. It was not possible to distinguish between the two J=2,3 possible total spin values, so only the $g\Gamma_n$ values were determined. The time-energy relation was obtained by fitting the n_TOF time of flight distance to reproduce the energies of the resonances of ^{197}Au in the ENDF/B-VII.0 evaluation, obtaining 184.878 m. The n_TOF capture yield is presented together with the results of the SAMMY fit in Fig. 7, for several neutron energy ranges.

We have obtained the statistical uncertainties in the resonance parameters from SAMMY, together with their correlations. Concerning the systematic uncertainties, the following contributions were considered:

1. Uncertainties due to the normalization. They were estimated by performing several fits (1000), each of them with a different normalization value, varied randomly according to a Gaussian distribution with standard deviation equal to the 3% uncertainty in the normalization. The systematic uncertainty of each fitted parameter was then estimated as the standard deviation of all the fitted values.

2. Uncertainties due to the temperature of the sample.

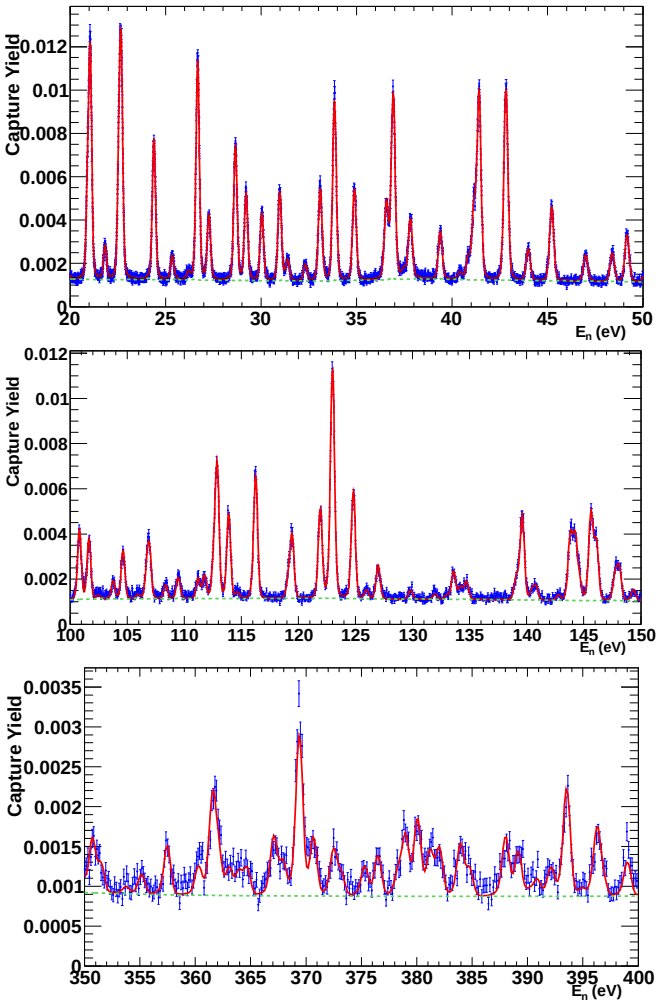

FIG. 7. Examples of the fitted n_TOF capture yield, in different energy ranges.

They were estimated in the same way as in the previous case, by varying the sample temperature according to 293±4 K.

3. Uncertainties due to the background component constant in time (Section III A). They were estimated in the same way as in the two previous cases, by varying this parameter according to its value: $a = 0 \pm 3 \cdot 10^{-5}\sqrt{eV}$.

4. Uncertainty due to the shape of the background. Due to the low beam time dedicated to the background measurements (Table III), it was necessary to integrate the background in large neutron energy intervals to reduce the statistical fluctuations. However, since the shape of the background is quite smooth (Fig. 3), we used an smoothed background for the resonance analysis. In order to estimate the uncertainties in the resonance parameters due to the smoothing procedure, different analysis were performed, each of them with a background smoothed with a different technique. The uncertainties in the fitted resonance parameters were then estimated as the standard deviation of the resulting fitted values.

5. Uncertainty due to the Doppler broadening model. Following the same approach than in the previous cases, we estimated this contribution by comparing the results of a fit performed with the free gas model and a fit performed with the crystal-lattice model [39]. In the latter case, we used the phonon spectrum of UO_2, since it has not been measured for AmO_2.

6. Uncertainty due to the sample inhomogeneities. The resonance integral ($I_0 = \int_{0.5eV}^{\infty} \sigma_\gamma(E)/EdE$) obtained after performing the fit is I_0 =1681 barn, which is significantly lower than any of the measured values presented in Table II. This discrepancy can be explained with the existence of inhomogeneities in the sample, which would affect the shelf shielding and multiple scattering corrections. The strongest resonance at 1.35 eV is the only one where these corrections are important (∼15%), and it contributes around 70-80% to the resonance integral. In the rest of the resonances the shelf shielding and multiple scattering corrections are much lower (8 resonances with corrections between 3% and 1%, the rest of the resonances below 1%). For this reason, the strongest resonance at 1.35 eV was not measured correctly. This is why the normalization to the transmission data was performed above 3 eV. In order to estimate the uncertainties due to the sample inhomogeneities, we compared the results of a fit performed with the nominal sample thickness with a fit performed with a double thickness, where the shelf shielding and multiple scattering corrections are larger.

The rest of the contributions, such are the ones corresponding to the dead time corrections or the resolution function, were considered negligible.

The values of the fitted resonance parameters are presented in Tables IV and V. The Γ_γ values with statistical uncertainties larger than 10% were fixed to the average radiative capture width, which was calculated from the rest of the values, all of them from resonances below 43 eV. Table IV provides as well the (quadratic) sum of the systematic uncertainties. In the case of the $g\Gamma_n$ parameters, the contributions to the systematic uncertainties associated with the temperature, the shape of the background and the Doppler broadening are negligible. In addition, since for nuclei with $\Gamma_\gamma \gg \Gamma_n$ the resonance area is nearly proportional to $g\Gamma_n$, the uncertainty in the $g\Gamma_n$ due to the normalization is the same 3% as the normalization uncertainty and has not been included in the tables. Thus, only the uncertainties due to the background component constant in time and the sample inhomogeneities were taken into account in the tabulated

values. Concerning the Γ_γ parameters, the normalization is the only negligible contribution to the total systematic uncertainty.

Above 43 eV, all the Γ_γ values were fixed to $<\Gamma_\gamma>=$ 42 meV, and only the energy and $g\Gamma_n$ values are given in Table V. At these energies, the estimated uncertainties due to the background component constant in time and the sample inhomogeneities are negligible, so only the statistical uncertainty and the uncertainty due to the normalization have to be considered.

More information concerning the correlations between the different resonance parameters and the different contributions to the systematic uncertainties can be found in [52], and they will be also available in EXFOR.

TABLE IV: Resonance parameters below 43 eV. The first uncertainty in each parameter corresponds to the statistical uncertainty, whereas the second one is the total systematic uncertainty. The $g\Gamma_n$ values have an additional 3% uncertainty due to the normalization.

E_0 (eV)	$g\Gamma_n$(meV)	Γ_γ(meV)
-2	0.5735	39
0.4151	0.00042	39
0.9798	0.00643 ± 0.00004 ± 0.00008	34.4 ± 0.4 ± 1.1
1.3526	0.48579 ± 0.00024 ± 0.02447	48.57 ± 0.04 ± 2.50
1.7395	0.11465 ± 0.00015 ± 0.00111	40.11 ± 0.12 ± 0.39
3.1251	0.00486 ± 0.00012 ± 0.00015	34.0 ± 2.4 ± 1.8
3.4160	0.1389 ± 0.0003 ± 0.0007	39.93 ± 0.24 ± 0.47
3.8382	0.00608 ± 0.00017 ± 0.00022	45.2 ± 2.9 ± 2.4
5.1122	0.1512 ± 0.0005 ± 0.0007	40.2 ± 0.4 ± 0.6
6.5378	0.4824 ± 0.0011 ± 0.0031	41.0 ± 0.3 ± 0.7
7.0467	0.0359 ± 0.0005 ± 0.0004	47.8 ± 2.1 ± 1.3
7.8434	0.6813 ± 0.0015 ± 0.0048	42.9 ± 0.3 ± 0.8
8.3658	0.00788 ± 0.00036 ± 0.00016	42
8.7480	0.0630 ± 0.0008 ± 0.0005	45.5 ± 1.8 ± 1.2
9.2931	0.0745 ± 0.0008 ± 0.0006	40.3 ± 1.6 ± 1.3
10.286	0.2384 ± 0.0013 ± 0.0009	53.5 ± 0.9 ± 1.0
10.870	0.00769 ± 0.00046 ± 0.00016	42
11.249	0.1458 ± 0.0013 ± 0.0007	41.1 ± 1.4 ± 1.0
11.661	0.0518 ± 0.0010 ± 0.0004	40.8 ± 2.8 ± 0.8
12.098	0.0855 ± 0.0012 ± 0.0006	42.3 ± 2.2 ± 1.0
12.846	1.189 ± 0.004 ± 0.008	43.5 ± 0.5 ± 0.9
13.124	0.713 ± 0.003 ± 0.003	46.1 ± 0.8 ± 1.7
15.098	0.03001 ± 0.00115 ± 0.00019	42
15.369	0.6881 ± 0.0032 ± 0.0021	44.0 ± 0.9 ± 1.3
16.178	0.2725 ± 0.0024 ± 0.0010	44.9 ± 1.6 ± 1.2
16.543	0.0978 ± 0.0015 ± 0.0004	42
17.830	0.1115 ± 0.0017 ± 0.0005	42
18.120	0.0200 ± 0.0011 ± 0.0003	42
19.496	0.1089 ± 0.0019 ± 0.0006	42
19.869	0.0425 ± 0.0015 ± 0.0005	42
20.933	0.2356 ± 0.0040 ± 0.0006	42
21.071	0.5822 ± 0.0054 ± 0.0018	42.8 ± 1.7 ± 1.3
21.840	0.0657 ± 0.0028 ± 0.0004	42
21.851	0.02369 ± 0.00224 ± 0.00006	42
22.580	0.3509 ± 0.0064 ± 0.0011	41.8 ± 2.7 ± 0.8
22.695	0.5875 ± 0.0070 ± 0.0014	42.5 ± 2.0 ± 1.5
24.404	0.4761 ± 0.0045 ± 0.0017	50.6 ± 2.0 ± 1.4
25.365	0.0797 ± 0.0024 ± 0.0006	42
26.208	0.0257 ± 0.0017 ± 0.0003	42
26.695	0.8469 ± 0.0062 ± 0.0020	44.6 ± 1.6 ± 1.4
27.284	0.2452 ± 0.0041 ± 0.0011	46.2 ± 3.3 ± 0.9
28.673	0.5589 ± 0.0057 ± 0.0015	45.3 ± 2.3 ± 1.3
29.230	0.3650 ± 0.0051 ± 0.0012	45.3 ± 2.9 ± 1.2
30.058	0.2916 ± 0.0043 ± 0.0009	42
30.994	0.4023 ± 0.0055 ± 0.0014	42.6 ± 2.9 ± 1.4
31.406	0.0937 ± 0.0033 ± 0.0006	42
32.339	0.0768 ± 0.0031 ± 0.0007	42
33.115	0.4816 ± 0.0064 ± 0.0016	51.5 ± 3.1 ± 1.2
33.862	0.9399 ± 0.0082 ± 0.0020	40.6 ± 2.0 ± 1.8
34.908	0.4928 ± 0.0064 ± 0.0012	42
36.583	0.4657 ± 0.0086 ± 0.0014	64 ± 4 ± 3
36.940	1.1680 ± 0.0113 ± 0.0020	57 ± 3 ± 3
37.498	0.0532 ± 0.0035 ± 0.0003	42
37.837	0.3786 ± 0.0071 ± 0.0015	54.8 ± 4.0 ± 1.2
39.399	0.3007 ± 0.0061 ± 0.0011	42
40.438	0.0456 ± 0.0033 ± 0.0005	42
40.861	0.1369 ± 0.0054 ± 0.0007	42
41.165	0.4730 ± 0.0096 ± 0.0007	42
41.438	1.342 ± 0.013 ± 0.003	44.5 ± 2.7 ± 2.1
42.845	1.493 ± 0.014 ± 0.003	43.5 ± 2.2 ± 2.3

TABLE V: Resonance energies and $g\Gamma_n$ parameters between 43 and 400 eV, the latter together with their statistical uncertainties. The systematic uncertainty in the values of the $g\Gamma_n$ is the same, and amounts to a 3% uncertainty due to the normalization.

E_0 (eV)	$g\Gamma_n$(meV)	E_0 (eV)	$g\Gamma_n$(meV)
44.016	0.2311 ± 0.0064	45.242	0.5887 ± 0.0092
47.018	0.2125 ± 0.0067	48.418	0.2416 ± 0.0073
49.189	0.4093 ± 0.0088	50.107	0.058 ± 0.006
51.144	0.507 ± 0.010	52.026	0.039 ± 0.006
52.916	1.043 ± 0.014	53.579	0.035 ± 0.007
53.868	0.325 ± 0.010	54.393	0.871 ± 0.015
54.617	0.153 ± 0.011	55.737	0.912 ± 0.014
57.194	0.051 ± 0.007	58.572	0.200 ± 0.010
58.953	0.447 ± 0.012	59.803	0.444 ± 0.012
60.605	0.590 ± 0.014	61.049	1.527 ± 0.020
62.370	0.139 ± 0.009	63.032	0.226 ± 0.010
63.489	0.067 ± 0.009	64.664	0.314 ± 0.012
66.067	0.728 ± 0.015	67.194	0.602 ± 0.015
67.836	0.644 ± 0.015	68.524	0.870 ± 0.018
69.502	1.93 ± 0.03	70.102	1.402 ± 0.023
71.530	0.094 ± 0.011	72.035	1.392 ± 0.023
72.711	1.647 ± 0.024	73.713	0.235 ± 0.013
74.131	0.266 ± 0.014	74.785	0.111 ± 0.012
75.253	1.67 ± 0.03	76.385	0.158 ± 0.013
76.818	0.301 ± 0.015	77.362	0.832 ± 0.020
78.040	0.212 ± 0.014	79.821	0.114 ± 0.013
80.396	0.290 ± 0.022	80.611	0.54 ± 0.03
80.899	1.75 ± 0.03	82.862	0.410 ± 0.018
83.309	1.37 ± 0.03	83.963	0.27 ± 0.07
84.011	0.79 ± 0.08	84.599	0.227 ± 0.016
85.267	0.92 ± 0.06	85.391	2.59 ± 0.07
86.436	0.983 ± 0.024	88.133	0.725 ± 0.023
88.740	0.819 ± 0.024	90.165	0.697 ± 0.023
91.002	0.607 ± 0.022	94.474	0.75 ± 0.03
95.081	0.105 ± 0.017	95.642	0.252 ± 0.020

TABLE V: (continued)

E_0 (eV)	$g\Gamma_n$(meV)	E_0 (eV)	$g\Gamma_n$(meV)
97.283	1.10 ± 0.03	98.509	0.218 ± 0.020
99.280	0.402 ± 0.023	100.870	1.83 ± 0.04
101.701	1.53 ± 0.04	102.521	0.212 ± 0.021
103.830	0.44 ± 0.03	104.690	1.26 ± 0.03
106.032	0.182 ± 0.022	106.793	0.96 ± 0.05
107.022	1.12 ± 0.05	108.425	0.43 ± 0.03
109.531	0.68 ± 0.03	111.280	0.61 ± 0.03
111.831	0.60 ± 0.03	112.651	1.14 ± 0.05
112.945	4.20 ± 0.08	113.955	2.79 ± 0.06
114.731	0.24 ± 0.03	116.120	0.14 ± 0.09
116.316	4.18 ± 0.04	119.186	0.62 ± 0.04
119.507	2.04 ± 0.06	121.983	3.14 ± 0.06
123.055	14.1 ± 0.3	124.880	4.07 ± 0.08
126.037	0.34 ± 0.03	127.053	1.13 ± 0.04
129.891	0.32 ± 0.03	132.060	0.31 ± 0.03
133.064	0.18 ± 0.03	133.669	1.05 ± 0.05
134.271	0.43 ± 0.04	134.795	0.65 ± 0.04
139.162	0.84 ± 0.05	139.682	4.07 ± 0.09
140.529	0.30 ± 0.04	140.871	0.53 ± 0.05
142.862	0.28 ± 0.04	143.893	2.80 ± 0.08
144.317	2.75 ± 0.10	144.701	0.95 ± 0.06
145.705	4.35 ± 0.11	146.182	2.78 ± 0.08
147.839	1.16 ± 0.07	148.190	1.44 ± 0.07
149.436	0.43 ± 0.04	150.717	0.44 ± 0.04
152.491	0.71 ± 0.05	153.616	2.19 ± 0.08
154.267	1.86 ± 0.07	155.065	0.52 ± 0.05
158.180	1.85 ± 0.07	158.815	0.50 ± 0.05
160.229	6.05 ± 0.15	160.612	0.96 ± 0.07
163.471	0.29 ± 0.04	164.396	2.66 ± 0.08
165.683	0.64 ± 0.06	166.120	1.01 ± 0.07
166.469	0.35 ± 0.06	167.567	3.80 ± 0.11
169.394	0.73 ± 0.05	172.200	3.60 ± 0.10
173.081	4.40 ± 0.13	174.257	2.12 ± 0.08
175.280	1.91 ± 0.08	176.326	1.89 ± 0.10
176.727	3.13 ± 0.11	179.537	1.39 ± 0.09
179.911	0.98 ± 0.08	180.470	0.63 ± 0.06
181.226	1.19 ± 0.07	182.516	0.75 ± 0.06
183.579	1.82 ± 0.09	184.070	2.21 ± 0.09
185.608	0.65 ± 0.06	186.227	1.49 ± 0.09
186.654	1.22 ± 0.08	187.517	4.42 ± 0.14
188.382	0.62 ± 0.06	189.884	0.69 ± 0.08
190.250	0.67 ± 0.08	191.064	2.04 ± 0.10
191.783	2.45 ± 0.10	192.902	5.38 ± 0.17
195.077	0.24 ± 0.05	195.821	0.72 ± 0.07
196.473	1.11 ± 0.08	197.187	3.01 ± 0.12
199.272	2.53 ± 0.11	201.999	0.52 ± 0.07
202.586	0.20 ± 0.05	204.043	0.82 ± 0.08
204.673	1.17 ± 0.08	206.078	0.92 ± 0.08
207.572	1.63 ± 0.09	208.859	2.14 ± 0.11
210.283	1.67 ± 0.13	210.640	2.05 ± 0.17
211.071	3.47 ± 0.17	212.793	0.36 ± 0.07
213.932	3.47 ± 0.14	216.325	1.25 ± 0.09
219.483	1.39 ± 0.10	220.063	0.78 ± 0.10
220.603	0.99 ± 0.10	222.118	0.41 ± 0.08
221.197	0.68 ± 0.08	222.656	0.42 ± 0.08
224.599	4.32 ± 0.17	225.471	1.82 ± 0.11
226.315	0.50 ± 0.09	226.798	1.49 ± 0.11
228.388	0.44 ± 0.07	232.332	4.45 ± 0.17
233.502	5.88 ± 0.23	235.447	0.65 ± 0.09
236.908	1.87 ± 0.12	238.468	1.08 ± 0.10

TABLE V: (continued)

E_0 (eV)	$g\Gamma_n$(meV)	E_0 (eV)	$g\Gamma_n$(meV)
239.061	0.75 ± 0.12	239.468	1.06 ± 0.12
241.136	0.59 ± 0.09	242.239	2.10 ± 0.13
243.670	0.84 ± 0.25	243.781	1.3 ± 0.3
244.558	1.20 ± 0.11	246.467	3.24 ± 0.16
247.913	5.54 ± 0.21	248.655	2.32 ± 0.15
251.053	2.88 ± 0.16	252.214	6.0 ± 0.3
254.482	0.90 ± 0.11	255.742	12.9 ± 0.6
256.329	1.12 ± 0.13	257.622	1.53 ± 0.13
258.561	1.49 ± 0.13	259.384	7.9 ± 0.3
260.652	2.70 ± 0.16	262.868	0.58 ± 0.10
265.358	1.23 ± 0.14	265.951	3.28 ± 0.22
266.598	5.3 ± 0.3	267.837	1.64 ± 0.14
271.683	5.9 ± 0.3	272.757	1.02 ± 0.12
273.987	7.4 ± 0.3	275.076	2.55 ± 0.17
276.909	1.35 ± 0.14	277.563	1.57 ± 0.15
278.924	2.91 ± 0.19	280.013	2.55 ± 0.18
280.910	0.51 ± 0.11	281.542	1.10 ± 0.15
282.317	3.8 ± 0.3	282.897	7.8 ± 0.4
285.633	1.18 ± 0.13	288.117	4.23 ± 0.24
289.485	4.9 ± 0.3	291.076	6.2 ± 0.3
295.672	3.39 ± 0.22	298.124	1.76 ± 0.16
299.693	0.97 ± 0.14	300.418	0.88 ± 0.14
301.363	1.43 ± 0.16	302.211	3.65 ± 0.24
303.571	0.66 ± 0.14	304.369	8.1 ± 0.4
307.084	1.86 ± 0.18	307.989	3.52 ± 0.24
310.268	0.69 ± 0.14	311.234	8.3 ± 0.4
312.223	1.40 ± 0.17	313.586	11.0 ± 0.6
315.387	4.7 ± 0.3	316.432	0.93 ± 0.15
317.607	2.25 ± 0.20	319.832	0.68 ± 0.14
320.986	9.6 ± 0.5	321.949	0.81 ± 0.15
325.731	0.74 ± 0.20	325.890	0.47 ± 0.22
326.558	4.0 ± 0.3	327.256	2.7 ± 0.3
328.915	0.40 ± 0.13	329.789	0.90 ± 0.18
330.480	0.96 ± 0.19	331.261	1.84 ± 0.22
332.280	4.7 ± 0.3	333.703	3.2 ± 0.3
334.963	2.8 ± 0.3	336.479	4.4 ± 0.3
337.849	1.92 ± 0.23	338.761	4.0 ± 0.3
341.211	2.55 ± 0.25	342.592	1.62 ± 0.21
344.105	1.16 ± 0.19	346.021	0.45 ± 0.14
347.545	7.5 ± 0.5	349.886	0.62 ± 0.16
350.889	2.4 ± 0.3	351.673	1.35 ± 0.20
353.935	0.47 ± 0.14	355.336	1.08 ± 0.18
357.665	2.44 ± 0.24	360.478	2.26 ± 0.24
361.742	4.4 ± 0.4	362.279	3.8 ± 0.4
363.254	1.47 ± 0.21	364.130	1.35 ± 0.22
364.859	1.50 ± 0.22	367.281	2.8 ± 0.3
368.092	1.74 ± 0.24	369.593	22.2 ± 1.6
370.875	3.6 ± 0.3	372.679	2.5 ± 0.3
373.365	1.09 ± 0.21	375.489	1.42 ± 0.21
376.691	2.4 ± 0.3	378.523	1.05 ± 0.22
379.189	3.9 ± 0.4	380.270	4.9 ± 0.4
381.400	3.1 ± 0.3	382.246	2.4 ± 0.3
384.143	2.9 ± 0.3	384.967	1.84 ± 0.25
388.234	3.3 ± 0.3	389.368	3.1 ± 0.3
390.358	0.71 ± 0.18	391.073	0.98 ± 0.20
392.314	1.66 ± 0.24	393.751	8.1 ± 0.6
395.109	0.53 ± 0.16	396.471	3.3 ± 0.4
396.987	1.5 ± 0.3	399.229	3.4 ± 0.3

The ratio between the n_TOF capture cross section

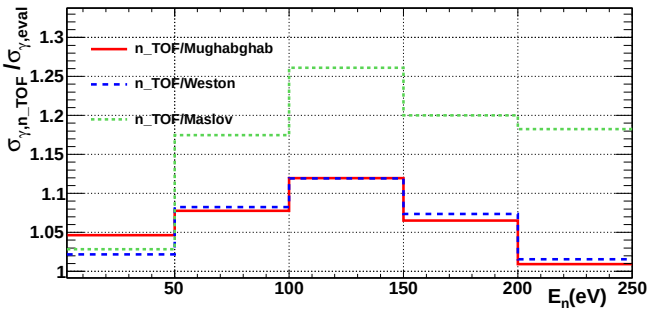

FIG. 8. Ratio between the n_TOF fitted capture cross section and the ones available in different evaluations ($\int_{E_1}^{E_2}\sigma_{\gamma,n\_TOF}(E)dE/\int_{E_1}^{E_2}\sigma_{\gamma,eval}(E)dE$), integrated in different energy ranges. The lower energy limit of the first bin is 3 eV, in order to avoid the strongest resonance at 1.35 eV.

and the most recent evaluations is presented in Fig. 8. The ratio has been performed with three different evaluations, carried out by: Mughabghab, adopted by the ENDF/B-VII.1 evaluation; Weston, adopted by the older ENDF/B releases and similar to the one by Mughabghab; and Maslov, adopted by the rest of the evaluations in this energy range: JEFF-3.1.2, JENDL-4.0, JENDL-3.3 [59], BROND-2.2 [60] and CENDL-3.1. In the 3-250 eV energy range, the n_TOF capture cross section is, on average, 6% larger than the Mughabghab and Weston evaluations and 13% larger than the Maslov evaluation. It should be said that new resonances have been found in this energy range, as well as 105 new resonances between 250 and 400 eV. In particular, the present evaluations contain 218 (Mughabghab and Weston) and 238 (Maslov) resonances up to 250 eV, whereas the n_TOF results have 248 resonances.

B. Statistical analysis of the resonance parameters

The average radiation width, $\langle\Gamma_\gamma\rangle$, was determined from the fitted values available in Table IV. We used the generalized weighted mean to take into account the correlations between the different parameters, but very similar results are obtained if the correlations are neglected. The resonances below 3 eV were not used to calculate $\langle\Gamma_\gamma\rangle$, due to the problems caused by the inhomogeneities in the vicinity of the strongest resonance at 1.35 eV. The resulting value was $\langle\Gamma_\gamma\rangle$=42.00±0.12±0.5±0.3±0.7±0.6 meV, where these uncertainties are, respectively: statistical, due to the sample temperature, due to the background component constant in time, due to the Doppler broadening model and due to the sample inhomogeneities. If all the systematic uncertainties are added linearly or quadratically we obtain a total systematic uncertainty of 2.1 or 1.1 meV, respectively.

An estimation of the s-wave average level spacing D_0 can be obtained, in principle, from $D_0 = \Delta E/(N-1)$ and $\Delta D_0/D_0 \approx 1/N$ [61], where N is the number of resonances observed in the neutron energy interval between E_1 and E_2 and $\Delta E = E_2 - E_1$. However, there are usually a certain number of small resonances which have not been detected (missing resonances), and their number has to be estimated as well. One of the most common used methods is based on fitting the reduced neutron width distributions, $\Gamma_n^0 = \Gamma_n \cdot (E_0/1eV)^{-1/2}$, which are assumed to follow, for each spin value J, the Porter-Thomas law of one degree of freedom, $p(x)dx = e^{-x/2}/\sqrt{2\pi x}dx$, were $x = \Gamma^0_{n,J}/\langle\Gamma^0_{n,J}\rangle$. Since the spins of the different resonances were not determined, we assumed that $1/D_{0,J} \propto (2J+1)$ and that $S_{0,J} = S_0$ (both assumptions are justified in Appendix D of [62]), where $S_0 = \langle g\Gamma^0_n\rangle/D_0$ is the s-wave neutron strength function. From these assumptions it follows that $\langle g_J\Gamma^0_{n,J}\rangle = \langle g\Gamma^0_n\rangle$, i.e., the value of $\langle g\Gamma^0_n\rangle$ is the same for both spin groups. Therefore, it is possible to consider only one Porter-Thomas distribution, where both spin groups are included, after making the change of variable from $x = \Gamma^0_n/\langle\Gamma^0_n\rangle$ to $y = g\Gamma^0_n/\langle g\Gamma^0_n\rangle$. With some manipulations of the Porter-Thomas distribution, it follows that, for a given energy interval, the number of resonances with $\sqrt{g\Gamma^0_n}$ greater than a certain value, x, is obtained from:

$$f(x) = N\frac{2}{\sqrt{\pi}\sqrt{2\langle g\Gamma^0_n\rangle}}\int_x^\infty \exp\left(-\frac{y^2}{2\langle g\Gamma^0_n\rangle}\right)dy \qquad (2)$$

where N is the number of resonances in the energy interval. This formula was used to estimate the number of missing resonances, by fitting the values of N and $\langle g\Gamma^0_n\rangle$, as it is presented in Fig. 9. The result was D_0=0.66(3) eV, where the uncertainty was estimated from the statistical uncertainty due to the number of resonances considered and from calculating D_0 in different energy ranges.

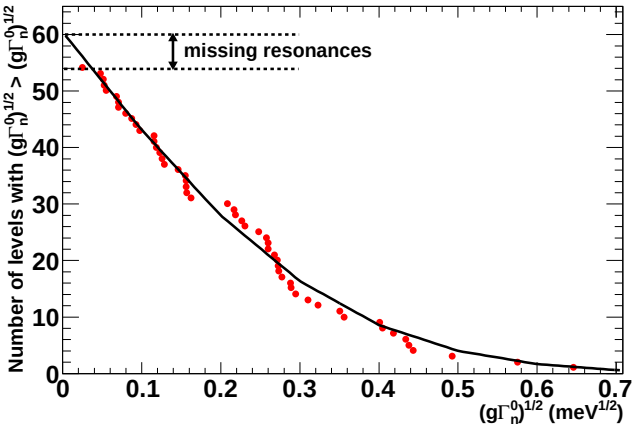

FIG. 9. Estimation of the number of missing resonances, performed in the 0-40 eV energy range. The experimental points were fitted to Equation 2.

The neutron strength function for s-wave resonances S_0 can be obtained from $S_0 = \sum_\lambda g\Gamma^0_{n,\lambda}/\Delta E$ and $\Delta S_0/S_0 =$

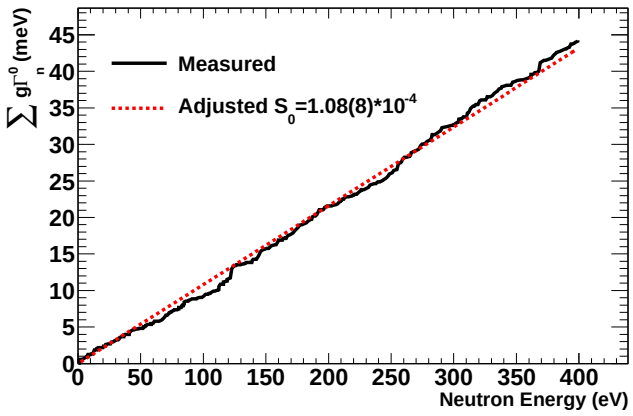

FIG. 10. Linear fit of $\sum_\lambda g\Gamma^0_{n,\lambda}$ as a function of the neutron energy.

$\sqrt{2/N}$ [61], and it was calculated from the slope of the experimental cumulative sum, as it is presented in Fig. 10. The result was $S_0 = 1.08(8) \cdot 10^{-4}$, with an additional 3% normalization uncertainty.

C. Analysis of the Unresolved Resonance Region

We have analyzed the energy range between 250 and 2500 eV as Unresolved Resonance Region (URR). Thus, the 250 - 400 eV energy region has been analyzed as both RRR and URR, the latter for comparison to the existing experiments and evaluations. The analysis has been performed with the SAMMY code, which contains a modified version of the FITACS code [39, 63], which uses Hauser-Feshbach theory [64] with width fluctuations.

SAMMY performs the fits in the URR to the capture cross section instead of the capture yield. In the URR the shelf-shielding and multiple scattering effects are negligible, so σ_γ was obtained directly by dividing the capture yield by the sample thickness, $\langle\sigma_\gamma(E_n)\rangle = \langle Y_\gamma(E_n)\rangle/n$. In the calculation of the capture yield, the background was subtracted without any smoothing procedure, since it is not straightforward to verify if the smoothed background is at the level of the measured yield between resonances, as it can be done in the RRR. Concerning the uncertainties, all the contributions to the systematic uncertainties mentioned in Section IV A are negligible in this energy range, with the exception of the uncertainty in the normalization. The largest contribution to the statistical uncertainties comes from the subtraction of the measured background.

The unique parameters which could be fitted with the n_TOF data were S_0 and $\langle\Gamma_\gamma\rangle_0$. The channel radius, distant level parameter R_l^∞ and fission parameters are not sensitive to this measurement, and the p-wave contribution starts to be important at higher energies. In particular, according to the ENDF/B-VII.1 evaluation, the p-wave contribution to the total capture cross section is around 11% at 2.5 keV, and a variation of 25% in the S_1 value induces a change of only 0.5% in the fitted value of S_0.

The fit of S_0 and $\langle\Gamma_\gamma\rangle_0$ was performed by using the results of the statistical analysis of the RRR as prior uncertainties, and the average level spacing was fixed to the obtained value (D_0=0.66 eV). The results of the fit were S_0=1.10(4)·10^{-4} and $\langle\Gamma_\gamma\rangle_0$=42.1(20) meV, with a correlation between them of -0.23. All these uncertainties and correlations are statistical, and there is an extra systematic uncertainty of 3% in the S_0 value due to the uncertainty in the normalization. If no prior knowledge of the parameters are assumed, compatible values of S_0 and $\langle\Gamma_\gamma\rangle_0$ are obtained, but with larger uncertainties and correlations.

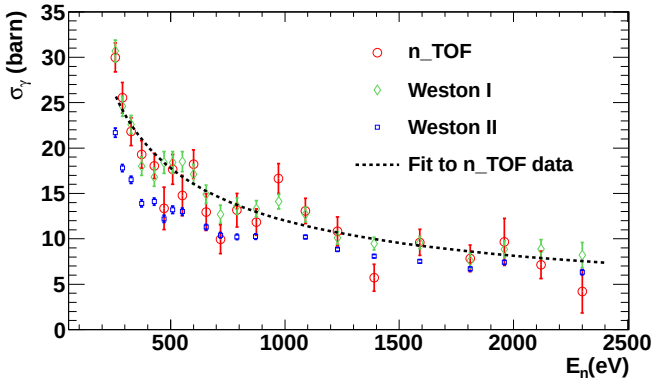

FIG. 11. Fitted n_TOF capture data in the URR together with the two different data sets provided by Weston *et al.*, in their common energy range.

The fitted n_TOF capture data is presented in Fig. 11, together with the only two available capture data sets at present in this energy range, tagged as "Weston I" [65] and "Weston II" [66]. Both of them have been provided by Weston *et al.* (see Table I), in the range from 250 eV up to 92 keV and differ significantly below 1.5-2 keV. The n_TOF data is compatible, in normalization and shape, with the Weston I data set, whereas it is not with the Weston II data. This is an important result, since the normalization of the n_TOF data to the available transmission experiments has been performed at low energies. On the other hand, all the present evaluations are much closer to the Weston II data set, underestimating the ^{243}Am capture cross section in this energy region between 7% and 20%.

We have extended up to higher energies the analysis of the URR, which ranges up to 40-42 keV in the present evaluations, with the data provided by Weston *et al.*, since they are compatible with the n_TOF data in their common energy range. The other available data set, Wisshak *et al.* (Table I), is about 10% lower. Note that above 2 keV, the two mentioned Weston *et al.* data sets are compatible. We performed a fit to the Weston *et al.* data in the 2.5-42 keV energy range by varying

TABLE VI. URR parameters (at E_n=0) obtained in this work compared with the ones obtained in other evaluations.

	D_0 (eV)	S_0 ($\times 10^{-4}$)	$\langle\Gamma_\gamma\rangle_0$ (meV)	S_1 ($\times 10^{-4}$)	$\langle\Gamma_\gamma\rangle_1$ (meV)
This work	0.66(3)	1.10(5)[a]	42.1(20)	1.65(24)[b]	52(34)[b]
Bellanova	0.62	0.65			
Berreth			42		
Simpson	0.68	0.96(10)	39		
Cote			43(3)		
RIPL-3 [61]	0.73(6)	0.98(6)	39(3)		
Mughabghab	0.60(6)	0.98(9)	39(1)		
Maslov[c]	0.57(5)	0.87(15)	43	2.176	43
BROND-2.2	0.67	0.93	39	2.44	39
JENDL-4.0	0.44	0.864	39	2.687	39
ENDF/B-VII.0	0.75	0.98	39	2.2	44
ENDF/B-VII.1	0.66	0.98	39.1	2.6	69.8

[a] This uncertainty has been obtained by adding quadratically the statistical uncertainty ($4 \cdot 10^{-4}$) to the 3% normalization uncertainty.
[b] Values obtained from the n_TOF+Weston *et al.* measurements.
[c] Values adopted by the JEFF-3.1, JENDL-3.3 and CENDL-3.1 evaluations.

S_1 and $\langle\Gamma_\gamma\rangle_1$ and fixing S_0 and $\langle\Gamma_\gamma\rangle_0$ to the values obtained from the n_TOF data analysis. The results were S_1=1.65(24)·10^{-4} and $\langle\Gamma_\gamma\rangle_1$=52(34) meV, with a correlation between them of -0.82. No systematic uncertainties were included in the calculations, since their description in [8] is not detailed enough, and thus only the statistical uncertainties available in EXFOR were taken into account.

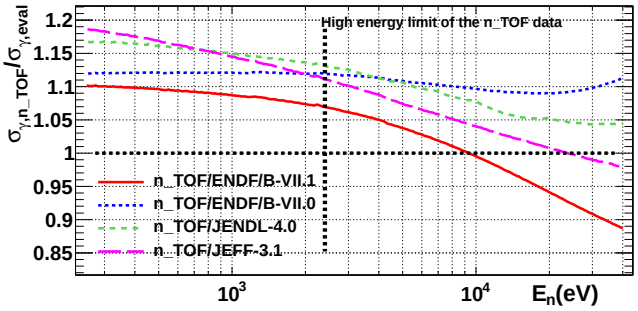

FIG. 12. Ratio between the n_TOF fitted capture cross section and and the ones available in different evaluations. JEFF-3.1 is the same as JEFF-3.1.2, JENDL-3.3 and CENDL-3.1, in this energy range.

The URR parameters obtained in this work are presented together with those obtained in other experiments and evaluations in Table VI. Note that in all the cases the parameter values are at neutron energy, E_n=0, and in the case of the n_TOF data the evolution of the URR parameters with E_n is the one described in [39]. The ratio between the n_TOF results and the capture cross sections of different evaluations are presented in Fig. 12. At low energies, the evaluations are 7%-20% lower than the n_TOF results because they seemed to use the Weston II data set instead of Weston I, which is the one compatible with the n_TOF data.

D. High energy region

Apart from the differential measurements of Weston *et al.* and Wisshak *et al.*, there are integral capture measurements in the fast energy range that can be considered for the determination of the capture cross section. One of these experiments is the PROFIL-1 irradiation experiment, where an ^{243}Am sample were irradiated in the fast PHENIX reactor in 1974 [33, 34]. Indeed, the changes in the ENDF/B-VII.1 evaluation with respect to ENDF/B-VII.0 were motivated by the results of this integral experiment [29]. The information which can be obtained from PROFIL-1 is the ^{243}Am effective capture cross section, $\sigma_{cap} = \int \phi(E)\sigma_\gamma(E)dE$, where $\phi(E)$ is the neutron flux at the irradiated sample position. We had access to the shape of the mentioned neutron flux, obtained from detailed Monte Carlo simulations [67], and used it to compare the experimental values of PROFIL-1 with calculations obtained from different capture cross sections.

The references [33] and [34] provide calculated to experimental ratios (C/E) of the mentioned effective capture cross section, σ_{cap}, each of them calculated with a different neutron data library. We did not have enough information to calculate these C/E values, but with the shape of the neutron flux we could calculate ratios between σ_{cap} values obtained from different libraries, i.e., we could calculate ratios between different C/E values. We used the C/E value provided by [34] with the ENDF/B-VII.0 evaluated library to normalize our results. With this normalization, we calculated the C/E values using several evaluated data libraries, and the results obtained are presented in the second column of Table VII. As it can be observed, they are in reasonable agreement with the values provided by the references, shown in the third and fourth columns. This indicates that the neutron flux used in this work is similar to the ones used by the references.

In a second step, we constructed several ^{243}Am capture cross sections by taking the results obtained from the analysis of the n_TOF+Weston data up to 42 keV (end of the URR in most of the evaluated libraries), and the high energy regions present in the different evaluated libraries. The corresponding C/E values obtained with these cross sections (with the previous normalization) are presented in the right column of Table VII. Since the experimental result has an estimated uncertainty of 5%, we can consider that only the results obtained when using the high energy regions of the ENDF/B-VII.1, JEFF-3.1, JEFF-3.0 [68] and CENDL-3.1 libraries are compatible with the PROFIL-1 integral experiment.

On the other hand, if we normalize the Wisshak *et al.* data to the Weston *et al.* data in their common energy

TABLE VII. C/E values of the PROFIL-1 irradiation experiment obtained with different libraries (second column), the same values provided by the references (third and fourth columns) and the C/E values obtained from the capture cross section resulting from taking the RRR and URR of this work and the part above 42 keV from the corresponding evaluated library.

	Library	[34]	[33]	This work
ENDF/B-VII.1	0.934	0.939		0.939
ENDF/B-VII.0	0.834[a]	0.834	0.85	0.889
JENDL-4.0	0.852			0.904
JEFF-3.1[b]	0.892			0.929
JEFF-3.0	0.936		0.99	0.959
CENDL-3.1	0.911			0.947
ROSFOND-2010	0.801			0.860
ENDF/B-V.0	0.585		0.62	0.730

[a] Value fixed to the value provided in [34] for normalization purposes. The rest of the values of this column were obtained from this value and the calculated C/E ratios.
[b] Same as JENDL-3.3.

range (which is reasonable, since n_TOF is compatible with Weston *et al.* and because the Wisshak *et al.* data is not compatible with the results of the PROFIL-1 irradiation experiment), then the capture cross sections provided by ENDF/B-VII.1 below 100 keV and JEFF-3.0 above 100 keV are not compatible with the differential data.

In conclusion, the ^{243}Am capture cross section constructed from the RRR and URR of this work up to 42 keV and the JEFF-3.1 or the CENDL-3.1 evaluations above 42 keV are in agreement with both the PROFIL-1 and the currently available differential capture data. In particular, this constructed cross section: (1) fits the n_TOF data between 0.7 eV and 2.5 keV; (2) fits the mentioned "Weston I" data between 0.25 and 2.5 keV; (3) fits both Weston *et al.* data sets between 2.5 and 42 keV; (4) fits the Wisshak *et al.* data up to 250 keV, if they are normalized to the Weston *et al.* data; (5) is compatible with the integral experimental results of the PROFIL-1 irradiation experiment; and (6) there is a continuous match between the URR and the high energy region, at 42 keV.

V. CONCLUSIONS

The ^{243}Am capture cross section has been measured at n_TOF using the segmented BaF_2 Total Absorption Calorimeter (TAC), in the energy range between 0.7 and 2500 eV. These are the first published analysis results of a differential ^{243}Am(n,γ) measurement below 250 eV.

The certified mass of the ^{243}Am sample provided by the manufacturers was not correct, and therefore we normalized the n_TOF capture cross section to the existing transmission measurements in the neutron energy range between 3 and 50 eV. This normalization was consistent with the sample mass obtained from a high resolution γ-ray spectrometry analysis and a low resolution measurement performed with the TAC. In addition, this normalization is consistent with one of the only two available capture measurements in the 250-2500 eV energy region.

Due to the large flight path of the n_TOF facility (185 m) and the statistics achieved, the results provide a better description of the resolved resonance parameters than the ones available in the current evaluated libraries, excluding the fission widths and the parameters of the biggest ^{243}Am resonance at 1.35 eV, which are based essentially in a single transmission measurement. The uncertainty in the resonance parameters have been reduced, new resonances have been found and the resolved resonance region has been extended from 250 eV up to 400 eV.

We have obtained a value of the resonance integral, $I_0 = \int_{0.5eV}^{\infty} \sigma_\gamma(E)/EdE$, which is significantly lower than the rest of the measured values. These differences can be explained with the existence of inhomogeneities in the sample, which would affect the shelf shielding and multiple scattering corrections. These inhomogeneities would only affect significantly the resonance parameters of the strongest resonance at 1.35 eV.

In the unresolved resonance region, it has been found that the n_TOF results are compatible with one of the two published capture measurements in the 0.25-2.5 keV energy range. Due to the fact that the current evaluations are closer to the other capture measurement, they underestimate the ^{243}Am(n,γ) cross section by 7-20% in the mentioned energy range. In addition, the 250-350 eV energy range is not well reproduced with the fitted unresolved parameters, so we recommend to extend the resolved resonance region at least up to 350 eV, in the future releases of the evaluated neutron data libraries.

We have completed the n_TOF ^{243}Am(n,γ) cross section data above 2.5 keV by using the data available in EXFOR and in the literature, including both differential and integral measurements. In particular, we have found an ^{243}Am(n,γ) cross section that reproduces, under some assumptions, all the differential data sets and the PROFIL-1 integral experiment.

Taking into account the n_TOF measurement, the ^{243}Am(n,γ) cross section presents its larger uncertainties at thermal energies, at the strongest resonance energy of 1.35 eV, and in the fast range for reactor applications. The experimental results of Jandel *et al.* [10] and Hori *et al.* [11], which have not been published yet, could reduce further some of the mentioned uncertainties.

ACKNOWLEDGMENTS

This work was supported partially by the NTOF-ND-XADS project from the European Union 5th Framework Programme, the IP-EUROTRANS project, the CIEMAT-ENRESA Agreement on the Separación y Transmutación de Residuos Radiactivos, the Spanish

Plan Nacional de Física de Partículas under Contract No. FPA2005-06918-C03-01, and the Spanish Consolider Project CPAN Ingenio-2010.

[1] M. Salvatores and R. J. (Eds.), *One possible optimization for target accuracy for innovative systems using recent covariance data evaluations*, Tech. Rep. 6410 (NEA/WPEC-26, Vienna, Austria, 2008).

[2] G. Aliberti, G. Palmiotti, M. Salvatores, and C. G. Stenberg, Nucl. Sci. Eng. **146**, 13 (2004).

[3] G. Aliberti, G. Palmiotti, M. Salvatores, T. K. Kim, T. A. Taiwo, M. Anitescu, I. Kodeli, E. Sartori, J. C. Bosq, and J. Tommasi, Annals of Nuclear Energy **33**, 700 (2006).

[4] T. S. Belanova, A. G. Kolesov, V. A. Poruchikov, G. A. Timofeev, S. M. Kalebin, V. S. Artamonov, and R. N. Ivanov, At.Energ. **40**, 298 (1976).

[5] O. D. Simpson, F. B. Simpson, J. A. Harvey, G. G. Slaughter, R. W. Benjamin, and C. E. Ahlfeld, Nucl. Sci. Eng. **55**, 273 (1974).

[6] J. R. Berreth and F. B. Simpson, Idaho Nuclear Corp. Reports **1407**, 66 (1970).

[7] R. E. Coté, L. M. Bollinger, R. F. Barnes, and H. Diamond, Phys. Rev. **114**, 505 (1959).

[8] L. W. Weston and J. H. Todd, Nucl.Sci.Eng. **91**, 444 (1985).

[9] K. Wisshak and F. Käppeler, Nucl.Sci.Eng. **85**, 251 (1983).

[10] M. Jandel, T. A. Bredeweg, M. A. Stoyer, C. Y. Wu, M. M. Fowler, J. A. Becker, E. M. Bond, A. Couture, R. C. Haight, R. J. Haslett, R. A. Henderson, A. L. Keksis, J. M. O'Donnell, R. S. Rundberg, J. L. Ullmann, D. J. Vieira, J. B. Wilhelmy, and J. M. Wouters, AIP Conf. Proc. **1090**, 220 (2009).

[11] J. Hori, M. Oshima, H. Harada, K. Furutaka, M. Koizumi, F. Kitatani, Y. Toh, S. Nakamura, A. Kimura, M. Igashira, M. Mizumoto, T. Ohsaki, T. Katabuchi, and J. Goto, in *Proceedings of the 2008 Annual Symposium on nuclear data (NDS 2008)*, JAEA-CONF 2009-004, edited by S. CHIBA (Ricotti, Tokai, Japan, 2009) p. 123.

[12] A. Kimura, T. Fujiib, S. Fukutanib, K. Furutakaa, S. Gokoa, K. Y. Haraa, H. Haradaa, K. Hirosea, J. Horib, M. Igashirac, T. Kamiyamad, T. Katabuchic, T. Kina, K. Kinod, F. Kitatania, Y. Kiyanagid, M. Koizumia, M. Mizumotoc, S. Nakamuraa, M. Ohtaa, M. Oshimaa, K. Takamiyab, and Y. Toha, Journal of Nuclear Science and Technology **49**, 708 (2012).

[13] A. Alekseev, A. Bergman, A. Berlev, E. Koptelov, A. Egorov, B. Samylin, B. Fursov, and V. Shorin, Atomic Energy **111**, 428 (2012).

[14] "Jeff-3.1.2: Joint evaluated fission and fusion file," (2012).

[15] "Rosfond-2010 library," (2010).

[16] Z. G. Ge, Y. X. Zhuang, T. J. Liu, J. S. Zhang, H. C. Wu, Z. X. Zhao, and H. Xia, in *Journal of the Korean Physical Society*, Vol. 59 (2011) pp. 1052 – 1056.

[17] F. Marie, A. Letourneau, G. Fioni, O. Druelle, C. Veyssière, H. Faust, P. Mutti, I. AlMahamid, and B. Muhammad, Nucl. Instrum. Methods A **556**, 547 (2006).

[18] M. Ohta, S. Nakamura, H. Harada, T. Fujii, and H. Yamana, J. Nucl. Sci. Technol. (Tokyo) **43**, 1441 (2006).

[19] Y. Hatsukawa, N. Shinohara, and K. Hata, Japan Atomic Energy Agency (JAEA).

[20] V. D. Gavrilov, V. A. Goncharov, V. V. Ivanenko, V. N. Kustov, and V. P. Smirnov, At. Energ. **41**, 185 (1976).

[21] S. H. Eberle, W. Robel, W. Jung, I. Bayat, H. J. Bleyl, E. Bojarsky, L. Schmidt, E. Gantner, J. Reinhardt, and C. Krueckeberg, *Actinides project. First half-year report*, Tech. Rep. 1456 (Karlsruhe Institute of Technology, Germany).

[22] R. L. Folger, J. A. Smith, L. C. Brown, R. F. Overman, and H. P. Holcomb, in *Nuclear Cross-Sections Techn. Conf.*, Vol. 2 (Washington, 1968) p. 1279.

[23] M. A. Bak, A. S. Krivokhatskii, K. A. Petrzhak, Y. G. Petrov, Y. F. Romanov, and E. A. Shlyamin, At. Energ. **23**, 316 (1967).

[24] C. H. Ice, *Production of the transplutonium elements at Savannah River.*, Tech. Rep. 66 (Du Pont, Savannah River Reports).

[25] J. P. Butler, M. Lounsbury, and J. S. Merritt, Can. J. Phys. **35**, 147 (1957).

[26] B. G. Harvey, H. P. Robinson, S. G. Thompson, A. Ghiorso, and G. R. Choppin, Phys. Rev. **95**, 581 (1954).

[27] C. M. Stevens, M. H. Studier, P. R. Fields, J. F. Mech, P. A. Sellers, A. M. Friedman, H. Diamond, and J. R. Huizenga, Phys. Rev. **94**, 974 (1954).

[28] S. F. Mughabghab, *Atlas of Neutron Resonances Resonance Parameters and Thermal Cross Sections Z=1-100* (Elsevier, 2006).

[29] M. Chadwick, M. Herman, P. Obloinsk, M. Dunn, Y. Danon, A. Kahler, D. Smith, B. Pritychenko, G. Arbanas, R. Arcilla, R. Brewer, D. Brown, R. Capote, A. Carlson, Y. Cho, H. Derrien, K. Guber, G. Hale, S. Hoblit, S. Holloway, T. Johnson, T. Kawano, B. Kiedrowski, H. Kim, S. Kunieda, N. Larson, L. Leal, J. Lestone, R. Little, E. McCutchan, R. MacFarlane, M. MacInnes, C. Mattoon, R. McKnight, S. Mughabghab, G. Nobre, G. Palmiotti, A. Palumbo, M. Pigni, V. Pronyaev, R. Sayer, A. Sonzogni, N. Summers, P. Talou, I. Thompson, A. Trkov, R. Vogt, S. van der Marck, A. Wallner, M. White, D. Wiarda, and P. Young, Nuclear Data Sheets **112**, 2887 (2011), special Issue on ENDF/B-VII.1 Library.

[30] M. Chadwick, P. Obloinsk, M. Herman, N. Greene, R. McKnight, D. Smith, P. Young, R. MacFarlane, G. Hale, S. Frankle, A. Kahler, T. Kawano, R. Little, D. Madland, P. Moller, R. Mosteller, P. Page, P. Talou, H. Trellue, M. White, W. Wilson, R. Arcilla, C. Dunford, S. Mughabghab, B. Pritychenko, D. Rochman, A. Sonzogni, C. Lubitz, T. Trumbull, J. Weinman, D. Brown, D. Cullen, D. Heinrichs, D. McNabb, H. Derrien, M. Dunn, N. Larson, L. Leal, A. Carlson, R. Block, J. Briggs, E. Cheng, H. Huria, M. Zerkle, K. Kozier, A. Courcelle, V. Pronyaev, and S. van der Marck, Nuclear Data Sheets **107**, 2931 (2006), evaluated Nuclear

Data File ENDF/B-VII.0.
[31] K. Shibata, O. Iwamoto, T. Nakagawa, N. Iwamoto, A. Ichihara, S. Kunieda, S. Chiba, K. Furutaka, N. Otuka, T. Ohsawa, T. Murata, H. Matsunobu, A. Zukeran, S. Kamada, and J. Katakura, J. Nucl. Sci. Technol. **48**, 1 (2011).
[32] O. D. Bank, *The JEFF-3.1 Nuclear Data Library, JEFF Report 21*, Tech. Rep. (2006).
[33] G. Palmiotti, G. Aliberti, M. Salvatores, and J. Tommasi, AIP Conf. Proc. **769**, 1436 (2005).
[34] A. Kahler, R. MacFarlane, R. Mosteller, B. Kiedrowski, S. Frankle, M. Chadwick, R. McKnight, R. Lell, G. Palmiotti, H. Hiruta, M. Herman, R. Arcilla, S. Mughabghab, J. Sublet, A. Trkov, T. Trumbull, and M. Dunn, Nuclear Data Sheets **112**, 2997 (2011), special Issue on ENDF/B-VII.1 Library.
[35] O. Schwerer, *EXFOR Format Description for Users*, Tech. Rep. 206 (IAEA Nuclear Data Section, Vienna, Austria, 2008).
[36] The n_TOF facility was closed at the end of the 2004 campaign. It was opened again in 2009 (Phase-2), with a different lead block and coolant circuit.
[37] U. Abbondano *et al.* (the n_TOF Collaboration), *CERN n_TOF Facility: Performance Report*, Tech. Rep. INTC-2002-037 (CERN, 2003).
[38] J. Pancin *et al.* (the n_TOF Collaboration), Nucl. Instrum. Methods A **524**, 102 (2004).
[39] N. Larsson, *Updated User's Guide for SAMMY: Multilevel R-matrix Fits to Neutron Data Using Bayes Equations*, Tech. Rep. (ORNL/TM-9179/R7).
[40] S. Marrone, P. Mastinu, U. Abbondanno, R. Baccomi, E. Marchi, N. Bustreo, N. Colonna, F. Gramegna, M. Loriggiola, S. Marigo, P. Milazzo, C. Moreau, M. Sacchetti, G. Tagliente, R. Terlizzi, G. Vannini, G. Aerts, E. Berthomieux, D. Cano-Ott, P. Cennini, C. Domingo-Pardo, L. Ferrant, E. Gonzalez-Romero, F. Gunsing, M. Heil, F. Kaeppeler, T. Papaevangelou, C. Paradela, P. Pavlopoulos, L. Perrot, R. Plag, J. Tain, and H. Wendler, Nucl. Instrum. Methods A **517**, 389 (2004).
[41] C. Guerrero *et al.* (the n_TOF Collaboration), Nucl. Instrum. Methods A **608**, 424 (2009).
[42] U. Abbondanno *et al.* (the n_TOF Collaboration), Nucl. Instrum. Methods A **538**, 692 (2005).
[43] E. Berthoumieux, *Preliminary Report on BaF2 Total Absorption Calorimeter Test Measurement*, Tech. Rep. (CEA-Saclay/DAPNIA/SPhN, 2004).
[44] S. Marrone, E. Berthomieux, F. Becvar, D. Cano-Ott, N. Colonna, C. Domingo-Pardo, F. Gunsing, R. Haight, M. Heil, F. Käppeler, M. Krtička, P. Mastinu, A. Mengoni, P. Milazzo, J. O'Donnell, R. Plag, P. Schillebeeckx, G. Tagliente, J. Tain, R. Terlizzi, and J. Ullmann, Nucl. Instrum. Methods A **568**, 904 (2006).
[45] C. Guerrero *et al.* (the n_TOF Collaboration), Phys. Rev. C **85**, 044616 (2012).
[46] E. Mendoza *et al.* (the n_TOF Collaboration), "Pulse pile-up and dead time correction methods applied to the digitized signals of a segmented baf_2 total absorption calorimeter used in (n,γ) cross section measurements," (2014), Nucl. Instrum. Methods A (submitted).
[47] Data buffers of different measurements, which can have not exactly the same energy calibration, are added artificially to perform the dead time corrections (see [46]).
[48] J. Tain and D. Cano-Ott, Nucl. Instrum. Methods A **571**, 719 (2007).
[49] S. Agostinelli *et al.* (the GEANT4 Collaboration), Nucl. Instrum. Methods A **506**, 250 (2003).
[50] C. Guerrero, D. Cano-Ott, E. Mendoza, J. Tan, A. Algora, E. Berthoumieux, N. Colonna, C. Domingo-Pardo, E. Gonzlez-Romero, M. Heil, D. Jordn, F. Kppeler, C. Lampoudis, T. Martnez, C. Massimi, and R. Plag, Nucl. Instrum. Methods A **671**, 108 (2012).
[51] E. Mendoza *et al.* (the n_TOF Collaboration), "The am-243 neutron capture measurement at the n_tof facility," in *Capture Gamma-Ray Spectroscopy and Related Topics* (World Scientific, 2013) Chap. 60, pp. 442–449, http://www.worldscientific.com/doi/pdf/10.1142/9789814383646_0060.
[52] E. Mendoza, *Measurement of the Am243 capture cross section at the n_TOF facility*, Ph.D. thesis, Universidad Complutense de Madrid (2014).
[53] R. L. Macklin, J. Halperin, and R. R. Winters, Nucl. Instrum. Methods **164**, 213 (1979).
[54] V. M. Maslov, E. S. Sukhovitskij, Y. V. Porodzinskij, A. B. Klepatskij, and G. B. Morogovskij, *Evaluation of neutron data for Americium-243*, Tech. Rep. INDC(BLR)-006 (IAEA, 1996).
[55] Simpson *et al.*, file EXFOR 10204.004, retrieved from the IAEA Nuclear Data Services website.
[56] Simpson *et al.*, file EXFOR 10204.005, retrieved from the IAEA Nuclear Data Services website.
[57] The energy ranges considered were, in eV: 3-50, 3-25, 3-10, 8.5-12.5, 10-17 and 14-25.
[58] S. Oh and L. C. Leal, *SUGGEL: A Program Suggesting The Orbital Angular Momentum of a Neutron Resonance from the Magnitude of its Neutron Width*, Tech. Rep. ORNL/TM-2000/314.
[59] K. Shibata, T. Kawano, T. Nakagawa, O. Iwamoto, J. Katakura, T. Fukahori, S. Chiba, A. Hasegawa, T. Murata, H. Matsunobu, T. Ohsawa, Y. Nakajima, T. Yoshida, A. Zukeran, M. Kawai, M. Baba, M. Ishikawa, T. Asami, T. Watanabe, Y. Watanabe, M. Igashira, N. Yamamuro, H. Kitazawa, N. Yamano, and H. Takano, J. Nucl. Sci. Technol. **39**, 1125 (2002).
[60] A. I. Blokhin, A. V. Ignatyuk, V. N. Manokhin, M. N. Nikolaev, and V. G. P. (ed.), *BROND-2.2, Russian Evaluated Neutron Reaction Data Library*, Tech. Rep. (IAEA-NDS-90 Rev.8, 1994).
[61] R. Capote, M. Herman, P. Obložinský, P. Young, S. Goriely, T. Belgya, A. Ignatyuk, A. Koning, S. Hilaire, V. Plujko, M. Avrigeanu, O. Bersillon, M. Chadwick, T. Fukahori, Z. Ge, Y. Han, S. Kailas, J. Kopecky, V. Maslov, G. Reffo, M. Sin, E. Soukhovitskii, and P. Talou, Nuclear Data Sheets **110**, 3107 (2009).
[62] A. Trkov, M. Herman, and D. A. Brown, *ENDF-6 Formats Manual: Data Formats and Procedures for the Evaluated Nuclear Data Files ENDF/B-VI and ENDF/B-VII*, Tech. Rep. BNL-90365-2009 Rev.2.
[63] F. H. Fröhner, Nucl. Sci. Eng. , 119 (1989).
[64] W. Hauser and H. Feshbach, Phys. Rev. **87**, 366 (1952).
[65] Weston *et al.*, file EXFOR 12951.002, retrieved from the IAEA Nuclear Data Services website.
[66] Weston *et al.*, file EXFOR 12951.003, retrieved from the IAEA Nuclear Data Services website.
[67] D. Villamarín, personal communication.
[68] O. D. Bank, *The JEFF-3.0 Nuclear Data Library, JEFF Report 19*, Tech. Rep. (2005).

Bibliography

[Abb04] U. Abbondanno et al., New experimental validation of the Pulse Height Weighting Technique for capture cross-section measurements, Nucl. Instr. Meth. A, 521:454, 2004.

[Abb05] U. Abbondanno et al., The data acquisition system of the neutron time-of-flight facility n_TOF at CERN. Nucl. Inst. Meth. A 538, 692-702 (2005).

[ADS02] NEA, Accelerator-driven Systems (ADS) and Fast Reactors (FR) in Advanced Nuclear Fuel Cycles (2002).

[Ale12] A. Alekseev et al., Atomic Energy 111, 428 (2012).

[Ali04] G. Aliberti et. al., Impact of Nuclear Data Uncertainties on Transmutation of Actinides in Accelerator-Driven Assemblies, Nucl. Sci. Eng. 146, 13-50 (2004).

[Ali06] G. Aliberti et al., Nuclear data sensitivity, uncertainty and target accuracy assessment for future nuclear systems, Annals of Nuclear Energy 33 (2006) 700-733.

[Bak67] M. A. Bak et al., Cross sections and resonance integrals for capture and fission in long-lived americium isotopes, Atomnaya Energiya, Vol.23, Issue.4, p.316 (1967).

[Bel76] T.S. Bellanova et al., Total Neutron Cross Section and Neutron Resonance Parameters of ^{243}Am, In the energy range of 0.4-35 eV, Sov.At.Energy 40, 368 (1976).

[Ber70] J. R. Berreth and F. B. Simpson, Total Neutron Cross Section of ^{243}Am from 0.01 to 25 eV, IN-1407, Idaho Nuclear Corporation (1970).

[Ber04] E. Berthomieux, Preliminary Report on BaF_2 Total Absorption Calorimeter Test Measurement, Tech. Rep. (CEA-Saclay/DAPNIA/SPhN, 2004).

[Blo94] A. I. Blokhin et al., BROND-2.2, Russian Evaluated Neutron Reaction Data Library, IAEA-NDS-90 Rev.8, International Atomic Energy Agency (1994).

[Boh36] N. Bohr, Nature 137, 344-348 (1936).

[Boh39] N. Bohr and J. A. Wheeler., The mechanism of nuclear fission, Phys. Rev., 56:426-450, 1939.

[Bur83] D.D. Burgess, R. J. Tervo: Background estimation for gamma-ray spectroscopy. NIM 214 (1983), 431-434.

[But57] J. P. Butler, The Neutron Capture Cross Sections of Pu238, Pu242, and Am243 in the Thermal and Epicadmium Regions, Canadian Journal of Physics, Vol.35, p.147 (1957).

[Cap09] R. Capote et al., RIPL-Reference Input Parameter Library for Calculations of Nuclear Reactions and Nuclear Data Evaluations, Nuclear Data Sheets 110 (2009), 3107-3214.

[CASxx] Castor Website: http://castor.web.cern.ch.

[Cha06] M. B. Chadwick et al., ENDF/B-VII.0 Next Generation Evaluated Nuclear Data Library for Nuclear Science and Technology, Special Issue on Evaluated Nuclear Data File ENDF/B-VII.0 Nuclear Data Sheets 107(12), 2931-3059 (2006).

[Cha11] M. B. Chadwick et al., ENDF/B-VII.1 Nuclear Data for Science and Technology: Cross Sections, Covariances, Fission Product Yields and Decay Data, Nuclear Data Sheets Vol. 112, Issue 12, 2887–2996 (2011).

[Cot59] R.E.Cote et al., Slow-Neutron Cross Sections of Pu240, Pu242, and Am243, Phys.Rev. 114, 505 (1959).

[Cox06] M. G. Cox et al., The generalized weighted mean of correlated quantities, 2006 Metrologia 43 S268.

[CRW09] IAEA, Classification of radioactive waste: safety guide, IAEA safety standard series, ISSN 1020-525X; GSG-1 (2009).

[Dig73] W. Digl et al., Level density parameters for the Back-Shifted Fermi Gas Model in the mass range $40<A<250$, Nucl. Phys. A217 (1973) 269-298.

[Ebe71] S. H. Eberle et al., Actinides project. First half-year report, Kernforschungszentrum Karlsruhe Reports, No.1456, p.45 (1971).

[ECWxx] http://ie.lbl.gov/atom.htm.

[ENSxx] Evaluated Nuclear Structure Data File (ENSDF), http://www.nndc.bnl.gov/ensdf.

[EURxx] http://nuklear-server.ka.fzk.de/eurotrans/Start.html.

[EUR05] IP-EUROTRANS Technical Annex. Contract proposal Nº 516520 (2005).

[EX1xx] http://www-nds.iaea.org/exfor/exfor.htm.

[EX2xx] http://www.nndc.bnl.gov/exfor/exfor00.htm.

[exf01] O. D. Simpson et al.: Data file EXFOR-10204.005. EXFOR data retrieved from the IAEA Nuclear Data Section, Vienna.

[exf02] O. D. Simpson et al.: Data file EXFOR-10204.004. EXFOR data retrieved from the IAEA Nuclear Data Section, Vienna.

[exf03] J. R. Berreth et al.: Data file EXFOR-10272.005. EXFOR data retrieved from the IAEA Nuclear Data Section, Vienna.

[exf04] L.W. Weston and J.H. Todd: Data file EXFOR-12951.002. EXFOR data retrieved from the IAEA Nuclear Data Section, Vienna.

[exf05] L.W. Weston and J.H. Todd: Data file EXFOR-12951.003. EXFOR data retrieved from the IAEA Nuclear Data Section, Vienna.

[exf06] K.Wisshak and F.Kappeler: Data file EXFOR-21863.011. EXFOR data retrieved from the IAEA Nuclear Data Section, Vienna.

[exf07] K.Wisshak and F.Kappeler: Data file EXFOR-21863.012. EXFOR data retrieved from the IAEA Nuclear Data Section, Vienna.

[exf08] K.Wisshak and F.Kappeler: Data file EXFOR-21863.008. EXFOR data retrieved from the IAEA Nuclear Data Section, Vienna.

[exf09] K.Wisshak and F.Kappeler: Data file EXFOR-21863.009. EXFOR data retrieved from the IAEA Nuclear Data Section, Vienna.

[Fol68] R. L. Folger et al., Foil Measurements Of Integral Cross Sections Of Higher Mass Actinides, Nuclear Cross-Sections Techn. Conf., Washington 1968, Vol.2, p.1279(H11) (1968).

[Fro89] F. H. Fröhner, Evaluation of the Unresolved Resonance Range of ^{238}U, Nucl. Sci. Eng. 103, 119-128 (1989).

[Fro00] F. Fröhner, Evaluation and analysis of nuclear resonance data, Tech. Rep. JEFF Report 18, OECD/NEA (2000).

[Gar76] V. D. Gavrilov et al., Thermal Cross Sections and Resonance Integrals of Fission and Capture Of ^{241}Am, ^{243}Am, ^{245}Cm, ^{249}Bk and ^{249}Cf, Atomnaya Energiya, Vol.41, Issue.3, p.185 (1976).

[GDR12] NEA, Geological Disposal of Radioactive Waste: National Commitment, Local and Regional Involvement, ISBN 978-92-64-99183-5 (2012).

[Ge10] Z. G. Ge et al., The Updated Version of Chinese Evaluated Nuclear Data Library (CENDL-3.1), Proc. International Conference on Nuclear Data for Science and Technology, Jeju Island, Korea, April 26-30, (2010).

[GEAxx] http://geant4.web.cern.ch/geant4.

[Gon00] A. J. González, The safety of radioactive waste management, IAEA bulletin, 42/3/2000 (2000).

[Gon09] E. González-Romero (Ed), Report of the Numerical results from the Evaluation of the nuclear data sensitivities, Priority list and table of required accuracies for nuclear data, NUDATRA Deliverable D5.11 from IP-Eurotrans (2009).

[Gue08] C. Guerrero, Measurements of the ^{237}Np and ^{240}Pu neutron capture cross sections at the n_TOF facility at CERN, Doctoral Thesis at the Universidad Complutense de Madrid, Spain, (2008).

[Gue09] C. Guerrero et al., The n_TOF Total Absorption Calorimeter for neutron capture measurements at CERN, Nucl. Inst. Meth. A 608, 424-433 (2009).

[Gue12.1] C. Guerrero et al., Monte Carlo simulations of the n_TOF Total Absorption Calorimeter, Nucl. Inst. Meth. A 671, 108-117 (2012).

[Gue12.2] C. Guerrero et al., Measurement and resonance analysis of the ^{237}Np neutron capture cross section, Phys. Rev. C 85, 044616 (2012).

[Har54] B. G. Harvey, Some pile neutron cross sections of isotopes of americium, berkelium, californium, and element 99, Physical Review, Vol.95, p.581 (1954).

[Har14] H. Harada et al. (coord.), Meeting Nuclear Data Needs for Advanced Reactor Systems, NEA/NSC/WPEC/DOC(2014)446.

[Hat97] Y. Hatsukawa et al., Measurements of Neutron Cross Section of the ^{243}Am Reaction, JAERI Reports, No.98,003, p.221 (1997).

[Hau52] W. Hauser and H. Feshbach, The inelastic scattering of neutrons, Phys. Rev. 87:366, 1952.

[HCN06] Handbook for calculations of nuclear reaction data, RIPL-2, IAEA-TECDOC-1506 (2006).

[Her09] M. Herman and A. Trkov (editors), ENDF-6 Formats Manual: Data formats and procedures for the Evaluated Nuclear Data File ENDF/B-VI and ENDF/B-VII, 2009.

[Hor09] J. Hori et al., Neutron Capture Cross Section Measurement on ^{243}Am with a 4π Ge spectrometer, JAEA-Conf 2009-004, 123-128 (2009).

[IADxx] International Atomic Energy Agency Nuclear Data Service, http://www-nds.iaea.org/exfor/endf.htm.

[Ice66] C. H. Ice, Production of the transplutonium elements at Savannah River, Du Pont, Savannah River Reports, No.66, p.69 (1966).

[Jam06] F. James and M. Winkler, MINUIT User's Guide, 2006.

[Jan09] M. Jandel et al., Neutron Capture and neutron-induced fission experiments on americium isotopes with DANCE, AIP Conf. Proc. 1090, 220 (2009), DOI:10.1063/1.3087017.

[JND05] OECD/NEA Data Bank, The JEFF-3.0 Nuclear Data Library, JEFF Report 19, OECD/NEA Data Bank (2005).

[JND06] OECD/NEA Data Bank, The JEFF-3.1 Nuclear Data Library, JEFF Report 21, OECD/NEA Data Bank (2006).

[Kah11] A. C. Kahler et al., ENDF/B-VII.1 Neutron Cross Section Data Testing with Critical Assembly Benchmarks and Reactor Experiments, Nucl. Data Sheets 112, 2997–3036 (2011).

[Kim12] A. Kimura et al., Journal of Nuclear Science and Technology 49, 708 (2012).

[Kni88] H-H. Knitter et al., Neutron-Induced Fission Cross Section of ^{243}Am in the Energy Range from 1 eV to 10 MeV, Nucl. Sci. Eng., Vol.99, p.1 (1988).

[Kno78] G. F. Knoll, Radiation Detection and Measurements, John Wiley and Sons (1978).

[Kob99] K.Kobayashi et al., Measurements of Neutron-induced Fission Cross Section of Americium-243 from Thermal Neutron Energy to 15 keV Using Lead Slowing-down Spectrometer and thermal Neutron Facility, J.Nucl.Sci.Technol.(Tokyo) 36, 20 (1999).

[Kop90] J. Kopecky and M. Uhl, Test of gamma-ray strength functions in nuclear reaction model calculations, Phys. Rev. C, Vol. 41-5, 1990.

[Kop07] S. Kopecky et al., Low energy transmission measurements of ^{240,242}Pu at GELINA and their impact on the capture width, Proc. Int. Conf. Nucl. Data for Sci. and Tech. 2007 (Nice - France), page 7391, 2007.

[KWE13] International Energy Agency, Key World Energy Statistics 2013, 2013.

[Lan58] A. M. Lane, R. G. Thomas, R-matrix theory of nuclear reactions, Rev. Mod. Phys. 30 (2) (1958) 257-353.

[Lar06] N.M. Larsson, Updated User's Guide for SAMMY: Multilevel R-matrix Fits to Neutron Data Using Bayes Equations, ORNL/TM-9179/R7, 2006.

[Lyn68] J.E. Lynn, The Theory of Neutron Resonance Reactions, Claredon Press, Oxford, 1968.

[Mac79] R. L. Macklin, J. Halperin, and R. R. Winters, Nucl. Inst. Meth. 164, 213 (1979).

[Mar04] S. Marrone et al., A low background neutron flux monitor for the n_TOF facility at CERN, Nucl. Instr. Meth. A, 517:389-398, 2004.

[Mar06.1] S. Marrone et al., Pulse shape analysis of signals from $BaF_2$and CeF_3 scintillators for neutron capture experiments, Nucl. Inst.Meth. A, 568, 904-911, 2006.

[Mar06.2] F. Marie et al., Thermal neutron capture cross-section measurements of ^{243}Am and ^{242}Pu using the new mini-INCA α- and γ-spectroscopy station, Nucl. Inst. Meth. A, 556:547 (2006).

[Mas96] V. M. Maslov et al. INDC(BLR)-006 (1996).

[MCN08] LA-CP-07-1473 MCNPX User's Manual version 2.6.0 (2008).

[Men07] A. Mengoni (editor) et al., Final Report of the n_TOF-ND-ADS Project, Deliverable 25, FIKW-CT-2000-00107 (2007).

[Men14] E. Mendoza et al., "Pulse pile-up and dead time corrections for digitized signals from a BaF$_{2}$ calorimeter", submitted to Nucl. Inst. Meth. A in March 2014.

[MFG09] NEA, Moving Forward with Geological Disposal of Radioactive Waste, ISBN 978-92-64-99057-9 (2008).

[Mol95] Moller et al., At. Nucl. Data Tables 59 (1995) 185.

[Mox63] M.C. Moxon and E.R. Rae, A gamma-ray detector for neutron capture cross-section measurements, Nucl. Instr. Meth. A, 24:445 (1963).

[Mox91] M. C. Moxon, A Least Square Fitting Program for Resonance Analysis of Neutron Transmission and Capture Data, AEA-InTec-0470, 1991.

[Mug84] S. F. Mughabghab, Neutron Cross Sections, Academic Press , Inc., 1984.

[Mug06] S. F. Mughabghab, Atlas of Neutron Resonances, Elsevier Holland, 2006.

[Mur96] B. D. Murphy et al., Preliminary calculational analysis of the actinide samples from FP-4 exposed in the Dounreay Prototype Fast Reactor, ORNL-6889 (1996).

[NEDxx] Nuclear Energy Agency, http://www.nea.fr/dbdata/eva.

[NNDxx] National Nuclear Data Center - Brookhaven National Laboratory, http://www.nndc.bnl.gov

[NPR12] Nuclear Power Reactors in the World 2012 Edition, IAEA-RDS-2/32, ISBN:978-92-0-132310-1, 2012.

[NTC03] The n_TOF Collaboration. CERN n_TOF Facility: Performance Report. CERN INTC-2002-037, 2003.

[NTOxx] http://pceet075.cern.ch.

[Oh00] S. Y. Oh. et al., SUGGEL: A Program Suggesting The Orbital Angular Momentum of a Neutron Resonance from the Magnitude of its Neutron Width, ORNL/TM-2000/314.

[Ohk05] S. Ohki, Validation of MA Nuclear Data by Sample Irradiation Experiments with the Fast Reactor JOYO, AIP Conf. Proc. 769, 472 (2005).

[Oht06] M. Ohta et al., J. Nucl. Sci. Technol., 43, 1441 (2006).

[ORExx] http://www.phy.ornl.gov/orela/orela.html.

[Pal05] G. Palmiotti et al., Integral Experiments Analysis for Validation and Improvement of Minor Actinide Data for Transmutation Needs, AIP Conf. Proc. 769, 1436 (2005).

[Pal11] G. Palmiotti et al., Report on INL Activities for Uncertainty Reduction Analysis of FY11, INL/EXT-11-23283 (2011).

[Pan04] J. Pancin et al., Measurement of the n_TOF beam profile with a micromegas detector, Nucl. Inst. Meth. A 524, 102-114 (2004).

[Por65] C. E. Porter (ed.), Statistical Theory of Spectra: Fluctuations, Acad. Press, New York - London (1965).

[PST06] NEA, Physics and Safety of Transmutation Systems, ISBN 92-64-01082-3 (2006).

[PTBxx] Physikalisch-Technische Bundesanstalt (PTB), http://www.ptb.de.

[Rei58] C.W. Reich and M.S. Moore, Phys. Rev. 111 (1958) 929.

[RP2xx] http://www-nds.iaea.org/RIPL-2.

[RP3xx] http://www-nds.iaea.org/RIPL-3.

[Ros91] P. F. Rose, ENDF-201, ENDF/B-VI Summary Documentation, BNL-NCS-17541, 4th Edition (1991).

[Rub98] C. Rubbia et al., A high resolution spallation driven facility at the CERN-PS to measure neutron cross sections in the interval from 1eV to 250MeV, CERN/LHC/98-02, 1998.

[Sal08] M. Salvatores and R. Jacqmin (Eds), One possible optimization for target accuracy for innovative systems using recent covariance data evaluations (BOLNA), NEA/WPEC-26, ISBN 978-92-64-99053-1 (2008).

[Sav64] A. Savitzky and M. J. E. Golay, Soothing and differentiation of data by simplified least squares procedures, Anal. Chem., vol. 36, pp. 1627–1639, 1964.

[Sch08] O. Schwener, EXFOR format description for users, IAEA-NDS-206, June 2008.

[See70] P. A. Seeger, LA-4420, p.138 (1970), EXFOR10063.

[SES13] Red Eléctrica de España, The Spanish Electricity System PRELIMINARY REPORT 2013, Dec. 2013.

[Shi02] K. Shibata et al., Japanese Evaluated Nuclear Data Library Version 3 Revision-3: JENDL-3.3, J. Nucl. Sci. Technol. 39, 1125 (2002).

[Shi11] K. Shibata et al., JENDL-4.0: A New Library for Nuclear Science and Engineering, J. Nucl. Sci. Technol. 48(1), 1-30 (2011).

[Sim74] O. D. Simpson et al. The Neutron Total Cross Section of Americium-243, Nucl.Sci.Eng. 55, 273 (1974).

[Ste54] C. M. Stevens, Curium Isotopes 246 and 247 from Pile-Irradiated Plutonium, Physical Review, Vol.94, p.974 (1954).

[Tai02] J. L. Taín et al., Accuracy of the Pulse Height Weighting Technique for capture cross section measurements, J. Nucl. Sci. Tech., Suppl. 2:689 (2002).

[Tai07] J. L. Taín et al., The influence of the unknown de-excitation pattern in the analysis of β-decay total absorption spectra, Nucl. Inst. Meth. A, 571, 719-727 (2007).

[TCE13] International Energy Agency, Tracking Clean Energy Progress 2013, 2013.

[Tsu03] K. Tsujimoto et al., Validation of Minor Actinide Cross Sections by Studying Samples Irradiated for 492 Days at the Dounreay Prototype Fast Reactor—II: Burnup Calculations, Nucl. Sci. Eng. 144, 129 - 141 (2003).

[Wan03] S. Wang et al., The RPI multiplicity detector response to γ-ray cascades following neutron capture in ^{149}Sm and ^{150}Sm, Nucl. Inst. Meth. A 513 (2003) 585-595.

[WEO12] International Energy Agency, World Energy Outlook 2012, 2012.

[Wes85] L.W. Weston and J.H. Todd, Neutron Capture Cross Section of 243Am, Nucl.Sci.Eng. 91, 444 (1985).

[Wig47] E. P. Wigner, L. Eisenbud, Higher angular momenta and long range interaction in resonance reactions, Phys. Rev. 72 (1) (1947) 29-41.

[Wis83] K. Wisshak and G. Käppeler, Neutron Capture and Fission Cross Section of ^{243}Am in the Energy Range from 5 to 250 keV, Nucl. Sci. Eng., 85, 251-260 (1983).

[WNAxx] World Nuclear Association, http://www.world-nuclear.org.

[Zab07] S. V. Zabrodskaya et al., ROSFOND - Rossiyskaya Natsionalnaya Biblioteka Nejtronnykh Dannykh, VANT, Nuclear Constants 1-2, 3 (2007).